SURFACE ENGINEERING SERIES
Volume 2

Chemical Vapor Deposition

SURFACE ENGINEERING SERIES
Volume 2

Chemical Vapor Deposition

Edited by

Jong-Hee Park
Energy Technology Division
Argonne National Laboratory

T.S. Sudarshan
Materials Modification Inc.

ASM International®
Materials Park, OH 44073-0002
www.asminternational.org

First printing, July 2001

Comments, criticisms, and suggestions are invited, and should be forwarded to ASM International.

Library of Congress Cataloging-in-Publication Data

Chemical vapor deposition/edited by Jong-Hee Park, T.S. Sudarshan.
p. cm. -- (Surface engineering series; v. 2)
1. Vapor-plating. 2. Refractory coating. I. Park, Jong-Hee, 1951-
II. Sudarshan, T.S., 1955-
III. Series.
TS695.C52 2001 671.7'35—dc21 2001022339

ISBN: 0-87170-731-4
SAN: 204-7586

ASM International®
Materials Park, OH 44073-0002
www.asminternational.org

Typeset in India by Emptek Inc., Scarborough, ON, Canada
Printed in the United States of America

Contents

Chapter 8

Chapter 9

Chapter 10

Chapter 11

Chapter 12

Chapter 13

Chapter 14

Preface

Chemical vapor deposition (CVD) is used widely in materials processing technology. The majority of its applications involve applying solid thin-film coatings to surfaces, but it is used also to produce high-purity bulk materials and powders, as well as to fabricate composites. Chemical vapor deposition has been used to deposit a wide range of materials in many different areas. The purpose of this book on CVD technology is to provide practical reference information, "how-to" guidelines, and application information on important surface engineering technologies for engineering design, development, and manufacturing. This book is intended to be a broad-based reference handbook for both experienced and novice users of the CVD process. It provides updated information for practicing engineers and research and development technologists who are involved in product design and/or development of new products or manufacturing systems. In addition, the contents should be suitable as a textbook or survey course book for graduate or advanced undergraduate engineering students. As editor of this volume, I thank all of the authors for their contributions, and the reviewers for the comments on each chapter. I am especially grateful to Steve Lampman of ASM International for his valuable assistance with this volume.

Jong-Hee Park, Ph.D.
Energy Technology Division
Argonne National Laboratory
Argonne, IL 60439

June 2001

Chemical Vapor Deposition
Jong-Hee Park, T.S. Sudarshan, editors, p1-22
DOI:10.1361/chvd2001p001

Chapter 1

Introduction to Chemical Vapor Deposition (CVD)

J. R. Creighton and P. Ho
Sandia National Laboratories
P.O. Box 5800, MS0601
Albuquerque, NM 87185-0601

Introduction

Chemical vapor deposition (CVD) is a widely used materials-processing technology. The majority of its applications involve applying solid thin-film coatings to surfaces, but it is also used to produce high-purity bulk materials and powders, as well as fabricating composite materials via infiltration techniques. It has been used to deposit a very wide range of materials. As indicated by the shaded boxes in Figure 1, the majority of the elements in the periodic table have been deposited by CVD techniques, some in the form of the pure element, but more often combined to form compounds.

CVD has an extensive literature, including a number of other books on the subject. The classic book by Powell, Oxley and Blocher[1] covers much of the earlier work up to the mid 1960s, while a bibliography by Hawkins[2] lists papers in CVD for the 1960-1980 time period. The handbook by Pierson[3] contains a very useful discussion of specific materials and CVD processes, as does the book by Morosanu.[4] The books by Hitchman and Jensen,[5] and by Sherman,[6] concentrate more on silicon microelectronics applications, while the books by Stringfellow[7] and by Jones and O'Brien[8] concentrate on compound semiconductor applications. The book by Kodas and Hampden-Smith[9] and the series of proceedings volumes, represented by Sandhu et al.[10] focus on CVD of metals. A separate series of books on CVD are the proceedings of the International Conferences on CVD held every two to three years since circa 1967, primarily sponsored by the Electrochemical Society. These provide useful "snapshots" of the field at various times,[11-13] are a few of the more recent volumes in this series. Books by Vossen and Kern[14] and Smith,[15] cover CVD as parts of their larger treatments of thin film deposition.

PERIODIC TABLE

IA	IIA	IIIA	IVA	VA	VIA	VIIA	VIII			IB	IIB	IIIB	IV	VA	VIB	VIIB	O
1 **H** 1.008																	2 **He** 4.003
3 **Li** 6.941	4 **Be** 9.012											5 **B** 10.81	6 **C** 12.01	7 **N** 14.01	8 **O** 16.00	9 **F** 19.00	10 **Ne** 20.179
11 **Na** 22.990	12 **Mg** 24.305											13 **Al** 26.98	14 **Si** 28.09	15 **P** 30.97	16 **S** 32.07	17 **CI** 35.45	18 **Ar** 39.948
19 **K** 39.098	20 **Ca** 40.08	21 **Sc** 44.956	22 **Ti** 47.90	23 **V** 50.942	24 **Cr** 51.996	25 **Mn** 54.938	26 **Fe** 55.847	27 **Co** 58.933	28 **Ni** 58.70	29 **Cu** 63.546	30 **Zn** 65.39	31 **Ga** 69.72	32 **Ge** 72.61	33 **As** 74.92	34 **Se** 78.96	35 **Br** 79.90	36 **Kr** 83.80
37 **Rb** 85.468	38 **Sr** 87.62	39 **Y** 88.906	40 **Zr** 91.22	41 **Nb** 92.906	42 **Mo** 95.94	43 **Tc** (99)	44 **Ru** 101.07	45 **Rh** 102.905	46 **Pd** 106.4	47 **Ag** 107.868	48 **Cd** 112.4	49 **In** 114.8	50 **Sn** 118.7	51 **Sb** 121.8	52 **Te** 127.6	53 **I** 126.9	54 **Xe** 131.30
55 **Cs** 132.905	56 **Ba** 137.33	57 **La** 138.9	72 **Hf** 178.49	73 **Ta** 180.948	74 **W** 183.85	75 **Re** 186.2	76 **Os** 190.2	77 **Ir** 192.22	78 **Pt** 195.09	79 **Au** 196.966	80 **Hg** 200.59	81 **TI** 204.37	82 **Pb** 207.2	83 **Bi** 209.0	84 **Po** (210)	85 **At** (210)	86 **Rn** (222)
87 **Fr** (223)	88 **Ra** (226)	89 **Ac** 227.0															

LANTHANIDES	57 **La** 138.9	58 **Ce** 140.115	59 **Pr** 140.1	60 **Nd** 144.2	61 **Pm** (145)	62 **Sm** 150.4	63 **Eu** 152.0	64 **Gd** 157.2	65 Tb 158.9	66 **Dy** 162.5	67 **Ho** 164.9	68 **Er** 167.3	69 **Tm** 168.9	70 **Yb** 173.0	71 **Lu** 174.96
ACTINIDES	89 **Ac** 227.0	90 **Th** 232.0	91 **Pa** 231.0	92 **U** 238.0	93 **Np** 237.0	94 **Pu** (244)	95 **Am** (243)	96 **Cm** (247)	97 Bk (247)	98 **Cf** (251)	99 **Es** (252)	100 **Fm** (257)	101 **Md** (256)	102 **No** (259)	103 **Lr** (257)

Fig. 1: Periodic table, where shaded boxes indicate elements that have been deposited using CVD.

In its simplest incarnation, CVD involves flowing a precursor gas or gases into a chamber containing one or more heated objects to be coated. Chemical reactions occur on and near the hot surfaces, resulting in the deposition of a thin film on the surface. This is accompanied by the production of chemical by-products that are exhausted out of the chamber along with unreacted precursor gases. As would be expected with the large variety of materials deposited and the wide range of applications, there are many variants of CVD. It is done in hot-wall reactors and cold-wall reactors, at sub-torr total pressures to above-atmospheric pressures, with and without carrier gases, and at temperatures typically ranging from 200-1600°C. There are also a variety of enhanced CVD processes, which involve the use of plasmas, ions, photons, lasers, hot filaments, or combustion reactions to increase deposition rates and/or lower deposition temperatures. There are also many derivatives of the CVD terminology, such as metal-organic chemical vapor deposition (MOCVD)[16,17] or, less commonly, organo-metallic chemical vapor deposition (OMCVD), which are sometimes used to note the class of molecules used in the deposition process. Some practitioners chose to differentiate epitaxial film deposition from polycrystalline or amorphous film deposition, so they introduced a variety of terms that include "epitaxy" in the acronym. Two of the more common variants are organometallic vapor phase epitaxy (OMVPE)[7] and metalorganic vapor phase epitaxy (MOVPE)[18] which are often used in the compound semiconductor epitaxy literature.

CVD has a number of advantages as a method for depositing thin films. One of the primary advantages is that CVD films are generally quite conformal, i.e., that the film thickness on the sidewalls of features is comparable to the thickness on the top. This means that films can be applied to elaborately shaped pieces, including the insides and undersides of features, and that high-aspect ratio holes and other features can be completely filled. In contrast, physical vapor deposition (PVD) techniques, such as sputtering or evaporation, generally require a line-of-sight between the surface to be coated and the source. Another advantage of CVD is that, in addition to the wide variety of materials that can be deposited, they can be deposited with very high purity. This results from the relative ease with which impurities are removed from gaseous precursors using distillation techniques. Other advantages include relatively high deposition rates, and the fact that CVD often doesn't require as high a vacuum as PVD processes.

CVD also has a number of disadvantages. One of the primary disadvantages lies in the properties of the precursors. Ideally, the precursors need to be volatile at near-room temperatures. This is non-trivial for a number of elements in the periodic table, although the use of metal-organic precursors has eased this situation. CVD precursors can also be highly toxic ($Ni(CO)_4$), explosive (B_2H_6), or corrosive ($SiCl_4$). The byproducts of CVD reactions can also be hazardous (CO, H_2, or HF). Some of these precursors, especially the metal-organic precursors, can also be quite costly. The other major disadvantage is the fact that the films are usually deposited at elevated temperatures. This puts some restrictions on the kind of substrates that can be coated. More importantly, it leads to stresses in films deposited on materials with different thermal expansion coefficients, which can cause mechanical instabilities in the deposited films.

CVD processes can be categorized according to the type of:

1. Application,
2. Process and reactor used, or
3. Precursor and chemical reaction used.

The next three sections of this chapter are arranged around such subdivisions. These sections are followed by a discussion of the fundamental processes underlying CVD, such as mass transport, thermodynamics, and chemical kinetics. Finally, we present a brief analysis of the historical and current status of CVD R & D.

CVD Applications

One of the earliest examples of a large-scale CVD application was a carbonyl process for

refining of nickel, as developed by Mond, Langer, and Quincke in 1890.[19] Many of the early applications involved refining or purification of metals and a limited number of non-metals by carbonyl or halide processes. Other early applications involved deposition of coatings for wear and corrosion resistance, and the fabrication of structural shapes and components. Most of the earliest work, up to the mid 1960s, is reviewed in the book by Powell, Oxley, and Blocher.[1] Many high volume applications, such as refining and the production of powders and pigments, are obviously still important economically, but most of the recent CVD R & D effort is aimed at thin-film deposition.

There is a great deal of ongoing R & D regarding CVD of thin films used primarily for their mechanical or chemical properties. Many of these are discussed in detail in other chapters of this book, so we only briefly mention them here. Chapter 11 discusses the use of CVD films for tribological applications, chapter 13 discusses CVD films used for corrosion protection, and chapter 14 discusses protective CVD coatings for tool steels. Chapter 10 discusses the CVD of diamond, and diamond-like carbon (DLC), which has generated a tremendous interest level in the past decade (see also last section, this chapter), and has significant commercial applications. Diamond films are mainly used for their hardness, but applications utilizing its high thermal conductivity, chemical inertness, or electronic properties are also important.

A great deal of CVD R & D in recent decades, however, is focussed on the semiconductor revolution. We devote somewhat more space here to these applications, as they are not covered elsewhere in this book. CVD has been a critical enabling technology in silicon-based microelectronics; it is even used at the earliest stage during the refining and purification of elemental silicon. Depending on the device, CVD processes are used for depositing thin films of the active semiconductor material (e.g. doped Si), conductive interconnects (e.g. tungsten), and/or insulating dielectrics (e.g. SiO_2), (see Figure 2).

The communications revolution also relies on a diverse set of CVD technologies. Some components are similar to those used in silicon microelectronics, but many are unique, involving complex epitaxial heterostructures of SiGe or compound semiconductor (e.g., AlGaAs) alloys that are required to yield high frequency (1-100 GHz) device operation.[20] The communication revolution also relies on optoelectronic components, such as solid state diode lasers (another complex heterostructure device), and these devices are often grown by CVD.[7,21] Even the fiberoptic cables that transmit the optical component of the communications network are manufactured using a CVD technique to achieve the desired refractive index profile.[22]

Optoelectronic material grown by CVD has many applications outside of the communications industry. One example is for solid state lighting using light emitting diodes (LEDs). Recently, Nichia Chemical was the first company to commercialize high brightness blue and green LEDs based on group-III nitride alloys, e.g. InGaN, which are grown on sapphire substrates using CVD technology.[23] This company also introduced the first long-life blue laser diode, based on the same material and technology. In addition to the myriad of lighting and signage applications using colored LEDs, there is a growing interest in generating solid state white light sources to replace incandescent and perhaps even fluorescent sources.[24] A solid-state white light source may be achieved by combining LEDs of different wavelengths, or by pumping a phosphor with an ultraviolet LED.

Another exciting technology utilizing CVD is the production of microelectromechanical structures, or MEMS.[25] Much of the MEMS technology is derived from the silicon microelectronics technology, so it is not surprising that CVD plays a crucial role. Most MEMS devices are fabricated from polycrystalline silicon (polysilicon) films deposited on silicon wafers, with intermediate sacrificial SiO_2 layers that are later removed by chemical etching. Figure 3 shows an example of such a device, in this case a set of interlocking gears that are ~50-200 microns in diameter. Both the polysilicon and oxide are deposited using

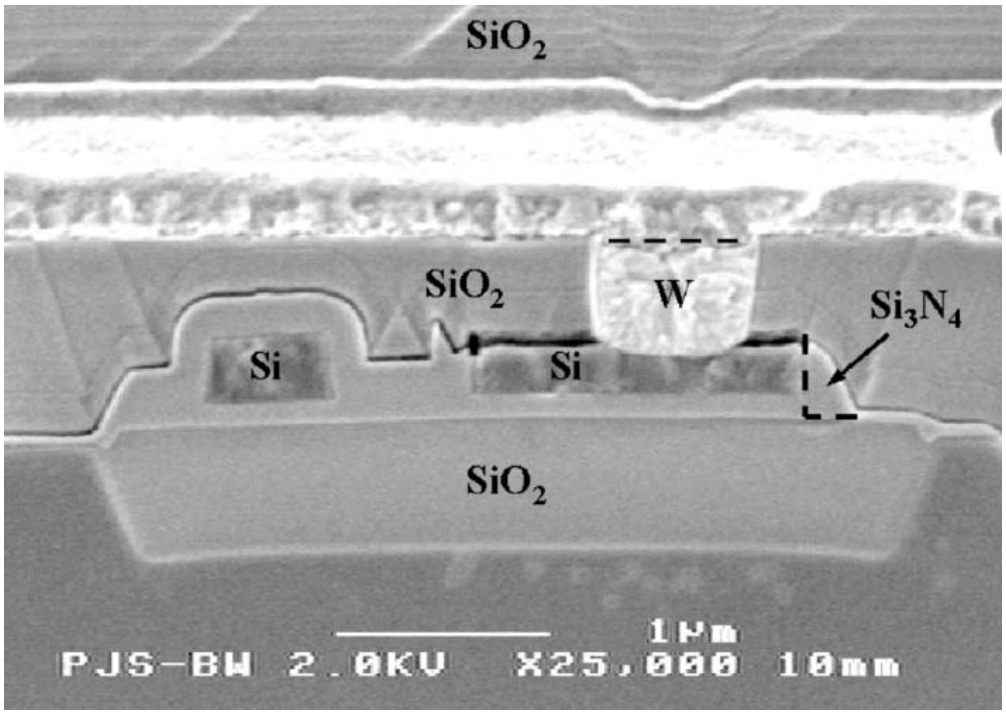

Fig. 2: Cross section of a silicon microelectronic memory circuit showing several materials deposited by CVD; polycrystalline silicon, tungsten (W), SiO_2, and Si_3N_4. Photo courtesy of Pat Shea, Sandia National Laboratories.

CVD or PECVD. The CVD steps define the structure of the device perpendicular to the silicon substrate, while numerous lithographic and etching steps define the structure in the other two dimensions. CVD is sometimes used to apply coatings to reduce friction after the 3-D structure is created. Work is also being done to integrate MEMS devices with silicon microelectronic devices on the same chip.

The field of nanotechnology has generated a lot of recent interest, and focused research programs have been initiated in almost all industrialized countries in the last five years. In 2000 the U.S. launched the National Nano-technology Initiative, with plans to nearly double the nanoscale R & D effort.[26] Nano-technology is an extremely diverse topic, but some of the best examples of existing nanoscale R & D are in the area of epitaxial heterostructures for laser diodes and LEDs grown by CVD.[7,23,27] Many of these devices contain two dimensional (2-D) quantum wells or superlattices composed of strained epitaxial layers that are 1-10 nm thick. An example of a strained layer superlattice is shown in Figure 4. In addition to quantum wells, laser structures such as the vertical cavity surface emitting laser (VCSEL) contain mirror stacks composed of a large number of alternating layers of semiconductor material that are typically 50-100 nm thick. The thickness of each layer often must be controlled with a precision better than 1 nm. Despite this requirement these devices can be grown routinely with relatively high yield in finely tuned and calibrated OMVPE reactors.[28] A related CVD technique that automatically yields subnanometer control is known as atomic layer epitaxy (ALE).[29]

An extension of 2-D quantum well R & D involves the generation of quantum wires (1-D) and quantum dots (0-D).[27,30] Quantum dots are

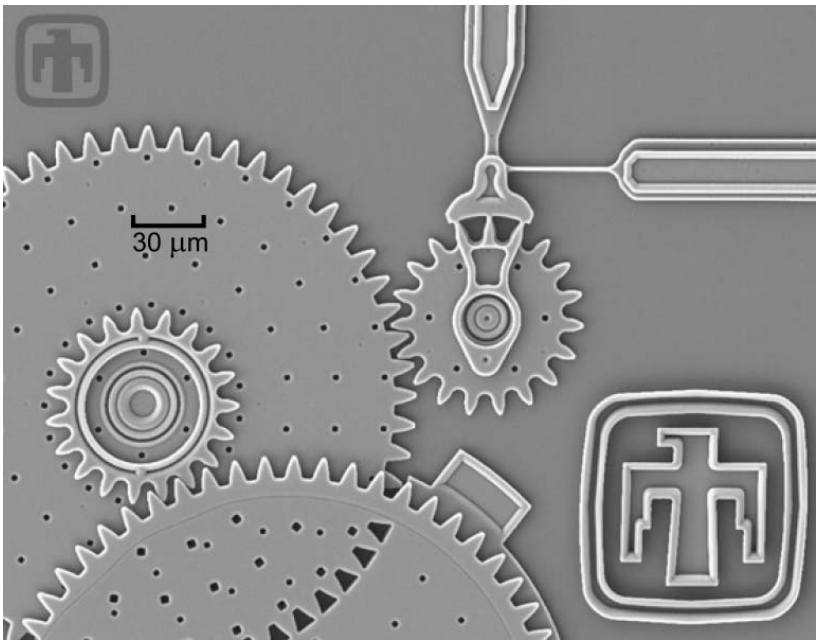

Fig. 3: Example of a silicon surface micromachined gear train. Courtesy of the Intelligent Micromachine Initiative, Sandia National Laboratories.

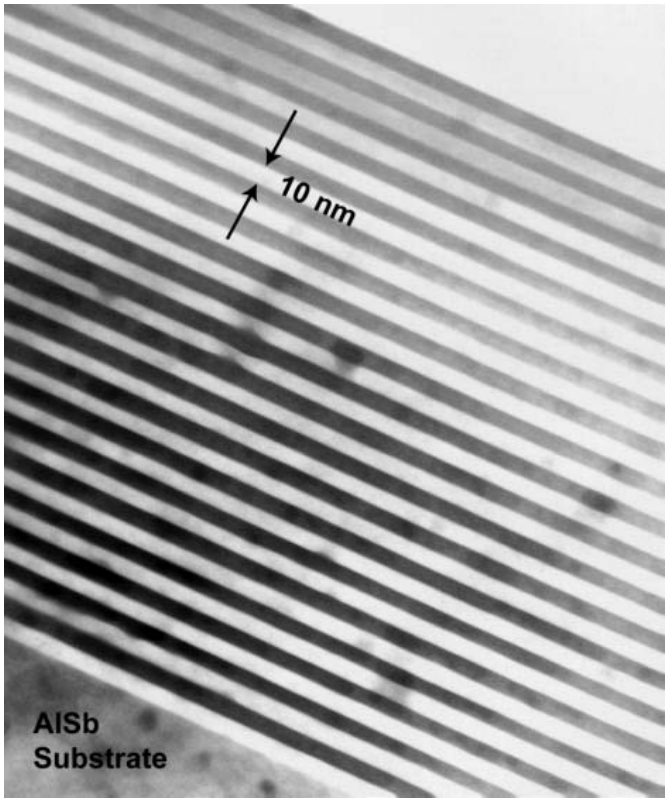

Fig. 4: Strained layer superlattice of InAsSb on InSb with 10 nm layer thickness. Photo courtesy of R. M. Biefeld, Sandia National Laboratories.

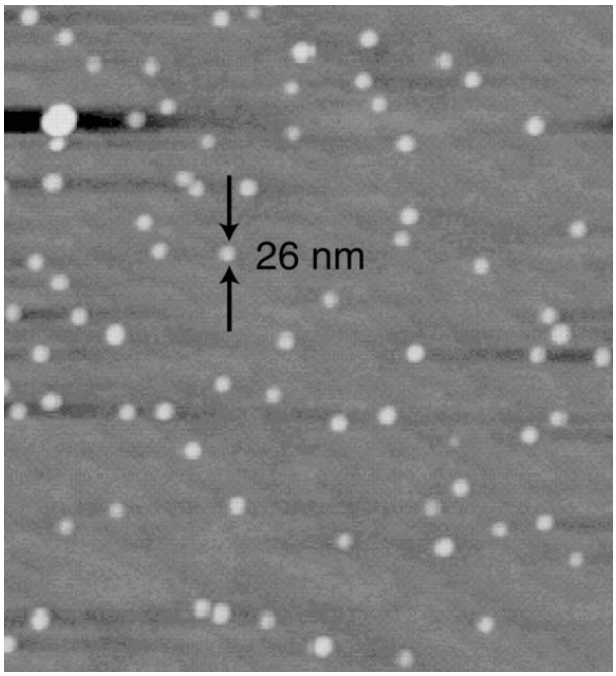

Fig. 5: Indium arsenide quantum dots deposited on gallium arsenide by OMVPE. Photo courtesy of Jeff Cederberg and R. M. Biefeld, Sandia National Laboratories.

often considered to be artificial atoms, where the effect of quantum confinement significantly perturbs the normal bulk electronic properties of the material. One method of growing quantum dots involves depositing one material on another with a large lattice mismatch. The example in Figure 5 is InAs on GaAs(100) by CVD. Due to the interfacial properties of this highly strained layer, InAs spontaneously forms islands on the 10-nm scale with a relatively narrow size distribution. The electronic and optical properties of the InAs quantum dots are dramatically different from bulk InAs, allowing for novel device fabrication.

In addition to the numerous electronic and optoelectronic applications mentioned above, novel applications of CVD are also being used to generate macroscopic components (10 cm as opposed to 1 nm). One interesting example is the production of Ir/Re thrust chambers for liquid rocket motors (see Figure 6).[31] For this structure a thick Rhenium CVD coating is applied to a sacrificial molybdenum mandrel, which is later removed by etching. Another example is the production of large-scale infrared optical materials (ZnSe and/or ZnS up to several feet across).[32]

CVD Reactor Types

As mentioned in the introduction, CVD encompasses a wide range of reactor and process types. The choice of process/reactor is determined by the application via the requirements for substrate material, coating material and morphology, film thickness and uniformity, availability of precursors, and cost. Here, we discuss the general types of reactors used for CVD, and refer the reader to the other chapters in this and other books for detailed information on specific systems.

Hot wall reactors represent one of the major categories of CVD reactors. In such systems,

Fig. 6: Rhenium rocket thrust chamber fabricated using CVD. Photo courtesy of B. H. Tuffias, Ultramet.[31]

shown schematically in Figure 7, the chamber containing the parts is surrounded by a furnace that heats the system. The parts are loaded into the system, it is heated to the desired temperature, then the reactive gases are introduced. The reactor may be equipped with shelves for coating many parts at once, or be sized for specific large parts. These systems are often run at very high temperatures, limited only by the materials used in constructing the furnace, and at reduced pressures, on the order of Torr to tens of Torr. Figure 8 shows a schematic for a hot-wall reactor that has been tailored to low-pressure CVD (LPCVD) batch processing in the microelectronics industry. In this case, a specialized support holds a large number (over a hundred) of closely-spaced silicon wafers for simultaneous processing. In general, hot wall reactors have the advantages of being able to process large batches of substrates, and having relatively uniform substrate temperatures and thus coating thicknesses. The primary disadvantages are that the walls get heavily coated, requiring frequent cleaning and causing particle problems, and that it involves higher thermal loads and energy usage.

Cold wall reactors are the other major category of CVD reactors. In such systems, the substrates are heated but the walls are cooled. Figure 9 shows an example of a cold wall rotating disk CVD reactor.[28,33] This system has water-cooled quartz walls, with a rotating holder for (silicon or compound semiconductor) wafers that is resistively heated from below. Other commercial cold-wall reactors include lamp heated single-wafer reactors that are widely used in microelectronics fabrication, and inductively heated horizontal flow reactors. Cold-wall reactors are often run at relatively high pressures, several hundred torr to atmospheric total

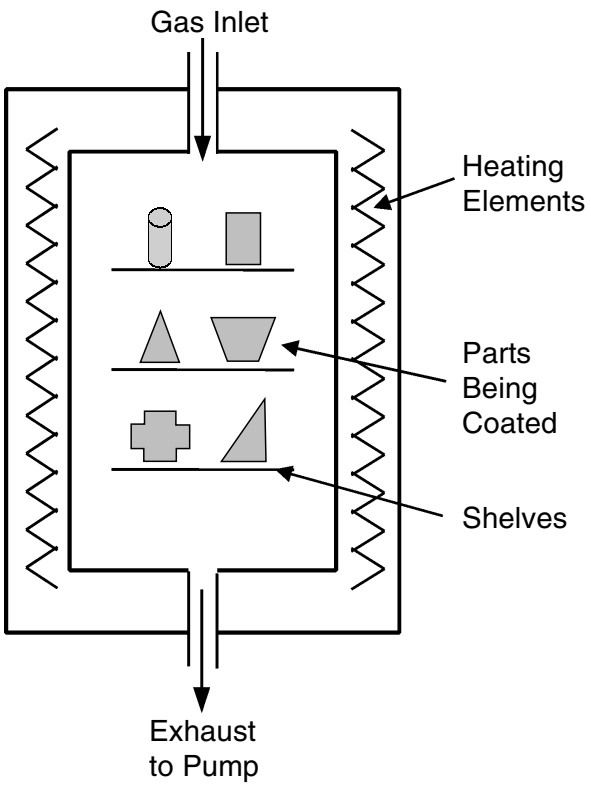

Fig. 7: Schematic drawing of hot-wall CVD reactor used to coat multiple parts.

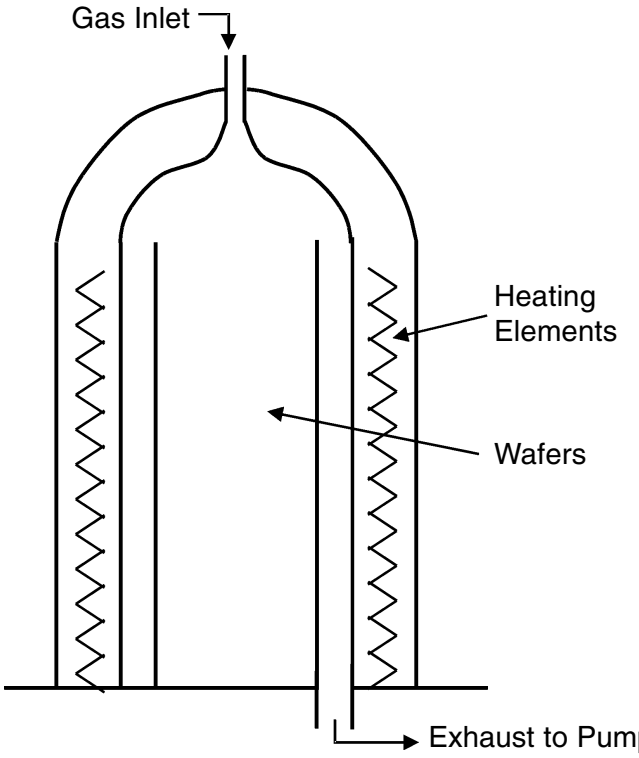

Fig. 8: Schematic drawing of LPCVD furnace for batch processing of multiple silicon wafers.

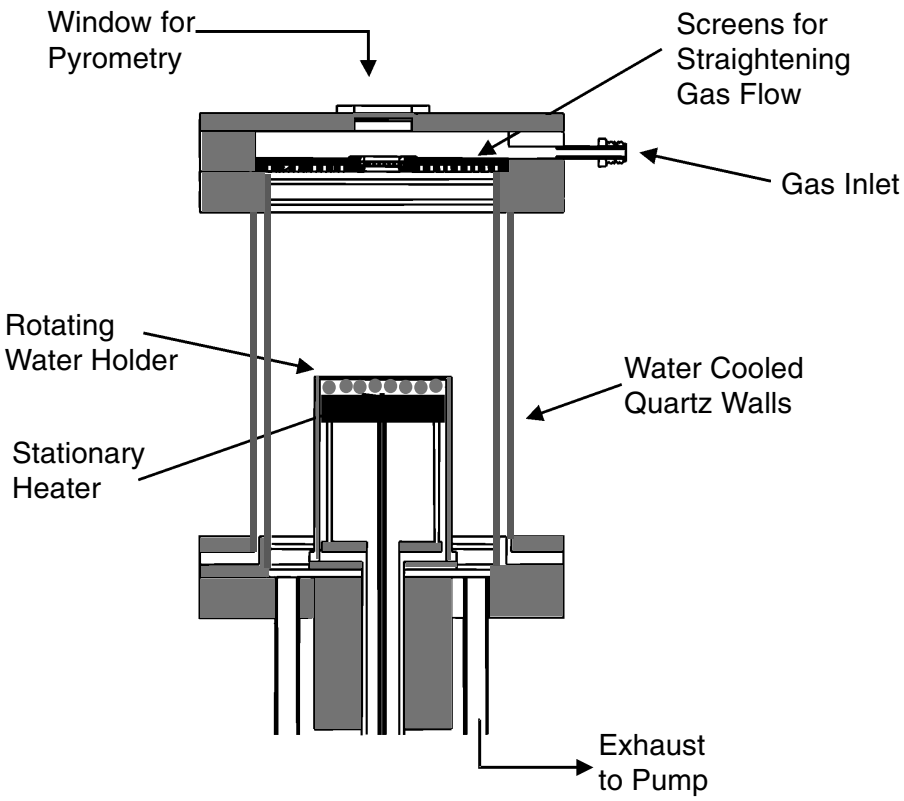

Fig. 9: Schematic diagram of a cold-wall rotating disk CVD reactor used for depositing thin films on semiconductor wafers.

pressure, and usually have the reactive precursors diluted in a carrier gas. Most compound semiconductor CVD processes use reactors of this type. Cold wall reactors have the advantages of reduced deposition of material on the walls, which means less cleaning, lower thermal loads on the substrates because of faster heat-up and cool-down times, lower energy consumption, and the avoidance of vacuum equipment. The primary disadvantages are larger temperature non-uniformities on the substrate, which may lead to film thickness non-uniformities, the smaller batch sizes, and possible thermal stresses on the substrates if the heating/cooling is too rapid.

A specialized variation of a cold wall reactor is the continuous reactor shown schematically in Figure 10. In this system, the surface to be coated moves underneath a set of gas injectors and is heated from below. In some cases, the substrates (wafers) are placed on a belt moving over a set of rollers. In other cases, such as the large-scale application of optical coatings (i.e. low-E coatings) to glass, the moving belt could be the float-glass sheet itself. These systems are essentially open to atmosphere – the reactive gases are contained by "curtains" of inert gas on either side of the deposition zone. Such systems have the advantage that they can do very large scale production, and avoid vacuum equipment. The disadvantages are a relatively high rate of gas consumption, potential non-uniformities in film thickness, relatively low operating temperatures because of the high volumes of gas involved, and relatively low efficiency for precursor use.

Plasma-enhanced (PECVD) or plasma-assisted (PACVD) CVD, (see chapters in Refs. 5, 14, and 15), constitute a smaller category of CVD processes that also involves a variety of reactor designs. In these systems, a plasma is

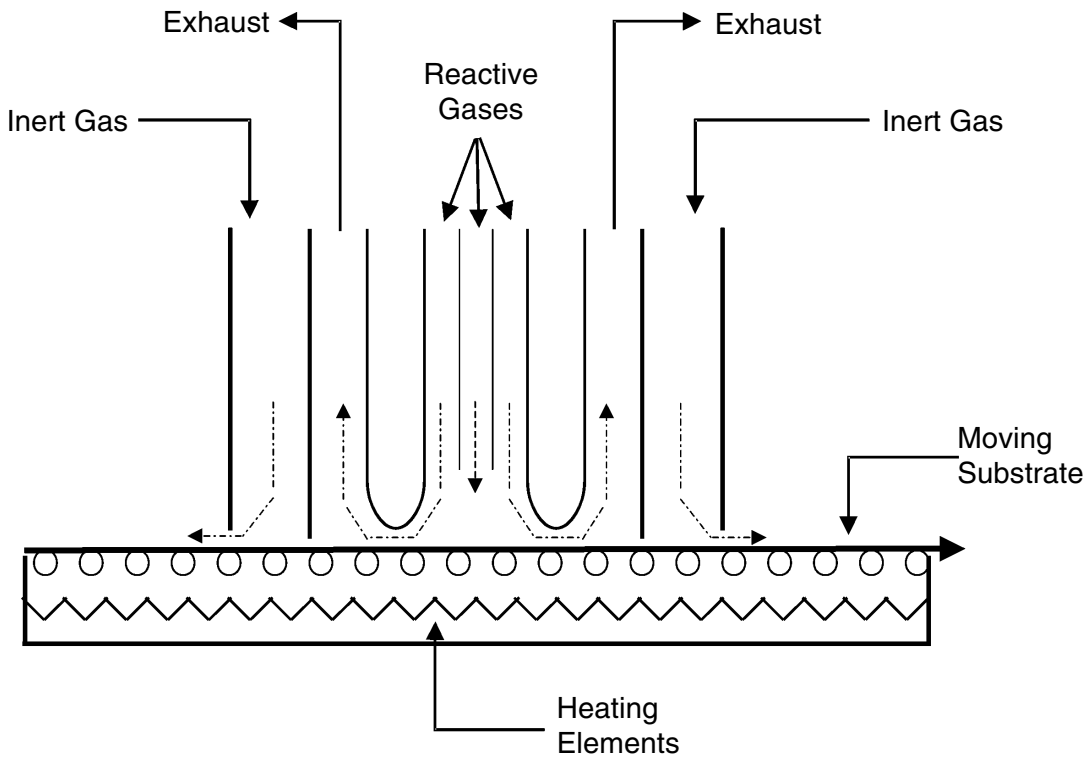

Fig. 10: Schematic diagram of a continuous flow, atmospheric-pressure CVD reactor.

used to dissociate the CVD precursor gas into smaller, more reactive, molecules. This allows deposition of a thin film to occur at significantly higher rates and/or lower temperatures. The substrate may still be heated, but usually to only a few hundred degrees. Plasma reactors are generally operated at pressures in the mTorr to several Torr range. Most PECVD systems involve low-temperature, or non-equilibrium plasmas (glow discharges) in which the electron temperatures are much higher than the neutral and ion temperatures. Such reactors have many configurations. In capacitively-coupled plasma reactors, the wafers are generally placed on the powered electrode. In inductively-coupled systems, shown schematically in Figure 11, the plasma is powered via a coil placed against part of the chamber, with the substrates placed on a surface below the plasma. In other systems (i.e., electron cyclotron resonance, ECR systems), magnetic fields are applied to confine and intensify the plasma. In comparison with thermal CVD processes, PECVD has the advantage of lower substrate temperatures, which means that films can be deposited on substrates that are not stable at high temperatures. The disadvantages, however, are often poorer film quality, in terms of rougher film morphology, higher impurity incorporation, and ion damage to the films and substrates. In addition to glow-discharge processes, there are also thin-film deposition processes that use high-temperature, or thermal plasmas. These are generally termed "plasma spray" processes rather than PECVD processes. In these systems, a high temperature plasma is used to dissociate precursors, which are then condensed onto the desired substrate. These plasmas are much more intense than the low-temperature plasmas and can atomize solid precursors. Thus they are more general than other CVD processes, but are harsh processes that can significantly heat or melt the surface.

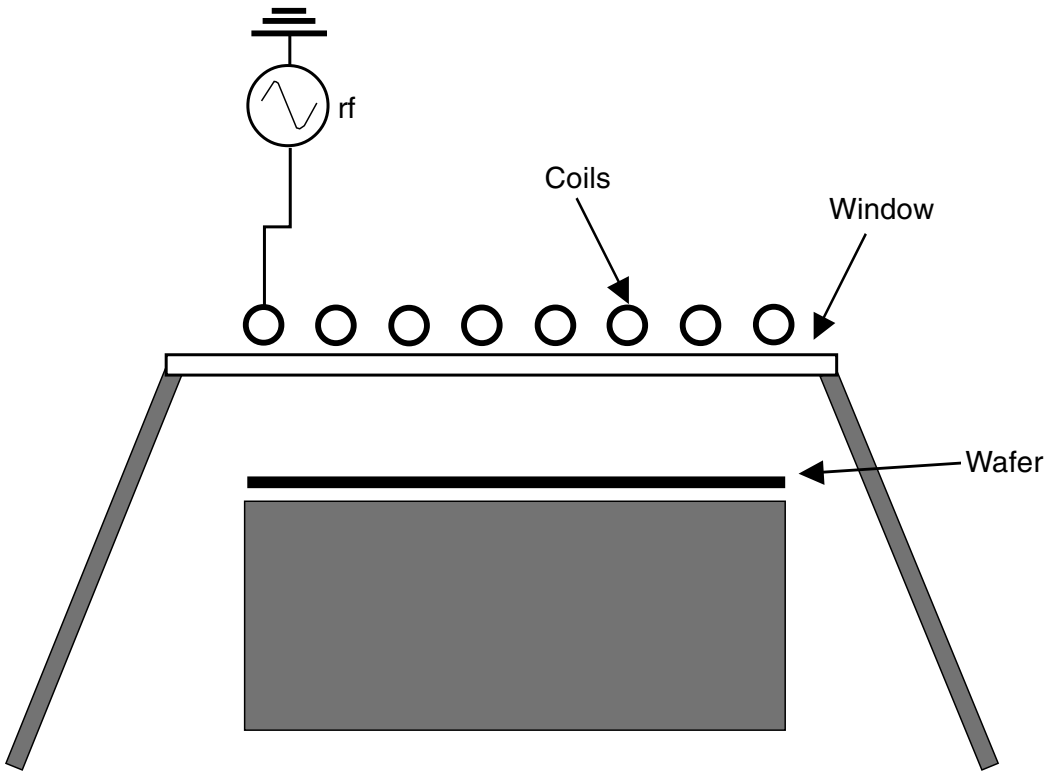

Fig. 11: Schematic diagram of an inductively-coupled plasma reactor.

Laser or photon assisted CVD is a specialized, not very common, category of CVD processes. In these cases, light from either a laser or a high-intensity lamp is used to promote the thin-film deposition. The photons can either be incident on the surface, or interact with the gas-phase molecules only. In both cases, the light can influence the chemical reaction either by simple heating of the gas/surface, or by electronic excitation or the molecules or solid. One of the advantages of laser-assisted CVD is for spatially-resolved deposition, where the laser is tightly focused and can be used to "draw lines" of deposited material. This is only practical in a limited number of cases involving very high-value materials, such as correcting design or manufacturing errors in prototypes, especially integrated circuits.

Hot filament CVD is another small category of CVD processes that has proven useful in recent years for the deposition of diamond and related materials. In this case, a very hot filament (1500-2000°C) is used to dissociate some of the CVD precursor gases, generally at pressures of 10-100 Torr, creating reactive radical species. The substrate is mounted nearby the filament in the process chamber, and is heated to more moderate temperatures (500-1000°C). Combustion CVD and chemical vapor infiltration (CVI) processes are covered in chapters 4 and 6 of this book, respectively, so we do not cover them here.

Types of CVD Precursors and Reactions

A wide variety of materials can be deposited using CVD techniques. As one would expect, a correspondingly wide range of chemical

precursors and reactions are involved. For any given material, there are generally a number of precursors and processes that can be used to deposit it. The choice of a particular process is based on the purity, morphology, and cost requirements for the product films, plus compatibility with the substrate materials. This section includes a general discussion of the types of precursors and reactions used in CVD. We refer the reader to the other chapters in the book for detailed discussions on the various CVD materials and applications. Comprehensive listings of precursors and reactions for specific materials can also be found in other books.[1,3,4]

Precursor molecules generally consist of the element(s) of interest (metal, semiconductor, oxide, etc.) chemically bonded to a variety of other atoms or groups of atoms (functional groups or ligands). These other atoms/groups react away during the CVD process leaving the desired species behind on the surface. Although pure-element precursors are occasionally used, the simpler precursors are generally small molecules where the central atom is bonded to other species such as hydride, halide (F, Cl, less commonly Br or I), or small organic radicals such as methyl or ethyl groups. Other precursors are more complex metalorganic molecules involving larger functional groups such as tertiary-butyl groups or ligands ranging from small carbonyl (CO) groups to large diketonates. Representative examples of these groups and ligands are shown in Figures 12 and 13, respectively.

The choice of a CVD precursor is determined by many factors in addition to the requirement that it contain the element(s) of interest. These considerations include the decomposition temperature required, vapor pressure of the precursor species, cost, and safety. Some of these chemicals are quite hazardous; the dangers range from high toxicity (i.e. $Ni(CO)_4$ or AsH_3), to pyrophoricity (i.e. SiH_4) or a tendency to explode (i.e. B_2H_6), to corrosiveness (i.e. $TiCl_4$ producing HCl byproducts), to combinations of the above. The metalorganic precursors often have lower vapor pressures, higher costs, and lower hazards than the hydrides and halides. The functional groups or ligands in these molecules can also lead to contamination in the material if they are incompletely removed, so a high purity requirement for the final product can count against a metalorganic precursor.

The chemical reactions used in CVD, though widely varied, can also be organized into classes, such as pyrolysis, reduction, or oxidation, which we discuss next. We write the chemical reactions very simply, showing only the overall conversion of reactants to products. Here we are not concerned with the details of the reaction kinetics, although detailed experimental and modeling studies have been done for both gas-phase and/or surface reactions, in some systems (see, for example, Refs. 34 and 35, respectively). CVD processes involve a trade-off between homogeneous and heterogeneous chemistry. To get high material purity and good film morphology, one often prefers that the rate-limiting chemistry occur at the surface rather than in the gas phase. However, this can lead to relatively low deposition rates. Increasing the deposition temperature for a given chemical reaction can lead to higher deposition rates. But this can also result in more extensive gas-phase reactions, which in turn can lead to gas-phase nucleation of particles or poor film morphology. Some applications, such as powder production, plasma assisted and combustion CVD processes, of course, involve substantial amounts of homogeneous chemistry by design.

Pyrolysis reactions are among the simplest, most straightforward CVD reactions. For example, silicon films are often deposited by thermally decomposing silane: $SiH_4 \rightarrow Si(s) + 2\ H_2$. If the conditions are chosen correctly, such as the presence of large amounts of H_2 as a carrier gas, the chemistry will occur primarily on the surface, rather than having substantial decomposition of the silane in the gas-phase. For these small, light molecules, the gas-phase unimolecular decomposition reactions are strongly pressure dependent, so the use of low pressures (~Torr), can also shut down the homogeneous reactions and allow the heterogeneous reactions to dominate. Other pyrolysis reactions used in CVD include the decomposition of methane to form diamond or diamond-like carbon: $CH_4 \rightarrow C(s) + 2\ H_2$, and the decomposition of nickel carbonyl to deposit nickel metal: $Ni(CO)_4 \rightarrow Ni(s) + 4\ CO$.

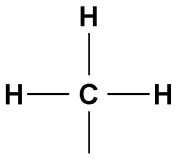

Methyl, Me, CH_3

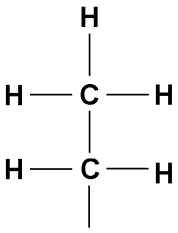

Ethyl, Et, C_2H_5

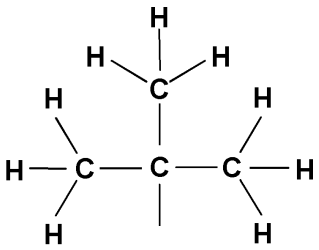

Tertiary-butyl,
t-Bu, C_4H_9

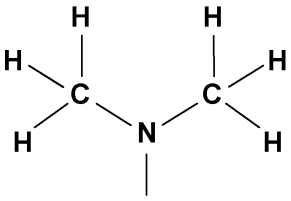

Dimethylamino,
DMA, $N(CH_3)_2$

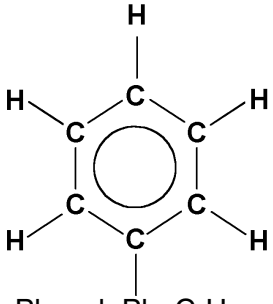

Phenyl, Ph, C_5H_6

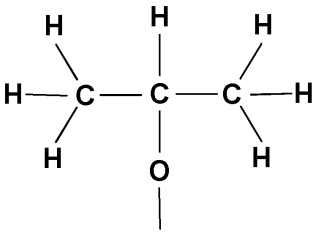

Isoproproxide,
i-PrO, C_3H_7O

Fig. 12: Examples of functional groups often used in CVD precursor molecules.

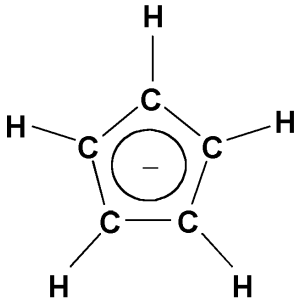

Cyclopentadienyl,
Cp, $C_5H_5^-$

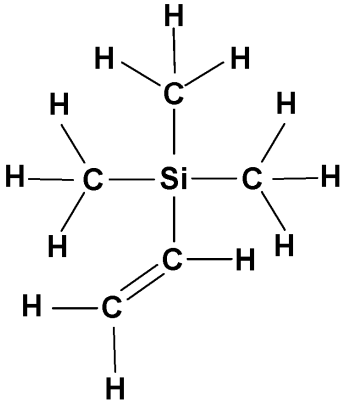

Vinyltrimethylsilyl,
VTMS, SiC_5H_{12}

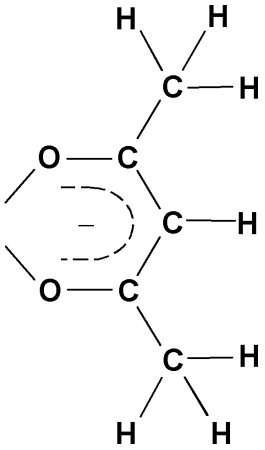

Acetylacetonate,
Acac, $C_5H_7O_2^-$

Fig. 13: Examples of ligands often used in CVD precursors.

Reduction reactions of halide precursors are very commonly used in CVD technologies. In many cases, the use of a hydrogen carrier gas provides the reducing agent in excess, as in the cases of tungsten deposition from the hexafluoride: $WF_6 + 3\ H_2 \rightarrow W(s) + 6\ HF$, or the deposition of silicon from a chlorosilane: $SiCl_4 + 2\ H_2 \rightarrow Si(s) + 4\ HCl$. In other cases, a separate reducing agent is added, as in the case of tungsten hexafluoride reduction by silane: $2\ WF_6 + 3\ SiH_4 \rightarrow 2\ W(s) + 3\ SiF_4 + 6\ H_2$. There are a few cases of intramolecular reduction, where both the halide and reducing groups are contained in the same molecule. An example of this is the deposition of silicon carbide from methyltrichlorosilane: $CH_3SiCl_3 \rightarrow SiC(s) + 3\ HCl$. Metal vapors are used as a reducer in certain processes, such as the case of titanium tetrachloride reduction by magnesium: $TiCl_4 + 2\ Mg \rightarrow Ti(s) + 2\ MgCl_2$. Alternatively, the solid substrate can act as a reducer, as in the case of tungsten hexafluoride reduction by silicon: $2\ WF_6 + 3\ Si(s) \rightarrow 2\ W(s) + 3\ SiF_4$. Such processes can also be called displacement reactions. In these cases, however, the deposition rate and final thickness of the CVD film become limited by interdiffusion of the reacting species through the solid, which can be quite slow.

Oxidation and hydrolysis reactions are widely used for the deposition of oxide materials. In these systems, oxygen or water is added to the system to oxidize the main precursor, removing hydrogen or halide atoms from the element of interest. A classic example is the oxidation of silane: $SiH_4 + 2\ O_2 \rightarrow SiO_2(s) + 2\ H_2O$, a mixture which incidentally can combust or explode. Ozone (O_3) is also used to accelerate oxidization, usually for cases of less-reactive precursors such tetraethoxysilane (TEOS). N_2O and CO_2 are also used as oxidizers, as in: $SiH_2Cl_2 + 2N_2O \rightarrow SiO_2(s) + 2\ HCl + 2\ N_2$, or $ZrCl_4 + 2\ CO_2 + 2\ H_2 \rightarrow ZrO_2(s) + 2\ CO + 4\ HCl$. Hydrolysis reactions are often used with metal chloride precursors: $2\ AlCl_3 + 3\ H_2O \rightarrow Al_2O_3(s) + 6\ HCl$, or $TiCl_4 + 2\ H_2O \rightarrow TiO_2(s) + 4\ HCl$. Solid substrates can also be directly oxidized, as in the steam oxidation of silicon: $Si(s) + 2\ H_2O \rightarrow SiO_2(s) + 2\ H_2$. This gives a high-quality oxide, but at a relatively slow growth rate.

Disproportionation reactions are those in which two similar molecules, or parts (groups) of a molecule, exchange parts to form non-identical products. Many, but not all, disproportionation CVD reactions are also pyrolyses. The decomposition of the copper diketonates is a sterling example of a CVD disproportionation. Cu(hfac)VTMS represents a copper atom bonded to a hexafluoroacetylacetonate ligand (hfac) and a vinyltrimethylsilane ligand (VTMS). Copper is in a formal +1 oxidation state in this molecule due to the neutral VTMS ligand. Two of these copper containing molecules can react on the surface, producing one deposited copper atom on the surface (0 oxidation state), a copper atom bound to two hfac ligands (+2 oxidation state), and two free VTMS molecules: $2\ Cu(hfac)VTMS \rightarrow Cu(s) + Cu(hfac)_2 + 2\ VTMS$. The pyrolysis of tetraethoxysilane (TEOS) to silicon dioxide: $Si(OC_2H_5)_4 \rightarrow SiO_2(s) + 2\ C_2H_4 + 2\ C_2H_5OH$, also illustrates disproportionation. Although the chemistry is actually much more complex,[36] it can be viewed as having two of the ethoxy groups in the TEOS molecule disproportionate, producing an ethylene molecule (C_2H_4) and ethanol molecule (C_2H_5OH), while leaving one of the O atoms behind, bonded to the Si atom. A different kind of disproportionation reaction is the case of aluminum deposition via the monochloride. In this case, AlCl is created in one region by the reaction of HCl or Cl_2 with Al(s). The AlCl is transported to the substrate, where it disproportionates to form $AlCl_3$ in the gas and Al(s) on the surface. This is representative of a chemical vapor transport process, which can be considered as a subset of CVD.

The last class of CVD reaction is what we will call co-deposition. This indicates deposition from a mixture of precursors, where atoms from several species contribute to the deposited film. This approach is generally used for the deposition of compound materials, where the desired film is composed of several elements. Examples of this kind of CVD system include the deposition of gallium arsenide from trimethylgallium (TMG) and arsine: $Ga(CH_3)_3 + AsH_3 \rightarrow GaAs + 3\ CH_4$, as well as the deposition of silicon nitride from silicon

tetrafluoride and ammonia: 3 SiF_4 + 4 NH_3 → Si_3N_4 + 12 HF. Most of the oxidation and hydrolysis CVD reactions also fall into the co-deposition category.

Fundamental Processes Underlying CVD

There is a variety of fundamental physical and chemical principles that can control the deposition rate and quality of a film resulting from a CVD process. We briefly introduce them here, but refer the reader to Chapter 2 and other books on CVD for more detailed discussions. The basic processes underlying CVD can be subdivided into mass transport effects and chemical effects, each of which can occur in both the gas and solid phases. Chemical effects can be further subdivided into thermodynamic effects and kinetic effects. In some cases, a particular effect can be separated out as rate limiting, and a CVD process can be said to be "mass-transport controlled" or "surface-kinetics controlled." In reality, transport and chemical reactions are closely coupled, with their relative importance varying with the details of the operating conditions.

Mass transport processes in the vapor phase carry the input CVD precursors, often in a carrier gas, from the injection point to the surface being coated. In most cases, the gas is in the continuum-flow regime, and is generally laminar, but occasionally has some turbulence. Mass transport effects are more likely to be rate limiting in larger CVD reactors, at higher temperatures and/or higher pressures. Especially at lower pressures, diffusional transport can be more important than convective transport. Mass transport has a much weaker dependence on temperature than chemical reaction kinetics. Thus, production CVD systems are often arranged to operate in a transport limited regime, in order to be more robust and easily controlled. Deposition rates can also be supply-limited, i.e., determined by the rate at which reactants are fed into the system, rather than the rate at which they are transported through the reactor to the surface. This can be manifested as loading effects, where the deposition rate varies strongly with the area of the surface being coated.

In addition to the reactor scale, which is measured in meters, vapor-phase mass transport effects can also be important in CVD at a much smaller scale, one measured in micrometers. This is often referred to as the "feature scale". On this scale, the gas is generally in the transition or molecular flow regimes, rather than continuum flow. Mass transport on this scale plays an important role in the CVI processes discussed in Chapter 6. These phenomena are also important in CVD involving high-aspect ratio features, which can occur unintentionally in some growth morphologies and deliberately in microelectronics applications.

Mass transport on the surface or within the solid can also affect CVD processes, primarily in the morphology of the growing film. Diffusion of atoms on the surface plays an important role in the initial steps of film nucleation, and, in competition with the chemical reactions depositing the atoms on the surface, can determine the film morphology and composition. Diffusion of atoms within the solid can also affect the composition of the film, especially in cases where the solid substrate comprises one of the reactants.

Chemical reactions occurring in the gas-phase can be more or less important in CVD, depending on the system, and can often be analyzed in detail.[34] Gas-phase reactions are more likely to be important with the use of high temperatures and high total reactor pressures, but less likely to be important at low reactor pressures. Many CVD systems are operated in ways that minimize gas-phase reactions in order to avoid particle formation that could interfere with the desired film deposition. Note that the absence of homogeneous nucleation of particles is not synonymous with the absence of gas-phase chemical reactions. In contrast, other CVD systems utilize gas-phase reactions to convert reactant molecules that are relatively unreactive at the surface into more reactive species. Examples where this strategy is used include the combustion CVD processes discussed in Chapter 4 and plasma-enhanced CVD processes.

Chemical reactions occurring on the surface are obviously responsible for the actual deposition of the desired film. The kinetics of such reactions can also be studied in detail[35,37,38]

although they may or may not determine the overall deposition rate. However, surface reactions generally play an important role in determining film composition, impurity incorporation, and, in concert with surface diffusion processes, film morphology.

An analysis of the thermodynamics of a CVD system, discussed further in Chapter 2, can provide valuable assistance in the choice of reactant concentrations, pressures and temperatures to use for a given chemical system. Such an analysis can also provide information on the composition of the deposited material as well as the maximum efficiency for use of reactants. However, a thermodynamical analysis only gives information on the theoretically-possible result, which may not actually be achievable. CVD systems are generally not operated at chemical equilibrium, although some systems, such as the deposition of silicon from chlorosilanes, come close.

The free energy of a proposed CVD reaction provides a feasibility indicator for a specified set of conditions. A negative change in free energy ($\Delta G = \Delta H - T\Delta S$) indicates that the process is likely to proceed in the desired direction (film deposition), whereas a positive change in free energy indicates that it is likely to proceed in the inverse direction (film etching). The free energy contains the heat of reaction (reaction enthalpy), but also contains an entropy term. Thus, an endothermic reaction (positive heat of reaction) can be used in a CVD process if the entropy change is positive enough or the temperature high enough. An example of this is the reaction between WF_6 and H_2, where the heat of reaction at 500 K is + 83 kJ/mol, but this can be overcome by a large increase in entropy to yield an overall free energy change of –84 kJ/mol. An exothermic reaction (negative heat of reaction) is more likely to be usable in a CVD process, regardless of the sign of the entropy change.

Thermodynamic analyses, in the form of calculations of chemical equilibrium state, have been done for many CVD systems. However, they require data on the enthalpy, entropy and heat capacity for all molecules to be considered, and such data are not always available, especially for the newer CVD precursors. Constraints can be imposed on equilibrium calculations as a way of starting to incorporate kinetic limitations. For example, if nitrogen is used as a carrier gas and has been experimentally shown not to participate in the process, species such as N atoms and solid nitride species would be omitted from the equilibrium calculation to account for the kinetic inaccessibility of these species.

The kinetics of a chemical reaction may prevent a reaction from occurring even though the thermodynamics indicates that it can occur. For example, silane is thermodynamically unstable relative to silicon and hydrogen even at room temperature, but is kinetically limited enough to allow it to be manufactured and shipped in gas tanks. In such cases, knowledge of the kinetics of a chemical reaction, either in the gas or on the surface, can prove crucial to understanding the CVD system. Acquiring knowledge of all the chemical kinetics of a CVD process is quite a large undertaking. Such a task requires chemical kinetic data acquired under conditions where there are no mass-transport limitations, which are often lacking for the molecules used as CVD precursors. Despite this, a number of detailed chemical reaction mechanisms have been developed for a CVD systems in recent years.[39] However, for a particular CVD process, it is often sufficient to identify a few reaction steps that are slow enough to be rate determining.

In recent years, the use of computational models that describe the details of these chemically reacting flows has been steadily increasing. They are being used to assist in the development of and optimization for CVD equipment and processes. This trend results from a convolution of several factors. First, the increasing complexity of CVD processes and more stringent requirements being placed on them means that the traditional Edisonian approach no longer works well enough and fast enough. Second, the cost of developing and building CVD equipment has notably increased, especially for the microelectronics and optoelectronics industries where a production-level CVD reactor can represent a multi-million dollar investment. Third, the rapidly decreasing cost of computational power has shifted the relative costs of cutting metal and numerical simulations in favor of the latter. This kind of

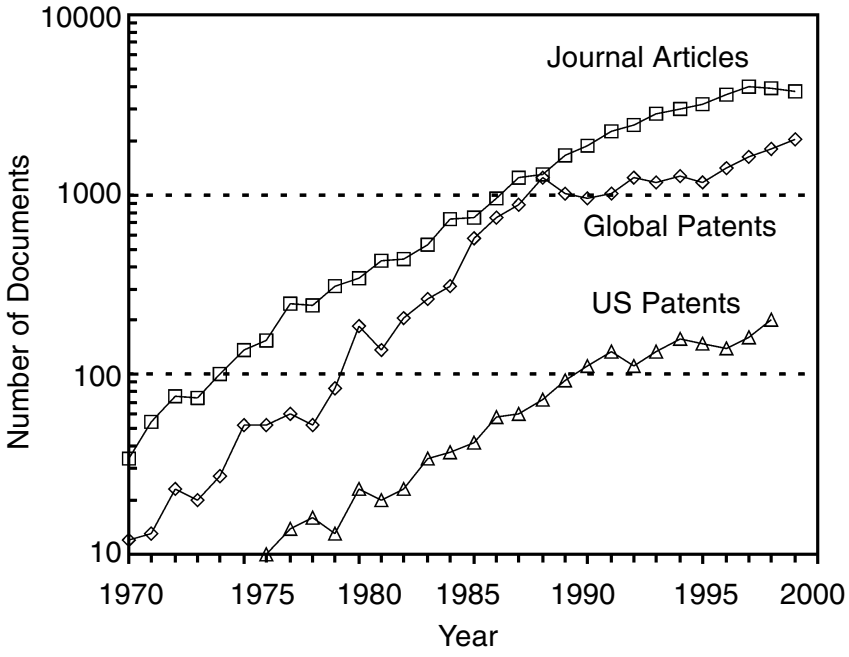

Fig. 14: Annual publications and patents in CVD R & D for the last 30 years.

modeling lies outside the scope of this book, but has been described elsewhere.[40]

Status of CVD Research and Development

After the development of CVD and its applications in the early part of this century, the scientific and technological interest in CVD continued to grow rapidly in the latter half of the 20th century. Here, we explore two quantitative metrics for the status of CVD R&D: publications/patents and government research grants.

Examining publications first, we note that between 1960-1980, approximately 5400 CVD-related publications were generated and are compiled in the bibliography by D. T. Hawkins.[2] More recent years, indexed in electronic databases, exhibit much higher publication rates. For example, Figure 14 shows the number of journal articles, worldwide patents, and US patents generated each year from 1970 to 1999, based on data in the Chemical Abstracts,[41] and US Patent Office databases.[42] These three measures exhibit similar trends, increasing more than 100-fold over this time period. Between 1970 and 1990 these publications were increasing at an annual rate of ~21% per year. This growth slowed somewhat in the 1990s, perhaps due to the maturity of the field or limits on funding and manpower. This deceleration is most noticeable in the number of journal articles, which has stabilized at approximately 4000/year during the last 5 years. Two other databases, the INSPEC®[43] and Science-Citation Index[44] were also examined and exhibited the same trend for number of journal articles published per year.

The number of grants awarded for CVD-related research is another measure for gauging the interest in or activity level of the topic. An analysis of the RaDiUs® database[45] shown in Figure 15, indicates that between 1993 and 1999 the U.S. federal government has funded an average of 240 research grants per year. (This number includes new starts and ongoing grants). The total number of grants has declined

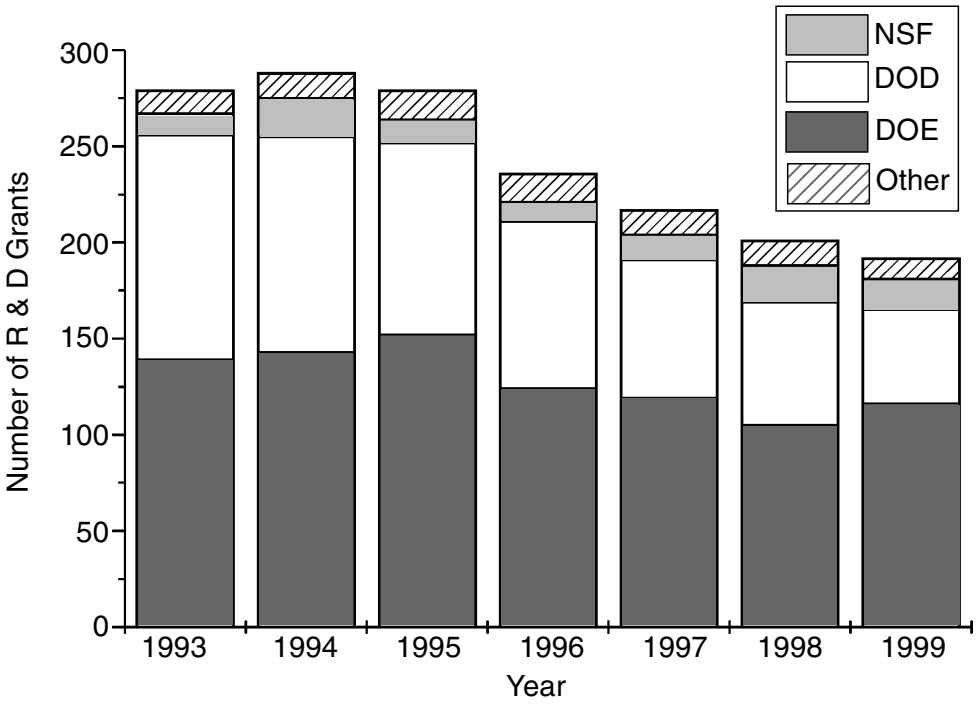

Fig. 15: Number of research grants in CVD funded by the U.S. government.

somewhat since 1995, which may be an indication of the maturity of CVD research, at least in the United States. Some of the decline in government funding is due to a slight downward trend in the number of National Science Foundation (NSF) grants, but the largest decline is in the number of Department of Defense (DOD) grants. The DOD was experiencing budget cuts during this time period, so the decline in CVD-related grants may simply be a reflection of the decline in the DOD R & D budget rather than a declining level of interest in CVD.

For the 1993-1999 period approximately 53% of the grants were awarded by the NSF, 36% awarded by the DOD, with the remaining fraction awarded by the Department of Energy (DOE), the National Aeronautics and Space Administration (NASA), and other federal agencies. While NSF primarily funds academic research, a significant amount of their CVD funding goes to small companies in the form of Small Business Innovation Research (SBIR) awards. The other agencies, such as DOD, may direct considerable resources towards companies in order to develop state-of-the-art products, as well as funding fundamental academic research. The NSF has a well-developed Internet accessible database back to 1989, so it is relatively easy to examine funding levels and trends. From 1990-2000 the NSF has averaged about 40 new CVD-related grants starts per year, with no discernable trend upwards or downwards. The total number of CVD grants funded by NSF ranges from 100-150 per year and exhibits a slight downward trend (see Figure 15), as mentioned above. Although the NSF grants are just one metric of CVD funding in the U.S., it is likely that agencies in other countries would show similar trends. The observation of a nearly constant NSF award rate could partially explain the nearly constant rate of journal article publication (see Figure 14) in the mid-1990s.

In addition to the number of grants, the actual funding level of CVD R & D would be

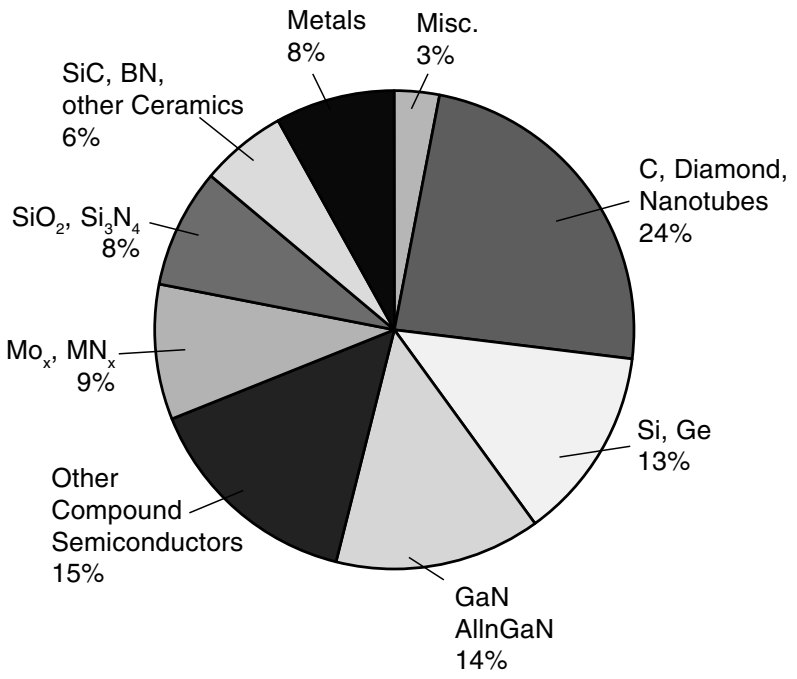

Fig. 16: CVD publications in 1999, categorized by material being deposited. (MO_x, MN_x are metal oxides and nitrides).

another interesting metric to examine. Unfortunately this information is difficult to obtain from most federal agencies, with the exception of NSF. The total integrated NSF CVD funding from 1989-1999 was approximately $103 million (U.S), representing 0.2% of the total NSF budget.

A different dimension of the publication record can be analyzed by examining the types of materials currently under investigation. Figure 16 shows a random sample of 750 journal articles published in 1999 categorized according to the material studied. Not surprisingly the results indicate a wide spectrum of interest, including semiconductors, metals, superconductors, insulators and ceramics. One CVD material that saw a rapid increase in interest in the 1990s is diamond and amorphous sp^3-carbon. Even more recently there has been a growing interest in synthesizing carbon nanotubes and fibers with CVD. Altogether, CVD of various forms of carbon accounted for about a quarter of all 1999 journal articles. Studies of elemental (Si, Ge) and compound (e.g. GaAs, GaN) semiconductors comprise a large fraction (~42%) of the literature, due to the numerous electronic and optoelectronic applications of these materials. Interest in the group-III nitride based semiconductors (e.g. GaN) has grown rapidly in the last few years and now accounts for about half of the compound semiconductor publications. Metals (e.g. W, Cu) account for 8% of the CVD publications, and metal oxides and nitrides account for another 9%. Most of the remaining literature deals with SiO_2, Si_3N_4, and a variety of other insulators and ceramics.

Summary

Chemical vapor deposition is a widely used technique for materials processing. The field encompasses a large variety of applications, reactor designs, materials and chemistries. CVD

R & D has grown rapidly over the last few decades and is a very active field today. However, a leveling-off of publications and government-funded research grants over the last few years suggest that the field may be maturing. This would be an expected result of a transition from government-funded R & D whose aim is publications, to privately-funded work in industry whose aim is proprietary intellectual property. This is consistent with the continued growth in patents in the late 1990s observed in Figure 14. CVD remains a critical enabling technology for many industries, including the computing and communications revolutions. It should continue to be an active field of R & D well into the 21st century, as new materials and applications develop.

Acknowledgment

This work was performed at Sandia National Laboratories, partially funded by the Division of Materials Science of the Office of Basic Energy Sciences. Sandia is a multiprogram laboratory operated by Sandia Corporation, a Lockheed Martin Company, for the United States Department of Energy under Contract DE-AC04-94AL85000. The authors also gratefully acknowledge the helpful scientific discussions with W.G. Breiland and M.E. Coltrin.

References

1. C.F. Powell, J.H. Oxley, and J.M. Blocher, Jr., eds, *Vapor Deposition,* John Wiley, NY, 1966.
2. D.T. Hawkins, *Chemical Vapor Deposition, A Bibliography,* Plenum, New York, 1981.
3. H.O. Pierson, *Handbook of Chemical Vapor Deposition, Second Edition,* Noyes Publications, Norwich, New York, 1999.
4. C.E. Morosanu, *Thin Films by Chemical Vapor Deposition,* Elsevier, Amsterdam, 1990.
5. M.L. Hitchman and K.F. Jensen, eds., *Chemical Vapor Deposition,* Academic Press, San Diego, CA, 1993.
6. A. Sherman, *Chemical Vapor Deposition for Microelectronics: Principles, Technology and Applications*, Noyes Publications, Park Ridge, NJ, 1987.
7. G.B. Stringfellow, *Organometallic Vapor-Phase Epitaxy: Theory And Practice,* Academic Press, San Diego, 1999.
8. A.C. Jones and P. O'Brien, *CVD of Compound Semiconductors,* VCH Publisher, NY, 1997.
9. T. Kodas and M. Hampden-Smith, eds., *The Chemistry of Metal CVD,* VCH Publishers, NY, 1994.
10. G.S. Sandhu, H. Koerner, M. Murakami, Y. Yasuda, and N. Kobayashi, eds., *Advanced Metallization Conference in 1998*, Materials Research Society, Warrendale, PA, 1999.
11. M.E. Allendorf and C. Bernard, eds., *Proceedings of the Fourteenth International Conference on Chemical Vapor Deposition,* The Electrochemical Society, Pennington, NJ, 1997.
12. T.M. Besmann, M.D. Allendorf, McD. Robinson, R.K. Ulrich, eds., *Proceedings of the Thirteenth International Conference on Chemical Vapor Deposition,* The Electrochemical Society, Pennington, NJ., 1996.
13. K.F. Jensen and G.W. Cullen, eds., *Proceedings of the Twelfth International Conference on Chemical Vapor Deposition,* The Electrochemical Society, Pennington, NJ, 1993.
14. J.L. Vossen and W. Kern, *Thin Film Processes II,* Academic Press, San Diego, CA, 1991.
15. D.L. Smith, *Thin-Film Deposition,* McGraw-Hill, New York, 1995.
16. P.D. Dapkus, Metalorganic Chemical Vapor Deposition, *Ann. Rev. Mater. Sci.,* Vol.12, 1982, p.243.
17. S.P. DenBaars and S. Keller, Metalorganic Chemical Vapor Deposition (MOCVD) of Group III Nitrides, *Semiconductors and Semimetals,* Vol.50, 1998, p.11.
18. T.F. Kuech, Metal-Organic Vapor Phase Epitaxy of Compound Semiconductors, *Mater. Sci. Rep.,* Vol.2, 1987, p.1.
19. L. Mond, C. Langer, and F. Quincke, Action of Carbon Monoxide on Nickel, *J. Chem. Soc.,* Vol.57, 1890, p.749.

20. R.A. Kiehl and T.C.L.G. Sollner, eds., *High Speed Heterostructure Devices,* Academic Press, Boston, 1994.
21. P.S. Zory, Jr., ed., *Quantum Well Lasers,* Academic Press, San Diego, 1993.
22. C. Yeh, *Handbook of Fiber Optics,* Academic Press, San Diego, 1990, pp.24-28.
23. S. Nakamura and G. Fasol, *The Blue Laser Diode: GaN Based Light Emitters and Lasers,* Springer, Heidelberg, 1997.
24. R. Haitz, F. Kish, J. Tsao, and J. Nelson, Another Semiconductor Revolution: This Time It's Lighting!, *Compound Semiconductor*, Vol.6, No.2, p.34-37.
25. J.J. Sniegowski and M.P. de Boer, IC-Compatible Polysilicon Surface Micromachining, *Annu. Rev. Mater. Sci*., Vol.30, 2000, pp. 299-333.
26. http://www.nano.gov.
27. Zh.I. Alferov, The History and Future of Semiconductor Heterostructures, *Semiconductors,* Vol. 2, 1998, pp.1-14.
28. W.G. Breiland, M.E. Coltrin, J.R. Creighton, H.Q. Hou, H.K. Moffat, and J.Y. Tsao, Organometallic Vapor Phase Epitaxy, *Mater. Sci. Eng.,* Vol.R24, 1999, pp.241-274.
29. T. Suntola, Atomic Layer Epitaxy, *Handbook of Crystal Growth 3: Thin Films and Epitaxy, Part B: Growth Mechanisms and Dynamics,* D.T.J. Hurle, ed., Elsevier, Amsterdam, 1994, p.605.
30. M. Grundmann, The Present Status of Quantum Dot Lasers, *Physica E*, Vol.5, 2000, pp.167-184.
31. Ultramet, Pacoima, CA. www.ultramet.com.
32. Rohm and Haas Company, Advanced Materials Division, Woburn, Massachusetts. www.cvdmaterials.com.
33. W.G. Breiland and G.H. Evans, Design and Verification of Nearly Ideal Flow and Heat Transfer in a Rotating Disk Chemical Vapor Deposition Reactor, *J. Electrochem. Soc.,* Vol.138, 1991, pp.1806-1816.
34. P. Ho, M.E. Coltrin, and W.G. Breiland, Laser-Induced Fluorescence Measurements and Kinetic Analysis of Si Atom Formation in a Rotating Disk Chemical Vapor Deposition Reactor, *J. Phys. Chem.,* Vol.98, 1994, pp.10138-10147.
35. J.R. Creighton and J.E. Parmeter, Metal CVD for Microelectronic Applications: An Examination of Surface Chemistry and Kinetics, *Critical Reviews in Solid State and Materials Sciences,* Vol 18, 1993, pp.175-238.
36. M.E. Coltrin, P. Ho, H.K. Moffat, and R.J. Buss, Chemical Kinetics in Chemical Vapor Deposition: Growth of Silicon Dioxide from Tetraethoxysilane (TEOS), *Thin Solid Films,* Vol.365, 2000, pp.251-263.
37. S.M. Gates, Surface Chemistry in the Chemical Vapor Deposition of Electronic Materials, *Chem. Rev.,* Vol.96, 1996, p.1519.
38. J.G. Ekerdt, Y.M. Sun, A. Szabo, G.J. Szulczewski, and J.M. White, Role of Surface Chemistry in Semiconductor Thin Film Processing, *Chem. Rev.,* Vol.96, 1996, p.1499.
39. C.R. Kleijn, Computational Modeling of Transport Phenomena and Detailed Chemistry in Chemical Vapor Deposition - A Benchmark Case, *Thin Solid Films,* Vol.365, 2000, pp. 294-306, and references therein.
40. M. Meyyappan, ed., *Computational Modeling in Semiconductor Processing,* Artech House, Norwood, MA, 1995.
41. SciFinder5, Chemical Abstracts Service (CAS), 2540 Olentangy River road, P.O. Box 3012, Columbus, Ohio, 43210, www.cas.org.
42. United States Patent and Trademark Office, Crystal Park 3, Suite 461, Washington, DC 20231, www.uspto.gov.
43. Information Service in Physics, Electrotechnology and Control (INSPEC), The Institution of Electrical Engineers, Michael Faraday House, Stevenage, Herts, SG1 2AY, U.K., www/iee.org.uk.
44. SciSearch® Database of the Institute for Scientific Information®, Inc., (ISI®), Philadelphia, Pennsylvania, USA, www.isinet.com.
45. Research and Development in the United States (RaDiUs®), database developed by RAND and the NSF; RAND, 1700 Main Street, P.O. Box 2138, Santa Monica, California 90407-2138, www.rand.org.

Chemical Vapor Deposition
Jong-Hee Park, T.S. Sudarshan, editors, p23-43
DOI:10.1361/chvd2001p023

Chapter 2

Basic Principles of CVD Thermodynamics and Kinetics

A.K. Pattanaik and V.K. Sarin
College of Engineering
Boston University
Boston, MA 02215

Introduction

Surface modification, in general, provides unique ways to change the surface and near surface regions of a material. In structural applications, it is typically used to improve durability, enhance resistance to tribological effects such as friction and wear, and increase resistance to chemical effects such as oxidation and corrosion. As the requirements become increasingly complex and technically demanding, a wide spectrum of properties are being desired from coating systems. There is, thus, a critical demand for systematically designed and controlled surface modification processes based on a fundamentally sound understanding of the coating system dynamics and process kinetics.

Chemical vapor deposition (CVD) is an atomistic surface modification process where a thin solid coating is deposited on an underlying heated substrate via a chemical reaction from the vapor or gas phase. The occurrence of this chemical reaction is an essential characteristic of the CVD method. The chemical reaction is generally activated thermally by resistance heat, RF, plasma and laser.[1] Furthermore, the effects of the process variables such as temperature, pressure, flow rates, and input concentrations on these reactions must be understood. With proper selection of process parameters, the coating structure/properties such as hardness, toughness, elastic modulus, adhesion, thermal shock resistance and corrosion, wear and oxidation resistance can be controlled or tailored for a variety of applications. The optimum experimental parameters and the level to which

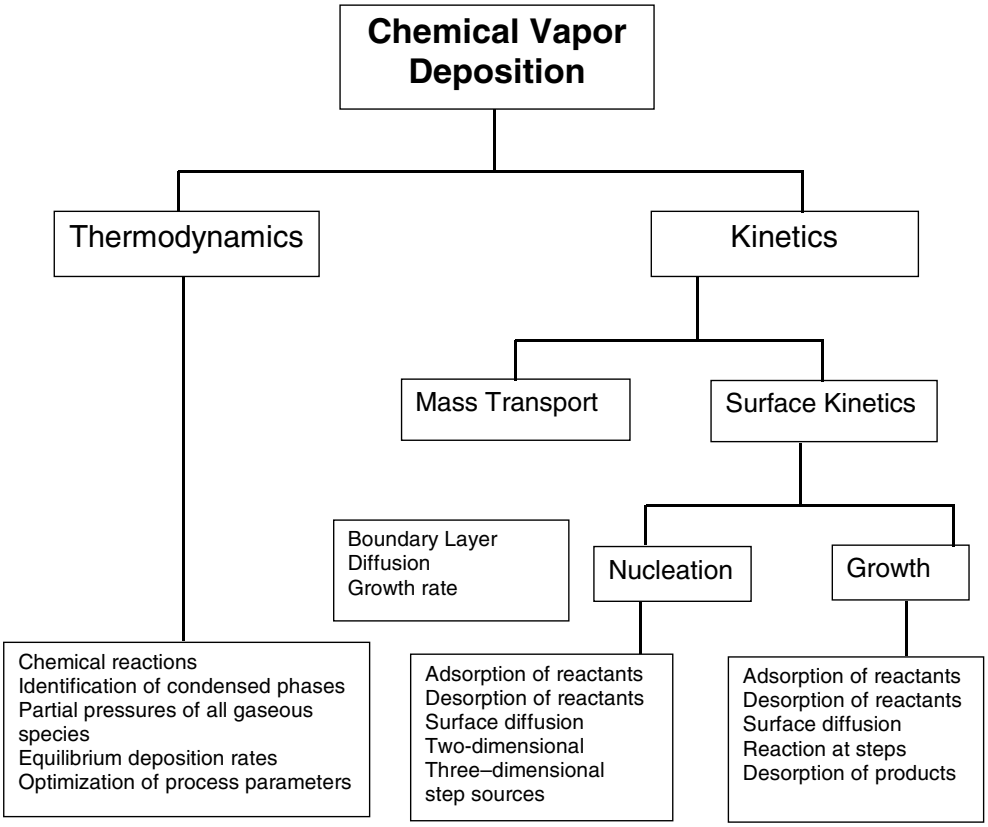

Fig. 1: Various fundamental aspects involved in a chemical vapor deposition process.

they must be controlled, in order to obtain reproducible results, requires a detail understanding of each individual system. However, the process can be controlled through the knowledge of the gas flow dynamics, mass transport, equilibrium thermodynamic yields, and possible chemical kinetic rate-limiting mechanisms of the system.

The logical approach to the development of a CVD coating is to first determine the feasibility of a particular coating system. The process itself is basically governed by the following two important mechanisms:

- Thermodynamics which determines driving force and
- Kinetics which determines the rate control of the chemical reactions.

This chapter discusses the basic principles of CVD thermodynamics and kinetics with a brief review of the CVD process. Various fundamental aspects involved in a chemical vapor deposition process are shown in Figure 1.

CVD Process

Chemical vapor deposition is a very complex process. There are numerous factors such as type, shape, and size of reactor, gas flow rate and arrangement that can affect the properties of the coating. Therefore, it is necessary to review briefly the process itself which includes reactor, reaction zones, temperature, pressure, precursors, and gas flow dynamics before discussing the thermodynamics and kinetics of the CVD.

In general, CVD process is classified and categorized in various ways such as low and high temperature, low and high pressure, cold and hot

wall, close and open system. Irrespective of type, a CVD process must have the basic three capabilities,

i. A process controller to deliver and control all precursors into the chamber,
ii. An energy source to drive the chemical reaction, and
iii. An exhaust system to remove the by-product and depleted gases from the chamber. Most commercial CVD reactors are either hot-wall or cold-wall.[2]

Hot-wall reactor is a high temperature chamber in which the substrate is placed for coating. In this reactor, including the substrate, all other parts (inlet and outlet tubes) inside the chamber get coated. On the other hand, in a cold-wall reactor only the substrate is heated, either resistively or inductively. Although the cold-wall reactor is more complex, it allows greater control over the deposition process. However, severe natural convection can occur due to the steep temperature gradient around the substrate. Depending upon the reactor geometry, the gas flow pattern can be quite complicated. In most cases, laminar gas flow is desirable but some local areas of turbulent flow may exist. The nature of the gas flow patterns is influenced by the kinetics of the various chemical reactions which may occur in the bulk gas or on the heated surfaces inside the reaction chamber.

For most coatings used in structural applications, the precursor gases frequently include inert gases such as argon and nitrogen, reducing gases such as hydrogen, and a variety of reactive gases such as methane, carbon dioxide, water vapor, ammonia, chlorine, arsine, boron trichloride, hydrogen chloride, hydrogen floride, tungsten hexafloride. Some of the high vapor pressure liquids e.g. titanium tetrachloride ($TiCl_4$), silicon tetrachloride ($SiCl_4$) are heated to a relatively moderate temperature (about 60°C), so that their vapor can be carried into the reaction chamber by bubbling a carrier gas (hydrogen or argon) through the liquid. Some precursors are formed by converting a solid metal or a compound into a vapor by a reaction, for example, between aluminum metal with chlorine or hydrochloric acid to form aluminum chloride ($AlCl_3$). Typically, for these gas mixtures, process temperatures range from about 600°C to about 1500°C, depending upon the coating/substrate combination. Furthermore, simultaneous deposition of more than one material to obtain composite (i.e. two-phase) coatings can be effectively used to tailor the structure and therefore the properties of such coating.[3-6] These coatings are found in numerous applications which includes microelectronics, decorative, corrosion and oxidation resistance, metal cutting, and nuclear. Wide commercialization of the CVD process is due to its ability to produce a large variety of coatings of pure and multi-component compounds.

Depending upon the applications, many variations of CVD processing are available.[7] One of the variants includes moderate-temperature or metal-organic CVD (MTCVD / MOCVD) in which reaction temperature fall in the range of 500 to 850°C. This is usually achieved by using metal-organic precursors, which decompose at relatively lower temperature.[1] Other variants include plasma-assisted (or -enhanced) CVD (PACVD or PECVD) and laser CVD (LCVD). Basically, the chemical reactions in the vapor phase are activated by the creation of a plasma in the gas phase, or by directing a laser beam into the gas mixture. This process facilitates more energetic activation of the vapor phase reactions and can lower the reaction temperature further.

Deposition reactions generally involve complicated chemical reaction schemes, however overall CVD reactions can be classified to include pyrolysis, reduction, oxidation, hydrolysis, disproportionation, or combinations of these.[8] Additionally, in certain cases the substrate may be a part of the reaction or may act as a catalyst. Coatings are generally grown at sub-atmospheric pressures, although high growth rate depositions have been done at (or close to) atmospheric pressures.

A sequence of physico-chemical process steps take place[1, 9-13] in a CVD process. First the reagents have to be supplied to the surface being coated. The zone between the bulk of the flowing gas and the substrate surface is the location of the first kinetic barrier, which has to be crossed by diffusion of gaseous species. Next the species are adsorbed on the substrate surface, and migrate, react and the product to be deposited is formed to form nuclei.

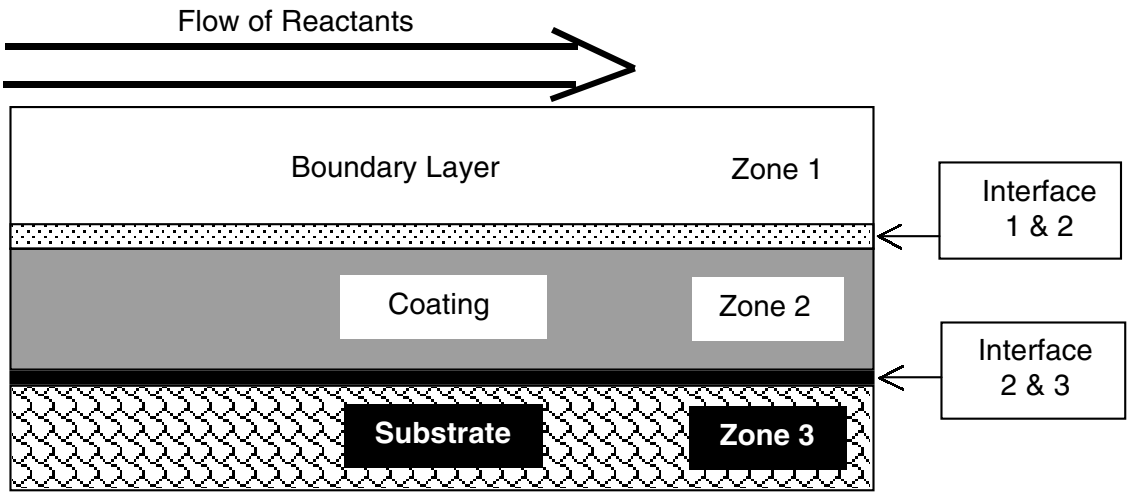

Fig. 2: A schematic diagram of the boundary layer model showing the reaction zones for Al_2O_3 coating.

In the case of laminar flow which is typically assumed in all models and calculations, the gas velocity is zero at the substrate surface and increases to a constant value (the bulk gas flow velocity) at some distance from the substrate. Boundary Layer Theory (BLT) provides the key to understanding the dynamics of these surface reactions.[1,2,9,12] It can help couple the chemical and mass transport processes occurring near or on the heated substrate surface as gas flows over it. For fluid dynamic reasons a more or less stagnant boundary layer occurs in the vapor adjacent to the substrate/coating interface. During the coating process, the gaseous reactants and products are transported across reaction zone 1 (Figure 2) as well as in the main gas stream, where homogeneous nucleation reactions in the vapor can occur. These reactions are usually undesirable, and can lead to flaky and/or non-adherent coatings. Heterogeneous reactions, which in many systems determine growth rate, occur at the interface between zones 1 and 2 (vapor/coating). The typically high temperatures used in CVD can and do lead to various solid state reactions (i.e. phase transformations, grain growth) during the deposition process in zones 2 and 3 (coating and the substrate). At the interface between these zones (2 and 3) diffusion can result in the formation of various intermediate phases, which are of importance to the adherence characteristics of the coating.

Thermodynamics of CVD

Significant progress has been made in understanding and predicting the thermodynamic behavior of the CVD process.[14-22] Thermodynamic calculations based on minimization of the Gibbs free energy of the gas-solid system are useful in predicting the influence of process variables such as temperature, pressure, inlet gas concentrations on the phase assemblage, the equilibrium deposition efficiency, and the concentration and the molecular species in the exhaust gas. The thermodynamic equilibrium state of the CVD system can be calculated for

i. Partial pressures of all the gaseous species,
ii. The identification of the condensed phase,
iii. Equilibrium deposition rates possible, and
iv. Their theoretical efficiencies.

Such calculations provide limiting criteria, and aid in establishing rate limiting gaseous species. The reliability of these calculations, is of course, dependent on the availability and accuracy of thermochemical data as well as the

identification of all the critical vapor species and condensed phases. Additionally, it should be noted that chemical equilibrium is rarely achieved under most CVD flow conditions.[1] Hence the thermodynamic calculations work as a guidance for the CVD process.

The evaluation of the equilibrium concentrations from the equilibrium constant might involve some trial and error since the number of gas species could be greater than two, the number of independent relations. One of these relations is the expression for the equilibrium constant in terms of the standard free energy of the reaction and the temperature and the other results from the condition that the system pressure is the sum of partial pressures. Using computer programs, calculations of the concentrations of gas and condense phase species are made to minimize the overall Gibb's free energy for a given system at a fixed temperature and pressure. The Gibbs free energy, G, of a system is given by,

$$G = H - TS \tag{1}$$

where H is the enthalpy, S is the entropy, and T is the temperature of the system. The free energy of formation of all vapor and condensed constituents of the system are the most useful data. The free energy of a chemical reaction (ΔG_r^o) can be calculated from the values of ΔG_f^o and ΔG_f^o according to the following equation.

$$\Delta G_r^o = \sum \Delta G_r^o \text{products} - \sum \Delta G_r^o \text{reactants} \tag{2}$$

where ΔG_r^o is related to the equilibrium constant k_p,

$$\Delta G_r^o = 2.3\ RT\ log\ k_p \tag{3}$$

the equilibrium constant is related to the partial pressure in the system as,

$$k_p = \frac{\prod_{i=1}^{n} P_i \text{ products}}{\prod_{i=1}^{n} P_i \text{ reactants}} \tag{4}$$

CVD normally involves a multi-component and a multi-phase system. There are various ways to calculate thermodynamic equilibrium in multicomponent systems.[23] The following is a brief discussion of the optimization method where the minimization of Gibbs free energy can be achieved. The free energy G of a system consisting of m gaseous species and s solid phases can be described by,

$$G = \sum_{i=n_i}^{m} (n_i^g \Delta G_{fig}^{\circ} + RTlnP + 2Tln\frac{n_{ig}}{N_g}) + \sum_{i=1}^{s} n_i^s \Delta G_{fis}^{\circ} \tag{5}$$

where n_i^g number of moles of gaseous species,

n_i^s number of moles of solid species

N_g total number of moles of gaseous species,

P total pressure,

ΔG_{fig}^o Free energy of formation at CVD, temperature of gaseous species,

ΔG_{fis}^o Free energy of formation at CVD, temperature of solid species.

The objective of optimization calculations is to determine the set of (n_i) which minimizes G. The solution to the above equation can be made using computer based programs such as SOLGAGMIX-PV[24,25] and FACT.[26] The accuracy and usefulness of the thermodynamic calculations depends strongly on the accuracy of the thermochemical data used. The database for these computer based programs are derived from various sources[27-29] and JANAF tables[27] which consists of thermal and formation functions. Both these functions are temperature dependent. Thermal functions are heat capacity, enthalpy increments, entropy, and Gibbs energy function. The formation functions consists of enthalpy of formation, Gibbs energy of formation, and the logarithm of the equilibrium constant of formation.

$$\Delta_f H^{\circ}(T) = \Delta_f H^{\circ}(298.15K) + [H^{\circ}(T) - H^{\circ}(298.15K)]_{compound} - \sum [H^{\circ}(T) - H^{\circ}(298.15K)]_{elements} \tag{6}$$

The Gibbs energy of formation is readily calculated from the enthalpy of formation when the entropies of the elememts are known. Thus,

$$\Delta_f G^{\circ}(T) = \Delta_f H^{\circ}(T) - T\{S^{\circ}(T)_{compound} - \sum S^{\circ}(T)_{elements}\} \tag{7}$$

The logarithm of the equlibrium constant of formation is thus found from the relation,

$$\Delta_f G^o(T) = -RT\ ln\ k_f \tag{8}$$

Figure 3 shows a typical JANAF thermochemical table for Al_2O_3.[27] This type of data is made available in the computer database. With specified temperature, pressure and input concentrations, the equilibrium compositions of gaseous and solid phases can be obtained. These calculations can then be used to determine the

Aluminum Oxide, Alpha (Al_2O_3) — Al_2O_3(Cr)

Enthalpy Reference Temperature = T_r = 298.15 K — Standad State Pressure = p° = 0.1 MPa

T/K	$C_p°$	S°	-[G°-H°(T_r)]/T	H°-H°(T_r)	Δ_fH°	Δ_fG°	Log K_f
	$JK^{-1}mol^{-1}$			kJ mol^{-1}			
0	0	0	Infinite	-10.020	-1663.608	-1663.608	Infinite
100	12.885	4.295	101.230	-9.693	-1668.606	-1641.642	857.506
200	51.120	24.880	57.381	-6.500	-1673.383	-1612.656	421.183
298.15	79.015	50.950	50.950	0	-1675.692	1582.275	277.208
300	79.416	51.440	50.951	0.147	-1675.717	-1581.698	275.398
400	96.088	76.779	54.293	8.995	-1676.342	-1550.226	202.439
500	106.131	99.388	61.098	19.145	-1676.045	-1518.718	158.659
600	112.545	119.345	69.177	30.101	-1675.300	-1487.319	129.483
700	116.926	137.041	77.632	41.586	-1674.391	-1456.059	108.652
800	120.135	152.873	96.065	53.447	-1673.498	-1424.931	93.038
900	122.662	167.174	94.296	65.591	-1672.744	-1393.908	80.900
1000	124.771	180.210	102.245	77.965	-1693.394	-1361.437	71.114
1100	126.608	192.189	109.884	90.535	-1692.437	-1328.286	63.075
1200	126.252	203.277	117.211	103.280	-1691.366	-1295.228	56.380
1300	129.737	213.602	124.233	116.180	-1690.190	-1262.264	50.718
1400	131.081	223.267	130.965	129.222	-1688.918	-1229.393	45.869
1500	132.290	232.353	137.425	142.392	-1687.561	-1196.917	41.670
1600	133.361	240.925	143.628	155.675	-1686.128	-1163.934	37.999
1700	134.306	249.039	149.592	169.060	-1684.632	-1131.342	34.762
1800	135.145	256.740	155.333	182.533	-1683.082	-1098.841	31.888
1900	135.896	264.067	160.864	196.085	-1681.489	-1066.426	29.318
2000	136.608	271.056	166.201	209.710	-1679.858	-1034.096	27.008
2100	137.319	277.738	171.354	223.407	-1678.190	-1001.849	24.920
2200	138.030	284.143	176.336	237.174	-1676.485	-969.681	23.023
2300	138.741	290.294	181.158	251.013	-1674.743	-937.593	21.293
2327.000	138.934	291.914	182.434	254.761	-----Alpha ↔ Liquid-------		
2500	140.206	301.922	190.360	278.905	-1671.142	-873.645	18.254
2600	140.959	307.435	194.757	292.963	-1669.279	-841.781	16.912
2700	141754	312.770	199.030	307.098	-1667.369	-809.990	15.670
2800	142.591	317.940	203.185	321.315	-2253.212	-776.335	14.483
2900	143.511	322.960	207.229	335.620	-2249.002	-723.665	13.035
3000	144.474	327.841	211.166	350.019	-2244.729	-671.139	11.686

Fig. 3: A typical JANAF thermochemical table for Al_2O_3.[27]

range of input conditions which will produce a specific condensed phase(s) at equilibrium.[30-35] This type of information can be represented by what has been known as "CVD Phase Diagrams".[19,20,36-38] These phase diagrams are therefore very useful in providing the range of process parameters.

For better understanding of the CVD phase diagrams, examples based on single component system such as tungsten carbide coating and multi-component system such as mullite coating are discussed below for various process conditions.

Tungsten carbide (WC) is known as refractory carbide and is widely used in cutting tool industry. Deposition of WC is considered according to the following chemical reaction using the WF_6-H_2-CH_4-Ar system.

$$WF_{6(g)} + H_{2(g)} + CH_{4(g)} \rightarrow WC_{(s)} + 6HF_{(g)} \quad (9)$$

The thermodynamic calculations were made at temperatures from 500-1200°C and total pressure from 20-200 torr.[19] The CVD phase diagrams (Figure 4) is a plot of the equilibrium condensed phases which are based on the WF_6 and CH_4 concentrations. It is observed that as the temperature decreases, the WC phase region expands. As the pressure increases, the WC phase region shifts toward a higher concentration of CH_4. Thermodynamic calculations predict that at a particular CH_4 concentration, WC or WC + C will form. The line delineating the W_2C + WC or the W_2C region from the WC region shows a linear relation to the WF6 concentration at higher W concentration. This can be expressed as,

$$X_{CH_4} = a + bX_{WF_6} \quad (10)$$

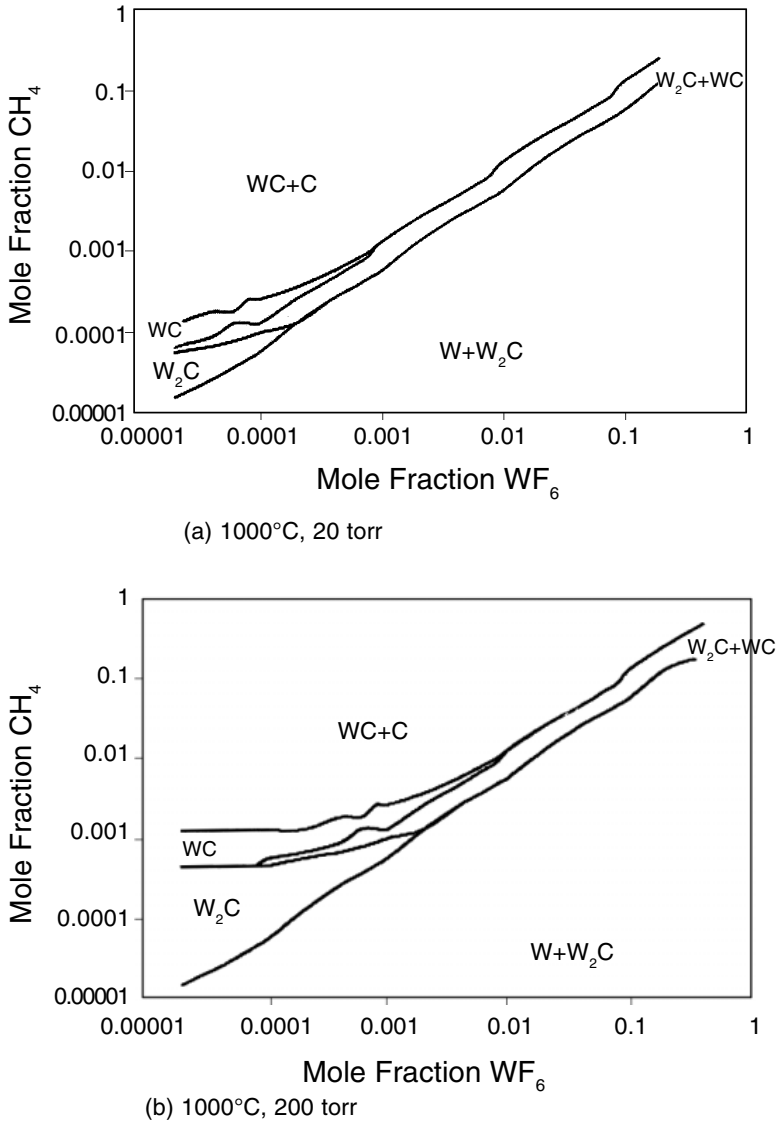

Fig. 4: CVD phase diagrams of the WF_6-H_2-CH_4-Ar system at 1000°C (a) 20 torr and (b) 200 torr.[19]

where a = 0.000511, and b = 1.15 for the conditions 900°C and 20 torr. Using the CVD phase diagrams, the initial experimental conditions were established. Experiments were carried out using WF_6 concentration of 0.00165 and CH_4 concentration of 0.0110 at 20 torr and at various temperatures. At a temperature of 850°C a mixture of W_2C and WC was obtained, monolithic hexagonal WC was obtained at temperature greater than 950°C. As expected the experimental results were not in total agreement with the phase diagrams. Monolithic WC could not be deposited below 900°C, rather, W_2C and W_3C are obtained. This is due to the slow decomposition rate of the CH_4 and the increased stability of hydrocarbons in the gas phase at lower temperatures. A typical SEM micrograph of the cross-section of the WC coating on a WC/Co substrate using the WF_6-H_2-CH_4-Ar system is shown in Figure 5.

Similarly, CVD phase diagrams for the mullite coatings from the $AlCl_3$-$SiCl_4$-CO_2-H_2

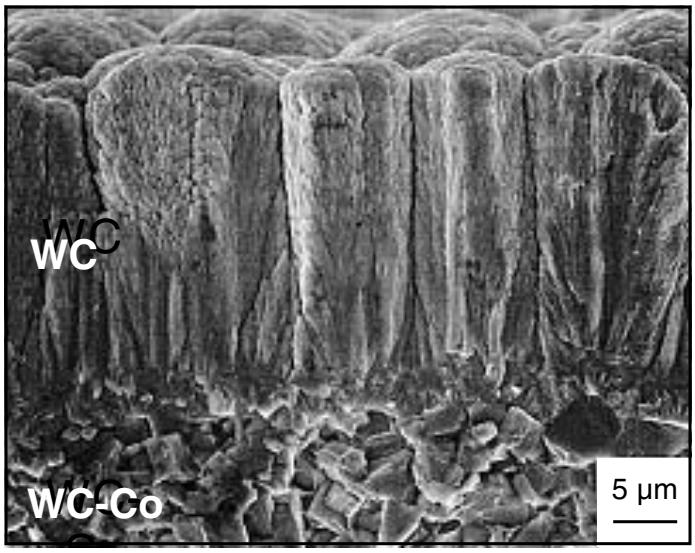

Fig. 5: Scanning electron micrograph of the cross-section of a typical WC coating on WC-Co using WF_6-H_2-CH_4-Ar system.[19]

system at various conditions are illustrated in Figure 6.[20] Mullite has been targeted as one of the prime protective coating materials for silicon based ceramics such as SiC and Si_3N_4 for elevated temperature applications. The overall chemical reaction for mullite coating using the $AlCl_3$-$SiCl_4$-CO_2-H_2 system is,

$$6AlCl_{3(g)} + 2SiCl_{4(g)} + 13CO_{2(g)} + 13H_{2(g)} \rightarrow 3Al_2O_3 \cdot 2SiO_{2(s)} + 13CO_{(g)} + 26HCl_{(g)} \quad (11)$$

Figure 6 shows a ternary CVD phase diagram of the $AlCl_3$-$SiCl_4$-CO_2-H_2 system at 1000°C and 75 torr. As is evident, Al_2O_3-based products are formed along the $AlCl_3$-CO_2 line and SiO_2-based products along the $SiCl_4$-CO_2 line. Pure oxides are predicted to form at high CO_2 concentrations, oxides + carbon in the medium CO_2 concentration, and oxides + carbides in the low CO_2 concentration. Excess carbon in the low CO_2 portion of the diagram can be attributed to the lack of availability of O_2 in the reaction to form the gaseous by-product CO. The calculations were made keeping the molar ratio of H_2:($AlCl_3$-$SiCl_4$-CO_2) at 5:1. According to the phase diagram, pure mullite can be obtained only as a line compound, between the mullite + Al_2O_3 and mullite + SiO_2 regions. Analysis of the phase diagrams revealed that mullite has higher Gibbs free energy of formation (ΔG = -1470.52 kcal/mole) than both Al_2O_3 (ΔG = -327.48 kcal/mole) and SiO_2 (ΔG = -248.38 kcal/mole). Thus thermodynamics predicted that all the oxygen available might be used to first form mullite, then Al_2O_3, and finally SiO_2. However, due to kinetic limitations this sequence is not observed experimentally. It is therefore projected that mullite can be obtained with these starting reactants if the stoichiometry of $AlCl_3$:$SiCl_4$ is maintained at the same level as that of mullite (Al:Si = 3:1). Similarly, thermodynamic calculations made at lower temperature, 800°C, predicted the formation of sillimanite ($Al_2O_3 \cdot SiO_2$) instead of mullite. Lower pressures are preferred for obtaining carbon-free mullite deposits as carbon has a higher affinity to form gaseous products such as CH_4 at lower pressure than forming a solid deposit. In order to optimize the process parameters, concentration and deposition efficiency curves (Figure 7) can be constructed, for example along the region marked by section AA of the phase diagram

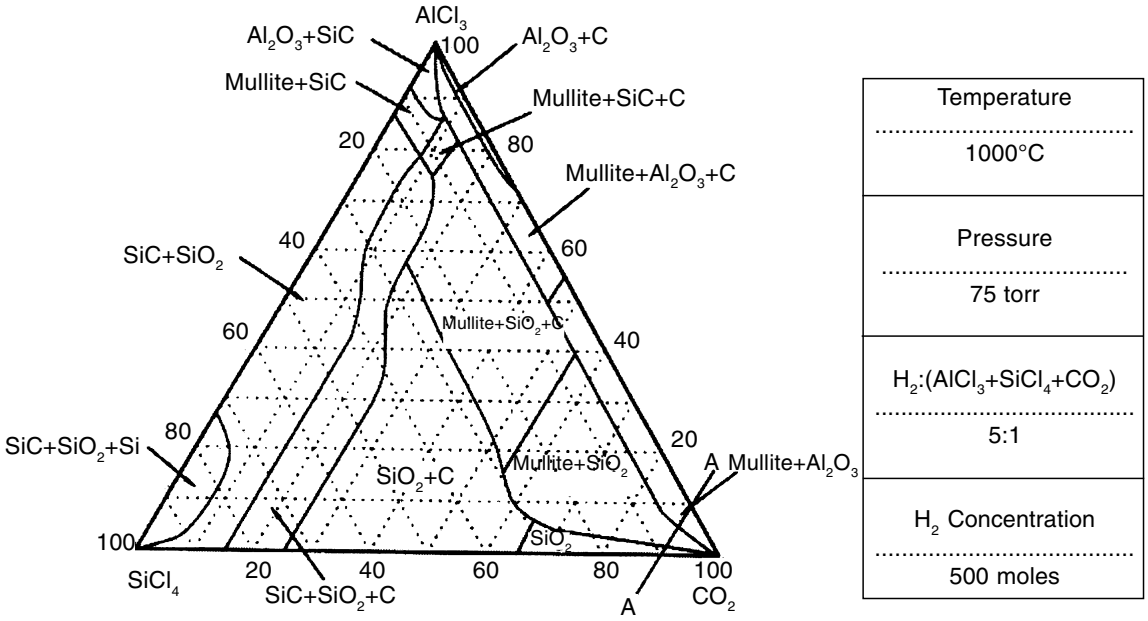

Fig. 6: CVD ternary phase diagram of the $AlCl_3$-$SiCl_4$-CO_2-H_2 system at 1000°C and 75 torr.[20]

(Figure 6). Accordingly, the initial process parameters were set CO_2 concentration at 90 moles and total chloride ($AlCl_3$ + $SiCl_4$) concentration at 10. A cross-section of a typical mullite coating on SiC at 950°C and 75 torr is shown in Figure 8. Figure 9 shows the cross-sectional TEM and electron diffraction pattern of a typical mullite coating on SiC. Initially at the substrate/coating interface a nano-crystalline zone is observed which converts to crystalline mullite when Al:Si = 3:1 in the coating. Various studies on CVD mullite coatings can be found from previous publications.[6,20,39-44]

CVD phase diagrams constructed using the SOLGAS-MIX-PV/FACT program have been shown to be powerful tools in the systematic development of CVD coatings. Their primary benefit is to initially establish the feasibility of a particular system and establish initial process parameters to obtain a particular deposit. Since equilibrium thermodynamics is used to generate CVD phase diagrams, they can only be used to establish trends because CVD process are typically non-equilibrium. With sufficient calculations the complete range of deposition parameters (temperature, pressure, starting gas composition) over which the CVD reaction is thermodynamically possible can be ascertained.

Kinetics of the CVD

Numerous studies on the kinetics and mechanisms of CVD reactions have been made.[1,12,39,45-48] These studies provide useful information such as activation energy and limiting steps of deposition reactions which are important for the understanding of deposition processes. The main problem in the CVD kinetics studies is the complexity of the deposition process. The difficulty arises not only from the various steps of the CVD process but also from the temperature and concentration gradient, geometric effects, and gas flow patterns in the reaction zones. Exact kinetic analysis is therefore usually not possible as the kinetic data are reactor dependent. There are several possible rate-limiting factors but mass transport and surface kinetics control are the most

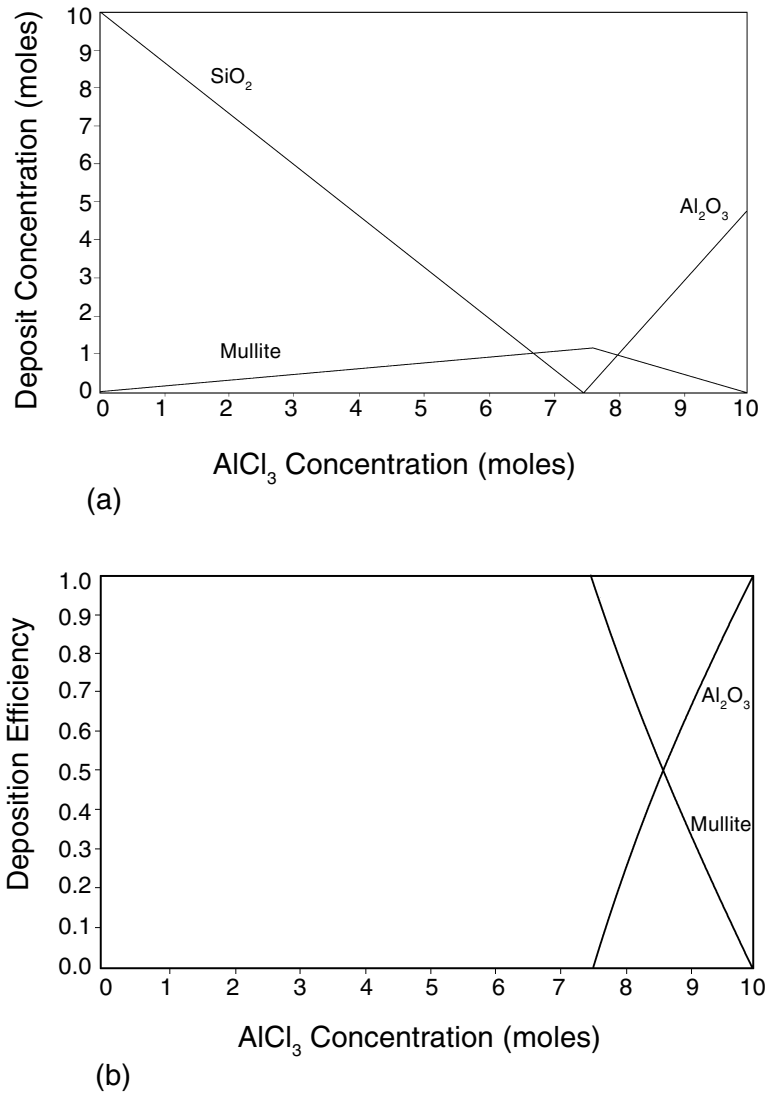

Fig. 7: (a) Concentration and (b) efficiency curves generated at section AA in Figure 6.[20]

predominant.[1,12,47,48] Mass transport control exists if the transport of the reactants/reaction products across the boundary layer determines the deposition rate. If the mass transport though the boundary layer is sufficiently large the system is controlled by surface kinetic reactions.

The reaction kinetics determine the rate at which a phase will form and whether its formation is limited by any step in the process. Figure 10 shows the seven mechanistic steps that have been hypothesized to occur during a vapor deposition process.[1,10,49-51] These steps include:

1. Transport of reactant gases into the reaction chamber,
2. Intermediate reactants form from reactant gases,
3. Diffusion of reactant gases through the gaseous boundary layer to the substrate,
4. Absorption of gases onto the substrate surface,
5. Single or multi-step reactions at the substrate surface,

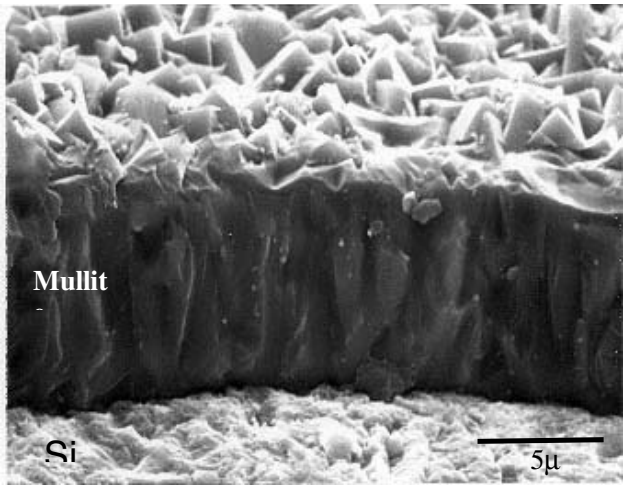

Fig. 8: Scanning electron micrograph of the cross-section of a typical mullite coating on SiC using $AlCl_3$-$SiCl_4$-CO_2-H_2 system at 950°C and 75 torr.

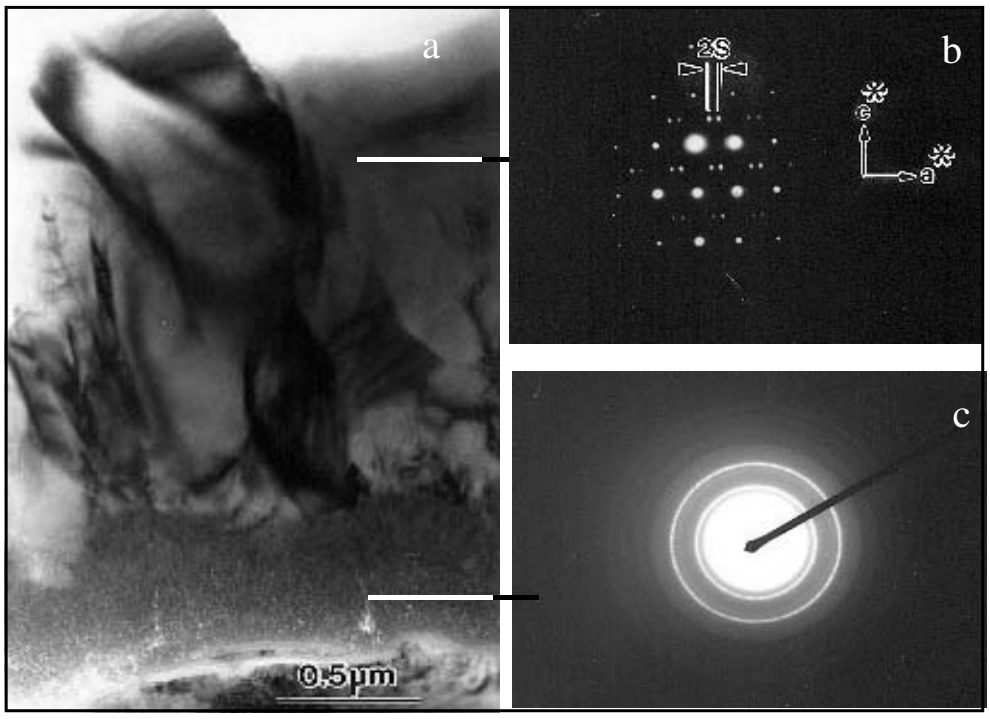

Fig. 9: (a) Cross-sectional TEM micrograph of CVD mullite coating on SiC with diffraction patterns from the two regions of the coating, (b) crystalline mullite, and (c) vitreous nano-crystalline layer.

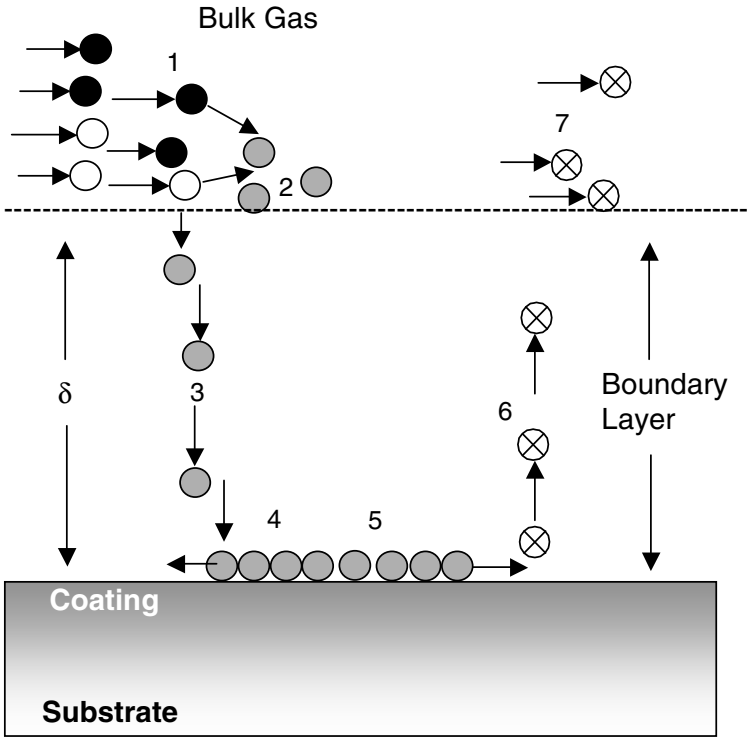

Fig. 10: Schematic diagram of the mechanistic steps that occur during the CVD process.

6. Desorption of product gases from the substrate surface, and
7. Forced exit of product gases from the system.

In this model, the steps can be classified into two categories, mass transport[1,3 and 7] and surface reaction steps.[2,4,5, and 6] The slowest of these steps determines if the process is mass transport or surface reaction limited. At lower temperatures the deposition rate is generally surface reaction limited. As the temperature increases, the surface reaction rate rises exponentially, resulting in a mass transport limited because transport becomes the slowest step in the series of deposition steps. Reaction resistances are often used to predict rate-limiting steps in CVD process.

If the process is mass transport limited, a typical rate limiting step can be diffusion of reactant species through the boundary layer. According to Fick's law, the reactant flux can be written as,

$$J_A = -\frac{D_{AB}}{RT}\frac{dc_A}{dx} \tag{12}$$

where J_A is the diffusion flux of specie A, D_{AB} is the diffusivity of the reactants, C_A is the concentration of specie A, x is the direction perpendicular to the substrate surface, *R* is the gas constant, and *T* is the absolute temperature. An approximation for the concentration gradient is,

$$\frac{dc_A}{dx} \approx \frac{\Delta c_A}{\Delta x} = \frac{c_{A_B} - c_{A_S}}{\delta} \tag{13}$$

where C_{A_B} is the bulk stream concentration of specie A and C_{A_S} is the surface concentration of specie A, and δ is the boundary layer thickness. Thus, the reactant diffusion through the boundary layer is described as,

$$J_A = -\frac{D_{AB}}{RT}\left(\frac{C_{A_B} - C_{A_S}}{\delta}\right) \tag{14}$$

The binary diffusivity, D_{AB}, of the reactants in which the Leonard-Jones parameters (σ, Ω) are available, is calculated through the Chapman-Enskog theory[52] by,

$$D_{AB} = 0.0018583 \frac{\sqrt{T^3(\frac{1}{M_A} + \frac{1}{M_B})}}{p\sigma_{AB}^2 \Omega_{D,AB}} \quad (15)$$

where T is the absolute temperature, M is the molecular weight, p is the pressure, σ_{AB} is the collision diameter, and $\Omega_{D,AB}$ is the collision integral, a dimensionless function of temperature and intermolecular potential. Multi-component systems are handled by considering an effective binary diffusivity for each species through the gas mixture. The reactant diffusivity in gas mixture is determined from a mass fraction as,

$$\frac{1 - x_1}{D_{im}} = \sum_{j=2}^{n} \frac{x_j}{D_{ij}} \quad (16)$$

where x_i is the mole fraction of the i^{th} species, D_{im} is the effective binary diffusivity for the diffusion of i in a mixture, and D_{ij} is the binary diffusivity for the diffusion of i in j.

In laminar gas flow, the reactant concentrations and gas velocity are zero at the substrate surface and increase to the bulk concentration and bulk stream velocity at some distance, δ, from the substrate surface and is given by,[53]

$$\frac{\delta}{x} = \frac{5.00}{Re^{\frac{1}{2}}} \quad (17)$$

The average boundary layer thickness, $\bar{\delta}$, is then calculated by integrating the above expression[17] over the length of the substrate and dividing the result by the length of the substrate as,

$$\bar{\delta} = \frac{10}{3} \sqrt{\frac{\mu_{mix} L}{\rho U}} \quad (18)$$

where L is the length of the substrate, ρ is the gas density, μ_{mix} is the viscosity of the gas mixture, and U is the free stream velocity. If it is assumed that the gas is well mixed, and there are minimal temperature gradients, then the diffusion path is determined by the concentration boundary layer, δ_c, which is related to the momentum boundary layer and is characterized by a Schmidt number of unity as,

$$Sc^n = \frac{\delta}{\delta_c} = 1 \quad (19)$$

The viscosity of a gas mixture, μ_{mix}, is calculated by,

$$\mu_{mix} = \sum_{i=1}^{n} \frac{x_i \mu_i}{\sum_{j=1}^{n} x_i \Phi_{ij}} \quad (20)$$

in which

$$\mu_i = 2.6693 \times 10^{-5} \frac{\sqrt{MT}}{\sigma^2 \Omega_\mu} \quad (21)$$

where M is the molecular weight, T is the absolute temperature, s is the collision diameter and Ω_μ is the collision integral for viscosity and

$$\Phi_{ij} = \frac{1}{\sqrt{8}} \left(1 + \frac{M_i}{M_j}\right)^{-\frac{1}{2}} \left[1 + \left(\frac{\mu_i}{\mu_j}\right)^{\frac{1}{2}} \left(\frac{M_j}{M_i}\right)^{\frac{1}{4}}\right]^2 \quad (22)$$

where x_i and x_j are the mole fractions of species i and j, n is the number of chemical species, μ_i and μ_j are the viscosities, and M_i and M_i are the molecular weights of i and j respectively.

The kinetics of coating growth is basically dependent on temperatures. A CVD reaction is divided into either surface kinetic or mass transport control. Figure 11 shows a model as how the growth process depends on the surface kinetics and mass control regimes.[54] C_g is the concentration of the bulk gas and C_s is the concentration at the substrate interface. The concentration of the reactants drops from the bulk to the substrate surface and the corresponding mass flux is given by,

$$J_{gs} = h_g(C_g - C_s) \quad (23)$$

where h_g is the gas mass transfer coefficient and is insensitive to variations in temperature. The flux consumed at the surface of the coating growth and can be approximated as first order by,

$$J_s = k_s C_s \quad (24)$$

where k_s is the rate constant for the slowest surface reaction. In a steady state conditions, $J_{gs} = J_s$, so,

$$C_s = \frac{C_g}{1 + \frac{k_s}{h_g}} \quad (25)$$

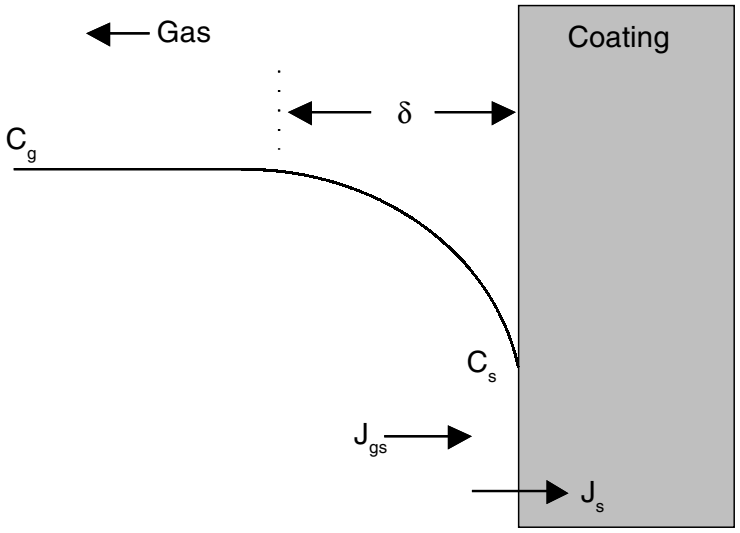

Fig. 11: Schematic diagram of the growth process model.[54]

If $k_s >> h_g$, the system is mass controlled where low gas transport rate through the boundary layer limits the rapid surface reaction. Surface reaction control dominates when $h_g >> k_s$ (C_s approaches C_g), the surface reaction is slow even through sufficient reactant gas is available. Additionally, h_g increases with increasing pressure and decreasing temperature, and k_s follows the Arrhenius equation. Thus surface reaction resistance increases more readily than h_g with decreasing temperature. Therefore surface kinetics control is readily achieved at low temperature, low pressure, low concentration of reactants, and high gas flow rates. Figure 12 show the schematic diagram illustrating the effect of temperature, pressure, and kinetics on the growth rate.[55]

Using these simplified models, process variables can be varied so that the deposition process is either limited by gas-phase diffusion to the substrate surface or by reaction at the substrate. Such control of the process is valuable because, for example, geometric surface irregularities in the substrate (grooves and corners) are coated uniformly in a kinetically controlled process, but in a process controlled by diffusion a protrusion receives a thicker coating while a depression is thinly coated.

The most important aspects of the deposition process are nucleation and growth.[56-59] This phenomena can be understood in terms of the kinetics of formation of the nuclei of a solid phase by the clustering of atoms in a gas phase, followed by the interaction of further vapor atoms with the growing surface. Classical nucleation involves the formation of a critical radius (balancing of Gibbs free energy involved in making the nucleus, and increase in the surface area of the cluster) whereas the critical radius is of atomic dimensions in most CVD reactions because of the high supersaturation.[57, 58, 60] The various steps during the heterogeneous nucleation of an element A on a substrate is schematically shown in Figure 13.[55] Due to reaction between hydrogen and AX, the A atoms formed are absorbed on the surface of the substrate. Surface diffusion and possibly direct impingement of A atoms from the vapor leads to nucleation. Lateral growth and coalescences results in the formation of an adherent coating. Several models have been developed to treat both the two and three dimensional cases.[61-63]

The rate of the nucleation can be calculated from the knowledge of free energy of formation of adatom of size *i* for individual molecules. The

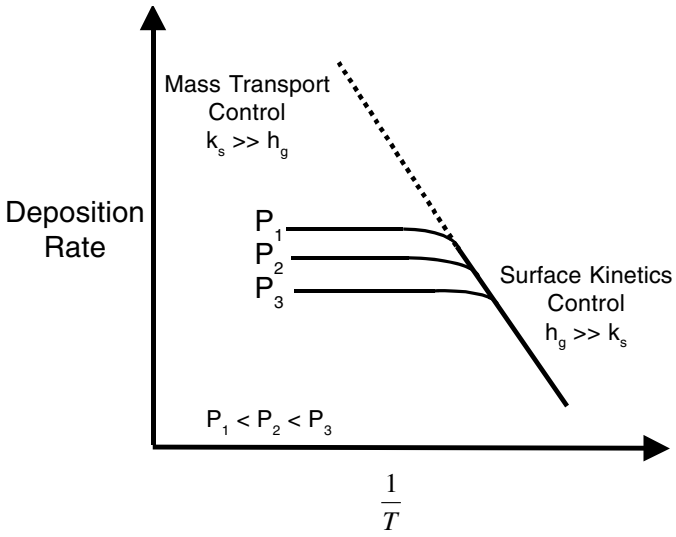

Fig. 12: Schematic diagram illustrating the effect of temperature, pressure and kinetics on the growth rate.[55]

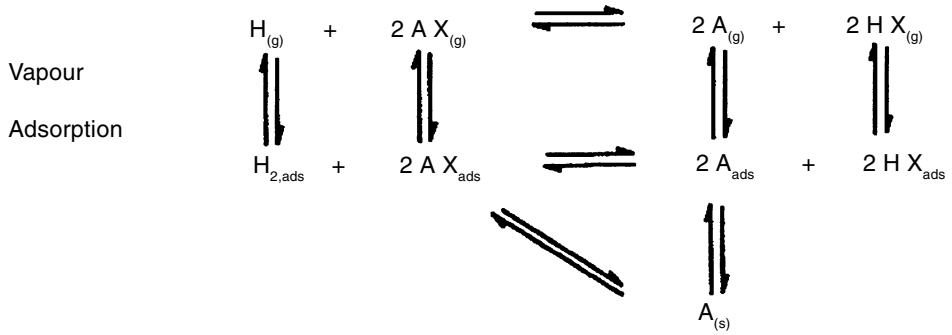

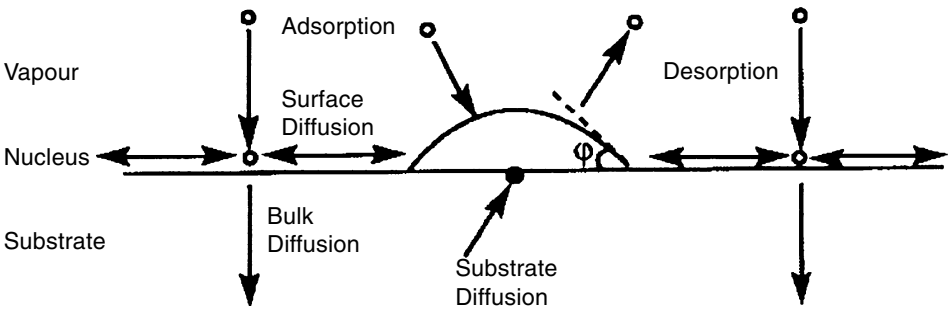

Fig. 13: Schematic representation of the various mechanistic pathways that can occur during the nucleation of A on a substrate during H_2 reduction of AX.[55]

nucleation rate is nothing but the rate at which single molecule collide with cluster of size *i*,

$$J = L^* \, w n_i^* \tag{26}$$

where L^* is the perimeter length of the cluster and is the surface diffusion related impingement rate and is given by,

$$\omega = n_a a \nu_0 \exp\left(\frac{-\Delta G_{sd}}{RT}\right) \tag{27}$$

ν_0 surface vibrational frequency

a jump distance for surface diffusion

and

$$n^* = n_1 \exp\left(\frac{-\Delta G_i^*}{RT}\right)$$

where n^* is the concentration of critical size nuclei.

Thus, the nucleation rate for heterogeneous nucleation is,

$$J = L^* a \nu_0 n_a^2 \exp - \left(\frac{\Delta G_{sd} + \Delta G_i^*}{RT}\right) \tag{28}$$

Based on the TLK (terrace, ledge and kink) model, growth on a perfect vicinal and singular surface proceed by a sequence of steps involving adsorption from vapor to form a surface adatom. This adatom diffuses to a kink site of the surface and incorporate into the crystal at the kink site. In order to determine the growth rate, the rate of formation of stable cluster must be determined. This is the rate at which cluster of radius r* grow by the addition of one incremental atom from the adlayer. The rate is given by,

$$J = Z(2\pi r^*) a n_a^2 \nu_d \exp\left(\frac{-\Delta G_{sd}}{RT}\right) \exp\left(\frac{-\Delta G^*}{RT}\right) \tag{29}$$

where Z is the non-equilibrium factor. It is found in practice that the pre-exponential part of the expression does not differ greatly from system to system and is on the order of e^{65}. The factor that influences *J* with changing *P* and *T* is ΔG^*, within the relation,

$$\Delta G^* = -\frac{RT}{\Omega} \ln\left(\frac{P}{P_0}\right) \tag{30}$$

where $\Omega = \frac{V}{N_{Av}}$ is the volume per atom

Thus, J in terms of $(P/P_0)_{crit}$, where J = 1 per cm^2 per sec lies in the range of (P/P_0), is given by,

$$(P/P_0)_{crit} = \exp\left(\frac{\pi h \Omega \gamma^2}{65 R^2 T^2}\right) \tag{31}$$

where $\gamma = \frac{\varepsilon}{h}$,

ε is the edge surface energy per centimeter of perimeter and *h* is the height of mono-atomic cluster. Thus, $(P/P_0)_{crit}$ is strongly dependent on both γ and T, making the critical factor of the growth of two-dimensional nuclei rate as,

$$\frac{\bar{x}}{\lambda} \tag{32}$$

where $\bar{x}$ is the mean free path for adatom diffusion on the surface and λ is the ledge spacing. This holds when an atom strikes the surface of the same substrate material. If $\lambda >> \bar{x}$, most adatom will desorb before reaching the ledges and the growth rate will be low. When $\bar{x} >> \lambda$, almost all adatom will reach the kink sites and growth rate will approach the ideal growth rate. Below $(P/P_0)_{crit}$, the growth rate will be very low and will rise to ideal rate with increasing $(P/P_0)_{crit}$. When the surface is imperfect, the imperfection allows growth at supersaturations much lower than $(P/P_0)_{crit}$.

The three basic growth modes are shown in Figure 14. Voller-weber or island mode (Figure 14a) is formed when the smallest stable clusters nucleate on the substrate and grow in a three dimensional way. This type of growth takes place when atoms or molecules in the deposit are bound to each other than to the substrate. The layer type of growth (Figure 14b) forms when the atoms or molecules in the deposit attract more strongly to the substrate than to each other. The intermediate mechanism follows with layer + island type growth (Figure 14c). The transition from two to three dimensional growth is not completely understood. This mode could be formed either due to the film substrate lattice mismatch or release of high energy at the deposit-intermediate layer interface. Thus, the composition and structure of the substrate can have a tremendous effect on the initial nucleation and growth of a coating. Figure 15 shows the surface morphologies of the mullite coatings growing under identical conditions on various

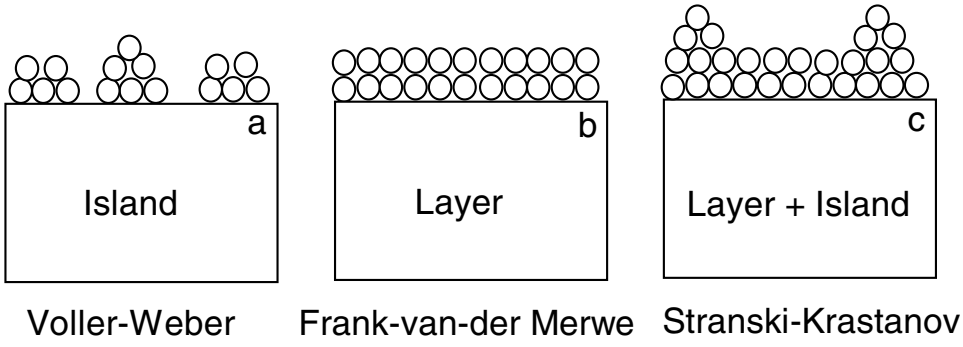

Fig. 14: Schematic diagrams of the three different modes of the thin film growth: (a) island, (b) layer, and (c) layer + island.

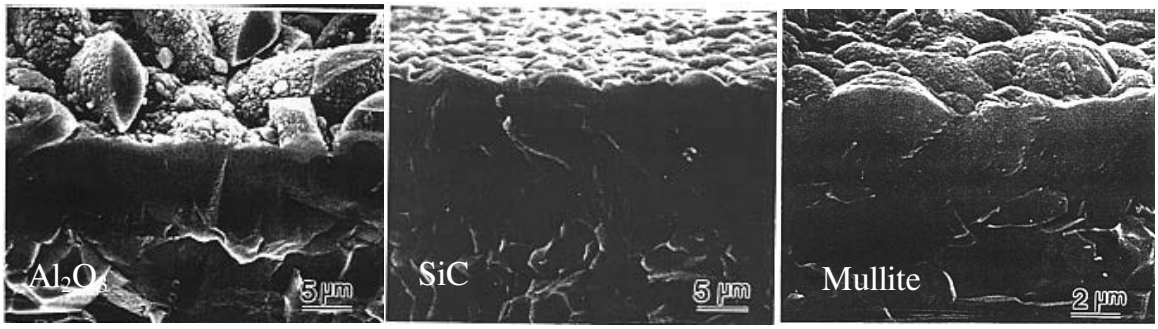

Fig. 15: The effect of substrate on the nucleation and growth of mullite coatings using a the gas mixture of $AlCl_3$-$SiCl_4$-CO_2-H_2.[63]

substrates.[64] As is evident, the nucleation and the growth rate on each of them is very different.

Supersaturation and deposition temperature (diffusion) are the two critical factors that can be effectively used to control the morphology of the coating[65] as can be seen in Figure 16a. The effect of changes in the supersaturation of the reactive gases combined with thermodynamic phase equilibria calculations can be effectively used to understand and therefore control the morphology of the deposit (Figure 16b). It was established that the formation of whiskers or polycrystalline TiC is dependent on the level of free carbon present in the $TiCl_4$-CH_4-H_2 gas mixture. A typical cross-section of a TiC coating and surface morphology of the TiC whiskers are shown in Figure 16. Control of the coatings microstructure is, of course, imperative to optimize its mechanical properties.[65-69] The most desirable coatings for structural applications (mechanical strength and fracture toughness) consist of very fine, equiaxed grains. Epitaxial deposits result from conditions of low reactant concentrations and sufficiently rapid surface diffusion. Deposits consisting of randomly oriented fine grains near the substrate surface which grow into larger columnar grains of preferred orientation at higher reactant concentrations and more limited diffusion.[70] This microstructure can typically be produced at still

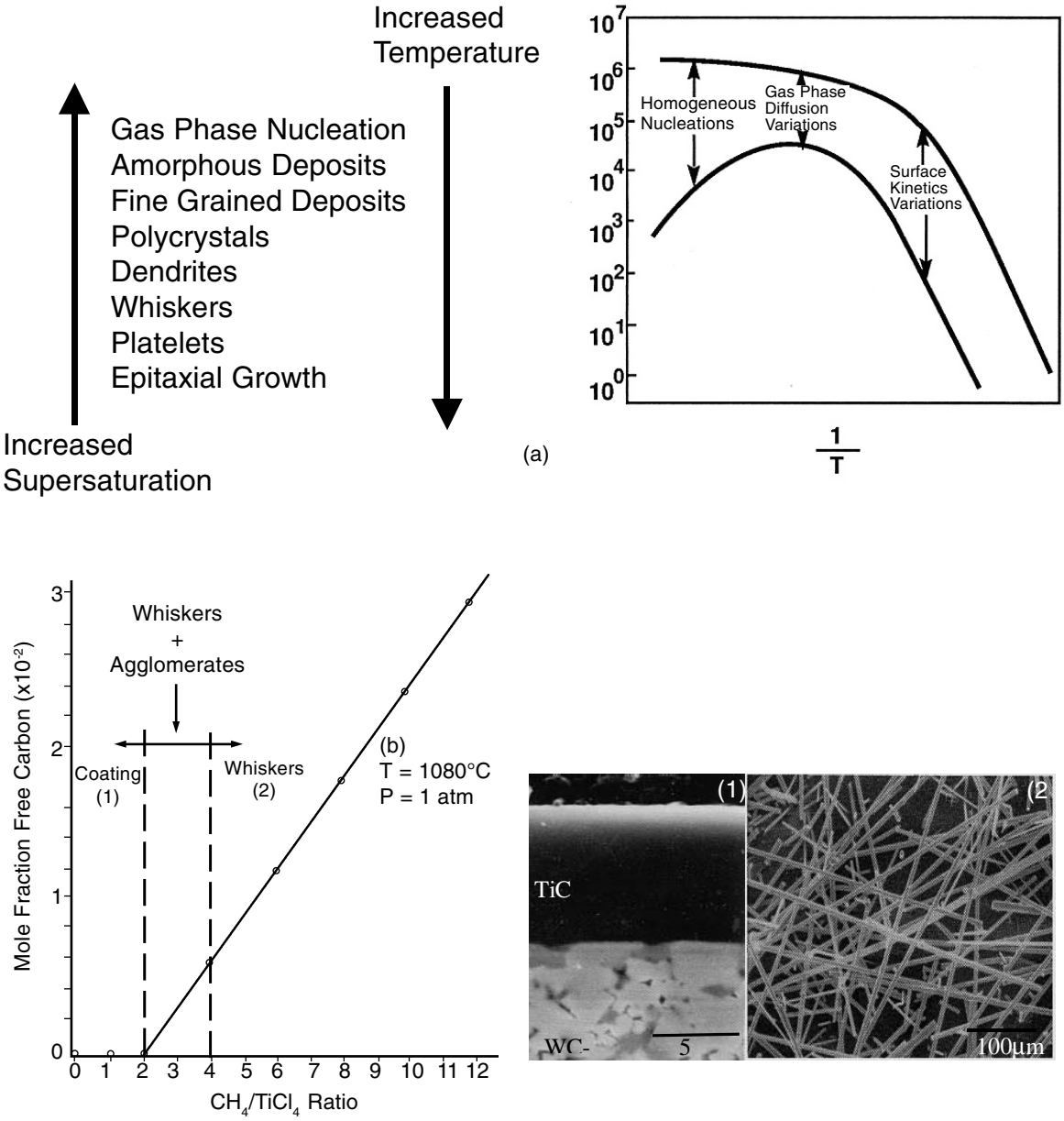

Fig. 16: (a) Effect of supersaturation-temperature-structure relationship on the vapor deposited coatings,[65] (b) the effect of free carbon on the morphology of the TiC deposition for a gas mixture of $TiCl_4$, CH_4 and H_2, (1) cross-section of the TiC coating on WC-Co, and (2) surface morphology of the TiC whiskers.

higher concentrations and conditions under which surface diffusion is limited.

Conclusions

This chapter discusses the thermodynamic and kinetics of the CVD process with particular emphasis on structural applications. Thermodynamic calculations can be used to guide and find the range of initial process parameters. Kinetically the CVD process is very complex and most established mechanisms are still some what controversial. Nevertheless, a insight into surface kinetic reactions, mass

transport phenomena, nucleation, and growth of the coating is necessary and helpful in the development of new or improved coatings. Knowledge of these basic principles involved in the CVD process are deemed necessary both for systematic development of coatings and for the pragmatic utilization of the CVD process itself.

References

1. K.F. Jensen, *Microelectronics Processing: Chemical Engineering Aspects*, D.W. Hess and K.F. Jensen, eds., American Chemical Society, Washington, DC, 1989, p.199.
2. K.H. Habig, *Journal of Vaccum Science Technology A,* Vol.4, No.6, 1986, p.2932.
3. V.K. Sarin, H.E. Hintermann and G. Gindraux, *US Patent 4,745,010,* 1988.
4. V.K. Sarin, H.E. Hintermann and G. Gindraux, *US Patent 4,751,109,* 1988.
5. W.A. Bryant, *Journal of Materials Science,* Vol.12, 1977, p.1285.
6. M.L. Auger and V.K.Sarin, *Proceedings of the 14th International Confernce on Chemical Vapor Deposition*, Paris, France, The Electrochemical Society, Pennington, NJ, 1997, p.302.
7. H.O. Pierson, *Proceeding of Advanced Materials Manufacture,* Vol.3, No.1, 1988, p.107.
8. K.K. Yee, Int. *Met. Rev*., Vol.1, 1978, p.19.
9. M.L. Hammond, *Solid State Technol.,* Vol.11, 1979, p.61.
10. J.O. Carlsson, *Less-Common Met.,* Vol.71, 1980, p.15.
11. J. Korec and M. Heyen, *Journal of Cryst. Growth,* Vol,60, 1982, p.286.
12. K.E. Spear, *Journal of Pure Appl. Chem.,* Vol.54, No.7, 1982, p.1297.
13. W.L. Holstein, J.L. Fitzjohn, E.J. Fahy, P.W. Gilmour, and E.R. Schmelzer, *Journal of Cryst. Growth,* Vol.94, 1989, p.131.
14. W.B. White, W.M. Johnsson and G.B. Dantzig, Journal *of Chem. Phys.,* Vol.28, 1958, p.751.
15. G. Eriksson, *Acta Chem. Scand.,* Vol.25, 1971, p.2651.
16. C. Bernard, *Proceedings of the 8th International Conference on CVD,* Gouvieux, France, The Elecrrochemical Society, Pennington, NJ,1981, p.3.
17. P. Sourdiaucourt, A. Derre, P. David, P. Delhaes, *Proceedings of the 14th International Confernce on Chemical Vapor Deposition*, Paris, France, The Electrochemical Society, Pennington, NJ, 1997, p.31.
18. E.Blaquet, A.M.Dutron, C.Bernard, G.Llauro and R.Hillel, *Proceedings of the 14th International Confernce on Chemical Vapor Deposition*, Paris, France, The Electrochemical Society, Pennington, NJ, 1997, p.23.
19. Mark Fitzsimmons and Vinod K Sarin, *Surface and Coating Technology*, Vol.76-77, 1995, p.250.
20. R.P. Mulpuri and V.K. Sarin, *Journal of Materials Research*, Vol.11, 1996, p.1315.
21. John L. Vossen and Werner Kern, *Thin Film Processes*, Academic Press, New York, 1978, p.257.
22. C. Bernard, *Proceedings of the Eighth International Conference on Chemical Vapor Deposition,* J.M. Blocher, G.E. Vuillard, G. Wahl eds., Electrochemical Society, New York, 1981, p.3.
23. F. Van Zeggeren and S.H.Storey, *The Computation of Chemical Equilibria*, Cambridge University Press, London and New York, 1970.
24. G. Eriksson, *Chem. Sc*., Vol.8, 1975, p.100.
25. T.M. Besmann, Rep. ORNL/TM-5775, Oak Ridge National Laboratory.
26. C.W. Bale, A.D. Pelton, and W.T. Thompson, F*A*C*T 2.1, Ecole Polytechnique de Montreal/Royal Military College, Canada, 1996.
27. M.W. Chase, Jr., C.A. Davies, J.R. Downey, Jr., D.J. Frurip, R.A. McDonald, and A.N. Syverud, JANAF Thermochemical Tables, 3rd Edn., National Bureau of Standards, NSRDS, 1985.
28. A.D. Mah, Bureau of Mines Report of Investigation BM-RI-6337, 1963.
29. I.Barin and O.Knacke, Thermochemical Properties of Inorganic Substances, Springer, Berlin, 1973.

30. L. Vandenbulcke, *Journal of Electrochem. Society,* Vol.128, 1981, p.1584.
31. F. Teyssandier, M. Ducarrior and C. Bernard, *Journal of Less-Common Met.,* Vol.78, 1981, p.269.
32. A.I. Kingon, L.J. Lutz and R.F. Davis, *Journal of American Ceramic Society,* Vol.66, No.8, 1983, p.551.
33. A.I. Kingon, L.J. Lutz, P. Liaw and R.F. Davis, Journal *of American Ceramic Society,* Vol.66, No.8, 1983, p.558.
34. F. Teyssandier, M. Ducarrior and C. Bernard, *Journal of Less-Common Met.,* Vol.78, 1981, p.269.
35. T.M. Besmann and K.E. Spear, *Journal of Electrochem. Soc.,* Vol.124, 1977, p.786.
36. K.E. Spear, *Proceedings of the 7th International Conference on CVD*, T.O. Sedgwick and H. Lydtin, eds., Electrochemical Society, Pennington, NJ, 1979, p.1.
37. E. Randich and T.M. Gerlach, *Thin Solid Films,* Vol.75, 1981, p.271.
38. H. Hannache, R. Naslain, and C. Bernard, *Journal of Less-Common Met.,* Vol.95, 1983, p.221.
39. V.K. Sarin and R.P. Mulpuri, *U.S. Patent No.*576008, 1998.
40. M.L. Auger and V.K. Sarin, *Surface and Coatings Tech.*, Vol.94-95, 1997, p.46.
41. A.K. Pattanaik and V.K. Sarin, *Surface Modification Technologies,* T.S. Sudarshan, K.A. Khor, and M. Jeandin, eds., ASM International, Materials Park, Ohio, Vol.12, 1998, p.91.
42. S.N. Basu, A.K. Pattanaik, and V.K. Sarin, *Emerging Trends in Corrosion Control*, A.S.Khanna, K.S.Sharma and A.K.Sinha, eds., NACE International (India Section), Academia Books International, New Delhi, India, Vol.2, 1999, p.1016.
43. Ping Hou, S.N. Basu and V.K. Sarin, *Journal of Mater.Res.*, Vol.14, No.7, 1999, p.2952.
44. S.N. Basu, Ping Hou, and V.K. Sarin, *International Journal of Refractory Metals and Hard Materials*, Vol.16, 1998, p.343.
45. J. Arndt and G. Wahl, *Proceedings of the 14th International Confernce on Chemical Vapor Deposition*, Paris, France, The Electrochemical Society, Pennington, NJ, 1997, p.147.
46. Francis Teyssandier and Mark D. Allendorf, *Proceedings of the 14th International Confernce on Chemical Vapor Deposition*, Paris, France, The Electrochemical Society, Pennington, NJ, 1997, p.15.
47. C.H.J. van den Breckel, *Acta Electron.,* Vol.21, 1978, p.209.
48. W.A. Bryant, *Surface Modification Engineering,* R. Kossowsky, ed., CRC Press, Boca Raton, FL, Vol.1, 1989, p.199.
49. V.K. Sarin, *Surface and Coating Technology*, Vol.73, 1995, p.23.
50. K.E. Spear, *Proceedings of 5th Eurpean Conference on CVD*, J.O. Carlsson and J. Lindstom, eds., Uppsala, Sweden, 1985.
51. M.E. Jones and D.W. Shaw, *Treatise on Solid State Chemistry,* N.B. Hannay, Plenum Press, NY, Vol.5, 1975, p.283.
52. R.B. Bird, W.E. Stewart, and E.N. Lightfoot, *Transport Phenomena,* Wiley, NewYork, 1960, p.495.
53. F.M. White, *Fluid Mechanics*, McGraw Hill Book Company, New York, *2nd* edn., 1986.
54. Milton Ohring, *The Material Science of Thin Films*, Academic Press, San Diego, 1992.
55. V.K. Sarin, *Journal of Hard Materials,* Vol.2, No.1-2, 1991, p.115.
56. J.H. Oxley, *Transport Processes in Vapor Deposition*, C.F. Powell, J.H. Oxley, and J.M. Blocher, Jr, *eds*., John Wiley & Sons, New York, 1966.
57. J.P. Hirth, *Am. NYAcad. Science,* Vol.101, 1963, p.805.
58. D. Walton, *Journal of Chem. Phys.,* Vol.37, 1962, p.2182.
59. J.P. Hirth and G.M. Pound, *Prog. Mater. Science,* Vol.2, 1963, p.41.
60. J. Bloem and W.A.P. Claassen, *Philips Tech. Rev.,* Vol.41, 1983, p.60.
61. J.B. Hudson, *Surface Science: An Introduction*, Butterworth-Heinemann, Stoneham, MA, 1992.
62. C.E. Neugebauer, *Handbook of Thin Film Technology*, L.I. Maissel and R. Glang, eds., McGraw-Hill, New York, 1970.
63. J.A. Venables, G.D.T. Spiller, and M. Hanbrucka, *Rep. Prog. Phys.,* Vol.47, 1988, p.399.

Chemical Vapor Deposition
Jong-Hee Park, T.S. Sudarshan, editors, p45-80
DOI:10.1361/chvd2001p045

Chapter 3

Stresses and Mechanical Stability of CVD Thin Films

M. Ignat
L.T.P.C.M. - E.N.S.E.E.G. BP. 75
Domaine Universitaire
38402 Saint Martin d'Héres, Cedex, France

Introduction

The use of thin films and coatings obtained by Chemical Vapor Deposition (CVD) expands continuously. Nowadays it includes rather different technological applications such as tribological applications, microelectronics or biotechnologies.

However, to consider any of the mentioned applications, a certain number of problems have to be understood and solved. Indeed, film on substrate systems are subjected to internal stresses produced by thermoelastic mismatch, or to external mechanical stresses applied monotonically or cyclically. Then they are likely to be damaged by mechanisms that produce bulk and/or interface failures. For example, after their deposition the mechanical stability of the films on their substrates, remains initially an essential point which defines their reliability.

The evolution of the mechanical stresses in the film on substrate systems and the related mechanisms: cracking, debonding, plastic relaxation, have been assembled with the notion of *Mechanical Stability,* which was introduced by Klokholm.[1] Using brittle fracture energy criteria,[2,3] this author demonstrated that the bulk cracking of a film and its detachment from the substrate are controlled by the intensity of the stored elastic energy. In the case of a thin film subjected to in plane isotropic stress, the elastic energy 'U' stored per unit area of film is expressed by the following relation:

$$U = \frac{1-\nu_f}{E_f}(\sigma_f)^2 h \quad (1)$$

in which σ_f is the normal stress component in the plane of the film. E_f, ν_f and h represent respectively Young's modulus, Poisson's coefficient and the thickness of the film. The film becomes mechanically unstable when the stored elastic energy reaches a critical value. For example, a film subjected to a tensile stress, cracks when U is equal to the film's bulk cracking energy. Conversely, a film subjected to a compressive stress may become detached when U is equal to the interface cracking energy.

The mechanical stability of the film therefore depends either on its bulk resistance to cracking or on its interface stability. Its bulk resistance may be characterized by the mechanics of continuous and homogeneous media failure. In contrast, analyzing its interface stability involves modeling the mechanics of non-homogeneous media failure,[4] and sometimes taking into account factors that are intrinsically linked with the nature of the interface. These factors, such as roughness[5] and the reactivity or crystallinity of media in contact govern adhesion, a parameter that cannot be reduced to a specific physical value.

Qualitatively speaking, the term *adhesion* designates the cohesion between two media, whether they be identical or not. However, it is more difficult to give a quantitative definition. This concept may be understood from three complementary angles:[6] fundamental adhesion, thermodynamic adhesion and experimental adhesion.

Fundamental adhesion is connected with the nature of the bonds producing cohesion between two media. These bonds may be classified into two categories, namely strong bonds (polar, covalent and metallic bonds) and secondary bonds (hydrogenous and Van der Waals bonds).[7] Different atomic or molecular models have been proposed to describe the electronic structure of interfaces.[8-10] None however, is sufficient for calculating the intensity of adhesion forces for systems of practical interest.

Thermodynamic adhesion is defined as the reversible work W_{ad} needed to create an interface of unit area between two media, A and B. It is often referred to as "adhesion work" in wettability studies[11] and is expressed by Dupré's relation:[12]

$$W_{ad} = \gamma_A + \gamma_B - \gamma_{AB} \quad (2)$$

where γ_A and γ_B are the free surface energies of the media A and B and γ_{AB} the free energy of the interface A/B.

Lastly, experimental adhesion is quantified by an interface cracking energy.[13] This energy is measured during mechanical adhesion tests. For a film/substrate system, the principle of such tests involves imposing a mechanical stress at the interface either through the film or substrate and then detecting the critical threshold above which interface failure begins to occur. Unfortunately, the wide variety of adhesion tests currently used means that the values of the interface cracking energy measured for the same system are often extremely scattered.[14]

To optimize the mechanical stability of a film deposited on a substrate or of a multilayer system, it is therefore necessary to understand the mechanisms causing bulk and interface damage. An analysis of this kind involves using a series of appropriate and complementary mechanical tests.

The results obtained from preliminary studies[15-16] have opened up new prospects for research into the mechanical behavior of CVD thin films.

Residual Stresses and Damage

The first mechanical problems of a fundamental nature may occur as soon as the thin film is deposited on the substrate, even before any further processing (as engraving for films intended for microelectronics). The film is far less rigid than the substrate at this point. In the absence of any external mechanical stress, the elastic interaction between film and substrate generates mechanical stresses. These are commonly referred to as "internal stresses" or "residual stresses". The latter expression will be adopted in this chapter. The deposited film is thin and homogeneous, and the residual stresses are considered to be flat and constant through the thickness of the film.

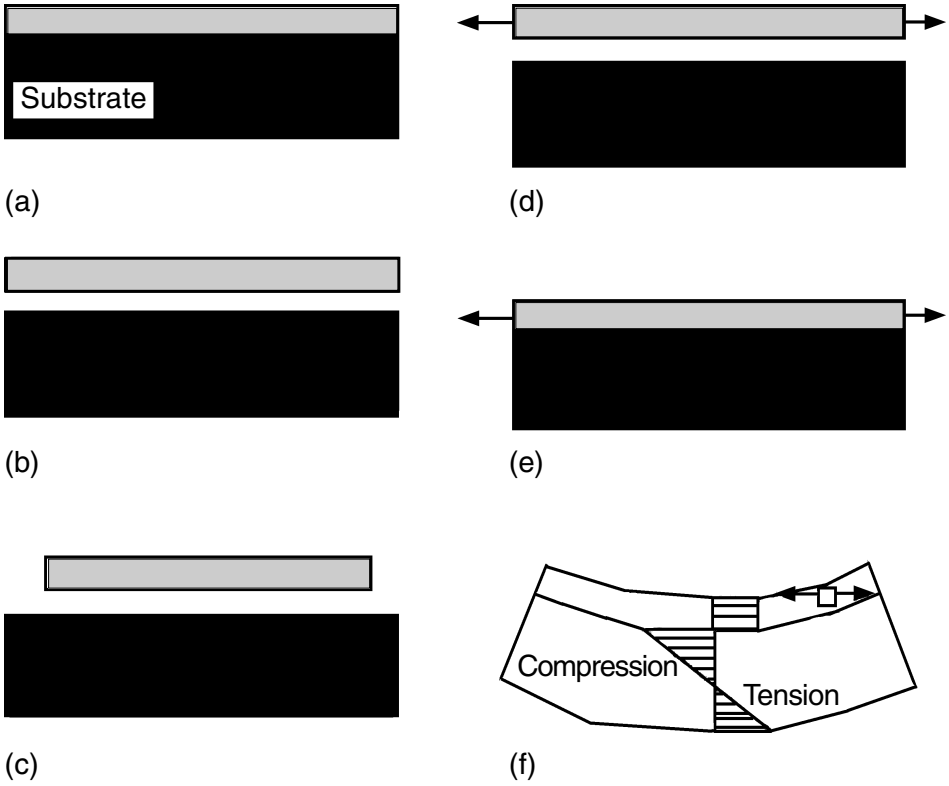

Fig. 1: Schematic representation of the elastic interaction between a thin film and substrate, generating residual stresses in the system, as described in the text.

In order to understand the presence of these residual stresses, the creation of a film/substrate system may be broken down as follows Figure 1.[17]

1. At the film deposition temperature T_d the system is free of any mechanical stress (Figure 1a).
2. If the film is detached from the substrate at the same temperature (Figure 1b), it is not under stress, and its longitudinal dimensions still correspond to those of the substrate.
3. Assuming, for example, that there is differential contraction in the film and substrate (Figure 1c). The film, now detached from the substrate, is still free of stress.
4. The film is now stretched so that it once again has the same dimensions as the substrate (Figure 1d).
5. The film is now made to adhere once again to the substrate (Figure 1e).
6. The stress is now no longer applied (Figure 1f). The film tends to contract but the rigid substrate to which it is adhering does not.

At mechanical equilibrium, the film/substrate system is therefore curved. In the example shown in Figure 1, the curve is concave and corresponds to a residual tensile stress in the film. A stress gradient is formed in the substrate, with compression occurring at the interface. Conversely, the system would be convex if the film were subjected to a residual compressive stress.

Residual stresses are therefore generated throughout the film/substrate system in which the dimensions of the film change in respect to those of the substrate (Figure 1c). These stresses will depend on the deposition conditions (temperature, pressure, gas flux, etc.) and on the heat treatment applied to the system after deposition.

Leaving aside the special case of epitaxial stresses resulting from parameter differences between two monocrystalline media, the residual stresses in a film/substrate system have two components, one thermoelastic and the other intrinsic.

Thermoelastic stresses are generated during a change from the deposition temperature T_d to another temperature T_1. The difference between the thermal expansion coefficients of the film (f) and substrate (s) cause deformation ε_{th}^{f} to occur in the film plane. This is constant throughout the thickness of the film, such that:

$$\varepsilon_{th}^{f} = \int_{T_d}^{T_1} \left[\alpha_s(T) - \alpha_f(T)\right] dT \qquad (3)$$

In this relation, α_s and α_f are the thermal expansion coefficients of the substrate and film. These depend on the temperature T. If the film is homogeneous and elastically isotropic, the in plane thermoelastic stress is expressed by:

$$\sigma_{th}^{f} = \frac{E_f}{1-\nu_f} \int_{T_d}^{T_1} \left[\alpha_s(T) - \alpha_f(T)\right] dT \qquad (4)$$

E_f and ν_f are respectively Young's modulus and Poisson's coefficient for the film. Furthermore, assuming that the thermal expansion coefficients are independent of the temperature, the thermoelastic stress increases linearly with the film deposition temperature.

As far as the intrinsic stresses are concerned, they are associated with the film growth process. If the incident atoms are not sufficiently mobile at the surface of the substrate, later atom rearrangements associated with changes in film volume may generate this type of stress.[18] Generally, these stresses decrease as the deposition temperature increases. Physical models describing the microstructural modifications that cause intrinsic stresses, are however scarce.[19] For example, the growth of grains,[20] the rearrangement of atoms at grain boundaries[21] or partial or total crystallization of amorphous films result in volume decreases that generate intrinsic tensile stresses. Moreover, the absorption of water by hydrophilic and micro-porous films causes their volume to increase, producing an intrinsic compressive stress. It should also be pointed out that the ion arrangement acting at the scale of the atomic structure also produces similar effects.

The overall residual stress in the film is equal to the sum of the thermoelastic component and intrinsic component. In the case of low deposition temperatures, the intrinsic stress is still the main contributing factor to the overall residual stress. In contrast, in the case of high deposition temperatures, the thermoelastic stress predominates. Therefore, while the signs of these stresses are identical, there is an intermediate deposition temperature for which the residual stress is minimised (Figure 2).

Examination of thin films, or structures built up of homogeneous CVD thin films indicates that they should be susceptible to spontaneous mechanical damage (Figure 3). For example a structure intended for microelectronics is in fact composed of a great variety of CVD and non CVD deposited materials, with very different physical, thermal and mechanical properties. Consequently, severe residual stresses are generated. Furthermore, from an initial multilayer a definitive structure for microelectronics has relatively complex geometric shapes with angular patterns. These act as mechanical singularities where stress concentrations are generated. They are potentially sensitive to mechanical stresses and damage may therefore tend to occur more often there.

The discussion here will be restricted to mechanical damage due to residual stresses alone, without considering other phenomena.

Regarding the damage mechanisms, spontaneous cracking and detachment of uniform films may occur in the early stage of a structure formation.[22] In the case of thin films subjected to residual tensile stresses, the film deposited on the substrate generally becomes mechanically unstable when the stored elastic energy U corresponds to the bulk cracking energy of the film (Figure 3a). As the crack spreads through the thickness of the film, it may produce plastic deformation of the substrate when it reaches the interface (Figure 3b) or be deviated at the interface and cause the film to become detached (Figure 3c), or propagate inside the substrate (Figure 3d). Figure 4 shows,

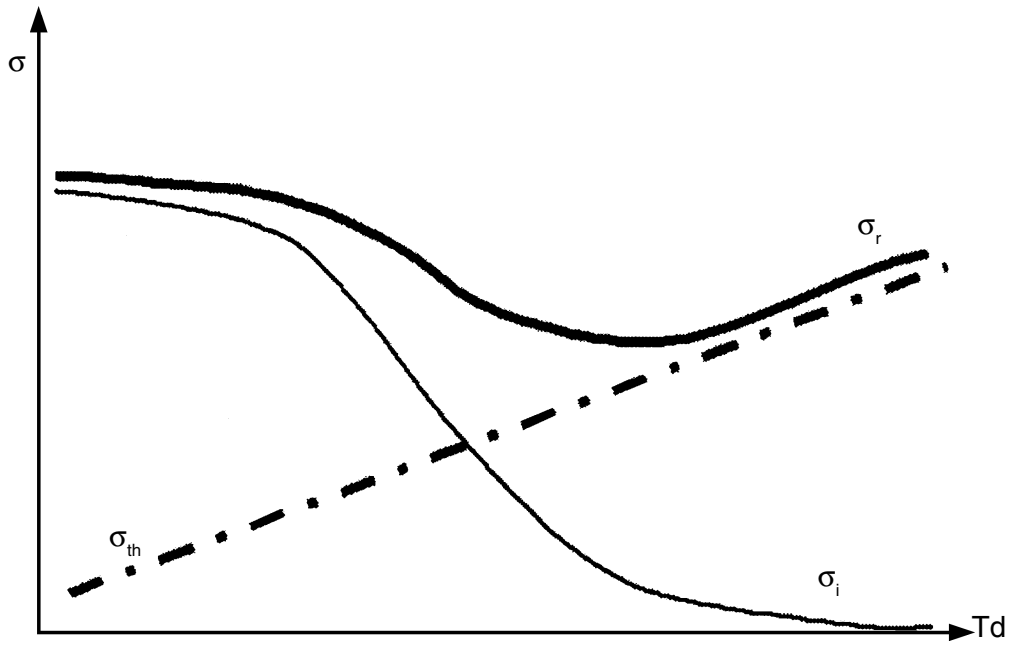

Fig. 2: Schematic representation of changes in thermoelastic stress σ_{th}, intrinsic stress σ_i and overall residual stress σ_r, in a thin film as a function of deposition temperature T_d.[21]

for example, the failure of a CVD film of silicon nitride, through cracking and detachment due to excessively high residual tensile stress and poor adhesion.

Conversely, if the residual stress is compressive, mechanical instability occurs when U is equal to the interface cracking energy. In this case, an interface crack that has already begun to form from a defect propagates when the detached part of the film buckles. This mechanism leads to the formation of a blister (Figure 3e). The interface crack may then propagate through the thickness of the film, leading to flaking (Figure 3f).

Other types of damage may be produced through thermomechanical effects. For example, when being annealed at 450°C a CVD aluminum film on a Si substrate is subjected to compressive thermoelastic stresses owing to the considerable difference between the thermal expansion coefficients of aluminum ($\alpha_{Al} = 23 \times 10^{-6}$ °C^{-1}) and the silicon substrate ($\alpha_{Si} = 3.5 \times 10^{-6}$ °C^{-1}). When cooling, the film may therefore contract by as much as 1%. Due to the combined action of residual stresses and temperature, diffusion mechanisms may be active, especially at grain boundaries. Aluminium atoms then accumulate at triple boundaries, producing hillocks on the free surface of the film.[23] They may be as high as the film is thick.

After cooling and by virtue of their shape, these hillocks form singularities where stress concentrations will encourage cracking and then flaking of any brittle thin passivation film after it has been deposited on the aluminum (Figure 5).

Consequently, considerable residual stresses may be generated as soon as a film is deposited. These usually include a thermoelastic component and an intrinsic component and can concentrate near singularities. Singly or in combination with external forces, they may activate different damage mechanisms within a single film or a multilayer. For example, aluminium films may be damaged by the formation of hillocks of thermal origin, by plastic deformation or extruding of grains or cavity formation. In addition, other brittle passivation films deposited may crack, become

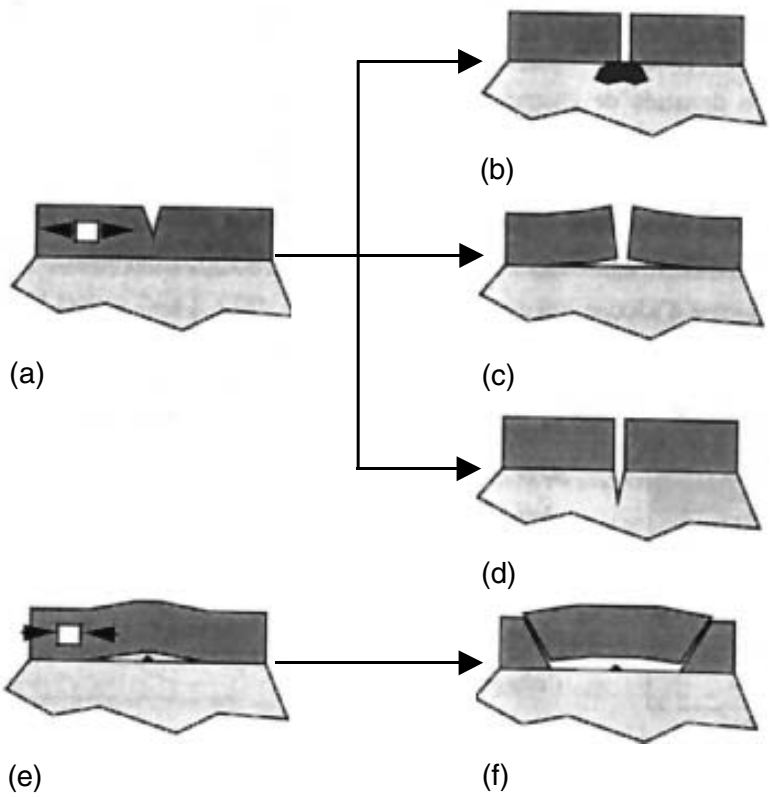

Fig. 3: Schematic representation of various types of failure associated with the mechanical instability of a film deposited on a substrate. (a) cracking of a thin film subjected to residual tensile stress, (b) plastic deformation of the substrate at the end of the crack, (c) deviation of the crack at the interface, (d) cracking of the substrate, (e) detachment and buckling (formation of a blister from an interface defect) of a film subjected to residual compressive stress, and (f) deviation of the crack through the thickness of the film (flaking).

detached or flake. These failures may strongly restrict any further application.

In order to analyze the reliability of these film(s) on substrate structures, it is therefore necessary to know the mechanical and microstructural properties of the various materials beforehand, and then study the mechanical stability of the complete assembly.

Experimental Analysis of the Mechanical Stability of CVD Films

A standard experimental method for studying the mechanical stability of films on substrates consists of straining the system in uniaxial tension. Then, a network of transverse cracks develops in a brittle film, while adhesion failure can occur at the interface. The progress of damage can be related to the mechanical properties of the system: Young's moduli of the film and substrate, yield stress of the substrate, fracture toughness of the film, strength of the interface, flaw distribution and residual stresses in the film.

Models describing the mechanics of cracking and loss of adhesion occurring in uniaxially stretched film/substrate systems are numerous.

Hu and Evans[24] have analyzed the cracking and decohesion of brittle Cr films deposited on Al and stainless steel substrates taking into consideration the critical values of non-

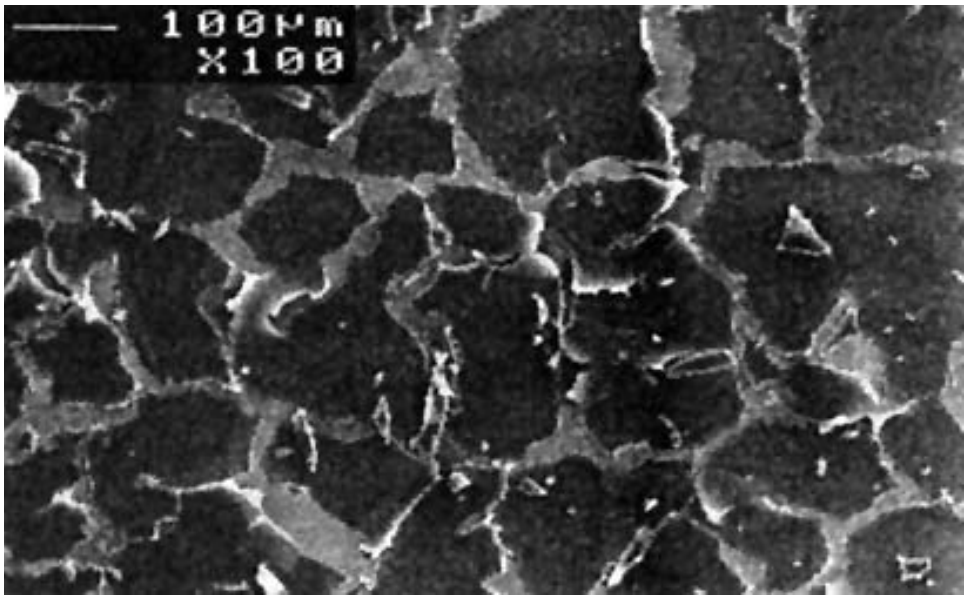

Fig. 4: SEM image showing spontaneous cracking and detachment of a film of PECVD silicon nitride (h = 0.18 µm) deposited on a aluminum substrate.

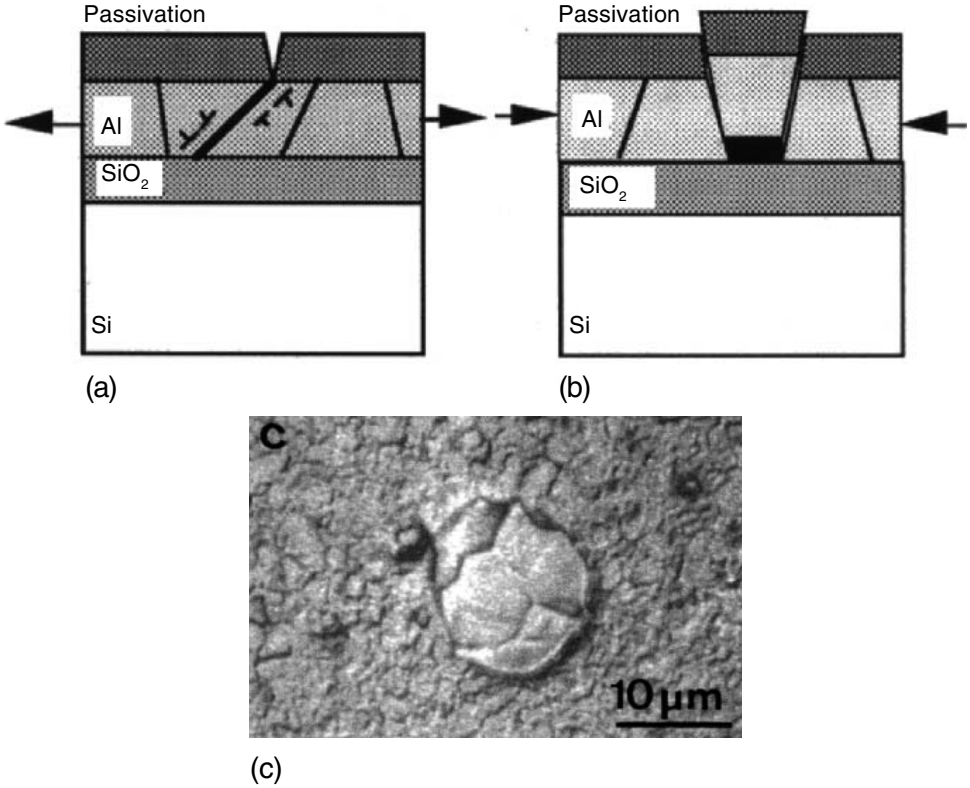

Fig. 5: (a) Plastic deformation of aluminum due to residual tensile stress and cracking of the passivation film ($T = T_{amb}$), (b) dislodging of a grain of aluminum due to residual compressive stress and cracking of the passivation film ($T > T_{d.Al}$), and (c) optical scan showing dislodging of grains in a uniform unpassivated aluminum film. This damage was produced by heating cycles at temperature up to 400°C.

dimensional parameters related to the elastic properties of the deposited films and the substrates.

Delannay and Warren[25] have studied the interaction between parallel cracks by considering the energy release rate associated with the propagation of a new crack among an already existing crack network.

More recently, the cracking in layered materials has been extensively reviewed by Hutchinson and Suo[26] and Ye et al.[27]

Statistical models of fracture describing the multiple cracking in hard coatings through the evolution of the crack density have been proposed by several authors. Gille and Wetzig[28] have described the dependence of the crack density on a random distribution of flaws in the brittle film. This statistical model derives the strength distribution function obtained as a Weibull law.[29] Mézin et al.[30] have analyzed the distribution of the distances between the cracks and the evolution of the crack density with the strain in Mo films deposited on steel substrates. This approach defines the evolution of the fracture probability of the film with the strain and leads to the measurement of the length of the zone in which the normal stress is relaxed on both sides of the cracks.

The interface shear strength of a SiO_2 film deposited on a Cu substrate has been evaluated by Agrawal and Raj[31] by considering the spacing distribution between the cracks for applied strains corresponding to the saturation of the network of transverse cracks.

Using fracture mechanics and the Griffith's energy criterion, Chow et al.[32] have derived an analytical relation to determine the interfacial fracture energy between a brittle film and a polymeric substrate.

Faupel et al.[33] have analyzed the adhesion of metal films deposited on polymer substrates strained in an optical microscope. The deadhesion energy was deduced from the difference in the stress versus strain curves between the film/substrate system and the substrate only.

Continuous observations of the evolution of damage, associated with the measurement of the corresponding stresses and strains, are necessary for a precise experimental study. Because of higher magnification and a better focusing depth, *in situ* tests in a scanning electron microscope permit efficient observations and analysis of the damage progress in film/substrate systems.[34-38]

In the following, we present two examples related to analysis of the mechanical stability of CVD films on substrates. One case describes systems intended for microelectronic devices (passivation films on a aluminium substrate), and the other describes coatings intended for wear and corrosion protection of steels.

Passivation Films Deposited by PECVD

As recalled in the introduction during the first manufacturing stages of integrated circuits, the coupling of metals for interconnections with materials for isolation and protection (passivation materials) is subject to reliability hazards, principally because of the large thermal expansion mismatch existing between the metals and the passivation materials.[39] Consequently, improvement of the mechanical stability of the film/substrate systems requires an understanding of their response to failure.

To begin, we present an example of the mechanical stability of systems consisting of brittle PECVD films of two kinds of passivation material, on Al substrates using an *in situ* tensile test. The passivation materials are silicon nitride (Si_3N_4) and 4.5 wt.% phosphorus doped silicon oxide (SiO_2:4.5 wt.% P). We also investigate the effects on damage progress by a thermally grown alumina (Al_2O_3) interlayer and by the presence of scratches on the Al surface. For each system, the experimental observations of the film cracking onset are analyzed through the approach of Hu and Evans.[24] Then, multiple film cracking is described by the evolution of the crack density with the longitudinal strain applied to the system. Finally, the interfacial strength is evaluated by extending the approach of Chow et al.[32] to the particular adhesion failure observed in the systems.

Samples and Microstructural Observations

The different PECVD film/substrate systems are schematically presented in Figure 6a. The substrates correspond to 99.99% pure Al, mechanically polished with a 0.3 μm alumina powder, then finally electrolytically in a 70% methanol-30% nitric acid solution. When exposed to air, a native aluminum oxide of about 3 nm is produced. The substrates were coated with a dielectric film of a passivation material: either Si_3N_4 or SiO_2:4.5 wt.% P. These systems are, respectively, denoted as system A and system C. The Si_3N_4 films were produced by plasma enhanced chemical vapor deposition at a temperature of 360°C, while the SiO_2: 4.5 wt.% P films were chemically vapor deposited at a temperature of 420°C. For both passivation materials, the thickness of the films was 0.8 μm.

Before film deposition, several Al substrates were annealed in air at 590°C for two hours. Under these conditions, a 40 nm thick thermally grown Al_2O_3 is formed.[40] With these substrates also coated with Si_3N_4 films (system B) and SiO_2: 4.5 wt.% P films (system E), the aim is to compare the mechanical behavior of systems with a native oxide interlayer (systems A and C) to that of systems having a thermally grown Al_2O_3 interlayer (systems B and E).

Finally, before the deposition of the SiO_2: 4.5 wt.% P film, the surface of an Al substrate was intentionally scratched by mechanical polishing. The scratches were about 1.5 μm wide, 1 μm deep, and were oriented 45° with respect to the longitudinal axis of the sample. This system (denoted as D), permits analysis of the effect of an interfacial roughness.

Unfortunately, it was not practical to determine directly the residual stresses and strains in the dielectric films for these samples. However, measurements on similar films showed compressive stress values of the order of 100 MPa for the Si_3N_4 films, and 50 MPa for the SiO_2:4.5 wt.% P films.[41] The corresponding residual strains are thus of the order of 0.001. Although these strains are not negligible, they are substantially smaller than the cracking strains we observed, but are within the uncertainties of our measurements. Consequently, we do not include them in our analysis.

The samples (Figure 6b) were loaded into an *in situ* tensile testing device adapted to a scanning electron microscope. Because the straining system induces a symmetrical displacement of the grips with respect to the center of the sample, the observation of damage progress does not need a systematic focusing and recovery of the image. For each system, four regions were chosen in the central part of the sample and were observed under a magnification of 200. In each region, the longitudinal and transverse strains in the film were determined locally from the displacement between surface imperfections. The absolute error on the measurement of the strain was ± 0.3%. A more precise description of the device has been presented elsewhere.[42,43]

In the five film/substrate systems, the damage progress presents characteristic stages with corresponding critical strains. Figure 7 presents a typical evolution of the damage observed during an *in situ* experiment when straining a sample of system C. For each system, the damage evolution can be characterized by the following stages as a function of the longitudinal strain applied to the system. For small strains of the order of a tenth of a percent, the film deforms elastically. Then, when increasing the strain to about 0.4% in systems A, B and E, 1.6% in system C and 1.3% in system D, primary cracking is activated in the film. The primary cracks are straight, perpendicular to the tensile axis and are regularly spaced. Their number increases rapidly with uniaxial elongation of the sample. For a strain of 4% in system A, 7% in system B, 10% in system C, 4% in system D and 9.5% in system E, a network of secondary cracks develops among the primary cracks. The propagation of these new cracks often shows a curved path and arrest, when getting close to the free surfaces produced by the primary cracking (Figure 7a). When the strain is increased, saturation of the network of transverse cracks is achieved. The saturation corresponds to a strain of 15% in system A, 18% in system B, 19% in system C, 12% in system D and 22% in system E. Previous

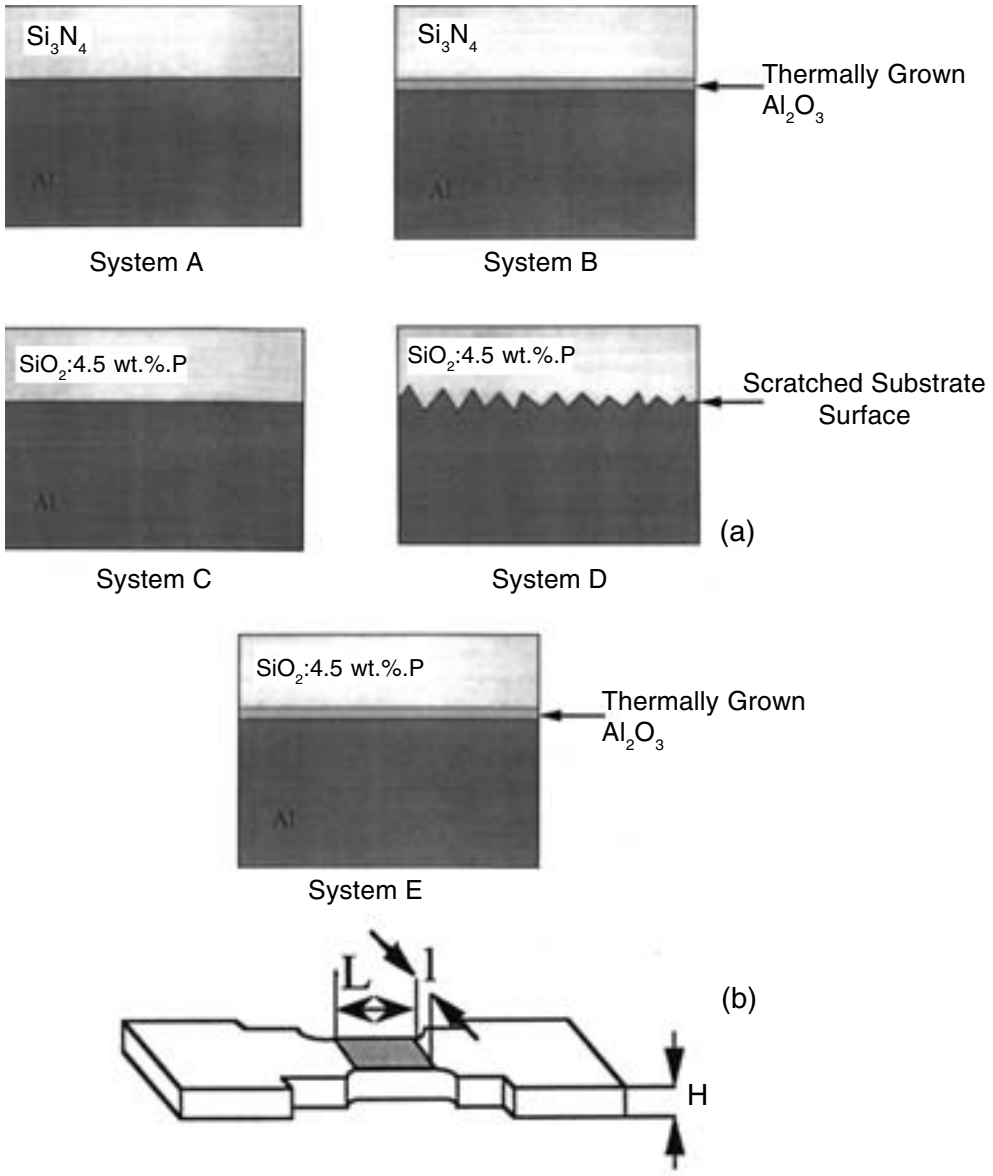

Fig. 6: (a) schematic cross sections of the five studied systems and (b) schematic representation of a sample showing the zone which is analyzed during the experiments (L = 2.5 mm, 1 = 1.8 mm, and H = 1.3 mm).

to this saturation stage, for strains of 8% in system A, 13% in system C and 3% in system D, the loss of adhesion and buckling of strips of the cracked film, extended perpendicularly to the longitudinal axis of the sample and bounded by two successive transverse cracks is observed (Figures 7b and 8). For systems with the Al_2O_3 interlayer, the stage of debonding and buckling is detected at the same time or slightly after the saturation of the network of transverse cracks. The corresponding strains are 21% in system B and 22% in system E. For higher strains, the buckled zones of the film strips break along the directions of the maximum shear in the substrate.

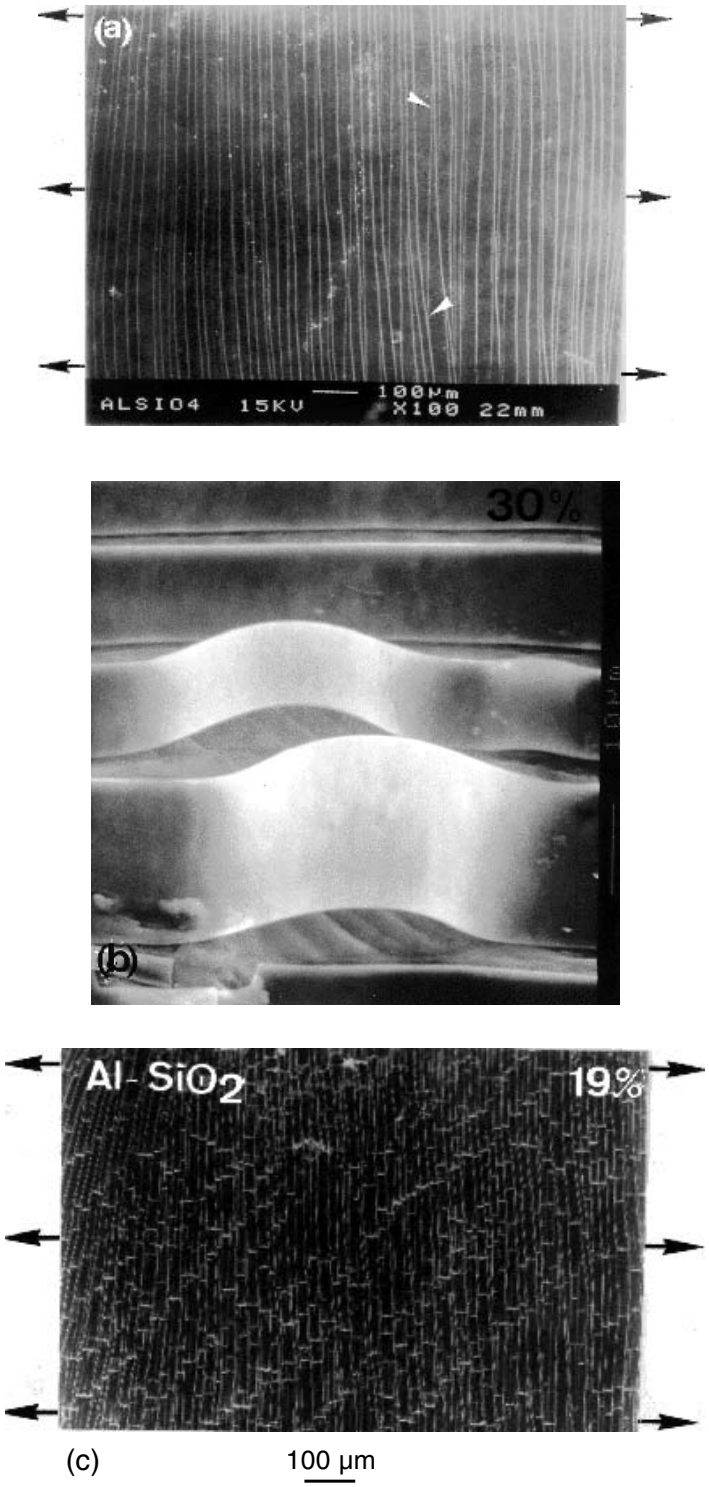

Fig. 7: Sequential micrographs of the evolution of the damage in a SiO_2: 4.5 wt.% P film deposited on an Al substrate subjected to a tensile test (system C, Figure 6). The black arrows show the tensile direction. (a) Networks of primary and secondary cracks perpendicular to the tensile axis (ε = 11%). The white arrows show a secondary crack which stops when getting close to primary cracks, (b) decohesion and buckling of the strips of film. Slip lines are observed on the Al surface under the buckled strips, and (c) transverse rupture of the buckled zones along the directions of maximum shear of the substrate (ε = 19%).

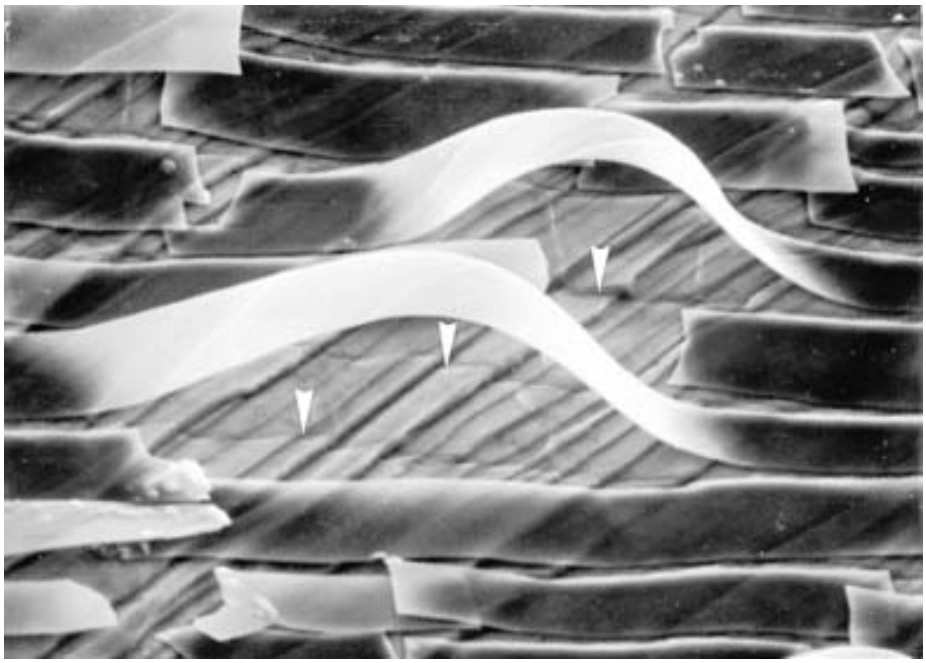

Fig. 8: Detailed views of decohesion and buckling among a cracked SiO_2: 4.5 wt.% P film deposited on a scratched Al substrate. The white arrows show the scratches. The buckled strips of the film are perpendicular to the tensile direction.

The critical longitudinal strains corresponding to the above-mentioned damage stages are presented in the diagram in Figure 9.

Multiple Cracking of the Films

A typical evolution of the crack density with the longitudinal strain is presented in Figure 10. After exceeding the critical cracking strain of the film, the number of primary cracks increases rapidly with the strain. Then, the evolution of the crack density slows down when the secondary cracking occurs until reaching a constant value, which corresponds to the stage of saturation, with no further transverse crack opening process.

In system E, the evolution of the crack density with the longitudinal strain shows that the presence of a thin thermally grown Al_2O_3 interlayer modifies the cracking response of the SiO_2: 4.5 wt.% P film. First, as noted previously, the onset of primary cracking is accelerated; second, the density of cracks at saturation increases from 78 to 95 cracks/mm. These effects are not observed for systems with a Si_3N_4 film, in which the crack density at saturation is about 60 cracks/mm, with or without the Al_2O_3 interlayer. These opposite cracking responses certainly result from the different strengths of the SiO_2: 4.5 wt.% P/Al_2O_3 and Si_3N_4/Al_2O_3 interfaces. Indeed, if we consider Si_3N_4/Al_2O_3 interfacial strength to be weak, so the Si_3N_4 film may locally debond near the transverse cracks present in the Al_2O_3. This process will restrain the propagation of the transverse cracks to the upper film (Figure 11a). On the contrary, the better adhesion between the SiO_2:4.5 wt.% P film and the Al_2O_3 interlayer could explain the increase in the crack density at saturation. In this case, the transverse cracks propagate straight through the interlayer and the film. The Al_2O_3 interlayer imposes its own cracking response on

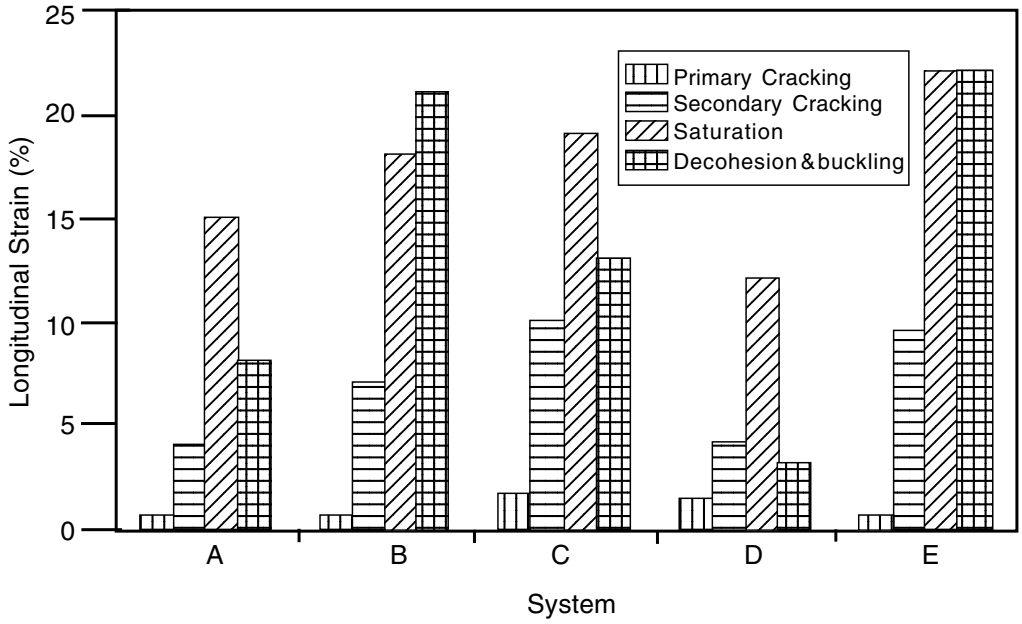

Fig. 9: Diagrams presenting the critical longitudinal strains (bold numbers) corresponding to the successive stages of damage. System A = Si_3N_4/Al, System B = Si_3N_4/Al_2O_3/Al, System C = SiO_2 : 4.5 wt.% P/Al, System D = SiO_2: 4.5 wt.% P/scratched Al, and System E = SiO_2 : 4.5 wt.% P/Al_2O_3/Al.

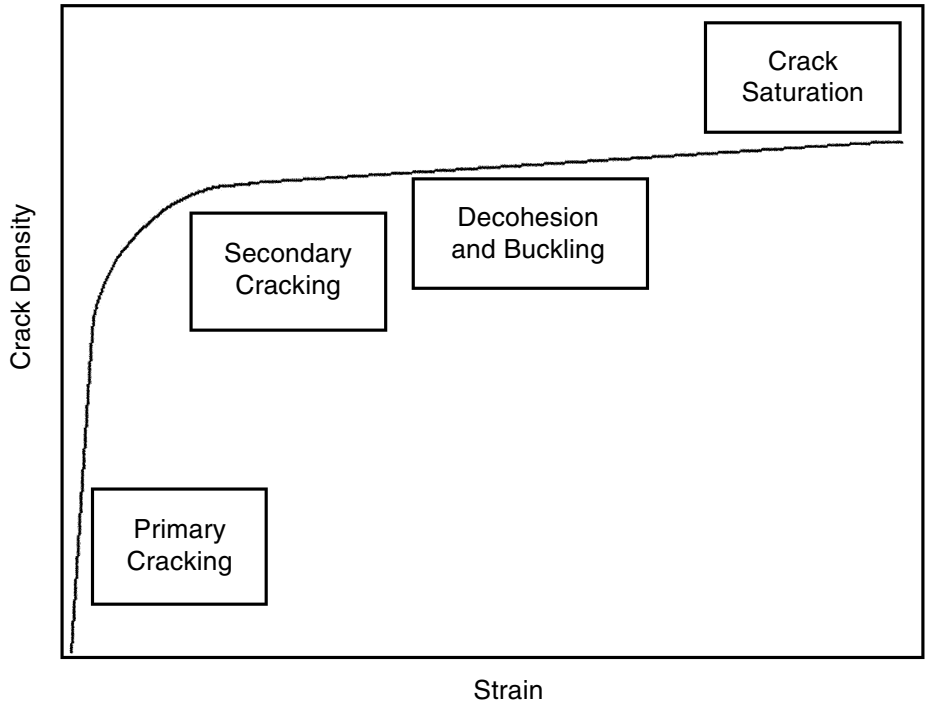

Fig. 10: Typical evolution of the crack density with longitudinal strain. The occurrence of the four damage stages is indicated.

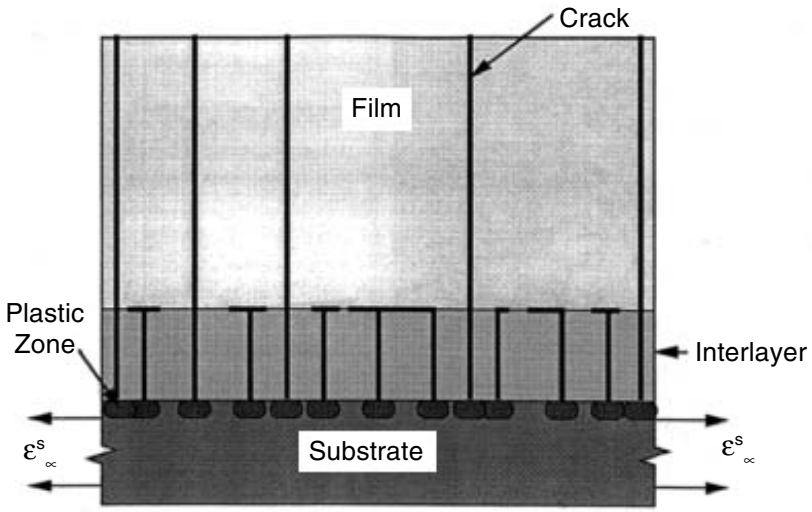

(a) Weak Interlayer/Film Interface

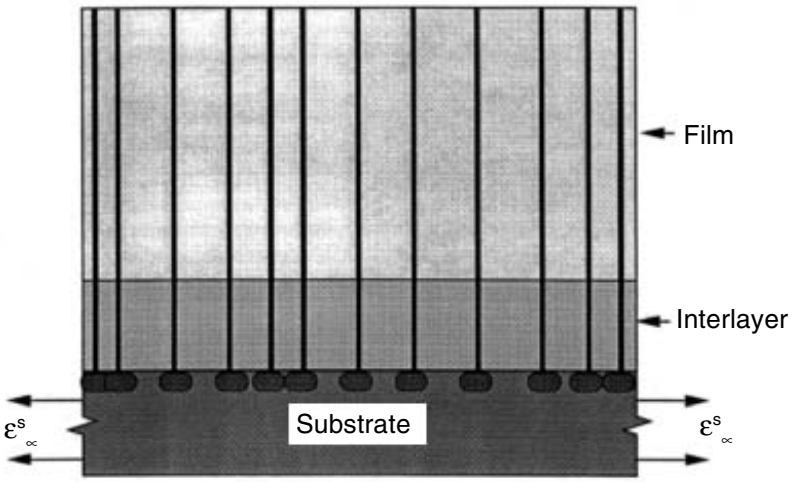

b) Strong Interlayer/Film Interface

Fig. 11: Schematic representation of the film cracking process when the system includes a thermally grown Al_2O_3 interlayer: (a) weak interface: decohesion is activated from the interlayer transverse cracks at the interlayer/film interface (system B) and (b) strong interface: straight propagation of transverse cracks both through the interlayer and the film (system D).

the SiO_2:4.5 wt.% P, producing numerous transverse cracks in the film (Figure 11b).

Although the critical cracking strain of the SiO_2: 4.5 wt.% P film is not affected by a scratched Al surface, the interfacial roughness has an impact on the multiple film crackings. The cracking rate is accelerated and the crack saturation is reached for a smaller strain: 12%, compared to 19% in system C. Yet, the crack density at saturation in system D (scratched

Table 1. Analytical Expressions for Crack Density vs Longitudinal Strain Obtained from the Empirical Law

System	Crack Density Relation (mm^{-1})
Si_3N_4/Al	$60\ (1 - \exp(-5.9\ (\varepsilon-0.004)^{0.32}))$
Si_3N_4/Al_2O_3/Al	$61\ (1 - \exp(-17.0\ (\varepsilon-0.004)^{0.85}))$
SiO_2:4.5 wt.% P/Al	$78\ (1 - \exp(-12.2\ (\varepsilon-0.016)^{0.79}))$
SiO_2:4.5 wt.% P.Al	$81\ (1 - \exp(-24.2\ (\varepsilon-0.013)^{0.83}))$
SiO2:4.5 wt.% P/Al_2O_3/Al	$95(1 - \exp(-7.3\ (\varepsilon-0.004)^{0.46}))$

aluminum surface) remains close to the value of system C (fine polished aluminum surface). However, the poor adhesion of the film on the scratched substrate should correspond to a lower value of the crack density at saturation. But the Al plastic flow blunts the film crack tips and also the interfacial asperities, which inhibits the debond from the crack/interface intersection. Thus, the crack density in the film can reach the same saturation level as in the case of a fine polished interface.

Directly from the in situ observations, the multiple film cracking is analyzed through the evolution of the crack density with the longitudinal strain applied to the system. Before any deformation, a representative zone of the sample is chosen. Its total length is 0.55 mm, extended parallel to the longitudinal axis of the sample. This initial length is denoted λ_0. For any further deformation, it is denoted $\lambda(\varepsilon)$ and corresponds to:

$$\lambda(\varepsilon) = \lambda_0\ (1 + \varepsilon) \tag{5}$$

ε is the longitudinal strain applied to the system. Then, the crack density, denoted $d(\varepsilon)$, is defined by:

$$d(\varepsilon) = \frac{N(\varepsilon)}{\lambda_0} \tag{6}$$

$N(\varepsilon)$ is the number of transverse cracks which intercept the length $\lambda(\varepsilon)$. The error introduced when counting the number of cracks is ± 2 cracks per millimeter. In order to describe the cracking response of our passivation films, the experimental values of the crack density as a function of the longitudinal strain are fitted by using:

$$\frac{d(\varepsilon)}{d_{sat}} = 1 - \exp\left[-A\left(\varepsilon - \varepsilon_c\right)^{\alpha}\right], \tag{7}$$

ε_c is the critical strain for the cracking of the film. d_{sat} is the density of cracks at saturation, *A* a constant parameter. α is a characteristic exponent of the law. ε_c and d_{sat} are determined from the experiments. A and α, are respectively, calculated from the intercept and the slope of a linear regression, when plotting $\ln(-\ln(1 - d/d_{sat}))$ as a function of $\ln(\varepsilon - \varepsilon_c)$. For each system, the relationship for the crack density as a function of the longitudinal strain is reported in Table 1. Figures 12 and 13 show the experimental results and the corresponding curves obtained from relation.[7] Such an empirical relationship can be useful for a statistical analysis of the cracking behavior of the film.[30,45]

Redistribution of Stresses in the Cracked Film

When considering a ductile substrate coated with a brittle film and subjected to a uniaxial strain ε^s_∞ during loading and before debond of the film (perfect adhesion), the displacement is assumed to be continuous at the interface. Then, the substrate deformation is entirely transmitted to the film through the interface. When exceeding the critical cracking strain of the film, a network of transverse cracks develops. At the interface, each crack tip will be surrounded by a

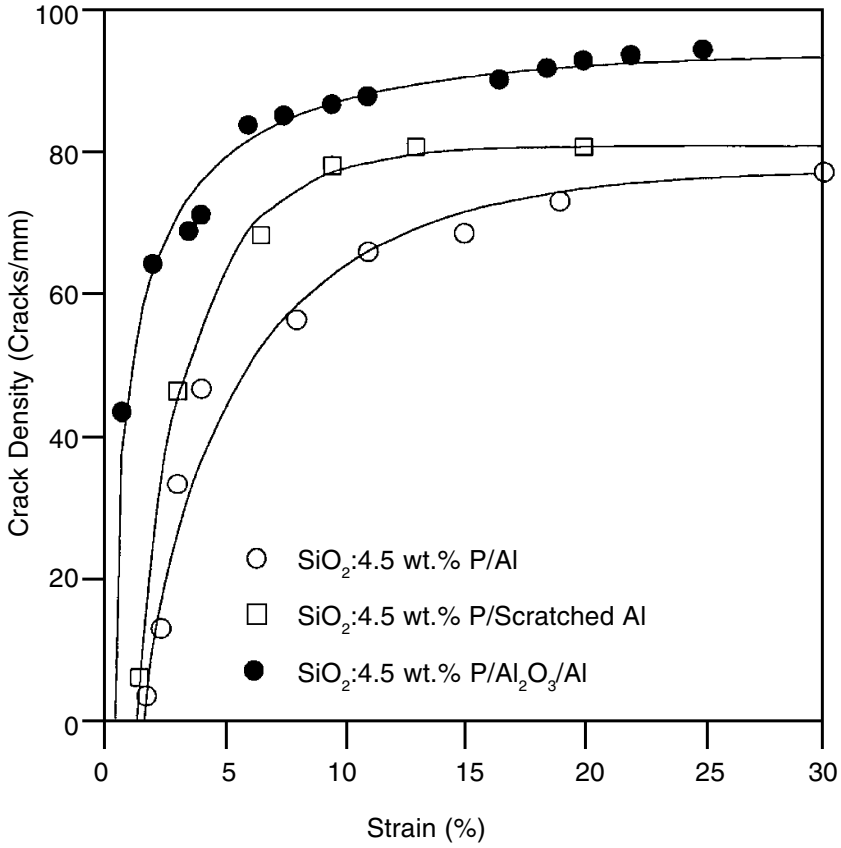

Fig. 12: Crack density vs longitudinal strain for the systems with a SiO_2: 4.5 wt.% P film. The circles correspond to the experimental results and the solid lines to the empirical fits (relation 7).

stress field which can locally induce plastic flow in the substrate (Figure 14a). Thus, the redistribution of the strain near the free surfaces of the cracks is associated with the relaxation of the normal component of stress σ^f_{xx} over a characteristic length r (Figures 14b and c). The rest of the film is assumed to remain uniformly deformed at the applied strain ε^s_∞. Consequently, in these unrelaxed parts of the film, the normal stress σ^f_{xx} can be described by two terms: the stress induced when straining the system, and the residual stress parallel to the x axis σ^f_r.

$$\sigma^f_{xx} = E_f \varepsilon^s_\infty + \sigma^f_r \qquad (8)$$

E_f is Young's modulus of the film. When transverse crack saturation is achieved the normal stress in each film strip is expected to be lowered, and no new transverse crack will open. The shear stress component is deduced from the force equilibrium condition of an element of film near a free surface of a crack, assuming that the normal stress σ^f_{xx} is uniform through the film thickness (Figure 15). At a distance x from the free surface, the interfacial shear stress τ_i is related to the normal stress σ^f_{xx} and the thickness of the film h by the relation:

$$\tau_i(\chi) = h\frac{d\sigma^f_{\chi\chi}(\chi)}{d\chi} \qquad (9)$$

Figure 14d shows the schematic evolution of the interfacial shear stress. It is zero in the unrelaxed part of the cracked film. When the response of the system remains in the elastic

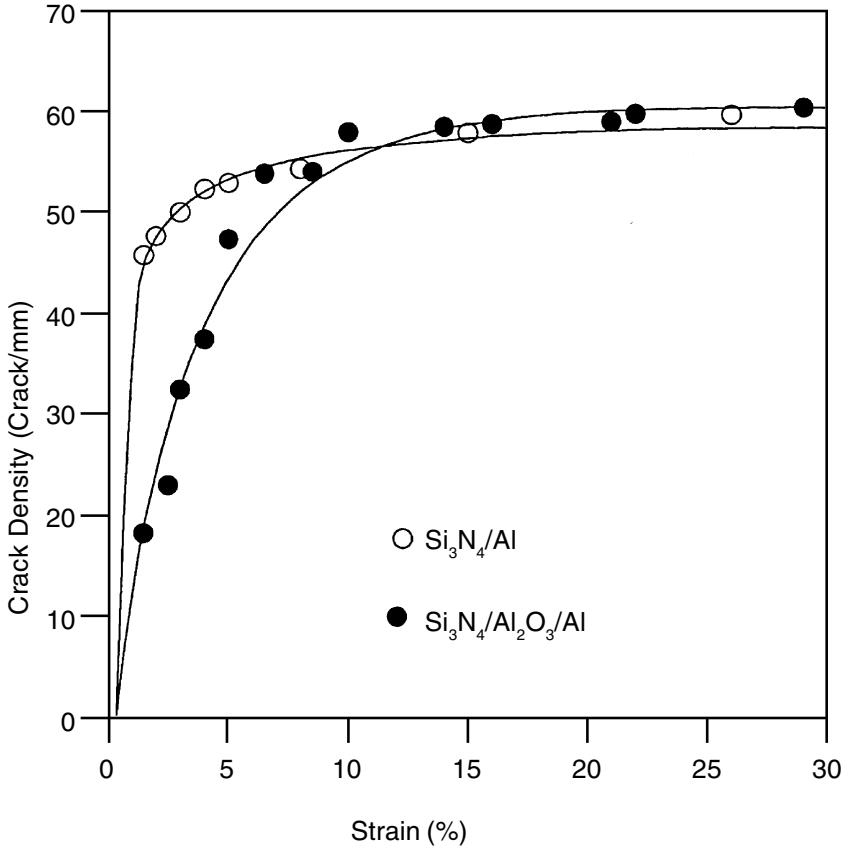

Fig. 13: Crack density vs longitudinal strain for the systems with a Si_3N_4 film. The circles correspond to the experimental results and the solid lines to the empirical fits (relation 7).

domain, the interfacial shear stress increases near the free surface of the crack. On the contrary, when plasticity is activated in the substrate at the crack/interface intersection, the interfacial shear stress passes through a maximum and decreases near the free surface of the crack.

The brittle film cracking with plastic deformation of the ductile substrate at the interface has been described by using the shear lag model.[24] This model, which was proposed in the analysis of the fragmentation of fiber composites,[44] develops a relation for the critical stress producing the steady-state cracking of the film. It assumes that the interfacial shear stress, on the one hand, is activated at each crack tip along the characteristic slip length r, and, on the other hand, is constant and equal to the yielding shear of the substrate τ^s_Y. Then, from relation (9), the normal stress in the film τ^s_Y along the characteristic slip length r at each side of the crack is (Figure 16):

$$\sigma^f_{\chi\chi}(\chi) = \frac{\tau^s_Y \chi}{h} \quad (0<\chi<r/2) \qquad (10)$$

Finally, the critical cracking stress of the film is deduced from the change in energy of the system caused by the through-thickness cracking. This change in energy corresponds to a balance among several energy terms: the strain energy released by the crack propagation through the film, the work done by the applied load, the released energy associated with the interfacial yielding, and the change in strain

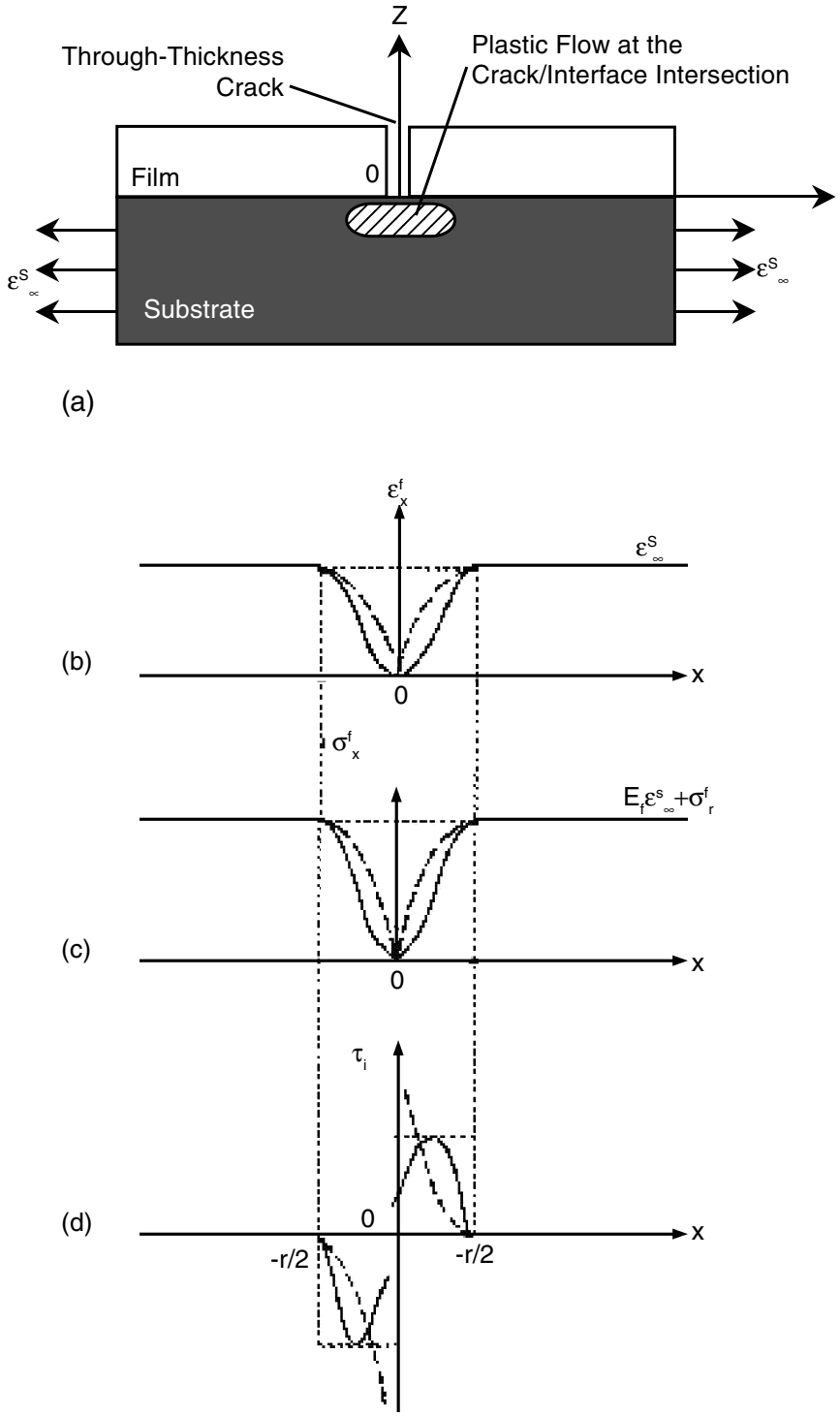

Fig. 14: Stress distribution in a cracked film. The dotted lines correspond to the elastic behavior of the film/substrate system, the solid lines to the presence of plasticity in the substrate at the crack/interface intersection (a) crack opening in a film deposited on a substrate which is uniaxially stretched, (b) longitudinal strain distribution in the film, (c) normal stress distribution in the film, and (d) shear stress distribution in the film at the interface.

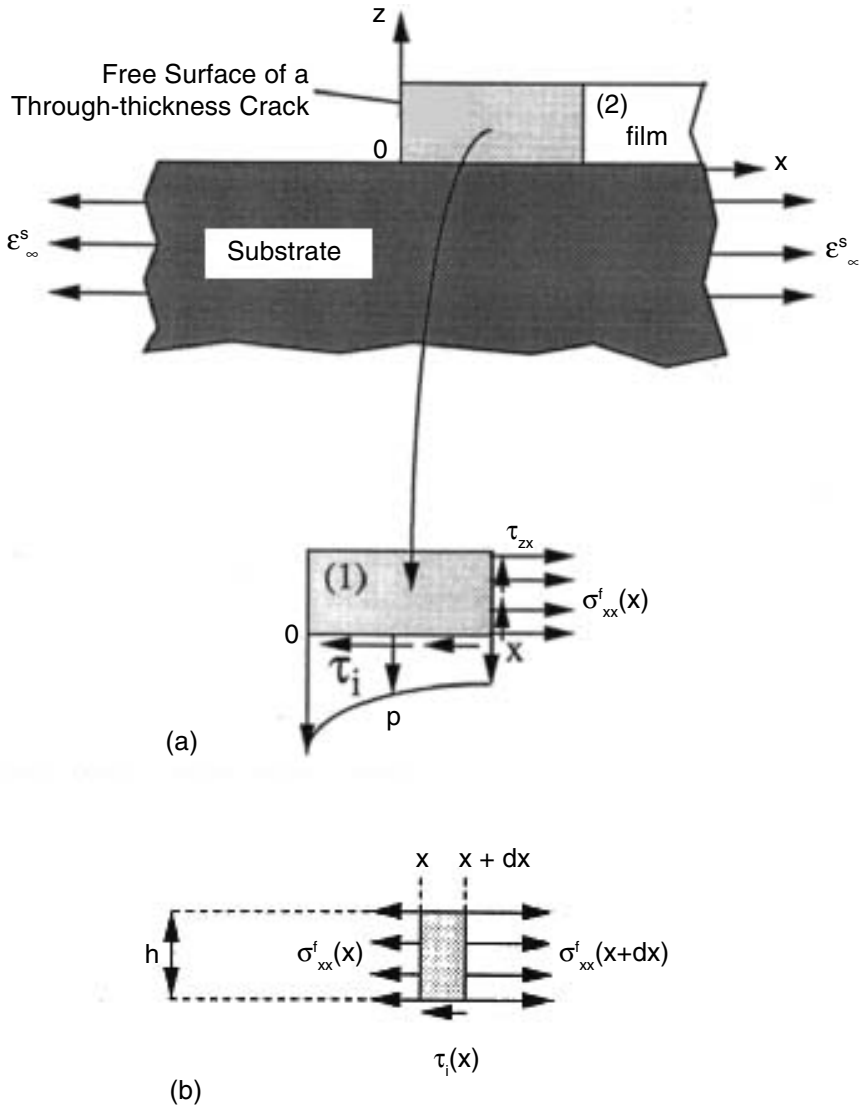

Fig. 15: (a) Schematic representation of the stress profiles in an adherent portion of film at a distance x from a free surface of a through-thickness crack. Interfacial shear stress τ_i and peel stress p correspond to the action of the substrate on region (1).[22] The normal stress parallel to the x axis, $\alpha^f_{xx}(x)$, is supposed to remain constant through the film thickness h. τ^f_{zx} is the component of shear stress which is tangential to the cross section and parallel to the z axis and (b) mechanical equilibrium in projection on the x axis of an element of film at a distance x from the free surface.

energy caused by interfacial sliding. Then, the critical stress for the cracking of the film σ^f_c is obtained from the following relation.[24]

$$\sigma_c^{f\,2}\left[\sigma_c^f\frac{h}{3\tau_Y^s}+\pi hF\right]=K_c^{f\,2}, \qquad (11)$$

K^f_c is the fracture thoughness of the film and τ^s_Y is the yielding shear stress of the substrate, which is related to its tensile yield stress σ^s_Y through the relation:

$$\tau_Y^s=\frac{\sigma_Y^s}{\sqrt{3}}. \qquad (12)$$

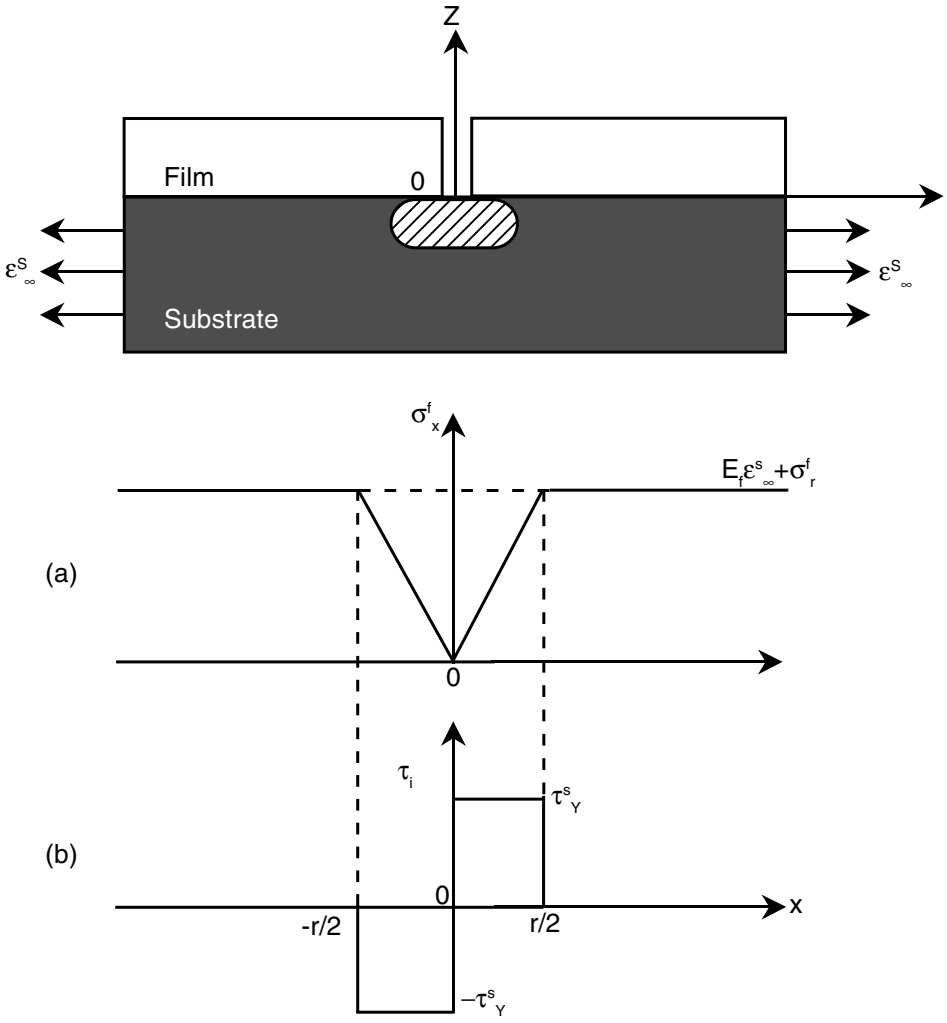

Fig. 16: Modeling of the stress distribution in a cracked film with plasticity at the interface using the shear lag approximation, (a) linear evolution of the normal stress σ^f_{xx} along the characteristic slip length r/2 and (b) sharp evolution of the interfacial shear stress τ_i along the characteristic slip length r/2.

F is a function of the ratio of Young's moduli of the film and substrate.

Assuming elastic response of the brittle film, the critical strain ε_c which induces the cracking of the film can be deduced from relation.[8] Typical material properties used in our calculations are given in Table 2. As discussed earlier, the residual strains are small relative to the critical strains, and are neglected in this analysis. The calculated critical cracking strains for both passivation films and for a thermally grown Al_2O_3 layer can be compared with the experimental results (Table 3).

Cracking Strains and Critical Parameters

An *in situ* tensile test in a scanning electron microscope permits the local observation of the first crack openings and propagations. For

Table 2. Material Properties

Material Properties	Al	SiO_2:4.5 wt.%P	Si_3N_4	Al_2O_3
α (10-6. °C-1)[36]	23	4	1	
E (GPa)[27,36]	70	100	150	390
ν[22]	0.35	0.25	0.25	
$\sigma^s Y$ (MPa)	30*			
$\sigma^f r$ (MPa)		-25 ± 10		
$K^f c$ (MPa.$m^{1/2}$)[28]		5**	2	3
$f(E_f/E_s)^3$		0.65	0.70	0.82
h (µm)		0.8	0.8	0.04

α : Thermal expansion coefficient
ν : Poisson's coefficient
σ : Residual stress in the film,
f(Ef/Es) : Modulus ratio function,[24]
E : Young's modulus
σY : Yield strength of the substrate
K_c^f : Fracture toughness of the film
h : Thickness of the film
* : This value has been obtained from a tensile test performed on a normalized tensile sample of 99.99% pure Al
** : This value is estimated from relation.[14]

Table 3. Critical Cracking Stresses and Strains Calculated from the Approach of Hu and Evans[24]

System	$\sigma^f c$ (MPa)	ε_c (Calculated) (%)	ε_c (Experimental) (%)
Si_3N_4/Al	570	0.38	0.4
SiO_2:4.5 wt.% P/Al	1140	1.14	1.6
Al_2O_3/Al	2225	0.57	

The experimental results are reported for comparison.

instance it has been shown that the Si_3N_4 film is more brittle than the SiO_2:4.5 wt.% P film. The first transverse cracks appear for a strain of about 0.4% in system A, compared to 1.6% in system C.

Concerning system C, little is known about the fracture toughness of the SiO_2:4.5 wt.% P. Considering a mode I crack opening (tensile), the fracture toughness parameter K_{IC} is estimated from the relation:

$$K_{1c} = \sigma_c (\pi a)^{1/2} \qquad (13)$$

where a is the length of the initial defect present in the material which propagates under the critical stress σ_c. By considering a full elastic response and the same initial length of defect for both passivation materials, the toughness of the SiO_2:4.5 wt.% P film can be related to the toughness of the Si_3N_4 film, which is better known, by the following empirical relation.

$$K_{lc,SiO_2} = \frac{E_{SiO_2}\varepsilon_{c,SiO_2}}{E_{Si_3N_4}\varepsilon_{c},Si_3N_4} K_{lc,Si_3N_4} \qquad (14)$$

ε_c and E are, respectively, the critical cracking strain and Young's modulus. A toughness of

5 MPa·m$^{1/2}$ is deduced for the SiO_2 : 4.5 wt.% P film. This value remains one order of magnitude higher than the fracture toughness of bulk silica: $K_{1c} = 0.75$ MPa . m$^{1/2}$.[46,47] However, concerning a PECVD silicon oxide film, its density increases when doped with phosphorus, and this improves its fracture toughness.[48,49] Moreover, this value appears to be realistic because the critical strains deduced from the experiments and those calculated by the model based on the shear lag approximation are similar. Concerning the system with Si_3N_4 (system A), the experimental and calculated strains remain in good agreement. Besides, the mechanical model also predicts a critical cracking strain of about 0.5% for the 40 nm thick thermally grown Al_2O_3 interlayer, which is close to the critical cracking strain of the Si_3N_4 film. But because of the uncertainty in the strain measurement, the effect of the brittle interlayer on the cracking onset in the Si_3N_4 film was not detected with accuracy. However for the SiO_2:4.5 wt.% P film and a brittle Al_2O_3 interlayer, the corresponding strain for initial cracking of the film was about 0.4% instead of 1.6%. This experimental result points out that the first transverse cracks in the brittle interlayer forward the cracking of the upper SiO_2:4.5 wt.% P film.

For the system with a scratched substrate surface (system D), the first primary cracks appear at a critical strain equivalent to the one observed in the case of a fine polished Al surface (system C). This observation suggests that, as long as the film remains adherent to the substrate, the roughness of the substrate will not influence the cracking onset of the film. However, as discussed in this section, the other main damage stages, which are multiple cracking and debonding, appear to be strongly dependent on the roughness of the substrate.

Debonding of the Films

For each system, the adhesion of the film to the substrate is characterized by an interfacial fracture energy value. The interfacial fracture energy term is calculated using an energetic approach which was proposed for analyzing the loss of adhesion of cracked films from the transverse crack/interface intersections.[32] By considering Griffith's energy release term, and when the rigidity of the substrate is much larger than the rigidity of the film, the analytical relation for calculating the interfacial fracture energy becomes

$$U = \frac{h}{2}\frac{E_f}{1-\upsilon_f^2}\varepsilon_{c\chi}^{*2}, \qquad (15)$$

where ε^*_{xc} is the critical longitudinal strain applied to the system which induces the debonding and ν_f is Poisson's coefficient of the film. It has been demonstrated that relation 15 remains valid when the substrate deforms plastically.[50] For our systems, it appears clearly that the Al substrate yields plastically before reaching saturation in transverse cracks. This plastic flow blunts the crack tips at the interface and inhibits longitudinal debonding of the film from the transverse crack/interface intersections. However, the adhesion failure occurs by the buckling of the strips of the cracked film under the effect of the transverse contraction of the substrate. The adhesion of our films is then analyzed from this characteristic stage of damage, using the above-mentioned analytical model to calculate the interfacial fracture energy associated with the debonding and buckling mechanism. The residual stress effects being neglected, the critical transverse strain ε^*_{cy} which induces the debonding of the strips of the cracked film is determined from the difference between the experimentally measured critical transverse strain ε_{cy} and the critical buckling strain $\varepsilon_{buckling}$ deduced theoretically (Figure 17).

$$\varepsilon^*_{cy} = \varepsilon_{cy} - \varepsilon_{buckling} \qquad (16)$$

The experimental critical transverse strain ε_{cy} is obtained by measuring the reduction in distance between two surface imperfections on a strip, which are aligned in the transverse direction and located at each side of a prebuckled region. $\varepsilon_{buckling}$ is the critical strain for the buckling process, determined by taking into account the dimensions of the observed de-adhered zones. These zones present a rectangular shape with length *a*, width *b* which is equal to the width of the strips, and thickness *h* of the film. The expression for the critical buckling strain is[51]

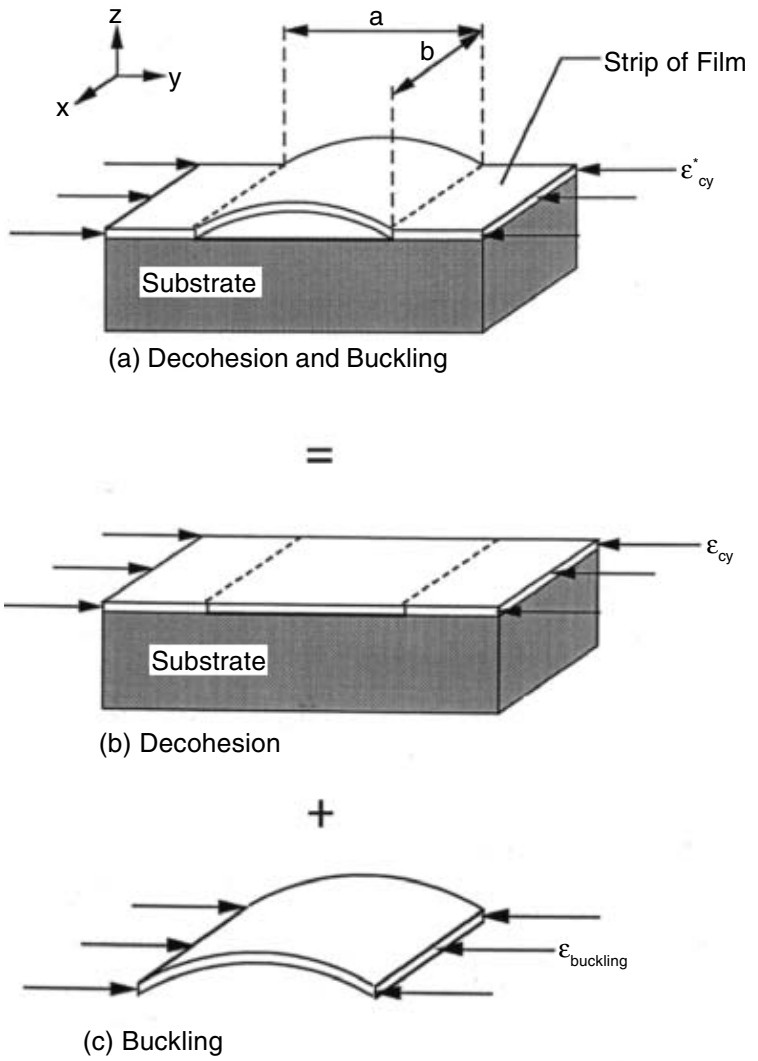

Fig. 17: Schematic representation of the interfacial failure process which is induced by the transverse contraction of the substrate in the y direction. The system is submitted to uniaxial tension in the x direction, (a) the decohesion and buckling of a strip of the cracked film, defined by two consecutive transverse cracks, is decomposed in, (b) a decohesion stage, and (c) a buckling stage of the decohered part of the strip.

$$\varepsilon_{buckling} = \frac{k\pi^2}{12(1-\upsilon_f^2)}\frac{h^2}{b^2}, \qquad (17)$$

where k is a function of the ratio of a to b.

The interfacial fracture energy associated with adhesion failure can then be calculated taking into account the elastic properties of the film and the defined critical strains.

$$\gamma = \frac{h}{2}\frac{E_f}{1-\upsilon_f^2}\left(\varepsilon_{cy} - \varepsilon_{buckling}\right)^2 \qquad (18)$$

Table 4 presents, for each system, the average dimension of the de-adhered areas, the critical strains, and the corresponding interfacial fracture energy.

The interfacial debond occurs after the through-thickness cracking of the films. It is activated by transverse contraction of the substrate which induces the buckling of the strips of the cracked films. The analysis of this particular adhesion failure mechanism provides insights concerning the interfacial strength of

Table 4. Decohesion Parameters: Average Dimensions of the Decohered Areas (a × b), Critical Strains (ε) and Corresponding Interfacial Fracture Energies (γ)

System	a × b (μm)	ε_{cy} (%)	$\varepsilon_{buckling}$ (%)	ε*c (%)	γ(J.m^{-2})
Si_3N_4/Al	15 × 20	-2.4 ± 0.3	-0.6	-1.8 ± 0.3	21 ± 7
Si_3N_4/Al_2O_3/Al	10 × 16	-3.4 ± 0.4	-1.1	-2.3 ± 0.3	24 ± 9
SiO_2:4.5 wt.% P/Al	15 × 15	-2.6 ± 0.4	-1.0	-1.6 ± 0.3	11 ± 4
SiO_2:4.5 wt.% P/Scratched Al	40 × 35	-1.1 ± 0.4	-0.2	-0.9 ± 0.3	3 ± 2
SiO_2:4.5 wt.% P/Al_2O_3/Al	8 × 11	-4.3 ± 0.5	-2.0	-2.3 ± 0.3	23 ± 6

film and substrate systems. This is done by measuring the critical debond strain, using a combination of elastic fracture mechanics and buckling theory of plates, and deducing an interfacial fracture energy. In the same way, an energy release rate term associated with the advance of a crack from a buckled debonded area has been proposed for uniformly compressed films.[52]

In the example described here, system A and system C show interfacial fracture energy values, respectively, of the order of 20 J.m^{-2} and 10 J.m^{-2}. However, thermodynamical studies on solid state metal/ceramic interfaces give work of adhesion varying from 0.1 J.m^{-2} to 3 J.m^{-2}.[53] This suggests that the work of adhesion is only a very small fraction of the interfacial fracture energy. This difference is due to the contribution of irreversible energy dissipation processes. For systems A and C, the plastic flow in the Al at the interfacial crack tip is certainly the prevailing contribution to the energy values we calculated. Indeed, slip lines on the Al surface are visible under the buckled strips of the SiO_2: 4.5 wt.% P film (Figure 7b). In addition to the effect of the plastic deformation of the substrate, the interfacial fracture energy depends on the trajectory of the interfacial crack, which in turn, is influenced by the test method.[54] Moreover, it is also affected by the presence of impurities at the interface and by roughness, as is shown here by the system D. In this system, asperities on the substrate surface locally increase the stresses and favor the debonding process. The interfacial fracture energy is then one order of magnitude lower, i.e., about 3 J.m^{-2}.

Yet, for systems A and C, the measured fracture energies remain low compared with the critical fracture energy of the bulk aluminum: 10^3 J·m^{-2}.[46] Moreover, we do not observe islands of passivation material on the Al fracture surface and, inversely, we do not observe Al on debonded surfaces of the passivation films. This suggests that the loss of interfacial adhesion is close to a *brittle* fracture process; despite the influence of plasticity of the Al substrate and crack blunting at the interface. This sort of brittle mode of interfacial failure, including plastic flow in a ductile material (the substrate), has been observed or discussed for a sapphire/Au interface.[55]

Even if the Al_2O_3 interlayer accelerates the activation of the transverse cracking, it seems to have the opposite effect on adhesion failure. Indeed, we observe for both systems with an Al_2O_3 interlayer (B and E) that the debonding and buckling are delayed. Therefore, the adhesion of the films is improved. The presence of this thermally grown Al_2O_3 interlayer increases the interfacial fracture energy values to about 15 J.m^{-2} in both systems. Two qualitative explanations can be proposed for the adhesion improvement. First, the Al_2O_3 certainly permits an increase in the number of O-Si bonds between the interlayer and the film. Second, prior to the

deposition of the film, the substrate annealing reduces the organic contamination which weakens the metal/ceramic interfacial strength.[56,57] Finally, from our calculations, the interfacial fracture energy value which corresponds to system E is close to the critical fracture energy value G_c of Al_2O_3, 20 $J.m^{-2}$.[46] This result may suggest a crack propagation in the Al_2O_3 interlayer, confirming the good adhesion of the SiO_2:4.5 wt.% P film on the thermally grown Al_2O_3.

Some Concluding Remarks about the Mechanical Stability of Passivation PECVD Films

The uniaxial determination stretching of this sort of sample, produces transverse cracking of the film, until the saturation of the crack network. The debonding and buckling of the strips of a cracked film is induced by the transverse contraction of the substrate.

The mechanical stability of each film/substrate system can be characterized by three steps.

1. Critical strain determination for the cracking of the film,
2. Evolution of the crack density with the longitudinal strain applied to the system, which can be fitted with an empirical law,
3. Interfacial fracture energy determination associated with the decohesion and buckling process.

In our examples, the systems with a Si_3N_4 film appear to be brittler than the systems with a SiO_2:4.5 wt.% P film. However, both films show good adhesion to the Al substrates. Besides, our experiments show that:

- On the one hand, the thin thermally grown Al_2O_3 interlayer improves the adhesion of both films, but
- On the other hand, the same interlayer imposes its own cracking response to the SiO_2:4.5 wt.% P film.

Because of high stress concentration at the interface asperities, a scratched Al surface significantly reduces the adhesion of the SiO_2:4.5 wt.% P film. Because the Al plastic flow blunts the crack tips reaching the interface, it delays the loss of adhesion of the film from the transverse crack/interface intersections. This plasticity of the Al substrate remains the prevailing contribution in the large interfacial fracture energies obtained for the five systems obtained by PECVD deposition.

PECVD SiC Coatings Deposited on Steel

Another interesting example of the mechanical stability of CVD films is ceramics coatings deposited on metals and/or alloys, which are likely to be used in applications in which wear, corrosion resistance and mechanical strength are needed. Using a PECVD process based on tetramethylsilane (TMS) and argon mixtures, steel substrates can be coated with a dense coating of the type $Si_xC_{1-x}(H)$. These coatings have a complex microstructure but promising physical chemical properties.[58,59] In order to maximize the performance of such coatings which have a very low dry coefficient of friction and low wear rates, their adhesion to a substrate must be as good as possible.

The competition between the interfacial reactivities, the residual stresses and the elasto-plastic behavior of the components will be strongly dependent on the mechanical stability of the coating-substrate combination. Mechanical stability control has been assessed when making ceramic/metal junctions at high temperature (700°C - 1000°C) during which thick reaction zones tend to form by reactive diffusion in volume intermediate layers.[60,61]

These problems concerning a micron-scale deposit and an in volume substrate have rarely been studied in the past. However, from a survey of literature on cases other than that of SiC on steel, it was found that one or several interlayers may change the stress levels in the ceramic. Moreover, once a critical thickness has been reached, these interlayers have a beneficial effect.[62] Some work has been carried out on TiN/SiC layers on a variety of substrates.[63-65] However, in all these studies, information on mechanical stability is fairly limited. Concerning the PECVD of SiC on cutting tools coated with TiN, adherence variations in relation to pretreatment processes were reported.[65]

Recently, the introduction of a metallic interlayer between a coating deposit and its substrate and its effects on mechanical properties were studied.[66,67] The authors experimented with a multilayer approach: a metallic layer sandwiched between two highly reactive layers. For the SiC system, no previous reference on the interposition of a ductile layer between the deposit and the substrate was found, and that motivate the study reports here.

It appears then that the role of an interlayer can be predominant in the mechanical stability of a coating on substrate system. Variable thicknesses may attenuate the difference between the residual stresses in the deposit and in the substrate. This should give the system more satisfactory behavior when subjected to external stresses.

The effect of different types of interlayer on thermoelastic residual stresses can be analyzed from finite-element calculations for a two-dimensional geometry, assuming perfect adherence and without taking into account any reactivity between the components.

From the results obtained, for SiC coatings several cases can be identified for which the Von Mises and shear stresses and their gradients with respect to the interface are low. For example, Ta, Mo, Ti, Nb, and TiN produce this effect, when interposed between the steel substrate and the SiC coating.

Subsequent preliminary comparative studies of the behavior of an SiC based layer on Ta, Mo, Ti and steel substrates showed that better mechanical stability was obtained with a coating deposited on tantalum.[68,69] This element was consequently considered to make PECVD deposit/interlayer/steel stacks. Tantalum can be produced by physical vapor deposition (PVD), at variable thickness, with reproducible morphology. Note that preparation by chemical vapor deposition with or without plasma assistance (CVD or PECVD) is possible at low temperature but would require an optimization study in order to be compatible with the deposition conditions of the silicon carbide layer, the aim being to increase the mechanical stability.

The stated aim of analyzing the change in mechanical stability, implies a prior knowledge of the mechanical properties of the components and the chemical nature of the interfaces. The samples considered here are therefore SiC/steel, SiC/interlayer and interlayer/steel dual layers and SiC/variable thickness interlayer/steel triple layers.

Samples and Mechanical Properties of the Components

The tantalum layer were prepared by PVD on previously polished substrates. The substrates are degassed under argon atmosphere (450°C, 0.2 Pa for 60 min) and then ionically cleaned (18 min, V = 200 V) prior to the deposition stage at 300°C (0.2 Pa, 4 kW, -50 V polarization). The layer obtained is dense but has a number of defects as nodules and craters dispersed over it's surface.

The silicon carbide-based ceramic layer is obtained by CVD activated by a microwave plasma (2.45 GHz) on the tantalum previously cleaned by an argon plasma (56 min, 133 Pa, 250 W) at a temperature identical to the deposition temperature (T_s = 570°C), lower than the substrate annealing temperature. After readjustment of the total pressure and microwave power by introduction of a precursor (TMS) in the argon flow, the SiC coating is produced under selected conditions (66 Pa, TMS/Ar = 0.2/5.5 $l.h^{-1}$, T_s = 570°C, 350 W) derived from a previous parametric study. Coatings obtained then presented low dry friction coefficients.[70]

The mechanical properties, which are essential in order to be able to appreciate the mechanical stability, were acquired by several methods:

- Conventional tensile test with extensometry on standard cylindrical test specimens, for solid commercial steel and tantalum,
- Instrumented nano-indentation (Nano Indenter II) under low applied loads (10 to 100 mN) for all the samples. The announced values are the average of the results of 6 indentations, each resulting from two consecutive load/unload cycles. Young's modulus is calculated by the software supplied with the indenter using data from the second unloading with the Berkovich pyramid indenter of known shape function.

Table 5. Young Moduli (E) of the Substrates, Obtained from Different Experimental Methods

Ref.	$E_{tensile}$ (GPa)	$E_{bending}$ (GPa)	$E_{indentation}$ (GPa)
30NCD14	213	204.5 ± 0.3	226 ± 4
Ta bar	170	187.7 ± 0.5	172 ± 4

- Dynamic bending for the coated plates and with reference layer on (steel and Ta).[71]

For the Young's modulus, the results obtained are presented in Table 5.

The results indicate that the Young's modulus (E) determined perpendicularly to the surface by instrumented nano-indentation on solid steel and Ta specimens were in good agreement (within 10%) with the values obtained by dynamic bending and by tensile testing. Such a result was corroborated by measurements obtained from other materials presenting different elastic responses.

Microstructural Observations: Damage Evolution

A 3-point bending test was applied to the coating/substrate systems. In this way it was possible to observe the increasing damage both on the surface and on one polished side (edge) of the sample, caused by a gradual increase of the applied load. This test and its results are described in several cases.[72-74] The purpose here is to report and discuss the bending and damage evolution with respect to the interlayer. The bending test on parallelepiped specimens with the coating on the outer layer (i.e., subjected to a tensile stress), produced transverse cracks (perpendicular to the longitudinal axis), which increased in number with the specimen deflection. For our samples we observed that the number of cracks increases until a constant value per unit length is reached, independently of strain.

At this stage, the distance d_s (distance to saturation) between two consecutive cracks no longer varies. As in the previously reported experiment, this change may be accompanied by flaking (surface separation) of the film,[75] by crack propagation into the substrate, or by interfacial deviation of the crack without flaking. As shown previously from experimental values, corresponding for example, to the appearance of the first cracks, and by using analytical models, it is possible to deduce the parameters quantifying failure behavior.

The parameters include the critical cracking energy G_{Crack}^{Crit} and the mode-I tensile toughness K_{Ic} of the coating. For the dual layer and triple layer systems presented here, the parameters deduced from three experiments for each type of sample are presented in Tables 6 and 7. The strain values are measured to an accuracy of ± 0.02% following a prior calibration. The applied stress is known to be within 0.1%, from a force sensor and the distance between two cracks is the average of twenty or so values determined to an accuracy of one micron in the central part of the specimen.

For the Ta/steel system, the results show that the induced strain associated with cracking is independent of thickness, and no separation occurs at the test limit. For the SiC/Ta/steel triple layer system, the strain associated with cracking is also independent of thickness, but debonding becomes easier as tantalum thickness increases. An increasingly smaller amount of energy is transferred to the external SiC layer through the tantalum, leading to a correlative increase in the inter-cracking distance. Observed transverse cracks are straight, with regular spacing, and stop at the steel-tantalum interface (Figure 18).

For the SiC/Ta and SiC/steel bilayers, the phenomenology is identical except that, in certain cases, transverse cracking is accompanied by separation (flaking) of the coating. The inter-crack distances are greater

Table 6. Bending Tests on bi Systems with and without Ta Interlayer

		Ta (PVD)/steel				
	SiC/steel	**0.3 µm Ta**	**0.6 µm Ta**	**1.2 µm Ta**	**2.6 µm Ta**	**SiC/Ta**
$\varepsilon_{crack}^{crit}$	0.55%	1.62%	1.62%	1.62%	1.62%	0.24%
$\varepsilon_{separ}^{crit}$ / $\varepsilon_{crack}^{crit}$	1.63	>2.24	>2.24	>2.24	>2.24	1.47
σ_{crack}^{crit} [MPa]	824	3330	3330	3330	3330	358
K_{Ic} [MPa]$\sqrt{m}$	1.0 to 2.7	1.3 to 1.7	1.9 to 2.5	2.7 to 3.5	3.9 to 5.2	0.3 to 0.8

The experimental results correspond to: $\varepsilon_{crack}^{crit}$: critical strain when cracking, σ_{crack}^{crit} corresponding stress. The ratio among the critical strain for debonding ($\varepsilon_{separ}^{crit}$) and the critical cracking strain ($\varepsilon_{crack}^{crit}$) is also indicated. K_{Ic} is the fracture toughness deduced from relations (19) and (20).

with smaller critical strains associated with cracking and separation. The coatings on a solid tantalum substrate (SiC/Ta) show early activation of these mechanisms, probably due to the poor surface condition of the substrate which was difficult to polish well. In this case, transverse crack propagation into the substrate occasionally occurs, but only to a limited extent.

Regarding the trilayered systems (SiC/Ta_x/steel), the critical strain values corresponding to cracking of the coating are of the same order of magnitude (about 0.5%) but crack propagation varies with coating thickness. The cracks still pass through the entire thickness of the silicon carbide deposit. They then extend preferentially into the tantalum layer when this layer is 0.3 µm thick whereas they deviate at the interface in the SiC/$Ta_{0.6\ \mu m}$/steel triple layer. However, in this latter case, sub-cracking of the tantalum occurs. The cracks have a spacing of 10-15 µm, a distance which is similar to that obtained in the case of the SiC/$Ta_{0.3}$/steel system (Figure 18). For greater tantalum layer thicknesses (SiC/$Ta_{1.2\ or\ 2.6\ \mu m}$/steel), the cracks blunt at the tantalum interface. When the strain induced by the test increases, the resulting damage is mainly in the form of debonding at the SiC/tantalum interface.

The ratio between strain at separation debonding to strain on cracking ($\varepsilon_{sepat}^{crit}$ /$\varepsilon_{crack}^{crit}$) is smaller than the same ratio for the SiC/steel reference system for thick tantalum layers (SiC/$Ta_{1.2\ or\ 2.6}$/steel), much higher for Ta/steel and SiC/$Ta_{0.3}$/steel deposits, and about the same for the SiC/$Ta_{0.6}$/steel system (see Tables 6 and 7). This provides qualitative information on the mechanical stability of these systems.

Critical Parameters

In, the central zone, the regular distribution of transverse cracks shows that the induced strain is rather homogeneous. Consequently, many analytical models can be applied in order to determine the intrinsic parameters of the coatings. The critical cracking energy G_{crack}^{crit} and the mode I fracture toughness K_{IC}^{crit} of the deposited silicon carbide film were assessed by means of the model presented previously. It should be remembered that it was first established and developed for composite materials based on research by Kelly[76] and subsequently by Hu[24], that when the stress normal to the coating reaches a critical value

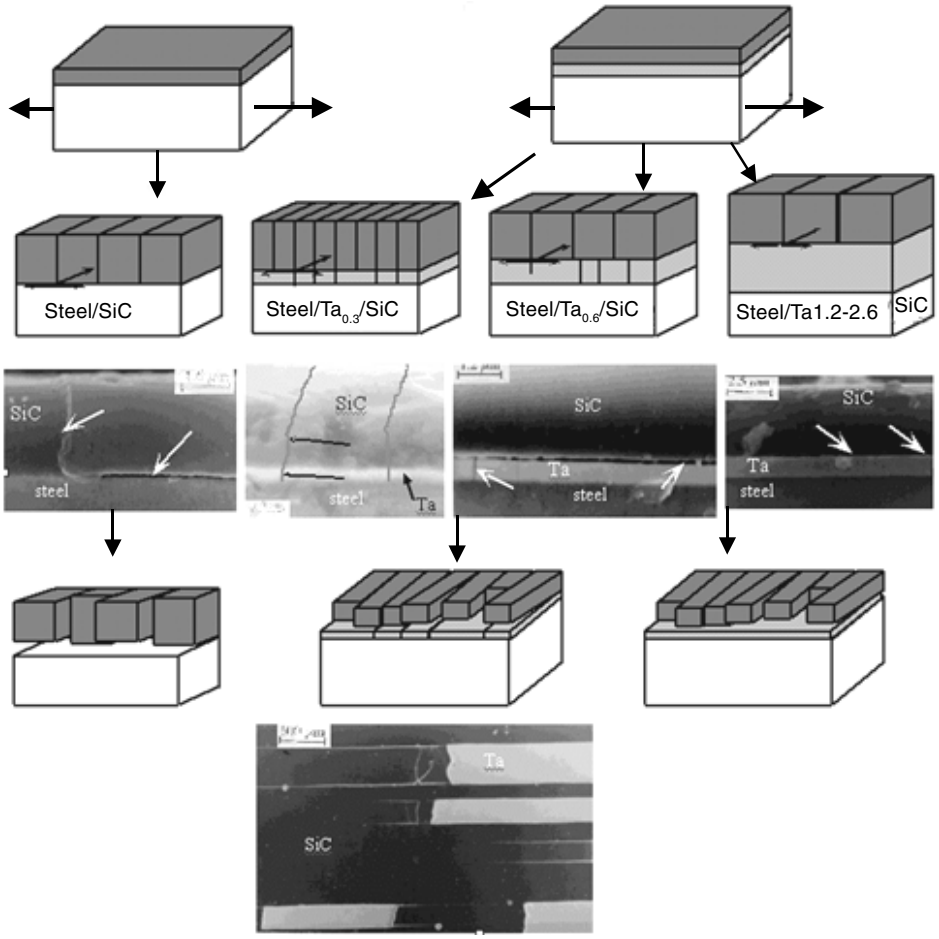

Fig. 18: Schematic representations and micrographs of damage: case of the SiC / steel reference system and SiC/ Ta_x/steel triple layers (x corresponds to the Ta interlayer thickness in microns).

σ_{crack}^{crit}, the layer cracks. In the vicinity of the free surfaces of the cracked film, the normal stress then tends to zero. Similar to relation 11 for the critical cracking energy, G_{crack}^{crit}, a relation can be deduced, taking into account the work performed by the external force during film cracking, the elastic energy dissipated when the cracks propagate in the film, the energy associated with plastic strain in the vicinity of the cracks and the change in energy induced by redistribution of the normal stress in the substrate.[24] By considering the residual stresses, σ_r^f, in the film, this critical cracking energy is expressed as:

$$G_{crack}^{crift} = \frac{(\sigma_{crack}^{crit} + \sigma_r^f)^2}{E_f} \left\{ \pi_f + \frac{\sigma_{crack}^{crit} + \sigma_r^f}{R_e \sqrt{3}} \right\} \quad (19)$$

In equation (19) which is similar to equation (11), πf is a function of the ratio of Young's moduli of the film and the substrate, and σ_{crack}^{crit} is the critical stress of the film which corresponds to the activation of primary transverse cracking. This parameter is directly deduced by applying the Hooke's relation to the film, deformed at a critical strain by the substrate, which is determined from the experiment. We may note

here that the residual stress term is considered. Assuming uniaxial stress application in the film plane, an apparent mode I- fracture toughness of the film (K_{Ic}^{s}) can then be calculated as:

$$K_{Ic}^{s} = \sqrt{G_{crack}^{crit} \cdot E_f} \quad (20)$$

The fracture toughness values of the silicon carbide deposits on steel thus calculated (cf. Table 6) are of the same order of magnitude as the toughness of a sintered silicon carbide (1 to 4 MPa.m $^{1/2}$).[77] On a tantalum substrate, these are lower. These differences are probably due to residual stresses which vary considerably depending on the nature of the underlying substrate.

Regarding PVD Ta, the values reflect the specific nature of this material compared to as cast tantalum. The observed increase in K_{Ic}^{f} with thickness may result from an interface contribution which is the greater as the deposited layer is thinner or from possible changes in the morphology of the layer in relation to its thickness.

The analytical approach developed by Schadler and Noyan,[78] allows calculation of the stress redistribution in cracked triple layer systems.[38] This approach assumes mechanical equilibrium of the cracked coating and the interlayer through perfectly adhering interfaces which transfer the applied stress to the substrate. It is thus possible to deduce expressions for stress distribution normal to the cracked film and shear stress distribution at the interlayer:

$$\sigma_{SiC} = \sigma_s E_{SiC} \{\cosh(\beta.x) / \cosh(d\beta/2) - 1\} / E_s \quad (21)$$

$$\tau(x) = G_{Ta} \sigma_s \sinh(\beta.x) / h_{Ta} E_s \beta \cosh(\beta d/2) \quad (22)$$

where d is the intercracking distance, and σ_s represents the stress imposed by the test on the substrate in the vicinity of the interface and where β is defined by:

$$\beta^2 = G_{Ta}(1/E_s h_s + 1/E_{SiC} h_{SiC})/e_{Ta} \quad (23)$$

The calculation hypotheses assumes continvity of displacements across the SiC/$Ta_{1.2\ \mu m}$/steel triple layer interfaces. The variation in shear stress calculated by the above-mentioned relationship is then used to make a comparison between the assumed perfect adherence of the calculations and the experimental observations.

As a numerical application, we can consider here a shear stress of 800 MPa, estimated from coating cracking stresses. Then the inter-crack distances resulting from perfect adherence can be calculated.[79] This distance can be compared to the experimental values in Table 7. For SiC/$Ta_{0.3}$/steel, there is good agreement between the theory (perfect adhesion) and the experimental observations. On the other hand, for the other systems, the significantly smaller theoretical distances compared with experimental distances is indicative of unsatisfactory interfacial attachment in the vicinity of the transverse cracks of the coating.

The Effects of an Interlayer

Trilayered systems can then be analyzed according to two different approaches: the first focused on the reactional aspects at the interfaces and the second concentrated on the mechanical stability of the triple layer system.

Concerning the SiC coating composition of our systems, SIMS analyses demonstrated the compositional homogeneity of the layer which is slightly hydrogenated. Regardless of the substrate (tantalum or steel) used to deposit the coating at 843 K for 15 min, a 0.3 - 0.4 μm thick diffusion-reaction zone is formed. However, in the case of SiC/steel deposits, no clear evidence could be found for the presence of Fe-Si bonds: because the oxygen present at the interface could mask it. At the Ta/steel interface, no peaks were detectable, but in view of the phase diagram which exhibits extensive solid solutions, the possibility of an interaction in the Fe-Ta system cannot be excluded.

As regards the SiC/Ta interface, the peak shifts (Si, C) reflect the changes in chemical environment of these elements and the existence of complex bonds in the Ta-Si-C-O and Ta-C systems. Note that Auger measurements performed on the denuded parts of the substrate obtained during scratch tests, and on these same parts obtained during bending tests, give evidence of a failure surface made of tantalum,

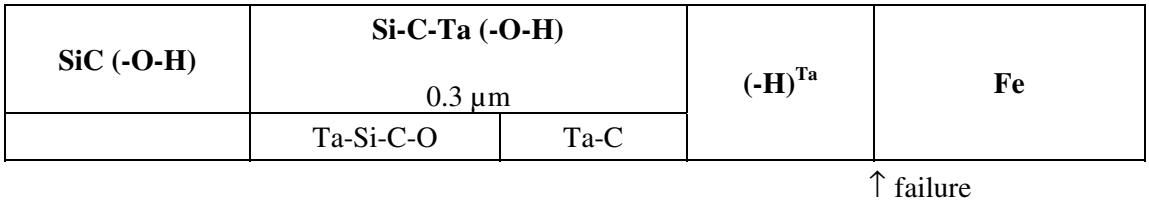

Fig. 19: Schematic representation of a SiC/Ta/steel systems deduced from SIMS and Auger analysis, including the possible site of debonding failure.

Table 7. Bending Tests on Triple Layer Systems

	$SiC/Ta_x/steel$			
	TMS6	**TMS5**	**TMS3**	**TMS4**
	0.3 μm Ta	0.6 μm Ta	1.2 μm Ta	2.6 μm Ta
$\varepsilon_{crack}^{crit}$	0.48%	0.54%	0.53%	0.51%
$\varepsilon_{separ}^{crit}/\varepsilon_{crack}^{crit}$	4.50	1.67	1.20	1.26
d_s^{exp}[μm]	17	27	37	57
σ_{crack}^{crit}[MPa]	720	806	798	766
σ_s[MPa]	1090	1210	2100	1150
d_s^{calc}[μm]	14	6.5	6	6

The strains ε are defined on Table 6, also σ_{crack}^{crit}. d_s^{exp} and d_s^{calc} are the experimental and calculated distances between two consecutive cracks at saturation, and σ_s is the stress applied during the test on the substrate in the vicinity of the interface.

regardless of the thickness of the intermediate tantalum layer (Figure 19).

If compared to normal indentation and scratch tests, identical qualitative ranking of mechanical stability of the trilayered samples was obtained.[79] The behavior of the TMS3 sample ($SiC/Ta_{1.2}$/steel) stands out clearly from the others. For this thickness of tantalum, the resistance to flaking caused by scratch and indentation tests reaches a maximum value with reduced flaking. This optimum thickness is to be linked to the state of residual stresses in the deposits as evidenced by the concomitant variations in the parameters involved (Figure 20). When the coating is under the highest residual stress, the best mechanical stability is obtained in the scratch and indentation tests. Several other authors have mentioned this relation in the past.[80] More recently, Kleer[81] showed that the critical load L_c increases when the state of stress in an AlN coating on silicon carbide gradually changes from tensile to compressive.

From another standpoint, the mechanical stability of various samples can be ranked by the bend test by referring to experimental data such as $\varepsilon_{separ}^{crit}/\varepsilon_{crack}^{crit}$. In particular, the

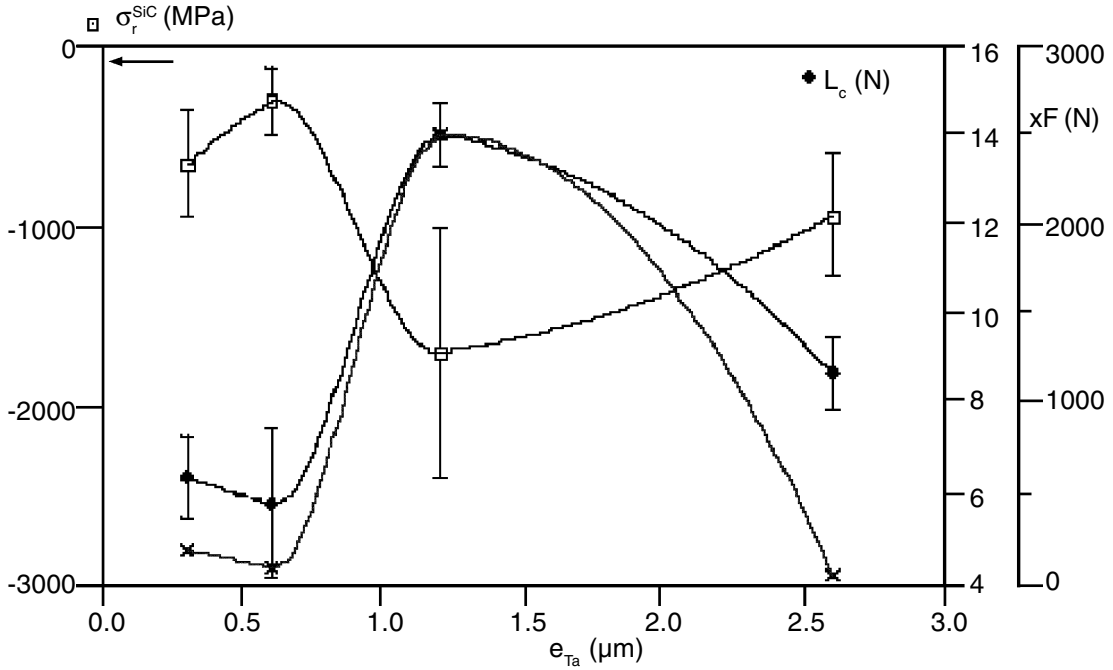

Fig. 20: Critical scratching load L_c, macro-indentation failure load F and residual stresses σ_r, SiC in the triple layer system. e_{Ta} corresponds to the thickness of the Ta interlayer.

characteristic parameters of the layers can be deduced, something that has not been possible up till now with the other methods used in this work. Thus the calculated fracture toughness values for a silicon carbide layer deposited on tantalum or steel (of the order of 1 MPa.m$^{1/2}$) are consistent with the order of magnitude of the usual values for ceramic materials. On the other hand, the fracture toughness tensile strength values of PVD tantalum layers are very low compared to those generally taken for in volume tantalum (between 20 and 40 MPa.m$^{1/2}$). These films therefore have specific properties.

The analytical lag approach, based on strain transfer by shearing of the intermediate layer, provides information on the separation mechanism. The coating with a 0.3 μm thick tantalum layer (sample TMS6) exhibits the most efficient transfer capacity without debonding. A close examination of the damaged crystallographic surfaces (polished edge of plates or indentation denuded surfaces along the extension of radial cracks) indicates the presence of cracks which extend into the tantalum. These cracks are all the more numerous as the interlayer thickness decreases. It is also found that, for thin tantalum layers, the cracks pass right through the layers to the substrate. However, when the interlayer thickness increases, the cracks tend to die out in the tantalum or deviate along the SiC/Ta interface. All things considered, the damage in a triple layer system will, as a first approximation, be governed by the mechanical properties of the interlayer and of the first interface.

The methods applied to assess mechanical stability give proof of the beneficial role of the interposition of a PVD tantalum layer between the PECVD deposited ceramic layer and the substrate: a factor of 2 gain in strain and in critical load with respect to the SiC/steel pair. However, it is nonetheless clear that the optimum thickness of the interlayer could not be established with certainty. At the present time, there does not appear to be any experimental explanation for this. The only factor that might be stressed is

that, given the existence of an interdiffusion-reaction zone between the coating and the metallic interlayer (see Figure 19), the improvement cannot be attributed to the change in residual stresses alone, and that the different tests induce different stress fields. Unlike the scratch and macro-indentation tests which quickly place the material under stress (just a few seconds), the bend test requires several minutes. Under these conditions, there is time for stress to redistribute and also relax by plasticity in the interlayer and at the top of the substrate.

In order to be able to optimize the mechanical stability of such systems, more tests must be performed along with in-depth microstructural examination of the interfaces.

Conclusions

Because of the processing method, CVD introduce residual stresses in the films on substrates.

These stresses can reach values as high as flow stress values, and then induce some stress relaxation mechanisms which can include plasticity and/or spontaneous cracking. Meanwhile, if the internal stress levels are lower, any external stress can be critical, and promote a damage mechanism, similar to those previously described.

Therefore, it is important to observe and study the mechanical response of film on substrate systems under external stresses, in particular when establishing the reliability of PECVD systems.

A lack of experimental information exist in this area that can be addressed by performing in-situ experiments.

The micromechanical experiments in a SEM, characterize the damage evolution on preselected areas of film on substrate systems.

The results on different PECVD films, showed that the failure of the systems was different, depending on the associated materials and on the interfacial behavior when the debonding occurred with buckling, or by interfacial crack deviation, the transverse crack saturation was reached at lower strains. No debonding showed higher crack saturation values. Following the activation of the mechanisms, which drive a system to its failure, critical parameters can be derived from the experiments as follows.

- The critical stresses and strains for cracking, the toughness of a layer,
- The critical length for stress transfer for the system presenting an interlayer;
- The interfacial fracture energy associated with the debonding of a layer.

The values of these parameters corresponding to intrinsic properties of the systems, can be cross checked and discussed with respect to parameters calculated from analytical models.

Finally, if may be emphasized that these experiments allow first to improve the information which is needed to validate theoretical models and second it allows to select film on substrate systems for defined applications.

References

1. E. Klokholm, Delamination and Fracture of Thin Films, *IBM Journal of Research and Development,* Vol.31(No.5), 1987, p.585.
2. A.A. Griffith, *Proceedings of First International Congress of Applied Mechanics, Delft,* 1924, p.55.
3. G.I. Barenblatt, Mathematical Theory of Equilibrium Cracks in Brittle Fracture, *Advanced Applied Mechanics*, Vol.7, 1962, p.55.
4. M. Toya, Fracture Mechanics of Interfaces, *JSME International Journal, Series I,* Vol.33(No.4), 1990, p.413.
5. D. Tabor, Surface Forces and Surface Interactions, *Journal of Colloid and Interface Science,* Vol.58(No.1), 1977, p.2.
6. K.L. Mittal, Adhesion Measurement of Thin Films, *Electrocomp. Science Technology,* Vol.3, 1976, p.21
7. R.J. Good, *Intermolecular and Interatomic Forces Dans Treatise on Adhesion and Adhesives*, R.L. Patrick, ed., M. Dekker Inc., New York, Vol.1, 1967, p.9.
8. D. Taylor and J.E. Rutzler, Adhesion Using Molecular Models, *Industrial Engineering*

Chemistry , Vol.50, 1958, p.928.
9. G. Bordier and C. Noguera, Electronic Structure of a Metal/Insulator Interface: Towards a Theory of Nonreactive Adhesion, *Physics Review B,* Vol.44(No.12), 1991, p.6361.
10. F.S. Ohuchi and M. Kohyama, Electronic Structure and Chemical Reactions at Metal/ Alumina and Metal/Aluminum Nitride Interfaces, *Journal of Amercian Ceramic Society,* Vol.74(No.6), 1991, p.1163.
11. N. Eustathopoulos, D. Chatain, and L. Coudurier, Wetting and Interfacial Chemistry in Liquid Metal/ceramic Systems, *Materials Science and Engineering*, Vol.A135, 1991, p.83.
12. E.D. Hondros, Bonding of Metal/Ceramic Interfaces, International Conference Science Hard Materials, *Institute of Physics Conference Ser.,* Vol.75(No.2), 1986, p.121.
13. T. Suga and G. Elssner, Determination of the Fracture Energy and the Fracture Resistance of Interfaces, *Journal of Physics,* Vol.C4(No.46), 1985, p.657.
14. D.S. Rickerby, A Review of the Methods for the Measurement of Coating/Substrate Adhesion, *Surface and Coatings Technology*, Vol.36, 1988, p.541.
15. A. Chouaf, Etude de la Stabilité Mécanique de Films de Tungsténe déposés Sur Des Substrats de Silicium, Thése, INPG, Grenoble, 1992.
16. P. Scafidi, Fissuration et Perte d'adhérence de Couches de Passivation Sur Substrats d'aluminum, DEA, INPG, Grenoble 1992.
17. W.D. Nix, The Mechanical Properties of Thin Films on Substrates, *Metallurgical Transactions,* Vol.A1, 1989, p.2217.
18. F.M. D'Heurle and J.M.E. Harper, Note on the Origin of Intrinsic Stresses in Films Deposited Via Evaporation and Sputtering, *Thin Solid Films,* Vol.171, 1989, p. 81.
19. M.F. Doerner and W.D. Nix, Stresses and Deformation Processes in Thin Films on Substrates, *CRC Critical Review Solid State Materials Science,* Vol.14, 1988, p.225.
20. P. Dhaudari, Grain Growth and Stress Relief in Thin Films, *Journal of Vacuum Science and Technology*, Vol.9(No.1), 1972, p.520.
21. R.W. Hoffman, The Mechanical Properties of Thin Condensed Films, Physics of Thin Films, G. Hass and R.E. Thurn, *eds.,* Academic Press, New York, Vol.34, 1966, p.211.
22. H.E. Evans, Cracking and Spailing of Protective Oxide Layers, *Material Science and Engineering*, Vol.A120, 1989, p.139.
23. M. Hershbovitz, I.A. Blech, and Y. Komen, Stress Relaxation in Thin Aluminum Films, *Thin Solid Films,* Vol.130, 1985, p.87.
24. M.S. Hu and A.G. Evans, *Acta Metallurgica*, Vol.37, 1989, pp.917-925
25. F. Delannay and P. Warren, *Acta Metallurgica,* Vol.39, 1991, pp.1061-1070.
26. J.W. Hutchinson and Z. Suo, *Advanced Applied Mechanical*, Vol.29, 1992, pp.63-95.
27. T. Ye, Z. Suo, and A.G. Evans, *International Journal of Solid Structures,* Vol.29, 1992, p.2639.
28. G. Gille and K. Wetzig, *Thin Solid Films*, Vol.110, 1983, pp.37-45.
29. W. Weibull, *Journal of Applied Mechanics,* Vol.18, 1951, pp.293-297.
30. A. Mézin, J. Lepage, N. Pacia, and D. Paulmier, *Thin Solid Films,* Vol.172, 1989, pp.197-215.
31. D.C. Agrawal and R. Raj, *Acta Metallurgica,* Vol.37, 1989, pp.1265-1279.
32. T.S. Chow, C.A. Liu, and R.C. Penwell, *Journal of Polymer Science,* Vol.14, 1976, pp.1305-1312.
33. F. Faupel, C.H. Yang, S.T. Chen, and P.S. Ho, *Journal of Applied Physics*, Vol.65, 1989, p.1911.
34. M. Ignat, A. Armann, L. Moberg, and F. Sibieude, *Surface and Coatings Technology*, Vol.49, 1991, pp.514-521.
35. M. Ignat, M. Ducarroir, M. Lelogeais, and J. Garden, *Thin Solid Films,* Vol.220, 1992, pp.271- 277.
36. M. Ignat, L. Fayette, F. Templier, and J. Torres, *Proceedings of Materials Research Society Symposium*, Vol.264, 1992, pp.207-213.
37. P. Seafidi and M. Ignat, *Proceedings of Materials Research Society Symposium,* Vol.309, 1993, pp.55-60.
38. M. Ignat, P. Scafidi, E. Duloisy, and J. Dijon, *Proceedings of Materials Research*

Society Symposium, Vol.338, 1994, pp.135-146.
39. P.A. Flinn, Stress Induced Phenomena in Metallization, C. Li, P. Totta, and P. Ho, eds., *Proceedings of AIP Conference*, New York, Vol.263, 1992, pp.73-79.
40. J. Bénard, *L'Oxydation Des Mdtaux*, Gauthier-Villars, ed., Tome II, 1964.
41. A. Chouaf, M. Ignat, P. Normandon, and J.M. Terriez, *Proceedings of Materials Research Society Symposium*, Vol.203, 1991, pp.177-182.
42. M. Ignat, *Key Engineering Materials,* Vol.116-117, 1996, pp.279-289.
43. M. Ignat, C. Josserond, and L. Debove, *Bulletin De La SFME,* Vol.14, 1995, pp.10-13.
44. J. Aveston, G.A. Cooper, and A. Kelly, *The Properties of Fiber Composites,* IPC Science Technology Press, U.K., 1971.
45. P.H. Wojciechowski and M.S. Mendolia, *Journal of Vacuum Science and Technology*, Vol.A7, 1989, pp.1282-1291.
46. M.F. Ashby and D.R.H. Jones, *Engineering Materials*, Pergamon Press, Vol.1, 1980.
47. G.R. Anstis, P. Chanttikul, B.R. Lawn, and D.B. Marshall, *Journal of Amercian Ceramic Society*, Vol.64, 1981, p.533.
48. P.A. Flinn, *Proceedings of Materials Research Society Symposium*, Vol.130, 1989, pp.41-52.
49. B. Bhushan, S.P. Murarka, and J. Gerlach, *Journal of Vacuum Science and Technology,* Vol.138, 1990, pp.1068-1075.
50. A. Davutoglu and I.A. Aksay, *Surfaces and Interfaces in Ceramic and Ceramic-Metal Systems*, University of California Berkeley Press, 1980, pp.64-70.
51. S.P. Timoshenko and J.M. Gere, *Theory of Elastic Stability*, Me Graw Hill, New York, 1961.
52. A.G. Evans and J.W. Hutchinson, *International Journal of Solids Structures,* Vol.20, 1984, p.455-465.
53. E.D. Hondros, *Institute of Physics Conference Ser.,* Vol.75, 1986, pp.121-128.
54. A.G. Evans, B.J. Dalgleish, M. He, and J.W. Hutchinson, *Acta Metallurgica,* Vol.37, 1989, pp.3249- 3260.
55. I.E. Reimanis, B.J. Dalgieish, M. Brahy, M. Rühle, and A.G. Evans, *Acta Metallurgica,* Vol.38, 1990, pp.2645-2663.
56. D.M. Mattox, *Deposition Technology for Films and Coatings,* R.F. Bunshah, ed., N.Y., 1982, p.63.
57. A.I. Sauter and W.D. Nix, IEEE *Transactions CHMT*, Vol.15, 1992, pp.594-603.
58. S. Scordo, M. Ducarroir, T. Grégoire, and C. Boher, French Patent No.9507999, 1995.
59. M. Ducarroir, L. Thomas, S. Scordo, R. Berjoan, M. Andrieux, and J.L. Jauberteau, *Annual Chemical Science Materials,* Vol.23, 1998.
60. R. Schiepers, Ph.D., Eindhoven University, The Netherlands, 1991.
61. W.A. Kaysser, A. Frisch, W. Zhang, and G. Petzow, Metal Ceramic Joining, the Minerals, *Metals and Materials Society,* Vol.13, 1991.
62. K. Suganuma, T. Okamoto, and M. Koizumi, *Journal of American Ceramic Society*, Vol.C256, 1984.
63. E. Cappelli, G. Giunta, A. Parretta, and V. Adoneecchi, *High Performance Ceramic Films and Coatings, 1991,* p.409.
64. G. Giunta, M. Fiorini, V. Vittori, and G. Marchesano, *Surface and Coatings Technology,* Vol.49(No.1-3), 1991, p.174.
65. V.A. Mernagh, T.C. Kelly, M. Ahern, A.D. Kennedy, A.P.M. Adriaansen, P.P.J. Ramaekers, L. Mcdonnel, and R. Koekoek, *Surface and Coating Technology*, Vol.49, 1991, p.462.
66. M. Nesladek, C. Asinari, J. Spinnewyn, R. Lebout, *Diamond and Related Materials,* Vol.3(No.4-6), 1994, p.912.
67. M. Nesladek, K. Vandierendonck, C. Quaeyhaegens, M. Kerkhofs, and L.M. Stals, *Thin Solid Films,* Vol.270, 1995, p.184.
68. A. Angelelis, M. Ducarroir, E. Felder, M. Ignat, and S. Scordo, *Annual Chemical Science Materials*, Vol.23, 1998.
69. M. Andrieux, M. Ducarroir, and A. Le Vide, *Science, Technique et Applications,* Vol.279, 1996, p.212.

70. C. Boher, M. Ducaroir, S. Scordo, and T. Grégoire, *Annual Chemical Science Materials*, Vol.23, 1998.
71. P. Mazot and S. Pautrot, *Annual Chemical Science Materials*, Vol.23, 1998.
72. M. Ignat, M. Ducarroir, M. Lelogeais, and J. Garden, *Thin Solid Films,* Vol.220, 1992, p.271.
73. M. Ignat, A. Armann, L. Moberg, and F. Sibieude, *Surface and Coating Technology,* Vol.49, 1991, p.81.
74. P.M. Ramsey, H.W. Chandler, and T.F. Page, *Thin Solid Films,* Vol.201, 1991, p.514.
75. S.P. Timoshenko, *Theory of Elastic Stability,* Mc Graw Hill, New York, 1961.
76. A. Kelly, *Strong Solids*, Clarendon Press, Oxford, 1973.
77. *CRC Handbook of Chemistry and Physcis*, 66th Edition, CRC Press Inc., Boca Raton, Florida.
78. L.S. Schadler and I.C. Noyan, *Proceedings of Materials Research Society Symposium*, Vol.239, 1992, p.151.
79. M. Andrieux, Thèse No.171D, Université De Perpignan, 21 Février 1997.
80. P.J. Burnet and D.S. Rickerby, *Thin Solid Films,* Vol.154, 1987, p.403.
81. G. Kleer, R. Kassner, E.M. Meyer, M.G. Schinker, and W. Doell, *Surface and Coatings Technology,* Vol.54-55, 1992, p.167.

Chemical Vapor Deposition
Jong-Hee Park, T.S. Sudarshan, editors, p81-102
DOI:10.1361/chvd2001p081

Chapter 4

Combustion Chemical Vapor Deposition (CCVD)

A.T. Hunt and Matthias Pohl
Micro Coating Technologies, Inc.
3901 Green Industrial way
Chamblee, Ga 30341

Abstract

Combustion Chemical Vapor Deposition (CCVD) allows deposition of thin films that confer special electronic, catalytic, or optical properties, corrosion and oxidation resistance. The CCVD process is a novel, open-atmosphere process that is environmentally friendly and does not require expensive reaction/vacuum chambers. Often coatings are of equal or better quality than those obtained by vacuum-based methods. Coating costs are significantly lower than for more traditional processes such as Chemical Vapor Deposition (CVD) and Physical Vapor Deposition (PVD). Equally important, this novel technology can be implemented in a production-line environment, thus enabling uninterrupted processing. To date over 70 different inorganic materials have been deposited onto a variety of substrates ranging from metals and ceramics to polymers. Compositionally complex films and multi-layered coatings are possible. CCVD has been shown to provide excellent stoichiometric control for such coatings.

Introduction to the Combustion CVD Process

The innovative Combustion Chemical Vapor Deposition (CCVD) process, patented[1] for applications other than the diamond coatings by the Georgia Institute of Technology and licensed exclusively to Micro Coating Technologies, Inc., (MCT, Chamblee, GA) has demonstrated its ability to overcome many of the shortcomings of traditional vapor

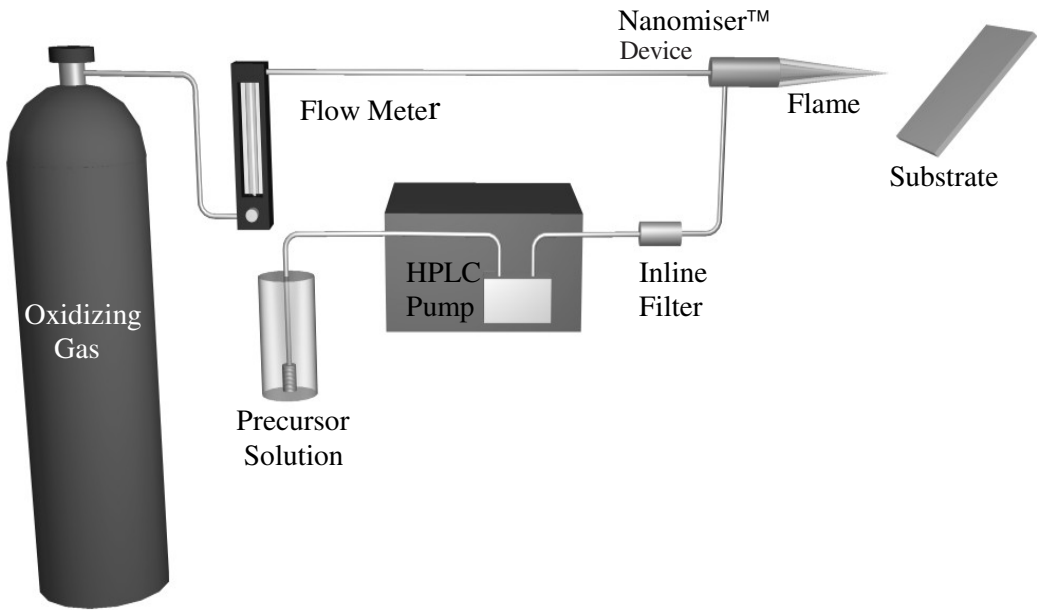

Fig. 1: Schematic representation of the open-atmosphere CCVD system showing its major components.

deposition techniques while yielding equal or better quality coatings at a lower cost. The key advantage of the liquid solution CCVD technology is its ability to deposit thin films in the open atmosphere (or any pressure above 10 Torr) using inexpensive liquid-based precursors or traditional high vapor pressure precursors. This obviates the need for costly furnaces, vacuum equipment, reaction chambers, and post-deposition treatment (e.g. annealing).

A schematic representation of a liquid solution CCVD system and its major components can be seen in Figure 1: typically, precursors are dissolved in a combustible solvent which also acts as the fuel for the flame. This solution is atomized to form submicron droplets by means of a proprietary technology (Nanomizer™ technology, patent pending). These droplets are then carried by an oxygen gas stream into a flame where they are combusted. Coating is accomplished by simply drawing combustion plasma containing the activated deposition species over the substrate's surface. The thermal energy from the flame provides the means to evaporate the droplets and for the precursors to react and deposit onto the substrate. The entire process generally takes no more than two hours from initial set-up to post-deposition cleaning. Multiple experimental utilizing the same solution require less than 30 additional minutes per run. Therefore, coatings and their properties can be optimized quickly in a systematic manner.

The liquid solution CCVD process does not deposit droplets (these evaporate in the flame environment) or powders as in traditional thermal spray processes. The CCVD technology is drastically different from spray pyrolysis: In spray pyrolysis, a liquid mixture is sprayed onto a heated substrate, while CCVD atomizes a precursor solution into sub-micron droplets followed by vaporization of said droplets. The resulting coating capabilities and properties described hereafter qualifies CCVD as a true vapor deposition process. For example, depositions are not line-of-sight limited and achieve epitaxy, 10 nm dielectric coatings onto silicon wafers in a Class 100 clean room resulted

in a capacitor yield of 100%. This result attests to the high quality of the coatings, which were found to be free of particles, pinholes and other defects. For some materials, substrate temperatures may be as low as 100°C, thus, enabling deposition onto a wide variety of materials including polymers.

By adjusting solution concentrations and constituents, a wide range of coating stoichiometries and compositions can be achieved. This is especially valuable for achieving specific composition and thin film characteristics. Conventional CVD requires precursors with sufficiently high vapor pressures to enable vapor phase transport. This frequently necessitates the use of expensive materials and often produces toxic fumes which must be carefully treated ("scrubbed"). In contrast, the liquid solution CCVD technique uses soluble precursors that do not need to have a high vapor pressure. Precursors for the CCVD process tend to be between 10 and 100 times less expensive than those used in traditional CVD processes. Physical structure and chemical composition of the deposited films can be tailored to the specific application requirements: This greatly facilitates the rational design of thin films.

In summary, the CCVD process offers the following capabilities.

- **No Need for Specialized Chamber:** Depositions are inexpensively performed at ambient conditions without the need for expensive, specialized equipment such as reaction furnaces and/or vacuum chambers, reducing repair times and costs.
- **Uses Inexpensive Precursors:** Soluble precursors are used instead of expensive, high vapor pressure organometallics.
- **Excellent Composition Control:** Solution properties is adjustable to allow for great versatility in depositing a wide variety of complex multi-component compounds with targeted stoichiometries.
- **Suitable for Continuous Production:** The equipment enables a robust production system which has been shown to operate without failure around the clock for several days. Substrates that have been coated include fiber tows, pins, industrial rollers, wire, radiators, and roll sheet material.
- **Straightforward Integration into Existing Production Processes:** Advanced materials can be deposited onto large surface areas, including assembled parts that would be difficult to place inside a traditional coating chamber.
- **Ability to Deposit Multi-Layered Structures:** CCVD flames are regularly used in sequence to deposit multi-layered structures.
- **Wide Choice of Substrates:** The CCVD process allows deposition on to many different substrate materials, including plastics which can be incompatible with vacuum processes. Different sizes and shapes can be processed including non-planar substrates.
- **Precise Control of Coverage Area:** Coating can be limited to specific areas of a substrate by simply controlling the dwell time.
- **No Line-of-Sight Limit:** Operating at atmospheric pressure randomizes atom trajectories through diffusion. This permits infiltration into high aspect ratio holes and vias, as well as complete coverage around fibers and wires. This contrasts with conventional long mean-free-path processes where the "shadowing" of molecular rays affects distribution of coatings over non-planar surfaces.
- **Outstanding Microstructure Control:** Microstructure of the deposited film is closely controlled, ranging from dense, *epitaxial* films to high surface area, nanoporous layers.
- **Accelerated Development Cycle for New Applications:** Development of coatings for specific applications is achieved more rapidly than with traditional technologies: a large number of samples are quickly prepared for testing and optimization.
- **Environmentally Friendly:** Relatively safe chemical precursors (non-toxic and halogen-free) are used, resulting in benign by-products, thus reducing environmental impact.

As a result, capital requirements and operating costs are reduced up to tenfold when compared to competing chamber-and vacuum-

Table 1. Partial list of Thin Film Materials Deposited by CCVD

Metals	Ceramics	Others
Ag, Au, Cu, Ir, Ni, Rh,Pt.	Al_2O_3, doped-Al_2O_3, Al_2O_3•MgO, $3Al_2O_3$•$2SiO_2$, $BaCeO_3$, $BaTiO_3$, BST, CeO_2, Cr_2O_3, Cu_xO, $[La_{.95}Ca_{.05}]CrO_3$, Fe_2O_3, In_2O_3, ITO, $LaAlO_3$, LSC, LSM, MgO, Mn_2O_3, MoO_3, Nb_2O_5, NiO, NSM, $PbTiO_3$, PdO, PLZT, PMN, PMT, PNZT, PZT, RbO_x, RhO_x, RuO_2, SiO_2, Spinels (e.g. $NiAl_2O_4$, $NiCr_2O_4$), Silica Glasses, doped-SnO_2, $SrLaAlO_4$, $SrRuO_3$, $SrTiO_3$, Ta_2O_5, TiO_2, V_2O_5, WO_3, $YBa_2Cu_3O_x$, $YbBa_2Cu_3O_x$,YIG, YSZ, YSZ•Al_2O_3, YSZ-Ni, ZrO_2, fully and partially stabilized ZrO_2 (Dopants: Y, Ce, Al).	$BaCO_3$, $LaPO_4$, $PbSO_4$.
Substrates Used		
Al, Brass, Ag, Cu, Pt, Ni, Stainless and C-Steel, Al_2O_3, Fiber Tows, Glass, Graphite, $LaAlO_3$, MgO, NAFION™, NiCr, Optical Fibers, Polycarbonate, Silica, Si, Si-Ti/Pt Wafers, SiC, Si_3N_4, Superalloys, Teflon™, Ti, TiAl alloy, YSZ.		
Possible Applications		
Architectural Finishes, Capacitors, Catalytic Applications, Corrosion Resistance, Cutting Tools, Electronics, Engines, Ferroelectric Materials, FGM, Fuel Cells, Integrated Circuits, Optics, Piezoelectrics, Replacement for Nickel Plating, Superconductors, Thermal Barrier, Thermal Control, Wear Resistance.		

based technologies (e.g. sputtering and most CVD). The ability to deposit thin films in the open atmosphere enables continuous, production-line manufacturing. Consequently, throughput potential is far greater than with conventional thin-film technologies, most of which are generally restricted to batch processing. Thus far CCVD has been used to prepare more than seventy distinct material compositions for a variety of applications. (Table 1).

Related Technologies and Processes

What follows is a review of the open and patent literature of thin film deposition processes that are related to Combustion Chemical Vapor Deposition (CCVD). This will help to distinguish the novel CCVD process from more classical processes such as CVD, spray deposition, and thermal spraying and to highlight its inherent advantages and limitations.

Combustion CVD vs. Traditional CVD

Chemical Vapor Deposition (CVD) has been defined as "*a materials synthesis process whereby constituents of the vapor phase react chemically near or on a substrate surface to form a solid product*."[2] With these traditional processes a reaction chamber and secondary energy (heat) source are mandatory making them different from the Combustion CVD process. Numerous flame-based variations of CVD have been used to generate powders, perform spray pyrolysis, create glass forms, and form carbon films including diamond films.

In the 1940's a CVD process using a flame to produce homogeneously nucleated (powder) oxides of titanium, zirconium, iron, aluminum, and silicon was reported.[3] A mixture of metal halide vapor and oxygen is injected through the central nozzle of a burner, with fuel gas and supplemental oxygen provided through two concentric outer rings. At 950ºC to 1100ºC flame temperature, the metal halide vapor decomposes to form very fine oxide powders.

Several patents[4-6] were granted for the production of glass in a flame using combustible gases and hydrolysis of silicon compounds. Furthermore, two-component powders have been made using a combustion flame in a reactor, here vaporized precursors were mixed with nitrogen and fed into a hydrogen-oxygen flame.[7] Diamond films have been deposited by a process known as the Hirose method which is diamond CCVD from the reducing portion of an acetylene oxygen flame.[8,9] (Note that this technology is different from MCT's CCVD process that can use dissolved precursors as the source material and has a much wider applicability than Diamond CCVD). Notably, all of these methods rely on gaseous and/or vaporized precursor materials whereas CCVD can employ liquid precursor solutions.

Coatings have also been accomplished using powders, sprayed or atomized solutions. For example, the Pyrosol® process involves deposition from a vapor which is generated by ultrasonification of dissolved organic or inorganic precursors.[10] Another non-CVD method, the Pyrolytic Spray™ process, produces aluminum coatings by atomizing warmed aluminum alkyl, as either a pure liquid or as a kerosene dilution, over a heated substrate in a reaction chamber.[11] Another approach is to directly feed reactive powders (*e.g.* metal-organics or halides) into a furnace and flash or pyrolize them in the furnace's hot zone.[12-14] High-quality films have been produced by this process suggesting that precursors are indeed vaporized. All of these processes require a reaction chamber or furnace and an external heat source and do not use a flame or combustion.

Finally, Vapor Phase Axial Deposition (VAD) is used for forming optical fibers.[15] This process uses two flames which are fed with a mixture of $H_2/SiCl_4$ and $H_2/SiCl_4/GeCl_4$, respectively (the hydrogen acts as the combustible fuel). This results in the deposition of silica soot onto the outer area of a porous preform, and the deposition of germanium-doped silica soot onto the inner area. This process involves combustion, but is not a homogeneous deposition process because a particulate glass particles forms *before* deposition onto the substrate.

Combustion CVD vs. Spray Deposition

In spray pyrolysis a solution is sprayed onto a heated substrate which is then heat-treated to yield the desired thin film. A similar deposition technique is the sol-gel process in which a layer of solution is applied to the substrate (dipped, spin- or spray-coated), dried, and then heat-treated to give the final material. In both cases liquid phases are applied to the substrate. Corning has patented a flame-based process for producing glass that at first appears to be a CVD process; quite correctly no explicit mention of CVD was made.[16] Here, a mixture of fuel gas/oxygen/$SiCl_4$ is combusted in a flame. An aerosol of an aqueous salt mixture is sprayed directly into this flame producing a transparent, homogeneous glass body consisting of at least two constituent oxides. While this process clearly is a close "cousin" to the CCVD process, it lacks the simplicity and elegance inherent in the latter and requires two nozzles and a gas flame as the primary heat source. Furthermore this process has never been extended into the realm of thin film manufacture but was confined to the production of glass bodies and forms.

Notably, there are at least two reports of spray pyrolysis that share some characteristics with the CCVD process. Koguchi and coworkers[17] deposited a 10 µm thick $YBa_2Cu_3O_x$ coating onto a YSZ substrate over the course of 10 minutes by atomizing an appropriate aqueous precursor solution and transporting the resulting mist to a hydrogen-oxygen flame. The resulting film had a strong c-axis preferred orientation and showed no resistivity at 90 K

following 850°C oxygen anneal for 8 hours. The authors termed their method flame pyrolysis, and were likely depositing at temperatures near the melting point of $YBa_2Cu_3O_x$. Solution concentrations and deposition rates reported were higher than those typically used in the CCVD process.

McHale and coworkers[18] obtained 75 to 100 μm thick films of $YBa_2Cu_3O_x$ and $Bi_{1.7}Pb_{0.3}Ca_2 Sr_2Cu_3O_{10}$ by either dissolving nitrates in liquid ammonia and combusting the sprayed solution in a N_2O gas stream, or by combusting nitrates dissolved in either ethanol or ethylene glycol in an oxygen gas stream. Results suggest that films were particulate and not phase pure. The $YBa_2Cu_3O_x$ coatings had to be annealed at 940°C for 24 hours, and the $Bi_{1.7}Pb_{0.3}Ca_2Sr_2Cu_3O_{10}$ coatings had to be annealed twice at 800°C for 10 hours and then at 860°C for 10 hours to yield the desired material. Even after oxygen annealing the best zero resistivity measurement was 76 K. Once again, solution concentrations and deposition rates reported were higher than what is typically used in vapor deposition and the CCVD process.

Combustion CVD vs. Thermal Spraying

Thermal spraying[19] typically produces thick films (>10 microns) by feeding powder into a gas combustion torch (flame spraying) or a plasma torch (plasma spraying) to melt the powdered coating material which is then splattered onto the object being coated, thus forming a film. Thermal spraying is considerably different from CVD, but there are variations that resemble CCVD.

In one modification of thermal spraying, powdered material is vaporized and the vapor is then condensed onto the substrate. This evaporation technique was used in early high-temperature superconductor research to deposit c-axis preferred orientation $YBa_2Cu_3O_x$ at deposition rates of up to 10 microns/min.[20]

Another embodiment of flame spraying feeds a solution instead of a powder into the flame. Aqueous solutions of yttrium, barium and copper nitrate were atomized in a hydrogen-oxygen flame to produce finely dispersed superconducting powders.[21,22] The flame vaporizes the water leaving particles of yttrium, barium, and copper nitrates. These then react with OH and O radicals yielding $YBa_2Cu_3O_x$ particles. It is interesting to note that the best powders were made using an over-ventilated diffusion flame at 700–900°C. These conditions minimize product decomposition and decrease formation of impurities such as $BaCO_3$.

The plasma spray method most similar to CCVD is spray-inductively coupled plasma (S-ICP).[23] Here, a precursor solution is atomized into fine droplets of 1-2 μm diameter. These droplets are carried into an ICP chamber. Oxidic thin films of a larger number of materials have successfully been deposited using this technique. Holding the substrate at an appropriate distance from the plasma was noted as being important in synthesizing dense films. CVD type coatings were achieved using ultrasonically atomized 05-1.0 M solutions of metal-nitrates in water which were fed into the ICP at 6–20 ml/h using an argon stream of 1.3–1.4 l/min.

Fundamentals of the CCVD Process

The morphology and stoichiometry of thin films deposited by CCVD are directly controlled by the following major process parameters:

a. Solution composition, precursor concentration, flow rate and atomization,
b. Flame (i.e. oxygen and fuel flow rate, pilot flames, temperature, atomization); and
c. Substrate conditioning (i.e. cooling, heating, motion, tilt angle, inert gas).

The effects of each of these process parameters will subsequently be discussed as it applies to the CCVD process that employs liquid precursor solutions. (Some of these results are applicable also to vapor-source CCVD).

Process Parameters – Solution

The easiest method utilizes a solution comprising of a flammable solvent (typically

toluene, isopropanol, ethanol, methanol, etc.) in which the precursors are dissolved. The solvent acts as a (a) combustible fuel to produce and sustain the deposition flame, and (b) as a transport medium for the dissolved precursor chemicals. Solution flow rate and stoichiometry can be precisely controlled, the latter by varying the reagent ratios in the solution. Using a proprietary nozzle technology (Nanomiser nozzle), the solution is nebulized (i.e. atomization or "spraying") to form nanosized droplets that enter the flame zone shortly after formation. Solutes with a low boiling point (less than 200°C) vaporize with the solvent in the flame. Solutes with higher boiling points form finely dispersed solute clusters as the solvent vaporizes and burns. Cluster size depends on solution molarity and droplet size. When small enough, the clusters vaporize in the flame, react then condense or adhere to the substrate, and finally bond/diffuse to form the coating.

Composition of Solution

There are several ways in which to adjust the composition of the solution. For one, different elemental precursor chemicals can be used. The choice of precursors depends on their solubility in a given solvent or solvent system. Similarly, the choice of solvent is primarily dictated by the requirement to fully dissolve the precursor. Furthermore, carbon-free solvents, such as water, and low carbon residue (soot) solvents, such as methanol, may be used to control the amount of elemental carbon in the flame. The elimination of impurities can also be extremely significant in certain applications. For example, sulfur and sodium can be detrimental to many coatings; in such cases solvents and precursors must be free of these and other common impurities.

Precursor Concentration in Solution

The appropriate concentration of the precursor solution is established empirically. Generally speaking, the higher the concentration, the higher the deposition rate. (Typically, concentrations are in the range of 10^{-2}–10^{-4} M). However, a high concentration can be detrimental in that the surface diffusion of the desired species may be too low to accommodate the deposition rate of certain materials. Some materials with low surface diffusion may require a lower concentration to form a uniform, dense film. Ordinarily, the highest solution concentration that provides a good film for a desired purpose is used to maximize the deposition rate.

Solution Flow Rate

The choice of solution flow rate, that is, the volume of solution that is fed to the flame in a given time period, affects the flame, the deposition rate and coating coverage. Generally, an increase in the flow rate results in a longer, wider flame and greater deposition rates. A higher solution flow rate often requires feeding supplemental oxygen to the flame while a lower solution flow rate requires a lower flow rate of supplemental oxygen.

Solution flow rate also affects the deposition rate: higher flow rates produce thicker films in a set amount of time compared to lower flow rates. However, some materials may not deposit well at higher flow rates. Higher flow rates may also be used when very high deposition temperatures (1300°C) are desired. The larger flame has a larger hot zone thereby maximizing the deposition area.

Generally, the highest flow rate that produces a film of the desired properties on a particular substrate should be used. Increasing the gas flow also reduces the diffusional boundary layer resulting in more uniform coating coverage at a higher deposition rate.

Process Parameter-Flame

The flame provides the "operating" environment for the CCVD process. The energy and radiation produced by the flame are used to form the reactive species and to heat the substrate, ultimately enabling surface reactions, diffusion, nucleation and growth of the thin film material.

Supplemental Oxygen

Flame characteristics can be modified by flowing supplemental oxygen (either pure

oxygen or air) around the flame. Its flow rate allows for control of the turbulence flow of gases and is important in maintaining a stable flame at high flow rates. This operational parameter should be adjusted in conjunction with the solution flow rate. A higher supplemental oxygen flow rate produces a fast flame that allows better material penetration into tight areas on a substrate yielding smoother coatings. A lower supplemental oxygen flow rate produces a slower, longer and wider flame. This flame is useful if a more rough, nodular film microstructure is desired as opposed to a smooth, dense film. These differences are somewhat arbitrary, though, and their occurrence or extent will differ from one deposited material to another.

The higher the percentage of oxygen, or the higher the deposition temperature, the more complete is the combustion (oxidation) that occurs. The oxidant-to-fuel (solvent) ratio helps to control the flame temperature, size and velocity. Using pure oxygen versus air results in a more efficient and rapid combustion: this in turn minimizes the formation of NO_x, carbon monoxide, and elemental carbon.

At times it might be necessary to employ gases other than oxygen (e.g. argon or air) to aid in the deposition of less noble metals or partially oxidized phases. Changing to gases other than oxygen will affect the flame, and process variables will have to be adjusted.

Pilot Flames

The pilot flames are arranged symmetrically around the spraying needle and are necessary whenever gas flow rates exceed the flame velocity to initiate combustion of the nebulized solutions. For a given deposition process there is generally an optimum distance from the needle tip to the pilot flames. This distance is rarely changed but can be altered, depending on the atomization conditions, to achieve suitable flame conditions. Generally, a mixture of oxygen and methane (or ethane) is used to form the pilot flames. Other flammable gases or gas mixtures (e.g. hydrogen or hydrogen/oxygen) can be used to reduce the potential for formation of carbon-containing phases.

Deposition Temperature

For the purposes of this discussion, deposition temperature is defined as the gas temperature close to the substrate. Due to the exhaust flow in the deposition hoods and the natural rising of hot air, the deposition temperature profile is skewed above the flame's longitudinal axis. The actual temperature of the substrate in the deposition zone depends upon the substrate material — size, absorption and emissivity characteristics — as well as the dwell time of the flame on one area of the substrate and whether or not any cooling is being applied to the substrate.

Deposition temperature is measured with a thermocouple held in the flame as close to the surface of the substrate as possible. The actual substrate temperature can be measured with a pyrometer or embedded thermocouple.

Atomization of Solution

Atomization refers to the process of creating a fine spray of the solution as it exits the spraying needle. Due to intellectual property concerns and a pending patent application, no further details can be communicated at this time on the operation of the Nanomizer device. Other atomization techniques can be used to perform liquid solution CCVD, but the smaller droplet size applied by the Nanomizer device creates a fuller, denser coating at an increased deposition rate.

Additional Parameters Affecting Deposition

Additional process variables that can be altered include:

a. Substrate temperature,
b. Motion control,
c. Substrate orientation, and
d. Environmental control.

Substrate Temperature

The substrate's location in the flame zone is dictated by the following conditions:

a. The need to heat the substrate enough to allow surface diffusion;
b. Sufficient reaction time for the precursors to chemically change to their final states; and

c. The need to deposit the material as a vapor while preventing agglomeration into clusters. However, if atomization is poor, a substrate too far into the flame could allow droplets to hit the substrate surface resulting in a spray pyrolysis effect.

Substrate Cooling

Cooling is most often used on substrate materials that cannot withstand the heat generated by the deposition flame (e.g. some metals and polymers). Substrate cooling can also be of advantage for depositing materials that deposit better or more efficiently on a cool substrate. The cooling is generally localized and moves in conjunction with the flame. One common method is to direct a stream of filtered air onto the back of a substrate directly in-line with the longitudinal flame axis. The farther back the cooling nozzle is positioned relative to the substrate, the larger the cooling zone and vice versa. In addition, depending on the amount of cooling required, the rate of air flow can be adjusted. Some materials are significantly affected by the cooling air and not only deposit faster on a cooled substrate but in the absence of a well-aligned air flow do not deposit efficiently and evenly. Other materials only require a cool surface without exact alignment. The amount of substrate cooling is material dependent and is experimentally determined for each material deposited with respect to substrate size and make-up.

Often it is not the deposited material that dictates the use of cooling but the substrate itself. Substrate degradation due to annealing, oxidation, or melting must be eliminated or minimized. Because many materials cannot be deposited onto a substrate cooled sufficiently to avoid substrate degradation, other means must be developed to protect the substrate. In some instances of oxidation or thermally induced film/substrate interaction it has proven beneficial to first apply a protective base thin film layer. The desired material is then deposited on top of this layer perhaps without or minimal substrate cooling. In other cases of substrate degradation, the film must be deposited while the uncooled substrate is moved quickly through the deposition zone — fast enough to avoid damaging the substrate but slow enough to allow time for deposition. Air is a common coolant, but liquids, such as water, have also been successfully used.

Substrate Heating

Some substrates must be heated for deposition. For example, large ceramic (brittle) substrates must be evenly heated to avoid large temperature gradients, which could result in fracture, across their surface. Many coating materials and phases also require a warm or hot substrate to deposit. This characteristic is related to the surface diffusion and thermodynamics of the materials. A material's dependence on a heated substrate may be only for the deposition itself to achieve a dense, continuous film or for the deposition of a particular phase or morphology. For example, many materials require a hotter substrate to form a crystalline film as opposed to an amorphous film.

Substrate Motion

Using a single point flame (versus a series or linear flame) to achieve a uniform coating requires moving the substrate under the flame or moving the flame over the substrate. The motion pattern depends upon the specifics of the substrate, flame, and thin film material. The coating of a large, flat substrate by a single-point flame is generally accomplished by moving the flame with respect to the substrate back and forth in a ladder-like pattern. Generally, the pattern should start at the bottom of the vertically positioned substrate. The deposition zone of a flame is a circular zone rather than a point. However, due to the natural rising of heat (and to a lesser extent the updraft of the exhaust hood), the total deposition zone is not perfectly circular but asymmetric with more area above the center of the flame. As the flame is coating the lower part of a substrate, the upper part is also receiving a very thin layer of coating. Thus, the motion pattern must accommodate this deposition pattern and allow for longer deposition times at the bottom of the substrate and for shorter times in the middle and upper areas of the substrate.

Near the edges of the substrate may also need additional dwell time of the flame because of close-to-edge effects. Close-to-edge effects result from a no "overspray" effect and the different conditions at the edge of a sample as compared to the center of a sample. Temperature, gas flow from the flame and the flow of cooling air at the back of the substrate may all vary. Coatings on high points and at sharp edges of the substrate tend to be thicker due to thinner diffusion boundary layers. Thus, the motion pattern must take these factors into account. The motion pattern can accommodate the many factors affecting a uniform deposition by allowing the flame to pass over an area multiple times, slowing the flame's travel across a substrate and allowing the flame to sit and dwell on a spot for a number of seconds. Most motion program patterns must be tested many times to achieve a completely uniform coating across a complex substrate's surface.

Diffusion Boundary Layer

Diffusion boundary layers are an important factor in producing high-quality thin films. During a deposition, a substrate acquires a so-called gas diffusion boundary layer through which the deposition materials must pass to form a film. The thicker the boundary layer, the less coating occurs. Brownian motion causes diffusion across the boundary layer. This layer is thinner or almost absent at the surface high points or edges of a sample due to the gas velocity of the flame across an edge. This results in thicker coatings at sharp edges of a substrate. The boundary layer can be minimized (*ceteris paribus*, resulting in thicker coatings) by:

a. Increasing the gas temperature at the substrate surface;
b. Decreasing the pressure by depositing inside a low pressure chamber;
c. Increasing the flame velocity and/or turbulence; or
d. Decreasing the substrate size.

In addition, angling the substrate by 30 to 60° to the flame direction can also decrease the boundary layer thickness through shear.

The tilt angle can be important in controlling the deposition of certain microstructures and phases. For example, at least some epitaxial coatings seem to be sensitive to the tilt angle. Smoother coatings may be possible on a tilted substrate compared to a substrate held perpendicular to the flame's longitudinal axis. The amount of acceptable tilt is controlled by the deposition efficiency at a certain angle.

Environmental Considerations

Streaming an inert or reducing gas (e.g. hydrogen, nitrogen, or argon) around the substrate can protect materials (substrate or film) from oxidation during the deposition process. These set-ups tend to limit substrate size if the deposition system is placed in an airtight, solid containment. However, one can restrict the application of inert or reducing gas to the flame zone only. The flame and substrate are, however, more susceptible to oxygen contamination using this approach.

Case Studies

This section highlights some of the process capabilities of CCVD.

Capacitor Coatings[24]

There is worldwide interest to develop processes capable of manufacturing high permittivity (high k) thin films for IC applications. The CCVD process is well suited for high-rate deposition (up to 1 μm/min) of dielectrics such as SiO_2. Multi-component perovskite thin films (e.g. barium-strontium-titanate, BST) with extraordinarily high dielectric constants have also been successfully deposited. Thin films comprising BST are very difficult to prepare by any competing thin film process. These films not only hold promise for small-area embedded capacitors, but have also significant potential for on-chip applications.

Additional work on dielectrics includes deposition of silica, PABS (lead aluminum boron silicates), PLZT (lead lanthanum zirconium titanate) and BST (barium strontium titanate) on Si-Ti-Pt wafers (Figure 2). The wafer specimens were patterned with metal electrodes and electronic properties were characterized.

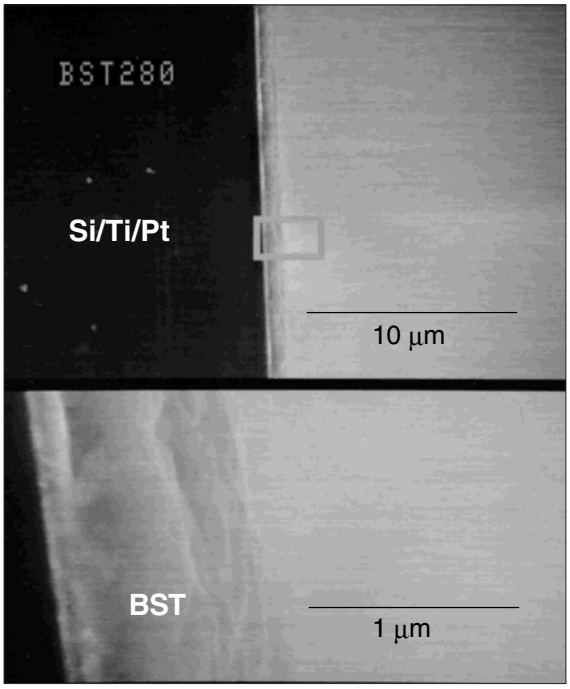

Fig. 2: SEM micrograph of dense thin film of BST on an Si/Ti/Pt substrate. The lower picture is a 10× magnification of the framed area in the upper picture.

Thickness and, correspondingly, capacitance variation was less than 2%. The absence of impurity peaks in XPS spectra of silica-coated specimens clearly demonstrates the achieved purity. Yield, defined as the percentage of functioning vs. total measured capacitors, was 100%. Breakdown field strength was in the range 1.1-5.4 MV/cm and leakage current was about 10^{-7}-10^{-9} A/cm^2 at 0.5 MV/cm. Capacitance density was 23-350 nF/cm^2 dependent on thin film thickness and materials. No breakdown was observed after 20 cycles between 0–40 V. Time dependent dielectric breakdown (TDDB) was 185 s at 40 V for ten of the patterned capacitors.

For capacitors on copper foil substrates, yield of initial samples was an impressive 83-90%. Capacitance density ranged from 20-242 nF/cm^2; this is approximately 50-100 times higher than that of laminated planar epoxy-glass capacitors.

CCVD Coating Conformality[25]

Many applications require the deposition of *conformal* coatings. However, due to the micro-roughness of many substrates, line-of-sight deposition processes (e.g. PVD processes) can suffer from "shadowing" of peaks. Shadowing, which results from long mean-free molecular paths, can cause pinhole defects in the resulting films. In contrast, short molecular mean-free-paths, characteristic of the CVD process, effectively randomize the path trajectories of the atoms thus minimizing shadowing. The coating effectively conforms to the topography of the substrate surface. An example is the conformal coating of over a thousand 12 μm diameter alumina fibers (NEXTEL™ 610) with $LaPO_4$ in a deposition at 900°C (Figure 3). More than 50% of the fibers exhibit a coating thickness from 300-500 nm, with no uncoated fibers.

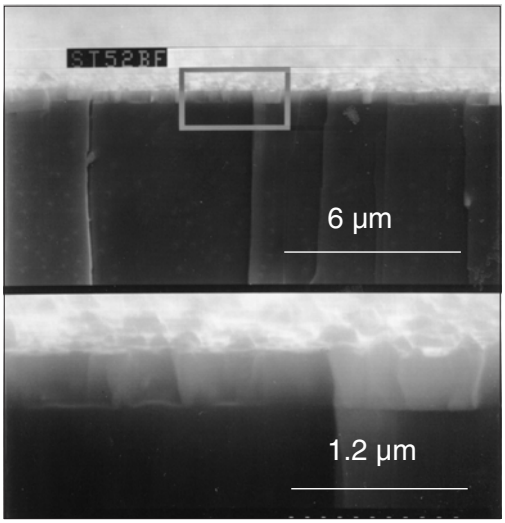

Fig. 3: An epitaxial layer of strontium titanate was successfully deposited onto a MgO single crystal. The lower picture is a 5× magnification of the inset in the upper picture.

Epitaxial Coatings[26]

Epitaxial $SrTiO_3$ was successfully deposited onto a MgO single crystal (Figure 3). A single cube-on-cube texture was displayed in pole figure x-ray diffractometry. The full-width at half-maximum (FWHM) values of the (110) and (200) planes are 2.020° ± 0.004° and 1.67° ± 0.01°, respectively. According to Oak Ridge National Laboratory (ORNL), these values are the best ever reported for a $SrTiO_3$ coating deposited on this substrate by any technique. The approximately 380 nm thick epitaxial coating is smooth and dense.

Cerium oxide (CeO_2) was deposited onto a (100) $LaAlO_3$ single-crystal substrate with a single cube texture and good in- and out-of-plane alignment. A φ scan of the (220) plane of the CeO_2 film yielded a FWHM of 2.45° ± 0.05°; the rocking curve of the (200) plane indicated a FWHM of 1.688° ± 0.006°. A layer of YSZ was then deposited by CCVD on top of this ceria layer. The majority of the YSZ deposited as one cube texture (Figure 3) with only a minor 45° film rotation (<1% intensity) present. The YSZ film exhibited good in- and out-of-plane alignment with a FWHM from the (220) plane of 3.37° ± 0.01and a FWHM from the (200) plane of 2.37° ± 0.01. Numerous other materials have also been deposited by CCVD as epitaxial films, for example, Ta_2O_5, PLZT, BST, YBCO, LSC, YSZ.

Frequency Agile Thin Films for Wireless Communications[27-29]

Recent advances in semiconductor IC fabrication technologies have stimulated research and development of integrated ferroelectric oxide thin films which can be used in various electronics applications including microwave devices, dynamic random access memory (DRAM), non-volatile ferroelectric random access memory (NVFRAM), and next generation gate oxide for IC transistors, to name a few. There has been a renewed interest in developing $Ba_{1-x}Sr_xTiO_3$ and $SrTiO_3$ thin films for frequency agile electronics because the required dc bias for tuning the communication devices can now be drastically decreased

because of significant reduction of ferroelectric coating thickness. Epitaxial barium strontium titanate and strontium titanate thin films were deposited on (100) MgO single-crystal substrates CCVD. The as-deposited films were patterned with gold electrodes to form an interdigitated structure and perform as electrically tunable devices, namely, coupled microstripline phase shifters (CMPS). Microwave dielectric properties were characterized at 11-20 GHz with an applied electric field up to ± 35 V/μm. A maximum figure of merit of 53°/dB at 20 GHz and 23°C was measured. Capacitance changes of BST films were 3.7% at 35 V and 302 K vs. 3.9% for PLD films. Dielectric constants of 390-510 were achieved. Thickness variation on 75 mm silicon wafers was less than 2% as measured by ellipsometry. The demonstrated high degree of tunability and relatively low loss showed great potential of these films for the targeted frequency agile device applications.

Protective Coatings for Ceramic Matrix Composites and Corrosion Resistance[30-39]

Ceramic Matrix Composites

Thus far, excessive costs have restricted ceramic matrix composites (CMCs) from fulfilling their significant commercial promise. To better position CMCs as a competitive material, it is imperative to develop a fiber coating system that combines the desired materials properties with ease of use and efficiency in a production environment. While alumina fibers have several desirable characteristics for CMC applications, uncoated fibers weaken in the composite due to chemical reactions between the fiber and surrounding matrix. This results in loss of strength. Hence, a thin film fiber coating of a debonding material, such as lanthanum phosphate, is required to form a reaction barrier. Coatings can also enhance the chemical and abrasion resistance as well as thermal protection of the matrix fibers.

Lanthanum phosphate coatings were deposited onto NEXTEL 610 alumina fibers of up to 3 feet in length. The coatings are dense and uniform with complete coverage around individual filaments (Figure 4).

Process temperatures were as low as 900-1000°C with only minimal fiber degradation. Beta aluminas, such as $LaAl_{11}O_{19}$ and $BaMg_2Al_{15}O_{27}$, required higher deposition temperatures and did not yield the desired stoichiometry and phases without fiber degradation. The strand strength for coated fibers is 2.72–2.81 kg and is unaffected by thermal aging. The coatings are phase-pure, columnar grained monazite and vary in thickness from 0.1 to 1.0 μm. Microstructure and compositional layering were uniform among tows comprising 420 and 1260 filaments.

Chromium Replacement Coatings[35-37]

The environmental hazards of traditional anti-corrosion coating technologies such as cadmium and chromium plating have motivated considerable R&D to develop environmentally benign alternatives. MCT has prepared several types of coatings that could be developed into alternatives to chrome. Figure 5 shows a scanning electron microscope (SEM) image of the cross section of a CCVD "nanolaminate" ceramic coating, composed of 22 alternating alumina and yttria-stabilized-zirconia layers with individual layer thickness on the order of 100 nm. Such "nanostructured" layers promise corrosion-resistance, excellent hardness, and crack-resistance. Figure 6 is an SEM image showing the cross-section of a 100 nm CCVD nickel coating on a glass substrate; note the smooth, dense, continuous nature of the coatings. Figure 7 shows a proprietary composite ceramic anti-corrosion coating in cross-section (patent pending). The rough surface of the pictured coating is advantageous in, for example, paint adhesion, although smooth coatings are possible with deposition parameter adjustments. The latter coating technology is in advanced development under Navy sponsorship as a chromate conversion coating replacement, having passed relevant ASTM and MIL-SPEC tests for corrosion-resistance. This coating has also passed Battelle salt fog testing for 1344 hours, surpassing MIL-C-83488 specifications for a Class I thickness

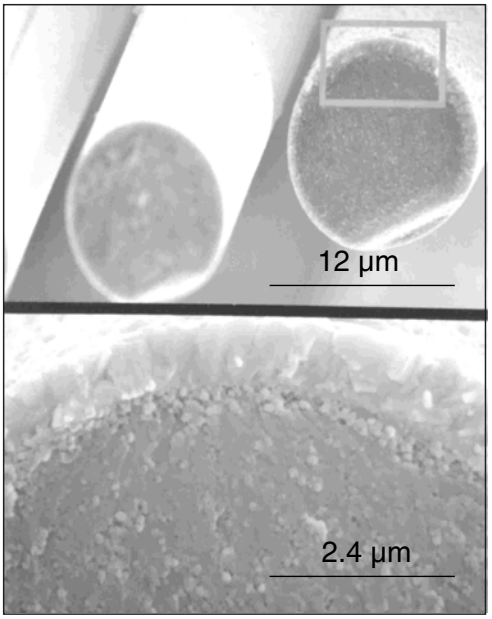

Fig. 4: Scanning electron micrograph of 300 – 400 nm thick Nextel alumina fibers coated with lanthanum phosphate. The lower figure is a 5× magnification of the inset in the upper figure.

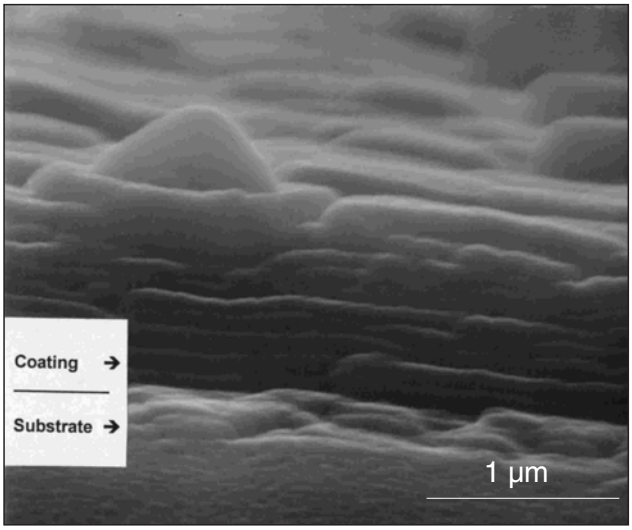

Fig. 5: Nanolaminate CCVD coating comprising 22 alternating layers of alumina and zirconia.

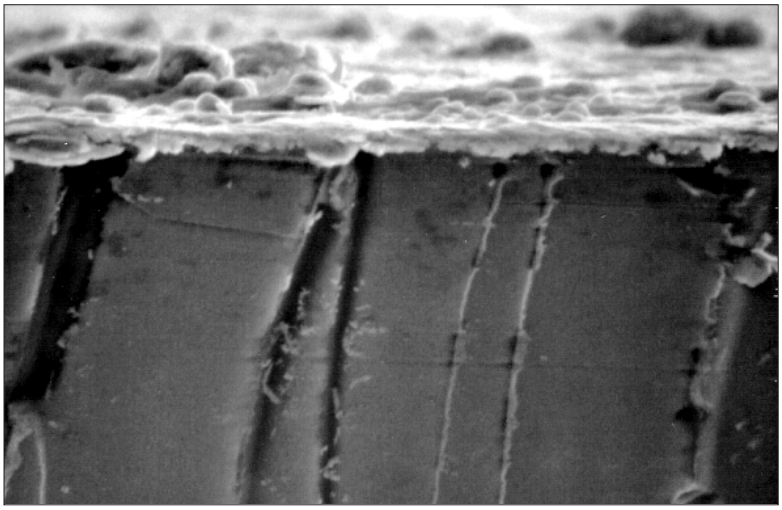

Fig. 6: Scanning electron micrograph of a cross-section of a nickel coating on glass (magnification 13,000×) showing the dense nature of the coating. Coating thickness is approx 100 nm.

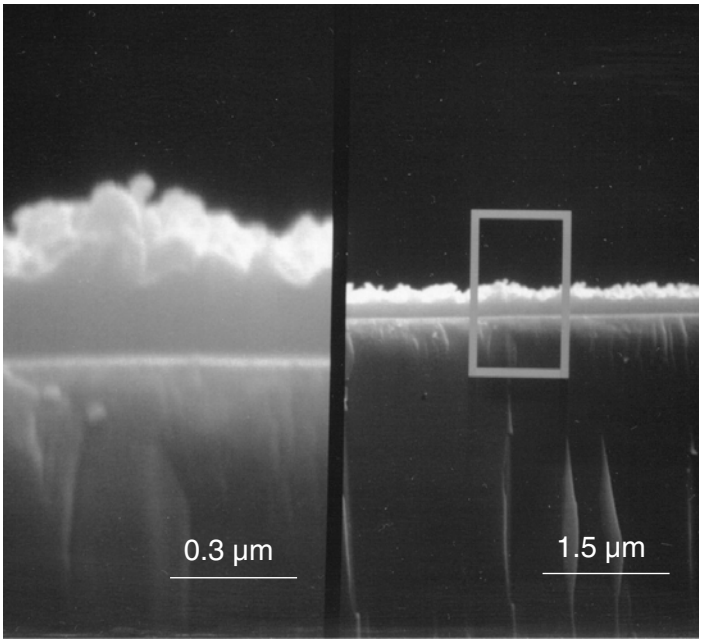

Fig. 7: Cross-section of a proprietary corrosion resistant coating, clearly showing its dense and high surface area nature. The left picture is a 5 × magnification of the framed area in the right picture.

with a chromate conversion coating. These results indicate that CCVD can be used to prepare dense, continuous, pore-free coatings with controlled composition and microstructure.

Resistor Coatings

The CCVD process is well suited to deposition of composite resistor layers. The CCVD reagent solutions can be pre-mixed to control the relative amounts of constituents in each resistor composition (patent pending). Precise control of these ratios permits tailoring of specific resistivity of the resistor layers over many orders of magnitude, ranging from 5 Ω/square to very high sheet resistivity values up to 500 kΩ/square. The resistor material comprises a metal (e.g. platinum or nickel) and a small amount of an oxide (e.g. ceria or silica) added to increase resistivity. There is a linear correlation between the log of resistance and weight percent of a component material in thin film resistors on fused silica substrates. This linearity greatly simplifies the materials engineering to meet desired resistance specifications. The initial test vehicles have been successfully fabricated with sheet resistivities of 100 Ω/square and 10 kΩ/square. In addition, the process can be used to deposit conducting oxide coatings such as bismuth ruthenium oxide. In amorphous form, these materials have a high resistivity and a positive temperature coefficient of resistance (TCR). In principle, bi-layered coatings consisting of a resistor layer deposited on top of a conductive oxide thin film will result in resistors with zero TCR (patent pending). MCT has already produced high-quality 100 nm resistor coating samples on 69 × 83 cm copper sheets and continuous rolled foil using a multi-flame CCVD system in close to 100% yield. This important preliminary result shows the great promise that the CCVD process has for manufacturing embedded passives.

Flame Characterization[40]

In the CCVD process, the flame provides the reactive zone in which precursor materials are pyrolized and ultimately deposited onto the substrate; hence, an in-depth understanding of flame characteristics and processes is a *sine qua non* for rational thin film design. Optical Emission Spectroscopy (OES) and flame pyrometry were used to study the Nanomiser device produced liquid jet flame during the deposition of barium strontium titanate ($Ba_xSr_{1-x}TiO_3$) films. While species distribution and vapor-substrate interactions have been studied for number of chemical vapor deposition (CVD) processes,[41–45] we were interested in correlating flame characteristics with thin film microstructure.

In a series of experiments, the dependence of flame-to-substrate distance and temperature on surface morphology of deposited films was studied. Depositions were performed at 700, 900, 1100 and 1400ºC gas temperature (corresponding to distances of 12.2, 11.4, 9.7, and 8.1 cm), respectively. In all cases, the substrate was mounted at a 45° angle with respect to the impinging flame centerline. A representative thermal image of the CCVD flame for an optimized BST deposition as measured by pyrometry is shown in Figure 8. Optical emission spectroscopy (OES) measurements were performed simultaneously with the flame pyrometry to obtain relative concentrations for emitting species in the flame. Although the observed spectrum provides information about the excited-state density, it does not directly reflect the ground-state population, since numerous vapor clusters are formed. OES is a powerful and simple diagnostics tool. The intensity of the OES signal for different species depends on both the species concentration and flame temperature, and can be used to approximate spatial distribution of emitting species. Images of individual species emission intensities after background subtraction are shown in Figure 9.

Both Ba and BaO reach their peak concentration about 1 cm from the nozzle after which they rapidly decay. The only discrete species emitting in the flame at the distances corresponding to the temperatures studied (8.1 to 12.2 cm) is SrOH and Na. The four films deposited in this temperature range (700 to 1400ºC) all yielded x-ray diffraction peaks

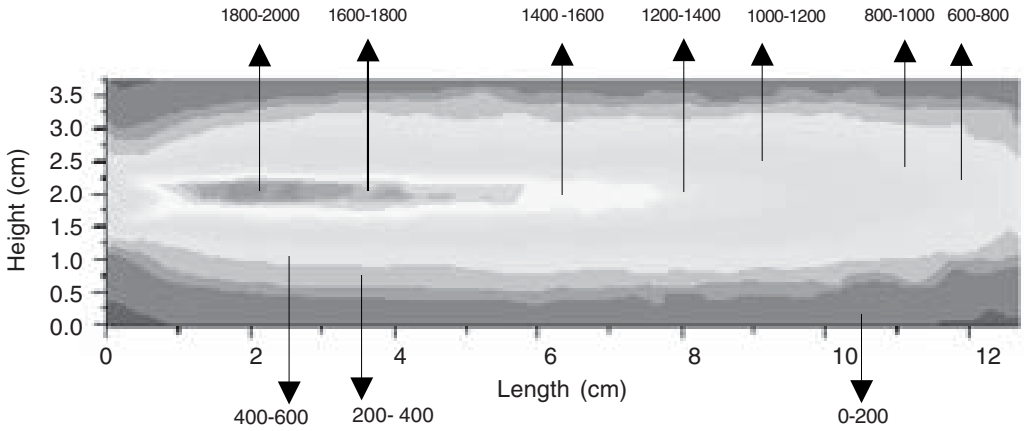

Fig. 8: Representative thermal image of the BST flame as measured by pyrometry.

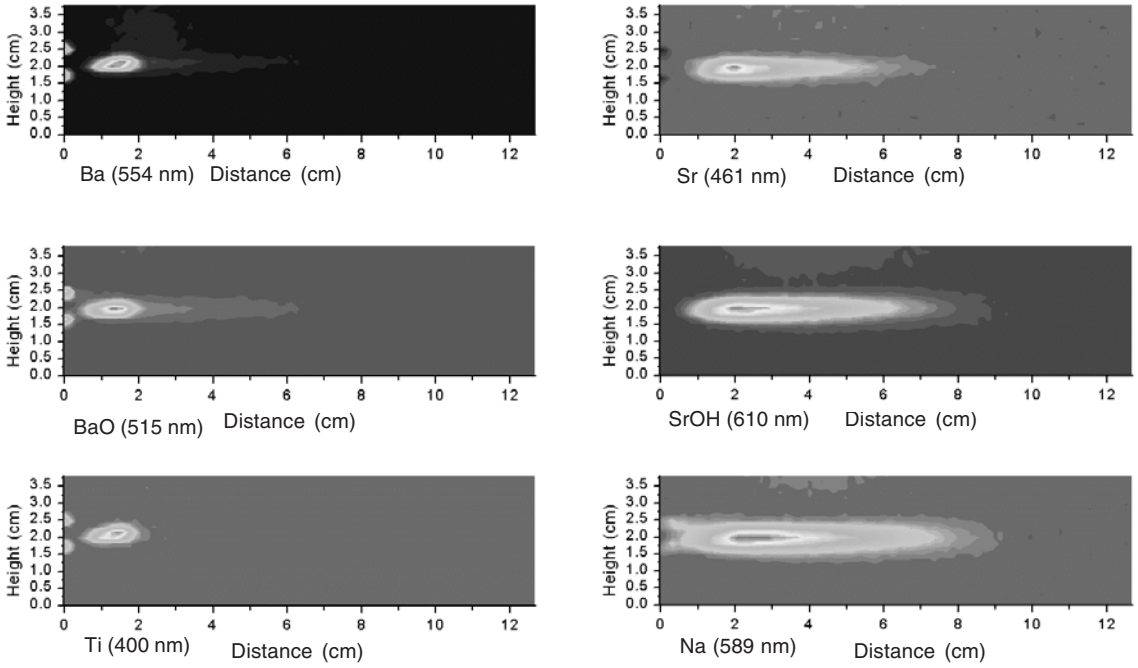

Fig. 9: Optical emission intensities for individual flame species while depositing epitaxial BST.

corresponding to the desired $Ba_xSr_{1-x}TiO_3$ phase. BST films deposited between 700-1100ºC were epitaxial; depositions at 1400ºC also yielded the desired phase but were not epitaxial.

By combining optical emission spectroscopy and pyrometry, it was possible to derive relative concentrations of short-lived, reactive species in a hydrocarbon flame. Although only relative, these measurements allowed determination of species spatial distribution within the flame and provided a better description of the flame interaction with

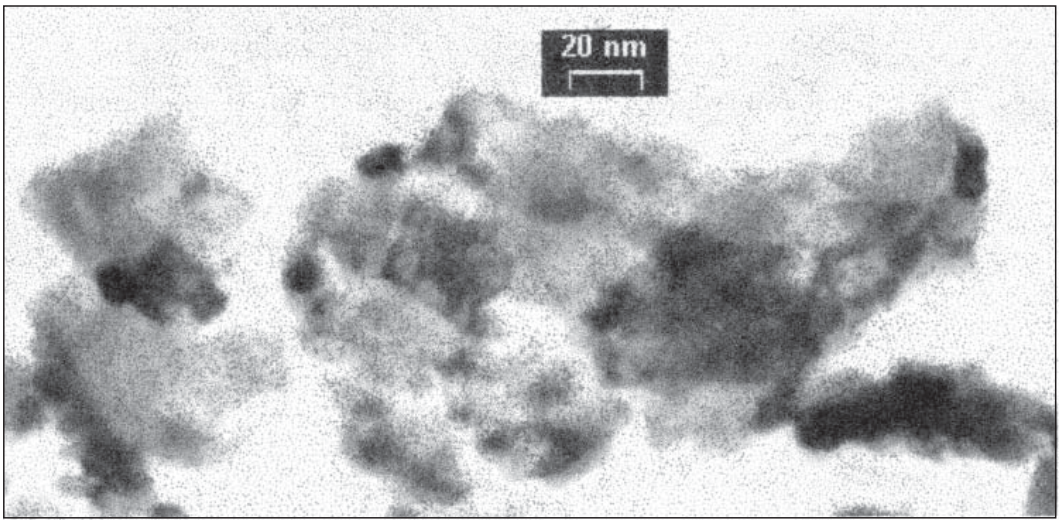

Fig. 10: TEM micrograph of platinum nano-particles deposited onto a Nafion membrane. The platinum is dispersed so finely that it appears as a darkening of the Nafion cluster. Darker material is a thicker cluster which was formed when the specimen was abraded from the sample onto the carbon grid for imaging.

the substrate. It has been demonstrated that the excited species emission from the flame reaches a maximum value of 1 to 2 cm from the nozzle exit. Determining the relative species concentrations also provided an insight into the mechanism of thin film growth. The observed surface morphology is controlled by the surface mobility of deposited clusters. At low flame and substrate temperatures, the surface mobility is low resulting in an even coating with a high surface energy. At higher temperatures, the surface mobility is higher resulting in smoother coatings with lower surface energy. The most important result of this study establishes that precursor pyrolysis, detected by UV-vis spectrascopy, occurs predominately prior to the substrate surface and high-quality vapor deposited coatings can be produced by this method.

Fuel Cell Applications

Fuel cells are of huge interest to the technology marketplace, as illustrated by sizable investments in the technology and market capitalization of fuel cell companies with little or no current revenues. This is because of their pervasive potential to power homes, offices shopping malls, automobiles, buses, trains, boats, personal computers, communication equipment and other increasingly distributed, power-demanding appliances of modern-day living. The overall market size for fuel cells is deemed to grow beyond that of transportation and stationary power into distributed 'personal power', to an estimated $1B to $200B annually by 2025. In a very real way, fuel cells will be to energy what integrated circuits have become to information.

For applications in solid oxide fuel cells it is important to increase the interfacial area and total surface area of the coating on the membrane electrode assembly (MEA) while maintaining uniformity. MCT has achieved promising results with the CCVD process to generate advanced catalytic coating structures. Figure 10 shows a transmission electron micrograph of a platinum layer deposited by CCVD onto Nafion: nanoscale platinum particles can be seen as a very fine dispersion of moderate to dark gray matter in the light gray membrane material. The scanning electron micrograph in Figure 11 is a cross-sectional view of a conductive lanthanum-strontium

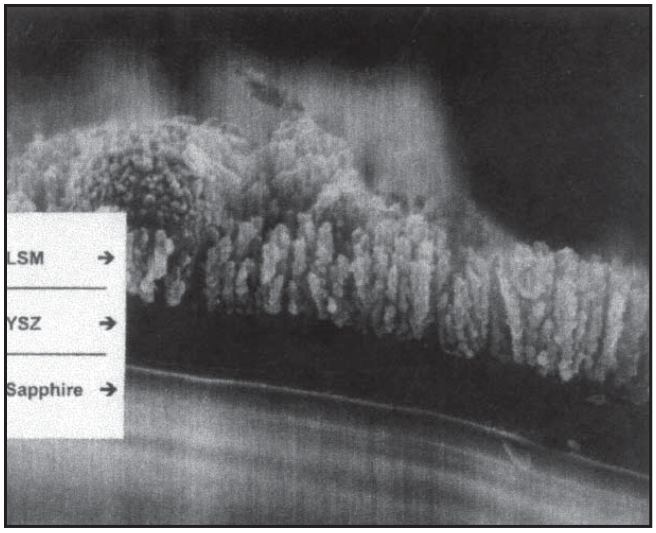

Fig. 11: SEM cross-section of a CCVD-deposited LSM conductive coating, showing the open columnar structure over a dense YSZ layer on a sapphire substrate.

manganate (LSM) layer with a ''loose'' columnar microstructure deposited onto a dense CCVD layer of yttria-stabilized zirconia. Fully dense YSZ coating have also achieved as have been nano-laminate structures (cf. Figure 5).

Summary, Conclusion, and Future Directions

The open-atmosphere CCVD technology has many advantages for producing advanced thin film materials when compared to current technologies, in particular, potential for an order-of-magnitude reduction in operating and capital costs, substantially higher thin film quality, and the ability to engineer materials for specific applications (e.g. great compositional and structural control). In addition, the ease-of-use of CCVD permits both rapid development of new coating/substrate combinations and straightforward implementation for production-friendly manufacturing. Finally, the CCVD process in conjunction with the Nanomiser uses only environmentally benign chemical precursors, minimizing safety and pollution concerns.

Acknowledgments

Public sector funding from Small Business Innovation Research (SBIR) grants and the Advanced Technology Program was instrumental in carrying out many of the research and development projects described in here or listed in the reference section. We would especially like to thank the Department of Defense (BMDO and Navy), the National Science Foundation, and the Department of Energy for their continued support. Special recognition has to go to the group of dedicated scientists, engineers, and technicians that has carried out the research and development work and without whom there would not be a CCVD process.

References

1. A.T. Hunt, W.B Carter, and J.K. Cochran, *Method and Apparatus for the Combustion Chemical Vapor Deposition of Films and Coatings*, U.S. Patent 5,652,021, 1997.
2. *Handbook of Thin Film Deposition Processes and Techniques*, K.K. Schuegraf, ed., Park

Ridge, NJ, Noyes Publication, 1988.
3. 1950, Swiss Patent 265,192.
4. R.H. Dalton, U.S Patent 2,239,551, 1941.
5. J.F. Hyde, U.S. Patent 2,272,342, 1942.
6. M.E. Nordberg, 1943, U.S. Patent 2,326,059.
7. S. Hori, Characterization and Processing of CVD Powders for Fabrication of Composite and Compound Ceramics. *Materials Research Society of Symposium Proceedings,* Vol.155, 1989, pp.3-12.
8. W.S. Zhu, B.E. Williams, and J.T. Glass, Growth and Characterization of Diamond Films on Nondiamond Substrates for Electronic Applications Proceeding IEEE (USA), Vol.79, No.5, 1991, pp.621-646.
9. M. Murakawa, S. Taeuchi, and Y. Hirose, An Experiment in Large Area Diamond Coating Using a Combustion FlameTorch in its Traversing Modelling, *Surface and Coatings Technology*, 1990, pp.22-29.
10. G. Blandenet, Y. Lagarde, and J. Spitz, Indium Oxide Deposition on Glass by Aerosol Pyrolysis, *Chemical Vapor Deposition*, 1975, pp.190-203.
11. J.C. Withers and L.C. Mccandless, Aluminum Coatings by a Pyrolytic Spray Chemical Vapor Deposition Processing, *Chemical Vapor Deposition*, 1970, pp.393-407.
12. C.M. Hollabaugh, L.A. Wahman, R.D. Reiswig, R.W. White, and P. Wagner, Chemical Vapor Deposition of Zirconium Carbide Made by Reactions of Zirconium Tetrachloride with Methane and with Propylene. *Nuclear Technology*, Vol.35, No.2, 1977, pp.527-535.
13. W.J. Lackey, W.B. Carter, J.A. Hanigofsky, D.N. Hill, E.K. Barefield, G. Neumeier, D.F. O'Brien, M.J. Shapiro, J.R. Thompson, A.J. Green, T.S. Moss, III, R.A. Jake, and K.R. Efferson, Rapid Chemical Vapor Deposition of Superconducting $YBa_2Cu_3O_x$, *Applied Physics Letters*, 1990, Vol.56, No.12, pp.1175-1177.
14. L.R Newkirk and F.A. Valencia, *Superconducting Articles of Manufacture and Method of Producing Same*, U.S. Patent 508,586, 1980.
15. T. Isawa and S. Sudo, *Optical Fibers, Materials and Fabrication*, Boston, D. Reidel Publishing Co.,1986.
16. E.N. Randall, *Method of Producing Glass in a Flame*, U.S. Patent 3,883,336, 1975.
17. M. Koguchi, Y. Matsuda, E. Kinoshita, and K. Hirabayashi, Preparation of $YBa_2Cu_3O_x$ Thin Film by Flame Pyrolysis, *Japan Journal of Applied Physics*, Part 2, Vol.29, No.1, 1990, pp.33-35.
18. J. McHale, R.W. Schaeffer, A. Kebede, J. Macho, and R.E Salomon, Preparation of High-Tc Oxide Films via Flaming Solvent Spraying, *Journal of Superconductors*, Vol.5, No.6, 1992, pp.511-518.
19. D. Matejka and B. Benko, *Plasma Spraying of Metallic and Ceramic Materials*, Chichester, John Wiley and Sons, 1989.
20. K. Terashima, K. Eguchi, T. Yoshida, and K. Akashi, Preparation of Superconducting Y-Ba-Cu-O Films by a Reactive Plasma Evaporation Method, *Applied Physics Letters*, Vol.52, 1988, pp.1274-1276.
21. M.R. Zachariah and S. Huzarewicz, Aerosol Processing of YBaCuO Superconductors in a Flame Reactor, *Journal of Materials Research*, Vol.6, 1991, pp. 264-269.
22. B.D. Merkle, R.N. Knisely, F.A. Schmidt, and I.E. Anderson, Superconducting Yttrium Barium Copper Oxide ($YBa_2Cu_3O_x$) Particulate Produced By Total Consumption Burner Processing, *Materials Science and Engineering*, Vol.A124, No.1, 1990, pp.31-38.
23. M. Kagawa, M. Kikuchi, R. Ohno, and T. Nagae, Preparation of Ultrafine MgO by the Spray-ICP Technique, *Journal of American Ceramic Society*, Vol.64, No.1, 1981, pp.C7-8.
24. W.Y. Lin, ''Embedded Capacitors for Electronic Circuits Based on Flexible Laminate Multichip Module/Printed Circuit Boards,'' Contract DMI 9561712, NSF SBIR Phase I Grant, 1996.
25. A.T. Hunt, "CCVD Processing of Lanthanum Phosphate and Beta-Alumina Fiber Coatings for Mullite Matrix Composites," Contract DMI 9561712, NSF SBIR Phase I Grant, 1996.

26. W.Y. Lin, Low Loss and Cost Thin Film for Frequency Adaptive Electronics, Contract DAAHO, 1-97-C-R230, DARPA STTR Phase I Grant, 1998 and S.S. Shoup, S. Shanmugam, D. Cousins, A.T. Hunt, M. Paranthaman, A. Goyal, P. Martin, and D.M. Kroeger, Low-Cost Combustion Chemical Vapor Deposition of Epitaxial Buffer Layers and Superconductors, *IEEE Transactions on Applied Superconductivity, submitted.*
27. W.Y. Lin, R.F. Speyer, T.R. Shrout, and W.S. Hackenberger, Dielectric Properties of $Ba_2Ti_9O_{20}$ Microwave Resonators Doped with Zirconium and Tin Oxides, *Journal of American Ceramic Society,* Submitted.
28. A.T. Hunt and H.G. Hörnis, *CCVD Theory and Processing of Ferroelectric Thin Films at Ambient Pressure. Invited presentation at the MOCVD Workshop for Silicon Processing*, Kyungju, Korea, 1995.
29. A.T. Hunt, J. Abbey, and H.G. Hörnis, *PZT, PLZT, LSC and Pt Thin Films Produced in the Open Atmosphere Using Combustion Chemical Vapor Deposition. Presented at the International Symposium on Integrated Ferroelectrics*, Colorado Springs, CO, 1995.
30. M.R. Hendrick, *The Effects of Combustion CVD-Applied Alumina Coatings on the High Temperature Oxidation of a Ni-Cr Alloy*, Thesis, Georgia Institute of Technology, Atlanta, 1996.
31. M.R. Hendrick, H. Shao, T.J. Hwang, and A.T. Hunt, *Low Cost Corrosion Protection of Metals by Combustion Chemical Vapor Deposited Coatings*, *Materials Solutions Conference*, Rosemont, Illinois, ASM International, Materials Park, Ohio, 1998.
32. M.R. Hendrick, J.M. Hampikian, and W.B. Carter, Combustion CVD-Applied Alumina Coatings and Their Effects on the Oxidation of a Ni-Based Chromia Former, *Journal of Electrochemical Society*, Vol.145, No.11, 1998, pp.3986-3994.
33. M.R. Hendrick, S. Shanmugham, and A.T. Hunt, *Elevated Temperature Oxidation Protection of Carbon Steel by Combustion Chemical Vapor Deposition*, *Symposium on High Temperature Coatings III, TMS Annual Meeting,* San Diego, CA., 1999.
34. M.R. Hendrick, J.M. Hampikian, and W.B. Carter, *Combustion Chemical Vapor Deposition of Alumina*, Gordon Research Conference on High-Temperature Corrosion, New London, New Hampshire, 1995.
35. M.R. Hendrick, S. Shanmugham, and A.T. Hunt, *Chrome Conversion Replacement Coatings via CCVD Processing*, *US Navy and Industry Corrosion Technology Information Exchange*, Louisville, Kentucky, 1998.
36. M.R. Hendrick, T.J. Hwang, H. Shao, H.G. Hörnis, J. Thomas, and A.T. Hunt, *Chrome Replacement and Thermal Corrosion Resistant Coatings Via Open Atmosphere CCVD Processing in 3rd Annual Advanced Techniques for Replacing Chromium*, Seven Springs, Pennsylvania, 1996.
37. A.T. Hunt, M.R. Hendrick, H. Shao, J.E. McEntyre, and T.J. Hwang, Chrome Replacement Coating Methods and the Potential Use of CCVD Processing, *Proceedings of ASM Materials Solutions Conference*, Indianapolis, IN, 1997.
38. A.T. Hunt, M.R. Hendrick, H. Shao, J.E. McEntyre, and T.J. Hwang, Thin Film Coatings for Aircraft via CCVD Processing, *Proceedings of AESF Conference*, San Antonio, TX., 1998.
39. T.J. Hwang, H. Shao, M.R. Hendrick, H.G. Hornis, and A.T. Hunt, Combustion Chemical Vapor Deposition (CCVD) of $LaPO_4$ Monazite on Alumina Fibers for Ceramic Matrix Composites, *Journal of Materials Science and Engineering*, Vol.A244, 1998, pp.91-96.
40. M. Oljaca, H.L. Luten, T. Tomov, and T. Metzger, BST Thin Films by Combustion Chemical Vapor Deposition, Dependency of Materials Properties on Flame Characteristics, *Combustion Flame*, to be submitted.
41. N.G. Glumac and D.G. Goodwin, Diagnostics and Modeling of Strained Fuel-Rich Acetylene/Oxygen Flames Used for Diamond Deposition, *Combustion*

Flame, Vol.105, 1996, p.321-331.
42. E.J. Corat and D.G. Goodwin, Temperature Dependence of Species Concentrations Near the Substrate During Diamond Chemical Vapor Deposition, *Journal of Applied Physics*, Vol.74, 1993, pp.2021-2028.
43. D.S. Green, T.G. Owano, S. Williams, D.G. Goodwin, R.N. Zare, and C.H. Kruger, Boundary Layer Profiles in Plasma Chemical Vapor Deposition, *Science*, Vol.259, 1993, pp.1726-1729.
44. A.G. Lowe, A.T. Hartlier, J. Brand, B. Atakan, and K. Kohse-Hoinghaus, In situ Temperature and Species Concentration Measurements by Laser Diagnostics and Molecular Beam Mass Spectrometry, *Combustion Flame*, Vol.118, 1999, pp.37-50.
45. R.J. Holdsworth, P.A. Martin, D. Raisbeck, and M.E. Pemble, In Situ, Monitoring of Atmospheric Pressure Tin Oxide CVD Using Near-Infrared Diode Laser Spectroscopy, *Journal de Physique IV*, Vol.9, 1999, pp.109-113.

Selected References

Additional publications about Combustion CVD by our scientists and collaborators:

1. W.B. Carter, G.B. Book, and A.T. Hunt, Combustion Chemical Vapor Deposition of $YBa_2Cu_3O_x$, *Applied Superconductivity*, 1993, p.391-394.
2. W.B. Carter, J.M. Hampikian, S. Godfrey, and T.A. Polley, Thermal Aging of Combustion Chemical Vapor Deposited Coatings, *Materials and Manufacturing Processes*, Vol.10, No.5, 1995, pp.1007-1020.
3. A.T. Hunt, W.B. Carter, and J.K. Cochran, Jr., Combustion Chemical Vapor Deposition, A Novel Thin-Film Deposition Technique, *Applied Physics Letters,* Vol.63, No.2, 1993, pp.266-268.
4. A.T. Hunt, *Combustion Chemical Vapor Deposition from Liquid Organic Solutions*, Dissertation, Georgia Institute of Technology, 1993.

We are aware of recent work by others concerning development of flame-based thin film deposition processes. However, our efforts and patents predate all of this work. Some key references:

5. K.L. Choy, I. Wiedman, and B. Derby, *Flame* Assisted Deposition of Functional Ceramic Thin Films, *Advance Science Technology*, Vol.5, 1995, pp.299-305.
6. K.L. Choy, Fabrication of Ceramic Coatings Using Flame Assisted Vapor Deposition, *Proceedings of British Ceramic*, Vol.54, 1997, pp.65-74.
7. K.L. Choy, W. Bai, and B.C.H. Steele, New Deposition Process for Dense YSZ Films onto Porous Electrodes, *Solid Oxide Fuel Cells*, Vol.97-40, 1997, pp.177-182.
8. K.L. Choy, S. Charojrochkul, and B.C.H. Steele, Fabrication of Cathode for Solid Oxide Fuel Cells using Flame Assisted Vapor Deposition Technique, *Solid State Ionics*, Vol.96, No.1-2, 1997, pp.49-54.
9. K.L. Choy, Laying it on Thick (or Thin), *Materials World*, Vol.6, No.3, 1998, pp.144-146.
10. G. Skandan, N. Glumac, Y.J. Chen, F. Cosandey, E. Heims, and B.H. Kear, Low-Pressure Flame Deposition of Nanostructured Oxide Films, *Journal of the American Ceramic Society*, Vol.81, No.10, 1998, pp.2753-2756.
11. Nanopowder Enterprises, Inc. (a division of SMI), *Low-Temperature Processing of Thick Film Ferroelectric Materials*, STTR (BMDO) Abstract, 1997.
12. N.G. Glumac, Y.J. Chen, and G. Skandan, Diagnostics and Modeling of Nanopowder Synthesis in Low Pressure Flames, *Journal of Materials Research*, 1998, Vol.13, No.9, pp.2572-2579.

Chemical Vapor Deposition
Jong-Hee Park, T.S. Sudarshan, editors, p103-181
DOI:10.1361/chvd2001p103

Chapter 5

Polarized Electrochemical Vapor Deposition

Eric Z. Tang, Thomas H. Etsell, and Douglas G. Ivey
Department of Chemical and Materials Engineering
University of Alberta, Edmonton, AB, Canada T6G 2G6

Abstract

The interfacing of thin film vapor deposition technologies and solid state ionic technologies has led to the development of polarized electrochemical vapor deposition (PEVD). PEVD utilizes a solid state electrochemical cell which can transport one or more reactants in the ionic state. Thus, under an electrochemical potential gradient, which is mainly provided by a dc potential, ionic reactants travel from the source side of a solid substrate to the sink side and react electrochemically with the surrounding vapor to form the desired solid product. PEVD has brought Wagner's scaling tarnishing theory to a new field for making synthetic products under well-defined thermodynamic and kinetic conditions. The immediate advantages of using a closed-circuit electrochemical cell in PEVD include easy control and monitoring. Furthermore, the PEVD product is capable of modifying the solid electrolyte/electrode interface both physically and chemically due to its unique crystallization and growth behavior.

PEVD has been applied to deposit auxiliary phases (Na_2CO_3, $NaNO_3$ and Na_2SO_4) for solid potentiometric gaseous oxide (CO_2, NO_2, and SO_2) sensors, as well as a yttria stabilized zirconia (YSZ) ceramic phase to form composite anodes for solid oxide fuel cells. In both cases, the theoretically ideal interfacial microstructures were realized. The performances of these solid state ionic devices improved significantly. Furthermore, in order to set the foundation for future PEVD applications, a well-defined PEVD system has been studied both thermodynamically and kinetically, indicating that PEVD shows promise for a wide range of technological applications.

Introduction

There are two types of conductivity in nature: electronic and ionic. The first does not involve mass or material transport while the second does. Thus, ionic conduction is capable of converting chemical energy to electrical energy, or vice versa. Since Wagner's early works in the 1930's,[1] defect solid state physics and chemistry has been an area of major scientific and technological interest with the resulting discoveries of solid state ionic materials and development of solid state ionic technology sustaining this interest. The stage has, therefore, gradually been set for a massive effort at developing applications.

The energy crisis in the early 1970's aroused a worldwide interest in energy converting applications based on ionic transport in solid state ionic materials. Since then this field has developed rapidly in order to serve ever-growing energy and environmental demands. Like solid state electronics, the device field of solid state ionics is quickly developing. The study of electronic-ionic processes in solid state ionic materials reflects the intimate relationship between science and technology; ''pure scientific'' results eventually find various practical applications. Present activity in this direction includes the development of small batteries for pacemaker implants, high power batteries for energy storage systems, fuel cells for high-efficiency power generation, electrochromic windows for energy conservation, sensors for chemical pollutant detection, etc.

In spite of the great promise solid state ionic devices offer, few commercial successes have been reported to date. The major problems faced today in the field of solid state ionic devices are still material related. At present, the key technical challenge is development of reliable and cost-efficient techniques to synthesize solid state ionic materials to serve as solid electrodes and electrolytes.[2] On the other hand, these materials are not used in isolation, but in an electrochemical system and must be in contact with each other. The response of solid state ionic materials in solid state ionic devices is highly related to the interface characteristics, which fix the external electrical conditions (electric potential and current density) and the external chemical conditions (chemical potential). The solid electrode/electrolyte interfaces must possess high ionic and electronic mobility. Thus, development of fabrication techniques to improve the interfaces assumes real significance.

The present availability of numerous types of solid electrolytes permits transport control of various kinds of mobile ionic species through those solid electrolytes in solid electrochemical cells, and permits electrochemical reactions to be carried out with the surrounding vapor phase to form products of interest. This interfacing of modern vapor deposition technology and solid state ionic technology has led to the recent development of polarized electrochemical vapor deposition (PEVD).[3] PEVD has been applied to fabricate two types of solid state ionic devices, i.e., solid state potentiometric sensors and solid oxide fuel cells. Investigations show that PEVD is the most suitable technique to improve the solid electrolyte/electrode contact and subsequently, the performance of these solid state ionic devices.

PEVD Fundamentals

Generally speaking, PEVD is a modified form of chemical vapor deposition (CVD). A comparison between PEVD and conventional CVD is schematically shown in Figure 1 for a product (D) formed from reactants (A) and (B). In a CVD process, both reactants (A) and (B) are supplied through a vapor phase at the same side of a solid substrate (E). They react chemically at the surface of the solid substrate (E), aided by some type of catalytic effect, to form a desired product (D). In a PEVD process, one reactant (A) is transported from one side (source) of a solid substrate (E) to the other side (sink) under well-controlled thermodynamic and kinetic conditions. At the sink side, reaction with (B) occurs to form (D). Further growth of (D) into a continuous thin film with the desired thickness in a PEVD process also relies on (A) transported in the solid state now through (E) and (D) to react with (B).

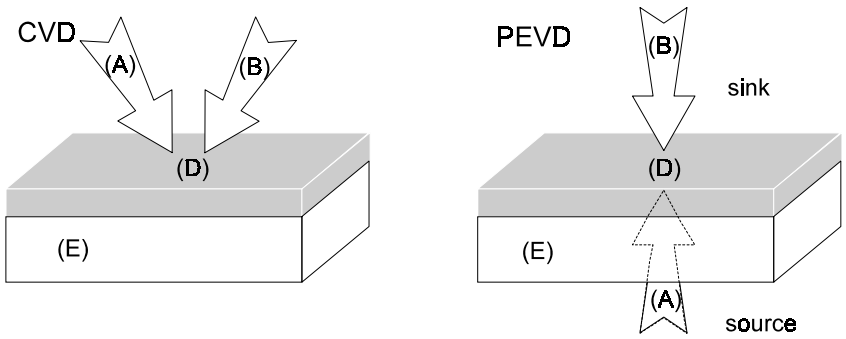

Fig. 1: Comparison of PEVD and CVD processes.

The reason that reactant (A) can be transported through the solid substrate (E) and the solid deposited phase (D) is because both (E) and (D) are solid state ionic materials,[4] in which the ionic state of reactant (A) is mobile. Thus, reactant (A) will be transported as a combination of corresponding ionic and electronic carriers under the mixed influences of chemical potential gradients and electric fields in the solids. Unlike the chemical reaction of vapor phase reactants (A) and (B) to form a deposit (D) in CVD, the reaction of the solid-state transported reactant (A) and the vapor phase reactant (B) to form a deposit (D) is electrochemical in nature in PEVD. The immediate advantage is that the deposition reaction in PEVD occurs at an electrochemically active area instead of a catalytically active area in the case of CVD. Consequently, reaction and deposition in PEVD take place only on the substrate, not on reactor walls, and there are no vapor phase reactions and powder deposition as might occur in CVD. The deposition products in PEVD are usually uniform and fully dense, due to the fact that the electrochemical potential gradient in (D) is the driving force for electrochemical reaction and deposition. Thus, where the film is the thinnest, the driving force is the greatest. Through this self-leveling effect, uniform coverage of PEVD products is expected.

PEVD can also be compared to another closely related vapor deposition technique, electrochemical vapor deposition (EVD), which was introduced by Isenberg at the Westinghouse R & D center in the late 1970's.[5,6] Both techniques utilize an electrochemical potential gradient as the driving force for solid-state transported reactant (A) diffusion through product (D) for further reaction and deposition. However, the way electronic carriers are transported distinguishes PEVD from EVD as schematically shown in Figure 2.

In EVD, electronic carriers flow with ionic carriers through the solid substrate (E) to the deposited product (D). The substrate (E) can either be an ionic or a mixed conductor, as long as the major mobile ionic species is (A^{z+}) or (A^{z-}). The driving force for reactant (A) transport through the solid substrate (E) and deposit (D) is (A)'s chemical potential difference between the two isolated compartments, i.e., the source and sink side of substrate (E). At the source side, the chemical potential of reactant (A) is usually maintained constant. At the sink side, the chemical potential of reactant (A) is fixed by EVD reactions.

In PEVD, an applied voltage is used to transport (A) through the substrate (E). Usually, (E) is an exclusive ionic conductor for (A^{z+}) or (A^{z-}). It serves as a solid electrolyte in a closed-circuit solid electrochemical cell, and is connected to an external electrical circuit with a dc electrical source by two electronic conducting electrodes at the sink and source sides of (E). Consequently, only ionic carriers can be transported through (E) to (D). The electronic

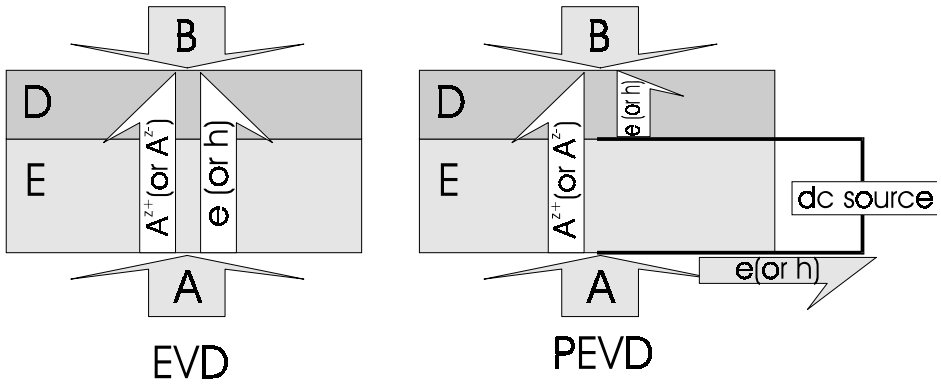

Fig. 2: Comparison of EVD and PEVD processes.

carriers flow separately to (D) through the external electrical circuit. Instead of only relying on the chemical potential difference of reactant (A) across the solid phase (E) as in EVD, the driving force for reactant (A) that is solid-state transported is mainly controlled by the applied dc electric potential in PEVD. Thus, PEVD offers more control of the chemical potential gradient across the deposit (D) than EVD. Furthermore, isolation between the source and sink side in a PEVD system is not necessary for delivering the driving force.

The transport mechanism for reactant (A) through deposit (D) for further growth in PEVD is the same as in EVD. The characteristic feature of both EVD and PEVD is that deposit (D) growth is driven by the presence of a chemical potential gradient of reactant (A) across deposit (D). Deposit (D) growth follows Wagner's electrochemical tarnishing theory and is parabolic in nature. Unlike the initial applications of Wagner's theory in corrosion, solid-state transporting of the reactant in both EVD and PEVD is under well-controlled thermodynamic and kinetic conditions, solely through sink and source vapor phases control in EVD, and mainly through dc electric potential control via a solid electrochemical cell in PEVD. Recently, a review of both EVD and PEVD was presented to illustrate the similarities and differences of both techniques.[7]

PEVD System Basics

A fundamental PEVD system is schematically shown in Figure 3. From left to right, it consists of

1. A source (O) to supply the solid-state transported reactant (A),
2. A substrate (E) in a solid electrochemical cell with an external electric circuit connected from the source side by a counter electrode (C) and from the sink side by a working electrode (W),
3. A product (D) deposited at the sink side surface of the substrate, and
4. A sink (S) to supply reactant (B) in the vapor phase.

As with CVD and EVD techniques, PEVD process design starts by considering the PEVD product (D). Either an anodic or cathodic half-cell electrochemical reaction at the sink side of the system can lead to product (D) formation and subsequent deposition.

$$\text{Anodic reaction: } A^{z-} + B - ze^- \Leftrightarrow D \qquad (1)$$

$$\text{Cathodic reaction: } A^{z+} + B + ze^- \Leftrightarrow D \qquad (2)$$

The equation of choice depends on whether the anion (A^{z-}) or cation (A^{z+}) of deposit (D) is transported through the substrate as well as the product. If doping is also required for a PEVD product (D), additional electrochemical reactions for doping should be considered at the same time.

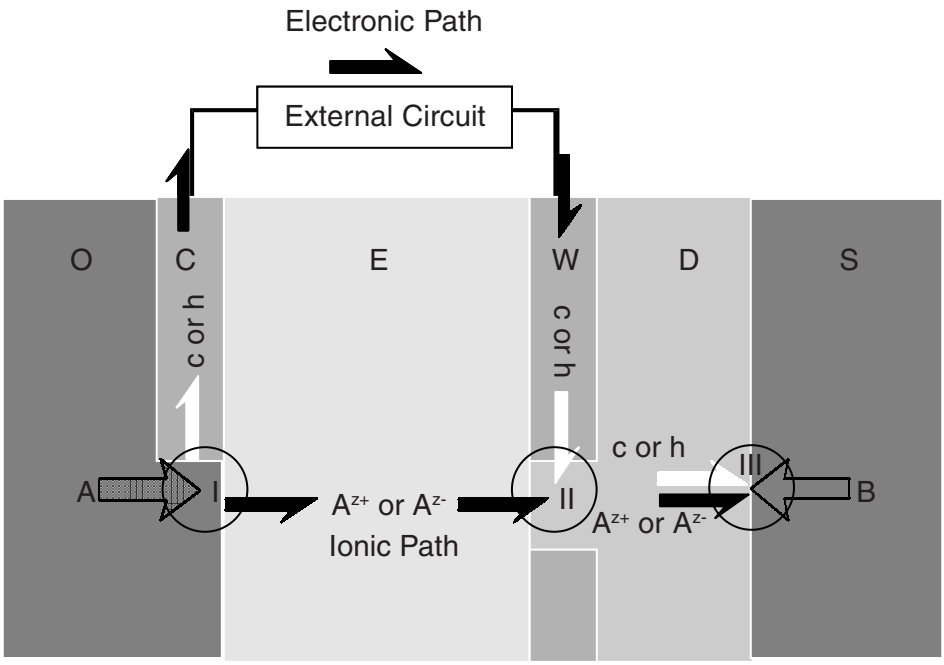

Fig. 3: Schematic of a fundamental PEVD system.

In order to carry out the electrochemical reaction for product (D) deposition in a PEVD process, the neutral reactant (B) and other possible reactants for doping are transported to the deposit (D) surface by diffusion in the sink vapor phase (S). Furthermore, if there are reaction products other than (D), they must be driven away from the reaction sites though the sink vapor phase.

The charged reactant for the sink electrochemical reaction is supplied by the solid electrochemical cell of a PEVD system. The solid phase (E) is an exclusive ionic conductor for (A^{z+}) or (A^{z-}), and serves as the solid electrolyte. (C) and (W) are solid electronic conducting phases, and contact (E) from both sides as counter and working electrodes, respectively. They connect with the external electric circuit, which consists of a dc source and other possible measurement devices. Because the conductivity changes in nature from ionic to electronic at the electrode/electrolyte interfaces, the solid electrochemical cell in a PEVD system effectively separates the transport paths of ionic and electronic charged carriers from the source (O) to the sink (S) of a PEVD system. Thus, the solid electrochemical cell in a PEVD system has two basic functions. First of all, it provides the substrate onto which PEVD products are deposited at the sink side. Secondly, it controls ionic (A^{z+} or A^{z-}) and electronic (e or h) reactant movement from the source (O) to the sink side (S) for participation in an electrochemical reaction and subsequent deposition through an external circuit. The requirements for a solid electrolyte in a PEVD system include:

- The only mobile ion in the solid electrolyte will be solid-state transported reactant (A^{z+}) or (A^{z-}).
- At the desired PEVD temperature, the solid electrolyte must have reasonable ionic conductivity when exposed to both sink and source side environments.
- Sufficiently high ionic current density must be obtained below the decomposition voltage.
- The solid electrolyte should be gas-impervious when the source and sink sides are exposed to difference gases or vapor phases.

- It should be stable in the PEVD environment.[8]

Usually, the working electrode (W) is a porous metallic electrode in PEVD. Thus, reactant (B) in the vapor phase can reach the surface of the solid electrolyte for initial electrochemical reaction at a three-phase boundary of solid electrolyte (E), working electrode (W) and sink vapor phase (S) as shown in Figure 3 (location II). All reactants for the sink side electrochemical reaction (1) or (2) are only available there. Subsequent reaction and deposition of the product (D) requires both electrons and ions to travel through product (D) to the surface to react with vapor phase reactant(s) electrochemically at location III in Figure 3.

The role of the source (O) in a PEVD system is to provide a constant supply of the solid-state transported reactant (A) during a PEVD process. Theoretically, it can be either a solid, liquid or vapor phase, as long as it can supply the ionic reactant (A^{z+}) or (A^{z-}) to the solid electrolyte (E) and the electronic reactant (e) or (h) to the counter electrode (C) via a source side electrochemical reaction. Therefore, the source must be in intimate contact with both solid electrolyte (E) and counter electrode (C) for mass and charge transfer between the source and solid electrochemical cell at location I of Figure 3. Practically, it is preferable to fix the chemical potential at the source. Any gas or solid mixture which does not react with the cell components and establishes a constant chemical potential of (A) is a suitable source. For instance, elemental (A) provides (A^{z+}) or (A^{z-}) according to the following reaction

$$A \Leftrightarrow A^{z+} (A^{z-}) + ze^{-}(-ze^{-}) \quad (3)$$

The overall cell reaction in a PEVD process is the combination of both source and sink half cell reactions. It can be expressed as

$$A_{(O)} + B_{(S)} \Leftrightarrow D \quad (4)$$

This reaction does not have to be a thermodynamically favorable one, since an external dc electric potential is applied via the solid electrochemical cell in the PEVD system to drive the reaction in the desired direction. Thus, the activity of (A) at the reaction site is controlled by the applied dc electric potential. Kinetically, this reaction can be monitored by an ammeter attached to the external electric circuit. Further discussion of mass and charge transport in a PEVD system will be given in the following.

Mass and Charge Transport in a PEVD System

According to the previous discussion, a PEVD process relies on mass and charge transport in two solid state ionic materials of a PEVD system, i.e., the solid electrolyte (E) and the product (D). Since mass and charge transport occur in solid state ionic materials, the conductivity mechanism imposes some restrictions, and fundamental considerations in a PEVD system can be obtained through the local equilibrium approach.[9] In the following, mass and charge transport in both phases will be discussed.

For convenience and simplicity, some assumptions are made. The solid electrolyte (E) is assumed to be an exclusive ionic conductor of mono-valent cation (A^{+}). Two porous electronic conducting electrodes (C) and (W) are attached to the solid electrolyte (E) from the source and sink side, respectively. An external electric circuit with a dc source is connected to the solid electrochemical cell via both electrodes.

During mass and charge transport in a PEVD system, the solid electrolyte serves as an ion-pass filter and the external electric circuit as an electron-pass filter. Consequently, two kinds of conducting passes are separated in the system as shown in Figure 3. One is the ionic conduction path from location (I) through the bulk of the solid electrolyte (E) to location (II), then across the bulk of the PEVD deposit (D) to location (III). The other is the electronic conduction path from location (I) through the source electrode (C), the external electric circuit, and the sink electrode (W) to location (II), then across the bulk of the PEVD deposit (D) to location (III).

In this PEVD system, the source (O) will be a vapor phase, which contains elemental solid-state transported reactant (A), and an anode half-cell reaction

$$A_{(O)} \Leftrightarrow A^{+}_{(E)} + e^{-}_{(C)} \quad (5)$$

prevails at the three phase boundary (I) of solid electrolyte (E), porous counter electrode (C) and source vapor phase (O). Assuming that the partial pressure of (A) in vapor phase (O) is constant during a PEVD process, the chemical potential of (A) at (I) is constant. The equilibrium equation for ionization of a neutral specie (A) at (I) is:

$$\mu_{A(O)} = \bar{\mu}_{A^{+}(E)} + \bar{\mu}_{e^{-}(C)} \quad (6)$$

in which $\mu_{A(O)}$ is the chemical potential of (A) in the source (O), $\bar{\mu}_{A^{+}(E)}$ is the electrochemical potential of (A^+) in the solid electrolyte at (I), and $\bar{\mu}_{e^{-}(C)}$ is the electrochemical potential of (e^-) in the counter electrode at (I).

At the sink side, once initial formation of (D) has occurred, solid-state transported reactant (A), in the form of (A^+) and (e^-) from the bulk of (D), reacts electrochemically with reactant (B) from the sink vapor phase (S) to form PEVD deposit phase (D) at (III). Thus, a cathodic half-cell reaction at location (III) can be expressed as:

$$A^{+}_{(D)} + e^{-}_{(D)} + B_{(S)} \Leftrightarrow D_{(D)} \quad (7)$$

Accordingly, the following equilibrium equation holds,

$$\bar{\mu}_{A^{+}(D)} + \bar{\mu}_{e^{-}(D)} + \mu_{B(S)} = \mu_{D(D)} \quad (8)$$

It is assumed that the partial pressure of (B) in the sink vapor phase is also fixed during a PEVD process. Thus, the chemical potential of (B) is constant. The chemical potential of product phase (D) is equal to its Gibbs free energy of formation. The chemical potential of (A), which is the combination of the electrochemical potential of (A^+) and (e^-) according to Eqn. 6, is fixed at location (III) at equilibrium. It is further assumed that the chemical potential of (A) at (I) is greater than its chemical potential at (III) in this PEVD system.

Because the cathodic reaction relies on the transport of both ionic and electronic species through product (D), it should be considered as a mixed conductor, even in the case where one carrier has a much higher conductivity than the other. In this case the conductivity of other charged species in (D) is assumed to be negligible. Deposit (D) is in contact with solid electrolyte (E) and working electrode (W) at (II), which is a three-phase boundary in the general electrochemical sense. At location (II), the exchange of solid-state transported reactant (A^+) between solid electrolyte (E) and product (D) can be expressed as

$$A^{+}_{(E)} \Leftrightarrow A^{+}_{(D)} \quad (9)$$

and the exchange of electrons (e^-) between the sink working electrode (W) and the product (D) is

$$e^{-}_{(W)} \Leftrightarrow e^{-}_{(D)} \quad (10)$$

Thus, product (D) should be in intimate contact with both the solid electrolyte (E) and working electrode (W) at (II) for a PEVD reaction to occur. If interfacial polarization is negligible, equilibria exist for both mass and charge transport across the interfaces at (II). Consequently, from Eqns. 9 and 10, the following electrochemical potential equilibrium equations at location (II) are valid:

$$\bar{\mu}_{A^{+}(E,II)} = \bar{\mu}_{A^{+}(D,II)} \quad (11)$$

$$\bar{\mu}_{e^{-}(W,II)} = \bar{\mu}_{e^{-}(D,II)} \quad (12)$$

Open Circuit Condition and Equilibrium Potentials of the PEVD System

Under open circuit conditions, the PEVD system is in equilibrium after an initial charging process. The equilibrium potential profiles inside the solid electrolyte (E) and product (D) are schematically shown in Figure 4. Because neither ionic nor electronic current flows in any part of the PEVD system, the electrochemical potential of the ionic species (A^+) must be constant across both the solid electrolyte (E) and deposit (D). It is equal in both solid phases, according to Eqn. 11, at location (II). The chemical potential of solid-state transported species (A) is fixed at (I) by the equilibrium of the anodic half cell reaction Eqn. 6; and at (III) by the cathodic half cell reaction Eqn. 8. Since (D) is a mixed conductor with non-negligible electronic conductivity, the electrochemical potential of an electron (which is related to the Fermi level, E_F) should be constant in (D) at the equilibrium condition. The transport of reactant

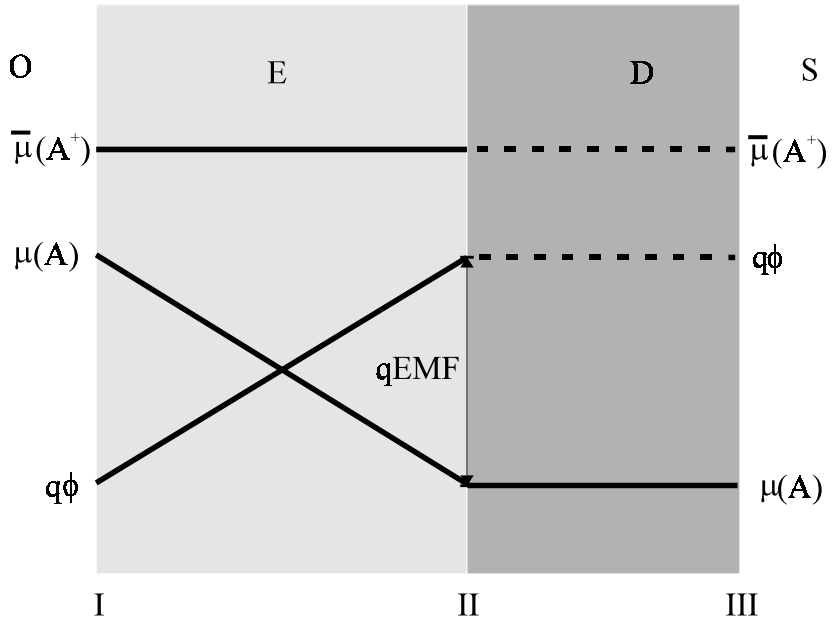

Fig. 4: Potential profiles in the PEVD system under open circuit conditions.

(A) inside (D) is the combination of both ionic and electronic conduction. Thus, the chemical potential of (A) is constant across deposit (D) and the chemical potential of (A) at (II) equals that at (III). Accordingly, the electric potential ϕ across deposit (D) must be constant.

The difference in chemical potential of (A) between the source and sink side of the PEVD system causes a gradient of the chemical potential of (A) across the solid electrolyte (E) between (I) and (II). In order to have a constant electrochemical potential of (A^+) inside (E) to prevent ionic current under equilibrium, an internal electric field is built up inside solid electrolyte (E). This is justified since electronic conductivity in (E) is negligible. The internal electric field causes an electric potential difference between (I) and (II). The value of the internal electric field is the EMF of the cell, and can be calculated from the change in chemical potential of (A) across the solid electrolyte (E) according to Nernst's equation. It can be measured by a high impedance electrometer in the external electric circuit. According to the Stockholm convention, EMF is taken as positive if the right-hand electrode of the galvanic cell is positive.[10] The flow of charge through the cell is called positive if a positive electric current flows from left to right through the cell. In this case, the value of the EMF is positive. It can be expressed as

$$EMF = \phi_{II} - \phi_{I} \tag{13}$$

In summary, the relation between the chemical potential of (A) at (I), (II) and (III) under open circuit conditions is:

$$\mu_A^{III} = \mu_A^{II} = \mu_A^{I} - qEMF \tag{14}$$

Closed Circuit Condition and Steady-State Potentials in a PEVD System

Under closed circuit conditions, the electric potential between the two electrodes (C) and (W) is set by an applied dc electric potential V_a.

$$V_a = \phi_{II} - \phi_{I} \tag{15}$$

Consequently, a gradient in the electrochemical potential of (A^+) exists inside the solid electrolyte (E), and electrons are able to conduct through the external circuit except when the applied dc electric potential is equal

to the open circuit EMF value. Under this condition, the applied dc potential prevents both ionic and electronic current flow through the PEVD system. The potential profiles in the PEVD system are now the same as for the open circuit condition except the electric potential difference at locations (I) and (II) is caused by the applied dc electric field instead of the internal electric field. The value of this applied electric potential corresponds to the stop electric potential E_{stop} commonly referred to for electrolytic cells. In theory, the value of the closed circuit stop potential is equal to the open circuit equilibrium EMF value at the steady-state condition. When $V_a < V_{stop}$, the electric potential difference between (II) and (I) is reduced, and this immediately causes an electrochemical potential gradient of (A^+). This gradient is initially equal to the difference between V_a and V_{stop}. An ionic current of (A^+) will flow from (I) to (II) under the electrochemical potential gradient. If the ionic transport of (A^+) is blocked at (II) or solid-state transport of (A) is blocked in the deposit (D), (A^+) will accumulate at (II), as do electrons (e^-) from the external circuit. This is equivalent to accumulation of the neutral species (A), and will increase the chemical potential of (A) at (II) until the electrochemical potential of (A^+) reaches the same level as at (I).

Thus, ionic current inside the solid electrolyte (E) and electronic current through the external electric circuit will cease after a short transition time. The chemical potential of (A) at (I) and (II) will then have the following relationship:

$$\mu_A^{II} = \mu_A^{I} - qV_a \tag{16}$$

Because ionic current cannot cross the interface at (II), the equilibria (Eqns. 11 and 12) at the interfaces at location (II) are not fulfilled. The chemical potential of (A) inside deposit (D) won't change and it will remain the same at (III).

Deposition in a PEVD system is accomplished by transporting both (e^-) and (A^+) across the interfaces at (II), and from (II) to (III) to react with (B) from the sink vapor phase. This is equivalent to the transport of neutral species (A) from (II) to (III) under a chemical potential gradient of (A). Consequently, the chemical potential of (A) at (II) is reduced. In order to restore it, transport of (A^+) inside the solid electrolyte (E) and (e^-) through the external electric circuit resume. Thus, under closed circuit conditions, the chemical potential of (A) is floating at (II), and electrochemical potential gradients of the charged species exist across both the solid electrolyte (E) and deposit (D). This causes mass and charge transport of reactant (A) from the source (O) to the sink (S) in the PEVD system. The entire PEVD system can be viewed as a reactor. The overall reaction is the combination of the anodic and cathodic reactions to form the desired PEVD product (D) and can be expressed as

$$A_{(O)} + B_{(S)} \rightarrow D_{(D)} \tag{17}$$

When both reactions in Eqns. 5 and 7 proceed to the right, the equilibria at both sides of the cell no longer exist. This will decrease the chemical potential of (A) at (I) and increase it at (III). If the current in the PEVD system is assumed to be very small, the change in chemical potential of (A) at both the source and sink side will not be significant. The steady state potential profiles of the PEVD system are illustrated in Figure 5.

When the current is limited by the solid transport of (A) in both the solid electrolyte (E) and product (D), the chemical potential of (A) at (II) for the PEVD system is related to the current in both phases. Thus, the chemical potential of (A) at (II) is critical to reveal the current and potential behavior in the PEVD system.

In the following, the floating chemical potential of (A) at (II) is solved under the assumption that the equilibria of mass and charge transport across the interfaces at (II) are rapidly reached during the mass and charge transfer in a PEVD process. In addition, some further assumptions are needed for steady-state conditions during a PEVD process:

- Despite the flow of current at (I) and (III), the change in chemical potentials of (A) at (I) and (III) is negligible,
- Only resistive overpotential in the bulk of (E) and (D) of the PEVD system is considered.
- Surface leakage current from the source (O) to the sink (S) in the PEVD system is negligible.

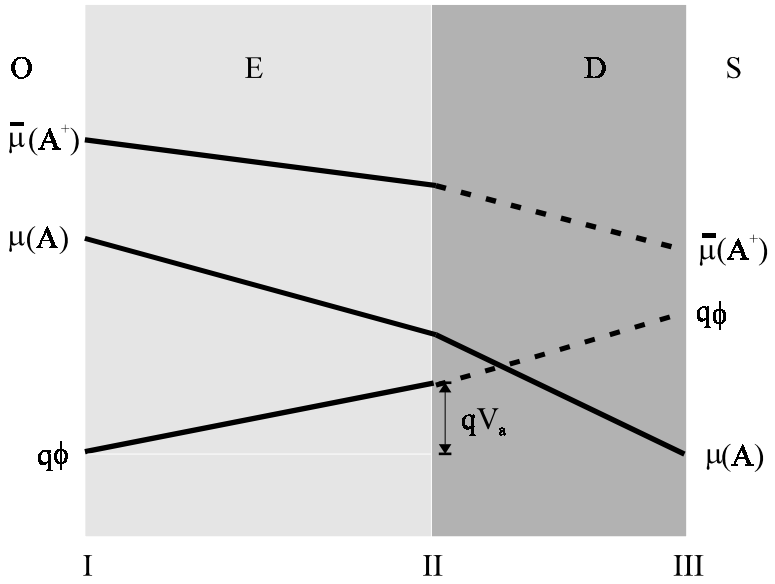

Fig. 5: Potential profiles inside the solid electrolyte (E) and product (D) under closed-circuit conditions.

Due to conservation of charges, the total current I_t in any part of the solid electrochemical cell of the PEVD system is the same.

$$I_{e,(W)} + I_{i,(W)} = I_{e,(E)} + I_{i,(E)} = I_t \quad (18)$$

Since the electronic current $I_{e,(E)}$ and the ionic current $I_{i,(W)}$ inside the solid electrolyte (E) and the external electric circuit, respectively, are negligible, the electronic current $I_{e,(W)}$ flowing through the external electric circuit equals the ionic current $I_{i,(E)}$ flowing through the solid electrolyte *(E)*.

$$I_{e,(W)} = I_{i,(E)} = I_t \quad (19)$$

Because all ionic and electronic current arriving at (II) will be drained away via the deposit (D), the ionic current $I_{i,(E)}$ flowing through the solid electrolyte equals the ionic current $I_{i,(D)}$ flowing through deposit (D) under steady-state conditions. The same is true for the electronic current through the external electric circuit and deposit (D). Thus, we have the following relation involving currents:

$$I_{e,(W)} = I_{i,(E)} = I_{e,(D)} = I_{i,(D)} \quad (20)$$

Consequently, the electronic current measured in the external electric circuit reveals the ionic current in solid electrolyte (E) and deposit (D), as well as the electronic current in deposit (D).

The current relation in Eqn. 20 is achieved by adjusting the chemical potential of (A) at (II) under closed circuit conditions. Since the gradient in electrochemical potential is the driving force for the flow of charged particles in the multiphase PEVD system, the current density carried by (A^+) in either the solid electrolyte (E) or deposit (D) can be written as:

$$i_{A^+}(x) = -\frac{\sigma_{A^+}(x)}{z_{A^+}q}\left(\frac{\partial \bar{\mu}_{A^+}(x)}{\partial x}\right) \quad (21)$$

where σ_{A^+} is the electric conductivity of (A^+).

Accordingly, the current density of (A^+) inside the solid electrolyte (E) is

$$i_{A^+,E} = -\frac{\sigma_{A^+,E}}{z_{A^+}q}\left(\frac{\bar{\mu}_{A^+,II} - \bar{\mu}_{A^+,I}}{L_E}\right) \quad (22)$$

assuming the solid electrolyte (E) is homogeneous. L_E is the thickness of solid electrolyte (E). Splitting the electrochemical potential into

both its chemical and electric potential components, and considering Eqn. 15, yields

$$i_{A^+,E} = -\frac{\sigma_{A^+,E}}{z_{A^+}q}\left(\frac{\mu_{A,II} - \mu_{A,I} + qz_{A^+}V_a}{L_E}\right) \quad (23)$$

In this equation, two variables exist. One is the applied potential, the other is the chemical potential of (A) at (II). The same equations apply to the current density of (A^+) inside deposit (D) when (D) is homogeneous and the thickness of (D) is L_D.

$$i_{A^+,D} = -\frac{\sigma_{A^+,D}}{z_{A^+}q}\left(\frac{\bar{\mu}_{A^+,III} - \bar{\mu}_{A^+,II}}{L_D}\right) \quad (24)$$

or

$$i_{A^+,D} = -\frac{\sigma_{A^+,D}}{z_{A^+}q} \cdot \left(\frac{\mu_{A,III} - \mu_{A,II} + qz_{A^+}(\phi_{III} - \phi_{II})}{L_D}\right) \quad (25)$$

Since the chemical potential of (A) is fixed by the cathodic reaction at (III), a chemical potential gradient of (A) exists inside product (D). This causes an open circuit internal electric field to build up to oppose the tendency of (A^+) to move across product (D). However, product (D) is a mixed conducting product. As in a scale product, the electronic leakage current weakens the internal electric field in (D). Thus, the electrochemical potential gradient in Eqn. 24 exists to move (A^+) from location (II) to location (III) to react with vapor phase.

The electric potential difference between interfaces (III) and (II) depends on the electronic conductivity of deposit (D). If the deposit is an exclusive electronic conductor, the difference is close to zero and the current is limited by ionic conduction in the deposit; on the other hand, if it is an exclusive ionic conductor, an internal potential close to the open circuit emf value is built up. Ionic conduction relies on the leakage electronic current. In either case, the electric potential difference across (D) can be expressed as

$$\phi_{III} - \phi_{II} = EMF_D = -\frac{t_{A^+}}{qz_{A^+}}(\mu_{A,III} - \mu_{A,II}) \quad (26)$$

where t_{A^+} is the transport number of (A^+).

Combining Eqns. 26 and 25 yields

$$i_{A^+,D} = -\frac{\sigma_{A^+,D}t_{e^-}}{z_{A^+}q}\left(\frac{\mu_{A,III} - \mu_{A,II}}{L_D}\right) \quad (27)$$

where t_{e^-} is the electronic transport number.

Both current densities are assumed to be uniform in solid electrolyte (E) with effective area A_E and in deposit (D) with effective area A_D. The ionic currents should be equal according to the charge conservation in Eqn. 20, and we have

$$A_E i_{A^+,E} = A_D i_{A^+,D} \quad (28)$$

If Eqns. 23 and 27 are substituted into Eqn. 28, then

$$-\frac{A_E\sigma_{A^+,E}}{z_{A^+}q}\left(\frac{\mu_{A,II} - \mu_{A,I} + qz_{A^+}V_a}{L_E}\right) = -\frac{A_D\sigma_{A^+,D}t_{e^-}}{z_{A^+}q}\left(\frac{\mu_{A,III} - \mu_{A,II}}{L_D}\right) \quad (29)$$

For simplicity, two conductances, G_E and G_D, can be defined as follows:

$$G_E = \frac{A_E\sigma_{A^+,E}}{L_E} \quad (30)$$

$$G_D = \frac{A_D\sigma_{A^+,D}t_{e^-}}{L_D} \quad (31)$$

Both G_E and G_D depend on the physical and geometrical properties of the solid electrolyte (E) and the deposit (D), respectively. Eqn. 29 then becomes

$$G_E(\mu_{A,II} - \mu_{A,I} + qz_{A^+}V_a) = G_D(\mu_{A,III} - \mu_{A,II}) \quad (32)$$

From Eqn. 32, the chemical potential at (II) can be expressed as

$$\mu_{A,II} = \frac{G_E\mu_{A,I} + G_D\mu_{A,III} - qz_{A^+}G_EV_a}{G_E + G_D} \quad (33)$$

According to the above equation, the chemical potential of the solid-state transported

reactant at (II) depends on a number of factors. These are the physical and geometrical properties of the phases in the PEVD system, except the applied dc potential V_a. Although varying physical and geometrical parameters affect a PEVD process, adjusting the applied dc electrical potential is the most effective way to control the driving force for ionic transport.

Electrochemical Control and Monitoring of a PEVD Process Through the Solid Electrochemical Cell of a PEVD System

The most distinguishing feature of PEVD process control is made possible because of the solid electrochemical cell involved in a PEVD system. Compared with other vapor deposition techniques, utilization of solid electrochemical cells is one of the most significant advantages of the PEVD technique, since deposition process control and monitoring are easy to realize. By connecting several measurement devices to the external electrical circuit of a PEVD system, the reaction in a PEVD process is easily monitored and possibly controlled by the electrical current and applied potential, respectively.[3]

PEVD Process Monitoring

The current, *I*, in a PEVD process can be recorded simultaneously by an ammeter in the external circuit to reveal the kinetics of the PEVD reactions. As discussed in the last section, solid-state reactant (A) needs to be transported as a combination of ionic and electronic species from the source to the sink side through the solid electrochemical cell to participate in a PEVD reaction with vapor phase reactant (B). The PEVD reaction rate, and subsequent product (D) formation rate, $\upsilon(t)$, can be expressed as

$$\upsilon(t) = \frac{1}{V}\frac{dn}{dt} \tag{34}$$

where *V* is the molar volume of the PEVD product (D), and *n* is the mole number of ionic species travelling through the PEVD system. From Faraday's law and Fick's second law discussed in the previous section, the current passing through the external circuit of a PEVD system is

$$I = \frac{dQ}{dt} = \frac{zFdn}{dt} \tag{35}$$

Combining Eqns. 34 and 35 yields.

$$I = \upsilon(t)VzF \tag{36}$$

Thus, the rate of PEVD product formation is proportional to the current flowing through the external electric circuit. Furthermore, taking into account the evolution of the cell with time, the amount of reaction product formed, *M*, at time *t* is easily monitored during PEVD by integrating the current from 0 to *t*.

$$M = \int_0^t Idt = \int_0^t \upsilon(t)VzFdt \tag{37}$$

Although it is not as severe in PEVD systems as in aqueous electrochemical systems in which various kinds of mobile ions are present in the electrolytes, it should be pointed out that, in the presence of reactants at the sink electrode surface, other electrochemical reactions might also take place in parallel with the desired one at the sink side. If side reactions exist, usually such parallel reactions' contributions to the measured current are not easy to quantify. If it is desired to use current to monitor the reaction and product formation in PEVD, side reactions should be eliminated or at least controlled. Fortunately, only one ionic species is usually mobile in a solid electrochemical cell because of the nature of the solid electrolyte. As long as the vapor phase is properly controlled, usually one electrode reaction is predominant over a wide range of PEVD applied potentials. Virtually 100% current efficiency for product formation can be expected.

Process Control via the Applied dc Electric Potential

Based on Eqn. 33, possible process control during PEVD includes many aspects, such as process temperature, the vapor phase at the sink side, the activity of the solid-state transported reactant (A) at both sink and source sides, etc. Further discussion of these factors is subject to the individual process and will be presented later. In this section, PEVD process control is

discussed under the assumption that all other parameters are constant. The current-potential behavior reveals that the thermodynamic driving force for the overall reaction and ionic transport are controllable by the applied external dc electrical potential in PEVD.

According to Eq. 33, adjusting the applied dc electrical potential controls the chemical potential of (A) at (II) and, accordingly, the chemical potential difference of the solid-state transported reactant (A) across the deposited product (D). Consequently, the applied potential controls the reaction rate in a PEVD system when solid transport of (A) through the product is the rate-limiting step for the process. Because the thermodynamic driving force for PEVD is not solely based on the chemical potential difference of the solid-state transported reactant between the sink and source side, isolation of both sides is not necessary. This provides a great practical advantage of PEVD over EVD.

In order to reveal the kinetics of the PEVD reaction, the chemical potential of (A) at (II) from Eqn. 33 is substituted into Eqn. 27,

$$I = I_{A^+,E} = I_{A^+,D} = -\frac{G_D}{qz_{A^+}}$$

$$\left(\mu_{A,III} - \frac{G_E\mu_{A,I} + G_C\mu_{A,III} - qz_{A^+}G_E V_a}{G_E + G_D}\right) \quad (38)$$

and therefore,

$$I = \frac{1}{qz_{A^+}}\frac{G_D G_E}{G_E + G_D}$$

$$\left(\mu_{A,I} - \mu_{A,III}\right) - \frac{G_D G_E}{G_E + G_D}V_a \quad (39)$$

G_t can be defined as the total conductance of the PEVD system,

$$G_t = \frac{G_D G_E}{G_E + G_D} =$$

$$\frac{A_E\sigma_{A^+,E}A_D\sigma_{A^+,D}t_{e^-}}{A_E L_D\sigma_{A^+,E} + A_D L_E\sigma_{A^+.D}t_{e^-}} \quad (40)$$

According to this definition, G_t depends on the physical and geometric properties of both the solid electrolyte (E) and product (D). G_t is fixed if the PEVD system is fixed. By substituting G_t into Eqn. 39, the current and applied potential have the following simple relation:

$$I = G_t\frac{\mu_{A,I} - \mu_{A,III}}{qz_{A^+}} - G_t V_a \quad (41)$$

In this ideal condition, the current vs. applied potential curve in a PEVD process is schematically shown in Figure 6. The applied dc potential V_a is linearly related to the current I, and the slope is $-G_t$. The stop potential at zero current is

$$V_{stop} = V_a = \frac{\mu_{A,I} - \mu_{A,III}}{qz_{A^+}} \quad (42)$$

Before discussing general conclusions regarding the current and applied dc potential in a PEVD system, the initial assumptions made in this discussion have to be examined carefully. The above discussion is based on the assumption that all interfaces at (I), (II), and (III) are ideal non-polarizable interfaces, and equilibrium electrochemical potentials of (A^+) and (e^-) prevail across these interfaces during mass and charge transport in the PEVD system. Thus, the aforementioned expressions for mass and charge transport in a PEVD system indicate that the transport rate (current) only depends on bulk material properties and simple geometric aspects. The thermodynamic equilibrium criterion at one interface between two phases is an equality of electrochemical potential of the charged particles. If establishment and maintenance of the equilibria are rapid, then the response of the interface to a non-equilibrium field is to drive the equilibrium predominantly in one of its component directions, which results in a basically non-resistive transfer of ideally reversible interfaces.[11] Only in this case can the bulk value of the electrochemical potential be substituted for the interface electrochemical potential in the aforementioned equations.

In practice, when current flows in the system, thermodynamic equilibrium conditions no longer exist at the interfaces. The response of the PEVD system is also related to the

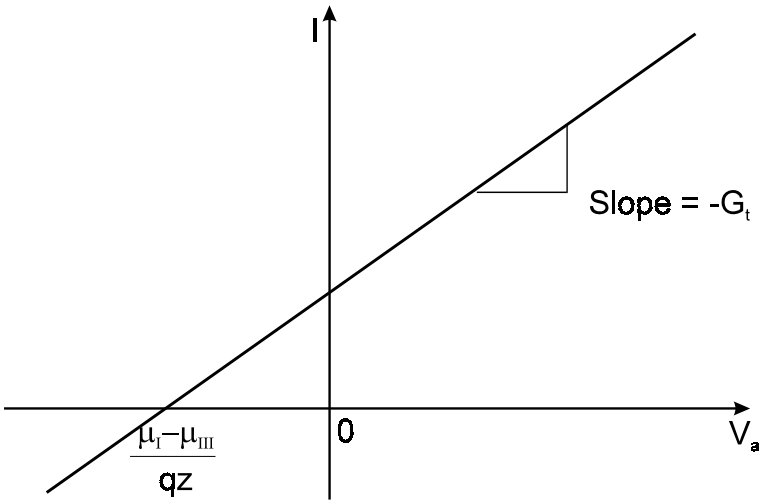

Fig. 6: Ideal current-applied potential behavior of a PEVD system

interface characteristics, which are fixed by the external chemical and electrical conditions for each phase. Polarization usually exists in the interface region. The interfaces need to be treated by kinetic considerations.[12] Nevertheless, mass and charge transport in a PEVD process at elevated temperatures are frequently determined by the rate of diffusion in the solid reaction product rather than by the rate of phase boundary charge transfer. On the other hand, overpotential in a PEVD reaction and product formation can be caused by other factors, such as gas phase diffusion and crystallization. The resultant current-applied potential curve could be more complicated than the ideal one in Figure 6. The details of those kinetic considerations on a well-defined PEVD system will be presented later.

General Product Deposition Behavior in PEVD

The advantages of PEVD are not only based on the close electrochemical control, but also arise from the unique electrocrystallization behavior during growth of PEVD products. In order to give the prerequisites for understanding the mechanism of PEVD product growth, it is necessary to consider the transport processes of the charged reacting species in the PEVD product phase.

Selective Deposition

As schematically shown in Figure 7a, initial PEVD reaction and product nucleation occurs at the three-phase boundary of solid electrolyte (E), working electrode (W) and the sink vapor phase (S) which contains vapor phase reactant (B). Only here are all reactants available for the half-cell electrochemical reaction at the sink side of a PEVD system. Although the ionic and electronic species can sometimes surface diffuse at elevated temperature to other sites to react with (B) in the vapor phase, the supply of the reactants continuously along the diffusion route is less feasible and the nuclei are too small to be stabilized under normal PEVD conditions. Only along the three phase boundary line are all the reactants available for further growth to stabilize the nuclei. Consequently, initial deposition in a PEVD process is restricted to certain areas on a substrate where all reactants for the sink electrochemical reaction are available.

Growth on Electrically Shorted Surfaces

The availability of reacting species for the electrochemical reaction also controls the crystal growth of the PEVD products. The further growth of product nuclei can be divided into two stages. During the first stage, the solid electrolyte (E) and working electrode (W) are

still exposed to the sink vapor phase (S). Since the ionic conductivity in the solid electrolyte (E) is generally much higher than that in the PEVD product, and the electronic conductivity in the working electrode (W) is much higher than in the product, two kinds of electrically shorted surfaces exist as shown in Figure 7b. One is an ionically shorted surface (X) along the solid electrolyte (E) and the other is an electronically shorted surface (Y) along the working electrode (W). Although the growth kinetics along these surface directions will still be parabolic, no ionic and electronic electrochemical potential gradient will be expected in the two directions, and charged species transport is driven by the concentration gradient of electrons and ions, respectively.[13] This is a unique case compared with common gas-solid reactions. The second stage starts when at least one of the electrically shorted surfaces is covered by PEVD product (D). The growth behavior in both stages is quite different if the PEVD reaction rate-limiting step is solid-state transport of reactant through PEVD product (D).

Along the X direction, i.e., the surface of the ionic conducting material, the reaction rate-limiting step is electron transport in the product phase (D). The growth distance, x, can be expressed as:

$$x = (V_D \sigma_e \Delta G t/F^2)^{1/2} \quad (43)$$

σ_e is the average electronic conductivity in the product phase (D), V_D is the molar volume of the deposit (D), t is time, and ΔG is the Gibbs free energy change of reaction (4) for product formation. Specifically,

$$\Delta G = \mu_{D,III} - \mu_{B,III} - \mu_{A,II} \quad (44)$$

Along the Y direction, i.e., the surface of the electronic conducting material, the reaction limiting step is mobile ionic reactant (A^+) transport in the product phase (D). No perceptible open circuit emf will be expected over the growth distance, and charged species are driven by the concentration gradient. The growth distance, y, can be expressed as:

$$y = (4/\pi)\,(V_D \sigma_{A^+} \Delta G t/F^2)^{1/2} \quad (45)$$

where σ_{A^+} is the average ionic conductivity in the product phase (D).

The ability of PEVD to deposit thin solid state ionic materials can be expressed by the ratio of the Y to X direction growth length, y/x, which can be written as

$$\frac{y}{x} \approx \frac{1.265\sqrt{\sigma_{A^+}}}{\sqrt{\sigma_e}} \quad (46)$$

This ratio is only related to the ionic and electronic conductivity of the PEVD product.[14] Thus, overgrowth along the electronic conducting surface indicates ionic conductivity is significantly higher than electronic conductivity in the PEVD product phase. For overgrowth along the ionic conducting surface, electronic conductivity must be significantly higher than ionic conductivity in the PEVD product phase.

Self-Leveling Effect

Once the working electrode (W) is covered by the ionic conducting product or the entire solid electrolyte (E) is covered by the electronic conducting product, no electrically shorted surface exists. Thus, further growth in thickness has to involve diffusion of both the ionic species and electrons to the surface to react with the gas phase. Practically, diffusion of one species is much faster than the other. However, electroneutrality must be maintained under this open circuit condition. The growth rate is determined by either migration of electrons or mobile ionic reactants in the deposit (D). In both cases, the increase in thickness should follow the parabolic law.[15]

$$\delta = (2kt)^{1/2} - (2kt_s)^{1/2} \quad (47)$$

where δ is the thickness of the product (D) at time t, k is the rate constant of Tammann's rate law[16] and t_s is the initial growth time along the x direction. This corresponds to the differential equation

$$\frac{\partial \delta}{\partial t} = \frac{k}{\delta} \quad (48)$$

and the boundary condition

$$\delta = 0 \text{ at } t = t_s \quad (49)$$

Because the increase in thickness is expected to follow parabolic behavior, the thicker the product, the slower the growth rate.

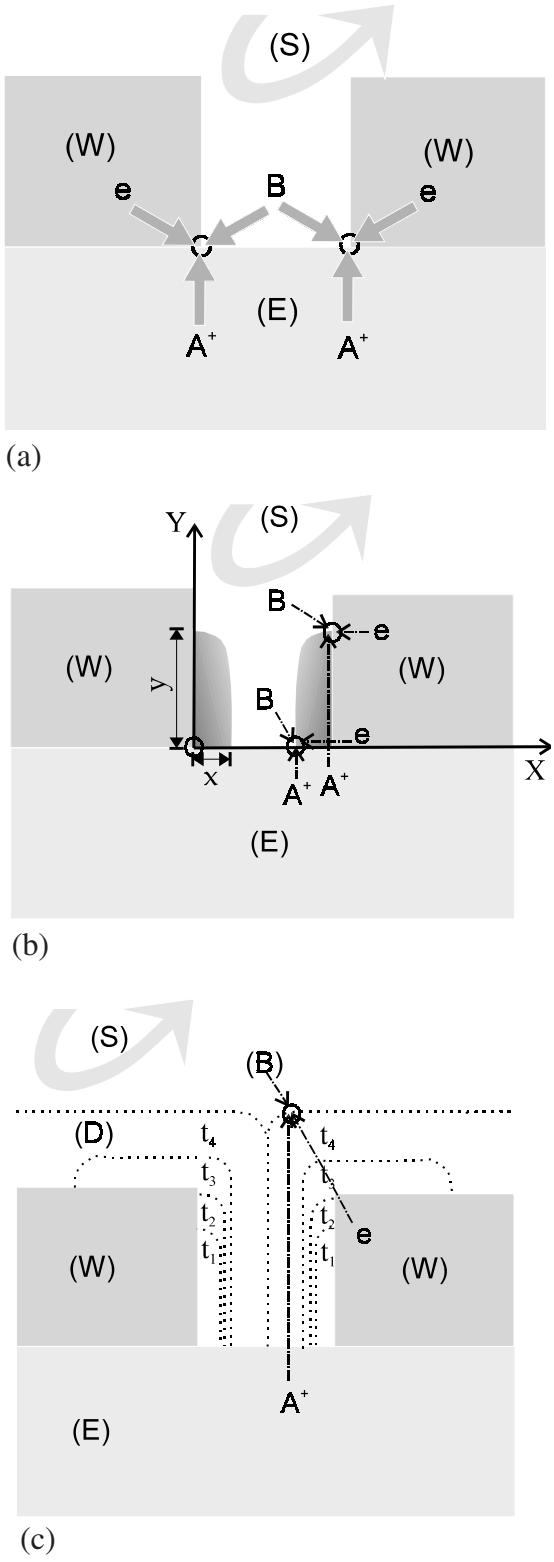

Fig. 7: (a) The initial PEVD reaction and product nucleation occurs at the three-phase boundary of solid electrolyte (E), working electrode (W) and the sink vapor phase (S), (b) PEVD product growth on both ionically and electronically shorted surfaces, and (c) The step by step increase of PEVD product (D) thickness which reduces the aspect ratio at the working electrode. From t_1 to t_4, the deposition time increases.

Thus, a dense and uniform coverage is expected decreasing the aspect ratio of the surface in a step-wise fashion, as indicated by the numbered dotted lines in Figure 7c.

PEVD Applications

Applying PEVD for Auxiliary Phase Deposition at Working Electrodes of Gaseous Oxide Sensors

PEVD was developed initially in the course of fabricating type III potentiometric sensors for gaseous oxide (CO_x, SO_x, and NO_x) detection.[3] Three kinds of PEVD products ($NaNO_3$, Na_2CO_3, and Na_2SO_4) were deposited as the auxiliary phases at the working electrode of NO_2, CO_2, and SO_2 sensors, respectively. Because of the underlying similarities, all discussion here will focus on CO_2 gas sensors. Cases of depositing $NaNO_3$ and Na_2SO_4 auxiliary phases for type III NO_2 and SO_2 potentiometric sensors, respectively, can be treated analogously.

Gaseous Oxide Sensors and Corresponding Kinetics

It is well known that gaseous oxides (CO_x, SO_x, and NO_x) are responsible for global environmental problems such as acid rain and the greenhouse effect. To date, these gaseous oxides have been analyzed mostly with analytical instruments based on IR absorption, UV absorption and chemiluminescence. Although these instruments provide precise analytical data, they are expensive with time-consuming procedures and hence do not fit well with a feedback control system. In order to treat combustion exhausts in chemical processes and to monitor the environment, there has been an ever-increasing need for compact, low-priced solid-state gas sensors[17,18] that are capable of detecting gaseous oxides in-situ. Various types of sensor prototypes have been studied.[19,20] Among them, solid electrolyte potentiometric gas sensors have attracted widespread attention in recent years, not only for process control due to their high stability, but also for the detection of air pollutants due to their high sensitivity and selectivity.

Previously, Weppner[21] classified potentiometric sensors into three types, depending on the gas electrode reactions at the working electrodes of the sensors.

Because of the unavailability of the requisite solid electrolytes to form a concentration cell of gaseous oxides, it is impossible to fabricate type I potentiometric sensors for detecting gaseous oxides.

In 1977, Gauthier and Chamberland[22] first demonstrated the possibility for type II potentiometric detection of gaseous oxides using solid electrolytes of inorganic radicals, such as K_2CO_3, $Ba(NO_3)_2$, and K_2SO_4. Since then, much effort has been devoted to the development of type II potentiometric sensors.[23-25] For instance, the simple cell (50) was employed to measure the equilibrium partial pressure of CO_2 in a gaseous mixture.[26,27] The galvanic cell arrangement is

$$\text{(ref.) Pt, } CO_2', O_2' | K_2CO_3 | CO_2, O_2, \text{Pt (working)} \quad (50)$$

It is an indirect CO_3^{2-} concentration cell with the overall cell reaction

$$CO_2' + \tfrac{1}{2}O_2' \Leftrightarrow CO_2 + \tfrac{1}{2}O_2 \quad (51)$$

The theoretical electromotive force (EMF) of the sensor is given by a Nernst equation:

$$EMF = \frac{RT}{2F} \ln \frac{P_{CO_2} P_{O_2}^{\frac{1}{2}}}{P_{CO_2'} P_{O_2'}^{\frac{1}{2}}} \quad (52)$$

where P_{CO_2} and P_{O_2} are the partial pressures of CO_2 and O_2, respectively. If the oxygen partial pressure is the same at both electrodes, then the EMF of the cell can be simplified to

$$EMF = \frac{RT}{2F} \ln \frac{P_{CO_2}}{P_{CO_2'}} \quad (53)$$

The partial pressure of CO_2 at the working electrode can be directly compared with the partial pressure of CO_2 at the reference electrode.

Although employing inorganic radicals in solid electrolytes opens the possibility to detect gaseous oxides by a potentiometric method, it is a chemical choice rather than a material choice for solid electrolytes. Since salts involving inorganic radicals are not usually good solid electrolytes due to limited chemical stability,

poor sinterability, phase transitions and low ionic conductivity, sensors made from those cells are unsuitable in practical applications.[28-30]

Instead of a chemical approach to solid electrolyte selection in type II potentiometric sensors, type III potentiometric sensors for gaseous oxide detection have been considered from a material approach by first selecting good solid electrolytes.[31] According to classic electrochemical theory, an indirect (exchange) electrode can be used in cells for the determination of thermodynamic data for reactions involving an element for which a solid electrolyte is not available. The indirect electrode then serves as an auxiliary phase where the activity of the component of interest can be related to the activity of another component in a solid electrolyte. Of particular importance is the applicability of this electrochemical technique to those gaseous species for which a solid electrolyte is not available. As a result, a large selection of solid electrolytes can be used for gaseous oxide sensors, especially several fast sodium ion conductors, such as β-alumina[32,33] and Nasicon ($Na_3Zr_2Si_2PO_{12}$).[34-37] For instance, a type III CO_2 potentiometric gas sensor, which obeys the following cell expression, has been widely recognized as the best potentiometric sensor prototype for CO_2 gas detection:[21,31,37,38]

$$\left(\begin{matrix}\text{reference}\\ \text{electrode}\end{matrix}\right)CO_2', O_2', Pt\left|Na_2CO_3\right|Na^+ - \beta''-$$

$$\text{alumina}\left|Na_2CO_3\right|Pt, CO_2, O_2\left(\begin{matrix}\text{working}\\ \text{electrode}\end{matrix}\right) \quad (54)$$

The sensing mechanism was studied in detail by Hotzel and Weppner[39] from a thermodynamic point of view. Under open circuit conditions, the equilibrium half cell electrochemical reaction at the reference electrode is

$$2Na^+ + CO_2' + \tfrac{1}{2}O_2' + 2e^- \Leftrightarrow Na_2CO_3 \quad (55)$$

and the equilibrium half cell electrochemical reaction at the working electrode is

$$Na_2CO_3 \Leftrightarrow 2Na^+ + CO_2 + \tfrac{1}{2}O_2 + 2e^- \quad (56)$$

The overall electrochemical reaction is

$$CO_2' + \tfrac{1}{2}O_2' \Leftrightarrow CO_2 + \tfrac{1}{2}O_2 \quad (57)$$

which is the same as for a type II potentiometric sensor. The EMF expression is also identical to a type II potentiometric sensor. However, an important feature of this kind of sensor is the Na_2CO_3 auxiliary phase. It provides a unique relationship between the partial pressure of the gaseous components (CO_2 and O_2) and the chemical potential of the mobile sodium ions in the solid electrolyte Na^+-β"-alumina. Thus, the auxiliary phases are of vital importance for type III potentiometric sensors. Generally, an auxiliary phase should be a fast mixed ionic and electronic conductor, be located at the area of change from ionic to electronic conductivity in the galvanic cell, and be involved in the cell reaction. The results obtained to date with type III potentiometric sensors have shown them to be successful and promising for detecting gaseous oxides. Recently, this topic was reviewed by Yamazoe and Miura.[38-40]

Although the basic principles of type III potentiometric sensors are applicable for gaseous oxide detection, this should not obscure the fact that these sensors still require further development. This is especially true in view of the kinetics of equilibria and charged species transport across the solid electrolyte/electrode interfaces where auxiliary phases exist. Real life situations have shown that, in practice, gas sensors rarely work under ideal equilibrium conditions. The transient response of a sensor, after a change in the measured gas partial pressure, is in essence a non-equilibrium process at the working electrode. Consequently, although this kind of sensor has been studied for almost 20 years, practical problems still exist and prevent its commercialization. These problems include slow response, lack of sensitivity at low concentrations, and lack of long-term stability.[41-43] It has been reported[41] that the auxiliary phases were the main cause for sensor drift, and that preparation techniques for electrodes with auxiliary phases were very important to sensor performance.[43]

Based on a newly developed sensor electrode reaction model,[44] the gas electrode reactions for type III potentiometric CO_2 sensors

in cell (54) are essentially charge transfer reactions between the Na_2CO_3 auxiliary phase and the gaseous species. These reactions certainly depend on the gas phase and the auxiliary phase, as well as the interface between them.[45]

This sensing model also implies that the geometric properties, instead of solely the physical properties of the auxiliary phase at the working electrode, are critical to kinetic performance. Accordingly, the four most important geometric criteria for an auxiliary phase are as follows:

1. The aspect ratio of the auxiliary phase at the working electrode should be as low as possible to improve gas phase diffusion.
2. The auxiliary phase should intimately contact the metallic electrode, and the interface should be as large as possible since transport of electrons is two-dimensional across the interface.
3. The auxiliary phase should be as thin as possible to allow readjustment of the Fermi level within the auxiliary phase.
4. The auxiliary phase should intimately contact the solid electrolyte to ensure transport of mobile ionic species. This will benefit the performance of sensors under certain conditions.

Besides the geometric requirements suggested by the above-mentioned gas-sensing model, two more criteria can be deduced from other considerations. First of all, as a general requirement of applying an indirect electrode,[14] the auxiliary phase should separate the reactants in the gas phase from the electrolyte. Otherwise, displacement reactions can damage the contact between the solid electrolyte and auxiliary phase layer and affect stability. These reactions can also generate a mixed sensor EMF response leading to selectivity and sensitivity problems. Thus:

5. The auxiliary phase should cover the entire solid electrolyte surface.

Secondly, from Wagner's theory, the metallic coatings forming the electrodes are viewed as mere electronic probes for the local electronic distribution in the auxiliary phase. They should be chemically inert. For operation in the lean regime, it is highly desirable that their chemical catalytic activities be as low as possible.[46] Hence:

6. The auxiliary phase should cover the entire metallic electrode. This also provides maximum interface contact as required in criterion (2).

Previously, several methods[47-49] have been reported for applying auxiliary phases to the porous metallic working electrodes of gaseous oxide sensors. Figure 8 compares the geometric structure of the ideal auxiliary phase arrangement (Figure 8a) according to the above six criteria to various reported techniques such as in-situ formation (Figure 8b), mechanically pressed discs (Figure 8c), physical vapor deposition (Figure 8d), and melting and quenching (Figure 8e). It is clear that none of these previously reported techniques meet all the geometric requirements for an ideal auxiliary phase. This will lead to sensor sensitivity, selectivity, stability and response time problems.

In what is the essence of materials engineering, structure and preparation will undoubtedly be of vital important to final properties. In order to deposit better auxiliary phases with close control to meet all six geometric criteria, PEVD has recently been applied to deposit auxiliary phases at the working electrodes of gaseous oxide sensors.[44]

Polarized Electrochemical Vapor Deposition to Deposit Auxiliary Phases at the Working Electrode of Type III Potentiometric CO_2 Sensors

PEVD Process Design

In the case of depositing a Na_2CO_3 auxiliary phase at the working electrode of a CO_2 potentiometric sensor, the substrate or solid electrochemical cell for this PEVD process is well defined. Although other solid electrolyte and metallic electrode combinations were reported in previous investigations, the use of Na^+-β"-alumina as the solid electrolyte and a porous Pt thick film as the metallic working electrode is the most common choice for type III potentiometric CO_2 sensors. A cross-section view of the substrate is schematically shown in Figure 9. The Pt thick films are highly porous (larger than 50 vol.% pore phase) and irregularly

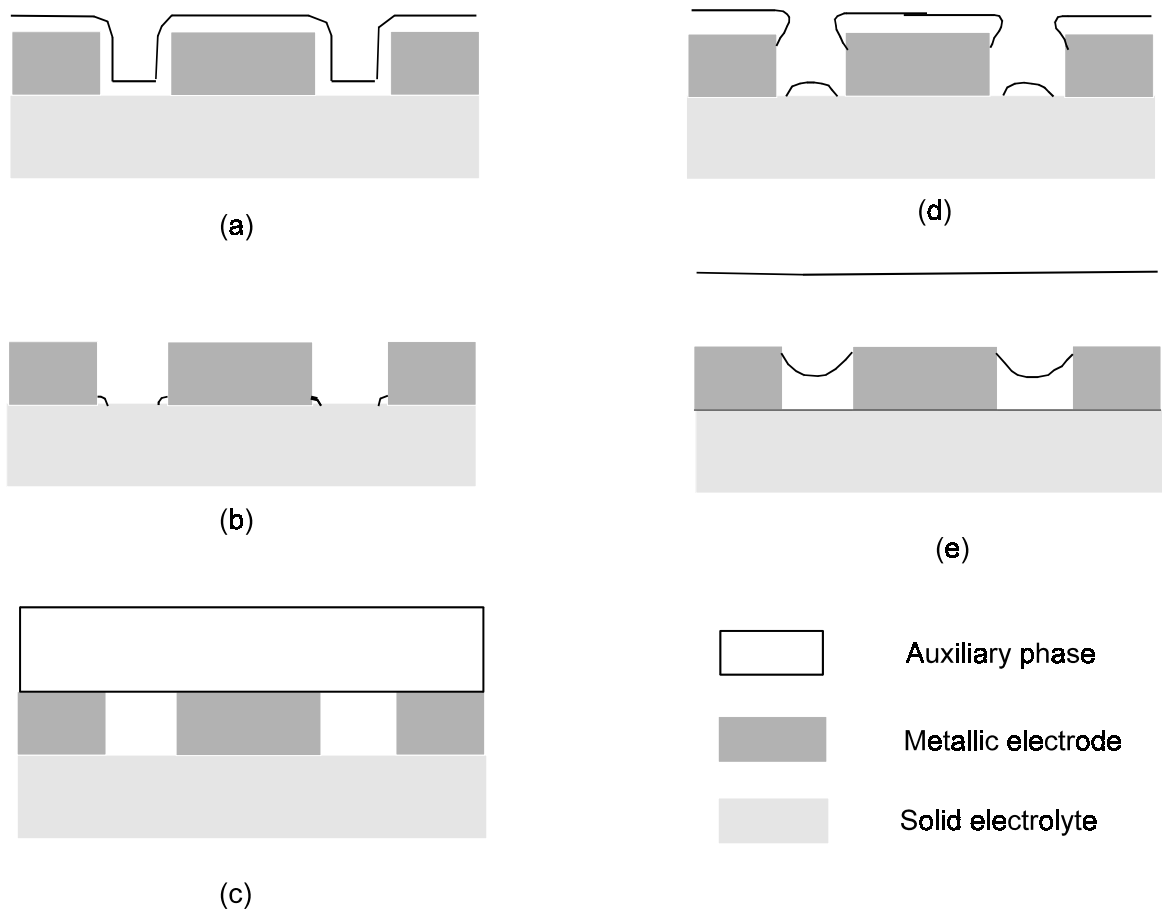

Fig. 8 Comparion of geometric structure of an ideal auxiliary phase (a) with those prepared by current techniques, such as in-situ formation (b), mechanically pressed discs (c), physical vapor deposition (d), and melting and quenching (e).

shaped, and they have very high aspect ratios (above 3). Depositing a compound thin film of Na_2CO_3 on such a substrate to meet all the above-mentioned geometric criteria by conventional deposition techniques is almost impossible.

Sodium is selected as the solid state transported reactant in PEVD. This is because not only is Na^+ a component in the PEVD product phase Na_2CO_3, but also the mobile ionic species in the solid electrolyte (Na^+-β"-alumina) and in the auxiliary phase of the sensor. Thus, PEVD can take advantage of the solid electrochemical cell (substrate) of the sensor to transport one reactant (sodium) across the substrate under an electrochemical potential gradient. This gradient is mainly provided by a dc electric potential under closed circuit conditions. The vapor (or gas) phase at the sink side of the PEVD system should be made up of the other components of the PEVD product Na_2CO_3, i.e., carbon and oxygen. This can be realized by using CO_2 and O_2 as the vapor phase reactants at the sink side of the PEVD system. Thus, the electrochemical reaction for PEVD Na_2CO_3 product formation will involve the solid state transport of sodium ions through the solid electrolyte to obtain electrons from the metallic electrode and react with CO_2 and O_2 from the sink side vapor phase. The cathodic half-cell electrochemical reaction at the sink side can be expressed as

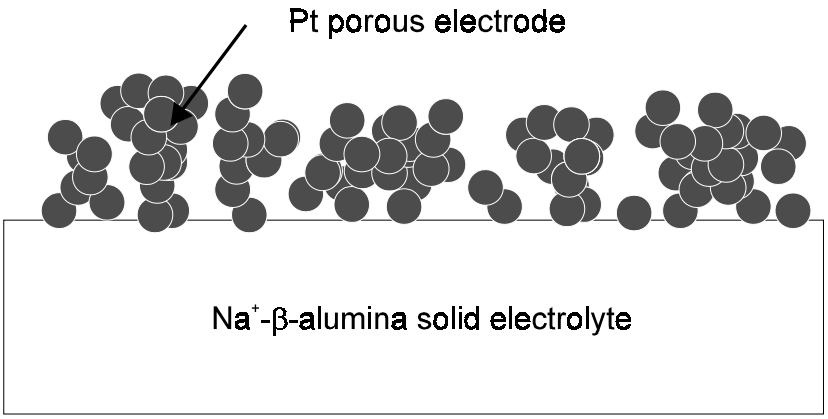

Fig. 9: Schematic cross-section of a Pt thick film electrode on a Na^+-β-alumina solid electrolyte of a type III potentiometric CO_2 sensor.

$$2Na^+ + 2e^- + CO_2 + \tfrac{1}{2}O_2 \rightarrow Na_2CO_3 \quad (58)$$

In order to sustain this reaction at the sink side of the PEVD system, a source is required at the other side of the substrate (anode) to supply sodium. Otherwise, depletion of sodium in the Na^+ -β"-alumina solid electrolyte will lead to an α-alumina phase buildup at the anode that will block the ionic transport path of the PEVD system. The electrolytic properties of the solid electrolyte in this PEVD system will then be lost. Elemental sodium, for instance, could be the source giving the following anodic reaction:

$$Na \rightarrow Na^+ + e^- \quad (59)$$

This kind of source has the advantages of the fixed chemical potential of sodium, good contact between liquid sodium and the solid electrolyte, and no additional electronic conducting electrode is needed as the counter electrode (C) to connect with the external electric circuit. In practice, elemental sodium is too active, and a very tight seal is required to prevent sodium vapor from migrating and reacting chemically with CO_2 and O_2 in the sink vapor phase. Consequently, the system setup becomes more complex. The choice of the source in the current study is a combination of Na_2CO_3, CO_2 and O_2 gas phase, and an inert Pt counter electrode. The anodic reaction will be a decomposition reaction of the Na_2CO_3 solid phase,

$$Na_2CO_3 \rightarrow 2Na^+ + 2e^- + CO_2 + \tfrac{1}{2}O_2 \quad (60)$$

This anodic reaction provides sodium ions and electrons to the solid electrolyte and the inert Pt counter electrode, respectively, at the source side. Both the sodium ions and electrons will then travel through the solid electrochemical cell along previously-mentioned ionic and electronic paths to sustain the PEVD cathodic reaction for Na_2CO_3 product formation at the sink side. Furthermore, based on anodic reaction 60, the chemical potential of sodium is fixed by the vapor phase at the source side. Under open circuit conditions, this type of source can also serve as the reference electrode for a CO_2 potentiometric sensor.

The PEVD system for Na_2CO_3 auxiliary phase formation at the working electrode of a type III potentiometric CO_2 sensor is schematically shown in Figure 10. The electrochemical cell for this PEVD process can be illustrated as:

$$(\text{source})\ O_2', CO_2', Na_2CO_3, Pt \mid Na^+ - \beta'' - Al_2O_3 \mid Pt, Na_2CO_3, CO_2, O_2 (\text{sink}) \quad (61)$$

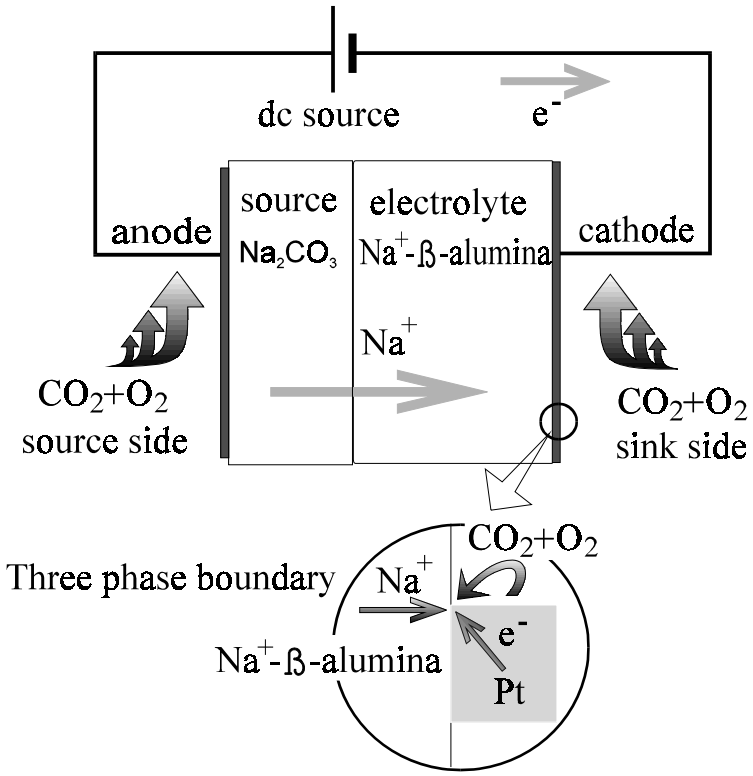

Fig. 10: PEVD process design for applying an auxiliary phase (Na_2CO_3) at the working electrode of a type III potentiometric CO_2 gas sensor.

The overall cell reaction is:

$$Na_2CO_3(\text{source}) \rightarrow Na_2CO_3(\text{sink}) \qquad (62)$$

This overall electrochemical cell reaction is equivalent to transporting the Na_2CO_3 phase physically from one side of the substrate to the other.

During the PEVD process, a chemical redox reaction takes place and the whole PEVD system can be viewed as a chemical reactor where the reactants are distributed over both the source and sink sides. According to the previous discussion, the driving force for this PEVD process can be solely provided by a dc electric potential, so that isolation of the source and sink vapor phases is not necessary. Consequently, the PEVD process is equivalent to physically moving a solid phase Na_2CO_3 through another solid phase (Na^+-β''-alumina) by electric energy. Furthermore, it should be pointed out that the overall cell reaction in this PEVD system is reversible.

$NaNO_3$ and Na_2SO_4 auxiliary phases can be deposited by a similar PEVD method for type III NO_2 and SO_2 potentiometric sensors, respectively.

Experimental

A commercially available fully dense Na^+-β''-alumina disc was used as the solid electrolyte. The working electrode (sink) of the system is a screen-printed platinum thick film of 7 μm in thickness. The porosity of the Pt thick film is in the range of 65 to 75%, and the average pore size is about 2 μm and ranges from 0.5-5 μm according to microstructure studies. A source Na_2CO_3 disc was made by pressing Na_2CO_3 powder. The green body was then co-sintered onto a Pt mesh with a spot-welded Pt lead.

The PEVD sample was placed into a lab-made PEVD apparatus, which is schematically

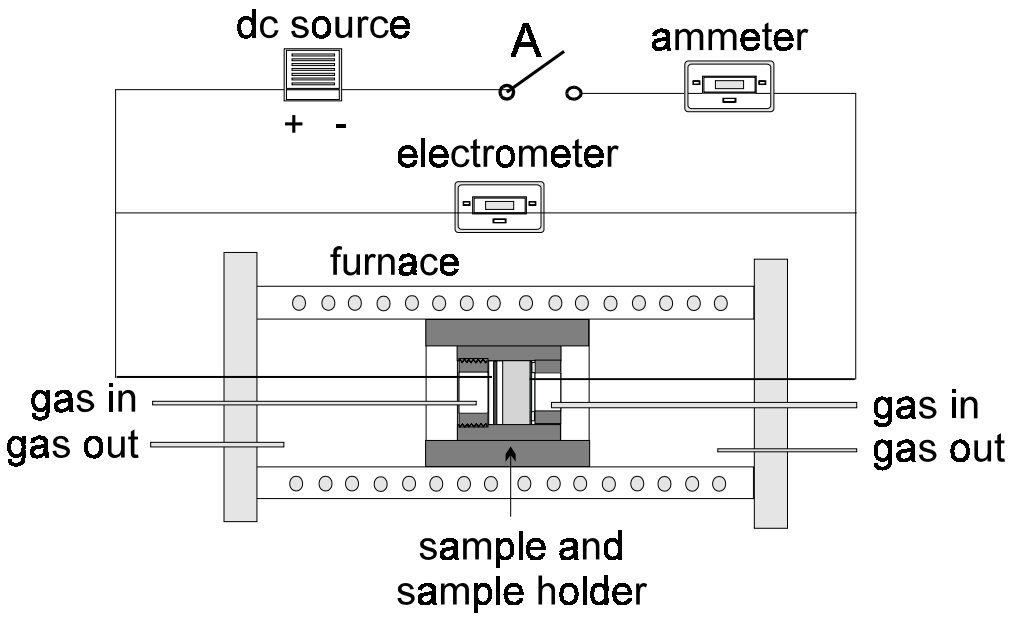

Fig. 11: PEVD apparatus for Na_2CO_3 formation at the working electrode.

shown in Figure 11. The apparatus has three basic functions, i.e., to set the processing temperature, to control the gas phases at both the source and the sink of the PEVD system, and to control and monitor the PEVD process through an external electric circuit.

Operating temperature affects the ionic conductivity in both the solid electrolyte and the PEVD product phase Na_2CO_3. The higher the operating temperature, the higher the ionic conductivity and, consequently, the PEVD current and reaction rate. Temperature also increases the electronic conductivity inside both solid phases. Although a higher electronic conductivity will increase the sodium solid-state transport rate inside the product Na_2CO_3 phase, it also increases the leakage current through the solid electrolyte. 500°C was selected for the current experiment. The samples were placed in a uniform temperature zone of a tube furnace.

In order to eliminate the driving force generated by a chemical potential difference between the sink and source side, the same vapor phase was used at both sides. The vapor phase consisted of air at atmospheric pressure. It was passed through a set of drying units before entering the PEVD apparatus. The flow rate of both inlet gases was in the range of 100-400 sccm.

An external electric circuit as shown in Figure 11 was connected to a PEVD sample through the Pt leads from both the source and sink sides. The driving force for the PEVD was supplied by a stable dc electric source. The sink and source side were set as the cathode and anode, respectively. A PEVD process started when gate A (Figure 11) was closed. Both potentiostatic (constant dc potential) and galvanostatic (constant PEVD current) methods could be applied in PEVD processes. An electrometer was used to measure the closed circuit applied potential during the PEVD process. An ammeter was used to monitor the current and, subsequently, the PEVD reaction rate according to Faraday's law.

In a potentiometric PEVD process, a dc potential of 2 V was applied. The resulting current, monitored over 50 hr, ranged from 52 to 205 μA. The current was relatively stable for the first 93 min, varying from 187 to 205 μA.

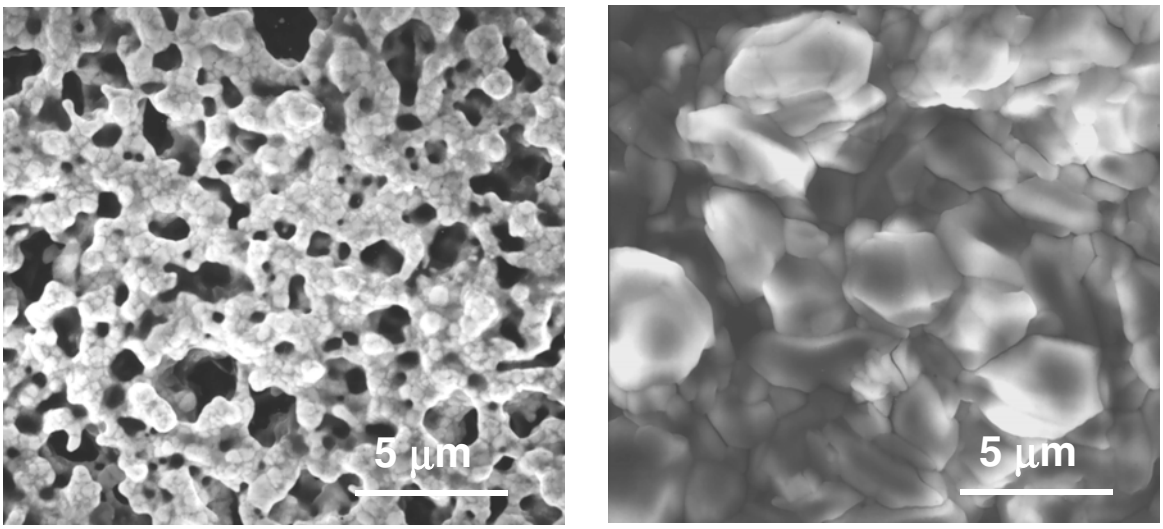

Fig. 12: SEM SE plan-view images of the working electrode (a) before and (b) after a PEVD process.

Then, it dramatically dropped to 56 μA within 12 min. After that, the current was again relatively stable for the remaining time.

The phases, microstructure and chemical composition at the sink side of the PEVD system were studied before and after the PEVD process by x-ray diffraction (XRD), scanning electron microscopy (SEM) and energy dispersive x-ray (EDX) spectroscopy, respectively.

Results

Figures 12a and b show SEM secondary electron (SE) plan-view micrographs comparing the sink side of a PEVD sample before and after a PEVD process, respectively.

Figure 13 is an SEM SE plan-view image of another PEVD sample, where the Pt thick film coverage at the sink side of the sample is not entirely continuous. After PEVD, the product (Na_2CO_3) only formed in area (A), where the Pt thick film of the working electrode is continuous and connected to the external circuit. No PEVD product formed in area (B), where the Pt thick film is discontinuous appearing as individual islands (white spots in the figure) on the Na^+-β"-alumina substrate.

Figure 14 is an SEM SE image of the sink side of a cleaved cross section sample after PEVD. It indicates that Na_2CO_3 can reach the bottom of deep holes of the very irregularly shaped, porous and high aspect ratio Pt thick film substrate. The Na_2CO_3 coverage on the Pt thick film is uniform and fully dense. Since the sample was prepared by cleavage, the ductile Pt thick film structure is well preserved. Although the image gives a good three-dimensional indication of how the PEVD product deposited on the sink side of the PEVD system, the Na_2CO_3 coverage close to the cleavage plane was damaged because of the brittle nature of solid Na_2CO_3.

In order to reveal Na_2CO_3 coverage more precisely, polished cross-section samples were also examined in this study. A cross-section SEM SE image in Figure 15, as well as corresponding x-ray maps of the same area in Figure 16, reveal the geometric structure of the product at the sink side of the PEVD system. The high dot density regions in the sodium element x-ray map correspond to PEVD Na_2CO_3. The high dot density areas in the aluminum and platinum element x-ray maps show the microstructures of the Na^+-β"-alumina

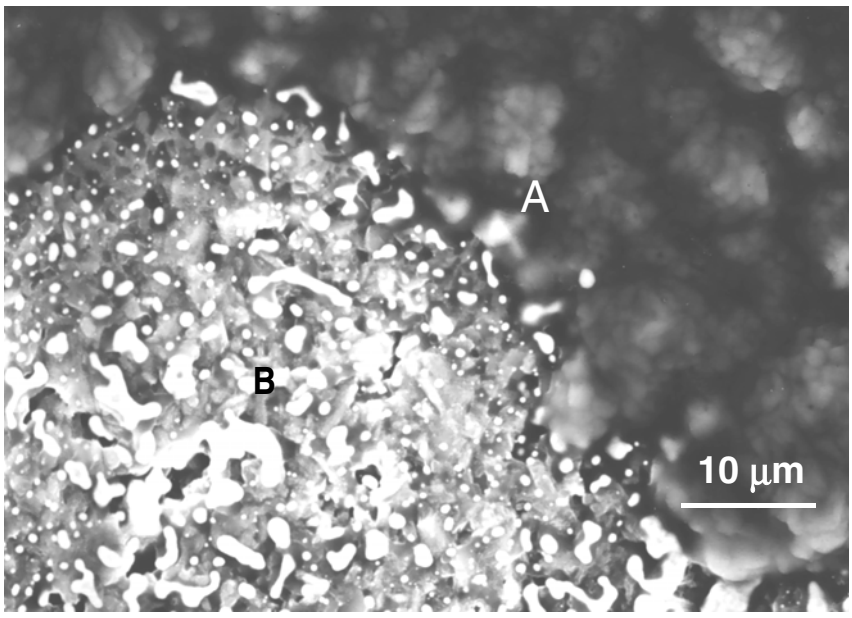

Fig. 13: Selective deposition: (A) continuous Pt thick film area; (B) discontinuous Pt thick film area.

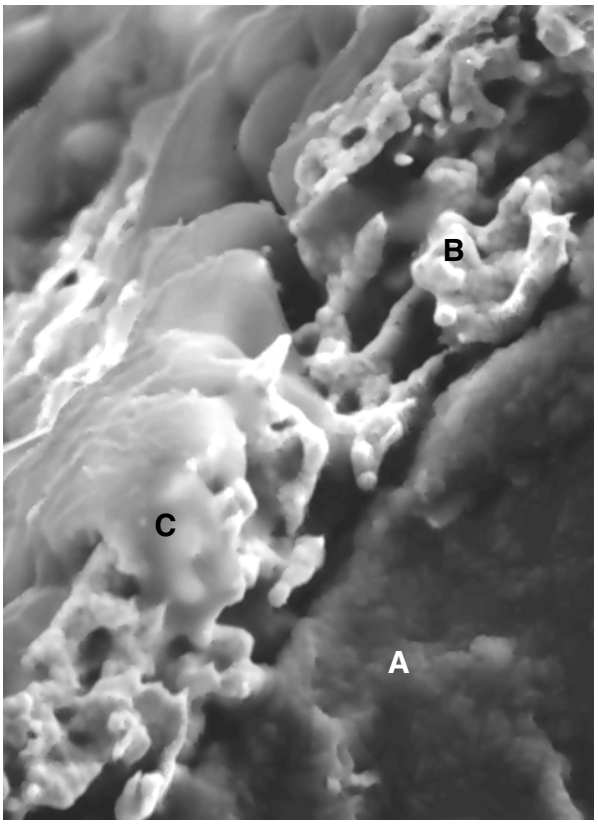

Fig. 14: Cross section SE image from a cleaved sample. Area (A) is the Na^{+}-β''-alumina solid electrolyte; area (B) is the Pt thick film electrode; and area (C) is the PEVD product Na_2CO_3.

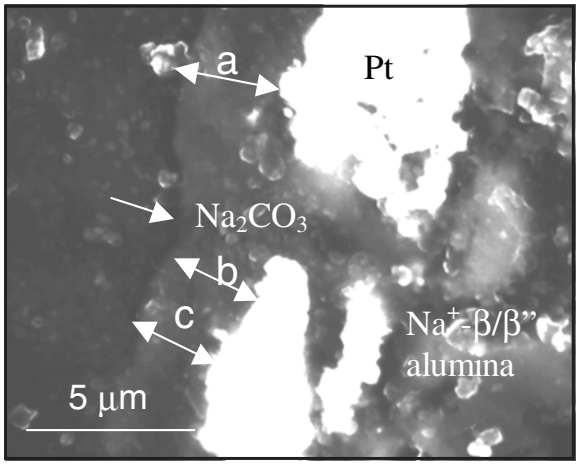

Fig. 15: Cross section picture from a polished sample; the average thickness of the Na_2CO_3 layer is about 2.5 μm according to the measurements along arrows a, b and c.

and the Pt coating at the cathode, respectively. It appears that the PEVD product not only intimately contacts the Na^+-β"-alumina and the Pt porous thick film, but also uniformly covers the Pt porous thick film. This is clearly revealed by a notch directly above a hole in the Pt thick film. The notch is indicated by an arrow in Figure 15. More careful examination of the SEM picture in Figure 15 shows that a boundary exists in the middle of the channel. It should be pointed out that the Pt area was not well preserved because of the ductile nature of the Pt thick film. Thus, small pores in the Pt thick film were destroyed during sample preparation. On the other hand, the PEVD product phase was well preserved.

Discussion

The mass and charge transport in the current PEVD process can be described as follows.

Under a negative dc applied potential, reaction (60) goes to the right resulting in Na_2CO_3 decomposition at the source side. Both sodium ions and electrons are given up by the source Na_2CO_3 disc at the anode of the electrochemical cell. Sodium ions travel through the solid electrolyte (Na^+-β"-alumina) to the sink reaction sites at the cathode. Electrons are conducted through the external electric circuit and the porous Pt thick film to the sink reaction sites. The sink side gas components, CO_2 and O_2, move through the pores in the porous Pt thick film to the same sink reaction sites. The PEVD reaction (58) proceeds to the right at the cathode. As a result, Na_2CO_3 is formed.

The potential profiles in this PEVD system are illustrated in Figure 17. Although there is no driving force due to a difference in the chemical potential of sodium in the current PEVD system, the applied dc potential provides the thermodynamic driving force for the overall cell reaction (62). Consequently, electrical energy is transferred in this particular PEVD system to move Na_2CO_3 from the anode to the cathode of the solid electrochemical cell by two half-cell electrochemical reactions. In short, this PEVD process can be used to deposit Na_2CO_3 at the working electrode of a potentiometric CO_2 sensor.

Selective deposition in PEVD is clearly indicated in Figure 13. As discussed previously, this is because of the unique feature of the electrochemical reaction for deposition. As schematically shown in Figure 18, the only area to meet the requirement for nucleation is the three phase boundary (point O) of Na^+-β"-alumina, Pt and gaseous phase, where Na^+, e^- and gaseous phase reactants ($CO_2 + O_2$) are all

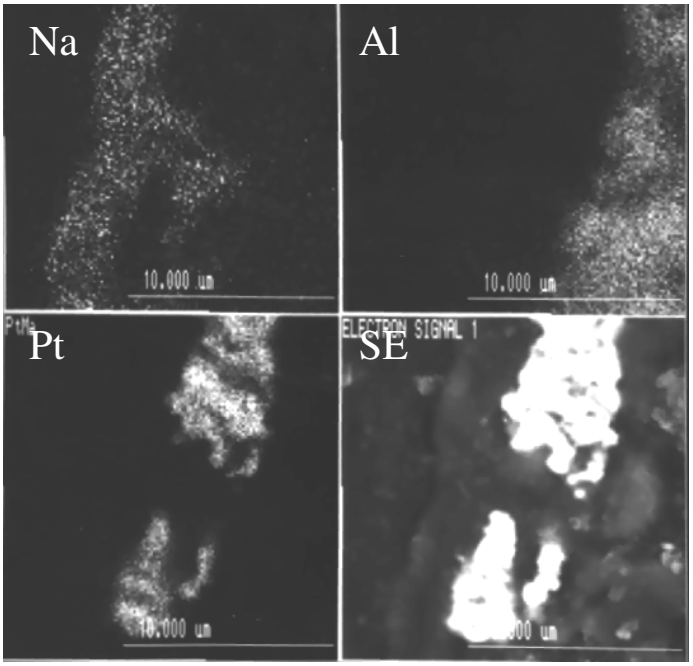

Fig. 16: X-ray maps of the same area as shown in Figure 15.

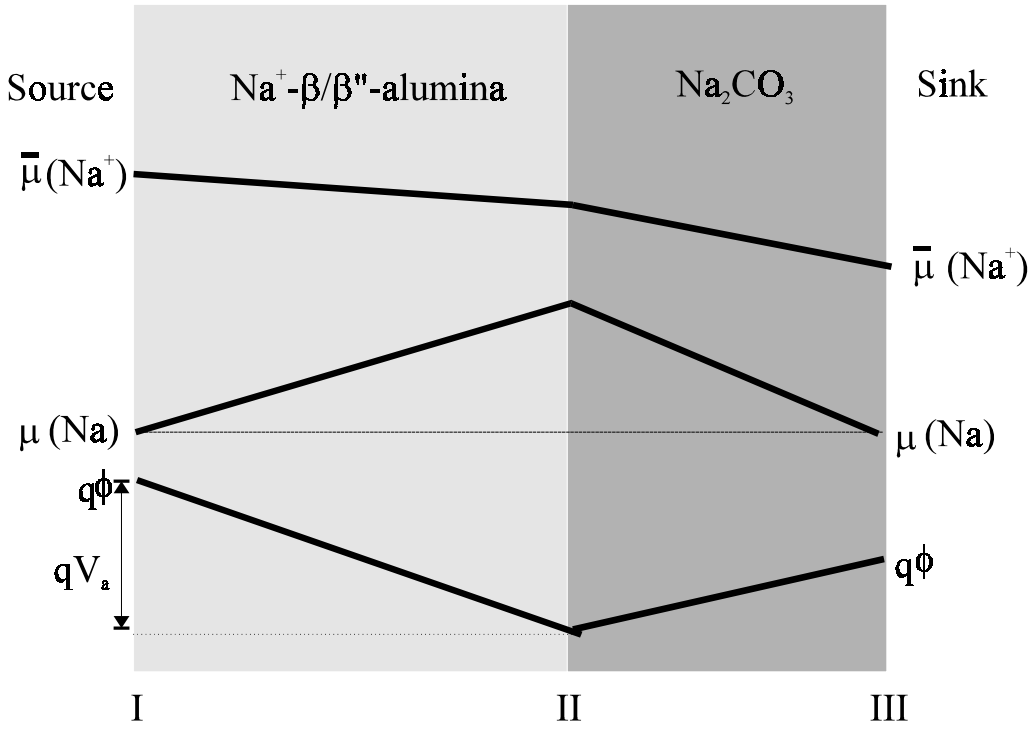

Fig. 17: Potential profiles in the PEVD system.

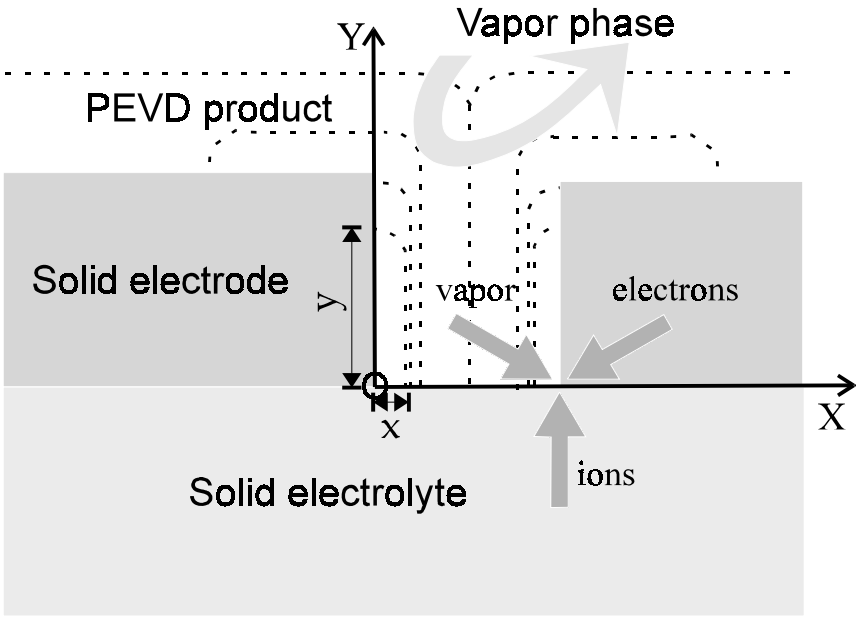

Fig. 18: Nucleation and growth of Na_2CO_3 at the working electrode of a type III potentiometric sensor.

available. Thus, any PEVD product Na_2CO_3 formed at the sink must be in intimate contact with both the solid electrolyte and electrode in the PEVD system to have both the ionic and electronic paths connected, respectively. In other words, the Na_2CO_3 auxiliary phase formed by PEVD must contact both the solid electrolyte and the Pt working electrode of a potentiometric CO_2 sensor. This feature makes the PEVD auxiliary phase fit geometric criteria (2) and (4). Furthermore, the selective deposition in PEVD indicates that the reaction for product deposition is surface dependent. In order to obtain uniform deposit coverage on the working electrode, the porous metallic electrode must be uniform and continuous.

After nucleation, PEVD product crystals can grow along two directions, *X* and *Y*, from point O. (In order to simplify the discussion, two dimensions instead of three will be used to discuss PEVD product phase growth at a cathode).

The X direction is along the surface of the solid electrolyte Na^+-β"-alumina, where Na^+ and the gaseous phase have easy access, but e^- have to diffuse through the PEVD product phase Na_2CO_3 to the reaction zone front.

The Y direction is along the surface of the Pt metallic electrode, where e^- and gaseous phase have easy access, but Na^+ has to diffuse through the PEVD product phase Na_2CO_3 to the reaction zone front.

If the cathodic reaction along the X direction is limited by electron migration through the product Na_2CO_3, the growth distance x at time t along the ionically shorted surface would be expressed by

$$x = \left(V_{Na_2CO_3}\sigma_e \Delta G t / F^2\right)^{1/2} \qquad (63)$$

where σ_e is the average electronic conductivity of the Na_2CO_3 phase, ΔG is the Gibbs free energy of reaction (58), and $V_{Na_2CO_3}$ is the molar volume of Na_2CO_3.

If the cathode reaction in direction Y is limited by sodium ion migration through the product Na_2CO_3, the growth distance *y* at time *t* along the electronically shorted surface would be expressed by

$$y = (4/\pi)\left(V_{NaNO_3}\sigma_{Na^+}\Delta G t / F^2\right)^{1/2} \quad (64)$$

The ratio of y to x is related to the conductivities of the sodium ions and electrons in the Na_2CO_3 phase.[13]

$$\frac{y}{x} \approx \frac{1.265\sqrt{\sigma_{Na^+}}}{\sqrt{\sigma_e}} \approx \frac{1.265}{\sqrt{t_e}} \quad (65)$$

Since Na_2CO_3 is a predominantly ionic conductor with a much higher ionic conductivity than electronic conductivity, the PEVD product Na_2CO_3 prefers to grow a thin layer along the Y direction, and wrap the entire Pt working electrode surface first. After the whole working electrode is covered, the Na_2CO_3 phase can only grow along the X direction to increase the thickness of the Na_2CO_3 auxiliary phase. The coverage should be uniform because of a self-leveling effect during the solid-state transport of sodium across the PEVD product for further growth. This is clearly indicated by both cross-section images in Figures 14 and 15.

Inside a pore of a Pt thick film, the thickness of the PEVD product will increase and eventually fill the pore as schematically illustrated by Figure 18, where the dotted lines indicate several consecutive PEVD processing steps. Accordingly, Na_2CO_3 grains from both side walls of a pore should meet at the middle of the pore, and leave a grain boundary in the middle of a pore and a notch on the top of a pore. Microstructural evidence of this growth model was captured in Figure 15, where a grain boundary exists in the middle of a pore and a notch exists on top of the pore (indicated by an arrow). A uniform increase in thickness will eventually reduce the high aspect ratio of the porous working electrode surface as schematically shown in Figure 18.

The current in a PEVD process reveals the kinetics of the PEVD cathode reactions which, in turn, indicates the PEVD product growth behavior. Since the electronic transference number in Na^+-β''-alumina is less than 10^{-6} and can be ignored under the current experimental conditions, it is reasonable to assume that the only current passing through the internal circuit of the PEVD system is the sodium ionic current. On the other hand, ionic current cannot flow in the external electrical circuit. All the Na^+ ionic current must be drained away by the gas electrode reactions, and the reaction rate, $\nu(t)$, can be expressed as

$$\upsilon(t) = \frac{1}{2V_{Na_2CO_3}}\frac{dn_{Na^+}}{dt} \quad (66)$$

where n_{Na+} is the number of mols of sodium ions at the cathode. Also, from Faraday's law,

$$I = \frac{dQ}{dt} = \frac{z_{Na^+}Fdn_{Na^+}}{dt} \quad (67)$$

Combining Eqns. (66) and (67) yields

$$\upsilon(t) = \frac{I}{2V_{Na_2CO_3}z_{Na^+}F} \quad (68)$$

Thus, the cathode reaction rate is proportional to the ionic current. Kinetic information about the gas electrode reactions can then be obtained by monitoring the current during a PEVD process.

For instance, the PEVD current-processing time behavior offers an easy way to control the thickness of the product layer. According to the mechanism for PEVD product growth, the reaction rate will decrease dramatically after the PEVD product covers the entire Pt surface. This corresponds to a sudden drop in the current. In order to deposit the thinnest possible film, this dramatic current decrease denotes the end point of a PEVD process.

Based on microstructure studies, the geometric structure of an auxiliary phase deposited by the PEVD technique is very similar to the previously discussed ideal auxiliary phase illustrated in Figure 8a. Table 1 compares the geometric properties of PEVD auxiliary phases with other reported techniques using the six proposed criteria.

The advantages of applying the PEVD process to deposit auxiliary phases are not only based on the mechanism of PEVD product crystal growth, but also arise from close control over the entire process achieved by adjusting the applied dc electric potential and monitoring current. Thus, the superiority of PEVD is obvious since the Na_2CO_3 auxiliary phase can be deposited in a well-controlled manner at the

Table 1. Geometric Properties of Auxiliary Phases Deposited by Various Techniques

Geometric Criteria	PEVD	Melting -Quenching	In-Situ	Disc
Contact to Electrode	Good	Good	Good	Poor
Contact to Electrolyte	Good	Poor	Good	Poor
Thickness Control	Good	Poor	Poor	Poor
Aspect Ratio	Low	Low	High	High
Coverage on Electrode	Good	Fair	Poor	Poor
Coverage on Electrolyte	Good	Poor	Poor	Poor

working electrode to meet all six geometric criteria. Furthermore, the success in realizing the geometric requirement of Na_2CO_3 auxiliary phases for potentiometric CO_2 sensors in our lab encouraged us to further apply PEVD to deposit the auxiliary phases $NaNO_3$ and Na_2SO_4 for NO_2 and SO_2 potentiometric sensors, respectively. The results are similar to those reported in this chapter. Thus, PEVD is the best technique to form auxiliary phases for gaseous oxide sensors.

Improvement of the geometric structures of the auxiliary phases using the PEVD technique will benefit the performance of gaseous oxide sensors in many ways, e.g., increasing selectivity and stability, shortening response time, and decreasing the influence of gas flow rate.[50]

Sensor Response Behavior Testing

Improvement of the geometric structure of the working electrode by a well-controlled PEVD process benefits the performance of a CO_2 sensor in many ways. To optimize kinetic behavior, the response and recovery times of CO_2 potentiometric sensors were studied at various auxiliary phase coverages. This was realized by a unique experimental arrangement to deposit the Na_2CO_3 auxiliary phase in-situ at the working electrode of type III potentiometric CO_2 sensors by PEVD in a step-wise fashion. Since the current and flux of solid-state transported material in a series of PEVD processes can be easily monitored to control the amount of deposit formed after each step of PEVD, the response behavior of the sensors after each PEVD auxiliary phase step increase can be characterized.

Experimental

As illustrated in Figure 19, the experiments in this study included three aspects:

a. Na_2CO_3 auxiliary phase deposition at the working electrodes of type III potentiometric CO_2 sensors by PEVD,
b. Sensor response behavior testing, and
c. Microanalysis of the working electrode of the sensor.

According to previous discussion, the amount of the Na_2CO_3 auxiliary phase deposited at the working electrode of a CO_2 potentiometric sensor can be recorded precisely during well-controlled PEVD processes. In this study, the amount of auxiliary phase at the working electrode of the sensors was increased in a step-wise fashion. After each step of the auxiliary phase deposition process, the sensor's response behavior was studied under open circuit conditions. Before moving forward to the next PEVD processing step, microstructural analysis of the covered working electrodes was performed with the SEM. Finally, results from 14 steps revealed the relationship between the response behavior of the sensor and the corresponding geometric structure of the auxiliary phases at the working electrodes of type III potentiometric CO_2 sensors.

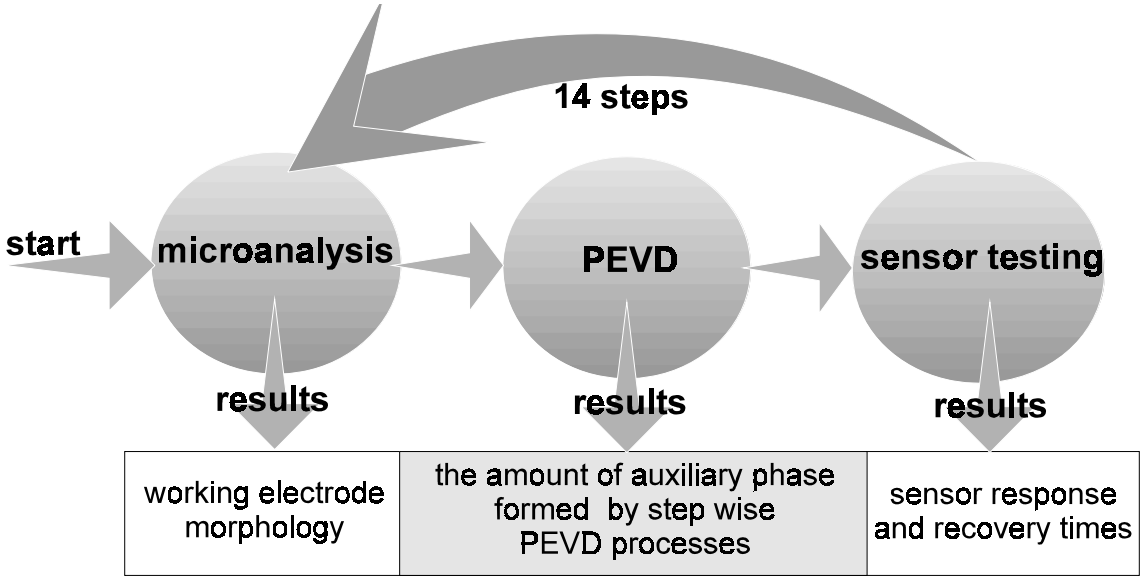

Fig. 19: PEVD auxiliary phase deposition and sensor testing procedure.

The sample system used in this investigation is similar to the one described previously. It consists of a solid electrochemical cell which has two functions, i.e., a closed circuit electrolytic cell (61) for the PEVD process and an open circuit galvanic cell (54) for sensor testing. Thus, the sink and source side of a PEVD system also act as the working and reference electrodes of a sensor. Figure 20a schematically shows the sample system in a gas-tight sample holder. Gas-tight seals were required to separate the reference electrode from the working electrode of the sensors in this investigation. Therefore, two Pt or Au rings were inserted at the source and sink side of the sample holder to ensure a gas-tight metallic seal between both sides of the solid electrochemical cell.

The sample holder was then put into a joint PEVD/sensor testing facility, as shown schematically in Figure 20b. The temperature during both PEVD processing and sensor testing was set at 500°C. Atmospheric pressure was maintained throughout the experiment in both chambers. In order to check the consistency of the results, the study was repeated on two sample systems.

During PEVD, a high gas flow rate (>>100 sccm) of type 1 gas, dry air with 293 ppm CO_2 (Praxair), was used at both the source and sink sides. In order to control the PEVD reaction rate, a galvanostatic method was used during the PEVD processes. The external electric circuit during PEVD processing is schematically shown in Figure 20b. A constant dc current of 100 μA was supplied by a steady dc source. The resulting potential was monitored by an electrometer.

After each step of auxiliary phase deposition, the PEVD process was stopped for sensor response behavior testing by opening Gate A (Figure 20b). Under the open circuit condition, the EMF of the sensor was indicated by the electrometer. A high flow rate at both sides remained until the equilibrium EMF value of the sensor, zero in this case, was reached.

During sensor response testing, the flow rate was initially reduced on both sides. Then, the gas at the working electrode was changed to a gas mixture of type 1 and type 2 (CO_2-free dry air), mixed at a ratio of 1:9 by a gas mixer. Thus, the virtual CO_2 partial pressure decreased by an order of magnitude at the working electrode

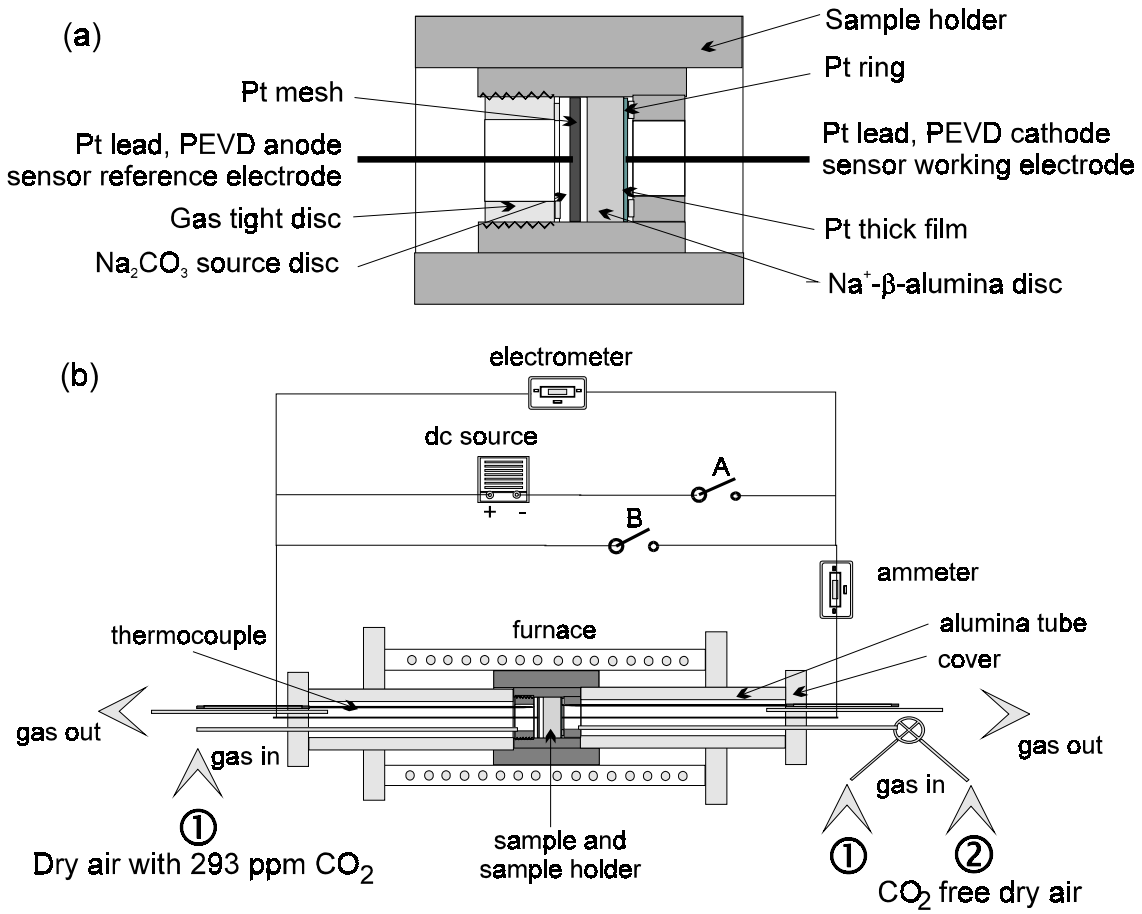

Fig. 20: Schematic of (a) sample holder and (b) a joint PEVD and sensor testing facility.

while the oxygen partial pressure remained the same at both sides. After the equilibrium EMF value of the sensor was reached, the gas at the working electrode was then changed back to type 1 gas. The EMF response of the sensors during CO_2 partial pressure change at the working electrodes was monitored and recorded by the electrometer connected to an analog recorder.

In order to reveal the influence of gas flow rate on the response behavior of the sensors, the response behavior has also been tested at two gas flow rates (40 or 80 sccm) at the working electrode side.

Before moving forward to the next round of auxiliary phase deposition and subsequent sensor response testing, the sample was taken out of the experimental apparatus for microanalysis to check auxiliary phase coverage. At the end of the experiment, cross-section samples were prepared by cleaving the sample to evaluate the thickness of the Na_2CO_3 product phase covering the working electrode of the sensors.

Results

Two identical samples (#1 and 2) were tested in this investigation. At a constant current of 100 μA, the resulting dc potential for both samples fell in the range of 0.5 to 5 V during the entire PEVD process. Accordingly, the flux of Na^+, in coulombs, through the PEVD system can be calculated. Consequently, the amount of product formed at the sink side (working

Table 2. PEVD Processing Time at Each Step for Both Samples at the Same Gas Flow Rate

Step	Sample #1			Sample #2	
	Processing Time (min)	PEVD Flux (C)	Micro-Analysis	Processing Time (min)	PEVD Flux (C)
0	0	0	a	0	0
1	78	0.468	b	66	0.396
2	91	0.546		76	0.456
3	127	0.762		106	0.636
4	157	0.942	c	142	0.852
5	193	1.158		180	1.080
6	235	1.410		213	1.278
7	274	1.644		254	1.524
8	310	1.860	d	296	1.776
9	346	2.076		329	1.974
10	383	2.298		365	2.190
11	428	2.568		408	2.448
12	467	2.802		452	2.712
13	512	3.072		485	2.910
14	540	3.240	e, f	530	3.180

electrode) could be obtained. The processing time and flux for both samples are reported in Table 2.

Figures 21a-e show SEM SE plan-view images of the first sample at five selected PEVD steps, indicated by a to e in Table 2. The auxiliary phase coverage at the working electrode of the sensor increased with PEVD processing time and PEVD flux from a to e. After 14 steps of auxiliary phase deposition and sensor response testing, the final thickness of the product was about 3 μm, which was estimated from an SEM SE image of a cleaved cross-section sample (Figure 21f).

According to the Nernst equation, the theoretical equilibrium EMF value of the sensor should be 76.7 mV at 500°C after the CO_2 partial pressure decreased by an order of magnitude at the working electrode. In this experiment, the emf value was slightly lower than the theoretical calculated value at about 76 mV.

The general response of the sensor after changing the CO_2 partial pressure at the working electrode is shown in Figure 22, which is the response curve obtained after seven steps of auxiliary phase deposition for the first sample. When the CO_2 partial pressure decreases at the working electrode, the emf of the cell increases dramatically at first and then slowly reaches an equilibrium value of 76 mV. The time to reach the equilibrium value is the recovery time of the sensor. The same is true when the partial pressure increases at the working electrode of the sensor, and the time to reach the equilibrium value is the response time of the sensor. In practice, researchers commonly use the time for

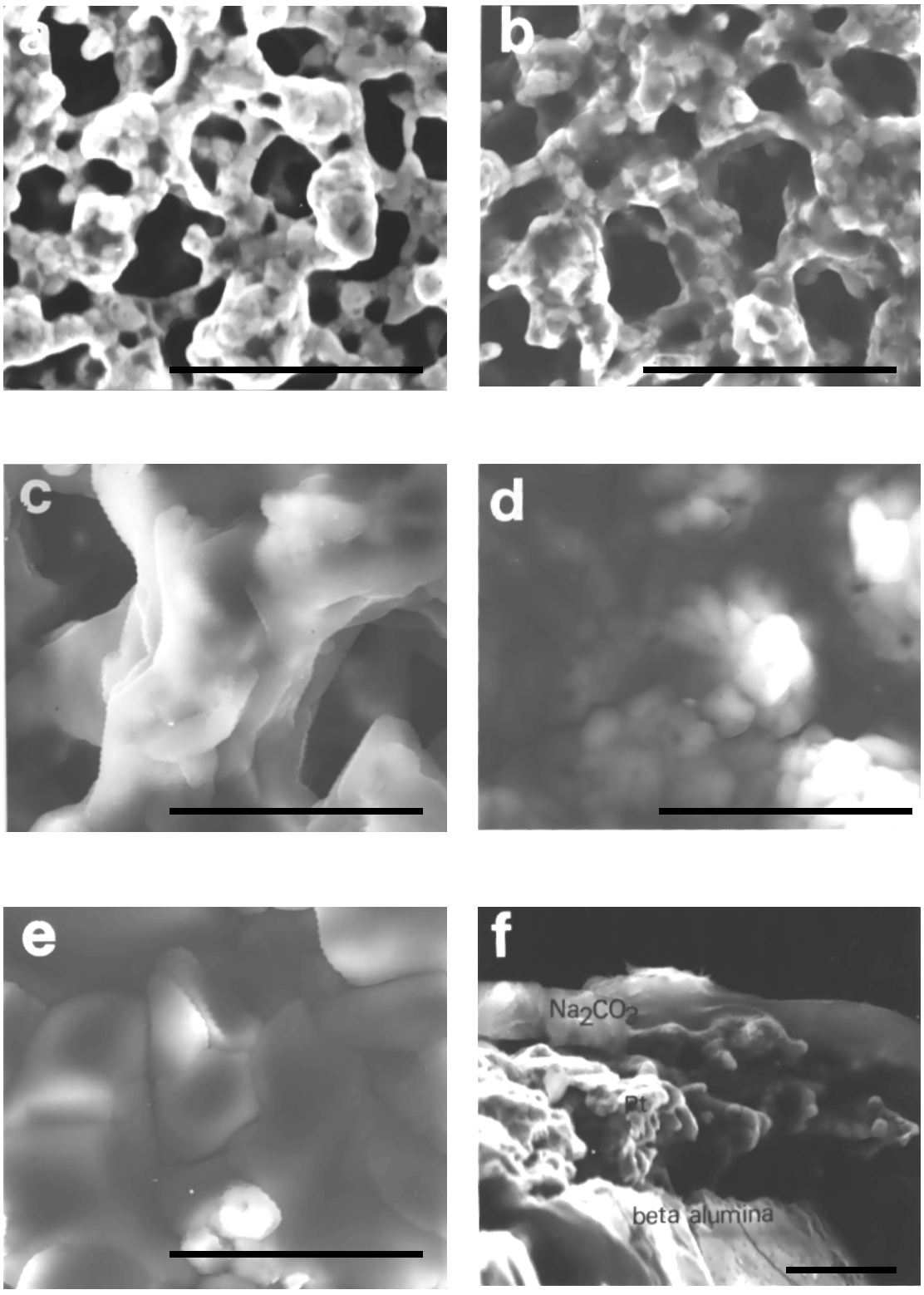

Fig. 21: SEM SE images of the working electrode: (a) before PEVD, (b) first stable EMF response, (c) when the response time of the sensor just passed the minimum point, (d) when the recovery time of the sensor just passed the minimum point, (e) final auxiliary phase coverage (plan view), and (f) final auxiliary phase coverage (cross-section). Bars equal to 5 μm.

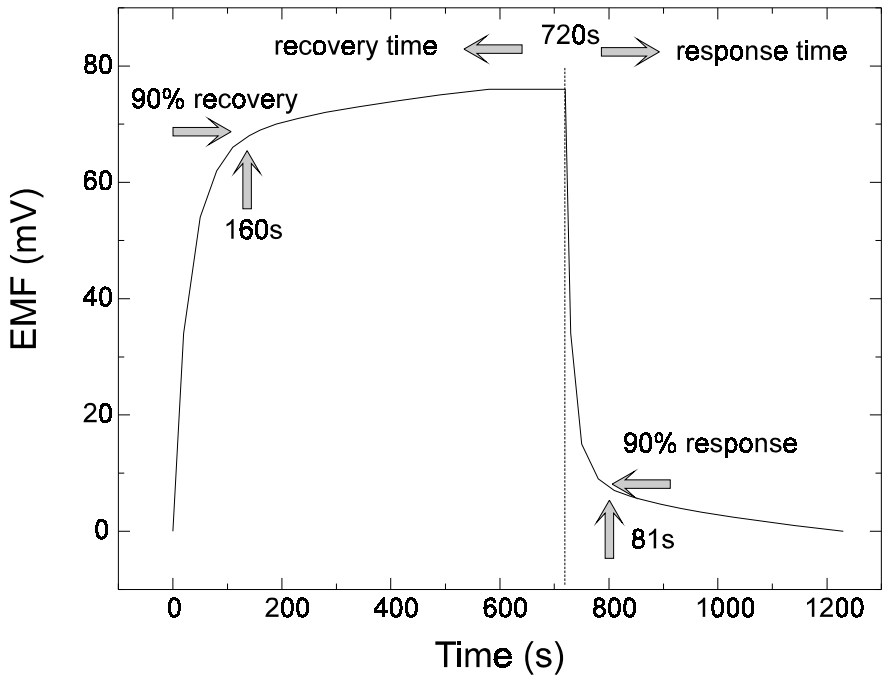

Fig. 22: A typical EMF response curve for a type III CO_2 potentiometric sensor.

90% attainment of the theoretical emf value change as the response and recovery time.[51] This convention will be used in the current investigation.

For sample #1, a stable EMF response from the sensor was obtained after passing about 0.468 C of Na ions. According to the previous discussion, this corresponds to the point where the PEVD auxiliary phase just covers the entire Pt thick film surface. The response times and recovery times of the sensor after each PEVD process step are recorded. Both response and recovery times are plotted against the Na ion flux through the solid electrolyte during the PEVD process in Figure 23. Curve (1) is the response time and curve (2) is the recovery time.

For sample #2, the sensor response was also tested at various flow rates at the working electrode. The response time and recovery time of the sensor at two flow rates are plotted in Figures 24a and b, respectively. After doubling the flow rate to 80 sccm, the data in curve (B) show a dramatic decrease (improvement) in response time for a small auxiliary phase thickness, and the response time does not change very much after reaching the minimum response time. The same is true for the recovery times.

Discussion

The response and recovery times of both samples at each PEVD step are compared at a working electrode flow rate of 40 sccm in Figures 25a and b, respectively. Because of the inability to fabricate a consistent Pt thick film at the working electrode of both sensors, the response and recovery curves do not exactly match. However, the curves from both samples follow the same trends. Taking into account the geometric factor for both samples, the results from this study can be considered to be fairly consistent.

The sensor response and recovery behavior for various auxiliary phase coverages at the working electrode of a type III potentiometric sensor are revealed for the first time through a combination of Figure 23 and Figures 21a-e.

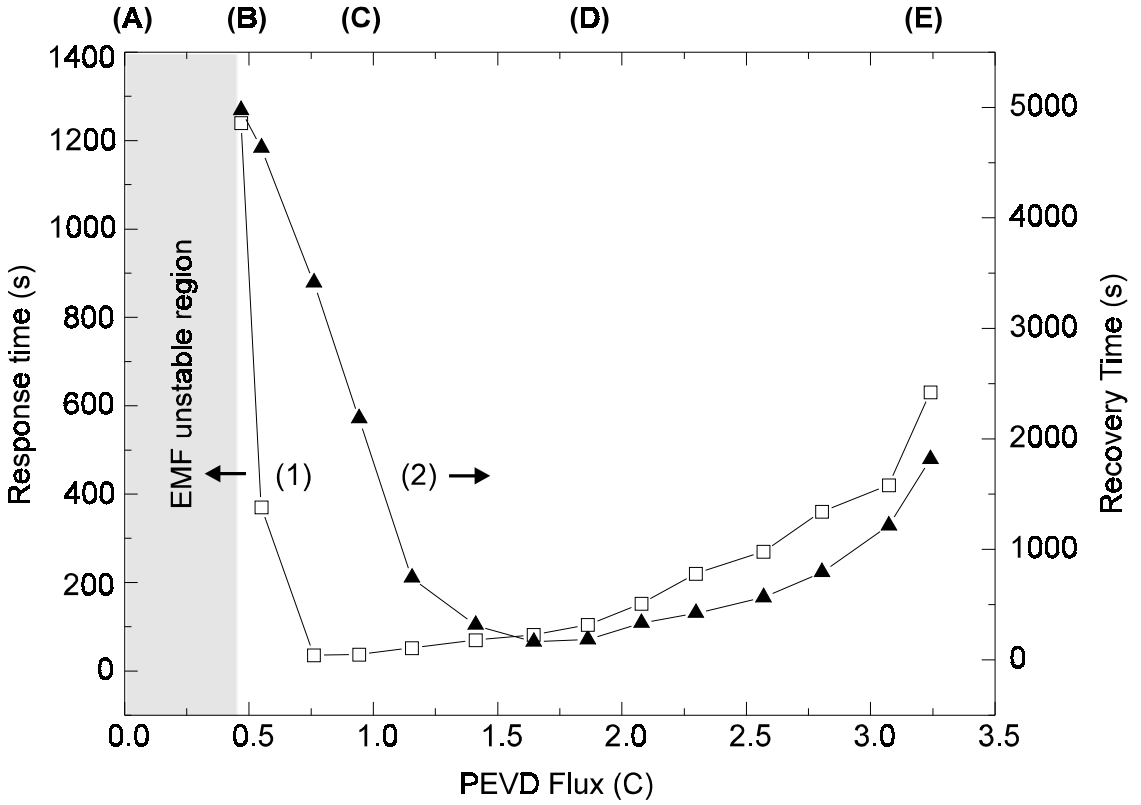

Fig. 23: The response (curve 1) and recovery (curve 2) behavior of the type III potentiometric CO_2 sensor (sample #1) with increasing PEVD auxiliary phase at the working electrode.

Furthermore, according to an earlier discussion, the increase in PEVD auxiliary phase thickness is uniform, and linearly related to the PEVD flux throughout the process. With the help of the cross-section SEM image in Figure 21f, the horizontal scale in Figure 23 can be converted to the thickness of the auxiliary phase on top of the Pt porous thick film at the working electrode. By taking the final thickness as 3 μm when the PEVD flux reaches 3.24 C after step 14, and an initial thickness of zero when the PEVD flux is 0.468 C at step 1, the sensor response behavior at various auxiliary phase thicknesses is plotted in Figure 26.

Both the response and recovery times first drop dramatically with increasing auxiliary phase thickness, reach a minimum point, and then increase steadily with increasing auxiliary phase thickness. The minimum response time is 35 s when the auxiliary phase thickness is about 0.3 to 0.5 μm. The minimum recovery time is 160 s corresponding to an auxiliary phase thickness of about 1.2 to 1.5 μm. Since most of the pores in the Pt thick film are under 3 μm in size and are filled with the auxiliary phase at this time, the aspect ratio of the working electrode of the sensor is very low (Figure 21d) when the recovery time of the sensor reaches its minimum value.

The results indicate that sensor response behavior is not only related to the thickness of the auxiliary phase, but is also controlled by other working electrode geometric factors - most likely the aspect ratio of the working electrode surface. Because of the high aspect ratio, the response and recovery times of the sensor are

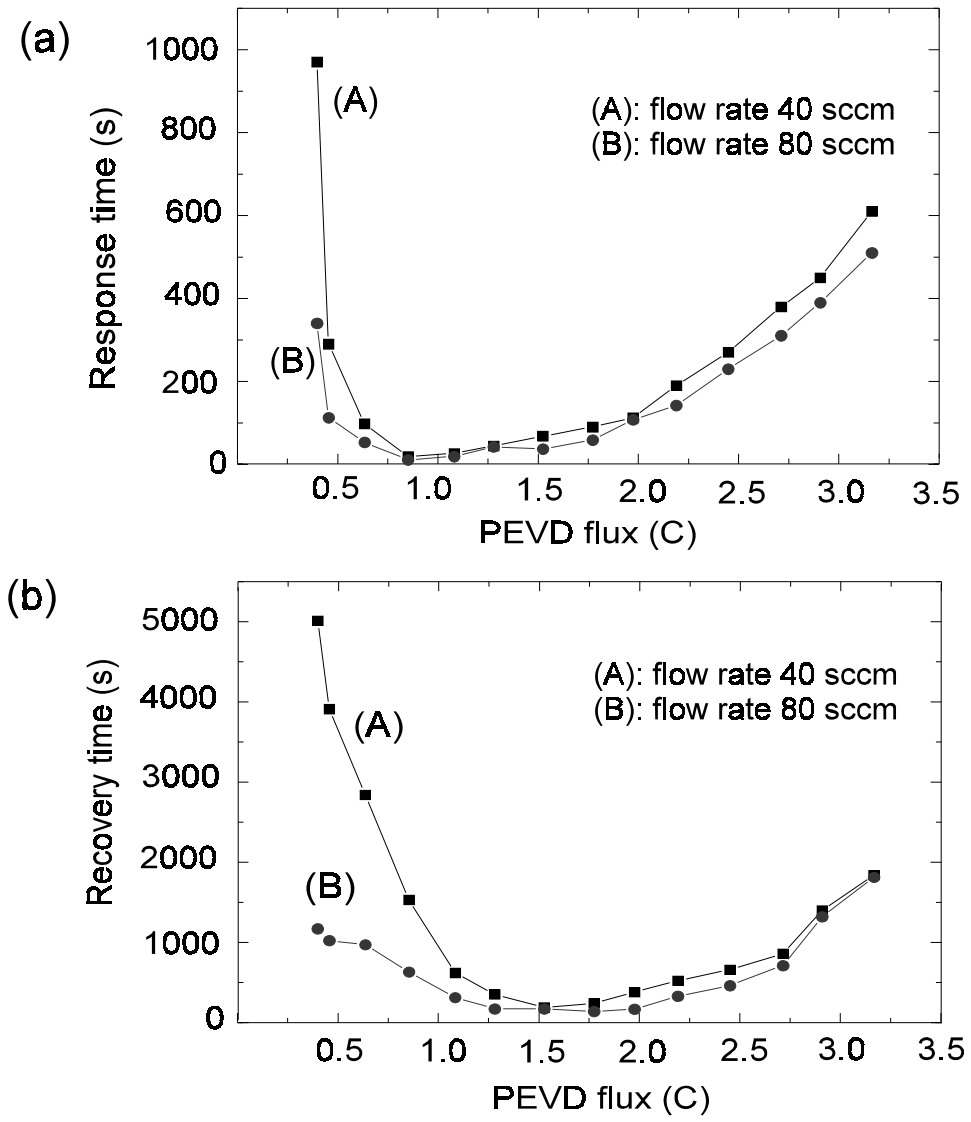

Fig. 24: The response time (a) and recovery time (b) of sample #2 at various gas flow rates (curve (A) at 40 sccm and curve (B) at 80 sccm).

limited by surface adsorption, desorption and gas phase diffusion at small PEVD auxiliary phase thicknesses.[33] Recovery time, which corresponds to a desorption process at the working electrode, is affected more by the aspect ratio than the response time, which corresponds to an adsorption process. Accordingly, in order to make a potentiometric sensor with a fast response, the best geometric structure for the working electrode is one which has a low aspect ratio and is covered with as thin a layer of auxiliary phase as possible. For Pt thick film metallic electrodes, this thickness is about 1 to 1.5 μm depending on the average pore size and thickness of the Pt electrode itself.

In conclusion, because of PEVD's ability to control the deposition process and its unique product phase growth behavior, it is possible to prepare, by means of PEVD, a working electrode with the best geometric structure. The response

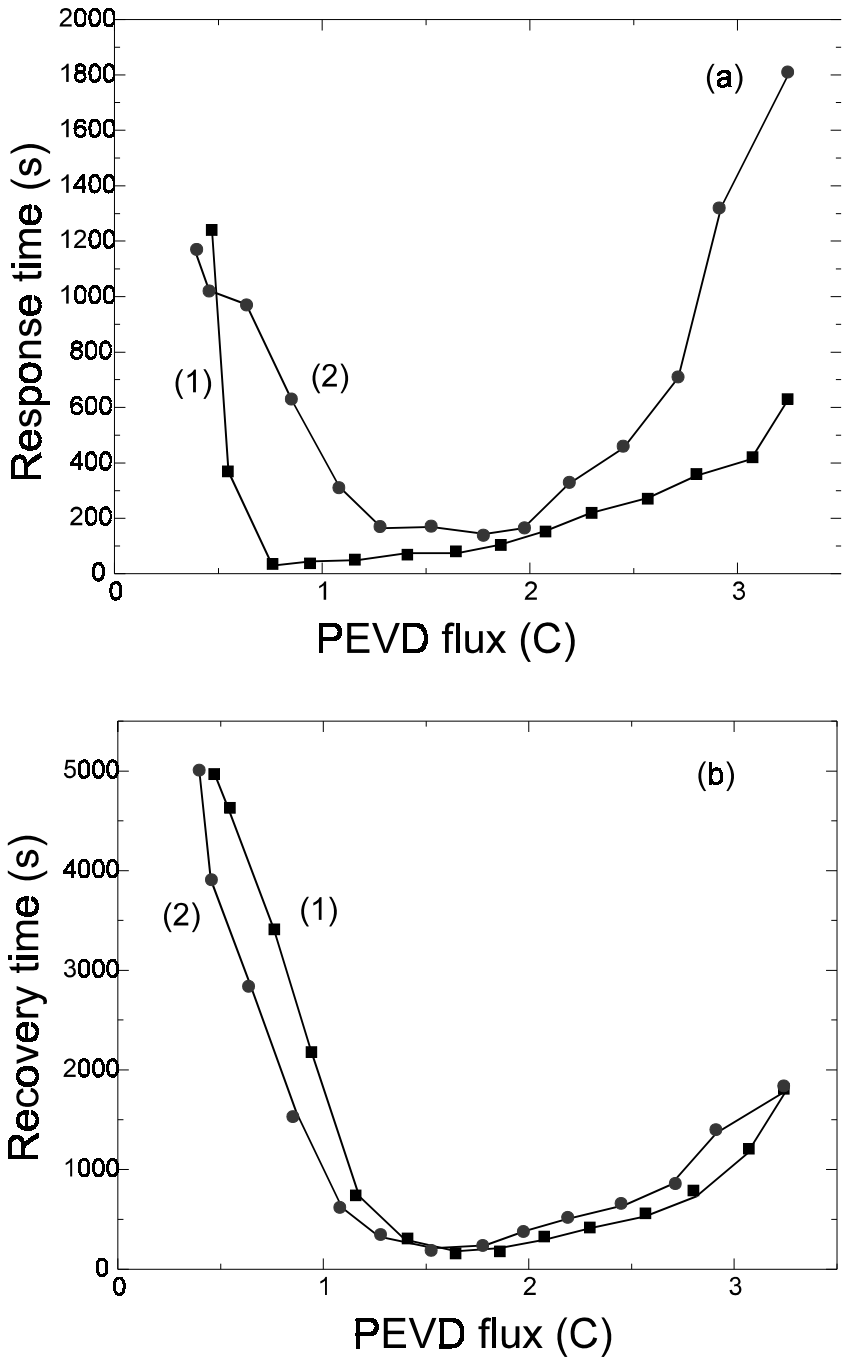

Fig. 25: Comparison of the response time (a) and recovery time (b) for the two sensors at the same working electrode flow rate of 40 sccm.

behavior of a potentiometric sensor depends on the thickness of the auxiliary phase and the aspect ratio of the working electrode surface. In an optimized condition, a potentiometric CO_2 sensor can be obtained with a response time of less than 1 min and a recovery time of less than 3 min, for a CO_2 partial pressure at the working electrode varying from 30 to 300 ppm at 500°C.

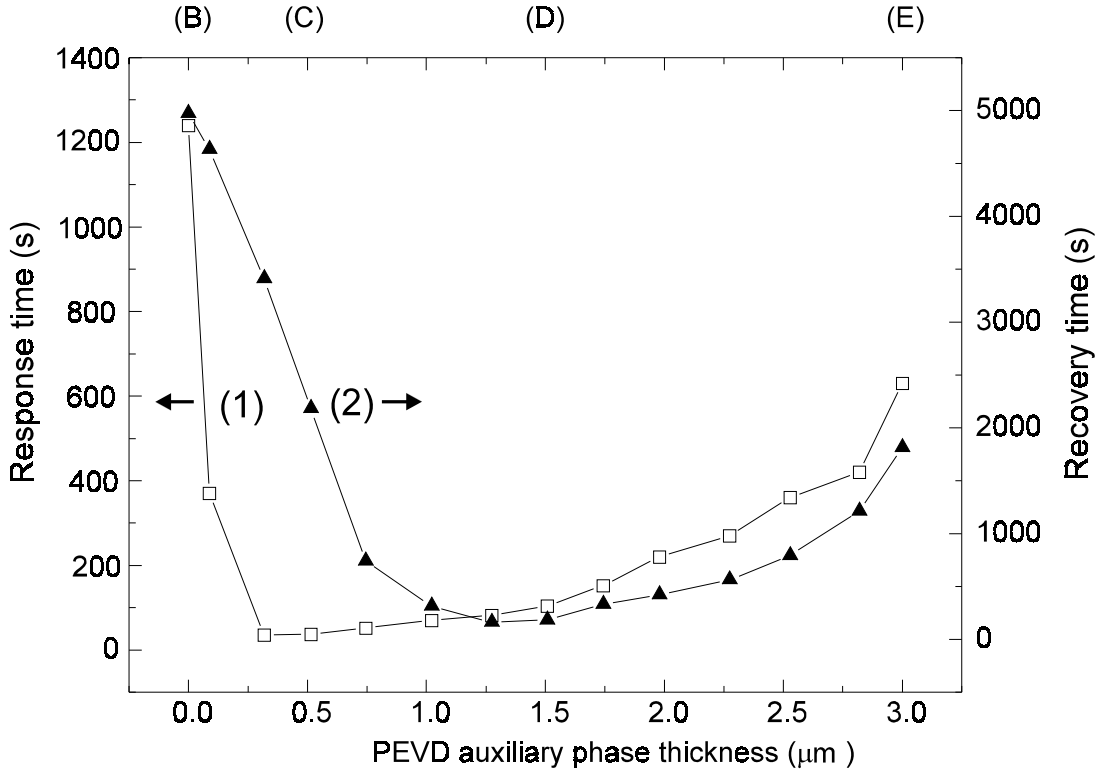

Fig. 26: Response and recovery times vs. the thickness of the auxiliary phase.

This is about 10 times lower than previously reported values under the same sensing conditions.[34,41-43]

This investigation not only confirms the reaction mechanism proposed, but also demonstrates the ability of PEVD to control auxiliary phase thickness and the aspect ratio of the working electrode of a sensor.

Applying PEVD to Composite Anode Fabrication for Solid Oxide Fuel Cells

Solid oxide fuel cells (SOFCs) are solid-state energy conversion devices with the potential advantages of high efficiency, silent operation and low emissions. However, the high operating temperature (1000°C) of SOFCs places stringent requirements on components, and the practical application of SOFCs is limited by a number of problems.[52-55] Among them, the performance of the anode is a significant one. Investigations have shown that approximately one-third of the total potential loss in a state-of-the-art SOFC is caused by anode polarization.[54,55] In addition, the compatibility of anodes with solid electrolytes and the long-term stability of anodes in an SOFC operating environment are not satisfied from a commercialization point of view.

Investigations in this field have indicated that it is imperative to fabricate efficient and compatible anodes for SOFCs to minimize polarization loss and concurrently achieve long term stability. In this section, a critical review of previous studies is given and several criteria for a theoretically ideal anode are summarized.

In searching for the best fabrication techniques for anodes in our laboratory, PEVD was used to fabricate efficient and compatible composite anodes in the hope of lowering polarization loss and simultaneously achieving long term stability in SOFCs.

SOFC Anodes

Previous Investigations of SOFC Anodes

According to the principle of SOFCs, at an SOFC anode, fuel gas is oxidized in the electrochemically active region, that is, close to a three-phase boundary of an ionic conducting phase, an electronic conducting phase and a vapor phase where all reacting species are available. The basic requirement of the anode materials is to possess both high electric conductivity and high anodic reaction rate.[53]

Since anodes work in a reducing fuel gas environment, theoretically pure porous metallic electrodes can be used. For instance, Ni,[54,56,57] Ru[55] and Pt[58] have been studied as anode materials. Pure metallic anodes have high electric conductivity. However, as schematically shown in Figure 27, contact between the pure metallic electrode and the solid electrolyte is two-dimensional in a solid state electrochemical system. Unlike an aqueous electrochemical system, the electrochemically active area is limited to the region close to the three-phase boundary along this contact surface. Thus, the number of electrochemical reaction sites is insufficient, particularly when SOFCs operate at low temperature and high current density. High overpotential loss is to be expected. In addition, because of the thermal expansion coefficient mismatch between the metallic electrode and solid electrolyte, induced stresses can be a problem. Since there is no "wetting" at a solid-solid contact, the thermal stresses can easily create cracks, which deteriorate the contact further after several heating and cooling cycles. Furthermore, vapor loss, sintering and poisoning of metallic electrodes over a long period of exposure to harsh SOFC operating conditions also cause serious stability problems.

In order to overcome the problems with pure metallic anodes, ceramic-metal (cermet) composite anode concepts have been overwhelmingly accepted. Many methods of producing composite anodes have been investigated during the past 10 years. These include slurry coating,[54,56,57] wet powder spraying[59] and vapor deposition.[60-66] Each of these methods offers advantages; however, each presents its own difficulties such as higher sheet resistance, high costs and performance degradation.

Among these techniques, a slurry coated cermet anode provides a compromise because it is an inexpensive method that has been shown to give reproducible results in terms of porosity and layer thickness.[67,68] The process consists of coating the electrolyte substrate with a slurry of mixed metallic and ceramic particles and, after drying, subjecting it to a number of sintering cycles. The microstructure of a slurry-coated cermet is schematically shown in Figure 28. The role of the cermet structure is to provide both ionic and electronic conducting paths through connected ceramic and metallic particles, respectively. In addition, there have to be sufficient contact points between the ceramic and metallic particles. Thus, a slurry-coated cermet anode expands the electrochemically active area from the region close to the three-phase boundary on a two-dimensional solid electrolyte/anode interface to the entire three-dimensional anode volume. This reduces overpotential loss and improves the performance of SOFCs significantly. For instance, Singhal[66] reported that a decrease in polarization was observed in a power generation test using a slurry-coated Ni/yttria stabilized zirconia (YSZ) cermet anode. However, in order to match the thermal expansion of the solid electrolyte of an SOFC, the metallic phase content in this kind of cermet anode must be as low as possible.[69] According to percolation theory,[56] no continuous metallic phase will exist to provide an electronic conducting path when the metallic phase content is lower than 30%. Even within this limitation, the mixed ceramic and metallic particles reduce the electronic conducting path dramatically, resulting in a high sheet resistance. Consequently, slurry-coated cermet anodes have their limitations; the reduction in overpotential loss is offset by increasing sheet resistance and thermal compatibility problems with the solid electrolyte.

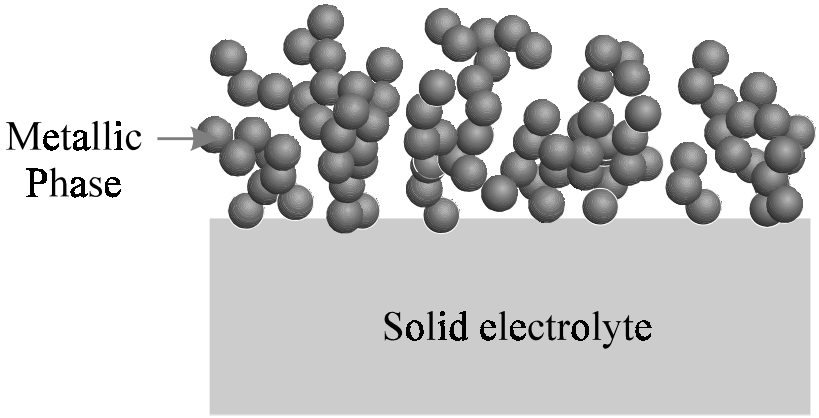

Fig. 27: Two-dimensional schematic of the microstructure of a pure metallic SOFC anode.

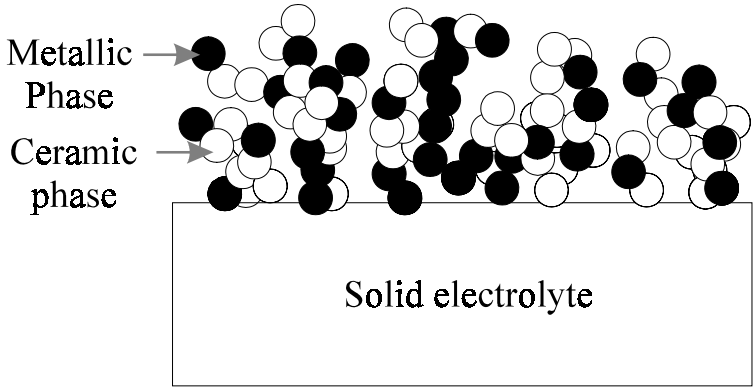

Fig. 28: Two-dimensional schematic of the microstructure of a slurry-coated cermet anode.

Furthermore, slurry-coated cermet anodes have various long-term stability problems, particularly due to the fine particle size of the metallic component.[54,70] It has also been reported that the tolerance for impurities in fuels is very limited.[71,72] High levels (100 ppm) of H_2S may cause significant irreversible performance loss due to anode poisoning.

The Criteria for a Theoretically Ideal SOFC Anode

Although the current performance of SOFC anodes is still far from satisfactory, they are mainly being studied solely in terms of the electrochemically active area, the electric conductivity, thermal expansion, stability and reactivity with the solid electrolyte. It is

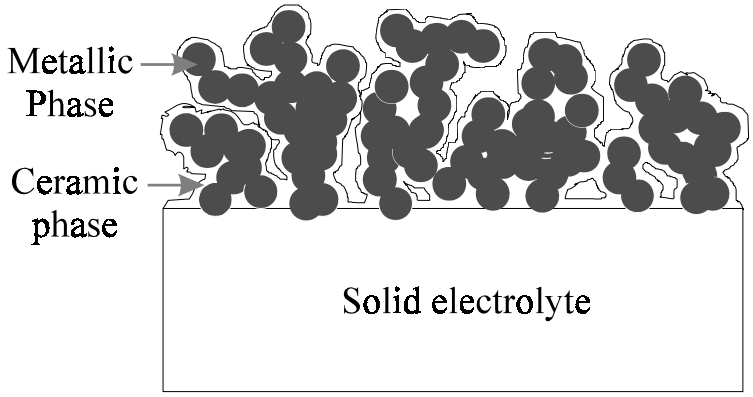

Fig. 29: Two dimensional schematic of the microstructure of the theoretically ideal composite anode.

commonly believed, however, that anode performance is not only attributable to the materials, but also to the interfacial structure. Consequently, previous investigations in this area have indicated the importance of a number of microstructural criteria for the best SOFC anodes. These criteria can be summarized as follows:

1. Overpotential loss is inversely proportional to the electrochemically active area. Thus, a composite anode with three phases is preferred, i.e., ceramic (ionic conduction), metallic (electronic conduction) and pore (gas diffusion) phases mixed together to expand the electrochemically active area to a three-dimensional anode volume.[56,62,67,73]
2. Ionic path impedance through the ceramic phase and electronic path impedance through the metallic phase have been found to be dominant factors in determining the electrode characteristics.[74] In order to provide a low sheet resistance anode, it is imperative that the metallic and ceramic phases have maximized continuous paths that allow ionic and electronic migration from the electrolyte/anode interface throughout the entire anode.
3. Due to thermal expansion incompatibility, a metallic phase will not by itself adhere very well to the solid electrolyte of an SOFC.[69] Thus, it is desirable to have a thermal expansion compatible ceramic phase in intimate contact with both the solid electrolyte and the metallic electrode at the anode/solid electrolyte interface of an SOFC for ''wetting'' purposes.
4. The metallic phase is vulnerable in SOFC operating environments. It suffers from vapor loss, sintering, and poisoning over time. Consequently, it is recommended that the ceramic phase both support and protect the metallic phase to achieve long-term stability.[55,60]

According to the above, the ideal anode microstructure is shown in Figure 29. However, finding a cost-efficient way to fabricate an SOFC anode with this kind of microstructure assumes real difficulties. The challenge of improving anode performance is not only based on having suitable materials to serve as anodes, but also having proper fabrication techniques to incorporate the materials into practical SOFC stack configurations. A good example is the development of electrochemical vapor deposition (EVD).[6,64,65] This technique has made it possible to fabricate fully dense thin ionic conducting films on a porous substrate as the solid electrolytes of SOFCs and, consequently, to minimize the internal resistance loss of the solid electrolytes.[75-77]

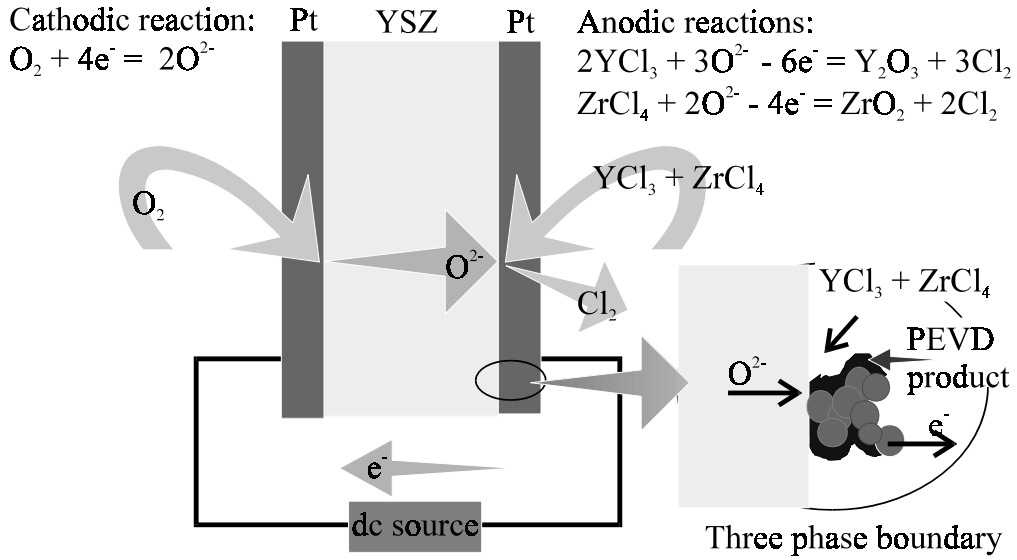

Fig. 30: PEVD process for fabricating a composite SOFC anode.

In searching for the best fabrication techniques for anodes, PEVD was applied to fabricate efficient and compatible composite anodes to lower polarization loss and simultaneously achieve long term stability in SOFCs.

PEVD Composite Anode Design

According to previous applications to solid state potentiometric sensors, PEVD seems to be a possible technique to deposit in-situ a layer of an oxygen ion conducting phase on a metallic anode of an SOFC. Thus, a composite anode with both a PEVD product and a metallic anode could be realized to overcome the aforementioned anodic limitations.

According to the principles of PEVD process design, consideration of PEVD processing starts with the PEVD product. Yttria doped zirconia was chosen to be the product in the current investigation due to its high stability and high oxygen ionic conductivity in the anode environment. The details of the PEVD process design for anodic PEVD reactions to form yttria-doped zirconia at a Pt thick film metallic anode of an SOFC are schematically shown in Figure 30.

The PEVD process takes advantage of the solid electrochemical cell of an SOFC. Oxygen is chosen to be the solid state transported reactant. At the source side (the cathode of the SOFC), oxygen in the source gas phase is reduced to oxygen anions (O^{2-}) through a cathodic reaction

$$O_2 + 4e^- \rightarrow 2O^{2-} \quad (69)$$

to supply the solid state transported reactant during the PEVD process.

Oxygen anions travel from the source side through the solid electrolyte to the sink side (anode) under the combination of the influence of an applied dc electric field and an oxygen chemical potential gradient. At the sink side (the anode of the SOFC), the oxygen anions react electrochemically with both zirconium and yttrium reactants from the sink vapor phase to form the desired product, yttria doped zirconia, and release electrons to the metallic anode. Electrons travel through the external electrical circuit back to the source side for further cathodic reaction.

$ZrCl_4$ and YCl_3 were chosen as sink vapor reactants due to their relatively high vapor pressures. As with conventional CVD, the Y

doping level or concentration of Y_2O_3 in the PEVD product (Y_2O_3-ZrO_2) can be controlled by the partial pressures of YCl_3 and $ZrCl_4$ in the sink vapor phase.

The main anode reaction for the PEVD process is:

$$ZrCl_4 + 2O^{2-} - 4e^- \rightarrow ZrO_2 + 2Cl_2 \quad (70)$$

The anode doping reaction is:

$$2YCl_3 + 3O^{2-} - 6e^- \rightarrow Y_2O_3 + 3Cl_2 \quad (71)$$

Since the chlorine released from both anodic reactions is in vapor form, it can be driven away easily through the sink vapor phase. The overall reaction for ZrO_2 formation in this PEVD process is:

$$ZrCl_4 + O_2 \rightarrow ZrO_2 + 2Cl_2 \quad (72)$$

and the overall doping reaction for Y_2O_3 formation is:

$$4YCl_3 + 3O_2 \rightarrow 2Y_2O_3 + 6Cl_2 \quad (73)$$

The PEVD process is closely related to electrochemical vapor deposition (EVD), which was developed to form gas-tight YSZ thin films as solid electrolytes at Westinghouse.[5,78,79] Recently, both PEVD and EVD techniques and their applications were reviewed by Tang et al.[7] It was shown that both processes have fundamental similarities in terms of mass and charge transport through the products required for further deposition. The differences between EVD and PEVD for depositing yttria-doped zirconia is that a solid electrochemical cell is used in PEVD to set the driving force for oxygen ion transport inside the solid electrolyte and the deposition product.

Utilization of solid electrochemical cells is one of the most significant advantages of the PEVD technique, since deposition process control and monitoring are easy to realize.

Experimental

The PEVD sample utilized in this investigation is a solid electrochemical cell with a ytterbia and yttria stabilized zirconia pellet ($8\%Yb_2O_3$-$6\%Y_2O_3$-ZrO_2) as the solid electrolyte to conduct oxygen anions from the source to the sink side. A commercially available Pt thick film paste was screen printed on the center of both surfaces of the solid electrolyte disk. Two Pt meshes, with spot welded Pt leads, were then pressed on the top of the porous Pt thick films, and co-sintered to ensure good electrical contact. The sample was then mounted on the end of a small fully dense alumina tube and secured with high-temperature cement.

Figure 31 shows a schematic diagram of a lab-made PEVD reactor for depositing yttria-doped zirconia. The sample tube was placed at the center of a large fully dense alumina reactor tube in an electric furnace. Thus, the sample tube separated the reactor tube into two chambers; the air chamber inside the sample tube and the chloride chamber between the sample and reactor tubes. Both chambers were evacuated separately.

Both sample electric leads were connected to a dc power supply as shown in Figure 31. The external electric circuit can be operated either under closed circuit or open circuit conditions via Gate A. The open circuit emf and the closed circuit applied dc potential were monitored by a digital electrometer. The closed circuit current was measured by an ammeter. The sublimation tubes for both chloride sources were made of quartz glass as shown in Figure 31. The working end of the tube was ''T'' shaped to store the chloride powders, and K type thermocouples were embedded in the tubes close to the powders. The positions of the sublimation tubes were adjusted manually during the deposition process to ensure that both $ZrCl_4$ (>99.9%) and YCl_3 (>99%) were heated at the proper sublimation temperatures for the desired vapor pressures. Each vaporized chloride was supplied to the reaction zone using Ar as a carrier gas, which passed through a series of driers and oxygen removal units before entering the chloride chamber. At the source side, air was bled into the sample tube.

In this PEVD process, the central reaction zone was maintained at 1000°C. The partial pressure ratio of $ZrCl_4$ vs. YCl_3 was 8:1. A dc applied potential of 450 mV was selected, and current in the range of 500 to 100 μA was recorded for 300 min. In order to examine the PEVD product at the anode of the samples, both plan-view and cleavage cross-section specimens were prepared. The phases, microstructure and chemical composition of the anode were studied using XRD, SEM and EDX, respectively.

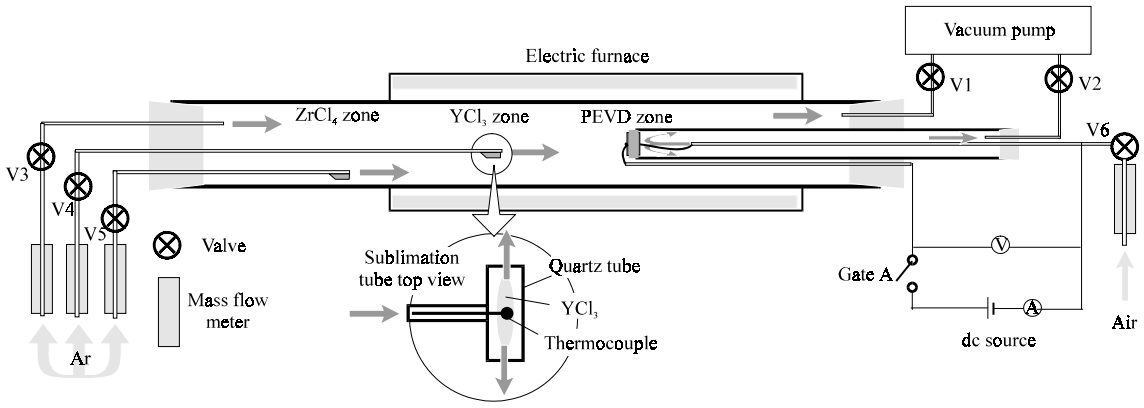

Fig. 31: PEVD reactor setup.

Results

Figures 32a and b are SEM secondary electron (SE) images of the anode of a plan-view sample before and after PEVD, respectively. PEVD products had formed at the edges of the pores, and the small step-like features of the Pt grains before PEVD had disappeared. This indicates that a layer of PEVD product had formed at the anode to wrap the Pt thick film. Since the porosity of the anode did not decrease much after PEVD and the grain boundaries of the Pt thick film are still visible in Figure 32b through the PEVD product at a 20 keV operating voltage in the SEM, the product layer covering the Pt metallic electrode must be quite thin (less than 1 μm).

In addition, anode crystallographic information after PEVD was obtained with XRD. The XRD spectrum of the PEVD composite anode is presented in Figure 33. Three phases exist in the XRD spectrum: a yttria stabilized zirconia phase (cubic), a pure zirconia phase (monoclinic) and a metallic Pt phase. The Pt phase shows up in the spectrum because the PEVD product on top of the Pt is thin enough to allow x-rays to penetrate the product phase to reach the underlying Pt phase. Based on the relative peak intensity, yttria stabilized zirconia is the major phase in the PEVD product. However, a certain amount of pure zirconia is evident. Thus, the zirconia in the PEVD product is partially stabilized (< 8%). It is worth pointing out that the equilibrium partial pressure ratio of YCl_3 to $ZrCl_4$ was set at about 1:8 during PEVD. The reason for this yttrium deficiency in the PEVD deposited phase requires further investigation.

The microstructure of the PEVD composite anode is further displayed by a cross-section SEM SE image in Figure 34. It shows that the deposited PEVD product phase (yttria stabilized zirconia) is in intimate contact with both the solid electrolyte and the Pt electrode. In the anode/solid electrolyte interface region, the deposited phase formed a dense layer encompassing the Pt electrode. This provides extra ''wetting'' for the metallic electrode and solid electrolyte contact. Conventional vapor deposition techniques are unable to deposit products at the bottom of this kind of high aspect ratio and irregularly shaped substrate. The deposited phase continuously covers the entire metallic electrode surface from its contact with the solid electrolyte to the top of the composite anode. Thus, there is little Pt phase shown in this cleavage sample, since the break is mainly through the pores in the anode region of the specimen.

In order to show the phase boundary between the solid electrolyte and PEVD product, an EDX line scan for Yb was performed along a 6 μm long dotted line between point A and C.

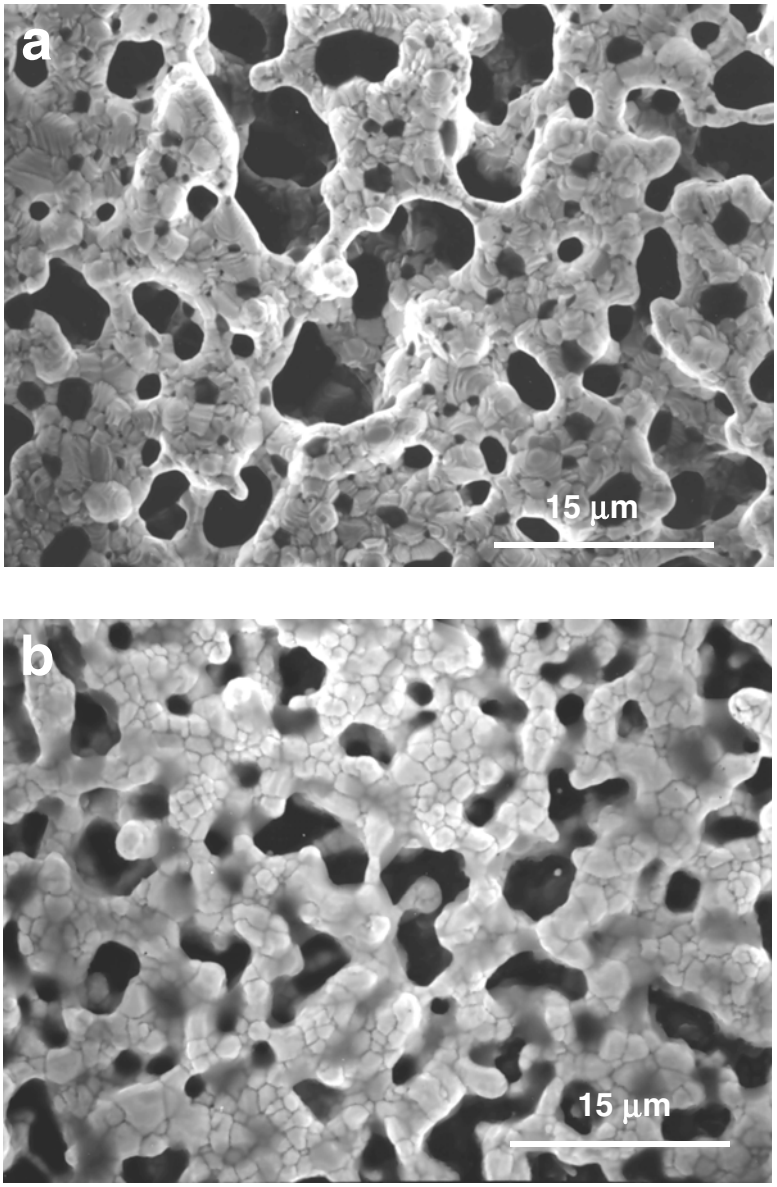

Fig. 32: SEM SE plan-view images of the anode of the sample before (a) and after (b) PEVD.

The electronic signal (gray level) and Yb Lα intensity are recorded in Figures 35a and b, respectively. The Yb x-ray intensity curve in Figure 35b dropped across the microscopic boundary. The valley in the gray level curve in Figure 35a indicates the position of the interface in the SEM SE image in Figure 34.

Discussion

Based on the preceding microstructural analysis results, it is clear that PEVD is capable of depositing a thin layer of yttria-doped zirconia to form a composite anode. This phase is not only in intimate contact with both the solid electrolyte and metallic electrode, but also covers

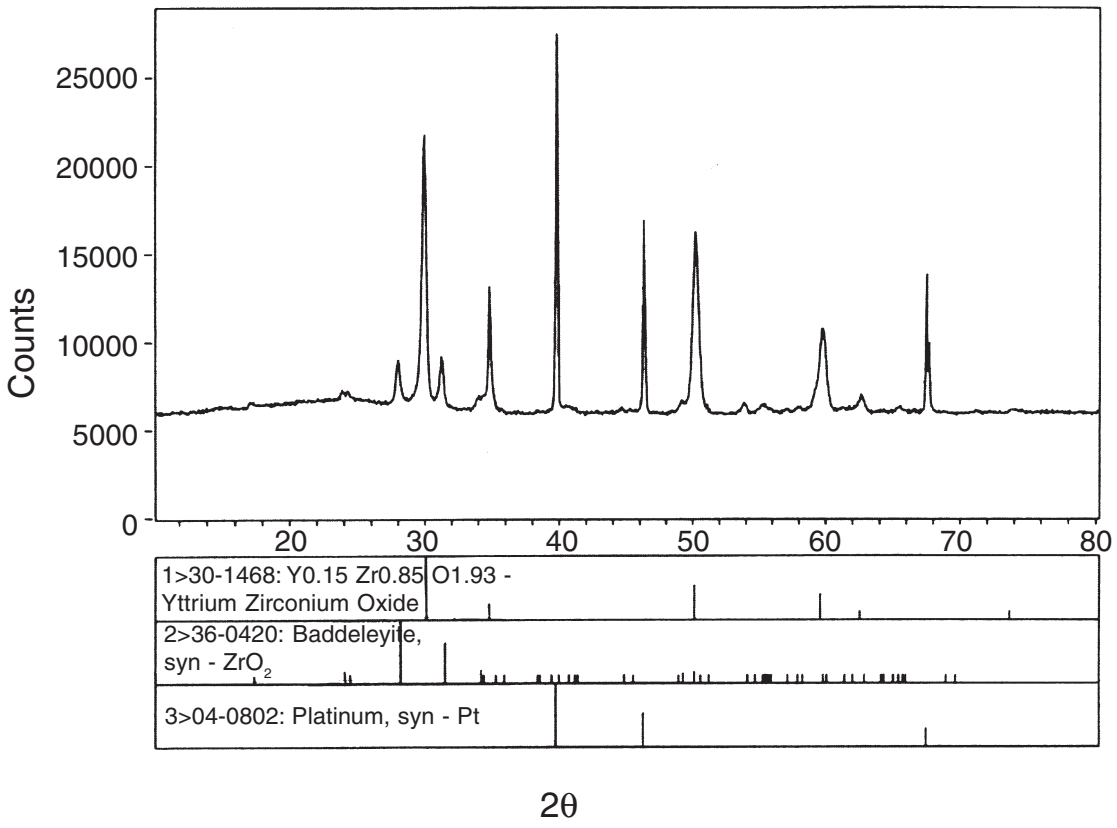

Fig. 33: XRD spectrum of the anode of the sample after PEVD. Also shown are representative spectra from standard Y_2O_3-ZrO_2, ZrO_2 and Pt specimens.

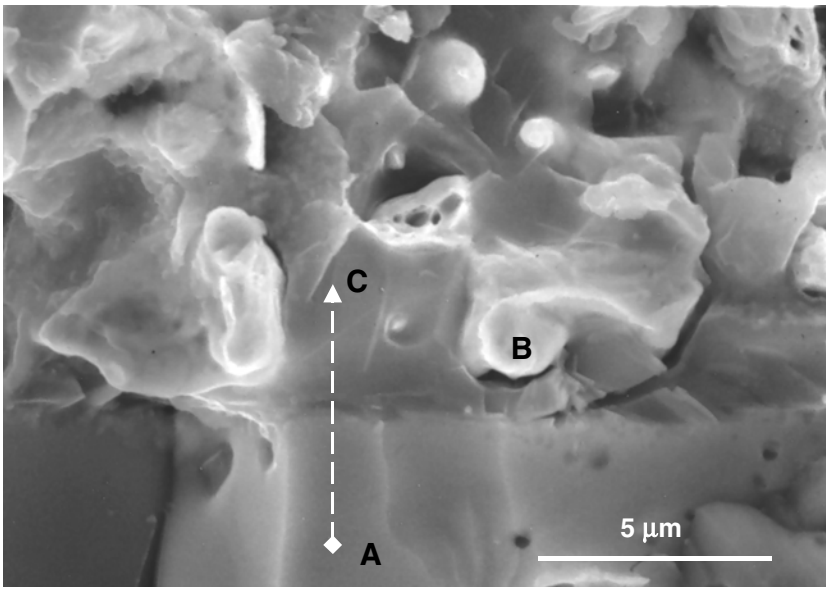

Fig. 34: SEM SE image of the anode/solid electrolyte interfacial region. (A) Substrate (ytterbia and yttria stabilized zirconia); (B) Pt metallic electrode; (C) PEVD product (yttria stabilized zirconia).

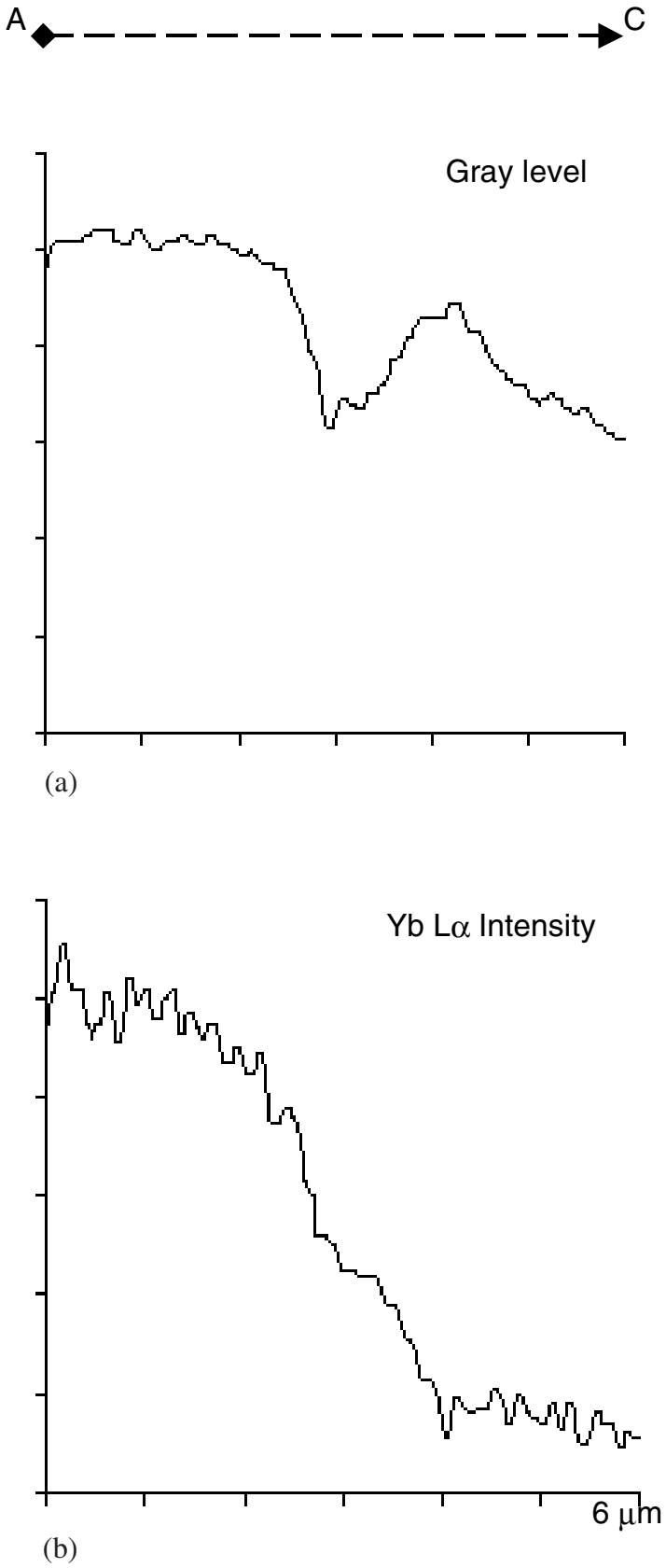

Fig. 35: EDX line scan from point A to point C. (a) gray level and (b) Yb Lα intensity.

the entire porous metallic (Pt) electrode surface. This coverage by the ceramic phase protects the metallic electrode from vapor loss, sintering and poisoning in the harsh SOFC operating environment. The intimate contact of the deposited ceramic phase in the interface region also improves the contact between the solid electrolyte and metallic electrode. Furthermore, at the interface between the solid electrolyte and composite anode, the ceramic phase is dominant. This increases the thermal shock resistance of the interface. PEVD yttria-doped zirconia also has continuous oxygen ionic conducting paths in the anode. Since the deposited ceramic phase is thinner at the other areas than the solid electrolyte/electrode interface, the porosity of the anode does not decrease significantly. This ensures that all three phases for the SOFC anode reaction coexist in the PEVD composite anode. This is the optimum way to expand the electrochemically active area to a three-dimensional anode volume. Unlike slurry coating of cermet anodes, formation of ionic conducting paths in PEVD composite anodes reduces the overpotential loss but does not sacrifice the electronic conducting path. Thus, the sheet resistance of the PEVD composite anode remains virtually the same as the pure metallic anode.

According to the previous discussions, the above mentioned PEVD composite anode microstructure is largely based on PEVD's unique electro-crystallization behavior.[3,80] Thus, PEVD has the capability of fabricating composite anodes to meet all the criteria for theoretically ideal anodes as illustrated in Figure 29. Furthermore, with regard to cost efficiency, PEVD is a single step process for composite anode formation. It can be conducted in situ to coat the pure metallic anodes, or even to repair damaged composite anodes for SOFCs.

PEVD Process Electrochemical Studies

In the previous sections, PEVD thermodynamic equilibrium relationships were discussed in connection with electro-crystallization phenomena occurring in PEVD processes for applications in sensors and fuel cells. However, the migration of charged ionic and electronic carriers in an electric field during PEVD is a kinetic process. Overpotential exists both in the bulk of the solid phases and within the diffuse double layer formed at the phase boundaries. Consequently, the applied potential and current in a PEVD process do not follow exactly the linear relations predicted from the thermodynamic equilibrium approach. Furthermore, it is necessary to discuss the changes at the working electrode during a PEVD process. Because such changes are accompanied by electrochemical reactions for PEVD product formation, the thermodynamic approach must, therefore, be complemented by kinetic considerations to evaluate electrocrystallization behavior during a PEVD process.

The task related to studying PEVD working electrode kinetics in this section is to explain the sequence of partial reactions constituting the overall PEVD electrochemical reaction for product formation at the working electrode. The dependence of current density, or of reaction rate, upon working electrode overpotential and temperature was studied by both a steady-state potentiostatic method and a dynamic potential sweeping method (solid electrolyte cyclic voltammetry), in the hope of resolving PEVD reaction rate-limiting steps. The results from this investigation will help in understanding the kinetics of the PEVD reaction and subsequent product formation at the working electrode of a PEVD system, improve knowledge of PEVD kinetics, and elucidate the possibility of further process control in PEVD.

Overpotential in a PEVD System

When a current flows through an electrochemical cell in the hypothetical PEVD system proposed in section 2, the applied dc potential V_a defines the potential difference V_{WC} between the working and counter electrode. This value deviates from its open-circuit value V°_{WC}, which is generally computable via a Nernst equation

$$V^{\circ}_{WC} = \frac{kT}{nz_A q}\ln\frac{a_{A^+(W)}}{a_{A^+(C)}} = \frac{\mu_{A,I} - \mu_{A,III}}{qz_A} \qquad (74)$$

where all terms have been defined in section 2.

According to the fundamental theory of overpotential for aqueous electrochemical systems,[81,82] the electrochemical cell overpotential is defined as the potential difference deviation from the open-circuit value. The electrochemical cell overpotential η_{WC} is then defined as:

$$\eta_{WC} = V_{WC} - V^{\circ}_{WC} = V_a - \frac{\mu_{A,I} - \mu_{A,III}}{qz_A} \quad (75)$$

Thus, the applied electric field and the chemical potential difference of solid-state transported reactant (A) between the sink and source determine the total overpotential η_{WC} of the PEVD system. Accordingly, Eqn. 41 can be expressed as

$$I = -G_t \eta_{WC} \quad (76)$$

where the PEVD current *I* and the total overpotential of the PEVD system η_{WC} are linearly related to each other. The slope is the conductance $-G_t$, which has been defined in section 2. However, this equation was obtained under the assumption that equilibria are attainable at all interfaces in the PEVD system. In practice, this assumption is valid only in a limited number of cases. Generally, when a current passes through the PEVD system, various kinds of overpotentials might exist at any part of the system, such as the counter electrode, solid electrolyte and working electrode. The overpotential η_{WC} of the electrochemical cell in the PEVD system is the sum of three terms:

$$\eta_{WC} = \eta_W + \eta_C + \eta_{E,WC} \quad (77)$$

where η_W, η_C are the overpotentials of the working (W) and counter (C) electrodes, respectively, and $\eta_{E,WC}$ is the ohmic overpotential due to the resistance of the solid electrolyte (E) between the working and counter electrodes. Thus, the current vs. applied potential curve in a PEVD process is usually not linear as expected from Eqn. 76. In order to further understand mass and charge transport during PEVD, the kinetics of a PEVD process and, consequently, various kinds of overpotential should be considered as well.

Since only the working electrode overpotential and current reveal, respectively, the thermodynamic and kinetic information of a PEVD reaction for product formation, it is imperative to distinguish the working electrode overpotential η_W from the total overpotential η_{WC}. This is possible with the help of a reference electrode (R). The overpotential between the working and reference electrodes can also be expressed as

$$\eta_{WR} = \eta_W + \eta_R + \eta_{E,WR} \quad (78)$$

where η_R is the overpotential of the reference electrode, and $\eta_{E,WR}$ is the ohmic overpotential due to the resistance of the solid electrolyte between the working and reference electrodes. During a PEVD process, no current flows through the open circuit between the reference and working electrode; therefore, both η_R and $\eta_{E,WR}$ are zero.[83-85] Thus, it is reasonable to assume that the potential difference V_{WR} between the working and reference electrode reveals the overpotential at the working electrode η_W only.

$$V_{WR} = \eta_W \quad (79)$$

The working electrode overpotential η_W can be measured by an electrometer between the working and reference electrodes.

When a PEVD system is at equilibrium under open circuit conditions, a thermodynamically defined reversible inner (or Galvani) potential ϕ°_W is set up at the working electrode. The equilibrium involved is a dynamic one, in which the rates at which charge carriers pass through the interface at the working electrode in both directions are equal. This rate is the exchange current density i_0.

$$i_+ = |i_-| = i_0 \quad (80)$$

When current flows through an electrode, its inner potential ϕ_W assumes a value different from the equilibrium inner potential ϕ°_W. This deviation of the electrode potential is the overpotential at the working electrode.[86]

$$\eta_W = \phi_W - \phi_W^{\circ} \quad (81)$$

An anodic (positive) and cathodic (negative) current always generates a positive and negative overpotential, respectively. Although working electrode overpotential is usually associated with working electrode/electrolyte interfaces in electrochemistry, in reality it refers to, and is measured as, deviations in the inner potential of the working electrode. The formation of the current-controlled overpotential in the working

electrode originates in the hindrance of the overall electrochemical reaction for PEVD product formation. The total working electrode overpotential can be divided into activation η_a, resistance η_Ω, concentration η_c and crystallization η_y overpotential according to the four possible types of rate control in PEVD electrochemical reactions. The total overpotential of the working electrode is given by the algebraic sum of the various components, since several of them usually operate simultaneously.

$$\eta = \eta_a + \eta_\Omega + \eta_c + \eta_y \quad (82)$$

Resistance overpotential η_Ω and activation overpotential η_a are characteristic of irreversible reactions and are, therefore, termed ''irreversible overpotentials''. Since deviations from the equilibrium potential due to changes in the concentrations of the reactants are largely reversible, concentration overpotential η_c is known as a ''reversible polarization''. Crystallization overpotential η_y is more complicated. It can be caused either by ''reversible polarization'' or ''irreversible polarization''. The details will be discussed later.

In electrode kinetics, as in chemical reaction kinetics, the slowest partial reaction is rate determining for the total reaction. The magnitude and type of working electrode overpotential is, therefore, governed by the slowest partial reaction which might have been included in the measurement. Thus, distinguishing various overpotentials during PEVD is critical to understand the kinetics of a PEVD process. However, the various components of the total working electrode overpotential can only be resolved under suitable conditions. If several of the reactions have slow reaction rates of similar orders of magnitude, the corresponding overpotentials are superimposed to form the total overpotential. Separation of the various components becomes very difficult. Before moving on to distinguish the overpotentials at the working electrode during a PEVD reaction, their causes will first be discussed.

Activation Overpotential

An overall electrode reaction differs from an overall chemical reaction in that at least one partial reaction of the overall electrode reaction must be a charge-transfer reaction. Activation overpotential at the working electrode of the PEVD system is due to slow charge transfer reactions at the working electrode/solid electrolyte interface (location (II) of Figure 3). During the charge-transfer reaction, charge carriers (A^+ and e^-) are transported against the potential controlled activation energy from solid electrolyte (E) and working electrode (W) into PEVD product (D) across the electrical double layer. The rate of the charge-transfer reaction is determined by the potential difference across the double layer. Thus, it is a measure of how easily charged particles (A^+ and e^-) cross the interfaces at location (II).

If only the charge-transfer reaction is hindered and not any of the other preceding or following partial reactions, the experimentally measurable total overpotential at the working electrode η_W of the PEVD system equals the activation overpotential η_a and is related to the PEVD current via the Butler-Volmer equation:[87]

$$I = I_o\left[\exp\left(\frac{\alpha_a F\eta}{RT}\right) - \exp\left(-\frac{\alpha_c F\eta}{RT}\right)\right] \quad (83)$$

where I_0 is the exchange current at the interface. It measures the polarizability of a solid electrolyte/electrode interface. It is worth noting that I_0 is, in general, strongly dependent both on temperature and on gas composition. α_a and α_c are the anodic and cathodic transfer coefficients, respectively, and were introduced by Erdey-Gruz and Volmer.[88] Generally, transfer coefficients have values ranging from zero to unity ($0 < \alpha < 1$). It has been experimentally shown that, within a certain potential range, this coefficient is independent of potential.

When $|\eta| > 100$ mV then the Butler-Volmer equation reduces to its ''high field approximation'' form:

$$\ln\left(\frac{I}{I_o}\right) = \frac{\alpha_a F\eta}{RT} \quad (84)$$

for anodic ($I > 0$, $\eta > 0$) operation and

$$\ln\left(-\frac{I}{I_o}\right) = \frac{\alpha_c F\eta}{RT} \quad (85)$$

for cathodic ($I < 0$, $\eta < 0$) operation. Thus, in a conventional Tafel plot of ln $|I|$ vs. η, a linear region (Tafel region) is obtained at $\eta > 100$ mV. The exchange current I_o can be obtained by extrapolating the linear part of the ln $|I|$ vs. η plot to $\eta_a = 0$. The slopes of the linear parts of the plot give the transfer coefficients α_a and α_c.

Resistance Overpotential

Resistance overpotential η_Ω, which corresponds to an ohmic potential drop at the working electrode, is usually negligible in a common electrochemical system, provided the electrode is sufficiently conductive. However, resistance overpotential can be created by a number of causes, such as the presence of surface films. In the PEVD system, the ''surface film'' is the product of the PEVD process. Thus, resistance overpotential could be a major contributor to the overall overpotential at the working electrode. The solid transported reactant (A) must migrate from location (II) through the deposit (D) to react with the sink vapor phase at location (III) of Figure 3. Accordingly, this transport process in a solid phase is the combination of both ionic (A^+) and electronic (e^-) carriers migrating under an electrochemical potential gradient. If the other overpotentials at the working electrode of the PEVD system are negligible, the transport rate is related to the total overpotential at the working electrode η_W and can be expressed as:

$$I = -G_D \eta_W \tag{86}$$

where G_D is the conductivity of (A) in deposit (D) as defined in section 2. Accordingly, if G_D is constant during a PEVD process, the transport rate or PEVD current is linearly related to the overpotential η_W at the working electrode.

Concentration Overpotential

Concentration overpotential η_c in a PEVD process is due to slow mass transfer of gaseous reactants and/or products involved in the overall working electrode reaction. During the passage of a current, the activities (or concentrations) of the gaseous reactants near the working electrode surface undergo a concentration change from the bulk sink gas phase, resulting in a corresponding shift in the equilibrium electrode potential. Concentration overpotential can be further subdivided into diffusion overpotential η_d and reaction overpotential η_r.

Diffusion overpotential η_d is caused by depletion or enrichment of the reactants at the surface of the working electrode. A transport process is involved in the overall electrode reaction by which the substances formed or consumed during the reaction are transported to or from the working electrode surface. This mass transport is necessary for the overall electrode reaction and takes place by diffusion to or from the surface, since the substances which are to be converted according to Faraday's law are present in sufficient quantities only in the bulk of the sink gas phase. Therefore, a concentration gradient or, more accurately, an activity gradient is established at the electrode surface. Pure diffusion overpotential η_d is encountered if mass transport by diffusion to or from the surface is the slowest process among the partial reactions involved.

Reaction overpotential η_r is caused by chemical reactions whose rates are lower than the preceding or following charge transfer reactions. The equilibrium concentrations required to produce the reversible EMF of the cell are not established quickly enough.

The diffusion and chemical reaction rates depend only on the concentration of gaseous reactants at the working electrode surface, and by definition, are independent of electrode potential. When concentration overpotential dominates the total overpotential at the working electrode, a limiting current I_L exists. This limiting current is the maximum current obtained when the electrochemical reaction is completely mass-transfer controlled.[89]

In aqueous electrochemistry, concentration overpotential is frequently important due to low reactant and/or product diffusivities in the aqueous phase and a low operating temperature. In the solid electrolyte cell of the PEVD system, mass transfer in the gas phase and chemical reaction at higher temperatures are usually rapid and, consequently, concentration overpotential is not that significant, especially at low PEVD currents and high PEVD operating temperatures.

Crystallization Overpotential

Crystallization overpotential is treated as a special type of overpotential. In the PEVD system, any barrier to the process by which atoms are incorporated into or removed from the crystal lattice of the PEVD product (D) leads to crystallization overpotential η_y.

According to Stranski's theory of crystal growth, each component of the deposited product (D) must first find its way to a suitable site at the edge of a lattice plane before it can be accepted into the lattice.[90] The additional overpotential observed when this reaction is inhibited is known as crystallization overpotential.

Electrocrystallization in PEVD may be split into the following three stages:

a. Transition,
b. Surface diffusion to the growth center, and
c. Inclusion in the lattice.

The characteristics of the observed crystallization overpotential are again determined by the stages which proceed at the lowest rate. Usually, step (c), inclusion into the lattice, is not a rate limiting step.

If step (a), the transition of charged components, is a limiting step, an inhomogeneous electric field is set up at the surface of the deposit (D) to guide the charged components into the active positions, and a linear relationship should, therefore, exist between the process rate and overpotential. This overpotential, which is due to distortion of the electric field, is usually small and is part of the resistance overpotential.

If step (b), surface diffusion to the growth center, is a rate limiting step, component concentration gradients are formed at the surface of the deposit (D). The observed overpotential could then be interpreted as a form of concentration overpotential, and is independent of the working electrode potential of the PEVD system.

On the basis of previous experimental evidence in this field, it has not as yet been possible to decide in favor of one or the other of the two theoretical transport mechanisms, as no unequivocal conclusions may be drawn from the measured steady-state current-potential curves. On the other hand, impurities will have a strong influence on crystallization overpotential.

PEVD System for Electrochemical Studies

PEVD System Setup

The PEVD process for Na_2CO_3 auxiliary phase deposition at the working electrode of a potentiometric CO_2 sensor was selected for the current electrochemical studies. Various kinds of overpotentials at the working electrode during the PEVD process were evaluated by both steady-state potentiostatic and dynamic potential sweeping methods in the hope of understanding the process kinetics.

The PEVD system used in this investigation is schematically shown in Figure 36. A Na^+-β/β''-alumina disc, 16 mm in diameter and 5 mm in thickness, was used as the solid electrolyte with a working electrode on one side and both counter and reference electrodes on the other. To simplify data interpretation, the same electrode material, a Pt thick film, was used for all three electrodes, so the measured potential difference V_{WR} could be directly related to the average inner potential difference between the working and reference electrode.[91,92] In order to make good electrical and mechanical contact, Pt meshes, with spot-welded Pt wires, were sintered on the Pt thick films as electron collectors and suppliers.

At the source side of the PEVD system, a counter electrode and a reference electrode were deposited on substrate areas of 1 cm^2 and 0.1 cm^2, respectively. The thickness of both electrodes was about 3 μm. Because rapid equilibration must be established for the electrochemical reaction at the source side during the electrochemical studies, it is important to minimize polarization at the counter and reference electrodes. Thus, the source Na_2CO_3 in this PEVD system wrapped both the counter and reference electrodes due to a melting and quenching technique. The Na_2CO_3 powder was first heated in an alumina crucible above its melting point at 852°C. Then the source side of the PEVD system was quickly dipped into the melt. After cooling to room temperature, a layer

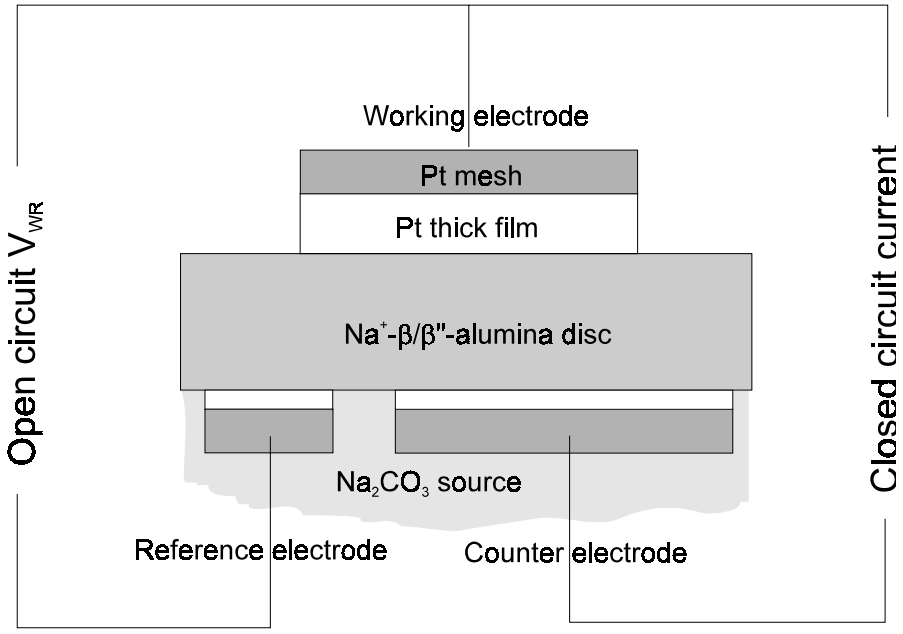

Fig. 36: The PEVD system setup.

of Na_2CO_3 covered both the counter and reference electrodes. This type of source had a lower overpotential loss.

At the sink side of the PEVD system, a porous Pt thick film about 7 μm in thickness was applied to a substrate area of 1 cm^2. As discussed in section 3, the PEVD process can be divided into two stages. In stage I the PEVD product does not cover the entire Pt thick film, while in stage II, it does. According to previous experiments, the kinetics of the PEVD process are different in both stages. In order to reveal the kinetics of PEVD working electrode reactions for stage I and stage II separately, two kinds of PEVD samples with working electrode Na_2CO_3 coverage corresponding to stage I and stage II were prepared by PEVD. The Na_2CO_3 depositions were similar to those discussed in section 3. Na_2CO_3 coverage at the working electrode was controlled during a potentiometric PEVD process by controlling processing current and, subsequently, confirmed by SEM microstructure studies.

During electrochemical studies, either a stage I or stage II PEVD sample system was placed in the constant temperature zone of a tube furnace to maintain a uniform temperature at both the sink and source sides. The same gas phase (ultrazero air) was fed into both sides of the system at a high flow rate (larger than 100 sccm). The three electrodes of the PEVD system were connected to the external circuit to give two solid electrochemical cells. One was a closed circuit cell from the counter electrode to the working electrode:

(counter) CO_2, O_2, Na_2CO_3, Pt|Na^+ - β/β"
-alumina|Pt, Na_2CO_3, CO_2, O_2 (working) (87)

The other was an open circuit cell from the reference electrode to the working electrode:

(reference) CO_2, O_2, Na_2CO_3, Pt|Na^+ - β/β"
-alumina|Pt, Na_2CO_3, CO_2, O_2 (working) (88)

Because the atmosphere at both the source and sink sides was the same, the chemical potential of sodium was equal and fixed by the Na_2CO_3 phase in equilibrium with the same atmosphere at all three Pt electrodes, when no electric field was present. At this point, the equilibrium electrochemical reaction

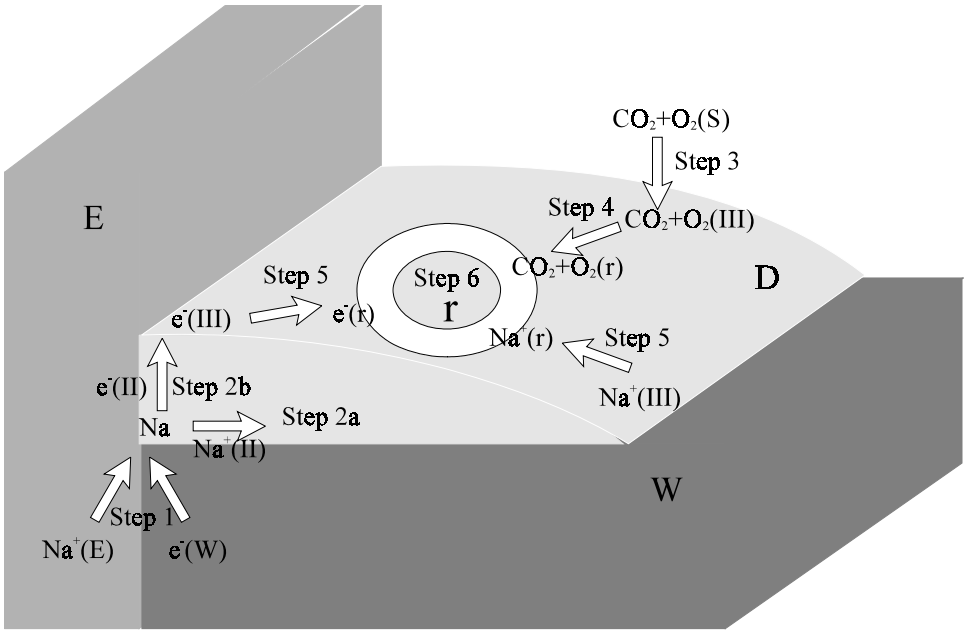

Fig. 37: The kinetic steps for PEVD reaction at the working electrode.

$$2Na^+ + 2e^- + CO_2 + \tfrac{1}{2}O_2 \Leftrightarrow Na_2CO_3 \quad (89)$$

prevailed at all three electrodes. Accordingly, the equilibrium potential was zero under both open and closed circuit conditions if there was no applied electric potential. By adjusting V_{WR} in the open circuit electrochemical cell, the working electrode overpotential η_W varied according to Eqn. 79. Correspondingly, the current through the closed circuit between the working and counter electrodes changed to reveal the kinetics of PEVD working electrode reactions as well as the mass and charge transport rate through the PEVD system. A negative V_{WR} or η_W increased the chemical potential of Na at the working electrode, and reaction (89) moved to the right forming Na_2CO_3 at the working electrode. A positive V_{WR} decreased the chemical potential of Na at the working electrode, and reaction (89) moved to the left resulting in Na_2CO_3 decomposition at the working electrode.

PEVD Reaction Rate Limiting Steps at the Working Electrode

For Na_2CO_3 formation at the working electrode of a PEVD sample, the overall electrochemical reaction can be divided into six rate-limiting steps as schematically shown in Figure 37. These steps are

Step 1: Charge transfer reaction at location (II).

$$Na^+(E) + e^-(W) \rightarrow Na(D) \quad (90)$$

If this step is the rate-limiting step for the PEVD reaction at the working electrode, the working electrode overpotential is dominated by an activation overpotential η_a.

Step 2: Solid-state transported reactant Na diffusion from location (II) to (III).

$$Na(II) \rightarrow Na(III) \quad (91)$$

If this step is the rate-limiting step, the working electrode overpotential is dominated by a resistance overpotential η_Ω. This can be considered separately for both stage I and stage II PEVD samples. For Na_2CO_3 formation at the working electrode of a stage I PEVD sample, the working electrode of the PEVD system has not been covered by the product. Thus, an electronically shorted surface exists to transport electrons from location (II) to (III). Growth is preferred along the Y direction (Figure 7b). The process is limited by the diffusion of Na^+ from location (II) to (III).

Step 2a: Na^+ (*II*) $\rightarrow$ Na^+ (III) (92)

For Na_2CO_3 formation at the working electrode of the PEVD system during stage II growth, the Pt electrode in the PEVD system has already been covered with a layer of Na_2CO_3. Further growth is in the X direction to increase the thickness of the product. According to the previous discussion, this step is limited by electron diffusion.

Step 2b: e^-(*II*) $\rightarrow$ e^- (*III*) (93)

Step 3: Gas phase diffusion and surface adsorption of CO_2 and O_2 from the bulk of sink gas phase (S) to the working electrode surface at location (III).

$$CO_2(S) + \tfrac{1}{2}O_2(S) \rightarrow CO_2(III) + \tfrac{1}{2}O_2(III) \quad (94)$$

If this step is the rate-limiting step for the PEVD reaction at the working electrode, the working electrode overpotential is dominated by a concentration overpotential η_c (diffusion overpotential η_d).

Step 4: Surface transport of neutral reactants at the working electrode surface to the reaction sites (r).

$$CO_2(III) + \tfrac{1}{2}O_2(III) \rightarrow CO_2(r) + \tfrac{1}{2}O_2(r) \quad (95)$$

If this step is the rate-limiting step, the working electrode overpotential is dominated by a crystallization overpotential η_y. This crystallization overpotential behavior is similar to a concentration overpotential.

Step 5: Surface transport of charged reactants at location (III), the product surface, to the reaction sites (r).

$$Na^+(III) + e^-(III) \rightarrow Na^+(r) + e^-(r) \quad (96)$$

If this step is the rate-limiting step, the working electrode overpotential is dominated by a crystallization overpotential η_y. This crystallization overpotential behavior is like a resistance overpotential.

Step 6: Chemical reaction at the reaction sites (r) to form the product Na_2CO_3.

$$2Na^+(r) + 2e^-(r) + CO_2(r) + \tfrac{1}{2}O_2(r) \rightarrow Na_2CO_3(r) \quad (97)$$

If this step is the rate-limiting step, the working electrode overpotential is dominated by a concentration overpotential η_c (reaction overpotential η_r).

Steady-State Potentiostatic Studies

The purpose of steady-state potentiostatic studies is to obtain a series of PEVD working electrode overpotentials and corresponding steady-state current values at various processing temperatures. According to the previous discussion, each possible kinetic limiting step for the overall PEVD reaction causes different effects in steady-state *I*-η curves. Furthermore, from the temperature dependence of the PEVD current, the activation energy for various PEVD processing conditions can be obtained to determine the possible reaction rate-limiting step.

Experimental Methods

During the steady-state potentiometric study, a potentiostat-galvanostat was connected to the three electrodes of the PEVD sample. A constant dc electrical potential V_{WR} across the open circuit electrochemical cell between the working electrode and reference electrode was set up manually with the potentiostat-galvanostat. According to Eqn. 79, V_{WR} is equivalent to the working electrode overpotential η_W of a PEVD system. At each η_W, a current *I*, that flows through the closed-circuit electrochemical cell between the working and counter electrode, was then measured by the potentiostat-galvanostat. However, it is current density, instead of current, that is directly related to the kinetics of a PEVD reaction at the working electrode. In order to relate the potentiostat-galvanostat measured current directly to the kinetics of a PEVD reaction at the working electrode, it is imperative to maintain the reaction area at the working electrode relatively unchanged during the time of testing. As discussed previously, the PEVD working electrode undergoes constant change due to the formation of PEVD products. This is especially true for a stage I PEVD sample. No steady-state current can be obtained at a constant V_{WR}. Thus, a steady-state potentiostatic study is unsuitable to study the kinetics of stage I PEVD reactions.

For a stage II PEVD sample, on the other hand, a steady-state current can be obtained at a constant V_{WR} after a period of charging time. This

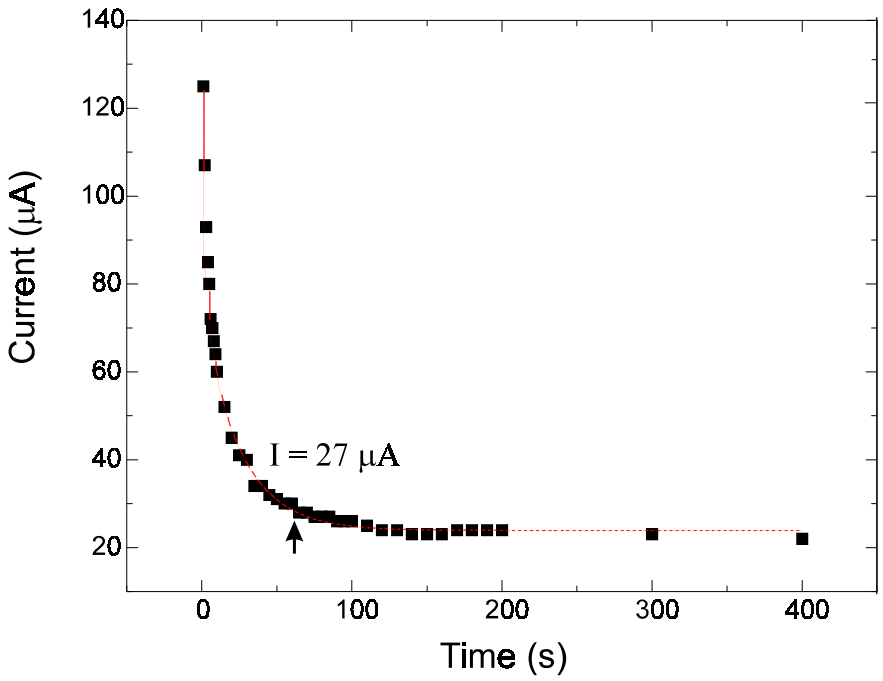

Fig. 38: Current decay during the charging process.

is because the working electrode surface reaction area is constant during stage II PEVD growth. For instance, the current response of a stage II PEVD sample after V_{WR} is increased from 20 to 40 mV at 530°C is recorded in Figure 38. The current increases sharply upon increasing V_{WR}, and then decays exponentially to approach a stationary value. This kind of current response is common for an electrochemical system with a non-negligible capacitance. In order to reach a steady-state current, a period of time is necessary to allow the charging current to die out. However, because the PEVD product thickness continues to increase at the working electrode during the delay time, the solid-state transport distance in the PEVD product will increase. Thus, it is advantageous to shorten the waiting time for the current reading at each step. According to Figure 38, a 60 s waiting time is a compromise solution, since the charging current component at 60 s is less than 20% of the final steady-state current. In this way, the *I*-η behavior for a stage II PEVD reaction was also experimentally repeatable.

Experiments on a stage II PEVD sample were conducted at six temperatures from 500 to 550°C at 10°C intervals. At each temperature, V_{WR} was increased step-wise from 0 to 450 mV with 60 s for each step. The resultant current flow through the working and counter electrode was measured simultaneously. Both V_{WR} and I were recorded by a dual channel analog recorder.

Results

Current - Overpotential Behavior

The PEVD reaction current, 60 s after changing the working electrode overpotential at each step, from a stage II PEVD sample is recorded. The results were repeatable. Two kinds of plots are commonly used to show the dependence of the current on overpotentials at various temperatures. One is a current vs. overpotential plot as shown in Figure 39; the other is a ln(current) vs. overpotential plot (Tafel plot) in Figure 40.

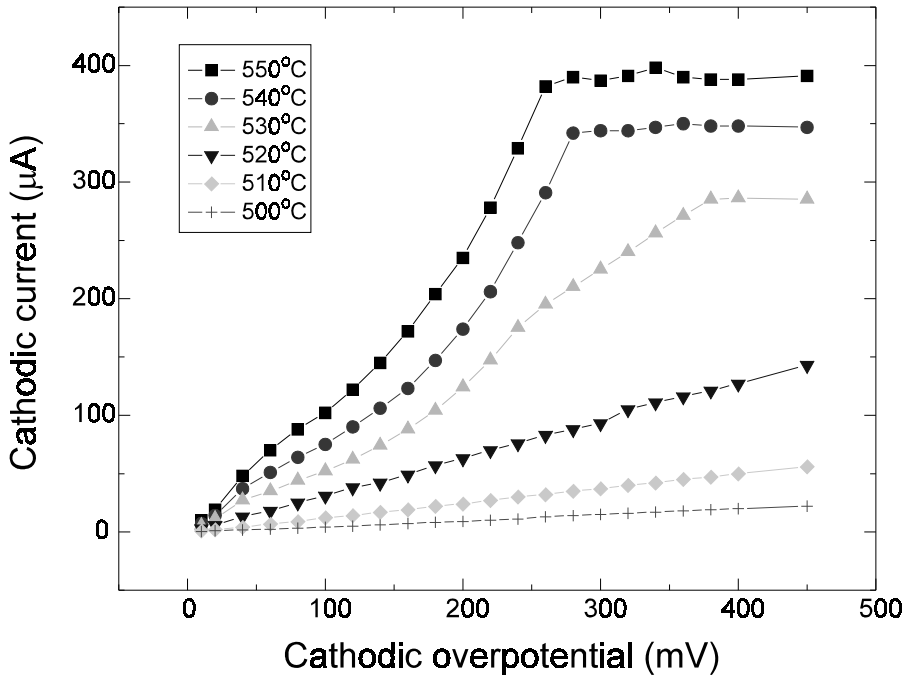

Fig. 39: Current-overpotential behavior (*I*-η curves) of a stage II PEVD process at various temperatures.

At lower temperatures, e.g. 500°C, the *I*-η curve is almost linear from the origin up to a cathodic overpotential of 450 mV. This kind of linear *I*-η behavior occurs since resistance or crystallization overpotential dominates the total working electrode overpotential. According to the previous discussion, the PEVD reaction rate-limiting step at the working electrode is either Step 2b (electron diffusion) or Step 5 (surface transport of charged reactants).

At higher temperatures, e.g. 550°C, the current-overpotential behavior is similar to that for common electrochemical systems. There are two regions separated at about 260 mV. In the lower overpotential region, a linear curve from 100 to 260 mV is obtained on the Tafel plot (Figure 40). This *I*-η logarithmic relation indicates that activation overpotential dominates the total working electrode overpotential, and the PEVD reaction rate-limiting step is Step 1 (charge transfer reaction). In the higher overpotential region, the current does not respond to further increase in overpotential. This limiting current can be caused by concentration overpotential η_c due to either Step 3 (diffusion overpotential η_d) or Step 6 (reaction overpotential η_r). This can also be caused by crystallization overpotential η_y due to slow surface transport of neutral reactants (Step 4).

The *I*-η behavior at four intermediate temperatures (540, 530, 520, and 510°C) was also studied to show the transition from lower temperature to higher temperature kinetic behavior. It was found that the 510 and 520°C curves are similar to the lower temperature one at 500°C, in which the current response to the overpotential is linear through the entire testing range. The 540°C curve resembles the 550°C curve, in which a linear logarithmic response is followed by a limiting current at higher overpotential. At 530°C, all three kinds of kinetic response, i.e., logarithmic, linear and constant with increasing overpotential, exist in the *I*-η curve. Thus, the kinetic transition from low temperature

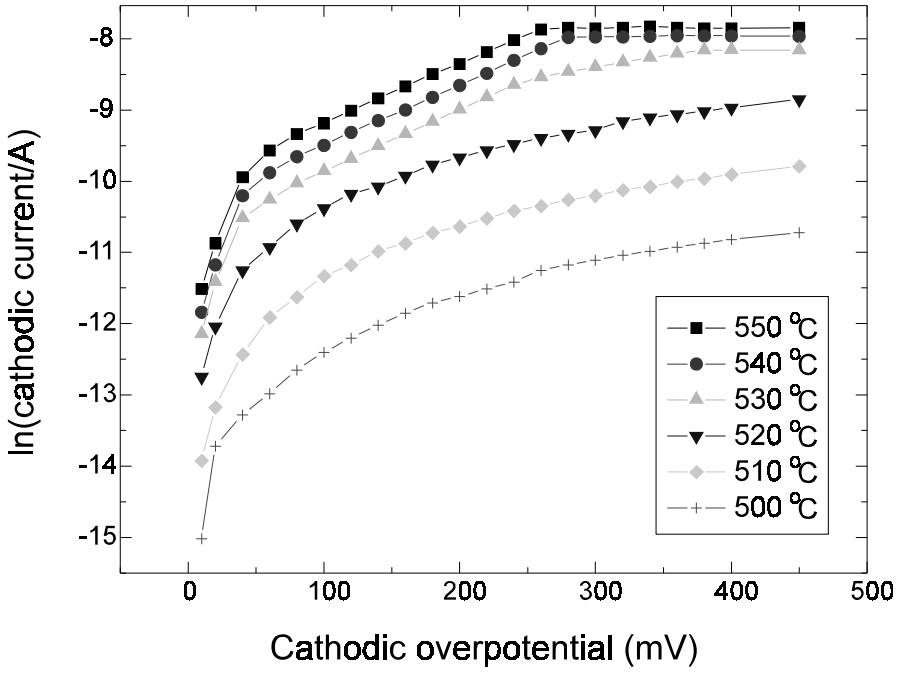

Fig. 40: Tafel plot (ln(*I*) vs. η) of the current-overpotential behavior in Figure 39.

to high temperature behavior in the current PEVD system occurs around 530°C.

Activation Energy of the PEVD Reaction

In order to further distinguish the PEVD reaction rate-limiting steps, activation energies of the PEVD reaction were studied at two overpotentials. Figure 41 is the Arrhenius plot of ln(*I*) vs. 1/*T* at an overpotential η_W = 100 mV. Two regions are resolved. In the higher temperature region above 530°C, an activation energy of 185 kJ/mol or 1.9 eV is obtained. This is close to the previously reported activation energy for a charge transfer reaction.[93,94] In the low temperature region below 530°C, an activation energy of 516 kJ/mol or 5.4 eV is obtained. This value is much higher than would be expected for Step 5, surface diffusion of charged particles. Thus, the possible kinetic limiting step is Step 2b, the diffusion of electrons in the product Na_2CO_3. However, the value of 5.4 eV is a little less than the activation energy for electronic conduction, which should be close to the bandgap E_g of the product. For inorganic oxysalts, the E_g is expected to be ~6.0 eV. One possible explanation is that impurity levels may exist between the conduction and valence band.[95]

Figure 42 is an Arrhennus plot of ln(*I*) vs. 1/*T* at an overpotential η_W = 400 mV. Again there are two regions. The slope of a linear regression curve in the low temperature region is similar to that at the lower overpotential, η = 100 mV. Thus, the kinetic limiting step is still Step 2b, the diffusion of electrons. The calculated activation energy E_a = 4.9 eV in this plot is actually a little lower than the previous one (5.4 eV). This difference could be due to the changes in the working electrode during product formation. Thus, the most reliable activation energy for Step 2b could be extracted from the slopes of the *I*-η curves at the lower temperatures as shown in Figure 43. Accordingly, the activation energy is 464 kJ/mol, or 4.8 eV.

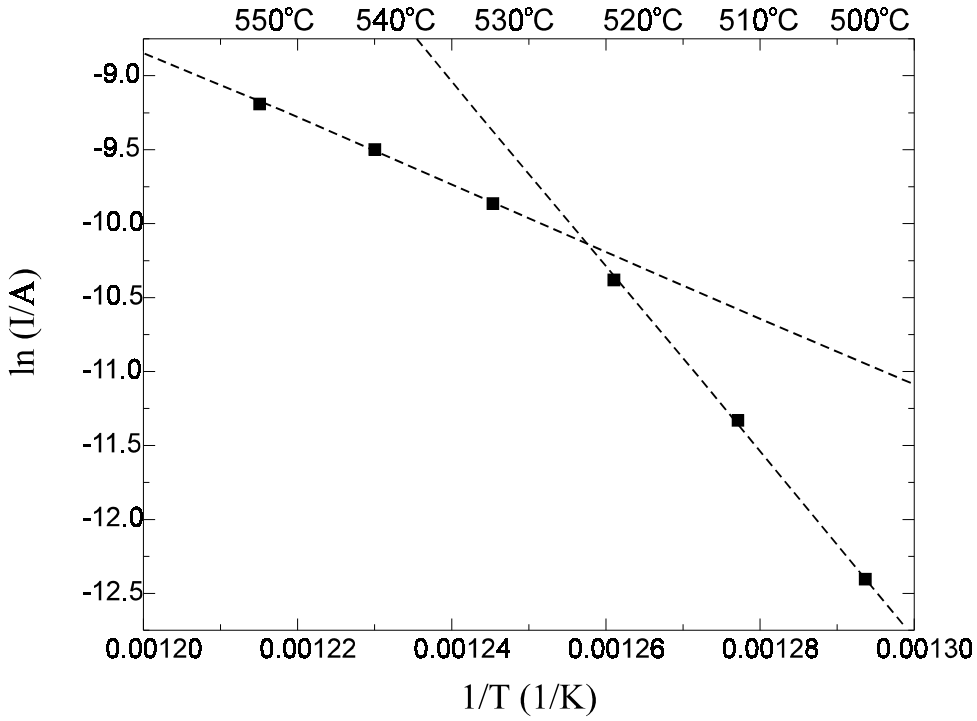

Fig. 41: Arrhenius plot at η = 100 mV.

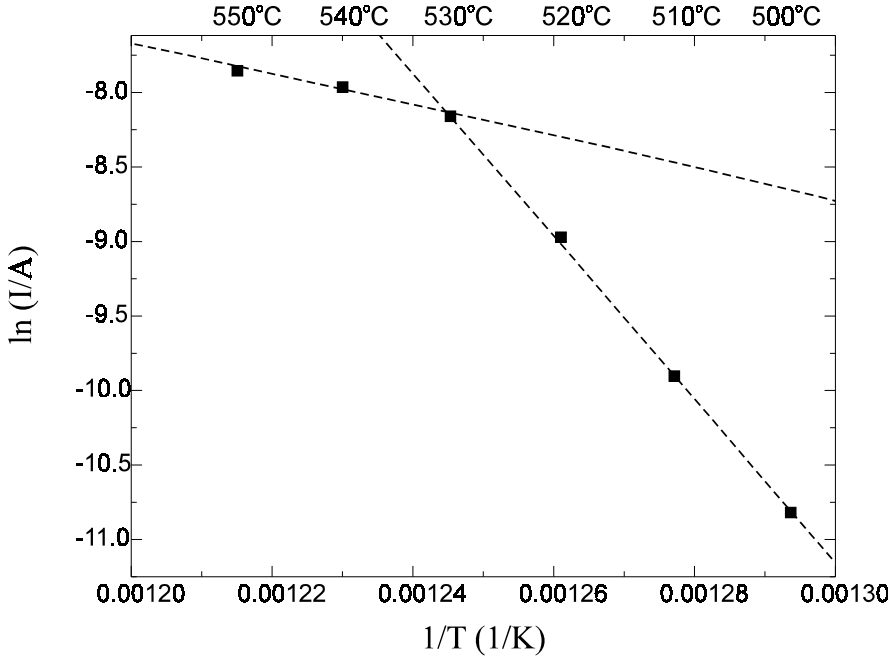

Fig. 42: Arrhenius plot at η = 400 mV.

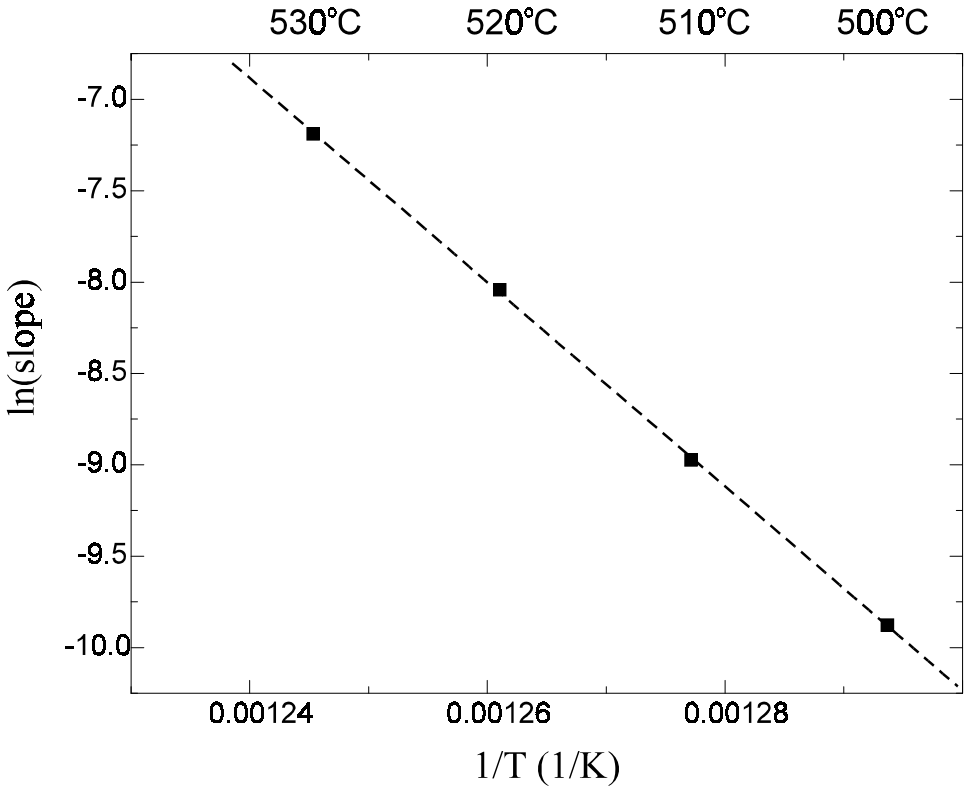

Fig. 43: Arrhenius plot of the slope of the *I*-η curves at lower temperatures.

At higher temperatures in Figure 42, an activation energy of 84 kJ/mol or 0.8 eV is obtained. Although increasing temperature will increase gas phase diffusion through an increase in molecular diffusion velocity, the mean free path will decrease. The result is only a weak thermal activation of gas phase diffusion for Step 3. The activation energy value is more likely due to Step 4 (surface diffusion of neutral reactants) or Step 6 (chemical reaction).

Exchange Current for the PEVD System

The exchange current I_0 and cathodic transfer coefficient α_c for the PEVD system can be extracted from standard Tafel plots (Figure 40) as described in detail previously, and provide a measure of the nonpolarizability of the solid electrolyte/electrode interface.[96,97] The values of I_0 and α_c at various temperatures are shown in Table 3. The activation energy of the exchange current can then be obtained from an Arrhenius plot in Figure 44 as 200 kJ/mole (2.1 eV), which fits in with those in the literature in the range of 1.2 to 2.7 eV.[98]

The cathodic transfer coefficient α_c is generally invariant with temperature.[99] A constant value from this experiment further indicates the reliability of using the steady-state potentiostatic method to study stage II PEVD reactions.

Summary

The current-overpotential behavior of the cathodic PEVD product formation at the working electrode during stage II of PEVD has been studied at various temperatures. The repeatability of the *I*-η curves in stage II of a PEVD process is fairly good. Thus, the change in geometric factor of the working electrode during the period of potentiostatic study is negligible. Accordingly, the PEVD reaction rate-limiting steps at the working electrode for a stage II PEVD process are collected in Table 4.

Table 3. Temperature Dependence of Exchange Current and Cathodic Transfer Coefficient

Temperature (°C)	Exchange Current I_0 (μA)	Cathodic Coefficient α_c
550	45.5	0.58
540	32.2	0.59
530	22	0.60

Table 4. Stage II PEVD Steady-State Potentiostatic Study Results

PEVD Parameters		I-η Relation	Dominant η	Rate Limiting Steps	Activation Energy (eV)
Temp. (°C)	η_W (mV)				
500, 510, 520	0 - 450	Linear	η_Ω	Step 2b, Diffusion of Electrons	4.8
530	0 - 220	Logarithmic	η_a	Step 1, Charge Transfer Reaction	1.9
	230 - 380	Linear	η_Ω	Step 2b, Diffusion of Electrons	4.8
	390 - 450	Limiting	η_y	Step 4, Surface Diffusion of Neutral Reactants	0.87
			η_c	Step 6, Chemical Reaction	
540, 550°C	0 - 260	Logarithmic	η_a	Step 1, Charge Transfer Reaction	1.9
	270 - 450	Limiting	η_y	Step 4, Surface Diffusion of Neutral Reactants	0.87
			η_c	Step 6, Chemical Reaction	

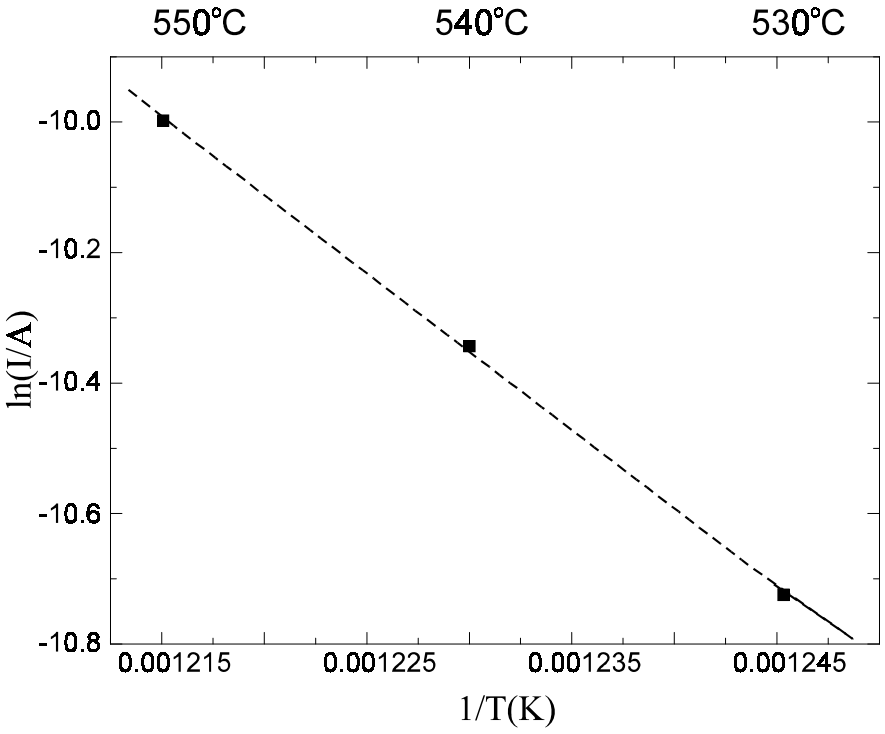

Fig. 44: Activation energy of the exchange current.

Cyclic Voltammetry Studies

The technique of cyclic voltammetry or, more precisely, linear potential sweep chronoamperometry, is used routinely in aqueous electrochemistry to study the mechanisms of electrochemical reactions.[99-103] Currently, cyclic voltammetry has become a very popular technique for initial electrochemical studies of new systems and has proven very useful in obtaining information about fairly complicated electrochemical reactions.[99] There have been some reported applications of cyclic voltammetry for solid electrochemical systems.[104-106] It is worth pointing out that, although the theory of cyclic voltammetry originally developed by Sevick,[107] Randles,[108] Delahay,[109] and Srinivasan and Gileadi[110] and lucidly presented by Bard and Faulkner,[99] is very well established and understood in aqueous electrochemistry, one must be cautious when applying this theory to solid electrolyte systems of the type described here, as some non-trivial refinements may be necessary.

Because of the geometric change at the working electrode due to growth of the PEVD product, the results from a steady-state potentiostatic study are not applicable to stage I of PEVD. In this study, a solid electrolyte cyclic voltammetry (SECV) method was applied for two reasons:

a. It is possible to resolve complicated electrochemical reactions and qualitatively reveal the general current-overpotential behavior.
b. Both anodic and cathodic potentials are applied during a single scan, which is fast enough to minimize the working electrode change of a PEVD sample during testing.

Experimental Setup

During the SECV study, the PEVD system and all experimental parameters were similar to those in the steady-state potentiostatic work. The only difference was the external circuit, in which a CAS-100 system (Gamry, Inc.) was used to connect with a PEVD sample. This setup

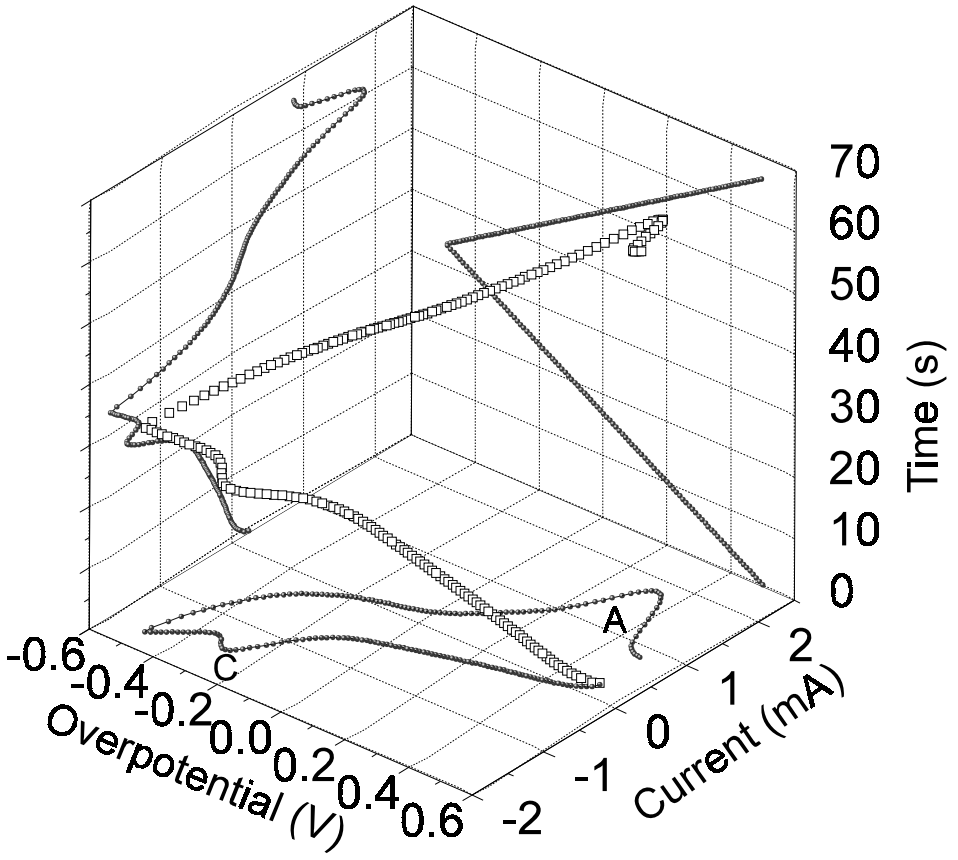

Fig. 45: A three-dimensional SECV spectrum and its projection planes for a stage II PEVD sample at 550°C.

permits linear variation in time of the working electrode potential with respect to the reference electrode V_{WR} according to

$$V_{WR} = V_{WR,1} + \upsilon t; \quad 0 < t \le \frac{\tau}{2}$$

$$V_{WR} = V_{WR,2} - \upsilon t; \quad \frac{\tau}{2} < t \le \tau \qquad (98)$$

$$\tau = 2\left(V_{WR,2} - V_{WR,1}\right)/\upsilon$$

where $V_{WR,1}$ is the initial ($t = 0$) working electrode potential corresponding to the beginning of each cycle, $V_{WR,2}$ is the switching potential, τ is the time for one scan and υ (V/s) is the sweep rate. The current I flowing between the working and the counter electrode can be recorded simultaneously to reveal the rate of the PEVD reaction taking place on the working electrode.

Results and Discussion for Stage II of PEVD

The validity of the SECV method was first tested for a stage II PEVD sample at 550°C. Thus, the results from SECV and the steady-state potentiostatic method could be compared.

General Features of an SECV Spectrum

Figure 45 shows a three-dimensional SECV spectrum for a stage II PEVD system at 550°C. This spectrum can be projected to three planes, i.e., the working electrode overpotential - PEVD current (V_{WR}-I) plane, the PEVD current - time (I-t) plane and the working electrode overpotential -time (V_{WR}-t) plane.

Traditionally, the most important projected curve, ‘‘cyclic voltammogram’’, is the one on the V_{WR}-I plane. The peaks labeled C and A are the major features of the voltammogram. The

cathodic peak C centered at V_{WR} = -290 mV corresponds to PEVD product (Na_2CO_3) formation at the working electrode; the anodic peak A at V_{WR} = 320 mV corresponds to Na_2CO_3 decomposition at the working electrode. The main reason that the current follows different paths on the V_{WR}-I plane upon increasing and decreasing V_{WR} is due to the fact that part of the current is used to charge the solid electrolyte/electrode interface, which has a nonzero capacitance C_d. The "thickness" ΔI of the cyclic voltammogram is of the order of $2\upsilon C_d$. Thus ΔI decreases with decreasing sweep rate υ and vanishes at $\upsilon = 0$, together with the cathodic peaks labeled C and the anodic peaks labeled A.[93,94,98] At this limit the entire cyclic voltammogram collapses into a single curve between A and C. The electrochemical literature[99] provides a more detailed discussion.

The projected curve on the I-t plane indicates the change in PEVD current as well as the reaction rate as a function of time. Conventionally, $I < 0$ corresponds to cathodic currents, i.e., I/F expresses the rate of supply of Na^+ to the working electrode. The area of the cathodic current peak on the I-t plane is 0.02631 C, which corresponds via Faraday's law to the reduction of 2.7×10^{-7} mol of Na to form 14 μg of Na_2CO_3. This amount of Na_2CO_3 is equivalent to an increase of about 12.5 nm in product thickness during stage II PEVD. Thus, the change to the working electrode is insignificant during a single scan.

The projected curve on the V_{WR}-t plane records the change of the imposed working electrode overpotential waveform during the V_{WR} scan. An important parameter in cyclic voltammetric studies is the sweep rate υ. The linear sweep rate for Figure 45 was 30 mV/s.

Effects of Sweep Rate

The cyclic voltammograms for various sweep rates at 550°C are reported in Figure 46. According to the theory of cyclic voltammetry,[99] the peak overpotential shift and peak current convey important information. A reversible redox reaction will not exhibit peak shifting with sweep rate change. In an aqueous electrochemical cell, the shift is generally caused by an irreversible redox reaction due to slow charge transfer compared with diffusion in the electrolyte. In such cases, the peak curent I_p linearly increases with υ.[99] However, when the charge transfer reaction does not involve a chemisorbed reactant, then, in practically all other cases, I_p varies linearly with $\upsilon^{1/2}$. In this study, the current for both peaks is linearly related to $\upsilon^{1/2}$ as shown in Figure 47.

Figure 46 also shows the effect of sweep rate υ on the cathodic peak potential $V_{WR,c}$. Increasing υ shifts $V_{WR,c}$ to more negative potentials. According to the theory of cyclic voltammetry, the magnitude of peak shift at various sweep rates permits direct computation of the cathodic transfer coefficient α_c:

$$\frac{dE_{p,c}}{d\ln\upsilon} = -\frac{RT}{\alpha_c F} \tag{99}$$

Figure 48 shows the usefulness of solid electrolyte cyclic voltammetry (SECV) for extracting transfer coefficients. The peak potentials are plotted against the logarithm of the sweep rates. The α_c value can be obtained from the slope of the linear regression curve. It is calculated to be 0.63, which is close to the value, 0.59, obtained from the steady-state potentiostatic study. Similarly, based on the equation for anodic peaks,

$$\frac{dE_{p,a}}{d\ln\upsilon} = \frac{RT}{\alpha_a F} \tag{100}$$

From the slope of the linear regression curve in Figure 49, the anodic transfer coefficient α_a is 1.

Effect of Holding Time

By holding the working electrode overpotential at 600 mV (anodic overpotential) for a period of time, then scanning to -1000 mV (cathodic overpotential), cyclic voltammograms are generated as shown in Figure 50. The cathodic peaks shift to lower (or more negative overpotentials) as the holding time increases. This indicates that the PEVD reaction is less limited by the higher overpotential limiting step. According to the results from steady-state potentiostatic studies (Table 4), the higher overpotential limiting step could be Step 3, Step

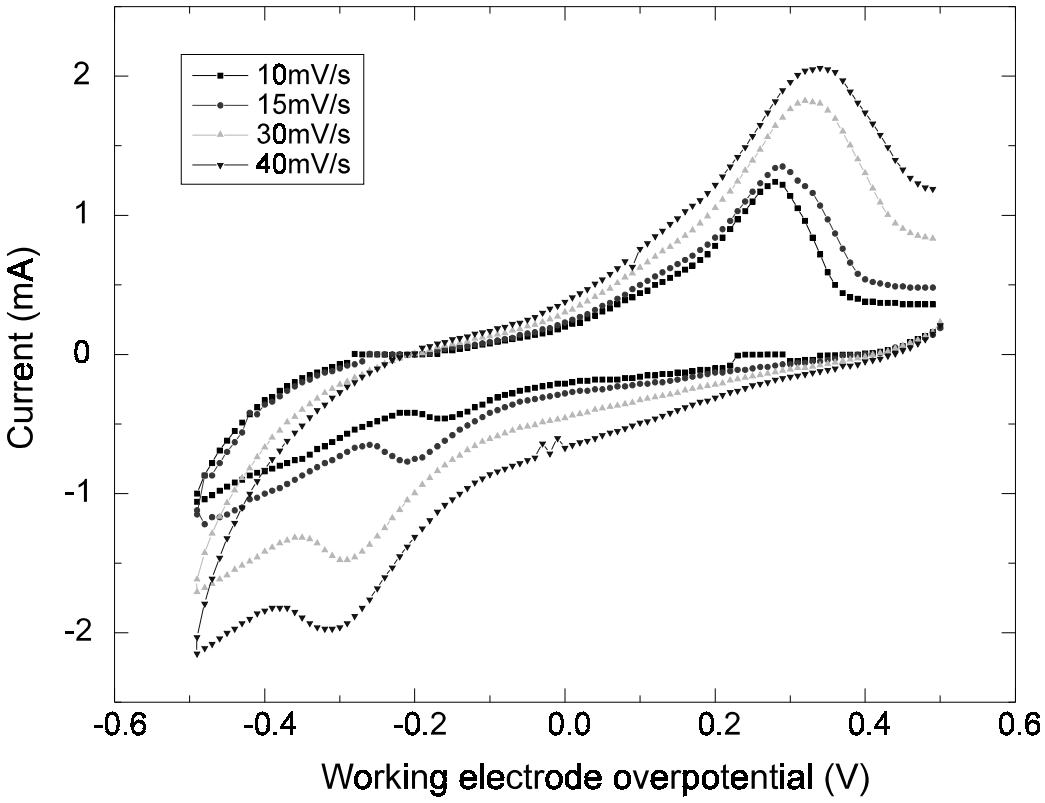

Fig. 46: Cyclic voltammograms at various sweep rates during stage II PEVD (550°C).

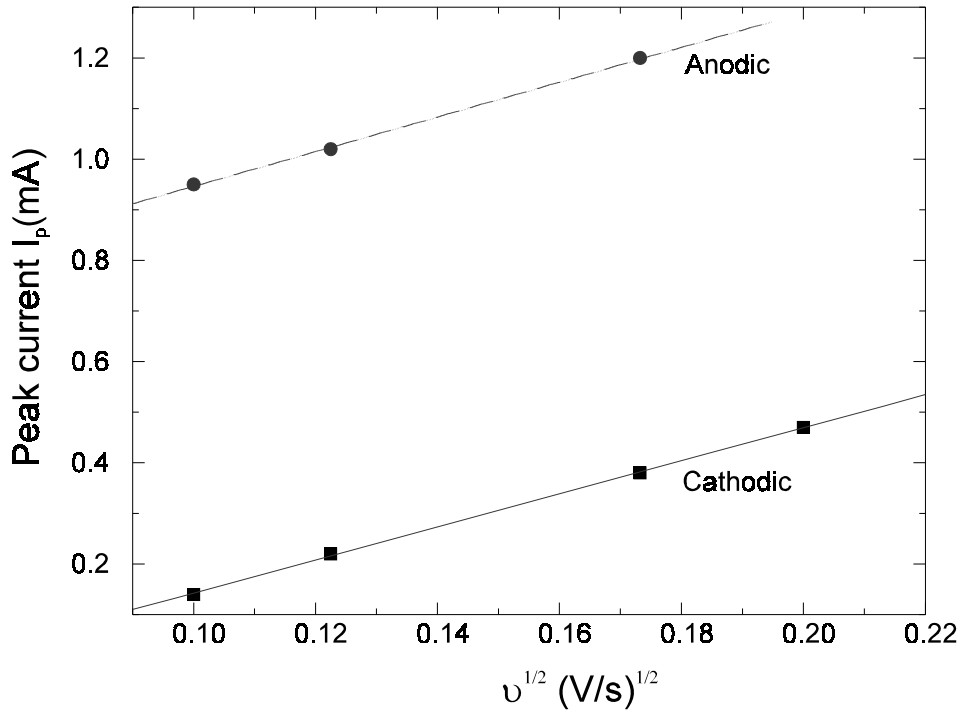

Fig. 47: Cathodic and anodic peak currents in Figure 46 vs. the square root of the sweep rate.

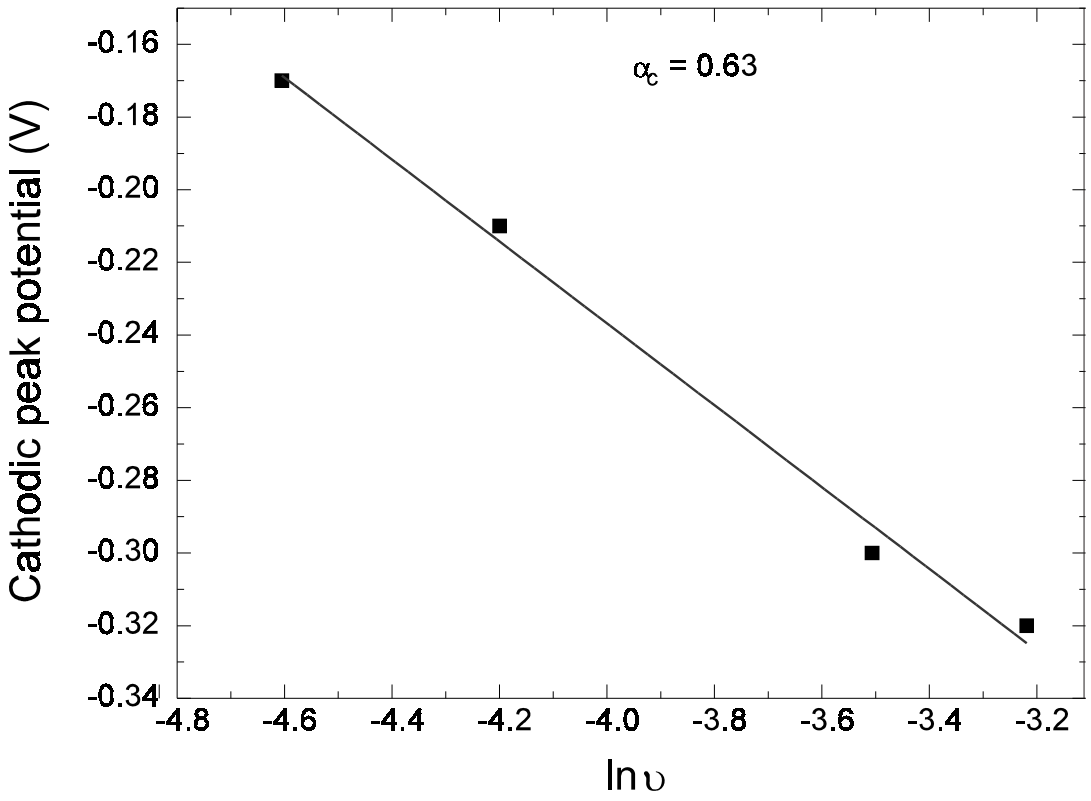

Fig. 48: Linear regression of cathodic overpotential vs. logarithm of sweep rate.

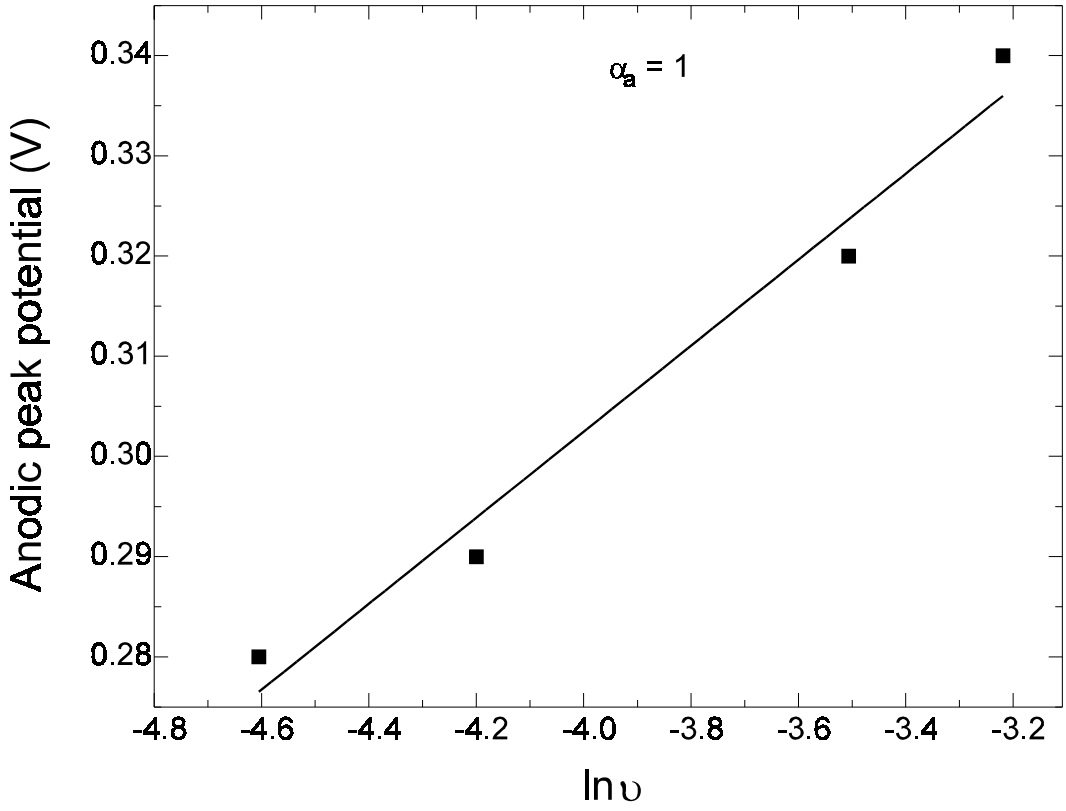

Fig. 49: Linear regression of anodic overpotential vs. logarithm of sweep rate.

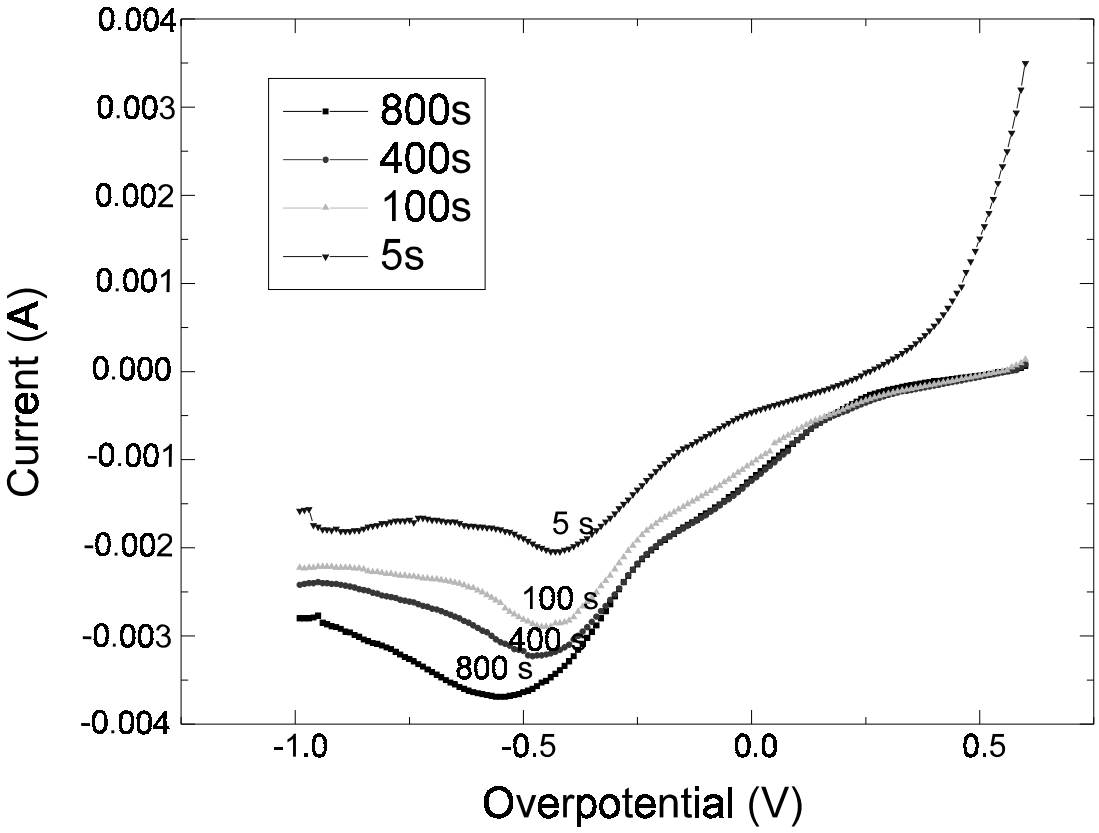

Fig. 50: Cyclic voltammetric curves at various holding times.

4 or Step 6. These experimental results indicate that Step 4 is more likely to be the higher overpotential limiting step, since Na_2CO_3 decomposes at the working electrode during the time of holding at an anodic overpotential. The longer the holding time, the more the decomposition proceeds. Step 3 and Step 6, gas phase diffusion and chemical reaction, respectively, will not be affected by this decomposition. On the other hand, surface diffusion of neutral reactants in Step 4 will be enhanced by the decomposition, since the products from decomposition are close to the reaction sites for formation. Thus, the limiting current for Step 4 will increase at the same working electrode overpotential. This delays the kinetic limitation step switch from Step 1 to Step 4. An interesting phenomenon is that the peak overpotential shift is linearly related to the holding time as shown in Figure 51.

Summary

In this section, a number of SECV experimental methods have been applied for the first time to study a PEVD system. The results from a stage II PEVD sample not only confirm the capability of SECV to distinguish various PEVD reaction rate-limiting steps, but also offer complementary information to the steady-state potentiostatic studies. For instance, SECV results further indicate that the rate limiting step at higher temperatures and higher overpotentials is Step 4. Since very little product is deposited on the working electrode during a single scan, SECV is also applicable to study stage I PEVD behavior.

Application of SECV to the Study of Stage I of PEVD

A stage I PEVD sample was tested at five temperatures (450, 475, 500, 525, and 550°C).

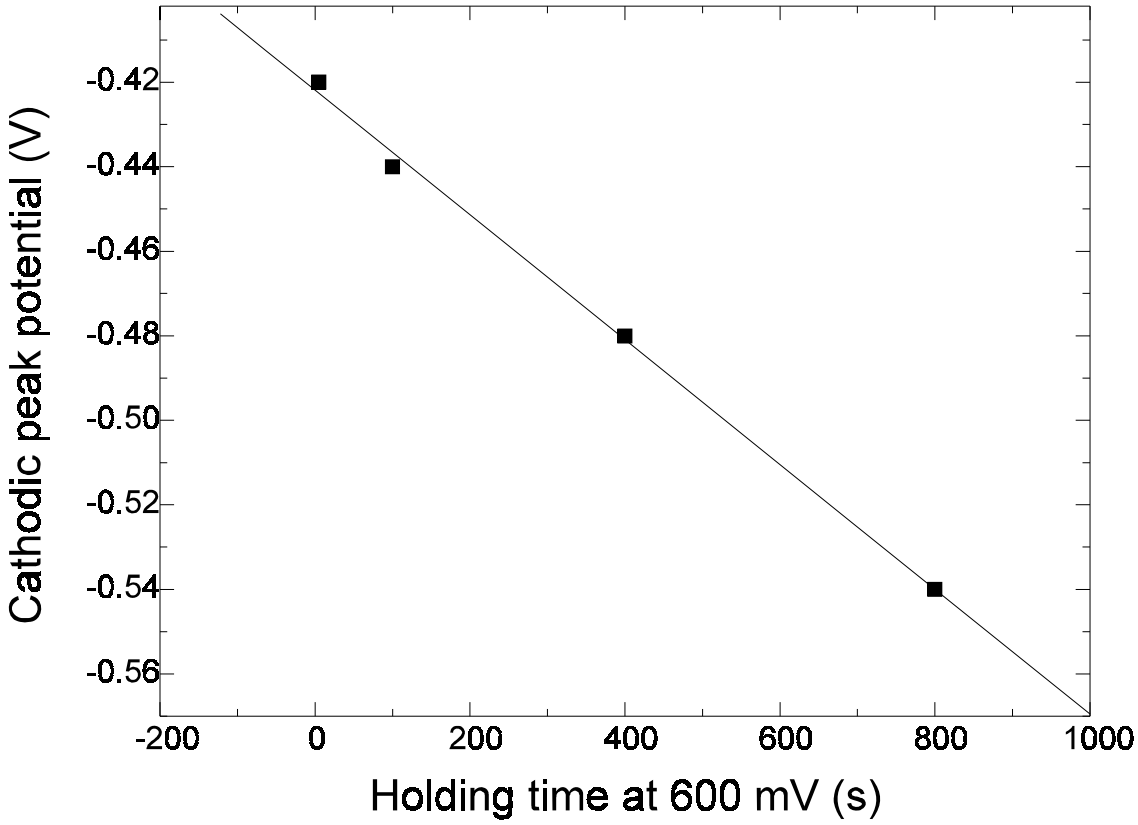

Fig. 51: Cathodic peak shift at various holding times.

Spectra at Lower Temperatures

Figures 52a, 53a, and 54a are cyclic voltammograms for various sweep rates at 450, 475, and 500°C, respectively. The voltammograms have similar features to those obtained from a stage II PEVD sample at a higher temperature (550°C). Only one pair of cathodic and anodic peaks exists. The cathodic and anodic peaks shift to more negative and positive potentials at higher sweep rates, respectively. Accordingly, PEVD reaction rate-limiting steps under these conditions are the charge transfer reaction (Step 1) at lower working electrode overpotentials and surface diffusion of neutral reactants (Step 4) at higher working electrode overpotentials.

Similar to the discussion for stage II, both cathodic and anodic transfer coefficients for the stage I PEVD sample can be obtained from the peak potential shifts resulting from changing sweep rates. The cathodic coefficients at each testing temperature are obtained by the peak overpotential vs. ln υ plots in Figures 52b, 53b, and 54b. Similarly, the anodic coefficients at each testing temperature are obtained by the peak overpotential vs. ln υ plots in Figures 52c, 53c, and 54c. The resulting α_c and α_a values are listed in Table 5, and are compared with those values from the stage II PEVD sample.

According to fundamental electrochemical theory, α_c and α_a should not change with processing temperature. The values for stage I are fairly constant. The significant increase in both coefficients from stage I to stage II is presumably due to the change in the solid electrolyte/working electrode interface during PEVD product (Na_2CO_3) formation. This indicates that the geometry of the auxiliary phase Na_2CO_3 at the working electrode is also kinetically related to the charge transfer reaction

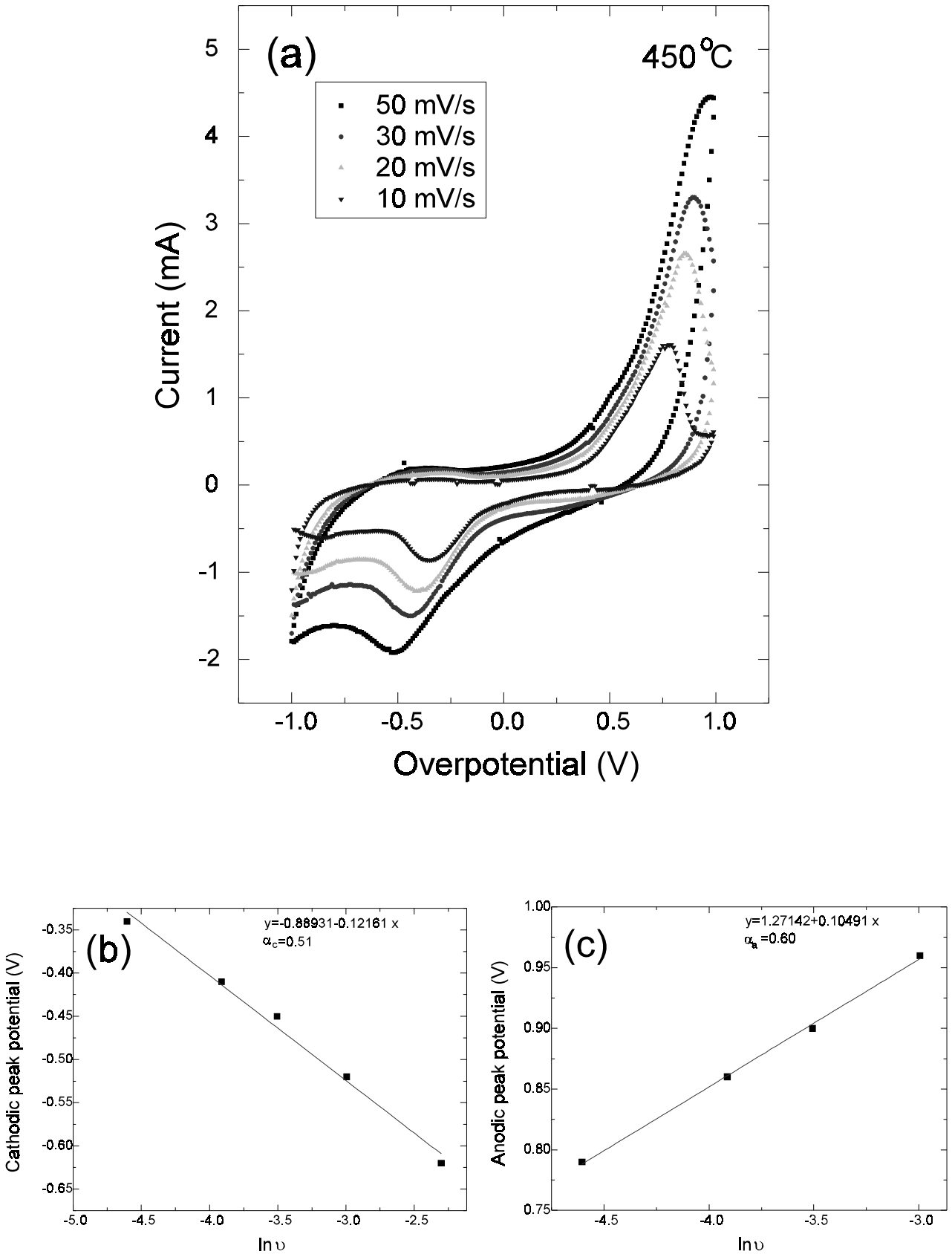

Fig. 52: (a) Cyclic voltammetric curves at 450°C, (b) cathodic coefficient, and (c) anodic coefficient.

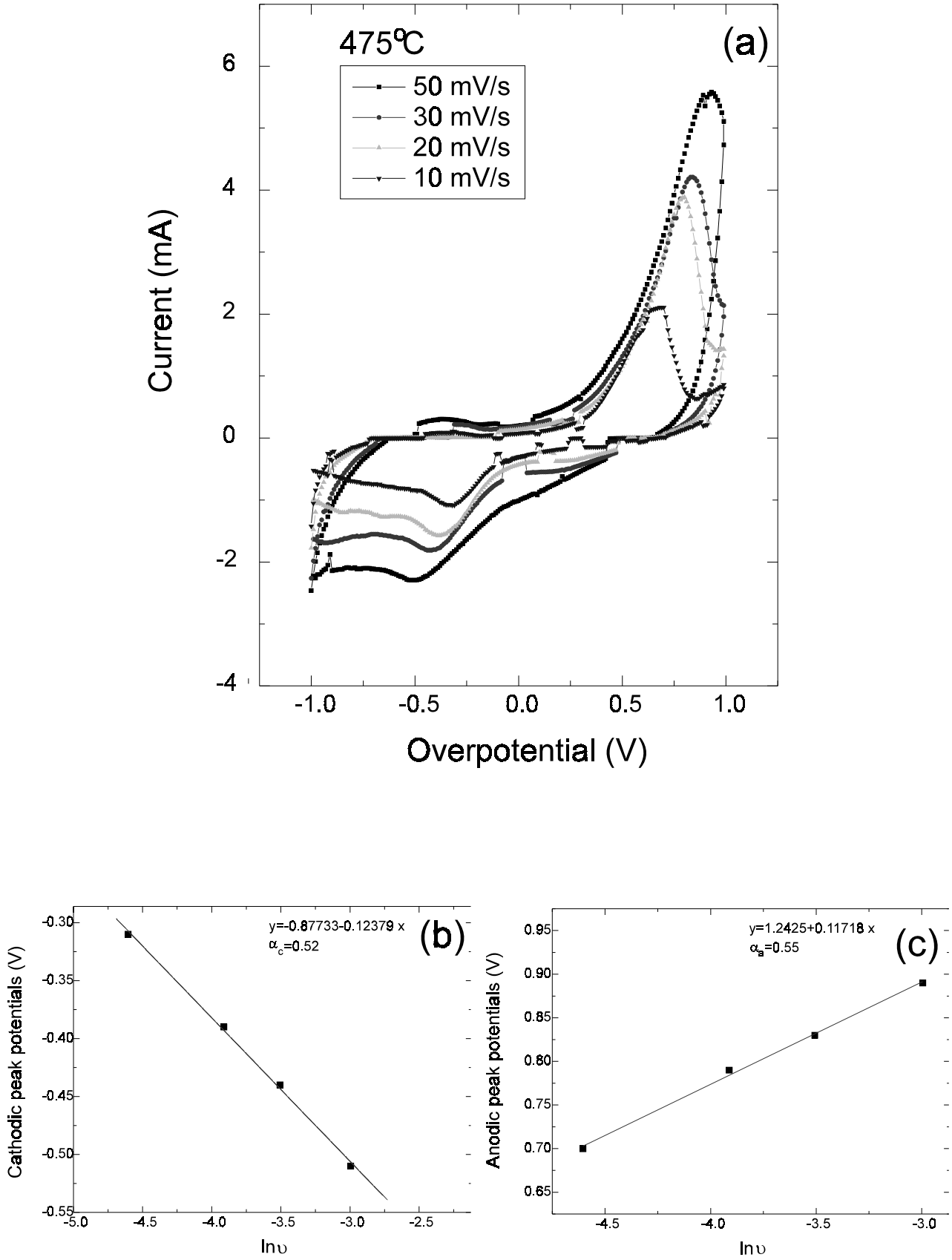

Fig. 53: (a) Cyclic voltammetric curves at 475°C, (b) cathodic coefficient, and (c) anodic coefficient.

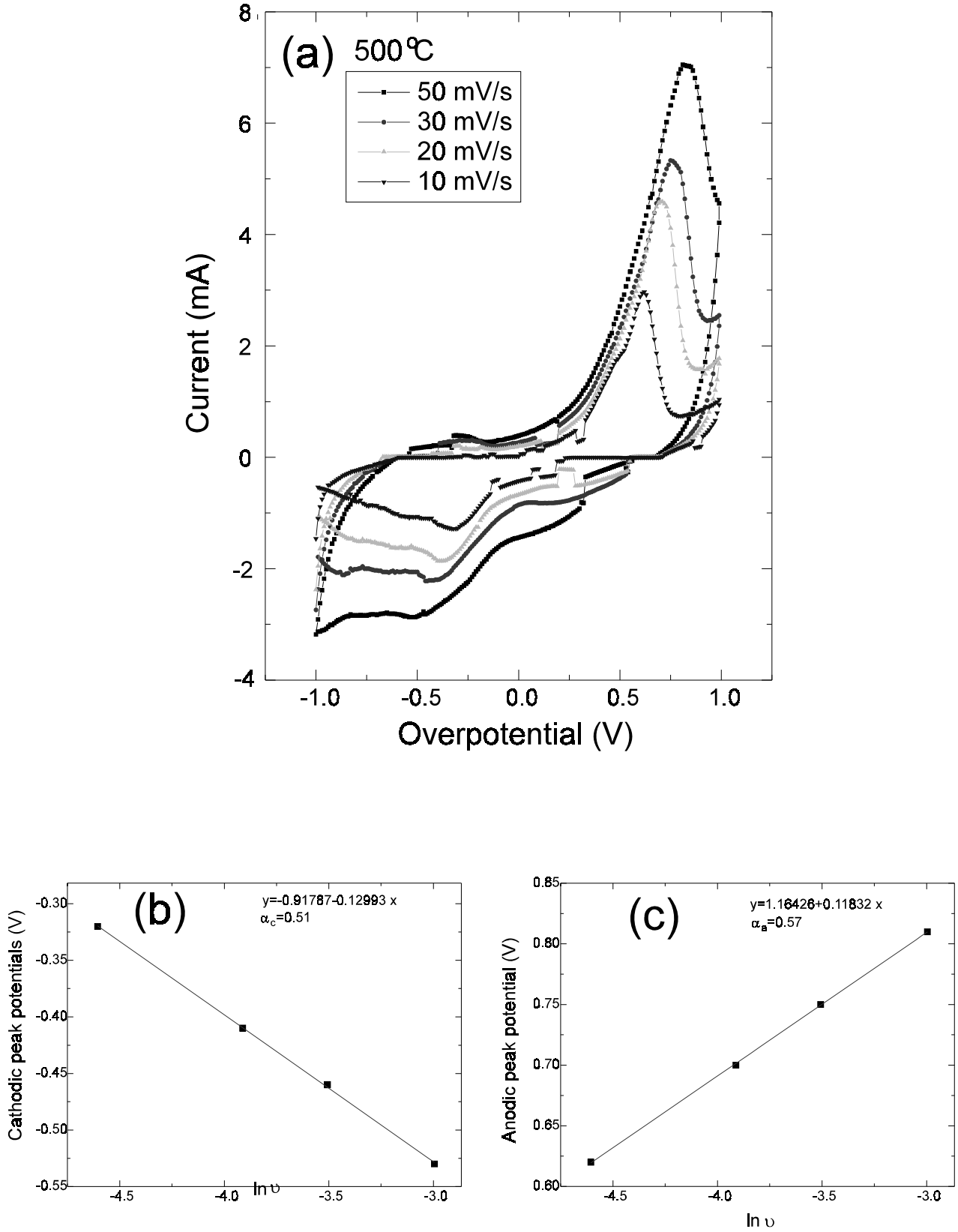

Fig. 54: (a) Cyclic voltammetric curves at 500°C, (b) cathodic coefficient, and (c) anodic coefficient.

Table 5. Comparison of the Cathodic and Anodic Transfer Coefficients from the Two Stages

PEVD Stage	Stage I			Stage II
Temperature	450°C	475°C	500°C	550°C
α_c	0.51	0.52	0.51	0.63
α_a	0.60	0.55	0.57	1

at the working electrode. A PEVD process improves the solid electrolyte/electrode interface.

Spectra at Higher Temperatures

The cyclic voltammograms for stage I PEVD reactions at higher temperatures are more complicated. The voltammograms for various sweep rates at 525 and 550°C are reported in Figures 55 and 56, respectively. Two pairs of peaks (labeled M and N for cathodic peaks, and M' and N' for anodic peaks) are distinguishable. Thus, extra PEVD reaction rate-limiting steps must be involved under these conditions.

Generally speaking, the cathodic and anodic peaks exist as a pair, and each pair of peaks represents a redox reaction. The second pair of peaks could be due to an additional redox reaction other than the one in Eqn. 90. However, a solid electrochemical system is usually very selective to only one mobile ionic species, which undergoes the charge transfer reaction. Previous investigation has found that double peaks could also result from different potential states in redox reactions for ionic species with higher valence.[82,111] For instance, during oxygen reduction, the oxygen has to obtain an electron twice to reduce to O^{2-}. In the current case, sodium ion is single valent. It is not likely to have two redox reaction potential states. Moreover, the shapes of the M peaks are different from those of redox reactions.

According to fundamental cyclic voltammetry theory, a peak results when an overpotential related rate-limiting step switches to another rate-limiting step. In the case of the N peaks, the PEVD reaction rate-limiting step switches from Step 1 to Step 4. As has been discussed previously, the diffusion of charged particles through the PEVD product is also a working electrode overpotential related step. Thus, it is possible that M peaks are due to a switch from Step 2a to Step 1 at certain working electrode overpotentials. Thus, a resistance overpotential is dominant at low working electrode overpotential. As a result, the PEVD current permitted by the charge transfer reaction is limited by the transport of Na^+ across the product under those PEVD conditions. It was also found that the repeatability of the M peaks in voltammograms was poor. The M peaks in these voltammograms do not have the same shape, peak overpotential and peak current under the same experimental conditions. This is possibly because M peaks are very sensitive to geometric factors at the working electrode of stage I PEVD samples during each SECV scan.

As shown in Figure 56, the cathodic M peaks are broader than the anodic M' peaks. The reason is that the PEVD processes for decomposition and formation at the working electrode are different. The broader M peak could result from diffusion of Na^+ across the product to form Na_2CO_3 in two steps,

$$\text{First step: } Na^+ + CO_3^{2-} \rightarrow NaCO_3^- \quad (101)$$

$$\text{Second step: } Na^+ + NaCO_3^- \rightarrow Na_2CO_3 \quad (102)$$

When the process is limited by the diffusion of Na^+ inside the product, the first step will increase the electrochemical potential of the sodium ion at the surface of the PEVD product (location (III)). Thus, the thermodynamic driving force will decrease causing further transport of Na^+ in the product to pursue the

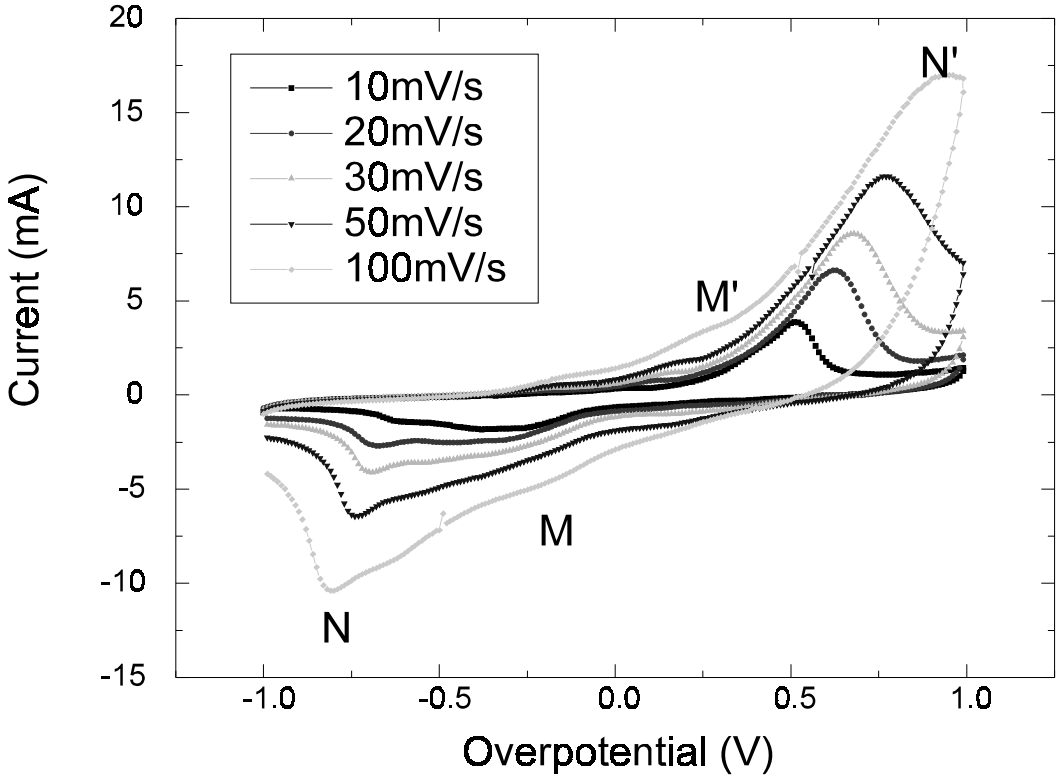

Fig. 55: Cyclic voltametric curves at 525°C.

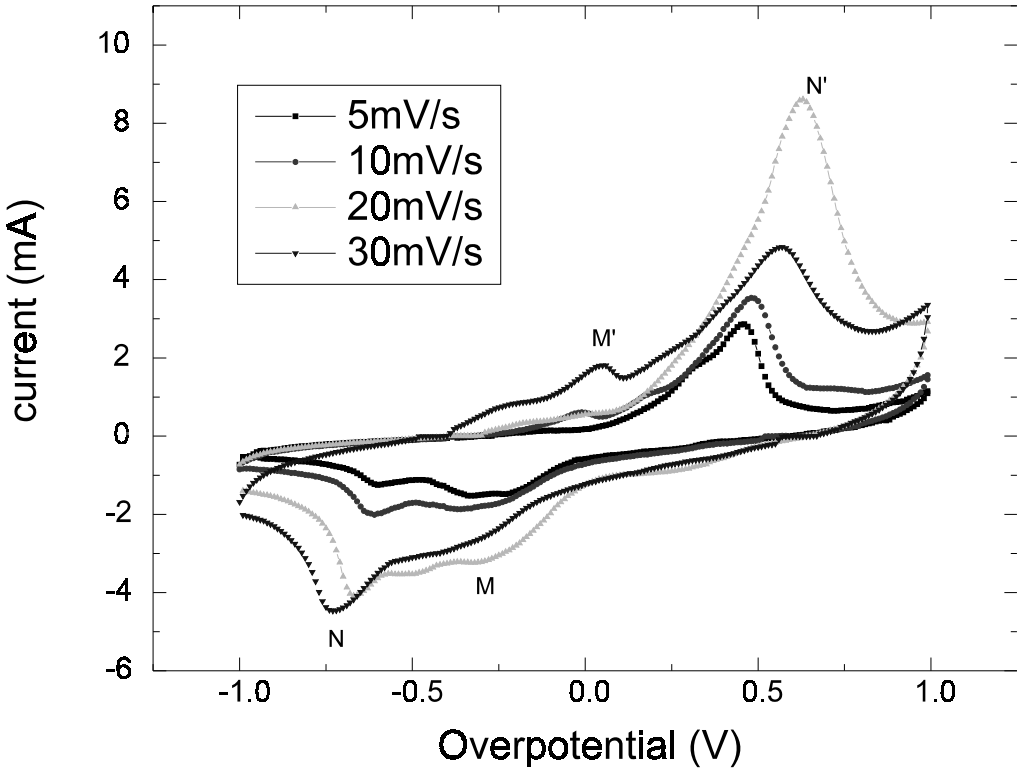

Fig. 56: Cyclic voltammetric curves at 550°C.

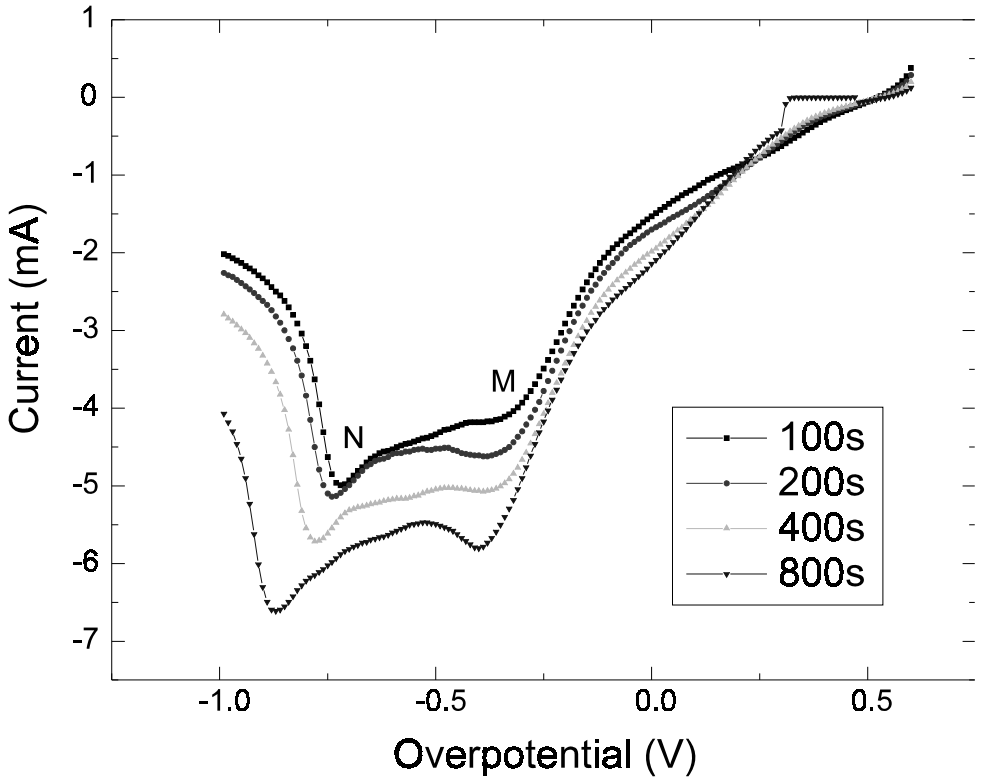

Fig. 57: The effect of holding time on cyclic voltammetric curves during the first stage of PEVD at 550°C.

second step. Two cathodic M peaks can indeed sometimes be resolved. The decomposition of Na_2CO_3 is a one step process.

$$Na_2CO_3 \rightarrow 2\ Na^+ + CO_3^{2-} \qquad (103)$$

The cause of the M peaks has been further confirmed with an SECV holding technique at 550°C. In this experiment, the V_{WR} was held at 600 mV for various times, then scanned negatively to -1000 mV at the cathodic side. The results are plotted in Figure 57. The longer the holding time, the more significant the M peaks vs. N peaks. As more decomposition of the product occurs, the Na^+ diffusion length decreases, and the PEVD current is less limited by Step 2a. The negative shift of the N peaks is a feature that has been discussed previously for a stage II PEVD sample.

Summary

Although SECV studies are not able to give quantitative results for stage I PEVD behavior, PEVD reaction rate-limiting steps are qualitatively revealed. At lower temperatures and working electrode overpotentials, the PEVD reaction rate-limiting step is Step 1, the charge transfer reaction. At higher temperatures and lower working electrode overpotentials, the rate-limiting step is Step 2a, the diffusion of Na^+ across the product. At higher working electrode overpotentials for all temperatures, the rate-limiting step is Step 4, the surface diffusion of neutral reactants.

Conclusions

During the last 20 years, we have witnessed the active development of solid state ionics associated with the study of ionic and electronic processes in solid state ionic materials. The investigation of energy converting applications to use ionic transport in solid state ionic materials is booming. The present availability of numerous types of solid state ionic materials allows for electrochemical reactions to be carried

out with the surrounding vapor phase to form products of interest. This recent interfacing of vapor deposition and electrochemistry has led to the development of polarized electrochemical vapor deposition (PEVD) during the course of the current study.

The significance of this new technique is that PEVD applies solid state ionic techniques to modify a widely accepted CVD technique under controlled conditions in a solid electrochemical cell. Compared with other solid state ionic techniques, PEVD takes advantage not only of energy transformation but also material transport itself during ionic and electronic transport in solids to form desired products. Thus, PEVD has brought Wagner's electrochemical tarnishing theory to a new field for making man-made products under well-defined thermodynamic and kinetic conditions.

PEVD holds promise of a wide range of potential applications for solid state ionic devices. During the course of the current research, PEVD has been applied for fabricating two types of solid state ionic devices, i.e., potentiometric gaseous oxide sensors and solid oxide fuel cells. These applications of PEVD have shown that PEVD is the most suitable technique to improve solid electrode / electrolyte contact and, consequently, the performance of those solid state ionic devices. Furthermore, the "active" use of material transport through the solid by PEVD offers more interesting opportunities not only for forming deposition products but also for studying the physical properties of the products under well-defined thermodynamic and kinetic conditions.

It has been more than 60 years since Wagner's electrochemical tarnishing theory was developed. Finally, the two parallel suggestions of material transport and energy transformation in the theory are interconnected, and newly developed PEVD will make solid state ionic devices better to serve today's ever-growing energy and environmental demands.

References

1. C. Wagner, *Z. Phys. Chem.*, Vol.B21, 1933, p.25.
2. T. Takahashi, *Superionic Solids and Solid Electrolytes*, *Materials Sciences Series*, A.L. Laskar and S. Chandra, eds, Academic Press, New York, 1989, p.1.
3. E.Z. Tang and T.H. Etsell, *Solid State Ionics*, Vol.91, 1996, p.213.
4. J. Hladik, *Physics of Electrolytes*, J. Hladik, ed, Academic Press, London, U.K., 1972, p.35.
5. A.O. Isenberg, *Proceedings of Symp. on Electrode Materials and Processes for Energy Conversion and Storage*, Electrochemical Soc., Princeton, NJ, Vol.77-6, 1977, p.572.
6. A. O. Isenberg, *Solid State Ionics*, Vol.3-4, 1981, p.431.
7. E.Z. Tang, T. H. Etsell, and D.G. Ivey, *High Temperature Materials and Processes*, Vol.19, 2000, p.25.
8. W.L. Worrell and J. Hladik, *Physics of Electrolytes*, J. Hladik, ed, Academic Press, London, U.K., 1972, p.747.
9. O. Tillement, *Solid State Ionics*, Vol.68 ,1994, p.9.
10. A.J. de Bethune, *Journal Electrochem. Soc.*, Vol.102, 1955, p.288.
11. D.O. Raleigh, *Proceedings of Electrode Processes in Solid State Ionics*, NATO Adv. Study Inst. Ser. C, Ajaccio, Corsica, M. Kleitz and J. Dupuy, eds., D. Reidel, Dordrecht/Boston, 1975, p.119.
12. H. Gerisher, *Proceedings of Electrode Processes in Solid State Ionics*, NATO Adv. Study Inst. Ser. C, Ajaccio, Corsica, M. Kleitz and J. Dupuy, eds., D. Reidel, Dordrecht/Boston, 1975, p.277.
13. C. Ilschner-Gensch and C. Wagner, *Journal Electrochem. Soc.,* Vol.105, 1958, p.198.
14. R.A. Rapp and D.A. Shores, *Physicochemical Measurements in Metals Research*, R.A. Rapp, ed., Interscience, New York, Vol.4, 1970, p.123.
15. N.B. Pilling and R.E. Bedworth, *Journal Inst. Met.*, Vol.29, 1923, p.529.
16. G. Tammann, *Z. Anorg. Chem.,* Vol.111, 1920, p.78.
17. W. Gopel, *Sensors and Actuators B*, Vol.18-19, 1994, p.1.
18. F. Forlani, *Sensors and Actuators B*, Vol.3, 1991, p.165.

19. M.J. Madou and S.R. Morrison, *Chemical Sensing with Solid State Devices* , Academic Press, Inc., Boston, 1989.
20. W. Gopel, *Sensors and Actuators*, Vol.16, 1989, p.167.
21. W. Weppner, *Sensors and Actuators*, Vol.12, 1987, p.107.
22. M. Gauthier and A. Chamberland, *Journal Electrochem. Soc.*, Vol.124, 1977, p.1579.
23. M. Gauthier, A. Chamberland, A. Belanger, and M. Poirier, *Journal Electrochem. Soc.*, Vol.124, 1977, p.1584.
24. W. L. Worrell and Q.G. Liu, *Sensors and Actuators*, Vol.2, 1982, p.385.
25. K. T.Jacob and D.B. Rao, *Journal Electrochem. Soc.*, Vol. 126, 1979, p.1842.
26. G. Adachi and N. Imanaka, *Chemical Sensor Technology*, Yamazoe, et al. eds., Kodansha Ltd., Tokyo and Elsevier, Amsterdam, Vol.3, 1991, p.131.
27. R. Cote, C. W. Bale, and M. Gauthier, *Journal Electrochem. Soc.*, Vol.131, 1984, p.63.
28. Y. Saito, K. Kobayashi, and T. Maruyama, *Solid State Ionics*, Vol.3-4, 1981, p.393.
29. Y. Saito, T. Murayama, and K. Kobayashi, *Solid State Ionics*, Vol.14, 1984, p.265.
30. Y. Saito,T. Murayama, Y. Matsumoto, K. Kobayashi, and Y. Yano, *Solid State Ionics*, Vol.14, 1984, p.273.
31. W. Weppner, German Patent DF 2926172 C2, 1979.
32. Y. Shimizu, Y. Okamoto, S. Yao, N. Miura, and N. Yamazoe, *Denki Kagaku*, Vol.59, 1991, p. 465.
33. R. Akila and K.T. Jacob, *Sensors and Actuators*, Vol.16, 1989, p.311.
34. N. Miura,S. Yao,Y. Shimizu, and N. Yamazoe, *Sensors and Actuators* B, Vol.13-14, 1993, p.387.
35. S. Yao, S. Hosohara, Y. Shimizu, N. Miura, H. Hutata, and N. Yamazoe, *Chem. Lett.*, Vol.1991, 1991, p.2069.
36. S. Yao,Y. Shimizu, N. Miura, and N. Yamazoe, *Chem. Lett.*, Vol.1992, 1992, p.587.
37. T. Maruyama, S. Sasaki, and Y. Saito, *Solid State Ionics*, Vol.23, 1987, p.107.
38. N. Yamazoe and N. Miura, *IEEE Transactions on Components, Packaging, and Manufacturing Technology*, Vol.18(A), 1995, p.252.
39. G. Hotzel and W. Weppner, *Proc. 6th Riso-Internat. Symp. on Transport-Structure Relations in Fast Ion and Mixed Conductors,* Riso Natl. Lab., Roskilde, Denmark, 1985, p. 401.
40. N. Yamazoe and N. Miura, *Sensors and Actuators B*, Vol. 20, 1994, p.95.
41. N. Miura, S. Yao, Y. Shimizu, and N. Yamazoe, *Journal Electrochem. Soc.*, Vol.139, 1992, p.1384.
42. W.F. Chu, D. Fischer, H. Erdmann, M. Ilgenstein, H. Koppen, and V. Leonhard, *Solid State Ionics*, Vol.53-56, 1992, p.80.
43. V. Leonhard, D. Fischer, H. Erdmann, M. Ilgenstein and H. Koppen, *Sensors and Actuators B*, Vol.13-14, 1993, p.530.
44. E.Z. Tang, T.H. Etsell, and D.G. Ivey, *Sensors and Actuators B*, Vol.45, 1997, p.131.
45. W. Gopel, *Progress in Surface Science*, Vol.20, 1985, p.9.
46. D.M. Haaland, *J. Electrochem. Soc.*, Vol.127, 1980, p.796.
47. T. Maruyama, X. Ye, and Y. Saito, *Solid State Ionics*, Vol.24, 1987, p.281.
48. T. Maruyama, *Materials Sci. and Eng. A*, Vol.146, 1991, p.81.
49. N. Miura, S. Yao, Y. Shimizu, and N. Yamazoe, *Sensors and Actuators B*, Vol.9, 1992, p.165.
50. E.Z. Tang, T.H. Etsell, and D.G. Ivey, Ceramic Sensors III, PV96-27, *The Electrochemical Society Proceeding Series*, The Electrochemical Society, Pennington, NJ, 1996, p.131.
51. J. Fouletier, H. Seinera, and M. Kleitz, *Journal Appl. Electrochem.*, Vol.4, 1974, p.305.
52. A. Negishi, K. Nozaki, and T. Ozawa, *Solid State Ionics*, Vol.3-4, 1981, p. 443.
53. T. Inoue, K. Eguchi, T. Setoguchi, and H. Arai, *Solid State Ionics*, Vol.40-41, 1990, p.407.
54. T. Kawada, N. Sakai, H. Yokokawa, M. Dokiya, M. Mori, and T. Iwata, *Solid State Ionics*, Vol.40-41, 1990, p.402.
55. M. Suzuki, H. Sasaki, S. Otoshi, A. Kajimura, and M. Ippommatsu, *Solid*

State Ionics, Vol.62, 1993, p.125.
56. D.W. Dees, T.D. Claar, T.E. Easler, D.C. Fee, and F.C. Mrazek, *Journal Electrochem. Soc.*, Vol.134, 1987, p.2141.
57. S. Murakami, Y. Akiyama, N. Ishida, Y. Miyake, M. Nishida, Y. Itoh, T. Saito, and N. Furukawa, *Denki Kagaku*, Vol.59, 1991, p.320.
58. T. Setogichi, K. Okamoto, K. Eguchi, and H. Arai, *Journal Electrochem. Soc.*, Vol.139, 1992, p.2875.
59. N.M. Sammes, M.S. Brown and R. Ratnaraj, *Journal Mat. Sci. Letters*, Vol.13, 1994, p.1124.
60. A.O. Isenberg, US Patent, 4,582,766, April 15, 1986.
61. A.O. Isenberg, US Patent, 4,597,170 (July 1, 1986).
62. Z. Ogumi, T. Ioroi, Y. Uchimoto, Z. Takehara, T. Ogawa and K. Toyama, *J. Am. Ceram. Soc.*, Vol.78, 1995, p.593.
63. U.B. Pal and S.C. Singhal, *Journal Electrochem. Soc.*, Vol.137, 1990, p.2937.
64. M.F. Carolan and J.N. Michaels, *Solid State Ionics*, Vol.37, 1990, p.189.
65. M.F. Carolan and J.N. Michaels, *Solid State Ionics*, Vol.37, 1990, p.197.
66. S.C. Singhal, *Proc. Second Internat. Symp. on SOFC*, Athens, Greece, F. Grosz, P. Zegers, S.C. Singhal, and O. Yamamoto, eds., Commission of the European Communities, Luxembourg, 1991, p.25.
67. S. Sridhar and U.B. Pal, *Powder Technology*, Vol.88, 1996, p.173.
68. R.E. Jensen, US Patent 4, 971, 830 1990.
69. T.E. Easler, B.K. Flandermeyer, T.D. Claar, D.E. Busch, R.J. Fousek, J.J. Picciolo, and R.B. Poppel, Abstracts of the 1986 Fuel Cell Seminar, Tucson, AZ, 1986, p.72.
70. S. Murakami, N. Akiyama, N. Ishida, T. Yasuo, T. Saito, and N. Furukawa, *Proceedings of Second Internat. Symp. on SOFC*, Athens, Greece, F. Grosz, P. Zegers, S.C. Singhal, and O. Yamamoto, eds., Commision of European Communities, Luxembourg, 1991, p.561.
71. J. Weissbart and R. Ruka, *Fuel Cells*, G.J. Young, ed., Reinhold, New York, Vol.2, 1963, p.37.
72. D. W. Dees, U. Balachandran, S.E. Dorris, J.J. Heiberger, C.C. McPheeters, and J.J. Picciolo, *Proc. Symp. on Fuel Cells*, R.E. White and A.J. Appleby, eds., The Electrochemical Society, Pennington, NJ, 1989, p.130.
73. A.O. Isenberg, Abstracts of the 1982 Fuel Cell Seminar, Newport Beach, CA., 1982, p.154.
74. T. Kawada, N. Sakai, H. Yokokawa, M. Dokiya, M. Mori, and T. Iwata, *Solid State Ionics*, Vol.40-41, 1990, p.402.
75. M. Doklya, N. Sakai, T. Kawada, and H. Yokokawa, *Proceedings of 1989 Intersociety Energy Conversion Engineering Conference*, Vol.3, 1989, p.1547.
76. Y. Balachandran, S.E. Dorris, J.J. Picciola, R.B. Poeppel, C.C. McPheeters, and N.Q. Minh, *Proceedings of 1989 Intersociety Energy Conversion Engineering Conference*, Vol.3, 1989, p.1553.
77. K. Eguchi, T. Setoguchi, H. Itoh, and H. Arai, *Extended Abstracts of 40th Meeting of the International Society of Electrochemistry*, Kyoto, Japan, 1989, p.362.
78. L.G.J. de Haart, Y.S. Lin, K.J. de Vries, and A.J. Burggraaf, *Journal Eur. Ceram. Soc.*, Vol.8, 1991, p.59.
79. J.P. Dekker, V.E.J. van Dieten, and J. Schoonman, *Solid State Ionics*, Vol.51 1992, p.143.
80. E.Z. Tang, D.G. Ivey, and T.H. Etsell, *Micron*, Vol.29, 1998, p.251.
81. K.J. Vetter, *Electrochemical Kinetics*, Theoretical and Experimental Aspects, Academic Press, New York, 1967.
82. C.G. Vayenas, S. Bebelis, I.V. Yentekakis, and H.G. Lintz, *Catalysis Today*, Vol.11, 1992, p.303.
83. S. Bebelis and C.G. Vayenas, *Journal Catal.*, Vol.118, 1989, p.125.
84. S. Neophytides and C.G. Vayenas, *Journal Catal.*, Vol.118, 1989, p.147.
85. C.G. Vayenas and S. Neophytides, *Journal Catal.*, Vol.127, 1991, p.645.
86. W.A. Caspari, *Z. Physik. Chem.*, Vol.30, 1899, p.89.
87. G. Hotzel and W. Weppner, *Solid State Ionics*, Vol.18-19, 1980, p.1223.

88. T. Erdey-Gruz and M. Volmer, *Z. Physik. Chem*. Vol.150A, 1930, p.203.
89. J.O'M. Bockris and A.K.N. Reddy, *Modern Electrochemistry*, Plenum Press, New York, Vol.2, 1970.
90. I.N. Stranski, *Z. Physik. Chem*., Vol.136 1928, p.259.
91. C.G. Vayenas, S. Bebelis, and S. Ladas, *Nature*, London, Vol.343, 1990, p.625.
92. S. Ladas, S. Bebelis, and C.G. Vayenas, *Surf. Sci*., Vol.251-252, 1991, p.1062.
93. D.Y. Wang and A.S. Nowick, *Journal Electrochem. Soc*., Vol.126, 1979, p.1155.
94. D.Y. Wang and A.S. Nowick, *Journal Electrochem. Soc*., Vol.128, 1981, p.55.
95. G. Couturier, J. Salardenne, C. Sribi, and M. Rosso, *Solid State Ionics*, Vol.9-10, 1983, p.699.
96. C.G. Vayenas, S. Bebelis, and S. Neophytides, *Journal Phys. Chem*., Vol.92, 1988, p.5083.
97. N.L. Robertson and J.N. Michaels, *Journal Electrochem. Soc*., Vol.137, 1990, p.129.
98. D.Y. Wang and A.S. Nowick, *Journal Electrochem. Soc*., Vol.126, 1979, p.1166.
99. A.J. Bard and L.R. Faulkner, *Electrochemical Methods: Fundamentals and Applications*, Wiley, New York, 1980.
100. B. Beden, F. Kadirgan, C. Lamy, and J.M. Leger, *Journal Electroanal. Chem*., Vol.142, 1982, p.171.
101. A. Papoutsis, J. M. Leger, and C. Lamy, *Journal Electroanal. Chem*., Vol.234, 1987, p.315.
102. E. Lamy-Pitara, L. Lghouzouani, Y. Tainon, and J. Barbier, *Journal Electroanal. Chem*., Vol.260, 1989, p.157.
103. C.G. Vayenas, A. Ioannides, and S. Bebelis, *Journal Catal*., Vol.129, 1991, p.67.
104. P. Fabry and M. Kleitz, *Journal Electrochem. Soc*., Vol.126, 1979, p.2183.
105. L.J. Olmer, J.C. Viguie, and E.J.L. Schouler, *Solid State Ionics*, Vol.7, 1982, p.23.
106. E.J.L. Schouler and M. Kleitz, *Journal Electrochem. Soc*., Vol.134, 1987, p.1045.
107. A. Sevick, *Collect. Czech. Chem. Commun*., Vol.13, 1948, p.349.
108. J.E.B. Randles, Trans. *Faraday Soc*., Vol.44, 1948, p.327.
109. P. Delahay, *New Instrumental Methods in Electrochemistry*, Interscience, New York, 1954.
110. S. Srinivasan and E. Gileadi, *Electrochim. Acta*, Vol.11, 1966, p.321.
111. Y. Jiang, A. Kaloyannis, and C.G. Vayenas, *Electrochim. Acta*, Vol.38, 1993, p.2533.

Chemical Vapor Deposition
Jong-Hee Park, T.S. Sudarshan, editors, p183-203
DOI:10.1361/chvd2001p183

Chapter 6

Chemical Vapor Infiltration: Optimization of Processing Conditions

Stewart K. Griffiths and Robert H. Nilson
Sandia National Laboratories
Livermore, California 94551-0969

Abstract

A combined analytical and numerical method is employed to optimize process conditions for composites fiber coating by chemical vapor infiltration (CVI). For a first-order deposition reaction, the optimum pressure yielding the maximum deposition rate at a preform center is obtained in closed form and is found to depend only on the activation energy of the deposition reaction, the characteristic pore size, and properties of the reactant and product gases. It does not depend on the preform specific surface area, effective diffusivity or preform thickness, nor on the gas-phase yield of the deposition reaction. Further, this optimum pressure is unaltered by the additional constraint of prescribed deposition uniformity. Optimum temperatures are obtained using an analytical expression for the optimum value along with numerical solutions to the governing transport equations. These solutions account for both diffusive and advective transport, as well as both ordinary and Knudsen diffusion. Sample calculations are presented for coating preform fibers with boron nitride.

Introduction

Chemical vapor infiltration (CVI) is widely used in advanced composites manufacturing to deposit carbon, silicon carbide, boron nitride and other refractory materials within porous fiber preforms.[1-3] Because vapor phase reactants are deposited on solid fiber surfaces, CVI is clearly a special case of chemical vapor deposition (CVD). The distinguishing feature of CVI is that reactant gases are intended to infiltrate a permeable medium, in part at least, prior to

deposition. Of course deposition also occurs, and is often greatest, on external surfaces where reactant concentrations are greatest.

CVI processes, employing a variety of chemistries, are usually performed in large batch furnaces at reduced pressures and elevated temperatures. In-furnace times typically range from a few hours to even weeks, resulting in costs ranging from $100 to over $1000 per kg for high-temperature high-performance composites.[4] Even under ideal conditions the processing time for these materials represents a significant fraction of the finished product cost, so optimizing processes conditions is important. In addition to the obvious benefit of lower product costs, lower prices are important to increasing the commercial applications for these materials, now largely limited to military and aerospace uses.

The most common application of CVI in composites manufacturing is in densifying the preform. In this use, reactant gases are employed to deposit solids within a fiber preform with the intent of filling all or most of the inter-fiber void. These solids bind the fibers together and form the continuous matrix of the composite. A second common use of CVI is in coating the preform fibers prior to densification. These coatings serve as high- temperature oxidation inhibitors and as debonding agents to permit limited motion between the fibers and the composite matrix. Such motion is desirable as it improves the mechanical properties of a composite.

In either densification or fiber coating, it is generally desirable to minimize processing time subject to constraints on the required coating thickness or degree of densification. In fiber coating processes it is sometimes sufficient that the coating thickness be everywhere greater than a prescribed minimum. However, it is usually desirable that the coating thickness or densification be relatively uniform through the part thickness. This ensures uniformity of mechanical properties and is often required to produce high strength. Uniformity is particularly critical in densification processes intended to fill most of the open porosity, because excess surface deposition may seal the external surface before the center reaches the required minimum density.

These conflicting goals of minimizing processing time while maintaining deposition uniformity can only be met by careful selection of processing conditions. For example, an increase in temperature will increase deposition rates and reduce process time, but only at the expense of reduced uniformity. This is because higher deposition rates cause greater depletion of reactant gases diffusing toward the preform center. As a result, reactant concentrations and deposition rates at the center will be smaller than those at the surface. This non-uniformity may be reduced by reducing the operating pressure, as this tends to lower reaction rates while not diminishing the diffusive mass flux. However, this pressure reduction strategy becomes counter-productive when the mean free path falls below the characteristic microscale dimension, because diffusion fluxes then fall with decreasing pressure. Thus, temperature, pressure, and preform microstructure are all important in determining the relative rates of species transport and chemical reaction.

In addition to process time and uniformity, other factors must be considered in selecting optimal conditions. As in any CVD process, a specific temperature range will usually be required to obtain a desired morphology of the deposited material. Specific process conditions may also be required either to induce or to inhibit certain gas-phase reactions, such as those involved in the production of necessary deposition precursors or those leading to undesirable gas-phase nucleation of particles. Here, we will present an optimization approach that can be used to maximize deposition rates subject to any of these constraints.

Mathematical modeling of the CVI process has been largely focused on the densification problem.[5-8] This is a difficult problem because the preform void fraction is altered significantly by the deposition process. The evolving microstructure strongly affects reactant transport through the preform, and so must be addressed in any meaningful analysis of densification. Because of this difficulty, most analyses of densification have employed numerical methods. Here we focus attention on the simpler problem of fiber coating. In this case, the microstructure may be considered invariant

through the deposition process, so long as the coating thickness is a small fraction of the original fiber size. Under this restriction, it is possible to derive analytical results that provide physical insights and scaling relationships not easily derived from numerical calculations.

The remainder of this article is devoted to mathematical modeling of the CVI fiber coating process. We begin by presenting the governing equations for one-dimensional transport and chemical reaction of a typical reactant or product species. The dimensionless parameters that control deposition uniformity are then derived, and the role of each is illustrated by presenting sample solutions to the governing equations. We then combine analytical and numerical methods to maximize the centerline deposition rate for CVI fiber coating processes involving a first-order deposition reaction. Two general expressions for the optimum pressure and optimum temperature are first derived using analytical methods. The optimum pressure is then obtained in closed form, while the optimum temperature is determined with the aid of numerical solutions to the governing diffusion and reaction equations.

These numerical solutions account for advective transport of the reactant gases, as well as both ordinary and Knudsen diffusion. Finally, we consider the influence on the optimum pressure of a constraint on the deposition uniformity. In this case, the optimum pressure maximizing centerline deposition rates is obtained in closed form using the method of Lagrange multipliers.

The results of this analysis are presented in a dimensionless form readily applicable to a range of preform thicknesses, fiber diameters, fiber volume fractions, and deposition chemistries. To illustrate the application of these results to a practical problem, the optimum process conditions are determined for a sample problem in which a boron nitride coating is deposited from boron trichloride and ammonia.

Governing Equations

To calculate centerline deposition rates, we consider the region within a preform, as shown in Figure 1. Diffusive and advective transport in the volume between fibers and the accompanying reactant depletion due to deposition on fiber surfaces are described by continuity equations for each gas-phase species, along with momentum and energy equations for the gas mixture. Here we consider one-dimensional transport in which species concentrations vary only with the transverse position through the preform thickness. Under this idealization, conservation of mass for a single reactive species may be written as

$$\frac{d}{dx}\left(\rho DD'\frac{df}{dx}\right)-\frac{d}{dx}(\rho uf)=S_{s_v} \tag{1}$$

where x is the distance from the preform center, ρ is the gas molar density, f is the reactive species mole fraction, D is the effective coefficient of binary diffusion for the reactive species, D' is the dimensionless effective diffusivity of the porous preform, and u is the local molar-average fluid speed. The preform specific surface area, s_v is the fiber surface area per unit volume, and S is the surface deposition rate.

Again assuming one-dimensional transport, continuity for the combined reactive and inert species can be expressed as

$$\frac{d}{dx}(\rho u)=\psi S_{s_v} \tag{2}$$

where the parameter ψ is the net molar yield of gaseous products per mole of reactant; that is, the molar ratio of gaseous products less reactants to reactants. By this definition, values of the parameter are limited to $\psi \geq -1$ because we are considering here only one reactive species. The limiting value of $\psi = -1$ corresponds to a simple single-species deposition reaction yielding solids but no gas-phase products.

If the deposition process is a first-order reaction having Arrhenius temperature dependence, the surface reaction rate, S, can be expressed as the product of the surface impingement rate and a reaction probability, ϕ. In terms of the gas molar density and reactant mole fraction this is

$$S=\frac{\bar{v}}{4}\rho f\phi \text{ where } \phi = be^{-E_a/RT} \tag{3}$$

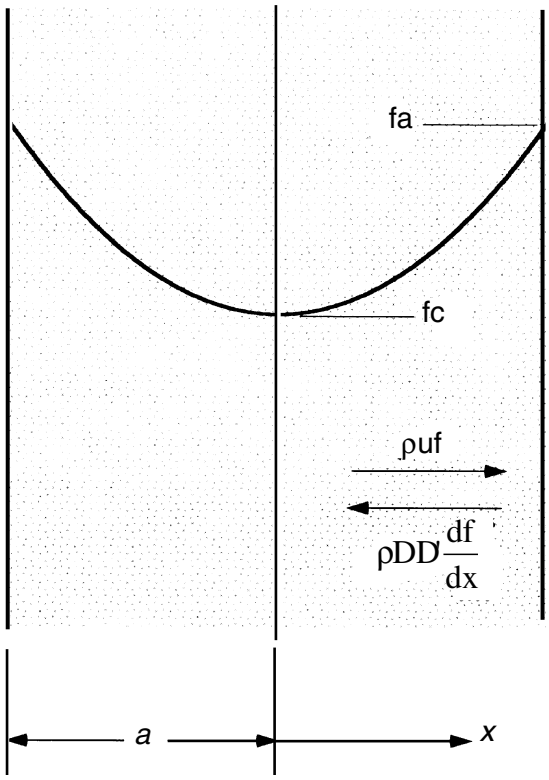

Fig. 1: Schematic cross-section of a porous fiber preform. Reactants diffuse from the preform surfaces toward the center, and are depleted by deposition on fiber surfaces.

The mean molecular speed, $\bar{\upsilon}$, of the reactive species is given by

$$\bar{\upsilon} = \left(\frac{8RT}{\pi m} \right)^{1/2} \tag{4}$$

where R is the ideal gas constant, T is the gas temperature, and m is the reactive species molecular weight. The parameters b and E_a are the surface reaction pre-exponential constant and the apparent activation energy, respectively.

The coefficient of diffusion in Eq.1 must account for both ordinary and Knudsen diffusion. At high gas densities, collisions of the reactive species with gas molecules are much more common than are collisions with fiber surfaces. In this limit, the diffusive flux of the reactive species is governed by ordinary diffusion. At sufficiently low pressures or sufficiently high temperatures, however, the mean free path of the reactive species becomes large relative to the size of the inter-fiber pores. In this limit, collisions of the reactive species with fiber surfaces are predominant, and the diffusive flux is controlled by Knudsen diffusion. To account for both of these conditions, the overall effective coefficient of binary diffusion for the reactive species can be approximated by the Bonsanquet interpolation formula,[9]

$$\frac{1}{D} = \frac{1}{D_m} + \frac{1}{D_{Kn}} \tag{5}$$

where D_m denotes the effective binary coefficient of ordinary diffusion for the reactive species in the gas mixture, and D_{Kn} denotes the

coefficient of Knudsen diffusion for the reactive species in the inter-fiber volume. Based on simple kinetic theory, Eq.5 may be rewritten as[10]

$$D = \frac{\bar{\upsilon}\lambda}{3}\frac{\alpha d}{d+\alpha\lambda} = \frac{\bar{\upsilon} d}{3}\frac{\alpha Kn}{1+\alpha Kn} \qquad (6)$$

where $\bar{\upsilon}$ is again the mean molecular speed of the reactive species, and $Kn = \lambda/d$ is the Knudsen number based on properties of the reactive species and the inter-fiber pore size. The effective mean free path for the reactive species alone is given by

$$\lambda = \frac{RT}{\sqrt{2}\pi N\sigma^2 p} \qquad (7)$$

where p is the total pressure, N is the Avogadro number, and σ is the molecular diameter of the reactive species.

The parameter α in Eq. 6 is the ratio of the effective binary coefficient of ordinary diffusion for the reactive species and the mixture of other void gases to the coefficient of ordinary self diffusion for the reactive species. As shown in the Appendix, this parameter depends only on the composition of the gas mixture and is independent of both the pressure and temperature for ideal gases. Thus for fixed gas composition, the parameter α is constant.

The continuity equations 1 and 2 must be accompanied by momentum and energy equations. In this analysis, we supplant the energy equations with an assumption that all gas species are at a uniform and constant temperature, T. Likewise, the momentum equation is replaced with an assumption that the pressure is uniform over the preform thickness.

The governing transport equations are closed using an ideal gas equation of state, $p = \rho RT$. Because both the pressure and temperature are uniform and constant, this relation requires that the gas molar density within the preform is also uniform and constant.

To complete the mathematical statement of the transport and deposition problem, boundary conditions must be specified for the reactive species fraction and fluid speed. The second-order equation governing the reactive species requires two conditions. One is imposed by symmetry, requiring that the gradient of the reactive species vanish at the origin. For the second we assume that the reactive species mole fraction is fixed at the preform surface.

$$\frac{df}{dx} = 0 \quad \text{at} \quad x = 0$$

$$f = f_a \quad \text{at} \quad x = a \qquad (8a,b)$$

In additon, the first-order equation governing the fluid speed requires a single boundary condition. Again this is obtained from a symmetry condition at the preform center,

$$u = 0 \text{ at } x = 0 \qquad (9)$$

requiring no flow into or out of the plane of symmetry.

To normalize the governing equations, we introduce a dimensionless position, $z = x/a$, and two dimensionless dependent variables, $f^* = f/f_a$ and $u^* = ua/DD'$. Note that the normalized velocity u^* is equivalent to a local Peclet number, indicating the relative magnitudes of the advective and diffusive fluxes of the reactive species. Applying these definitions to the transport equations yields the dimensionless governing equations

$$\frac{d}{dz}\left(\frac{df^*}{dz}\right) - \frac{d}{dz}\left(u^* f^*\right) +$$

$$\frac{1}{D}\frac{\partial D}{\partial f^*}\left(\frac{df^*}{dz} - u^* f^*\right)\frac{df^*}{dz} = \beta f^* \qquad (10)$$

for the reactive species, and

$$\frac{du^*}{dz} + \frac{u^*}{D}\frac{\partial D}{\partial f^*}\frac{df^*}{dz} = \psi^*\beta f^* \qquad (11)$$

for total species conservation. The constant β on the right of these equations is

$$\beta = \frac{S_{s\upsilon} a^2}{\rho DD' f} = \frac{3}{4}\frac{1+\alpha Kn}{\alpha Kn}\xi^2 e^{-E_a/RT} \qquad (12)$$

and the new parameters appearing here are the normalized preform thickness,

$$\xi^2 = \frac{bs_{\upsilon} a^2}{dD'} \qquad (13)$$

and the normalized reaction yield, $\psi^* = \psi f_a$. Boundary conditions for the normalized

variables follow from Eqs. 8 and 9 in the obvious manner.

The usual interpretation of the parameter β, referred to here as the deposition modulus, is that it is the square of the ratio of the characteristic time for diffusion to the characteristic time for surface deposition. In this view it is equivalent to the square of the Thiele modulus commonly appearing in analyses of porous-bed catalysis. Another useful interpretation of this parameter is that it is the ratio of two rates - the rate of deposition on the preform fiber surfaces, $S_{s_V}a$, to the maximum rate of diffusive transport, $\rho DD'f_a/a$. Thus when β is small, the actual rate of diffusive transport will be less than this maximum, and the mean gradient of the reactant fraction will be smaller than the maximum value of f_a/a. Under any of these interpretations, small values of β are associated with high uniformity of both the reactant fraction and coating thickness.

One additional relation can be obtained from Eqs.1 and 2 by integrating each equation once and combining the two results. This yields

$$u^* = \frac{\psi^*}{1+\psi^* f^*}\,\frac{df^*}{dz} \tag{14}$$

giving the normalized fluid speed in terms of the normalized reactant mole fraction and its derivative alone. This relation applies everywhere and so is useful in separating the coupled reactive species and total conservation equations. Substituting Eq.14 into either Eq.10 or 11 to eliminate u^* gives

$$\frac{d}{dz}\left(\frac{1}{1+\psi^* f^*}\,\frac{df^*}{dz}\right)+ \frac{1}{1+\psi^* f^*}\left(\frac{df^*}{dz}\right)^2 \frac{1}{D}\frac{\partial D}{\partial f^*} = \beta f^* \tag{15}$$

This species equation can now be solved without explicit knowledge of the local fluid speed. Fluid speeds can be computed after the fact from Eq. 14.

Equation 15 further provides useful insight into the relation between advective and diffusive fluxes of the reactive species. In dimensional form the advective flux at any position is ρuf , while the magnitude of the diffusive flux is $\rho DD'\,df/dx$. The local ratio of advective to diffusive fluxes is therefore given by

$$\frac{\rho uf}{\rho DD'df/dx} = \frac{u^* f^*}{df^*/dz} = \frac{\psi^* f^*}{1+\psi^* f^*} \approx \frac{\psi^*}{1+\psi^*} \tag{16}$$

where the approximate equality on the right is due to the fact that $f^* \approx 1$ when the deposition rate is fairly uniform over the preform thickness. Taking into account the signs for each flux, we see that the total flux of the reactive species differs from the diffusive flux by a factor of $1/(1 + \psi^* f^*)$. This is also apparent in Eq.15, where this term serves as an apparent diffusivity in what otherwise appears as a simple diffusion-reaction equation. When ψ^* is positive, the total flux of the reactive species is therefore reduced by the flow of gas toward the preform surface. When ψ^* is negative, the total flux is increased by flow toward the preform center. Note that the total flux is quite sensitive to the deposition chemistry- For a net production of only one mole of gas per mole of reactant, $\psi = 1$, the advective transport reduces the net flux of reactive species toward the preform center by up to a factor of two. As such, this advective inhibition of diffusion in the inter-fiber volume may significantly reduce deposition uniformity when the reactant fraction is large.

The derivative of the diffusivity on the right of Eq. 15 is the order of the diffusivity with respect to the reactant fraction. From Eq. 6 it is given by

$$\frac{1}{D}\frac{\partial D}{\partial f^*} = \frac{1}{1+\alpha Kn}\,\frac{1}{\alpha}\,\frac{\partial \alpha}{\partial f^*} \tag{17}$$

However, under a rather broad range of conditions its value is near zero. For a simple binary mixture of the reactant and a single diluent gas, $\partial\alpha/\partial f^*$ is exactly zero because binary diffusivities of low-pressure gases do not depend on species concentrations. Further, effective binary diffusivity of the reactant and a gas mixture also shows no dependence on the reactant fraction provided that the composition of the mixture does not vary with the reactant fraction. This of course is the case whenever the reactant fraction is small.

Under the simplifying assumption that the diffusivity is independent of the reactant fraction, the governing conservation Eq. 15 may be written as

$$\frac{d}{dz}\left(\frac{1}{1+\psi^* f^*}\frac{df^*}{dz}\right)=\beta f^* \tag{18}$$

In the limit $\psi^* \to 0$, Eqn. 18 possesses the well known solution[11]

$$f^* = \frac{\cosh\left(\sqrt{\beta}\, z\right)}{\cosh\left(\sqrt{\beta}\right)} \tag{19}$$

No such closed-form solution exists for the more general case $\psi^* \neq 0$. The general form of Eq. 18 can be solved for small values of the deposition modulus, β, though as we will see later, such solutions are not applicable to the problem of interest.[12] Fortunately, very accurate numerical solutions to the boundary value problem posed by Eqs. 8 and 18 are readily obtained using a numerical shooting technique.

Normalization of Variables

To solve generally for the optimum conditions and to plot resulting deposition rates, it is useful to rewrite the pressure, temperature, density and deposition rate in terms of normalized variables. For this purpose, the normalized values are defined as $p^* = p/p_R$, $T^* = T/T_R$, and $\rho^* = \rho/\rho_R$. Similarly, the normalized deposition rate and molecular speed are $S^* = S/S_R$ and, $\bar{\upsilon}^* = \bar{\upsilon}/\bar{\upsilon}_R$. The reference temperature, density and speed for a first-order deposition reaction are taken as

$$T_R = \frac{E_a}{R}, \quad \rho_R = \frac{\alpha}{\sqrt{2}\pi d N \sigma^2}, \quad \bar{\upsilon}_R = \left(\frac{8RT_R}{\pi m}\right)^{1/2} \tag{20}$$

We additionally require that the reference density, pressure and temperature satisfy the ideal gas equation of state, $p_R = \rho_R R T_R$.

The normalized density and normalized molecular speed follow directly from the reference values,

$$\rho^* = \frac{p^*}{T^*} = \frac{1}{\alpha Kn} \quad \text{and} \quad \bar{\upsilon}^* = \sqrt{T^*} \tag{21a,b}$$

Now taking $S_R = b\,\rho_R \bar{\upsilon}_R f_a/4$ as the reference deposition rate, the normalized deposition rate may be written as

$$S^* = \rho^* \bar{\upsilon}^* f^* e^{-1/T^*} = \frac{p^*}{\sqrt{T^*}} f^* e^{-1/T^*} \tag{22a,b}$$

A second useful normalization of the deposition rate is the simple modification of S^* given by $S^{**} = \xi^2 S^*$. Note that the normalized centerline deposition rate can be obtained from Eqs.22a, b simply by taking $f^* = f_c^*$ where f_c^* is the normalized reactant fraction at $z = 0$. The pressure, temperature and all other variables in these expressions are uniform over the preform thickness.

Finally, Eq.12 may be rewritten to obtain an expression for the deposition modulus that depends only on the normalized pressure, temperature and preform thickness.

$$\beta = \frac{3}{4}\frac{p^* + T^*}{T^*}\xi^2 e^{-1/T^*} \tag{23}$$

Thus, because, β and ψ^* are the only parameters in Eqs. 10 and 11, the normalized deposition rate at the preform center is uniquely determined by the normalized pressure, temperature, preform thickness and reaction yield.

Discussion of Deposition Rates

The deposition modulus at low temperatures is small, and the profile of the reactant concentration through the preform thickness is very uniform. In this case, the deposition rate at the center is nearly as large as that at the preform surface. With increasing temperature, the deposition modulus increases and the reactant concentration at the preform center falls. In this case, the centerline deposition rate becomes small relative to that at the surface. This behavior is illustrated in Figure 2. Here we see that the normalized centerline reactant fraction falls monotonically with increasing values of the deposition modulus. The centerline reactant fraction does not exhibit any sort of maximum, as is well known, and the deposition uniformity, $U = f_c^*$, falls smoothly as the deposition modulus is increased.

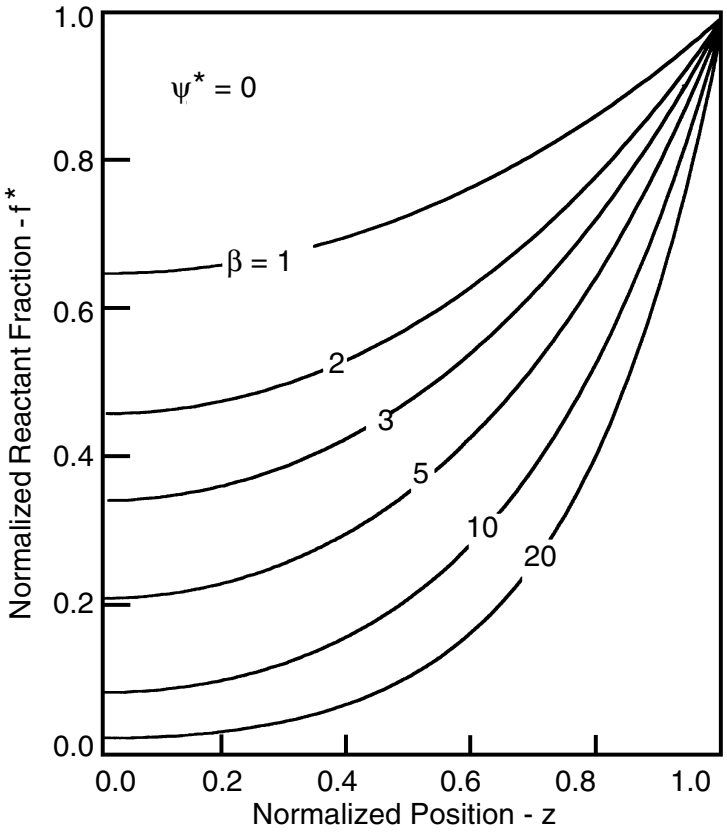

Fig. 2: Distribution of normalized reactant fraction through the preform thickness. Reactant fractions depend only on the dimensionless reaction yield, ψ^*, and the deposition modulus, β.

Although uniformity always falls with increasing values of the deposition modulus, this observation provides no insight into how the magnitude of the centerline deposition rate varies as the temperature and deposition modulus are increased. Low temperatures necessarily correspond to small deposition rates. As such, the deposition rate on the centerline is comparable to that at the surface when the temperature is low and the deposition modulus is small, but the rates everywhere within the preform, including the preform center, are small. In contrast, when the temperature is high and the deposition modulus is large, the deposition rate at the preform surface is large, but reactant depletion through the preform thickness is severe. In this case, the deposition rate at the preform center is very small compared to that at the surface, and the centerline deposition rate is again small. Between these extremes of temperature lies the maximum centerline deposition rate.

Figure 3 shows sample calculations of the normalized deposition rate through the preform thickness. We see that the deposition rate at the preform surface increases monotonically with increasing values of the deposition modulus. At the preform center, however, the deposition rate increases only up to a value of $\beta \approx 4$. At still larger values the centerline rate begins to fall, gradually approaching zero as $\beta \to \infty$. Thus for the conditions shown, the centerline deposition rate exhibits a maximum when the deposition modulus is about $\beta \approx 4$.

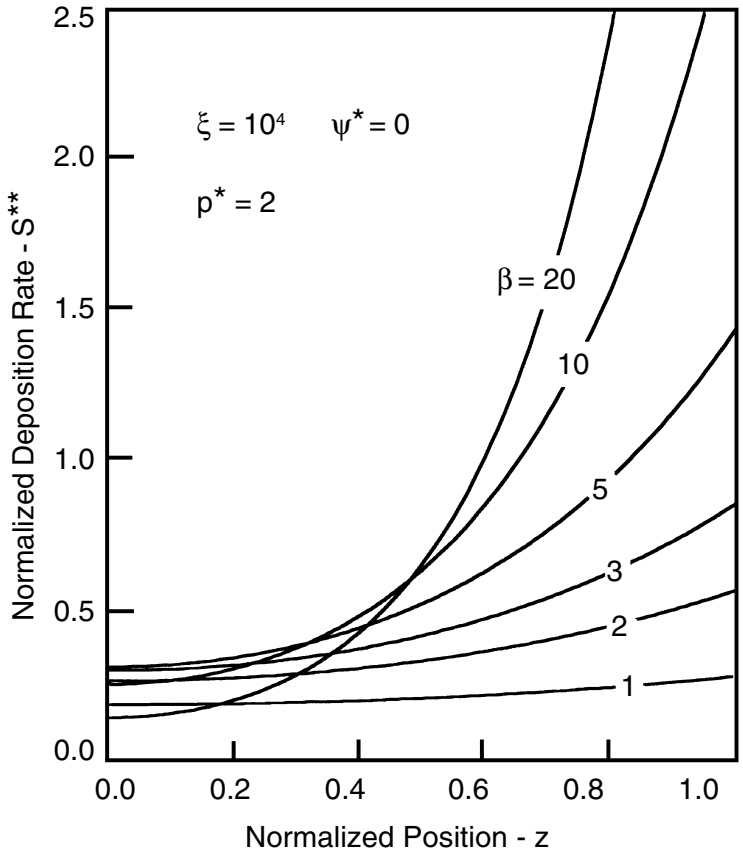

Fig. 3: Normalized deposition rate through preform thickness. Maximum centerline deposition rate occurs at a specific value of the deposition modulus, β; its value is $\beta \approx 4.453$ for the conditions shown.

The conditions giving rise to the maximum centerline deposition rate do not yield the maximum surface rate, nor do they yield the maximum mean deposition rate. This is shown in Figure 4, where the centerline, surface and mean normalized deposition rates are shown as a function of the normalized temperature. Here we see that both the surface and mean rates increase smoothly with increasing temperature and that only the centerline rate exhibits a maximum. For the conditions shown, this maximum occurs at $T^* \approx 0.0491$, corresponding to $\beta \approx 4.453$ and a deposition uniformity of $U = f_C^* \approx 0.239$.

Maximum Centerline Deposition Rate

To identify optimum conditions for the CVI fiber coating process, we seek to maximize the deposition rate at the preform center. This maximum deposition rate is defined by the requirement that the variation in rate with respect to both the pressure and temperature is zero. Because the pressure, temperature and deposition rate are all normalized only by constants, these conditions apply equally to the dimensional and normalized derivatives. The

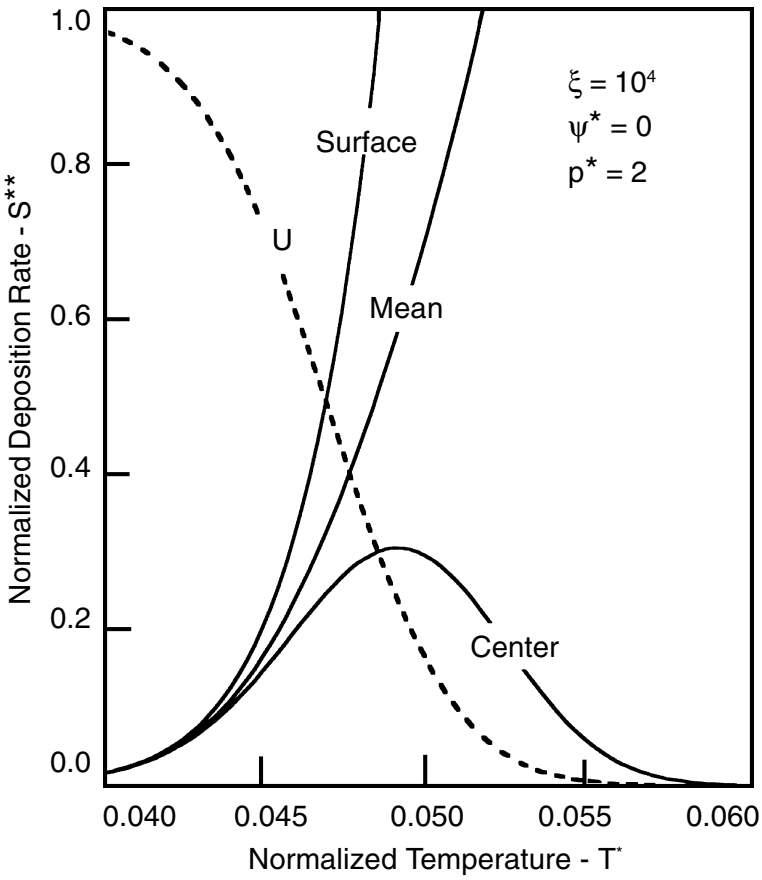

Fig. 4: Surface, mean and centerline deposition rates. For a given pressure, the maximum centerline deposition rate occurs at a specific temperature and corresponding value of the deposition modulus.

conditions for the maximum in terms of the normalized variables are

$$\frac{\partial S^*}{\partial p^*} = 0 \quad \text{and} \quad \frac{\partial S^*}{\partial T^*} = 0 \tag{24a,b}$$

where both derivatives of the deposition rate are evaluated at $z = 0$. Now using Eq. 22b for the normalized deposition rate, Eq. 24a may be written as

$$\frac{1}{S^*}\frac{\partial S^*}{\partial p^*} = \frac{1}{p^*} + \frac{\beta}{f_c^*}\frac{\partial f_c^*}{\partial \beta}\frac{1}{\beta}\frac{\partial \beta}{\partial p^*} = 0 \tag{25}$$

where again f_c^*, is the normalized reactant fraction at the preform center. Similarly, Eq. 24b may be written as

$$\frac{1}{S^*}\frac{\partial S^*}{\partial T^*} = \frac{1}{T^*}\left(\frac{1}{T^*} - \frac{1}{2}\right) + \frac{\beta}{f_c^*}\frac{\partial f_c^*}{\partial \beta}\frac{1}{\beta}\frac{\partial \beta}{\partial T^*} = 0 \tag{26}$$

The derivatives of the deposition modulus with respect to pressure and temperature can now be obtained from Eq. 23. They are

$$\frac{1}{\beta}\frac{\partial \beta}{\partial p^*} = \frac{1}{p^* + T^*} \tag{27}$$

and

$$\frac{1}{\beta}\frac{\partial \beta}{\partial T^*} = \left(\frac{1}{T^*} - \frac{p^*}{p^* + T^*}\right)\frac{1}{T^*} \tag{28}$$

Combining these results with Eqs. 25 and 26 then yields

$$1+\frac{T^*}{p^*}=-\frac{\beta}{f_c^*}\frac{\partial f_c^*}{\partial\beta} \tag{29}$$

for Eq. 24a, and

$$\frac{1}{T^*}-\frac{1}{2}=-\frac{\beta}{f_c^*}\frac{\partial f_c^*}{\partial\beta}\left(\frac{1}{T^*}-\frac{p^*}{p^*+T^*}\right) \tag{30}$$

for Eq. 24b. This pair,of equations, along with a solution to the boundary value problem to obtain the derivative $\partial f_c^*/\partial\beta$, can now be solved to obtain the optimum pressure and optimum temperature yielding the maximum centerline deposition rate.

We would generally expect that Eqs. 29 and 30 must be solved together to obtain the optimum pressure and temperature as a pair. Surprisingly, this is not the case here. Combining these to eliminate the derivative on the right of each yields

$$\frac{1}{T^*}-\frac{1}{2}=\left(1+\frac{T^*}{p^*}\right)\left(\frac{1}{T^*}-\frac{p^*}{p^*+T^*}\right) \tag{31}$$

which can be rearranged to eliminate the normalized temperature and give the simple result

$$p^*=2 \tag{32}$$

for the optimum pressure alone. Using the definition of the normalized pressure, the dimensional optimum pressure is

$$p=2p_R=\frac{\sqrt{2}\alpha E_a}{\pi d N\sigma^2} \tag{33}$$

This is a remarkable result in that the optimum pressure does not depend on the process temperature, the preform specific surface area, or the preform thickness. It depends only on the activation energy for the deposition reaction, the composition of the gas mixture, species properties of the mixture gases, and the inter-fiber pore size.

Using this result for the optimum pressure, the optimum temperature can now be obtained from Eq. 29 as

$$1+\frac{T^*}{2}=-\frac{\beta}{f_c^*}\frac{\partial f_c^*}{\partial\beta} \tag{34}$$

Given $\partial f_c^*/\partial\beta$ as a function of T^* from numerical solutions to Eq.18, this expression can be solved for the optimum normalized temperature.

For the special case of $\psi^* \to 0$, again corresponding to no net reaction yield or to a very small reactant fraction, Eq.19 yields

$$\frac{\beta}{f_c^*}\frac{\partial f_c^*}{\partial\beta}=-\frac{1}{2}\sqrt{\beta}\tanh\sqrt{\beta} \tag{35}$$

giving an optimum temperature specified by

$$2+T^*=\sqrt{\beta}\tanh\sqrt{\beta} \tag{36}$$

Under the further restriction that $\xi \to \infty$, corresponding to $T^* \to 0$, the last term on the left of Eq. 36 may be neglected. This special case yields $\beta \approx 4.2656$ and a corresponding centerline reactant fraction of f_C^*, ≈ 0.2495. The optimum temperature can then be obtained by using the optimum pressure, $p^* = 2$, in Eq. 23. This gives

$$\left(\frac{2}{T^*}+1\right)e^{-1/T^*}=\frac{4}{3}\frac{\beta}{\xi^2}\approx\frac{5.6875}{\xi^2} \tag{37a,b}$$

This equation can be solved easily by successive substitution. Using a guessed value of the temperature in the first factor on the left of Eq.37a, the exponential term is inverted to obtain an improved value for the guess. When repeated, this procedure converges in just a few cycles for all conditions of practical importance. For $\xi = 10^4$, the temperature obtained from Eq. 37b is $T^* = 0.04898$. The maximum centerline deposition rate can be computed from Eqs.19 and 22b once the pressure and temperature have been obtained.

When T^* is not small, Eqs. 36 and 37a must be solved together as an implicitly coupled system. Similarly, when ψ^* is not negligible, Eqs. 34 and 37a must be solved together, along with an appropriate solution of Eq. 18 to provide $\partial f_c^*/\partial\beta$ and f_c^*.

Optimum Conditions

Sample calculations of the optimum pressure and optimum temperature and the maximum centerline deposition rate are shown in Figure 5 as a function of the normalized preform thickness, ξ. These results are all for the special case of negligible reaction yield, $\psi^* = 0$. As noted

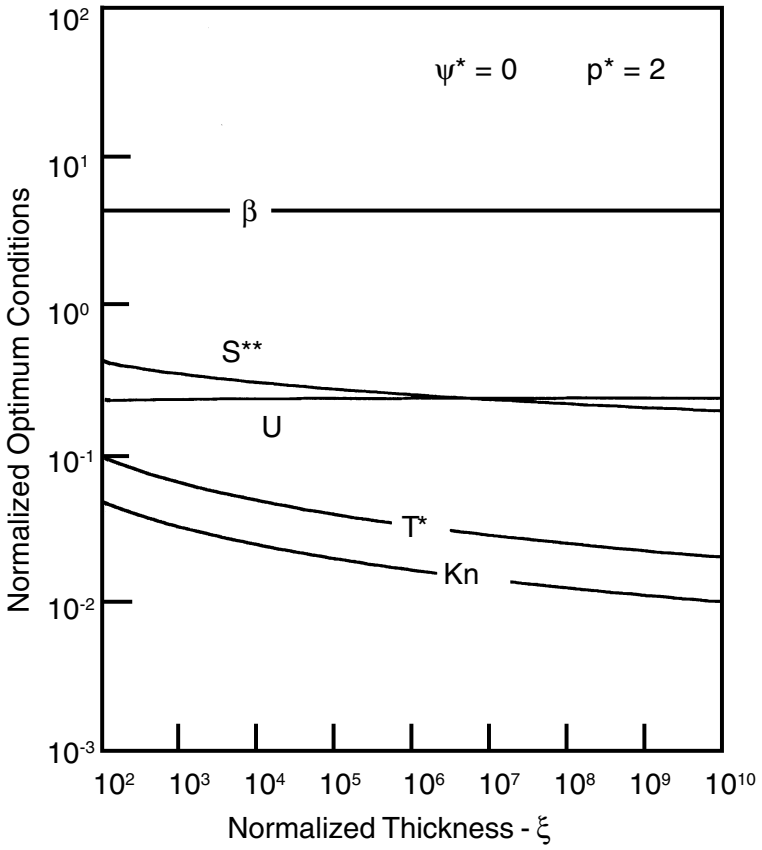

Fig. 5: Normalized optimum conditions as a function of normalized preform thickness. Optimum deposition uniformity is insensitive to preform thickness, but maximum deposition rates fall as $S \propto S^{**}/\xi^2$.

above, the optimum pressure is independent of ξ and is given by $p^* = 2$. The most surprising feature of this figure is that the deposition modulus and deposition uniformity at the optimum conditions vary by only about 15% as the normalized preform thickness varies by eight orders of magnitude. In essence, the optimum conditions yielding maximum centerline deposition rate occur when the centerline reactant fraction is f_c^*, = $U \approx 0.25$, regardless of the preform thickness. This result provides a very simple practical method of determining the optimum conditions. In addition, because the optimum deposition modulus is nearly constant at $\beta \approx 4.3$, Eq. 12 provides a simple means of adjusting the process temperature to maintain the optimum value as the preform thickness is varied.

Despite these weak variations in the optimum process conditions, the maximum normalized deposition rate varies inversely with the square of the preform thickness. The reason for this is that the normalized temperature is small over the range of conditions shown. In this limit of $T^* \rightarrow 0$, Eqs. 22b and 23 can be combined to express the normalized deposition rate in terms of the normalized preform thickness: $S^* \approx 4\sqrt{T^*}\,\beta f_c^*/3\xi^2$. Thus the maximum deposition rate differs by less than a factor of three from a squared dependence on the preform thickness as the thickness varies from 10^2 to 10^{10}.

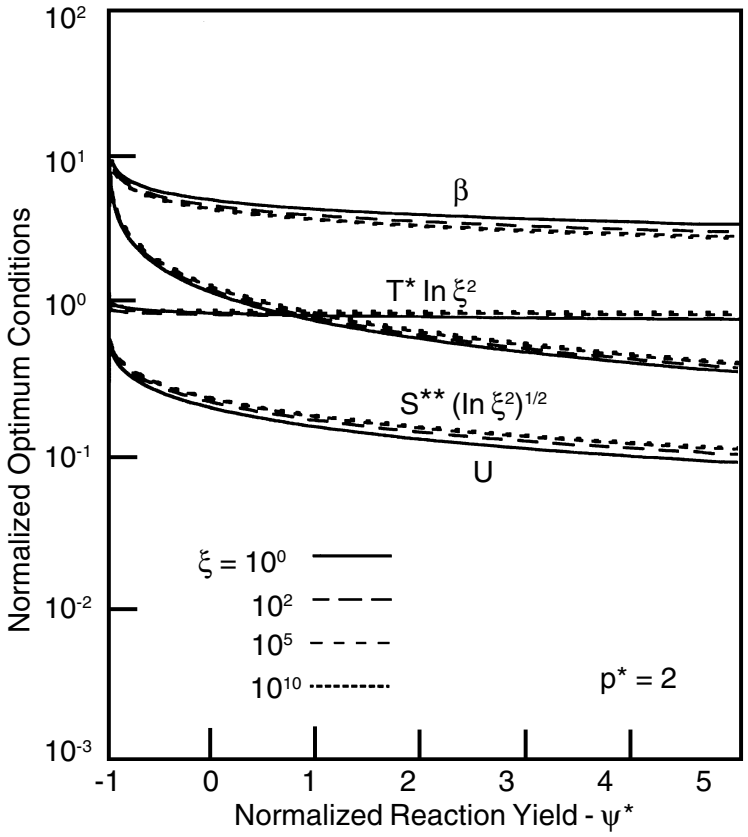

Fig. 6: Normalized optimum conditions as a function of normalized reaction yield. Larger reaction yields require slightly lower temperatures and give significantly reduced maximum deposition rates.

The results presented so far have been for the special case of no normalized reaction yield, $\psi^* = 0$. In general this parameter will not be small unless the ambient reactant fraction is negligible, $f_a << 1$. To examine the effects of non-zero reactant yields, we have computed the optimum temperature, deposition modulus, deposition rate, and centerline reactant fraction for a wide range of ψ^*. Note that the optimum pressure does not depend on ψ^*, and so is still given by $p^* = 2$. These results are shown in Figure 6. By the noted additional normalization of the temperature and deposition rate, this single Figure gives the optimum conditions for all practical values of both the normalized reaction yield and normalized preform thickness.

We see in Figure 6 that the optimum deposition modulus, uniformity at the optimum, and the maximum deposition rate all decrease significantly with increasing values of the normalized reactant yield. The reason for this is that positive values of the reaction yield correspond to a net production of gas in the deposition reaction and a corresponding flow away from the center toward the preform surface. This outward flow impedes the inward diffusion of the reactive species, and so gives rise to greater nonuniformity, lower reactant fractions at the preform center, and correspondingly lower centerline deposition rates. This increased resistance to diffusion therefore requires a reduced temperature to maximize the centerline deposition rate. Note that although the normalized

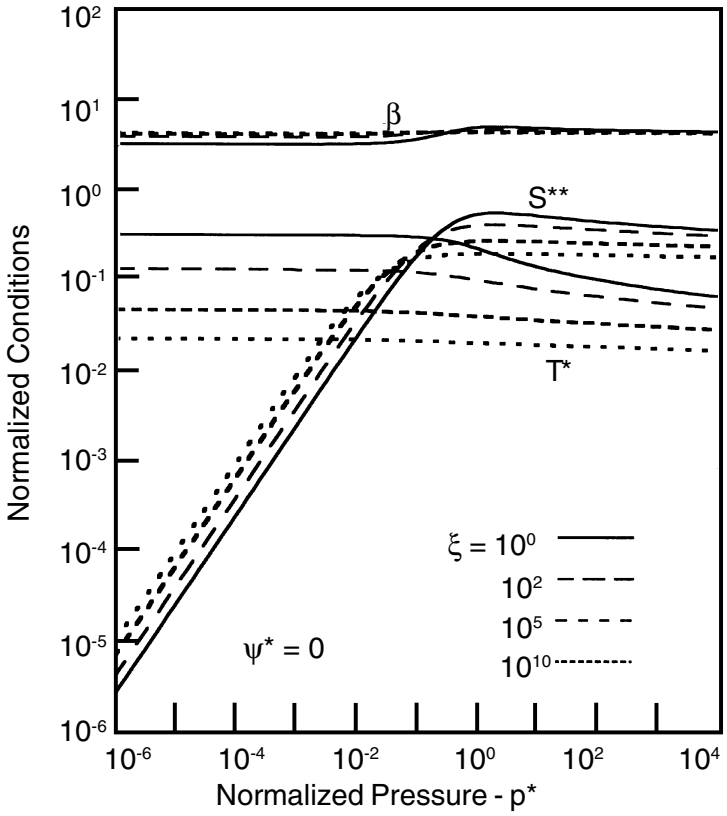

Fig. 7: Normalized deposition rates near the optimum pressure. Deposition rates exhibit a weak one-sided maximum with the deposition rate falling slowly at pressures above the optimum.

temperature appears nearly constant over this range of ψ^*, the very small variation present gives rise to a large effect on the optimum deposition modulus and the maximum centerline deposition rate. For this reason, the value of T^* is most accurately determined by solving Eq.37a using the value of β read from Figure 6.

Character of Maximum Deposition Rate

Although Eqs. 32 and 34 define optimum conditions giving the maximum deposition rate at the preform center, they provide no insight into the character of this maximum. To gain this insight, we need to examine the variation of the deposition rate in the vicinity of the optimum conditions. This is depicted in Figure 7. Here the normalized deposition rate is shown as a function of the normalized pressure, for fixed values of the normalized preform thickness. At each pressure along each curve, the corresponding temperature and normalized deposition rate are computed from Eqs. 30 and 22b. Using this approach, the centerline deposition rate is maximized with respect to the temperature, even though the pressure is not necessarily optimum.

We see in Figure 7 that the deposition rate exhibits a weak one-sided maximum; at all pressures above the optimum value, the deposition rate is nearly constant. The reason for this lies in the tradeoff between the linear pressure dependence of the deposition and the nonlinear pressure dependence of the

diffusivity. Combining Eqs. 25 and 26, and setting $\partial S^*/\partial T^* = 0$, Eq.25 may be rewritten as

$$\frac{p^*}{S^*}\frac{\partial S^*}{\partial p^*} = \frac{T^*\left(2-p^*\right)}{2p^*\left(1-T^*\right)+2T^*} \tag{38}$$

At very low pressures Knudsen diffusion is dominant, corresponding to $\alpha Kn = \alpha\lambda/d = T^*/p^* >> 1$. In this limit, Eq. 38 yields a linear relation between the pressure and deposition rate.

$$\frac{p^*}{S^*}\frac{\partial S^*}{\partial p^*} \to 1 \qquad \text{as} \qquad p^* \to 0 \tag{39}$$

Similarly, at high pressures ordinary diffusion is dominant, corresponding to $T^*/p^* << 1$. In this limit, the deposition rate gradually falls to a constant

$$\frac{p^*}{S^*}\frac{\partial S^*}{\partial p^*} \to -\frac{T^*}{2\left(1-T^*\right)} \qquad \text{as} \qquad p^* \to \infty \tag{40}$$

as the pressure increases without bound.

Optimum Pressure at Fixed Uniformity

The conditions yielding the unconstrained maximum centerline deposition rate give a deposition uniformity of only about 25%. While this may well be acceptable for some fiber coating processes, there are likely applications for which it is not. We now consider the problem of maximizing the centerline deposition rate, subject to an additional constraint that the deposition uniformity satisfies some minimum requirement. Assuming that the required uniformity is better than that obtained in the unconstrained case, the constrained maximum centerline deposition rate should occur when the uniformity constraint is just marginally satisfied. This permits replacing the inequality constraint of a minimum uniformity by an equality constraint that is satisfied exactly.

The constrained maximum deposition rate is defined by the requirement that the variation in rate with respect to all independent variables is zero along the direction of constant uniformity. To obtain this maximum we employ the method of Lagrange multipliers.[13] This technique introduces one new unknown constant for each constraint and yields one additional equation for each independent variable. The two new equations are

$$\frac{\partial S^*}{\partial p^*} - \kappa\frac{\partial U}{\partial p^*} = 0 \qquad \text{and} \qquad \frac{\partial S^*}{\partial T^*} - \kappa\frac{\partial U}{\partial T^*} = 0 \tag{41}$$

where κ, the Lagrange multiplier, is the new unknown constant. Together with the original constraint on the deposition uniformity, this pair of equations can be solved for the optimum pressure and temperature yielding the constrained maximum centerline deposition rate.

Rearranging Eqs. 41a and 41b to eliminate κ. yields

$$\frac{\partial S^*}{\partial p^*}\frac{\partial U}{\partial T^*} = \frac{\partial S^*}{\partial T^*}\frac{\partial U}{\partial p^*} \tag{42}$$

By the definition $U = S^*_c/S^* = f_c^*$, the derivatives of the uniformity with respect to pressure and temperature may be written as

$$\frac{1}{U}\frac{\partial U}{\partial p^*} = \frac{\beta}{f_c^*}\frac{\partial f_c^*}{\partial \beta}\frac{1}{\beta}\frac{\partial \beta}{\partial p^*} \tag{43}$$

and

$$\frac{1}{U}\frac{\partial U}{\partial T^*} = \frac{\beta}{f_c^*}\frac{\partial f_c^*}{\partial \beta}\frac{1}{\beta}\frac{\partial \beta}{\partial T^*} \tag{44}$$

Now using these results along with the definitions given previously in the left of Eqs. 25 and 26, Eq. 42 above can be expressed as

$$\frac{1}{\beta}\frac{\partial \beta}{\partial T^*} = \frac{p^*}{T^*}\left(\frac{1}{T^*}-\frac{1}{2}\right)\frac{1}{\beta}\frac{\partial \beta}{\partial p^*} \tag{45}$$

Finally, using the definitions of Eqs. 27 and 28 for the derivatives of the deposition modulus, Eq.44 becomes

$$\frac{1}{T^*}-\frac{1}{2} = \left(1+\frac{T^*}{p^*}\right)\left(\frac{1}{T^*}-\frac{p^*}{p^*+T^*}\right) \tag{46}$$

This is exactly the same as Eq.31 obtained previously, and again this can be rearranged to give

$$p^* = 2 \quad \text{or} \quad p = \frac{\sqrt{2}\alpha E_a}{\pi d N \sigma^2} \tag{47}$$

Thus, we find that the optimum pressure maximizing the centerline deposition rate for a

specified uniformity is the same as that obtained in the unconstrained problem. The optimum temperature in this case can now be obtained directly from the prescribed deposition uniformity and a numerical solution to Eq. 18.

Optimization Strategies

The preceding results suggest a strategy for optimizing process conditions in coating processes: first, the pressure is fixed at the optimum value; the temperature is then varied until the desired uniformity is obtained, keeping in mind that the maximum possible centerline deposition rate will occur at a uniformity of about 25%. Using this strategy, the time-consuming process of empirically varying both the pressure and temperature to produce at once both the desired uniformity and maximum deposition rate can be avoided.

This result also suggests a possible strategy for minimizing in-furnace times for the more complex densification process. As described earlier, preform transport properties vary significantly during densification, and this might have a strong influence on the optimum time dependent pressure and temperature histories. This influence appears, however, to be limited to effects on the temperature. The optimum pressure does not depend on transport proper- ties, but instead depends only on the preform effective pore diameter, and pore diameters fall by at most about an order of magnitude during most densification processes. We also know from Figure 7 that deposition rates are relatively insensitive to pressure in the vicinity of the optimum value. Thus a good strategy for densification might be to fix the pressure somewhat above the optimum value based on the initial pore size and to hold this constant during the process. The pressure would then be a bit high early in the process, but would be a bit low toward the end. At this fixed pressure, the temperature history alone can then be varied to obtain the desired final uniformity and final degree of densification. This strategy should yield mean deposition rates comparable to those of a full optimization of the pressure history, but again avoids simultaneous variation of both pressure and temperature. Decoupling the problem in this way should greatly reduce the experimental or computational effort needed to obtain an optimum process cycle.

The recoummended optimum pressures for these coating and densification strategies are in good agreement with previous numerical results. Ofori and Sotirchos determined the optimum pressure and temperature to densify a preform to some specified extent in the minimum time, subject to a constraint on the deposition uniformity.[14] That analysis considered the deposition of silicon carbide from a mixture of hydrogen and methyl-trichlorosilane (MTS) under isobaric, isothermal conditions. Here we compare their results with the optimum pressure given by Eq.47. The required molecular properties of the two gases are m_1 = 149 g/mol, m_2 = 2 g/mol, $\sigma_1 = 5.87$ Å, and $\sigma_2 = 2.83$ Å, where the subscript 1 refers to MTS and 2 refers to hydrogen.[15] By Eq.A5 of the Appendix, these values give a diffusivity ratio of $\alpha = 11.2$ for all species mole fractions. The remaining required parameters are $N = 6.02 \times 10^{23}$ molecules/mol and E_a = 120 kJ/mol.[14] These values yield p = 59 kPA for $d = 50\ \mu$m. For $d = 5\ \mu$m and $d = 0.5\ \mu$m, Eq. 47 gives p = 590 kPa and p = 5.9 MPa.

The optimum pressures read from Figures 1, 5, 7, and 9 of the Ofori and Sotirchos paper range from about 40 to 90 kPa for $d = 50\ \mu$m, from about 400 to 900 kPa for $d = 5\ \mu$m, and from about 4 to 9 MPa for $d = 0.5\ \mu$m. Although it is difficult to pick these optima very accurately from the Figures, these ranges of values are in excellent agreement with the values obtained from Eq. 47. Aside from this good quantitative agreement, we note that their optimum pressures consistently exhibit the inverse dependence on pore size given by Eq. 47. Their Figures 1, 5, 7, 8, 13, and 15 further suggest that the optimum pressure for densification, even under a uniformity constraint, does not depend on transport properties of the preform, the pre-exponential deposition rate constant, or the specified deposition uniformity. This again is in agreement with Eq. 47.

Sample Calculations

To illustrate the application of this analysis, we consider the sample problem of depositing a thin coating of boron nitride on fibers within a preform using boron trichloride and ammonia. The preform half-thickness is a = 5 mm, fiber diameter is $d_f = 10\,\mu$m, and the porosity is $\in = 0.6$. From simple geometry, the preform specific surface area is given by $s_v = 4(1-\in) / d_f = 1.6 \times 10^{-5}$ m^{-1}. Likewise, the effective pore diameter is given by $d = 4\in /s_v = 15\ \mu$m.[16] For simplicity we assume that the fibers are arranged in a regular hexagonal array. Effective thermal conductivities, equivalent to the effective diffusivity, have been computed for this geometry. The result at a fiber porosity of 0.6 is $D' = 0.43$.[17]

Boron trichloride and ammonia react rapidly in the gas phase to form $C1_2BNH_2$ and HCI.[18] For arbitrary flow rates of these two gases, this gas-phase reaction can be described by

$$BC1_3 + G\ NH_3 \rightarrow 4\ HCl + C1_2BNH_2 + (G - 1)\ NH_3 \quad (48)$$

where G is the ratio of the volumetric flow rate of ammonia to that of the boron trichloride. The $C1_2BNH_2$ species is then the deposition precursor for the surface reaction given by

$$C1_2BNH_2 \rightarrow BN(s) + 2\ HCl \quad (49)$$

Form these two reactions the reactant fraction is given by $f_a = 1 / (G + 1)$ provided that the reactant flow rates are sufficiently large that product gases do not significantly accumulate inside the furnace. Under this restriction, the reactant fraction is $f_a = 0.33$ for a relative flow rate of $G = 2$. From the surface reaction we see that two moles of gas-phase product are produced for each mole of reactant, giving $\psi = 1$ and a normalized reactant yield of $\psi^* = \psi f_a = 0.33$. The parameters E_a and b for the surface reaction probability are approximately 147 kJ/mol and 446, respectively.[19]

The diffusivity ratio, α, is computed using kinetic theory,

$$\frac{1}{\alpha} = \frac{1}{1-x_1}\sum_{j=2}^{n} x_j \left(\frac{\sigma_1+\sigma_j}{2\sigma_1}\right)^2 \left(\frac{2mj}{m_1+m_j}\right)^{1/2} \quad (50)$$

where the mole fractions of Cl_2BNH_2, NH_3 and HCl are $x_1 = x_2 = x_3 = 0.33$, and the corresponding species molecular weights are 98, 17, and 36 g/mol. The molecular diameters are 4.7, 2.6 and 3.3 Å, respectively.[15] These values yield $\alpha = 2.3$. A more accurate estimate of the diffusivity ratio could be computed using, for example, the more complete Chapman-Enskog theory for the transport properties of gases.

Using these basic parameters, the normalized preform thickness can be computed from Eq.13 as $\xi = 1.66 \times 10^4$. The reference pressure and temperature given by Eq.20 are $p_R = 38$ kPa (290 torr) and $T_R = 17680$ K, yielding a reference deposition rate of $S_R = 5.39 \times 10^4$ mol/m^{2}s. Now from Figure 6, or from the solution of Eqs.18, 29, and 30, the optimum conditions are given by $p^* = 2$ and $T^* \approx 0.0465$, corresponding to a dimensional optimum pressure of 77 kPa (580 torr) and optimum temperature of 549°C. The deposition modulus at these conditions is $\beta \approx 4.18$, the associated uniformity is $U \approx f_c/f_a = 0.216$, and the normalized centerline deposition rate is $S^{**} \approx 0.253$. This corresponds to a dimensional deposition rate of $S = S_R S^{**}/\xi^2 = 1.74 \times 10^{-5}$ mol/m^{2}s. At a BN solid density of 2.0 g/cm^3 and molecular weight of 24.8 g/mol, this gives a centerline deposition rate of 0.78 μm/hr.

Note that even the small normalized reaction yield of our sample problem significantly affects the optimum conditions and maximum deposition rate. If we take $\psi^* = 0$, but leave all other problem parameters unchanged, the resulting optimum temperature increases to 551°C and the maximum centerline deposition rate increases to 0.92 μm/hr. Thus a normalized reaction yield of only $\psi^* = 0.33$ has reduced the maximum deposition rate by over 15%.

As illustrated in Figure 7, the deposition rate is insensitive to pressure over a wide range of values near the optimum. In our sample problem, reducing the pressure an order of magnitude to 7.7 kPa (58 torr) still gives a maximum centerline deposition rate of 0.67 μm/hr at an optimum temperature of 642°C. Again reducing the pressure to 770 Pa (5.8 torr) yields a maximum deposition rate of 0.23 μm/hr at a temperature of 704°C. Thus a pressure two orders of magnitude below the optimum value only reduces the maximum deposition rate by about

a factor of three in this sample problem. However, reducing the pressure just one more decade, to 77 Pa (580 mtorr), yields a maximum centerline deposition rate of just 0.030 μm/hr at an optimum temperature of 717°C. At this pressure the deposition rate is falling about linearly with the pressure and will continue this behavior as the pressure is further reduced.

Over the pressure range from about 0.8 to 80 kPa (6 to 600 torr), the maximum centerline deposition rate increases by about a factor of three while the optimum temperature decreases from 642 to 549°C. This insensitivity to pressure may permit placing additional constraints on the process conditions without seriously reducing deposition rates. For example, the morphology of deposited BN may depend on the process temperature. If higher temperatures yield the desired morphology, then lower pressures may be preferred. Likewise, the gas-phase reaction of boron trichloride and ammonia is known to precipitate solid ammonium chloride if pressures are sufficiently high. In this case, the total pressure may need to be reduced below the optimum value. By reducing the pressure and slightly increasing the temperature, precipitation can be avoided, again without significantly reducing the deposition rate.

Summary

To help optimize CVI process conditions, we have derived analytical expressions describing the pressure and temperature giving the maximum centerline deposition rate for a first-order deposition reaction involving a single reactive species. These analytical expressions account for both diffusive and advective transport and both ordinary and Knudsen diffusion. The resulting optimum conditions are a function of only two dimensionless parameters: the normalized preform thickness; and the normalized reaction yield indicating the relative importance of advective transport away ftom the preform center due to the evolution of product gases from the deposition reaction. Although these results also have use in optimizing preform densification, the analysis employed here is strictly applicable only to fiber coating processes wherein the coating thickness remains small compared to the original fiber diameter.

The optimum pressure is obtained in closed form. Its value is proportional to the activation energy of the deposition reaction and inversely proportional to the characteristic preform pore size. Surprisingly, the optimum pressure does not depend on the preform thickness, specific surface area or effective diffusivity, nor does it depend on the reaction yield.

Optimum temperatures are obtained from the analytical expressions describing the optimum conditions, along with the derivative of the centerline reactant fraction with respect to the deposition modulus. Using an analytical solution to provide the derivative of the centerline reactant fraction, a closed-form implicit expression for the optimum temperature is obtained for the special case of no normalized reaction yield. For the more general case, this derivative is computed from numerical solutions to the equations governing transport and deposition. Optimum temperatures are presented graphically for a very wide range of the normalized preform thickness and normalized reaction yield.

As we would expect, the optimum temperature and maximum centerline deposition rate depend strongly on the preform thickness. Surprisingly, however, the deposition modulus and deposition uniformity at the optimum conditions are nearly independent of the thickness for a given normalized reaction yield. This provides a simple means of identifying optimum conditions for preforms of varying thickness once the optimum is known for a single case. The optimum temperature for a new thickness is obtained when the deposition uniformity is unaltered, as determined experimentally or by using a simple algebraic relation to give the same deposition modulus for the new preform thickness.

The optimum conditions yield a weak one-sided maximum of the centerline deposition rate. The deposition rate falls linearly at pressures well below the optimum value, but remains nearly constant at all values above. The reason for this behavior lies in the tradeoff

between the linear pressure dependence of the deposition reaction and the nonlinear pressure dependence of the diffusivity in the transition between the ordinary and Knudsen regimes. At very low pressures, Knudsen numbers are large, Knudsen diffusion is dominant, and the centerline deposition rate at the optimum temperature increases linearly with increasing pressure. At very high pressures, however, Knudsen numbers are small, ordinary diffusion is dominant, and the maximum centerline rate falls weakly as the pressure becomes infinite.

Conditions yielding the maximum centerline deposition rate give a deposition uniformity of only about 25%. That is, the deposition rate at the preform surface is roughly four times that at its center. Because this is probably not acceptable for some coating applications, we have also examined the influence on the optimum conditions of a constraint on the deposition uniformity. Using the method of Lagrange multipliers, we find that the optimum pressure in this constrained maximization of the centerline deposition rate is the same as that obtained in the unconstrained case. This surprising result suggests that a good strategy for optimizing both fiber coating and densification processes is to fix the pressure at the optimum value, and then vary only the temperature or temperature history to obtain the desired final state of the preform. The recommended optimum pressure, obtained here analytically, is in good agreement with the values obtained in a previous numerical analysis of the optimum conditions for preform densification when the deposition uniformity is constrained.

Although the discussions presented here focus on fibrous preforms, all of these results are equally applicable to particulate materials.

Nomenclature

a Preform Thickness

b Deposition Reaction Pre-Exponential Constant

d Inter-Fiber Pore Size

D Effective Binary Diffusivity

D' Effective Diffusivity of Porous Preform

D_m Effective Ordinary Binary Diffusivity

D_{Kn} Reactant Knudsen Diffusivity ($D_{\mathrm{kn}} = \bar{v}\, d/3$)

E_a Deposition Reaction Activation Energy

f Reactive Species Mole Fraction

Kn Knudsen Number ($\mathrm{Kn} = \lambda/d$)

m Reactive Species Molecular Weight

N Avogadro Number

p Total Gas Pressure

R Ideal Gas Constant

S Surface Deposition Rate

T Temperature

u Fluid Speed

U Deposition Uniformity ($U = f_c/f_a = f_c^*$)

$\bar{\upsilon}$ Reactant Mean Molecular Speed

x Transverse Position

z Normalized Transverse Position ($z = x/a$)

α Ratio of Diffusivities

β Deposition Modulus

λ Reactant Mean Free Path

ξ Normalized Preform Thickness

ρ Total Molar Density

σ Reactive Species Molecular Diameter

ϕ Reaction Probability

ψ Net Molar Yield of Deposition Reaction

Subscripts and Superscripts

a At Preform Surface

c At Preform Center

R Reference Value for Normalization

$*$ Asterisk Denotes Normalized Variable

Appendix

The parameter α is the ratio of the effective binary coefficient of ordinary diffusion for the reactive. species and the mixture of other furnace gases to the coefficient of ordinary self

diffusion for the reactive species. Denoting the coefficient for the mixture as D_{lm} and the coefficient for the reactive species only as D_{11}, this may be written

$$\alpha = \frac{D_{1m}}{D_{11}} \tag{A1}$$

The values of the terms on the right of Eq.Al may be computed by any number of methods, ranging from the very simple to very complete. Here we consider a very simple method based on kinetic theory and the rigid sphere approximation.

The effective binary coefficient of ordinary diffusion for the reactive species in a gas mixture may be expressed as.[10]

$$\frac{1-x_1}{D_{1m}} = \sum_{j=2}^{n} \frac{x_j}{D_{1j}} \tag{A2}$$

where x_j are the mole fractions of each species, and D_{1j} is the binary coefficient of ordinary diffusion for the reactive species paired with species j. In this case the subscript $j = 1$ refers to the species of interest, while $j = 2$ and above refer to all other species in the mixture. Combining Eqs. A1 and A2 yields an expression for α in term of the binary coefficients of diffusion only.

$$\frac{1}{\alpha} = \frac{1}{1-x_1} \sum_{j=2}^{n} x_j \frac{D_{11}}{D_{1j}} \tag{A3}$$

Now assuming the hard sphere molecular behavior, the ratio D_{11}/D_{1j} may be written as

$$\frac{D_{11}}{D_{1j}} = \left(\frac{\sigma_1 + \sigma_j}{2\sigma_1} \right)^2 \left(\frac{2m_j}{m_1 + m_j} \right)^{1/2} \tag{A4}$$

where σ_j and m_j are the atomic diameter and molecular weight of the jth mixture species. Note that neither the pressure nor temperature appear in this relation because D_{11} and D_{1j} always share the same functional dependence on both. Finally, combining Eqs. A3 and A4 gives the desired expression for α.

$$\frac{1}{\alpha} = \frac{1}{1-x_1} \sum_{j=2}^{n} x_j \left(\frac{\sigma_1 + \sigma_j}{2\sigma_1} \right)^2 \left(\frac{\sigma_1 + 2m_j}{m_1 + m_j} \right)^{1/2} \tag{A5}$$

We now see that the rigid sphere molecular model gives a value for α that depends only on the mixture composition and the molecular diameter and weight of all the mixture species. However, a more rigorous treatment based on Chapman-Enskog theory would yield a slight pressure and temperature dependence for the ratio D_{11}/D_{1j}. The value of α in that case would also show a weak dependence on the process conditions for a fixed mixture composition.

We should also keep in mind that the process conditions may directly influence the composition of the furnace gas mixture, so in this sense the diffusivity ratio α will vary with pressure and temperature due to variations in x_j, whether or not the ratios D_{il}/D_{1j} are constant. In this case, the present analysis may be combined with a simple zero or one-dimensional auxiliary model of reactant injection and transport within the furnace. Using the specified injection rate and assumed trial values for the optimum pressure and temperature, the results presented here can be used with such an auxiliary model to compute the composition of the furnace gas mixture. From this estimate of the composition, a value for α and new candidate values for the optimum pressure and temperature can then be calculated. This computational procedure may then be repeated, each time using the final estimates of the optimum conditions as initial guesses for the next iteration. This method should converge quickly because the value of α is a fairly weak function of the composition.

Acknowledgment

The authors wish to thank Dr. G.S. Thurston of Textron Specialty Materials and Dr. Craig Shumaker of DuPont Lanxide Composites for sharing with us their broad experience in composites manufacturing. This work was funded in part by the Defense Advanced Research Projects Agency (DARPA) High Temperature Structural Materials Program under the leadership of Dr. William Barker and in part by the US Department of Energy Office of Industrial Technologies, Advanced Industrial Matgerials Program under the leadership of Dr. Charles Sorrell.

References

1. P. McAllister and E.E. Wolf, Modeling of Chemical Vapor Infiltration of Carbon in Porous Carbon Substrates, *Carbon*, Vol.29, 1991, p.387.
2. B.W. Sheldon and T.M. Besmann, Reaction and Diffusion Kinetics During the Initial Stages of Isothermal Chemical Vapor Infiltration, *Journal of American Ceramic Society,* Vol.74, 1991, p.3046.
3. V. Cholet and L. Vandenbulcke, Chemical Vapor Infiltration of Boron Nitride Interphase in Ceramic Fiber Preforms; Discussion of Some Aspects of the Fundamentals of the Isothermal Chemical Vapor Infiltration Process, *Journal of American Ceramic Society,* Vol.76, 1993, p.2846.
4. G. Savage, *Carbon-Carbon Composites,* Chapman and Hall, London, 1993, p.372.
5. R.J. Melkote and K.F. Jensen, Gas Diffusion in Random-Fiber Substrates, *American Institute of Chemical Engineers Journal*, Vol.35, 1989, p.12.
6. B.W. Sheldon and H.C. Chang, Minimizing Densification Times During the Final Stage of Isothermal Chemical Vapor Deposition, *Ceramic Transition*, Vol.42, 1994, p.81.
7. S.V. Sotirchos, Dynamic Modeling of Chemical Vapor Infiltration, *American Institute of Chemical Engineers Journal*, Vol.37, 1991, p.1365.
8. J.Y. Ofori and S.V. Sotirchos, Structural Model Effects on the Predictions of Chemical Vapor Infiltration Models, *Journal of Electrochemical Society,* Vol.143, 1996, p.1962.
9. C. Bonsanquet, and T.A. Report, BR 507, 1944. See also W.C. Pollard and R.D. Present, *Physics Review*, Vol.73, 1948, p.762.
10. R.B. Bird, W.E. Stewart, and E.M. Lightfoot, *Transport Phenomena*, John Wiley & Sons, New York, 1960, pp.510 and 571.
11. E.W. Thiele, Relation Between Catalytic Activity and Size of Particle, *Industrial Engineering Chem*ical, Vol.31, No.7, 1939, p.910.
12. S.K. Griffiths and R.H. Nilson, Deposition Uniformity, Particle Nucleation and the Optimum Conditions for Chemical Vapor Deposition in Multiwafer Furnaces, *Journal of Electrochemical Society*, Vol.144, No.4, 1997, p.1399.
13. W. Kaplan, *Advanced Calculus*, Addison-Wesley, Reading, MS, 1973, p.184.
14. J.Y. Ofori and S.V. Sotirchos, Optimal Pressures and Temperature for Isobaric, Isothermal Chemical Vapor Infiltration, *American Institute of Chemical Engineers Journal*, Vol.42, No.10, 1996, p.2828.
15. R.C. Reid, J.M. Prausnitz, and T.K. Sherwood, *The Properties of Gases and Liquids,* Third Edition, McGraw-Hill, New York, NY, Mts Properties were Computed Based on Critical Conditions of 517 K and 3.28 MPa and an Estimated Acentric Factor of 0.26, 1977, pp.24 and 679.
16. G.L. Vignoles, Modeling Binary, Knudsen and Transition Regime Diffusion Inside Complex Porous Media, *Journal of Physics Colloq*. IV, Vol.C5, 1995, p.159.
17. W.T. Perrins, D.R. McKenzie, and R.G. McPhedran, Transport Properties of Regular Arrays of Cylinders, *Proceedings of Royal Society,* Vol.A369, 1979, p.207.
18. M.D. Allendorf and T.H. Osterheld, Chemical Reactions in the CVD of Boron Nitride from $BC1_3$ and NH_3, *Proceedings of 13th International Conference Chemical Vapor Deposotion,* Vol.96, No.5, 1996, p.16.
19. N. Patibandla and K.L. Luthra, Chemical Vapor Deposition of Boron Nitride, *Journal of Electrochemical Soc*iety, Vol.139, No.12, 1996, p.3558.

Chemical Vapor Deposition
Jong-Hee Park, T.S. Sudarshan, editors, p205-241
DOI:10.1361/chvd2001p205

Chapter 7

Metal-Organic Chemical Vapor Deposition of High Dielectric (Ba, Sr) TiO_3 Thin Films for Dynamic Random Access Memory Applications

Cheol Seong Hwang
Seoul National University, School of Material Science and Engineering
San #56-1, Shillim-Dong, Kwanak-ku
Seoul 151-742, Korea

Introduction

Since the early suggestion that ferroelectric thin film materials could be the high dielectric layer in the capacitor of the ultra large scale integrated dynamic random access memory devices (ULSI DRAMS) made by Parker and Tasch,[1] there has been a great deal of research effort to deposit multi-component ferroelectric oxide thin films as well as more recent industrial activity. The term "ferroelectric" indicates the property of certain materials that have remnant electric polarization in the absence of the electric field, and the direction of the remnant polarization can be reversed by the reversal of the applied field. Most of the ferroelectric oxide materials, such as Pb(Zr, Ti)O_3, show much larger dielectric constants than those of the non-ferroelectric dielectric materials, such as TiO_2, ZrO_2, etc. Therefore, in some literatures the terms ferroelectric and high dielectric are not classified. However, in principle, ferroelectric polarization does not necessarily imply large dielectric constant as in the case of $BaTiO_3$. In

the $BaTiO_3$ crystal, the dielectric constant is about 180 along the c-axis, which has the ferroelectric polarization, whereas the value along the a-axis is about 4000 at room temperature.[2] Therefore, in this chapter, the terms ferrociectric and high dielectric have specific meanings.

Even though some ferroelectric materials, especially the relaxor ferroelectrics, have an extremely large dielectric constant, which is a very desirable property for the dielectric layer of capacitors in ULSI DRAMS, the usually large dielectric loss prevents the materials from being used in the DRAMS. Furthermore, the quite large number of component cations of the relaxor ferroelectric materials makes it almost impossible to deposit thin films using chemical vapor deposition (CVD) which is believed to be the method of choice for mass production of the devices.

There is a different application for ferroelectric materials in solid state memory devices the ferroelectric RAM (FeRAM). However, in this chapter, the FERAM and related issues will not be considered because the subject would be too diverse.

$(Ba,Sr)TiO_3$ (BST) thin films are the dielectric material of choice for the cell capacitor of DRAMs having giga-bit densities, such as 4 and 16 giga-bit DRAMs, because it offers reasonably large dielectric constant with small dielectric loss and leakage current.[3-6] Although current mass production CVD processes in the semiconductor industry are limited to the simple binary materialsy such as SiO_2, Si_3N_4 and TiN etc., there is a strong belief that reliable deposition of BST thin films containing three cations can be achieved by CVD.[5,6] Although the film material properties have been proven to be adequate as capacitor dielectrics in terms of thermal and mechanical stability and dielectric properties, including leakage current, dielectric constant, loss factor as well as frequency, temperature and voltage dependencies of all these important parameters,[7,8] actual integration into DRAM devices has been slow because of unsolved problems related to the electrodes. Material selection and fabrication processes must produce extremely small sizes. Another obstacle to their use is the lack of reliable, mass-production compatible processes, especially for the BST film deposition.

Before the metal-organic CVD (MOCVD) process of the BST film is discussed, the reasons for using the CVD process, despite its difficulties should be described. The storage node size of the capacitors in the current state-of-the-art DRAMs is about $0.15 \times 0.35 \times 1.0\ \mu m^3$ with minimum spacing of about 0.15 μm between the nodes when the dielectric layer is a SiO_2/Si_3N_4 bi-layer or Ta_2O_5, and the electrode materials are poly-Si. Here 1 μm is the height of the nodes. Even smaller lateral dimensions are expected when DRAMs use a BST thin film as the capacitor dielectric layer. Even though the BST films have a much smaller t_{ox} value, which ensures a much larger capacitance per unit area compared to conventional dielectric layers, the three dimensional shape of the nodes is still required because of a very stringent design rule. There are two typical shapes for a storage electrode, shown in Figure 1, in which one is the node type and the other is the concave type. For both cases, we can clearly see that a conf6rmal deposition technique is required for the dielectric layer as well as the top electrode layer. It should be remembered that current technology for capacitor fabrication requires CVD formation of the Si_3N_4 dielectric layer followed by oxidation of it to form the SiO_2/Si_3N_4 bi-layer followed by poly-Si CVD for the top electrode. For the case of the concave capacitor structure, a conformal CVD technique for the bottom electrode is also required. The most probable electrode materials for the BST are noble metals, such as Pt and Ru. Research efforts for the development of the MOCVD processes for these metal layers become more and more active.[9-11] Some experimental results on the CVD of these metal layers are also included in this article.

In contrast to the CVD processes for conventional dielectric layers, which have excellent precursors having gaseous or liquid form to produce stable and reproducible deposits, the BST CVD process still does not have proper precursors. It is well known that synthesis of the CVD precursors for alkaline earth elements, such as Ba and Sr, is very difficult due to their large ionic size and

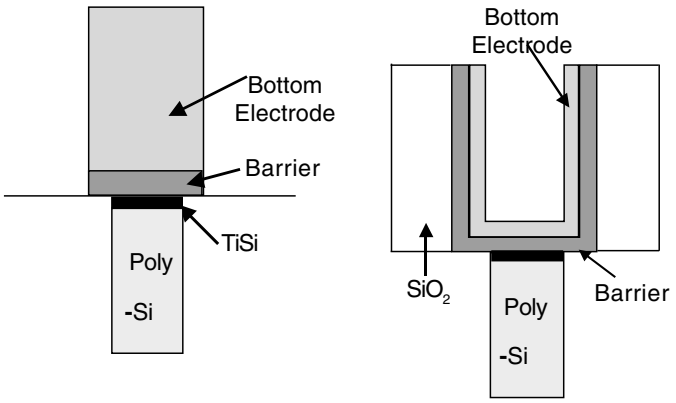

Fig. 1: Two representative shapes for storage electrodes.

polarizability.[12,13] The inorganic halogenated compounds do not show any useful volatilities at normal vaporization temperatures, and their decomposition requires very high temperatures which render these compounds almost useless for DRAM processes. Therefore, it seems quite reasonable to start this chapter with a review and discussions of precursors which maybe used for mass production. A discussion of the delivery technique for the precursors is also included because it is very important for reproducible deposition, and is one of the important components for a hardware system.

The CVD system components will be described briefly to indicate the specific features for BST CVD compared to conventional dielectric CVD system. The CVD processes for BST thin films are then dealt with from the view point of mass production compatibility. As with other CVD processes, the deposition characteristics of the BST CVD are quite dependent on the kind of precursors used. In this article, experimental results on deposition using different precursors are described. Some reported results from other groups are also summarized in order to reach a general conclusion.

The electrical characteristics of the films should produce stable operation of DRAM devices. The most important electrical properties are a small t_{ox}, all dielectric loss and low leakage current, which should be less than roughly 0.5 nm, 0.5% and 1 fA/cell, respectively. Even though the long term reliability properties, such as time dependent dielectric breakdown (TDDB) and time dependent resistance degradation (TDRD), are also important for reliability, they are not well understood yet. Therefore, some selected electrical properties of CVD BST films are described in comparison with sputtered BST films. It is believed that this section will help the readers understand the nature of BST CVD, which is one of the most complex CVD processes.

As mentioned previously, we include reports and discussions of CVD processes for metallic electrodes and diffusion barrier layers. The diffusion barrier layer is interposed between the electrode and poly-Si plug to prevent chemical reaction between them. It becomes quite clear that all these CVD processes should be developed simultaneously because of the structural complexity of capacitors and process integration requirements.

We include process integration for the completeness of the discussion. We are mindful of the fact that awareness of the CVD process of the BST films can be attained only when the objective of the processing is correctly understood. It is believed that a brief description of the process integration is helpful, irrespective of whether one is acquainted with DRAM

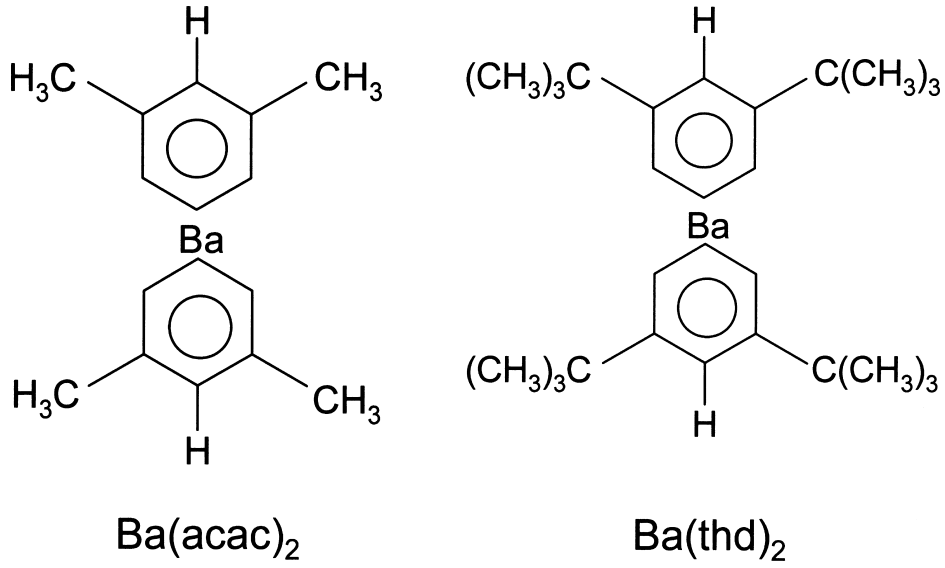

Fig. 2: Molecular structures of Ba(acetylacctonate)$_2$ and Ba(thd)$_2$.

processes, to understand the implications of the CVD processes and to anticipate the future direction of research.

Precursors for CVD

Precursors for Group II Elements: Ba and Sr

Synthesis of metal-organic precursors for the group II elements, Ba and Sr, having proper vapor pressure (> 100 mTorr) is quite difficult because of the bulky and heavy nature of the ions. For instance, the Ba^{2+} ion have a radius of 0.135 nm and a weight of 2.28×10^{-22} g/ion, compared the group IV, Ti^{4+} ion, which has an ionic radius of 0.068 nm and a weight of 7.95×10^{-23} g/ion. Furthermore, the large polarizability of the group II ions promotes formation of multinuclear aggregates which have even poorer volatility. Only those Ba compounds with multidentate sterically encumbered anions have proven useful for CVD applications.

Ba(thd)$_2$ (thd = 2,2,6,6-tetramethyl-3,5-heptanedionate) and Sr(thd)$_2$ constitute the most widely used CVD precursors due to their stability in air and moderate vapor pressures. These compounds are derived from the more simple β-diketonate compounds, such as acetylacetonates. Figure 2 shows the molecular structures of Ba(acetylacetonate)$_2$ and Ba(thd)$_2$. It can be understood that the more bulky structure of the thd ligand screens the metal ions from each other which reduces intermolecular attraction and improves volatility. These materials for white powders at room temperature and seem to degrade when they are exposed to air for a long time due to reaction with H_2O and CO_2. It has been observed that the vapor transport efficiencies of these precursors degrade with time when they are heated to temperatures higher than 200°C to obtain the proper vapor pressure. Purity and water content in the precursors seem to seriously affect their transport efficiency. Figure 3 shows typical TGA data of the Ba(thd)$_2$ from two different suppliers. It can be understood that vaporization of the material requires rather high temperature, and the behavior is quite dependent on the synthesis routes taken by different suppliers. Therefore, it is not simple to select proper commercial precursors for successful deposition.

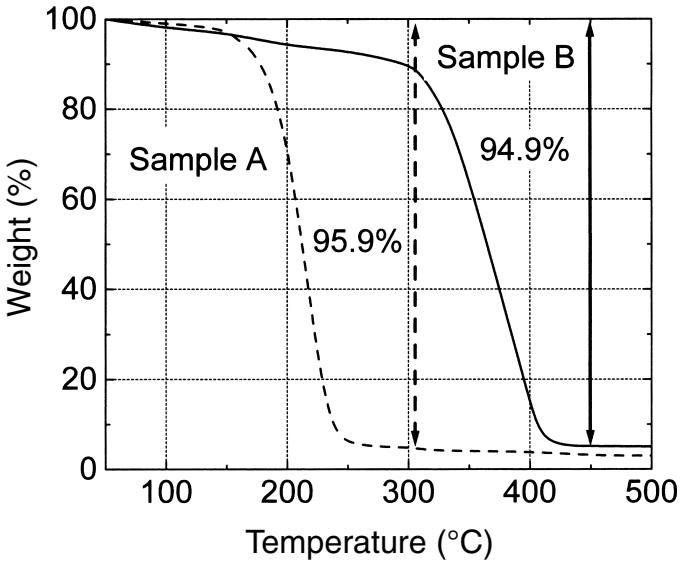

Fig. 3: TGA data for $Ba(thd)_2$ from two different suppliers.

Molecularity of the precursors having the thd ligand in the solid state is polymeric, and the precursor molecules tend to aggregate even in the vapor phase during transport. Actually, $Ba(thd)_2$ is more properly described as $Ba_4(thd)_8$ in the solid state because of its tendency to saturate the coordination number of Ba^{2+} ions. Therefore, sublimation of the $Ba(thd)_2$ and $Sr(thd)_2$ usually requires temperatures higher than about 180°C. From this point of view, there has been much effort to improve the volatility of group II precursors by adding an "adduct" to the $Ba(thd)_2$ and $Sr(thd)_2$. The adducts saturate the coordination number of the metal ions and reduce the tendency to aggregate.

One of the most extensively used adducts is tetraglyme ($C_{10}H_{22}O_5$); the $Ba(thd)_2$tetraglyme and $Sr(thd)_2$tetraglyme were commercialized by ATMI in the USA and have been tested by CVD system companies[14] and many device makers.[15] It appears that the addition of the adducts successfully increases the shelf life of the precursor at room temperature in solution for liquid delivery as well as in the solid state. However, dissociation of the adduct easily occurs during sublimation at high temperature, which cannot be any help in improving the repeatability of film deposition.

B. Vaartstra et al.[16] tried to improve adhesion between the adduct and the metal ion by adopting the simple or poly-amine adduct utilizing multiple metal - nitrogen bondings. Among the various adducts, 1,1,4,7,7-pentamethyidiethylenetriamine (pmdt) was commercialized as $Ba(thd)_2$pmdt and $Sr(thd)_2$pmdt. The multiple bonding between the metal ion and N ions of the adduct improves the thermal stability of the precursor which results in improved transport characteristics when liquid delivery is used. However, the pmdt adduct also dissociates in the temperature region between 120-150°C at 50 mTorr of pressure which also makes $Ba(thd)_2$pmdt less desirable as a CVD precursor. Figure 4 shows the molecular structure of the $Ba(thd)_2$pmdt molecule.

T. Kimura et al.[17] tested a large number of candidate materials as adducts. They can drastically reduce the melting point of the $Sr(thd)_2$ and increase the vapor pressure; examples are triethylenetetramine (trien) or tetraethylenepentamine (tetraen). The decrease in melting point of the precursor indicates that

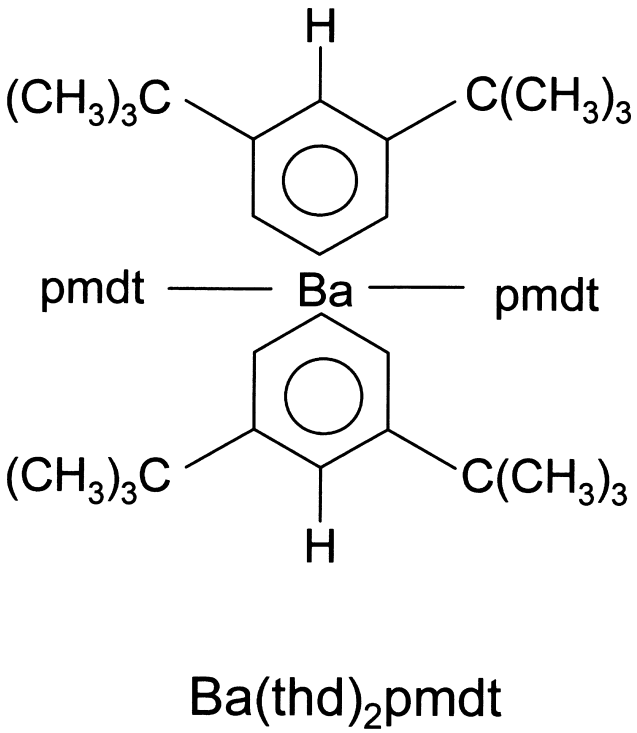

Fig. 4: Molecular structure of $Ba(thd)_2pmdt$.

intermolecular aggregation was effectively reduced by the saturation of the Sr^{2+} ion with the adduct. The melting points of $Sr(thd)_2trien_2$ and $Sr(thd)_2tetraen_2$ are 43.3 and 74.9°C, respectively. The result is that transport of the precursors is quite reproducible even using a conventional bubbling technique. The bubbling of precursors having liquid form does not results in surface area reduction which is a direct cause of reduction in vapor pressure with time for solid precursors. This precursor can be used for 60 hours at 130°C without any noticeable vapor pressure drop to deposit $SrTiO_3$ thin films.

Because of limited success due to adding adducts to the $Ba(thd)_2$ molecule, a new precursor having a modified thd ligand was recently developed. In $Ba(methd)_2tetraglyme$, one of the CH_3 group in the thd ligand is exchanged with the $CH_2OCH_2CH_2OCH_3$ group which appears to surround the Ba^{2+} ion more effectively than the simple thd ligand does due to its more bulky structure.[18] Schematic molecular structure of this material is shown in Figure 5. This material is liquid at room temperature and is very viscous, which does not permit conventional bubbling at temperatures lower than 100°C. It is still required to heat the material up to 160°C which makes the adduct unstable. Experimental data on the deposition of BST films using this precursor are not yet sufficiently available. However, some preliminary data show that the decomposition characteristics are rather different from those of $Ba(thd)_2tetraglyme$.[16]

The more electronegative and bulky F ions instead of the CH_3 group in the ligand were expected to decrease intermolecular forces and increase volatility of the precursors. A typical fluorinated precursor of Ba is Ba bis-hexafluoroacetylacetonate ($Ba(hfa)_2$). L. Wills and B. Wessels[19] used $Ba(hfa)_2tetraglyme$ to deposit $BaTiO_3$ thin films, where they sublirned the precursor at temperatures ranging from 105 to 125°C which is much lower than for $Ba(thd)_2$. M. Nyman and S. Desu[20] have reported better volatility of Pb bis-heptafluorodimethy-

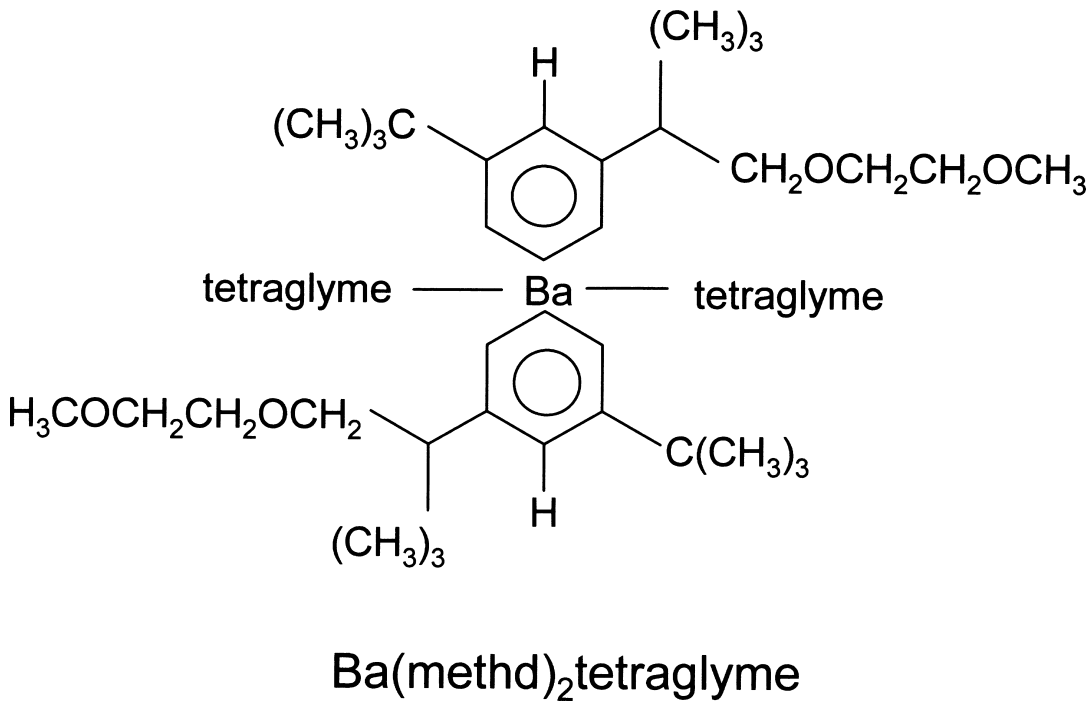

Fig. 5: Molecular structure of $Ba(methd)_2$tetraglyme.

loctadione $Pb(fod)_2$) compared to $Pb(thd)_2$ although these are not Ba precursors. Figure 6 shows the molecular structures of $Ba(hfa)_2$tetraglyme and $Pb(fod)_2$. Even though fluorinated precursors show better sublimation performance than the compounds having the thd ligand, the formation of a thermally stable fluoride, such as BaF_2, discourage their use as precursors.[21] However, the author's research group recently found that the incorporation of a small amount of F into the BST film improves the electrical performance of the thin film capacitors.[22] This issue will be discussed further in section 6.

Another strategy to improve transport efficiency of the $Ba(thd)_2$ and process reproducibility is to use NH_3, which is a simple amine adduct, as a carrier gas for the precursor. This idea was suggested by A. Baron in 1990 for the MOCVD of high T_c, superconducting oxide films containing Ba ions.[23] J. S. Lee et al. recently reported in - situ mass spectroscopic analysis results of the MOCVD of $SrTiO_3$ thin films using the NH_3 carrier gas for the $Sr(thd)_2$ precursor instead of the conventional Ar.[24] They observed that the concentration of Sr in the reaction chamber was maintained constant during the 100 min deposition time, whereas when using Ar carrier gas, it decreases with time. The better electrical performance of films deposited using the NH_3 carrier gas is due to uniform and reproducible transport of the precursor materials. It is believed that during saturation of the NH_3 gas with the precursor addition of adduct (NH_3) to the precursor molecule would happen to a certain extent and improve the transport efficiency of the precursor. Therefore, use of NH_3 as the carrier gas for precursors having thd ligands should be more extensively studied.

Precursors for group IV Elements: Ti

Contrary to the group 11 elements, we have many CVD precursors for Ti. The inorganic

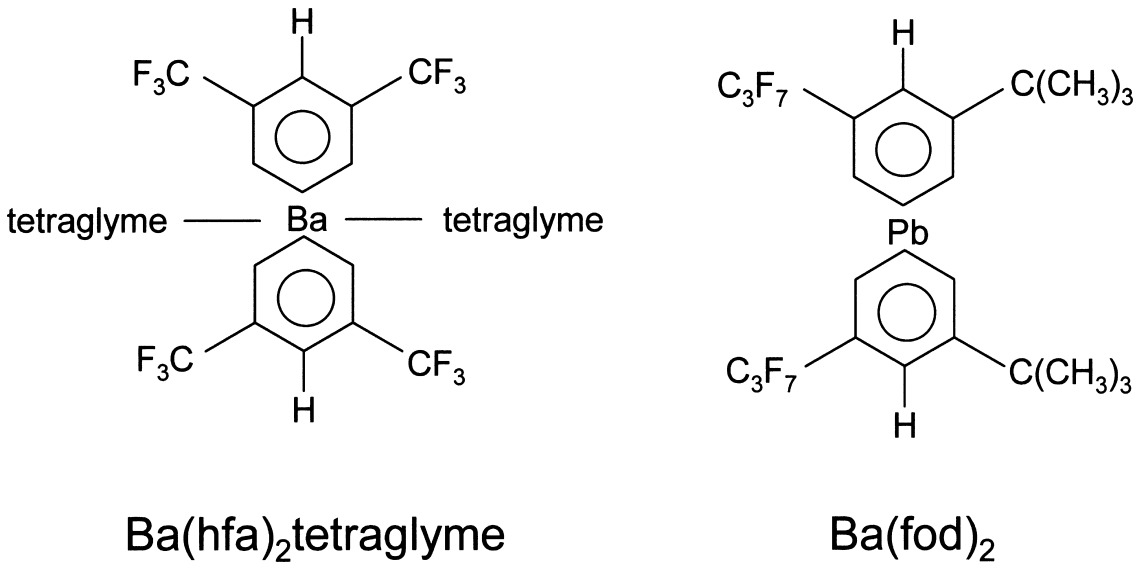

Fig. 6: Molecular structures of $Ba(hfa)_2$tetraglyme and $Pb(fod)_2$.

$TiCl_4$[25] has been extensively used for the deposition of TiN thin films as the top electrode for Ta_2O_5 dielectric capacitors as well as for barriers layers in Al or Cu metalization because it has sufficient vapor pressure and is non-viscous liquid at room temperature. However, thermal decomposition of this precursor and elimination of Cl contamination in the film usually requires high deposition temperatures (> 600°C). As discussed later, the BST CVD process requires a low deposition temperature, less than roughly 450°C, due to issues of process integration and conformal deposition which render the, $TiCl_4$ useless for this case. We need a metal-organic precursor.

There are several simple alkoxides of Ti having sufficient volatility.[26] The most extensively used alkoxide precursor is Ti-isopropoxide ($Ti(i\text{-}OC_3H_7)_4$) due to its high vapor pressure with good thermal stability. NEC group[27] in Japan has used this precursor in combination with $Ba(thd)_2$ and $Sr(thd)_2$ for the deposition of BST films using an electron cyclotron resonance (ECR) MOCVD. However, it is highly probable that a ligand exchange reaction occurs between the precursors having the thd and isopropoxy ligands, respectively, due to the different affinity of the ligands for the metal ions. The chemical reaction can result in macro-molecules which act as nuclei for homogeneous reaction in the gas phase. Therefore, a new Ti precursor which has a more similar chemical structure to that of the Ba and Sr precursors is required.

$Ti(thd)_2(i\text{-}O\text{-}P_r)_2$, where $P_r = C_3H_7$, has proven to be more useful to use than simple $Ti(i\text{-}OC_3H_7)_4$ in combination with Ba and Sr precursors[28]. However, even with the modified ligand structure of $Ti(thd)_2(i\text{-}O\text{-}P_r)_2$, incorporation of the Ti ions into BST films as a function of temperature is still quite different from those of the $Ba(thd)_2$ and $Sr(thd)_2$ which makes the cationic composition of the BST films very dependent on the deposition temperature.[29] This phenomenon will be explained in detail in section 4.

Mitsubishi researchers reported that conformal deposition of the BST film on a patterned wafer is improved when $TiO(thd)_2$ is used instead of the $Ti(thd)_2(i\text{-}O\text{-}P_r)_2$[30]. It was believed that the smaller sticking coefficient of the $TiO(thd)_2$ compared to that of the $Ti(thd)_2(i\text{-}O\text{-}P_r)_2$ improves the conforinality of the depositions.[30] They also reported a further improvement in conformal deposition by

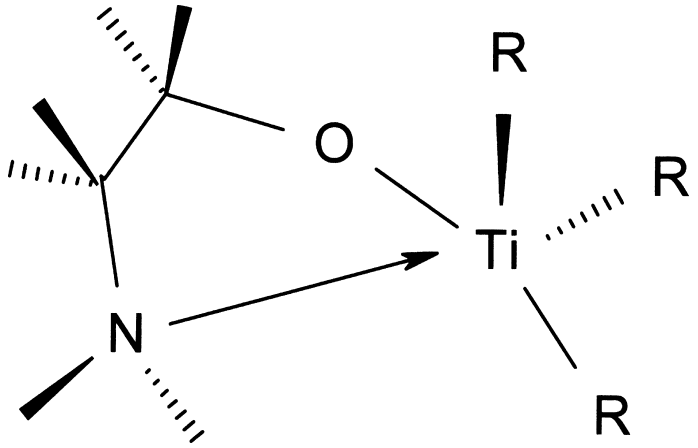

BST-NT1

Fig. 7: Molecular structure of BST-NT1.

utilizing $Ti(thd)_2(t\text{-}O\text{-}Bu)_2$ instead of $TiO(thd)_2$[31]. When BST films are deposited at 450°C with this Ti precursor, about 80% step coverage was obtained on the trench pattern of width : depth ratio of 1 : 3. The sticking coefficient of. the $Ti(thd)_2(t\text{-}O\text{-}Bu)_2$ was calculated to be only 1/5 that of the $TiO(thd)_2$.

Recently, one more Ti precursor has been introduced, Ti(MPD)$(thd)_2$ (MPD = methyl-pentanedioxide), but its effects on the BST film deposition are not yet well known. It is generally understood that the optimum Ti precursor must have chemical compatibility with the Ba and Sr precursors, such as non-interaction in solution or in the gas phase and similar decomposition characteristics to the Ba and Sr precursors, in addition to volatility. Most of the Ti precursors discussed above have much better volatilities and thermal stabilities than those of the precursors of the group II elements but are still lacking appropriate chemical compatibility with them. It is known that the thermal decomposition of $Ti(thd)_2(i\text{-}O\text{-}P_r)_2$ is quite different from that of the $Ba(thd)_2$ and $Sr(thd)_2$ from the increasing Ti concentration in the BST film with increasing temperatures.[29] It is believed that the thermal decomposition of $Ti(thd)_2(i\text{-}O\text{-}P_r)_2$ requires more activation energy compared with $Ba(thd)_2$ and $Sr(thd)_2$ due perhaps to the rather strong Ti-O bonds in the precursor. To overcome this problem, a new chemical containing weaker Ti-N bonding was developed having the code name of BST-NT1[32] the structure of which is shown in Figure 7. However, as discussed in the comparison of conformality of films using $Ti(thd)_2(i\text{-}O\text{-}P_r)_2$ and $TiO(thd)_2$, the easy thermal decomposition may possibly degrade conformality of the deposited thin films on a patterned surface.

Hardware Systems

Delivery Techniques for Precursors

Conventional Technique and Bubbling

Even though the simplest way of delivering the solid or liquid precursors is sublimating the precursors by heating to a proper temperature and carrying the vapor with a carrier gas. this technique, called bubbling, does not work with precursors for the MOCVD of BST films. As mentioned previously, the oligomerization of the

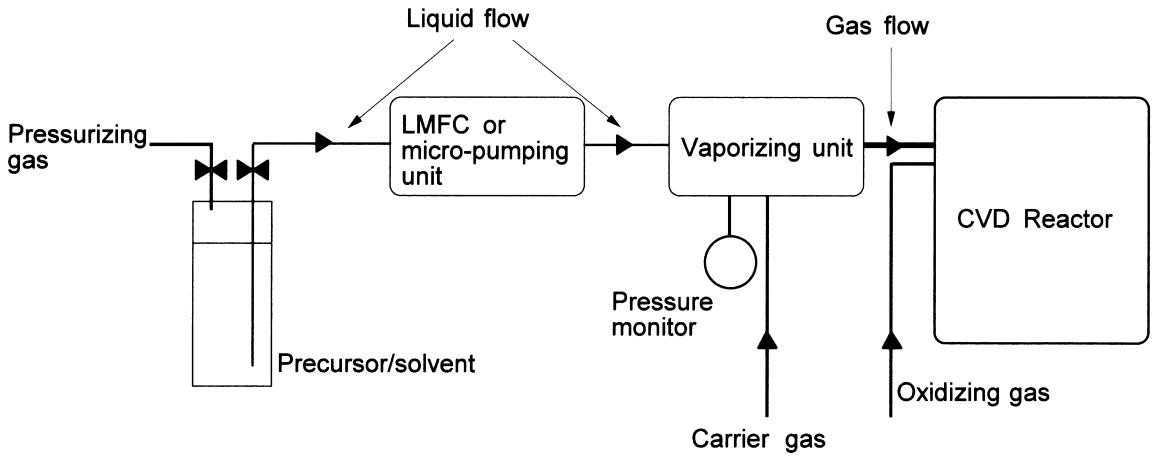

Fig. 8: Generalized schematic diagram of a liquid delivery system.

precursors at the bubbling temperature, especially for group II elements, rapidly drops the vapor pressure of the precursors, even when they have adducts, so that the deposition process becomes very unreproducible. For solid precursors in powder form, including Ba and Sr precursors, the decreasing surface area with volatilization decreases the transport efficiency of the material even if oligomerization is effectively suppressed. Liquid precursors do not have this problem. Thus synthesis of precursors having liquid form is highly desirable if the only allowed option for delivery is bubbling. Unfortunately, it seems that with precursors for BST thin fihns, degradation in the vapor pressure with time by oligomerization is so serious that mass production is not possible with this technique. We need a different way of delivering the precursors which does not degrade the volatility of the precursors, such as a liquid-delivery technique. Moreover, liquid precursors usually have higher vapor pressure than solid precursors. Thus, the synthesis of the liquid precursors is still desirable even with the liquid delivery technique.

Liquid Delivery Technique

The liquid delivery technique presently appears to be the only option that we have for mass production. This technique is based on the concept of the point of use of the required amount of the precursors. In this technique, precursors are usually dissolved in the proper solvents to make a "liquid source" when only solid precursors are available and to decrease the viscosity of liquid precursors. A small flux, usually a few tenths ml/min, of the solution is extracted by a micro-pump or liquid mass flow controller (LMFC) from the source reservoir which is stored at room temperature so that the oligomerization reaction is minimized. The small flux is flash vaporized in the "vaporizer" when the liquid contacts the hot surfaces of metal sponge or disks which are contained in the vaporizer. Then the vaporized precursors, accompanied by the vapor of the solvent, are directed into the CVD reactor by the carrier gas as in the case of conventional bubbling. Figure 8 shows a generalized diagram of the liquid delivery system.

There are many precautions for successful implementation of the liquid delivery technique for the MOCVD of BST films. First of all, there must be a proper solvent that can dissolve enough of the precursors. In addition, the boiling point of the solvent should be as close as possible to that of the precursors. Otherwise, the concentration of precursors in the source liquid would be increased during the transport which makes the performance of the vaporizer unstable. Mitsubishi[28,30,31] have exclusively used tetrahydrofuran (THF; C_4H_8O) as the solvent for

$Ba(thd)_2$ and $Sr(thd)_2$ as well as $TiO(thd)_2$. THF is an appropriate solvent because it not only dissolves a reasonable amount of the precursors (0.1 mol/L) but also appears to act as an adduct to the Ba and Sr precursors. However, the boiling point (65-66°C) of THF is much lower than that of the precursors. Another solvent is n-butylacetate supplied by ATMI. Samsung[29] used solutions of $Ba(thd)_2$tetraglyme, $Sr(thd)_2$ tetraglyme and $Ti(thd)_2(i\text{-}O\text{-}P_r)_2$ dissolved in n-butylacetate with a concentration of 0.15 mol/L for Ba and Sr precursors and 0.4 mol/L for the Ti precursor. The n-butylacetate has a boiling point of 124-126°C.

Fortunately, most of the β-diketonate precursors have quite good solubilities in a variety of solvents which opens many new combinations of precursors and solvents for stable delivery. Indeed many new combinations are under test.

The most critical factor determining overall performance of the liquid delivery system is the design and performance of the vaporizer. The design concept of the vaporizer is that the hot surface area of the material that contacts the source should be as large as possible for effective volatilization with the effective conduction of heat from the heat source to the hot surface to maintain temperature as constant as possible. Needless to say the hot surface material should be chemically inert to the source chemicals at the vaporization temperature. Unfortunately, these two factors are not mutually compatible, with the result that many hardware companies design their own vaporizers using different design concepts. The use of metal sponge as the contact material, for example ATMI's LDS 300B, is very effective in increasing the surface area, but the heat transfer from the heating jacket which surrounds the vaporizer is not so efficient due to the many small pores in the metal sponge. If the heat transfer is not efficient, a small variation in the flow of the cool liquid or flow of the flushing solvents might produce variation in the temperature of the vaporizing unit resulting in degradation of performance. The degradation in overall performance of the vaporizer is usually caused by clogging of the vaporizing unit which results from incomplete vaporization of the precursors, selective vaporization of the solvents and possible oligomerization in the vaporizer. To alleviate this issue, some manufacturers advise to flush the vaporizing unit using the solvents between each run. However, flushing induces a temporary variation of the vaporizer temperature, and the performance is even further degraded when heat transfer is not efficient. Therefore, still special care and many trials are required to establish optimum operation conditions of the liquid delivery system. For the precursors of BST thin films the vaporizer temperature is usually set between 240 and 250°C.

When the vaporizer function is not perfect, we can reduce the risk of catastrophic failure of the system by monitoring *in-situ* the status of the vaporizer. One method is to monitor the change of pressure inside the vaporizer with running time. When vaporizer clogging starts, the pressure increases abruptly, indicating that the vaporizer needs service. By gathering and inspecting data on the variation of the pressure with running time, the user can understand the experimental parameters that affect the vaporizer performance.

Control of liquid flow does not seem to be a problem. There are two versions of liquid flow control; one is to use a micro-pump or double cylinder to pressurize the liquid and the other is to use a liquid mass flow controller. In either case, the control of liquid flow seems to be accurate enough for CVD. One design precaution is to minimize the volume of the liquid lines, otherwise changing the source composition takes a long time with a large waste of expensive precursors.

Up to now, the precursor solutions for Ba, Sr, and Ti are usually contained in separate reservoirs to permit variation in the input ratio of the cationic elements. However, for mass-production it is much more desirable to use the "cocktail" source which contains all three precursors in one reservoir for more reproducible deposition. Use of the cocktail source is not proper for research because changing the cationic composition is not easy. Furthermore, the cationic composition of BST films is not only dependent on the input precursor ratio but also on the deposition temperature, as discussed below. Therefore, use of a cocktail source is possible only

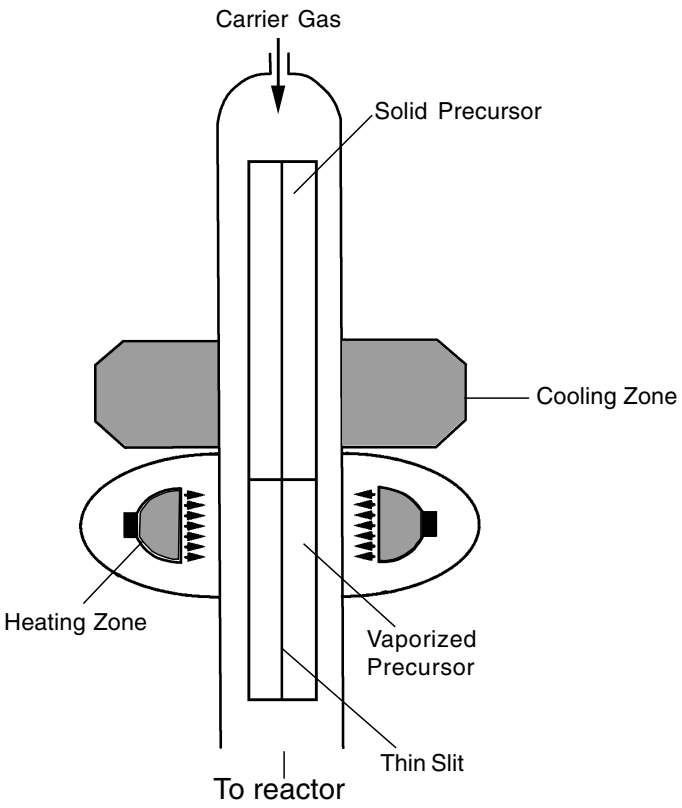

Fig. 9: Schematic diagram of a solid delivery system.

when all the experimental parameters are fixed for optimum deposition conditions.

Solid Delivery Technique

Another design to deliver precursors having powdery form is the solid delivery technique. Solid delivery is described as follows. Quartz glass tubing having a thin slit opening filled with the powder precursor mixture is provided with a steep temperature gradient heating zone, usually using a halogen lamp, and cooling zone, using cooling water, resulting in the steady vaporization of the precursors. A schematic diagram of this delivery system is shown in Figure 9. Z. Lu used this technique to grow epitaxial $LiNbO_3$ thin films.[33] J. C. Shin et. al. deposited (Pb, La)TiO_3[34] ferroelectric thin films using thd precursors with a solid delivery technique. The technique is very effective in precisely controlling the composition of the film to obtain reproducibility. Because this technique does not require any other chemicals except the precursors, potential influence of solvents on the deposition characteristics is eliminated. Furthermore, the system is much more simple and easy to install in the CVD reactor compared to the liquid delivery system. All these factors make the technique useful for acaden-tic research. However, continuous deposition is limited by the length of the precursor tube, which cannot be made very long, in addition to the rather serious particle generation problem. These two factors prevent the technique from being widely adopted as a mass-production compatible process. No commercial hardware for this technique is available at this moment, but it is believed that this technique is viable considering its excellent vapor transport capability, easy installation and low cost.

Deposition Reactors

Reactor Types

There are two general types of CVD reactors, one is the chamber type and the other is the tube type. The tube type reactor is typically a hot wall reactor and has been used in the semiconductor industry for the deposition of simple binary thin films such as Si_3N_4. This type of deposition reactor usually has quite large throughput because a few hundred wafers can be loaded and processed. However, the CVD precursors should have large diffusivities in the gas phase and be stable over the homogeneous reactions to produce uniform deposition on a large number of wafers. For tube type reactors, as for all hot wall type reactors, the CVD reaction occurs on the wall of the reactor as well as on the wafers. This increases the consumption of the precursors. Therefore, CVD reactors for BST thin films are the other type, except for a very recent report from Toshiba of Japan.[6] They reported CVD of BST thin films utilizing a tube type reactor which had a rotatory wafer holder to improve the uniformity of deposited films. Details of the CVD reactor have not been reported yet, thus, in this section only the details of chamber type reactors are discussed.

Chamber type CVD reactors for BST films usually have warm wall configuration to prevent condensation of the precursors during deposition. The walls are heated to a temperature approximately 250°C, a little higher than the evaporation temperature of the precursors. The most critical factors for performance of the chamber are design of the wafer heater and the method of precursor gas injection.

Heater Block

When deposition is controlled by surface chemical reaction conditions in the low temperature regime, uniformity over the wafer surface and repeatability between runs are almost entirely determined by the uniformity and repeatability of wafer temperature. This is the case for BST thin films for DRAM applications, as mentioned previously, so that a very stringent requirement is control of the wafer temperature. Usually, the [(max. - min.)/ 2average] uniformity value less than 1% is required, which means the maximum allowed temperature variation over an 8" wafer is only a few degrees ceisius when the processing temperature is about 450°C. To satisfy this requirement, a two zone heating method, in which the central and outer heating elements are separated and controlled independently, is usually used. It is worth noting that the actual temperature of the wafer is far different from that of the heater. To compensate for this difference, the wafer temperature is calibrated with the heater temperature, which is usually monitored during the processing, utilizing a so called thermocouple wafer which has several embedded thermocouple beads in a Si wafer. One important fact that should be remembered is that the actual wafer temperature is very dependent on the type of thin films on the wafer. Figure 10 shows the difference in temperature between the bare and platinized Si wafers as a function of the heater temperature. A special thermocouple wafer that has a 100-nm-thick Pt thin film was fabricated for this measurement. We can understand that the platinized wafer is much more effectively heated than the bare Si wafer due to the large reflection of photons into the wafer due to the Pt thin film. It should be remembered that the major heat transfer mode in this case is radiation from the heating element to the backside of the wafer. We can see that the difference is not constant over the temperature range. This result implies that the actual temperature and its distribution over the wafer can be further varied when the metal film is patterned. It was observed that the temperature of the center region of the platinized wafer was higher when the film was continuous whereas the edge region was hotter when it was patterned with the storage node shape under the same heating condition. All these factors require that special care be taken for the design of the heater.

Close contact of the wafer to the surface of the heater block is another important factor that determines uniformity and reproducibility of the deposition. In addition, the heating time of the wafer to the desired temperature after chamber loading, which takes normally a few minutes and reduces throughput, also depends on the contact status. The electrostatic chuck (ESC) may

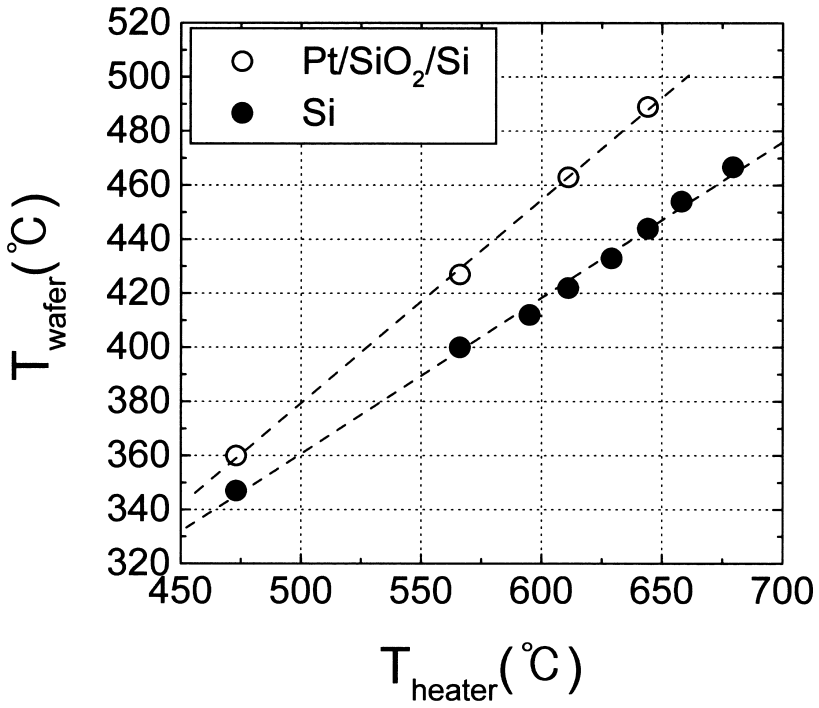

Fig. 10: Differences in temperature between bare and platinized Si wafers as a function of heater temperature.

improve the situation but there has not been any report on this issue. It seems that the low temperature version of the BST CVD process compared to a process which uses a temperature higher than 600°C, makes the adoption of the ESC highly probable.

The size of the heater block is usually slightly larger than that of the wafer, such as 10 or 12" for an 8" wafer, to compensate for heat loss from the wafer edge. However, the larger size brings unwanted deposition of the film material on the exposed heater surface which then generates particles after repeated depositions. This occurs even if the wall temperature is well controlled so as not to decompose and condense the precursors on the wall. This problem has been minimized by reducing heater size, as reported by joo et al.[35]. They designed a heater having almost the same size as that of the wafer by taking special care to maintain uniformity of temperature. This improvement may increase the up time of the chamber and its throughput.

Methods of Precursor Injection

Nozzle Type Gas Injector

It appears that there are two major types of precursor injection for BST CVD: simple nozzle injector and shower head. The simple nozzle injector is easy to fabricate as well as to operate. However, for uniform deposition with this nonuniform precursor injection, certain improvements in reactor geometry or substrate rotation are required. The high speed rotatory substrate holder produces uniform deposits on large wafers for compound semiconductor use. For this case the various gases are injected by separate nozzles which are installed on the inner top surface of the reactor. High speed rotation of the substrate generates a very thin and uniform fluid-dynamical and chemical boundary layer with uniform mixing of the gases which ensures uniform thickness and chemical composition of the deposited films. Recently, this technology has been applied to multi-component oxide CVD.[36] However, it is not still

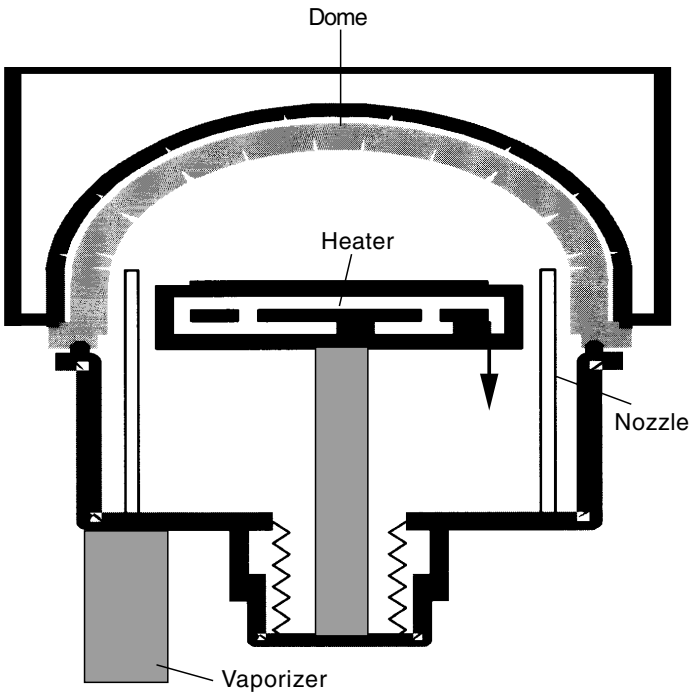

Fig. 11: Schematic diagram of a CVD reactor having a simple nozzle type gas injector. (courtesy of JUSUNG Engineering).

proven that this type of rotatory action of the substrate does not affect the long term reliability of the hardware system and the production throughput. A system that contains mechanically moving parts generally has more problems than a stationary system.

Another type of reactor using a simple injector is a reactor with a dome type cover.[37] In this case, the injector is installed on the bottom plate of the reactor. Figure 11 shows the typical configuration of this type of reactor. In this case the dome is usually heated to a proper temperature by a separate heater to prevent precursor condensation on it. It is rather difficult to expect uniform deposition of a thin film from this asymmetrical gas injection geometry. However, it has actually been proved that good thickness and compositional uniformity are obtained over the 8" wafer surface for Ta_2O_5 thin films. Figure 12 shows the typical variation in thickness of a Ta_2O_5 thin film using this reactor. An understanding of the possibility of uniform deposition using this type of non-uniform gas injection can be obtained from Figure 13. When the precursor molecules are injected through the injector nozzle from the bottom of the reactor to the dome wall, they stick to the inner surface of the dome for a very short time. Then they are desorbed from the dome surface and move to the wafer surface by diffusion process through the gas phase. During this short adsorption/desorption process, the precursor molecules lose their original directionality. The result is a uniform supply of precursor molecules on the large wafer surface due to the spherical shape of the dome. In addition to the capability of uniform supply, the warm dome surface supplies the precursor molecules with the proper thermal energy during the adsorption/desorption process. The "warmed-up" molecules appear to improve the uniformity and reproducibility of the deposition reaction.

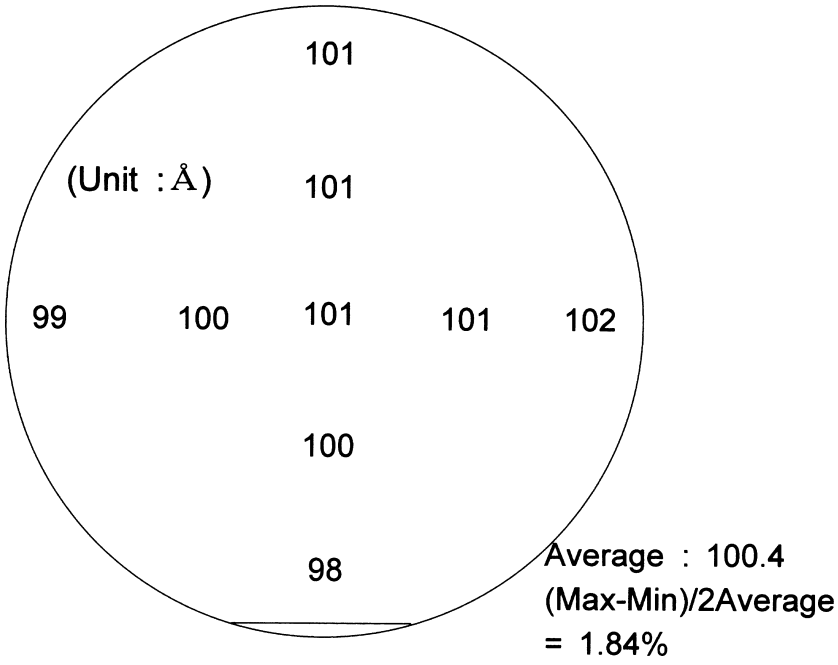

Fig. 12: Typical variation in the thickness of a Ta_2O_5 thin film using a dome type reactor.

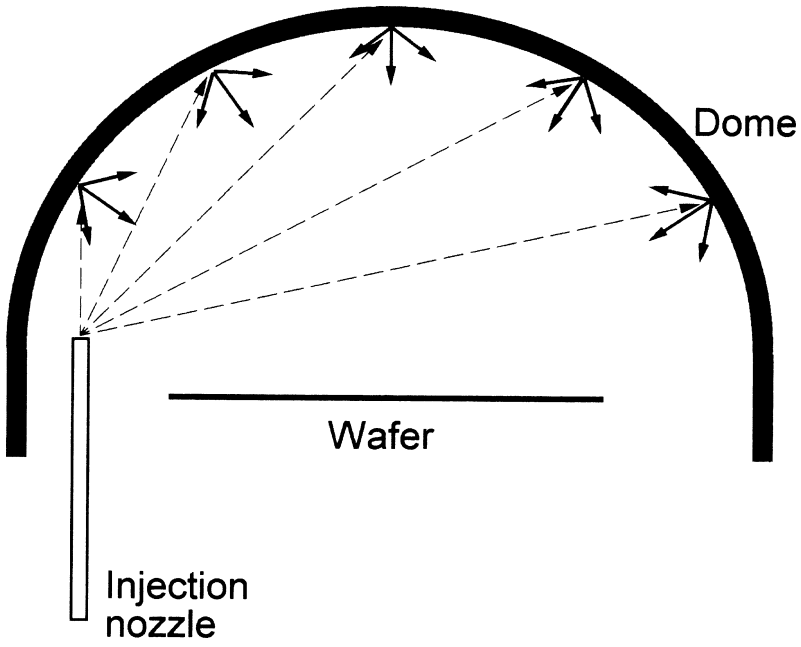

Fig. 13: The kinetics of injected gas molecules take on inner wall of a dome type reactor.

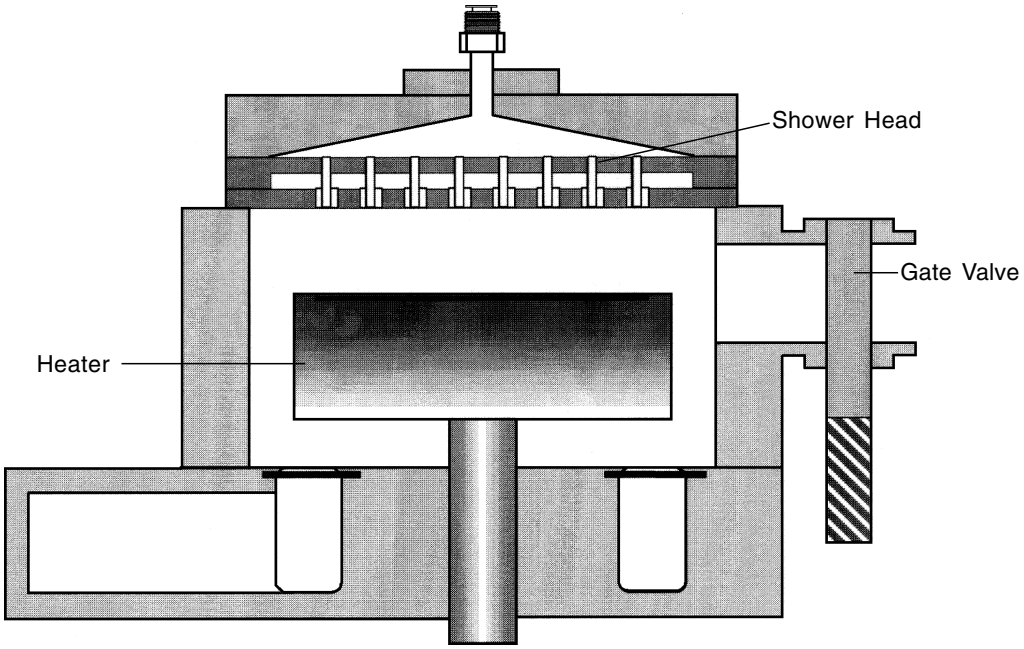

Fig. 14: Typical shape of the shower head for MOCVD BST. (courtesy of ULTECH Co.).

Shower Head Type Gas Injector

To ensure a uniform supply of precursor molecules over the wafer surface, shower head type gas injectors have been successfully used in many CVD chambers. Uniform deposition of BST thin films by MOCVD also has been attained by adopting shower heads.[29] Typical shower head shape for MOCVD BST is shown in Figure 14. For this application, the metal-organic precursor molecules usually carried by Ar gas and reactant gases, such as O_2 and N_2O, are supplied separately by a double shower head configuration into the shower head to alleviate the premature reaction between them, as shown in the figure. Although this type of gas injection usually ensures uniform supply of the gases over the wafer, some special precautions are required to obtain reproducible deposition. Because the CVD reaction temperature is quite high, > 600°C, for the high temperature version of BST deposition, the exit plate of the shower head, which is in a face to face position with the wafer, is usually heated to a temperature which is higher than the thermal decomposition temperature of the precursors if a proper cool down mechanism is not adopted. The proper cool down mechanism is usually circulation of cool nitrogen or thermofluid inside the shower head plate. When the shower head plate temperature is monitored *in-situ,* the temperature variation was observed to be less than ± 0.5°C, when the thermofluid is used. However, the thermofluid system requires some space and makes the CVD system more bulky and complicated. For the low temperature version of BST film deposition, < 450°C, the thermofluid acts to heat the shower head plate protecting the precursors from condensing inside the shower head. If either thermal decomposition or condensation of the precursors take place, the system generates numerous particles and deposition reproducibility seriously deteriorates. Therefore, it can be stated that the shower head usually ensures more uniform supply of reactant gas molecules over the wafer surface, but it costs more and requires more maintenance labor compared to simple nozzle type gas injectors.

Film Deposition Processes

The much larger dielectric constant of a BST film (>200), compared to that of a polyerystailine Ta_2O_5 film on Si (20~25) or amorphous SiO_2/SiN bi-layer (6 ~ 7), is due to its perovskite crystal structure, in which a large dipole moment is induced when the electric field is applied. Therefore, deposition of BST films with good crystalline quality is extremely important to obtain a large capacitance. In most deposition methods, the higher the deposition temperature the better the crystalline quality of the film as long as the stoichiometric composition is maintained.

However, there are several problems related to the high temperature deposition process. Firstly, oxidation of the barrier resulting in a increased contact resistance with increased deposition temperature limits the deposition temperature depending on the deposition method. Secondly, as discussed below, the conformal deposition property of the film on a three dimensional patterned geometry, i.e. the step coverage, usually degrades with increasing CVD temperature. Giga bit density DRAMs are anticipated to have a storage pattern with aspect ratio (width : height) of more than 1 : 3 and minimum feature size of far less than 0.15 μm. Therefore, good step coverage of the deposited thin films is also very important to ensure the reliability of the device. Even though it is not an important issue, the higher deposition temperature of BST films results in larger leakage current mainly due to increased roughness of the bottom electrode surface.

Therefore, it is quite logical to emphasize low temperature MOCVD (wafer temperature of less than roughly 500°C) of BST thin films even though the status of the research is still behind that of the high temperature deposition process (wafer temperature of higher than roughly 600°C). Data on films from high temperature CVD is discussed only for reference purposes.

Composition Control of the Thin Films

Figure 15 shows a typical variation of the cationic composition ratio with deposition temperature ranging from 405 to 570°C when $Ba(thd)_2$tetraglyme, $Sr(thd)_2$tetraglyme and $Ti(thd)_2(O\text{-}i\text{-}Pr)_2$ dissolved in n-buthyl acetate are used as the source chemicals for Ba, Sr and Ti, respectively. For this specific case, the oxidant was a N_2O/O_2 mixture, as originally suggested by the ATMI group. Because of the lower thermal decomposition of the Ti precursor compared to the Ba and Sr precursors, the chemical input ratio was controlled to be Ba : Sr : Ti = 1.00 : 1.00 : 1.68. The reaction chamber pressure was 1 Torr. Stable delivery of the precursors was obtained by adjusting the vaporizer temperature and the total liquid flow rate to be 240°C and 0.1 mil/min, respectively. More detailed experimental results can be found in the literature.[29]

The deposition temperatures can be divided into three regions. A, B, and C as shown in the figure, according to compositional and morphological behavior which will be discussed in the next section. The regions B and C roughly correspond to the high temperature deposition process and region A comprises the low deposition temperature region. As clearly shown in the figure, the high temperature process usually ensures highly reproducible deposition in terms of film composition and thickness. It produces reproducible electrical characteristics because cationic composition and film growth rate are quite insensitive to the temperature variation in this region. It is believed that the deposition process is controlled by gas phase diffusion of the chemical species rather than the surface reactions in this temperature region, which inevitably results in poor step coverage. It is well known that CVD in the diffusion controlled regime usually generates films with poor step coverage because the diffusion of chemicals onto topological features is not uniform.

However, in region A, the chemical composition of the deposited thin films is very sensitive to the minute variation of temperature because in this region the thermal decomposition rate of the Ti precursor is very sensitive to temperature; i.e. surface chemical reaction controls the deposition. The variation of mass concentration of the constituent ions estimated by x-ray fluorescent spectroscopy (XRF) is

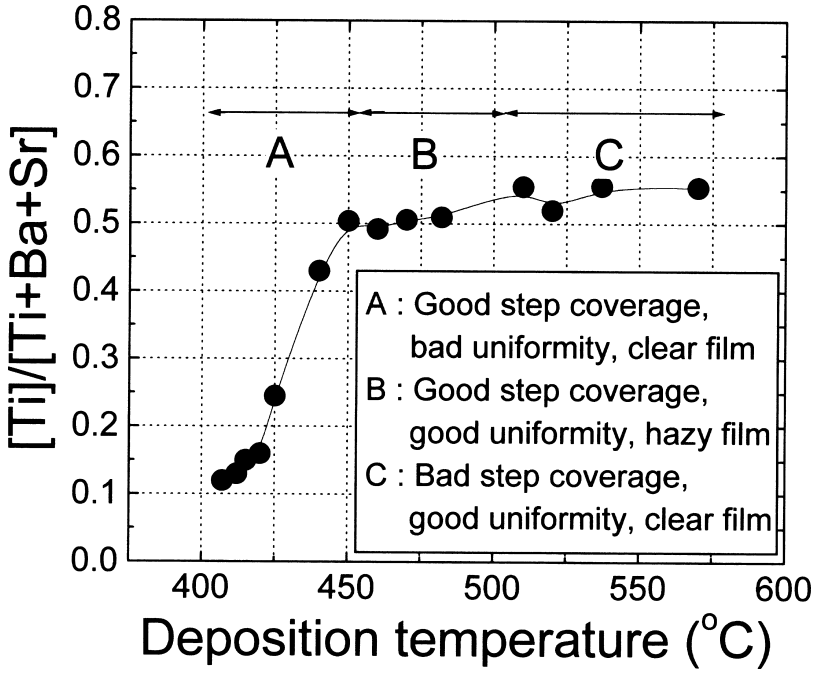

Fig. 15: Typical variation of the cationic composition ratio with deposition temperature when the precursors are $Ba(thd)_2$tetraglyme, $Sr(thd)_2$tetraglyme and $Ti(thd)_2(O\text{-}i\text{-}P_r)_2$ dissolved in n-buthyl acetate.

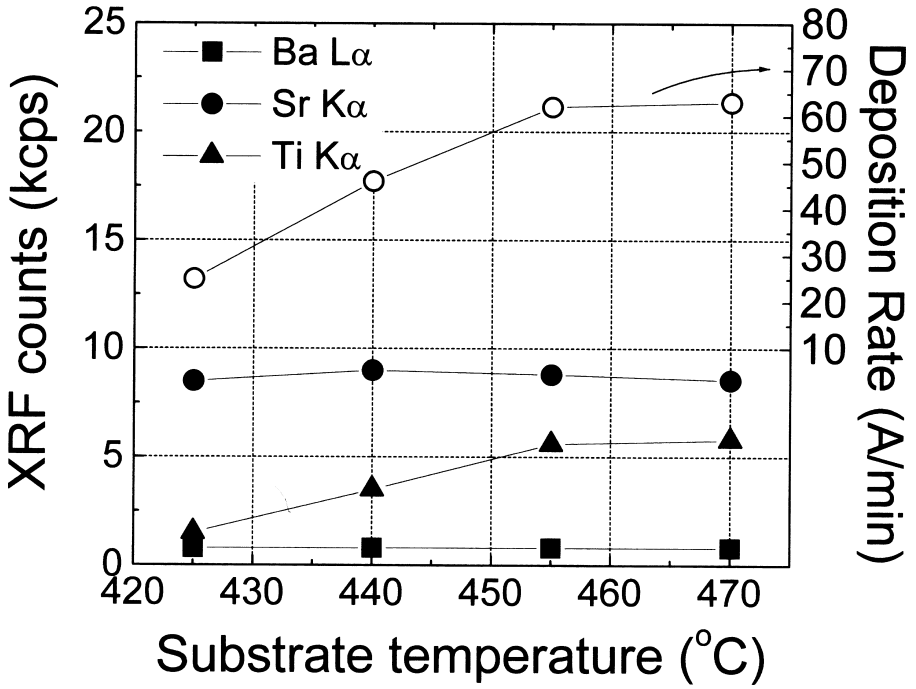

Fig. 16: The variation of mass concentration of constituent ions estimated by X-ray fluorescent spectroscopy.

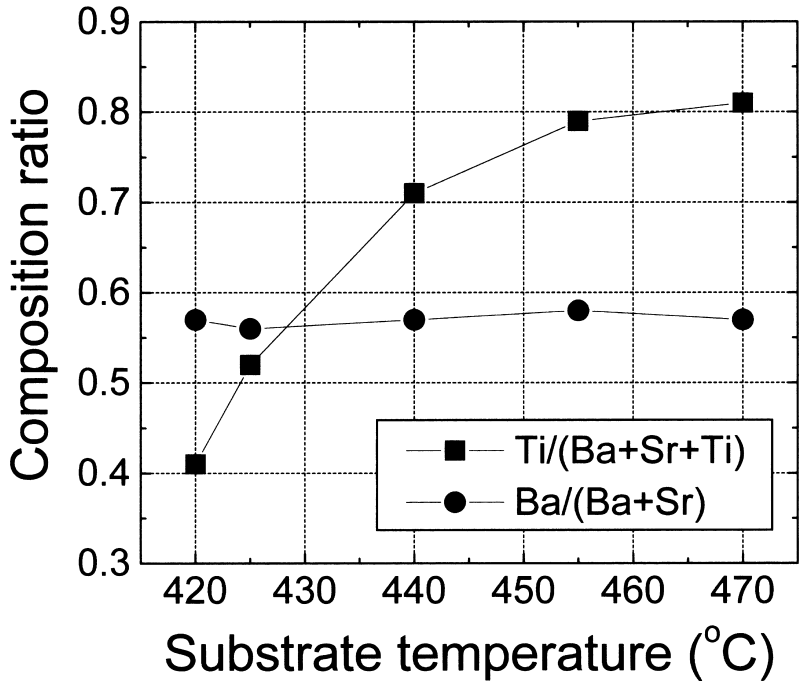

Fig. 17: Cationic composition ratios calculated from XRF utilizing a sensitivity factor.

shown in Figure 16 along with the variation of film growth rate in the temperature range from 420 to 470°C. For this set of experiments, the chemical input ratio of Ba : Sr : Ti was changed to 1 : 1 : 4.92 considering the poor incorporation of Ti in this temperature region. The cationic composition ratios calculated from XRF utilizing a sensitivity factor is shown in Figure 17. It can be understood that the different ligand structure of the Ti precursor from those of the Ba and Sr precursors and the stronger bonding strength between the Ti ion and its ligand make the thermal decomposition of the Ti precursor more difficult compared to the Ba and Sr precursors. Therefore, incorporation of Ti into the film is surface chemical reaction controlled whereas those of the Ba and Sr are much more diffusion controlled in this temperature region. Yamamuka et al. also reported the same behavior in the variation of the cationic composition of the films as a function of the deposition temperature when the $Ba(thd)_2$, $Sr(thd)_2$ and $TiO(thd)_2$ precursors dissolved in THF were used[30]. For that case, surface chemical reaction controlled incorporation of Ti was observed up to 500°C, in contrast to the case shown in Figure 17 due perhaps to the stronger bonding between the Ti ion and the O(thd) ligand and the significantly increased input of Ti, where the Ba : Sr Ti input ratio was 1.00 : 0.75 : 12.5.

An interesting observation results from the comparison between the Ti concentrations in Figures 15 and 17. When the Ti precursor input rate is increased by a factor of 2.93 (4.92/1.68) the Ti concentration of the film is increased by a factor of only 1.6 for a wafer temperature of 470°C, whereas it is increased by a factor of 2.73 when it is 420°C. This implies that as the deposition temperature increases, a type of self-regulating mechanism of film composition to the stoichiometric one is present, as in the case of Pb incorporation into PZT thin films. This kind of self-regulating mechanism can not generally be understood from simple therrnodynamic calculations which usually predict formation of

the most energetically stable phases under the assumption of a closed system, i.e. the total input material remains within in the system. It is more reasonable to assume that the mechanism is kinetic. However, thermodynamic calculation sometimes helps one understand the underlying kinetic processes.

Thermodynamic calculations on phase formation in the Ba-Sr-Ti-O-C-H system as a function of temperature for the given concentration of the each component, were done by Han et al.[38] They calculated the equilibrium concentrations of the possible solid phases, including the Ti-containing $(Ba,Sr)TiO_3$, $(Ba,Sr)_2TiO_4$, $Sr_4Ti_3O_{10}$ and TiO_2 in addition to $(Ba,Sr)CO_3$, (Ba,Sr)O and graphite, which do not contain Ti, in the relevant temperature range for the MOCVD process using the total energy minimization principle. It was assumed that C and H were incorporated into the system from the ligands of the precursors. They did not assume a liquid delivery situation so that the incorporation of C and H from the solvent were not taken into account which makes the calculation a bit different from the actual situation.

It was concluded that the most probable phase is BST in the temperature range from 500 to 1500 K, with the minor formation of other Ti-containing phases. Especially, when the temperature is less than 900 K, the formation of TiO_2 increases with decreasing temperature with slightly diminished formation of the BST phase whereas formation of other Ti-containing oxides is greatly suppressed. It should be noticed that the total Ti concentration of the system should be constant irrespective of the temperature in this calculation. However, it might be reasonable to assume that the quite complex Ti-containing phases, such as $(Ba,Sr)_2TiO_4$ and $Sr_4Ti_3O_{10}$, are not formed due to limited kinetics in this temperature range. In this case, we only need to consider the BST and TiO_2 phases because their structure is simpler and their kinetics are easier. Now, when the Ti input was increased by the same factor at high and low wafer temperatures, the enhanced formation of TiO_2 at the low temperature compared to the high temperature increases the incorporation efficiency of Ti into the film.

Owing to the very rapid variation of the composition with the temperature in region A, uniformity and reproducibility of deposition seriously degrade as the wafer temperature drops below 450°C. Figure 18 shows the variation of [(max. - min.)/2average] non-uniformity of the cation concentration and the film thickness over the 6" wafer surface with temperature. The small temperature variation over the wafer surface generates such a much non-uniformity in region A due to the exponential dependence of the incorporation rate of Ti on temperature in this region. It is quite insensitive to the temperature variation in region B and C due to mass transfer limited deposition in those regions. Therefore, development of a stable process recipe becomes difficult as the deposition temperature decreases even though, unfortunately, the integration process requires low temperature processing.

Another problem of the low temperature MOCVD process is incorporation of impurities, such as C and H, into the film during deposition. It is not difficult to imagine that decomposition of metal-organic precursors at low temperatures is not complete, and impurities originating from the ligands can remain in the film. If these impurities are not properly removed by post-annealing, dielectric properties of the films are degraded. It has indeed been observed that the low temperature MOCVD films have a lower dielectric constant than those of sputtered films even when the deposition and post-annealing temperatures are the same with the same thicknesses. Therefore, one should consider what is happening in a chemical sense during low temperature deposition in order to achieve successful processing. Again, considering thermodynamic calculation data greatly helps us gain insight into the phase formation in such a complex situation.

Thermodynamic calculations, done by Han et al.[38] for the Ba-Sr-Ti-O-C-H system predict that the stable solid phases will be Ti-containing $(Ba,Sr)TiO_3$, $(BaSr)_2TiO_4$, $Sr_4Ti_3O_{10}$, and TiO_2 in addition to the $(Ba,Sr)CO_3$, (Ba,Sr)O. The graphite phase is also stable in the temperature range roughly below 600K, but its concentration goes to almost zero due to excess oxygen or a slight increase of temperature, so that we can

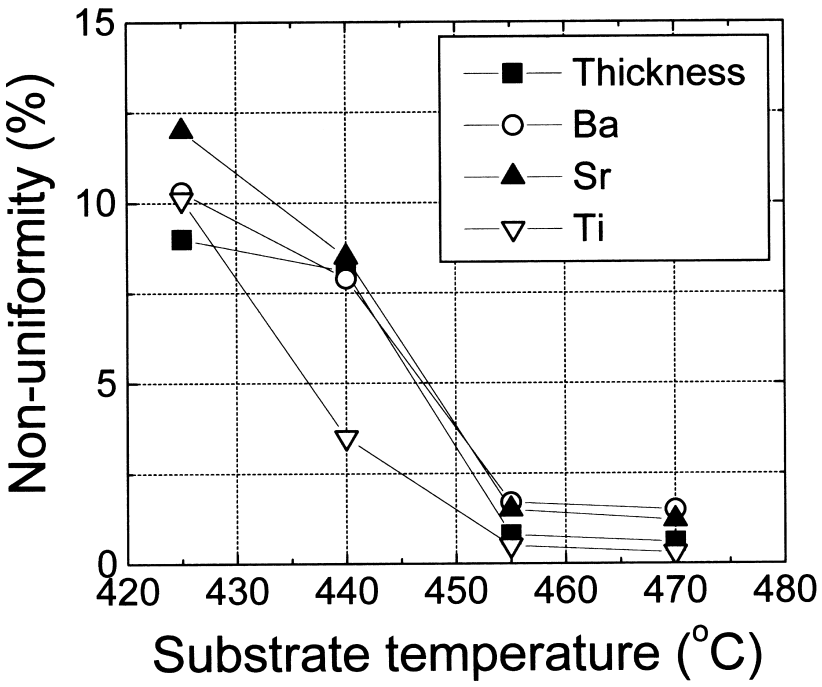

Fig. 18: Variations of [(max. -min.)/2average] non-uniformity of cation concentration and film thickness over the 6" wafer surface with temperature.

disregard it. The $(BaSr)_2TiO_4$, and $Sr_4Ti_3O_{10}$ phases can also be disregarded since their concentrations are a few orders of magnitude lower than the others, and the kinetics are quite limited due to their complex crystal structure in the temperature region of 600-800 K. The concentration of (Ba,Sr)O is also very low. Now the problematic impurity phases to be considered are (Ba, Sr)CO_3 and TiO_2. We consider the effects of three important process parameters on phase formation: temperature, Ti concentration for the given (Ba + Sr) concentration and the amount of oxygen.

When the material input ratio is fixed at Ba : Sr : Ti : 0 = 1 : 1 : 2 : 50, i.e. the cation stoichiometric composition, the formation of (Ba, Sr)CO_3 and TiO_2 is minimized to far less than 1% at 900 K (627°C). With decreasing temperature the formation of the two phases increases very rapidly with the same proportion, and at 700 K (427°C) their concentrations go up to a few% with a corresponding decrease in the concentration of the desired (Ba,Sr)TiO_3 phase. Below 600 K, the CVD reaction occurs too slowly so that we no longer consider that temperature. Actually, in such an extremely low temperature region, the formation of graphite is enhanced even with excess oxygen. Therefore, even if we supply the cations in the stoichlometric ratio by proper adjustment of the input ratio of each precursor taking into account the different thermal decomposition properties, we can see that roughly 10% of the Ba, Sr, and Ti are consumed to form the impurity phases, (Ba,Sr)CO_3 and TiO_2, with presence of carbon at around 400°C due merely to thermodynamic reasons.

When Ti input increased to a value higher than stoichiometric, the formation of (Ba, Sr)CO_3 is drastically suppressed with a corresponding increase in TiO_2 concentration. If the Ti input decreased to less than the stoichiometric value, the excess Ba and Sr react with C and O to form (Ba, Sr)CO_3. It has been

reported that the MOCVD deposition process as well as the electrical properties of the BST thin films are very stable when the film has a slightly Ti-excess composition during high temperature MOCVD.[39] This may be due to the successful suppression of formation of the detrimental (Ba, Sr)CO_3 phase with insignificant formation of TiO_2. However, excess Ti also generates a large amount of TiO_2 which also degrades the dielectric property of the films.

The last controllable parameter is the input of oxygen. When the O_2/Ba ratio is smaller than approximately 30 at 800 K, formation of graphite is quite extensive. If the film contains graphite it will be electrically conductive. The formation tendency of graphite is enhanced as temperature is decreased. Therefore, excess oxygen is absolutely necessary for the CVD reaction. With increasing oxygen, formation of (Ba,Sr)CO_3 and TiO_2 increases slightly even though their concentration is quite low for the case of stoichiometric supply of the cations. Accordingly, we can understand that the (Ba,Sr)CO_3 and TiO_2 impurity phases can not be completely eliminated by an increase of oxygen.

The above thermodynamic consideration shows that the low temperature MOCVD of BST inevitably involves the (Ba, Sr)CO_3 and TiO_2 impurity phases even though supply of the cations is at the right proportion, as long as the incorporation of carbon is not completely eliminated. This is primarily due to the slightly smaller formation free energies of the (Ba,Sr)CO_3 and TiO_2 phases compared to that of $BaTiO_3$: -1032.8, -809.7, and -1456.5 kJ/mol, respectively, at 700 K.

When solid state (Ba,Sr)CO_3 and TiO_2 are formed, the formation of (Ba, Sr)TiO_3 from these two phases by solid state reaction usually requires a temperature higher than 1100°C, which is unacceptable in the DRAM capacitor process. One factor to consider is that the actual chemical bond status of the carbon in the films may not be that of stable (Ba, Sr)CO_3 but can be more unstable which renders the elimination of the carbon or related impurities more feasible by a proper post-annealing than thermodynamics predicts. One must consider the atmosphere and surface status of the films during the annealing process. It is highly probable that incorporation of carbon containing impurities into the film is due to the incomplete decomposition of the Ti precursors in the low temperature region as will be discussed below. Therefore, the impurities may be loosely bonded to the Ti ions in the as-deposited thin films and may then combine with some of the Ba and Sr ions during post-treatment as the thermodynamics predict.

Step Coverage

Conformal deposition during CVD is the basic reason for use of the MOCVD process for BST films in,spite of various difficulties compared to the sputtering process. AS for general CVD, step coverage improves with decreasing deposition temperature. A typical variation of step coverage with deposition temperature is shown in Figure 19 where geometry of the test structure is 0.6 μm (width) × 0.9 μm (height) line/space pattern made of SiO_2. We can see that when deposition occurs in the mass transfer controlled region, T > 480°C, step coverage drops below 50% whereas it has values higher than 80% during surface chemical reaction controlled deposition, T < 480°C. There is a 30°C offset in the border temperature between the two controlling mechanisms for deposition between Figures 15 and 19. This is due to the different substrate surface states; for Figure 15 case surface is covered with a Pt thin film which increases the wafer temperature by about 30°C compared to the patterned wafer (in Figure 19) which does not have the metal layer.

The reason for good or poor step coverage in the two distinct temperature regions is obvious. In the surface chemical reaction controlled deposition regime, the deposition rate is determined solely by the temperature of the wafer. Temperatures at each point of the topological wafer surface having submicron features can hardly have local temperature variation, thus, conformal deposition is ensured. However, in the diffusion limited deposition region, the deposition rate is determined by gas phase diffusion of the reactants and/or reaction by-products which must be very dependent upon the topology of the surface.

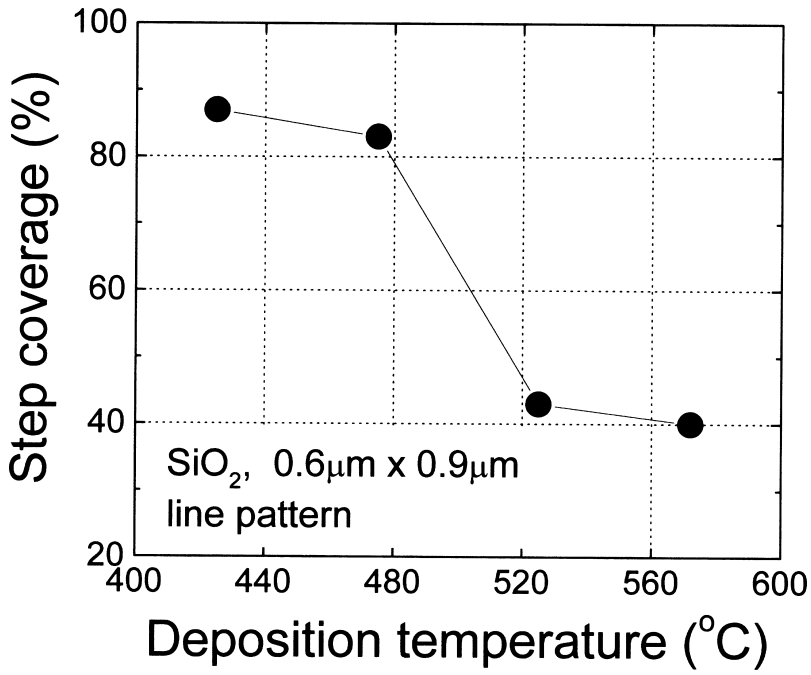

Fig. 19: Variation of step coverage with deposition temperature.

However, even in the surface chemical reaction controlled region, the stringent three dimensional topology of the storage node pattern of the DRAM capacitors makes the conformal deposition difficult. The Mitsubishi CVD group has published several papers on the effects of different Ti precursors, $Ti(O\text{-}i\text{-}C_3H_7)_4$[28], $TiO(thd)_2$[30] and $Ti(t\text{-}BuO)_2(thd)_2$[31] on the conformal deposition properties of the BST film when the deposition occurs in the surface chemical reaction controlled temperature region. They showed that the more bulky and stronger adhesive properties of the ligands to the metal ions accompany the smaller sticking coefficient of the precursor molecules onto the surface, which results in improved step coverage. For those experiments, the Ba and Sr precursors were also involved in the deposition reactions so that it can not be explicitly stated that step coverage is solely determined by the sticking property of the Ti precursor. However, as was shown in the previous section, the rate limiting step of the deposition in the low temperature region is incorporation of Ti. Therefore, it is not unreasonable to assume that step coverage is largely determined by the Ti incorporation reaction. The sticking coefficient of the most bulky Ti precursor, $Ti(t\text{-}BuO)_2(thd)_2$, was only 0.001, which is smaller by an order of magnitude than those of $Ti(O\text{-}i\text{-}C_3H_7)_4$ or $TiO(thd)_2$ at 420°C. With this small sticking coefficient, step coverage of more than 80% of the BST film was obtained on a trench pattern with aspect ratio of 3-4.

Figure 20 shows excellent step,coverage of one of the MOCVD BST films deposited by the dome type reactor with single injection nozzle at a wafer temperature of 413°C. The substrate has a linelspace pattern with an aspect ratio of 1 : 6 made of SiO_2 covered with a very thin Pt film. The step coverage is more than 80%. The featureless surface morphology of the film implies that the film has an amorphous structure which should be crystallized by proper post-annealing. As discussed previously, however, the hydrocarbon incorporation problem for low temperature CVD must be considered.

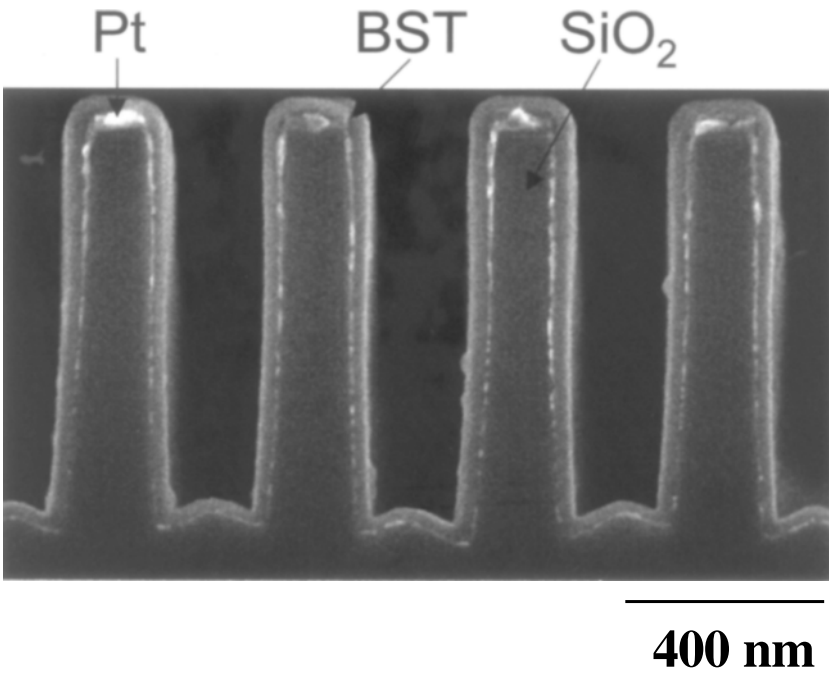

Fig. 20: SEM micrograph showing excellent step coverage of the MOCVD BST film deposited in a dome type reactor with single injection nozzle at a wafer temperature of 413°C.

Surface Morphology

The typical crystalline structure of the stoichiometric BST thin film on a Pt electrode is polycrystalline with partially faceted grains having average grain size of about 30 to 50 nm when the films are thinner than 50 nm and deposited at temperatures higher than roughly 500°C. The root mean square roughness measured by atomic force microscopy (AFM) is about 1 - 2 nm, which increases slightly with temperature. When the films are deposited under roughly 400°C, they are usually amorphous with featureless surface morphology. The crystallization temperature is rather dependent on the precursor material. However, for intermediate temperatures, the surface morphology is quite different from that of films deposited at high temperature as well as low temperature.

In Figure 15, the temperatures region above 450°C was divided into B and C regions even though both regions correspond to mass transfer controlled deposition. The reason for the division is the very different surface morphologies of the films deposited in regions B and C. Within region C, very uniform and reproducible thin films having average grain size of a few tens nm were obtained. The films are relatively well crystallized with good electrical characteristics similar to those of sputtered thin films. However, films deposited in region B show a very nonuniform and hazy appearance. Figure 21 shows the surface morphology of a film deposited at 470°C observed by SEM. The film is composed of protruded material (region a) and uniform film material (region b). The sizes of the protrusions are rather nonuniform having diameters from 100 nm to a few microns. Fine BST grains of average size 20 to 30 nm comprise the uniform film region. TEM analysis of the protruded material showed that it is also composed of perovskite grains with average size 20 to 30 nm. Both a and b regions contain a small amount of amorphous material. Local compositional analysis of the two regions by micro AES showed that the protruded material contains more Ti by a few atomic percent

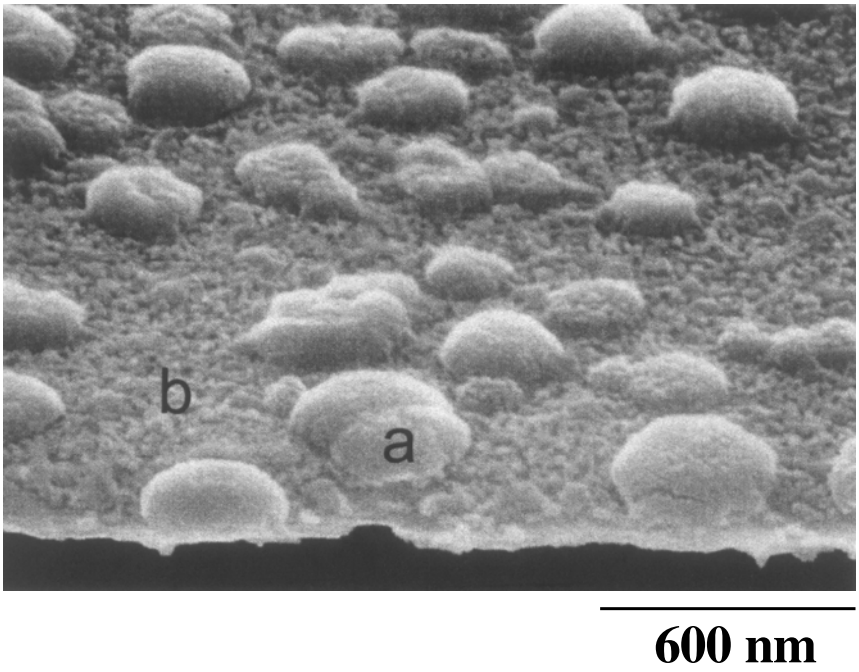

Fig. 21: SEM micrograph of the surface morphology of a BST film deposited at 470°C showing non-uniform film deposition.

compared to the matrix film even though exact quantification could not be performed due to the absence of proper standards. The protruded material also contains much more carbon than the flat film region. By post-annealing at 750°C for 30 min. under 95% N_2 + 5% O_2 atmosphere, the protrusion height decreases. Analysis by TEM and XRD showed that the crystalline qualities of both the a and b regions of the film were improved. The difference in Ti content between the protruded area and the matrix film was also decreased with corresponding decrease in carbon concentration in the protrusions.[29]

Formation of the rough and irregular surface morphology of the films in temperature region B could not be completely alleviated by any change in deposition parameters, such as gas flow rate, chamber pressure and wafer to shower head distance as long as the cation concentration is close to stoichiometry. When the Ti precursor was changed from $Ti(O\text{-}i\text{-}P_r)_2(thd)_2$ to $Ti(t\text{-}Bu)_2(thd)_2$, the higher end temperature of region B was extended to about 600°C with the same lower end temperature. The formation of protrusions was rather nonuniform over the 6" wafer surface. Due to unstable deposition characteristics in this temperature region, the electrical performance of the film was also unstable with poor reproducibility.

From the above observations, it can be assumed that the formation of protrusions is due to incomplete thermal decomposition of the Ti precursors in the relatively low temperature region. The non-cracked ligands incorporated into the film hinder the formation of a uniformly crystallized thin film. It is reasonable to assume that the protruded region contains some carbonate material even though the crystallographic analysis did not detect any carbonate phase due probably to the fact that the carbon containing phase has non-crystalline structure.

Another example of the formation of protrusions is shown in Figure 22 which shows a cross-sectional TEM micrograph of the BST film deposited in a dome type CVD reactor at a

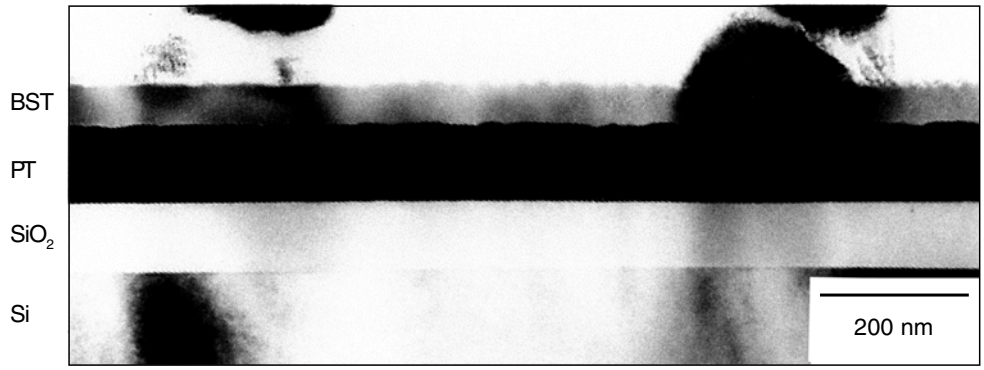

Fig. 22: Cross-sectional TEM micrograph of a BST film deposited in a dome type CVD reactor at a wafer temperature of 420°C.

wafer temperature of 420°C. In this case the protrusions are formed from the bottom electrode interface even at this lower temperature. The rest of the film is composed of amorphous material. These experimental results imply that formation of the non-uniform surface has a close relationship with the thermal cracking properties of the precursors, especially the Ti precursor. Up to now, no report has been made on the successful elimination of protrusions in the intermediate temperature region. Therefore, current research activity is more concentrated on the low temperature region in which the protrusion problem does not occur. Actually, the low temperature process is required to obtain excellent step coverage in addition to uniform surface morphology. However, the process temperature window for uniform and conformal deposition is still limited by the protrusion problem. A Ti precursor that has quite identical decomposition properties to those of the Ba and Sr precursors is greatly needed, as discussed in section 2-2.

Electrical Characteristics

Electrical properties such as the dielectric constant, dielectric loss and leakage current, of thin BST films are greatly dependant on interfaces with the electrodes. When metal electrodes, Pt or Ru, are used, the BST films make Schottky type contacts with the electrodes, which include an interface potential barrier and carrier depletion region. For our thickness region of interest the films are totally depleted due to either the large work function of the electrode or the interface trap density. The dielectric constants of thin BST films are usually smaller than bulk BST material. This can be attributed to the lower processing temperature and the space charge in the film. The space charge induced by carrier depletion generates a quite large internal static electric field (E_i), which decreases the dielectric constant of the material. It has been observed that the dielectric constants of the high dielectric materials, such as BST and PZT, decrease with increasing electric field, and the Landaw - Ginzburg - Devonshire theory has explained this phenomenons. The strength of Ei depends on the space charge density (N_d) as well as the film thickness. When the N_d is $10^{19}cm^{-3}$ and the film thickness is 50 nm, Ei at the cathodic interface goes up to a few hundred kV/cm, which is comparable to the applied electric field by the bias voltage.[41] The large field enhancement effect at the cathodic interface greatly affects the leakage current characteristics because the field at that interface is the controlling factor for electron transfer irrespective of whether the conduction mechanism is Schottky or tunneling

type. The field enhancement effect by the large Nd has been observed in sputter deposited BST thin films.[41] It was considered that energetic particle bombardment on the film surface during deposition generates the large N_d.

However, it appears that BST films deposited by MOCVD have lower defect density, by at least an order of magnitude compared to sputter deposited films, thus, smaller N_d. This can be inferred from the film thickness independent leakage current density (J) vs. applied field strength (E) of the MOCVD films[42] whereas J increases with increasing film thickness at a given applied field for sputtered films.[41]

It has been reported that the dielectric constant of thin BST films decreases with decreasing film thickness when metal electrodes are adopted even without any interfacial non-perovskite material.[43] This is due to the intrinsic interfacial low dielectric layer that originates from the termination of the chemical bonding of the perovskite structure at the interfaced. The large dielectric. polarizability of the perovskite can not penetrate into the metal layer due to the extremely high carrier concentration of the metal.

However, for the oxide electrode, such as $SrRuO_3$, the structural similarity of the electrode and dielectric material allows a certain penetration of the dielectric polarization into the oxide electrode.[45] As a result, the formation of the intrinsic low dielectric interfacial layer is effectively suppressed and film thickness independent dielectric constants are obtained, as reported by the author for the case of sputtered BST films on IrO_2 electrodes[43] and more recently reported by Toshiba researchers for the case of MOCVD BST films on $SrRuO_3$ electrodes.[6] Under these circumstances dielectric constants are solely determined by processing conditions. The stoichiometric composition and good crystallization of the films are the two most important parameters for a high dielectric constant.

Good crystalline quality of the films can be obtained when the deposition and post-annealing temperatures are high enough, roughly > 600°C. However, as discussed previously, owing to the poor step coverage of the high temperature MOCVD process as well as the oxidation problem of the diffusion barrier, the low temperature MOCVD process is required which usually results in amorphous or weekly crystallized as-deposited thin films. Therefore, high temperature post-annealing is an absolute necessity. The upper limit temperature of the post-annealing is about 800°C considering the interdiffusion between the BST and electrodes at higher temperature and process integration issues such as degradation of the metal contact resistance.

Under this limited process window, the importance of post-annealing process is growing. The films deposited at around 400°C contain a lot of hydrocarbons which may or may not be eliminated by post-annealing depending on how the process was performed. We need to think about the thermodynamic states and the kinetic pathway for the formation of the various solid phases. Sometimes the evolution of the hydrocarbons is too abrupt and large voids form in the film which critically deteriorate the electrical performance of the film. Figure 23 show the ε_r - V and J - V curves of a 32 nm thick BST film deposited at 400°C and post-annealed at 750°C after the top electrode deposition. There were two samples. One was the film annealed at 500°C for 30 min before the top electrode deposition, and the other was not. Pre-annealing at a relatively low temperature gradually evolved the impurity from the film. The film was well crystallized during the final annealing. We can see the large difference in the dielectric constant, dielectric loss and leakage current performance between the two samples.

The leakage current with high bias, > 1.5V in Figure 23, is due mainly to Fowler-Nordheim tunneling whereas with low voltage it is mostly due to the relaxation type current. The mechanism for the relaxation current is not fully understood. If the relaxation is large, an appreciable portion of the stored charge in the capacitor disappeared during the refreshing cycle of the operation of the DRAM. The large dielectric loss generally results in a large relaxation current. One of the merits of MOCVD films over sputtered films is that the dielectric loss is smaller: from 0.2 to 0.4% for the MOCVD films and from 0.6 to 0.9% for sputtered films

at 10 kHz, depending on fabrication conditions. It has not yet been proven whether this slightly large dielectric loss of for sputtered BST film causes any problems in the operation of the device especially in the expected operating frequency range of a few hundred mega - Hz.

The C-V characteristics are also important because the integrated area of the curve is the amount of stored charge. The upper limit voltage of the integration is $V_{cc}/2$, which is expected to be about 1 V for 1 giga DRAM, and the lower limit voltage is about a few tens mV depending on the, operation of the sense amplifiers. Symmetrical C-V characteristics with respect to the bias polarity are required due to the $V_{cc}/2$ operation scheme of current DRAMS. For thin BST films, the ratio of C_{min}, C at $V_{cc}/2$, to C_{max}, C at 0V, decreases with improving crystalline quality. Therefore, for the practical assessment of the dielectric performance of the film, one must be concerned about C-V characteristics not just the dielectric constant or the oxide equivalent thickness, t_{ox}, at 0V.

The electrical characteristics, such as t_{ox} and leakage current density, of high temperature version MOCVD films are comparable to those of the sputtered films when the deposition temperature and the film thickness are the same. However, films from the low temperature version MOCVD have usually a little smaller dielectric constant than sputtered films even when the processing temperatures are the same. This is believed to be due to impurity contamination for the case of MOCVD films, as mentioned previously. Therefore, research on the reduction of film contaminants by the post-deposition process is of prime importance when reproducible deposition system and recipes are available. Currently, low temperature (420°C) MOCVD BST films having t_{ox} of about 0.4 nm with physical thickness of 15 nm can be obtained when Pt electrodes are adopted. On the $SrRuO_3$ electrodes, a BST film having t_{ox} of about 0.31 nm with physical thickness of 25 nm has been reported.[6]

CVD Processes for Electrodes and Diffusion Barriers

To complete this chapter, it is reasonable to briefly discuss the CVD processes for electrodes and barriers. Because of the three dimensional capacitor structure of the giga-bit density DRAMs, the plate electrode as well as the BST film should be deposited by CVD. The space between the nodes after BST deposition is expected to be about 50 nm with the node height from 300 to 500 nm. Therefore, the requirement of conformal deposition for the plate electrode is rather stringent. In addition, some type of integration scheme, such as the concave structure as shown in Figure 24(b), requires a CVD process even for the bottom electrode.

It is expected that a multi - layer rather than a single metal layer will be adopted as the plate electrode of the capacitors because of the following reasons. The electrical potential of the plate electrode should be set to $V_{cc}/2$ during device operation which requires metal contact to the plate electrode. If the AI or W plug directly contacts to the metal, interdiffusion between the plugging metal and plate electrode occurs which degrades the contact resistance and the dielectric performance of the BST cell around the contact. Therefore, a diffusion barrier layer, such as TiSiN or TiAIN, should be deposited on the plate electrode. This barrier layer also acts as a glue layer between the plate electrode and the IMD (inter metal dielectric) layer which is usually SiO_2. In addition, the material comprising the plate electrode, such as Pt or Ru, is very expensive. CVD precursors for these metals are much more expensive than the metals themselves. Therefore, we must minimize plate electrode thickness for cost effectiveness of device production.

One method to achieve this goal is to deposit very thin metal electrodes just to form the interfacial potential barrier and then deposit the diffusion barrier layer with the necessary thickness. These two factors make a CVD process for barrier layer necessary.

Another requirement for the CVD barrier layer comes from the so called buried barrier scheme, as shown in Figure 24c. As the storage node size decreases to about 100 nm, oxidation of the barrier primarily proceeds from the side wall area rather than the interface with the storage electrodes. One way to alleviate this problem is to “bury” the barrier layer in the

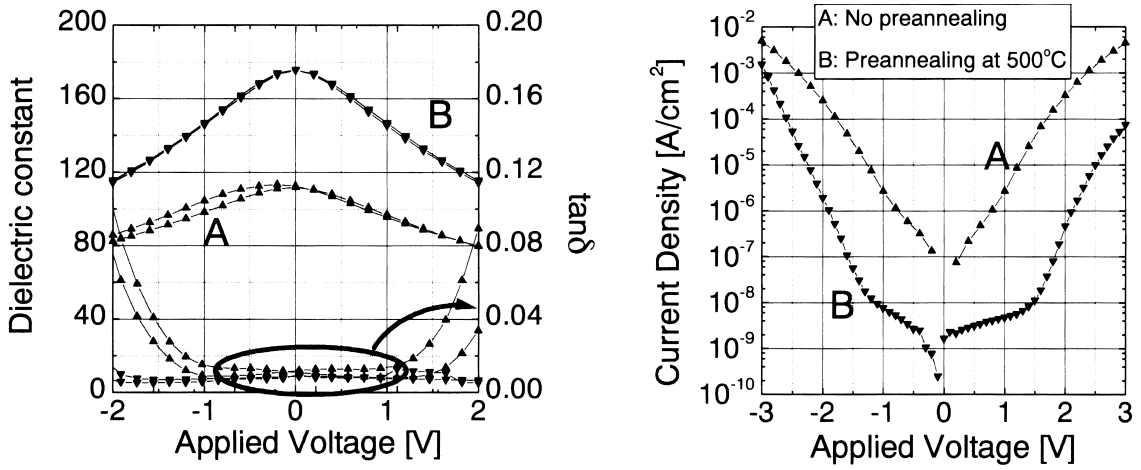

Fig. 23: The ε_r - V and J - V curves of a 32 nm thick BST film deposited at 400°C and post-annealed at 750°C after top electrode deposition.

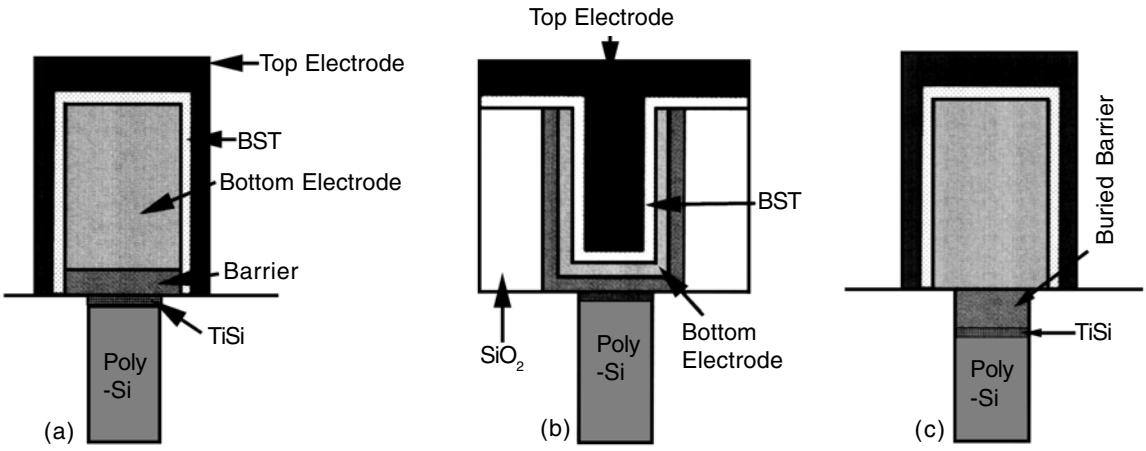

Fig. 24: Three different capacitor structures according to the (a) node, (b) concave and (c) buried barrier integration schemes.

contact plug. The formation of the buried barrier is accomplished by the deposition of the barrier layer by CVD on the recessed poly-Si plug followed by the chemical mechanical polishing (CMP) or etch back of the barrier layer to remove the barrier material from the top surface of the ILD (inter layer dielectric). Then the storage electrode material is deposited and patterned. This buried barrier electrode structure does not contain the exposed side wall area of the barrier,

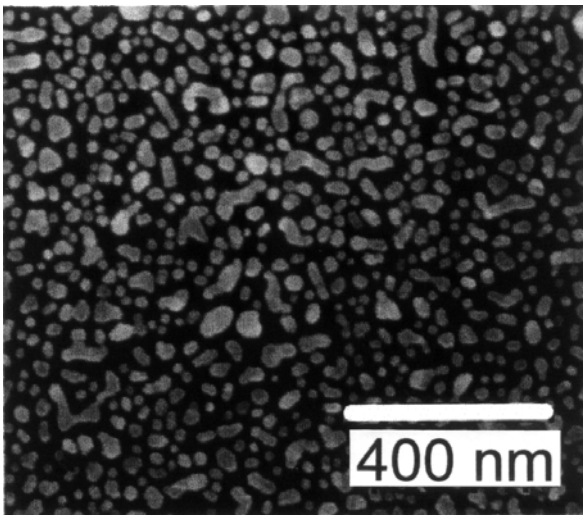

Fig. 25: Plan-view SEM micrograph of Pt grain islands on a SiO_2/Si wafer.

thus, the oxidation resistance is improved compared to the just stacked barrier/electrode structure, shown in Figure 24a. The burying process for barrier also requires a CVD technique.

MOCVD of Pt for DRAM applications has been reported by Lee et a1.[47] They used Pt-hexafluoroacetylacetonate ($Pt(hfa)_2$) and the Methylcyclopentadienyl-Pt-trimethyl ($MeCpPtMe_3$) as precursors, and the film depositions were performed at temperatures ranging from 300 to 400°C at a chamber pressure of 3 Torr. For both precursors, sufficient addition of oxygen was necessary to obtain thermal decomposition of the precursors. At the optimum oxygen flow rate and a deposition temperature of 325°C a minimum resistivity value of 13 μΩcm, which was close to the bulk resistivity of Pt, was obtained implying that the deposited films were rather pure. However, surface roughnesses of the films deposited on the SiO_2 films were too large to be used as the bottom electrode of the BST capacitor. This rough surface morphology was ascribed to low nucleation density on the oxide material. Figure 25 shows a plan-view SEM micrograph of the Pt grain islands on the SiO_2/Si wafer which clearly indicates the low nucleation density.

For the case of the $Pt(hfa)_2$, fluorine in the ligand reacts with the underlying SiO_2 Which results in an etching reaction of the Sio_2.[47] This unwanted reaction was another reason for the low nucleation density. The surface morphology should be improved by some kind of surfade modification technique which increases the nucleation density. However, the Pt films deposited on BST films show a much better surface morphology due perhaps to the larger nucleation density on the BST film.

The larger nucleation density of a Pt film on the BST also appears to have some relationship with the incorporation of the F at interfaces. It was observed that the top and bottom electrode interfaces came to have a noticeable amount of F impurity because the chemical bonding of Ba and Sr with F is quite strong and the fluorides are not volatile at the deposition temperature. Interestingly, the dielectric constant and leakage current density of the BST film having F impurity by the Pt top electrode are better than those of the film having a sputtered Pt top electrode.[22]

Another problem of MOCVD Pt is poor step coverage. Up to now, satisfactory conformal deposition has not been obtained. The poor step coverage property might also be improved by a

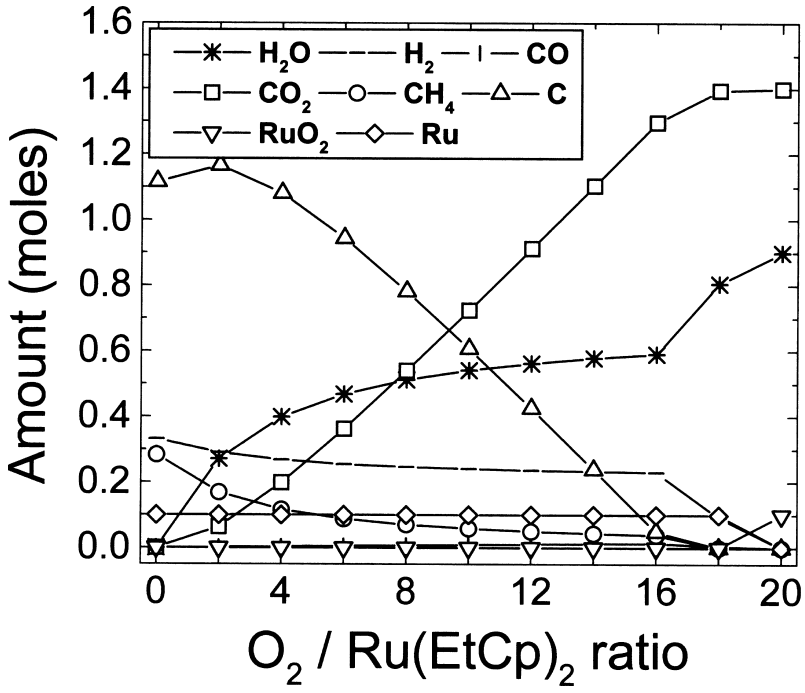

Fig. 26: Variation of calculated equilibrium molar concentrations of possible phases as a function of oxygen/Ru(EtCp) input ratio at 300°C.

proper surface modification technique and deposition temperature control.

MOCVD of Ru is being investigated by several research institutes. There are several precursors for this MOCVD including bis-(ethyl-π-cyclopentadienyl)Ru ($Ru(EtCp)_2$). Our preliminary experiments show that a high deposition rate (>20 nm/min.) with pure phase Ru film can be easily obtained,in a temperature region from 250 to 400°C. Interestingly, thermal cracking of the precursor also requires sufficient oxygen. However, as one might expect, an excess oxygen might oxidize the film. We performed the thermodynamic calculation using the SOLGASMIX-PV source chord[48] to predict the thermodynamic stability range of the Ru phase against the oxygen supply. Figure 26 shows the variation of the equilibrium molar amounts of possible phases as a function of oxygen/ Ru(EtCp) input ratio at 300°C. In this case, the initial input of the precursor was 0.1 mole. We can see that the system is under highly reducing atmosphere even with the large supply of oxygen because of the presences of carbon and hydrogen which originate from the ligand. Until all the carbon and hydrogen are oxidized to mostly CO_2 and H_2O, the RuO_2 phase is not formed. When the oxygen/Ru(EtCp) input ratio is smaller than 17 the stable solid phases are Ru and C. There appears to be a quite narrow process window in the oxygen/Ru(EtCp) input ratio, from approximately 17 to 18, for carbon and RuO_2 free metal film deposition. More detailed calculation results will be reported.[49] Figure 27 shows the "CVD phase diagram" for the formation of the solid phases with temperature and $O_2/Ru(EtCp)_2$ ratio. In the whole temperature range, the border $O_2/Ru(EtCP)_2$ ratio for the RuO_2 formation is 18 irrespective of temperature. The border $O_2/Ru(EtCP)_2$ ratio for C formation decreases with increasing temperature implying that the deposition process window for the C free Ru films increases with increasing temperature. However, lower

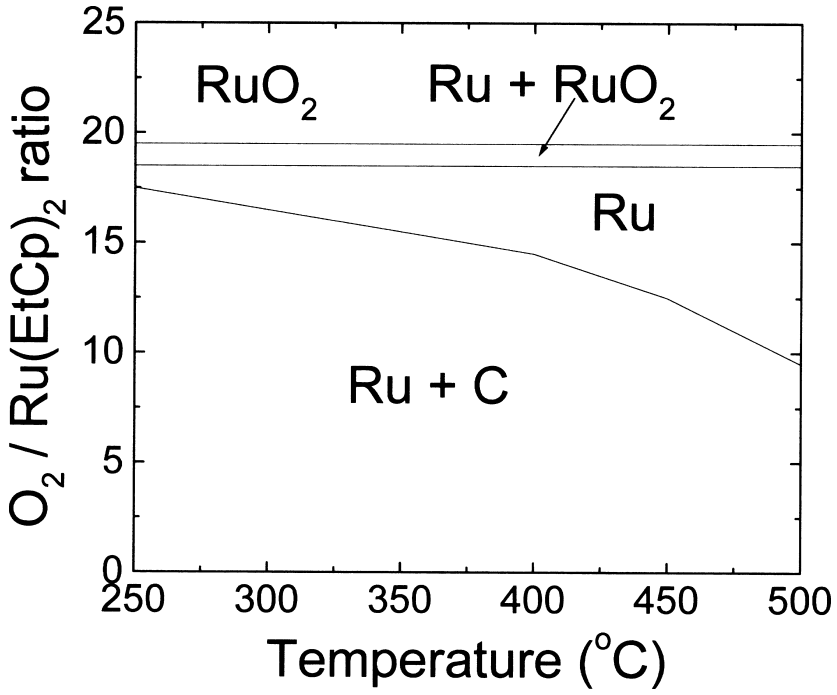

Fig. 27: "CVD phase diagram" for the formation of solid phases as a function of temperature and $O_2/Ru(EtCp)_2$ ratio.

temperatures are preferred for the integration process considering the improved step coverage with decreasing temperature.

The experimental results of the thin film deposition are presented in comparison with thermodynamic calculations. Figure 28 shows the XRD patterns of thin films deposited at 300°C with various input oxygen flow rates. All films have the same thickness of about 200 nm. Up to the oxygen flow rate of 200 sccm, RuO_2 is not detected. At the oxygen flow rate of 400 sccm, a small XRD peak corresponding to the RuO_2(101) plane is detected implying the formation of RuO_2 under this excessive oxygen flow condition. Therefore, the experimental results qualitatively correspond to the thermodynamic calculations presented in Figure 26. However, in a more quantitative sense, there is a big discrepancy; the oxygen flow rate of 100 sccm corresponds the $O_2/Ru(EtCp)_2$ ratio of about 50 at which the thermodynamically stable phase is RuO_2 rather than Ru as shown in Figures 26 and 27. To reconcile this contradiction we assume the following deposition mechanism.

Thin film deposition by CVD usually proceeds by means of heterogeneous nucleation and growth on the substrate. For Ru CVD, we can also reasonably assume that the Ru precursor and oxygen molecules adsorb on the substrate surface and decompose following which the thermodynamic reactions occur. Therefore, we should take into account the sticking probability of each constituent reactant to precisely predict the deposition reaction in addition to thermodynamics considerations. Even though the sticking coefficients of the two reactants on the SiO_2/Si substrates are not measured or found in the literature at the deposition temperature, it is not unreasonable to assume that the sticking probability of oxygen is smaller than that of $Ru(EtCp)_2$ considering the much larger vapor pressure of oxygen. Therefore, the actual quantity of oxygen that reacts with the Ru

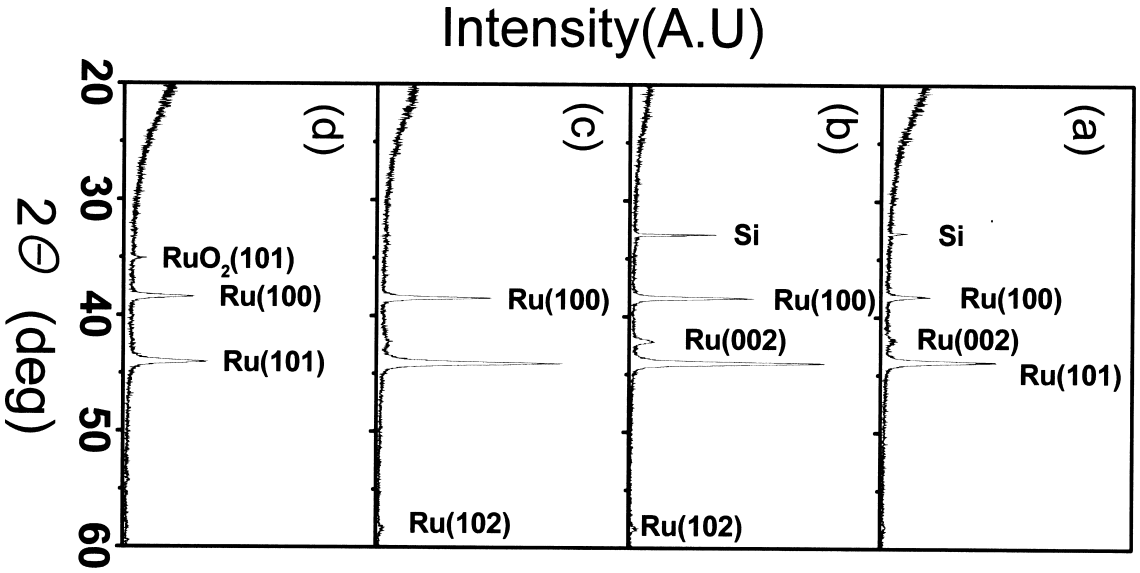

Fig. 28: XRD patterns of thin films deposited at 300°C with various input oxygen flow rates

precursor on the substrate during the deposition must be much smaller than the supplied quantity. Therefore, a larger O_2/Ru(EtCp)$_2$ supply ratio is required for the decomposition of the Ru precursor than thermodynamics predicts.

Summary and Future Directions

MOCVD techniques for BST capacitor technology for next-generation ULSI DRAMs were reviewed. Although it has been proven that the material properties of BST films are good enough for DRAM applications, integration of the BST film into the devices requires further research, especially in terms of BST film deposition techniques and electrode fabrication technologies.

MOCVD is the process of choice for the deposition of BST films considering the requirement of conformal deposition on three dimensional storage nodes. The precursors and hardware systems for MOCVD were discussed keeping in mind the mass production compatibility of the processes. The quite different chemical properties of group II (Ba and Sr) and group IV (Ti) elements result in CVD precursors having different structures and different thermal decomposition properties. The precursors basically have thd ligands or their derivatives which help the massive group II elements vaporize. Ligands of the Ti precursors have been modified to improve compatibility with group II precursors, so as to not induce ligand exchange during transport while exhibiting similar thermal decomposition. However, there is still not a Ti precursor that is completely compatible with Ba and Sr precursors, so that the deposition process becomes very complicated, especially for the case of low temperature deposition. Conformal deposition and non-oxidation of the barrier can be attained only by the low temperature CVD process. However, the larger activation energy for thermal decomposition of Ti introduces impurities from the ligands so that the deposition process as well as electrical performance of the films are unreliable for the case of low temperature CVD. The liquid delivery technique, to alleviate the thermal degradation problem of the precursors, also introduces large amounts of hydrocarbon material into the reaction chamber. Contrary to high temperature CVD, incorporation

of the hydrocarbon impurity in the deposited thin film cannot be underestimated for low temperature CVD. All these problems make MOCVD of BST very complicated. Even with these difficulties, some very promising experimental results, t_{ox} of less than 0.4 nm with low enough dielectric loss and leakage, are obtained using low temperature CVD which also has demonstrated good step coverage resulting from intensive R & D during the last couple of years. It is believed that the major, hurdle that should be overcome is not the CVD process itself but the integration issues involving the electrode, barrier and contamination control.

The choice of material, structure and fabrication technique for the electrode are still the subject of serious disagreement between major DRAM companies. This is due not only to material and process issues, such as deposition and etching, but also to the timing of the introduction of BST capacitor technology to the DRAM product which depends on the strategies of the different companies. One major problem that should be taken into account more seriously is the cost of the process. For example, some CVD precursors for noble metals are almost twenty times more expensive than the noble metal itself. It can hardly be believed that the commercial production of DRAM is possible with this extremely expensive process. Therefore, a future research direction must be to lower the cost of BST capacitor technology. In this sense, the very recent report on the deposition of BST thin films in a tube type CVD system is important because it maximizes effective usage of the precursors.[6] Development of technology that uses more conventional electrode materials, hopefully poly-Si, will be essential in reducing production cost.

The very tight design rule of future giga bit density DRAMs will require dielectric layers having extremely large dielectric constants. Therefore, a new high dielectric technology would be a good research topic especially for academic or similar research institutions. This might include the modification of anion composition as well as cation composition of the perovskite materials.

References

1. Parker and Tasch, *IEEE Circuits and Devices Magazine,* Japan, 1990, p.17.
2. W.J. Merz., *Physics Review*, **76**, 1949, p.1221.
3. C.S. Hwang, S.O. Park, H.J. Cho, C.S. Kang, H.K. Kang, S.I. Lee, and M.V. Lee, *Applied Physics Letters*, **67**(19), 1995, p.2819.
4. K. Takemura, S. Yamamichi, P.Y. Lessaicherre, K. Yokashiki, H. Miyamoto, H. Ono, Y. Miyasaka, and M. Yoshida, *Japan Journal of Applied Physics,* **34**, 1995, p.5224.
5. B.T. Lee, C.Y. Yoo, H.J. Lim, C.S. Kang, H.B. Park, W.D. Kim, S.H. Joo, H. Horii, K.H. Lee, H.W. Kim, S.I. Lee, and M.Y. Lee, *Proceedings of International Electron Devices Meet.,* IEEE, New York, 1998, p.815.
6. K. Hieda, K. Eguchi, N. Fukushima, T. Aoyama, K. Natori, M. Kiyotoshi, S. Vamazaki, M. lzuha, S. Niwa, Y. Fukuzumi, Y. Ishibashi, Y. Kohyama, T. Arikado and K. Okumura, *Proceedings of International Electron Devices Meet.,* IEEE, New York, 1998, p.807.
7. Y. Tsunemine, T. Okudaira, K. Kashihara, K. Hanafusa, A. Yutani, Y. Fujita, Matsushita, H. Itoh, and H. Miyoshi, *Proceedings of International Electron Devices Meet.,* IEEE, New York, 1998, p.811.
8. R.B. Khamankar, M.A. Kressicy, M.R. Visokay, T. Moise, G. Xing, S. Nemuto, Y. Okuno, S.J. Fang, A.M. Wilson, J.F. Gaynor, T.Q. Hurd, D.L. Crenshaw, S. Sumrnerfeit, and L. Colombo, *Proceedings of International Electron Devices Meet.,* IEEE, New York, 1997, p.245.
9. M.L. Green, M.E. Gross, L.E. Papa, K.L. Schnoes, and D. Brasen, *Journal of Electrochemical Society,* **132**, 1985, p.2677.
10. J.M. Lee, C.S. Hwang, and H.J.Kim, *Integrated Ferroelectrics,* Vol.13, 1996, p.79.
11. J.M. Lee, J.C. Shin, C.S.Hwang, and H.J. Kim, C.C. Suk, *Journal of Vacuum*

Science Technology, **A16**(5), 1998, p.2768.
12. A. Cleizes, S. Sans-Lenain, D. Medus, and C.R. Acad, *Science*, Paris, **313**, 1991, p.761.
13. R. Belcher, C.P. Cranicy, J.R. Majer, W.I. Stephen, and P.C. Unden, *Anal., Chim. Acta*, **60**, 1972, p.109.
14. P.C. Van Buskirk, R.Cardiner, P.S. Kirlin, and S.B. Krupanidhi, *Proceedings of 8th International Symposium Applications of Ferroelectrics,* Creenville, SC, 1992, p.340.
15. J. Fair, *Novellus Corporation Private Communication*.
16. B.A. Vaartstra, R.A. Cardiner, D.C. Condon, R.L. Ostrander, and A.L. Rheingold, *Proceedings of Material Research Society Symposium,* 1993.
17. T. Kimura, H. Yamauchi, H. Machida, H. Kokubun, and M. Yamada, *Japan Journal of Applied Physics*, **33**, 1994, p.5519.
18. Asahi Denka, New Chemical Product.
19. L. Wills and B.Wessles, *Proceedings of Material Research Society Symposium,* **243**, 1993, p.217.
20. M. Nyman and S. Desu, *Proceedings of Material Research Society Symposium,* **243**, 1993, p.381.
21. G. Maladrino, D.S. Richerson, T.J. Marks, D.C. DeCroot, J.L. Schindier, and C.R. Kannewurf, *Applied Physics Letters,* **58**, 1991, p.182.
22. Jong Myeong Lee, Sang Yeol Kang, Ju Cheol Shin, Won Joon Kirn, Cheol Seong Hwang, and Hyeong Joon Kim, *Applied Physics Letters*, in press.
23. A. Baron, *The Strem Chemiker*, **8**(1), 1990, p.1.
24. J.S. Lee, H.W. Song, K.5. Kim, B.G. Yu, Y.H. Jeong, Z.T. Jiang, and K. No, *Journal of Vacuum Science Technology*, **A15**, 1997, p.72.
25. R.I. Hedge, R.W. Fiordalice, E.O. Travis, and P.J. Tobin, *Proceedings of Material Research Society Symposium,* **250**, 1992, p.199.
26. D.C. Bradly, R.C. Mehrotra and D.P. Caur, ed., *Metal Alkoxides*, Academic Press, London, 1978, p.63.
27. H. Yamaguchi, T. Izuka, H. Koga, K. Takemura, S. Sone, H. Yabuta, S. Yamamichi, P.Y. Lesaicherre, M. Suzuki, Y. Kojima, K. Nakajima, N. Kasai, T. Sakuma, K. Kato, V. Miyasaka, M. Yoshida, and S. Nishimoto, *Proceedings of Conference on International Electron Devices,* IEEE, New York, 1996, p.675.
28. T. Kawahara, M. Yamamuka, T. Makita, K.Tsubahara, A.Yuuki, K. Ono and Y. Matsui, *Japan Journal of Applied Physics,* **33**, 1994, p.5897.
29. C.S. Kang, H.J. Cho, C.S. Hwang, B.T. Lee, K.H. Lee, H. Horii, W.D. Kim, S.I. Lee, and M.Y. Lee, *Japan Journal of Applied Physics*, **36**, 1997, p.6846.
30. T. Kawahara, M. Yamamuka, A. Yuuki, and K. Ono, *Japan Journal of Applied Physics,* **35,** 1996, p.4880.
31. K. Ono, T. Horikawa, T. Shibano, N. Mikami, T. Kuroiwa, T. Kawahara, S. Matsuno, F. Uchikawa, S. Satoh, and H. Abe, *Proceedings of International Electron Devices Meet.,* IEEE, New York, 1998, p.803.
32. S.W. Lee, Private Communication.
33. Z. Lu, Ph.D Thesis, *Stanford University*, Stanford, CA, 1995.
34. J.C. Shin, J.M. Lee, C.S. Hwang, H.J. Kim, J.W. Hong, and Z.G. Kim, *Japan Journal of Applied Physics*, **37**, 1998, p.5123.
35. J.H. Joo, J.B. Park, Y. Kim, K.S. Lee, J.A. Lee, J.S. Roh, and J.J. Kim, *Japan Journal of Applied Physics*, **38**, 1999, p.L195.
36. Anounced in 99 *International Symposium Integ. Ferro*., Colorado, 1999.
37. D. Y. Yang, Private Communication.
38. J.H. Han, H.K. Ryu, C.H. Chung, B.G. Yu, and S.H. Moon, *Journal of Electrochemical Society*, **142**, 1995, p.3980.
39. P.C. Van Buskirk, S.M. Bilodeau, J.F. Roeder, and P.S. Kirlin, *Japan Journal of Applied Physics*, **35**, 1996, p.2520.
40. C. Basceri, S.K. Streiffer, A.I. Kingon, and R. Waser, *Journal of Applied Physics,* **82**, 1997, p.2497.
41. Ju Cheol Shin, Jaehoo Park, Cheol Seong Hwang, and Hyeong Joon Kim, *Journal of Applied Physics,* in press.

42. G.W. Dietz, M. Schumacher, R. Waser, S.K. Streiffer, C. Basceri, and A.I. Kingon, *Journal of Applied Physics*, **82**, 1997, p.2359.
43. C.S. Hwang, B.T. Lee, C.S. Kang, K.H. Lee, H.J. Cho, H. Hideki, W.D. Kim, S.I. Lee, and M.Y. Lee, *Journal of Applied Physics,* **85**, 1999, p.287.
44. K. Natori, D. Otani, and M. Sano, *Applied Physics Letters,* **73**, 1998, p.632.
45. O.G. Vendik, S.P. Zubko, and L.T. Ter-Martirosayn, *Applied Physics Letters*, **73**, 1998, p.37.
46. C. S. Hwang, *Journal of Material Science, Engineering* B, **B56**, 1998, p.178.
47. J.M. Lee, C.S. Hwang, H.J. Cho, and H.J. Kim, *Journal of Electrochemical Society,* **145**, 1998, p.1066.
48. T.M. Besmann, SOLCASMIX-PV, A Computer Program to Calculate the Equilibrium Relationships in Complex Chemical Systems, Oak Ridge National Laboratory Report No.ORNL/TM-5775, *Union Carbide Corporation*, Oak Ridge, TN, 1977.
49. S.Y. Kang, K.H. Choi, S.K. Lee, C.S. Hwang, and H.J. Kim, submitted to *Journal of Electrochemical Society.*

Chemical Vapor Deposition
Jong-Hee Park, T.S. Sudarshan, editors, p243-285
DOI:10.1361/chvd2001p243

Chapter 8

Chemical Vapor Deposition of Polymers: Principles, Materials, and Applications

Ramakrishna Vedula, Swaroop Kaza, and Seshu B. Desu
201 Marcus Hall, Electrical and Computer Engineering Department
University of Massachusetts
Amherst, MA 01002

Abstract

In the last several years, polymer thin film deposition using chemical vapor deposition (CVD) has become increasingly popular. CVD of polymers offers numerous unique advantages over other polymer synthesis techniques and has been exploited for a multitude of applications in microelectronics, optical devices, biomedical industry, corrosion resistant and protective coatings, and even in the automobile industry. CVD of polymers (also referred to as chemical vapor polymerization, CVP, or sometimes Vapor Deposition Polymerization, VDP) differs from inorganic CVD (such as for metallic or ceramic thin films) and must be developed and optimized for each material and application. Deposition is usually accomplished by thermal or plasma activated processes. This paper reviews the fundamental processes involved in CVD deposition including the primary differences between inorganic CVD and CVP. Later, various materials deposited using CVP and their applications are discussed in detail. Commercial interest in polymer CVD is largely driven by the microelectronic and optical devices industries, for instance, in ultralarge-scale integrated circuits (ULSI) for intermetallic dielectrics. Hence, emphasis is placed on these materials and processes. Several research groups including our own have synthesized a variety of polymers using CVD and the materials and processes are

reviewed. Most recently, CVD of polymers is emerging as a powerful technique to synthesize novel molecular level inorganic-organic nanocomposites, the synthesis and properties of which are briefly presented.

Introduction

Without loss of generality, chemical vapor deposition (CVD) can be defined as a deposition technique, in which chemical components in the vapor phase react on a surface to form a solid film. This technique has been the workhorse of the industry for a large number of applications involving thin film depositions, as will be discussed in the later sections. This is primarily due to the unique advantages CVD has to offer, some of which are listed below:

1. Excellent film uniformity and conformality:

One of the primary differences between CVD (or in the case of polymers, commonly referred to, as chemical vapor polymerization or CVP) and other conventional deposition techniques, particularly for polymer thin films, is that CVD is a dry process. There is no liquid intermediate between the gas phase reactants and the resultant solid thin film and thus, problems due to surface tension such as pulling away from the corners, sharp edges etc, are not present. Additionally, CVD enables deposition of uniform thin films in recesses, holes and other difficult three dimensional configurations unlike solution based techniques which are limited to planar substrates. In the terminology of thin film device fabrication, CVD films have excellent gap-filling and step coverage characteristics.

2. High purity:

CVD eliminates the problems of solution based synthesis techniques such as solvent retention and contamination. Retention of volatile solvents subsequent to film formation can cause out gassing resulting in formation of pinholes, voids etc. Also, substituent groups used to provide solubility frequently result in degradation of the material properties of the host polymer. These problems are absent in CVD. Further, the dry nature of CVD results in high purity as it eliminates the problem of contamination from dust, molecular oxygen etc.

3. Ease of deposition over large substrates:

Solution based techniques offer several problems when depositing over large areas such as uniformity in thickness and properties. CVD films can be deposited over substantially large areas with excellent uniformity in thickness and properties. This is particularly advantageous when fabricating devices over a large area substrate as is the case, for instance, in ULSI. Also, CVD is not restricted to line-of-sight deposition, like a number of physical vapor deposition (PVD) processes such as sputtering, laser ablation etc.

4. Ease of fabricating multilayered and heterojunction films

To fabricate different polymer layers in a device using solution based techniques, mutually exclusive solvents have to be identified, which is often very difficult. CVD eliminates these difficulties and excellent heterojunctions and multilayered films can be fabricated relatively easily. Also, the capability to co-deposit compounds can be achieved. This ease of co-depositing compounds has enabled the synthesis of several inorganic-organic hybrids, which can also be tailored as nanocomposites at the molecular level.

5. Compatibility with manufacturing technology

Fabrication of most components in state of the art devices is done using vapor deposition techniques, such as thermal evaporation or CVD. Solution deposition of a polymer layer in the device could be an elaborate, expensive and slow step. CVD of polymers simplifies device integration and enables substantial reduction in the complexity of the manufacturing process.

It must be noted however, that CVD has a few drawbacks, the major one being the commercial non-availability of some of the precursors.

Although CVD (or CVP) is a well established deposition technique, the deposition process needs to be developed and optimized for each material and application. In order to exploit the capabilities of this technique fully,

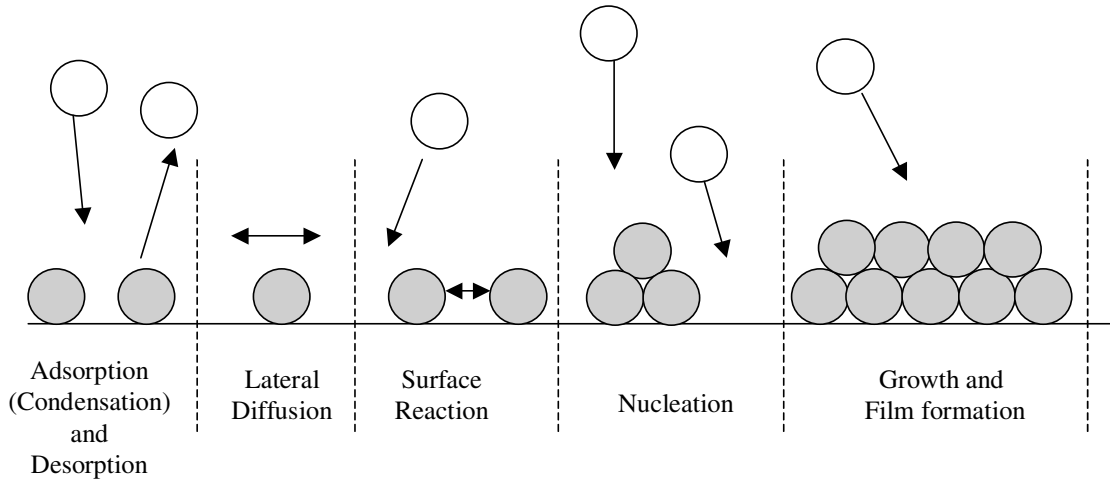

Fig. 1: Schematic of the underlying processes involved in a typical thin film deposition by CVD.

first, a thorough understanding of the processes involved in film growth is essential. The next section details the various processes involved in a typical CVD deposition of thin films with emphasis on polymer thin films.

Chemical Vapor Polymerization

Fundamentals of CVD

In this section, the fundamentals of chemical vapor deposition process (CVD) are briefly reviewed. For further details on this section, the reader is referred to excellent articles in literature.[1-3] Also the differences between polymer and other inorganic (for instance, metallic or ceramic materials) CVD processes are noted.

The following steps are common to almost all CVD processes. All these steps are schematically represented in Figure 1.

- **Transport of gaseous chemical reactants to the surface:**

This is usually done by evaporating (or sublimating) the precursor in a separate chamber, and subsequent formation of reactant species, followed by transport of these species into the deposition chamber where the substrate is placed. This is commonly achieved using pressure differential in a vacuum system.

- **Adsorption of the species on to the surface (commonly referred to as condensation):**

The reactant species impinging from the vapor phase is attracted to the surface of the substrate mainly due to the instantaneous dipole moment of the substrate surface atoms.[4] Adsorption of the condensed species is accompanied by lateral diffusion, i.e., the species moves along the surface of the substrate for a particular distance before it resides on the surface. An aggregate of condensed reactant species that reside on the surface of the substrate is termed a "nucleus". This could vary from a single atom or molecule to a cluster of species, and the process is referred to as nucleation. Nuclei are usually three dimensional island type structures formed on the surface of the substrate and nucleation is usually the initial stage of the film formation. It is worthwhile to note that, while simple condensation is usually exothermic, CVD adsorption and subsequent film formation is usually an endothermic reaction with few exceptions.

- **Reaction of the species on the surface:**

There are three possible sub-processes that any newly condensed molecule could undergo in the deposition chamber, viz., it could form a new nucleus, it could be incorporated into an existing nucleus in which case, the nucleus is referred to be "growing", or it could reenter the gaseous phase. If the condensed atom does not reenter the gas phase, a chemical reaction occurs between the existing nuclei and the incoming species, resulting in coalescing of the island type nuclei. This eventually leads to the formation of a continuous film.

- **Desorption of the gaseous byproducts of the chemical reaction:**

The chemical reaction mentioned above results in the formation of a film, along with some byproducts. The presence of these undesired byproducts in the vicinity of the film distinguishes CVD from other condensation processes. These byproducts are usually gaseous and hence carried away. However, in very few cases, it is possible that some of the byproducts are trapped in the film, and this could lead to contamination.[5]

- **Transport of byproducts away from the surface:**

Commercial CVD processes are usually performed in vacuum systems and hence, the transport of the byproducts away from the surface of the substrate is easily accomplished. It should be noted however, that the partial pressure of the gaseous byproducts could play an important role in the deposition kinetics.

- **Incorporation of the reaction products into the bulk of the film:**

Once a continuos layer of the film is formed, (often referred to, as a monolayer), further film growth is a reenactment of the nucleation-growth processes occurring under steady state conditions. During this stage, the film evolves into any of, amorphous, polycrystalline or single crystal forms, depending on several parameters such as substrate temperature, nature of the film deposited, and so on.

It is worthwhile to note that steps 2, 3, and 6, which essentially determine the film growth are all dependent on substrate temperature. All these processes are driven by individual activation energies. Hence, the deposition rate in any CVD process is strongly dependent on substrate temperature along with other parameters such as the partial pressure of the reactant species in the gas phase, etc.

Rate Controlling Steps

Generally in most CVD processes, either step 1 or steps 3 and 6 combined, are the potential growth rate controlling factors. If step 1 is the rate controlling factor, the deposition process is usually referred to as "mass transport controlled", whereas if the steps 3 and 6 are rate controlling, it is referred to as "surface reaction or diffusion controlled". Mass transport controlled process means that the kinetics of surface reaction and film formation is must faster than the transport phenomena. In such cases, careful reactor design taking into consideration the mass transport phenomena, such as fluid dynamic transport characteristics, is essential. On the other hand, in a surface reaction controlled process, kinetics of film formation is relatively slower, and therefore parameters such as uniformity of the substrate temperature play a major role. All these issues need to be considered when optimizing a process for any thin film deposition using CVD.

Inorganic vs. Polymer CVD

CVD of polymers has several distinguishing features from inorganic CVD processes. In inorganic CVD, the reactant species is usually an atom or a molecule. Also, the reaction of the incoming species is restricted to the surface of the film in inorganic CVD, whereas in polymer CVD, the incoming reactant species can diffuse into the bulk of the film, owing to its high mobility, and react below the surface. CVD of polymers in general, follows a reaction pathway, similar to any free-radical polymerization, via the initiation, propagation and termination route. Monomers are the incoming reactant species and they adsorb on the surface of the substrate. When the local adsorbed monomer concentration

reaches a critical value, chain initiation occurs. This critical monomer concentration requirement virtually eliminates polymerization in the gas phase. Whereas, in inorganic CVD, it is possible and is a common problem, that nucleation could occur in the gas phase, leading to particulate formation (also called "snow" effect), if the deposition conditions are not properly optimized.

After initiation, chain propagation rapidly occurs. Growth termination would occur when the free radical end of the growing polymer chain reacts with another of its kind, or when it is buried too deep into the bulk of the film where the incoming monomer species is unlikely to reach.

In general, during CVD growth, the rate of polymer chain propagation exceeds those of initiation and termination and is a strong function of the substrate temperature. This rate varies inversely with substrate temperature, i.e., decreases with increasing substrate temperature and vice versa. As mentioned earlier, chemical reactions on the surface, lateral diffusion of the incoming species, vaporization, are all characterized by activation processes and obey an Arrhenius temperature dependence of the form:

$$\frac{\partial \ln K}{\partial (1/T)} = -E_K / R \qquad (1)$$

where, K is the rate constant, E_K is the activation energy required, R is the universal gas constant and T is the absolute temperature.[6] The value of EK, the activation energy is negative for polymers while in the case of inorganic CVD processes, the corresponding value is positive. Gorham presented an activation energy for film growth in paraxylylene polymers of –9 kcal/mol.[7] Similar negative values of activation energies have been reported by other researchers as well.[8] In comparison, thermal CVD of epitaxial silicon (Si) from chlorosilanes requires an activation energy of 40 kcal/mol.[9] Thus, in most polymer systems, as the substrate temperature increases, the deposition rate decreases unlike in inorganic CVD systems. Consequently, it follows that, at low substrate temperatures, polymer CVD processes are driven in mass-transport controlled regime whereas, inorganic CVD processes are in surface-reaction controlled regime. As the substrate temperature is increased, polymer CVD processes undergo a transition from a mass-transport controlled regime to a surface-reaction controlled regime. This is in contrast to inorganic CVD processes, where the transition occurs from surface-controlled regime at low substrate temperatures, to mass-transport controlled regime at higher substrate temperatures.

Types of CVP

In general, several possible chemical reactions can occur in a CVD process, some of which are thermal decomposition (or pyrolysis), reduction, hydrolysis, oxidation, carburization, nitridization and polymerization. All of these can be activated by numerous methods such as thermal, plasma assisted, laser, photoassisted, rapid thermal processing assisted, and focussed ion or electron beams. Correspondingly, the CVD processes are termed, thermal CVD, plasma assisted CVD, laser CVD and so on. Among these, thermal and plasma assisted CVD techniques are widely used, although polymer CVD by other techniques has been reported.[10]

Thermal CVD

As the name suggests, thermal CVD process involves a chemical reaction by thermal activation. The principle of thermal CVD can be easily understood from the following example of paraxylylenes:

Poly-paraxylylenes are deposited by a thermal CVD process popular in the microelectronics industry as the "Gorham process".[11] The starting material for this deposition process (precursor) is usually a paracyclophane dimer (DPX). The dimer dissociates to form reactive monomer species, which then undergoes nucleation and growth leading to polymer thin film formation. The following reaction ensues:

$$\mathrm{DPX} \xrightarrow[\text{Vacuum}(<1\ \text{torr})]{600-700^{\circ}\mathrm{C}} \mathrm{PPX}$$

The details of polymerization and thin film growth are presented in later sections. Poly-

paraxylylene thin films deposited in this manner are rigorously pursued as low dielectric constant materials for interconnections in ultra-large-scale integrated circuits (ULSI).

Plasma Assisted CVD (also known as Plasma Enhanced CVD or PECVD)

In a number of industrial applications, the high temperatures involved in the thermal process are unacceptable. It has been long known that the presence of charged particles could open up new reaction pathways, with lower activation energies than that of their thermal counterpart.[12] This is achieved by the formation of excited species of the reactants in the presence of plasma, which allows the reaction to proceed at substantially lower substrate temperatures. A detailed description of plasma chemistry and plasma-gas interactions is beyond the scope of this paper, and is well presented in literature.[12-14] The presence of plasma creates a more than equilibrium number of free radicals, which react at sufficiently low temperatures and result in acceptable deposition rates. In addition to lowering the substrate temperature, the use of plasma also offers some distinct advantages. For instance, energetic charged particle collisions could produce certain metastable species, which otherwise cannot be created by thermal CVD alone. For this reason, several hydrocarbons, which do not contain conventionally easily polymerizable groups such as methane, ethane and cyclohexane can be polymerized using PECVD. In the realm of polymer thin films, PECVD is extensively used to deposit several polymers such as, poly-fluorohydrocarbons, and poly-perfluorocarbons in the past,[15,16] and more recently, an entirely new class of materials called plasma polymerized fluorinated monomers (PPFM) or fluoropolymers.[17,18] The details of deposition and the properties of these films will be discussed in the next few sections.

Polymers using CVP: Materials and Synthesis

CVD of polymer thin films (CVP) requires the following:

1. Initiation must occur exclusively on the surface, to eliminate polymerization in the gas phase,
2. Rate of propagation must greatly exceed the rates of initiation and termination,
3. The surface mobility of the monomers must be high and
4. The monomers must be stable under the deposition conditions. In spite of the apparently simple requirements CVP imposes and the numerous advantages it offers, there are relatively few polymers synthesized using this technique.

Only recently, there has been a tremendous surge of interest in these coatings, particularly in the microelectronic industry, although the deposition of polymers by CVP dates back to 1947.[19] The key to the growing interest can be attributed to both the material properties of the films such as low dielectric constant, low moisture absorption, excellent corrosion resistance as well as the unique capabilities of the CVP process. These polymers and their polymerization mechanisms along with the properties of the films obtained are the focus of this section. The following polymers are discussed in detail separately.

1. Poly-p-Xylylenes (Parylenes)
2. Polyimides
3. Polynapthalenes
4. Polyphenylene Vinylenes
5. Polyazomethines

Figure 2 shows an example of polymers belonging to each of these families. Each of these polymers, their polymerization and deposition mechanisms will be discussed below.

In addition to the above mentioned, there have been reports of other polymers deposited using CVP, but extensive studies have not been done. Reports on 4-fluorostyrenes,[20] polypyrrole[21] and epoxy-amine polymers[22] can be foundelsewhere, and are not discussed in detail in this paper.

Poly-p-Xylylenes (Parylenes)

There have been several parylene polymers deposited using CVP. Essentially, they are all derivatives of paraxylylene. The unsubstituted

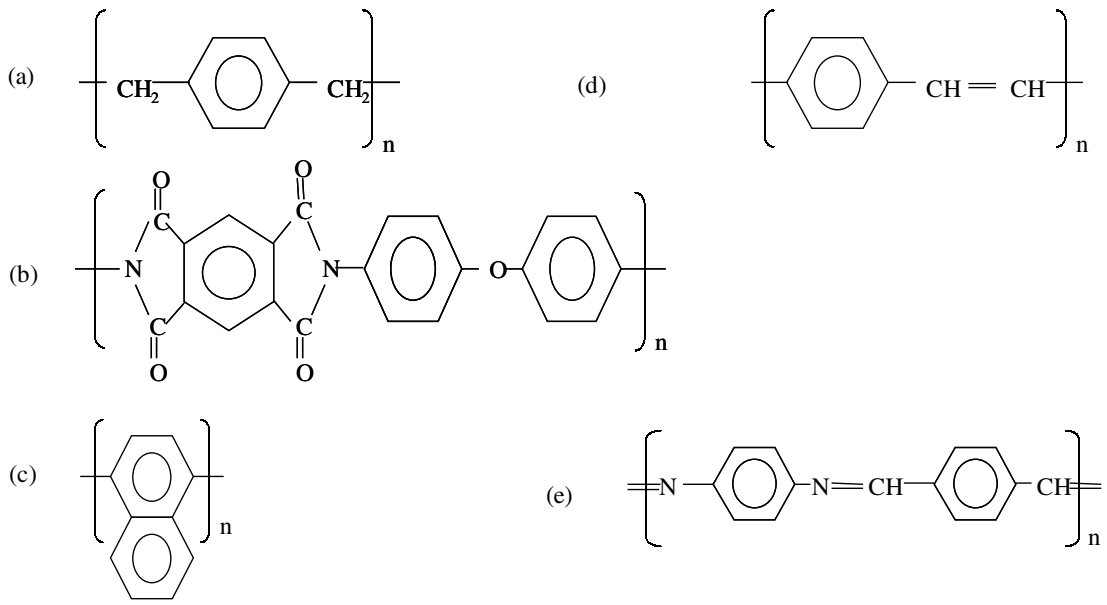

Fig. 2: The families of polymers currently deposited using CVP (a) paraxylylene, (b) polyimide, (c) poynapthalene, (d) poly p-phenylene vinylene, and (e) polyazomethine.

parylene is referred to as parylene-N. In the following discussion, only parylene-N will be considered and its analogues will be discussed later.

One of the first reports on the vapor phase synthesis of parylenes was by Szwarc.[23] He published a series of papers detailing the chemistry and applications of parylene in coatings technology.[23,24] In his pioneering work, he reported spontaneous polymerization of p-xylylenes on condensation to form poly-p-xylylene. However, this technique has several practical limitations such as low yield, contamination with byproducts and the polymers obtained were loosely crosslinked. Later, a new synthesis route to deposit linear parylenes was demonstrated by Gorham,[11] which initiated commercial applications of parylene coatings. This polymerization scheme is widely popular in literature and will be referred to hereafter as the Gorham process. It was shown that di-p-xylylene ((2,2) paracyclophane) is quantitatively cleaved at low pressures (< 1 mm) undergoing vapor pyrolysis at ~600°C to form a uniform coating of parylene. The basic concepts of polymerization were developed later by several researchers.[25-27]

Although Gorham process is the most popular method of parylene polymerization, there are reports of at least two other polymerization schemes for parylenes.[28] Figure 3 shows the different polymerization schemes used for CVP of parylene thin films. However, in this paper, only the Gorham process will be discussed, the details of alternate polymerization schemes can be found elsewhere.[28]

Polymerization Mechanism and Thin Film Formation

Chemical vapor polymerization of parylene thin films occurs through free radical polymerization. A generalized schematic of the chemical vapor polymerization reactor, employing the Gorham process is shown in Figure 4. The mechanism of polymerization is as follows:

1. The precursor, paracyclophane sublimates under vacuum (T ~150°C) and when the

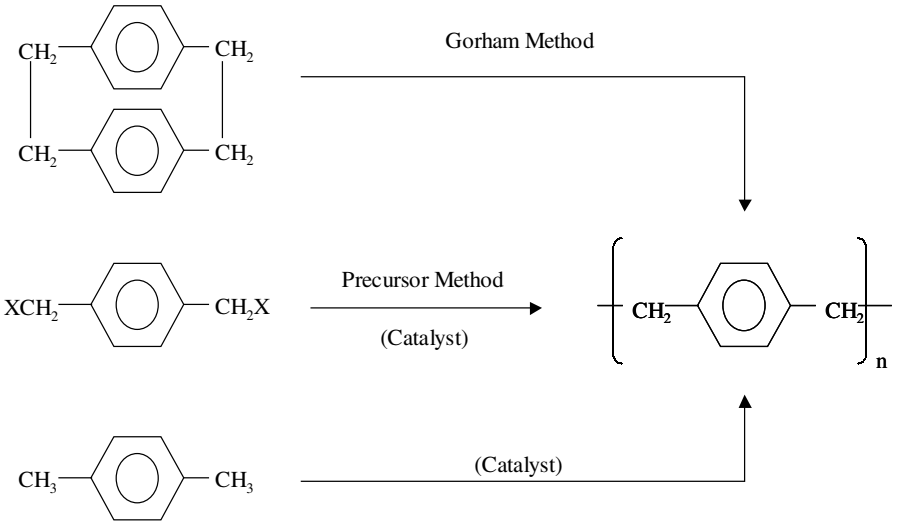

Fig. 3: Different synthesis techniques studied for parylene thin film deposition.[28]

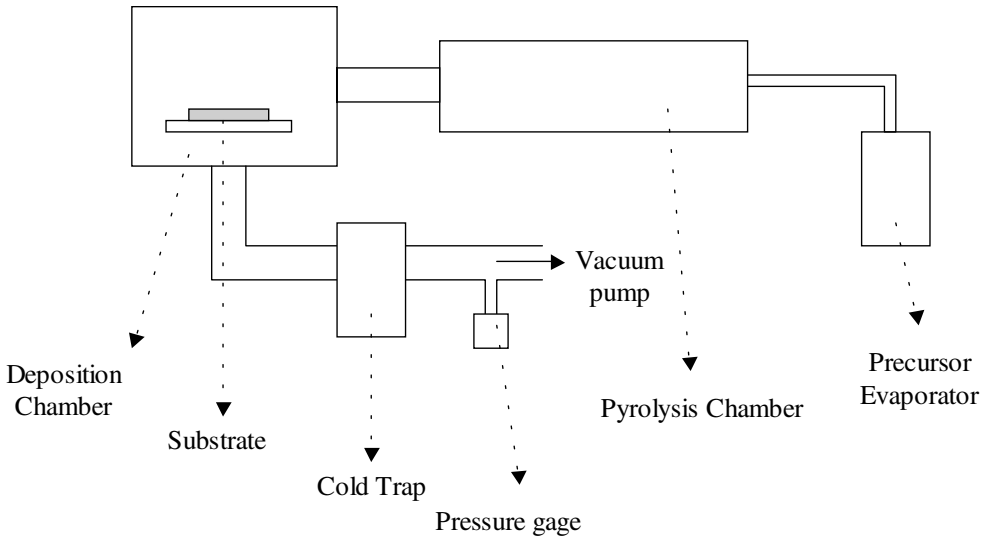

Fig. 4: Generalized schematic of the deposition system employing a Gorham technique for parylene deposition.

vapors are transported to a high temperature pyrolysis chamber (maintained at around 600°C), cleavage of the two CH_2-CH_2 bonds occurs. This results in the formation of two monomer p-xylylene (PX) molecules. Experimental evidence for this disassociation and the resultant monomer formation was found both directly and indirectly by several researchers.[11,29] The PX monomer has a ground state tetraolephinic

(or quinonoid) structure and is diamagnetic (singlet), while in the excited state, it possesses a benzoid structure and is biradical (triplet). The energy difference between these two structures is only 12 kcal/mol., and hence there is a substantial fraction of the biradicals (triplets) after pyrolysis. Further, theoretical calculations show that even in the quinonoid state, the molecule is extremely reactive and free radical additions can readily occur.[27]

2. Chain initiation occurs when two monomer radicals are coupled to form a dimer biradical and proceeds further.[11] This is an endothermic reaction requiring a heat of formation of 16 kcal/mol. Because of energetic concerns, chain initiation is unlikely to happen in the gas phase at low pressure. When the monomers are adsorbed onto the surface of the substrate, it is believed that, the high local concentration of monomers promotes the formation of biradicals assisted by van der waals forces. Models developed for vapor deposition polymerization of parylene-N indicate that initiation is a third order reaction with an activation energy of 24.8 kcal/mol.[25,26]
3. Chain propagation occurs when the monomer molecules of free radicals react with the biradicals on the surface. Addition of a monomer unit to the dimer-biradical is an exothermic process by 18.4 kcal/mol.[25,26] Consequently, the rate of propagation is several orders of magnitude greater than that of initiation, enabling thin film formation. Beach suggested a penetration depth, i.e., the distance into the film that the monomer molecules can diffuse before reacting, during the propagation step to be approximately 400 nm, although the rate decreases drastically with depth.[25]
4. Although no data on the chain termination mechanism is available in literature, it is generally considered that termination occurs when two biradicals at chain ends react or when the free radical end of the propagating chain is buried too deep in the film. Evidence of the active polymer chain ends has been provided by detection of high concentrations of paramagnetic centers in freshly prepared films.[27]

The resulting polymers are crystalline, and it is generally assumed that crystallization follows polymerization. The reaction sequence of the pyrolytic polymerization reaction is shown in Figure 5.

Influence of Deposition Parameters on Film Growth

The quantitative models developed enabled a thorough understanding of the parylene deposition process.[25,26] Further, these models suggested several deposition parameters that could be varied to tailor the thin film deposition for various applications. They indicate that the rate of consumption of the monomer during propagation is much larger than that during initiation, and is determined primarily by the monomer partial pressure and the substrate temperature. Influence of these two parameters viz., pressure and substrate temperature will be discussed here.

1. Pressure:

For parylene, Beach,[25] and more recently Gaynor and Desu,[26] formulated the following equation relating the deposited polymer film growth rate to the pressure:

$$\gamma = \left(\frac{2}{\lambda\rho^3}\right)^{1/4} \left(k_i k_p D^2\right)^{1/4} \left(\frac{\rho}{K_H p_0}\right)^{1.5} p^{1.5} \qquad (2)$$

where, γ is the growth rate, ρ is the mass concentration of the monomer (in g/cc), p is the monomer pressure, k_i and k_p are the initiation and propagation rate constants respectively, D is the diffusion constant of the monomer into the film, and p_o is the monomer vapor pressure, and K_H is Henry's constant. As can be seen in the equation the growth rate increases as the monomer vapor pressure is increased. This could be attributed to the fact that, as the monomer vapor pressure is increased, the number of active monomer species which can take part in the chemical reaction leading to film formation, increases.

Figure 6 shows the experimental evidence for this dependence of growth rate on pressure.[30] The deposition rate of parylene-N increases as $p^{1.5}$, as predicted by the models.

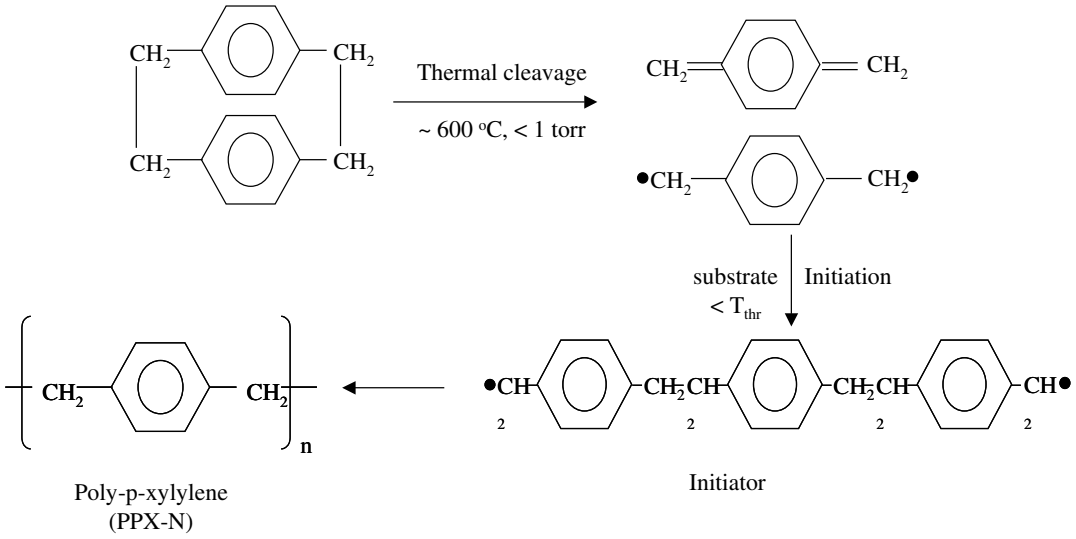

Fig. 5: Polymerization mechanism of Paraxylylene with paracyclophane as the starting material.[11]

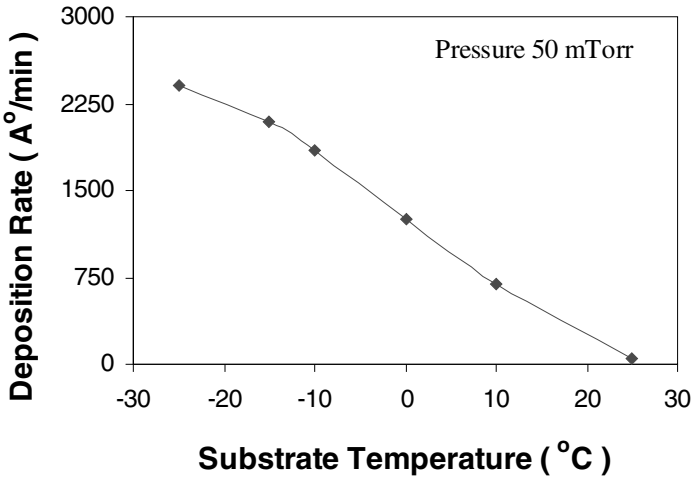

Fig. 6: Deposition rate of parylene-N as a function of substrate temperature.[30]

1. Substrate Temperature:

In their models, Beach,[25] Gaynor and Desu[26] also developed equations for the substrate temperature dependence of growth rates as follows:[25,26]

$$\frac{\partial \ln \gamma}{\partial (1/T)} = \frac{-E_i - E_p - 2E_D + 6\Delta H_v}{4R} \qquad (3)$$

where, E_i, E_p, E_D are the activation energies of chain initiation, propagation and diffusion processes respectively, and ΔH_v is the heat of vaporization. Here, as mentioned earlier, E_p = 8.7 kcal/mol, E_i = 24.8 kcal/mol, and the composite activation energy given by

$$E_\gamma = -R\left(\frac{\partial \ln \gamma}{\partial (1/T)}\right)$$

was reported as -9 kcal/mol.[25] The deposition rate law given by Cariou et al suggests a value of -6.22 kcal/mol for the same.[31] Both these

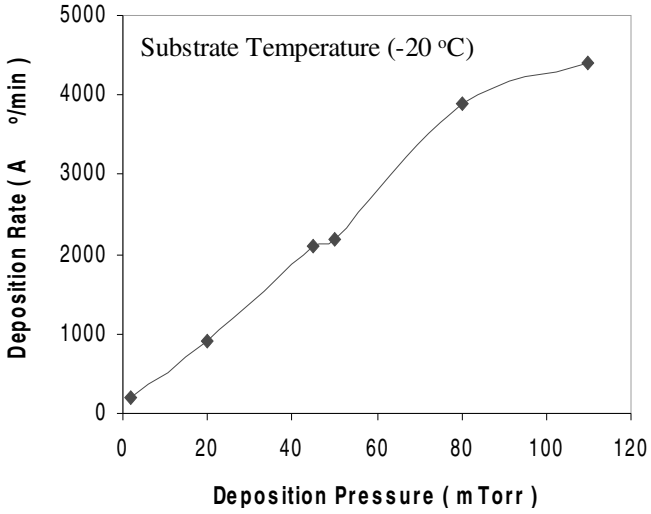

Fig. 7: Deposition rate of parylene-N as a function of pressure.[30]

calculations show negative activation energy of deposition, which means that, as the substrate temperature is increased, the growth rate decreases. Consequently, there is a maximum substrate temperature above which the rate of deposition becomes negligible. This maximum temperature is usually referred to, as threshold temperature or "ceiling" temperature (T_{thr}). The ceiling temperature is an important practical parameter of CVD of parylenes, as it could determine the limits of their applicability. Accordingly, later studies confirm the inverse dependence of deposition rate with substrate temperature (refer to Figure 7). Clearly, very high deposition rates (close to 250 nm/min) can be obtained when the substrate is maintained at sufficiently low temperatures.[30] This is in clear contrast to inorganic CVD systems.[1]

Both pressure and substrate temperature, not only determine the growth rate of the polymers, but also the average molecular weight of the resultant polymer.

Substituted Derivatives of Parylene-N

Since the procedure to deposit paraxylylene was first developed by Gorham,[11] several research groups have synthesized numerous substituted analogues of parylene-N. Figure 8 shows the structures of commonly reported polymers belonging to the parylene family. Among these, the more popular ones are, poly-chloro-p-xylylene (parylene-C), poly-bromo-p-xylylene (parylene-B), poly-dichloro-p-xylylene (parylene-D), poly-tetrafluoro-p-xylylene (parylene-F or sometimes also called AF-4). All of these are vapor depositable using the Gorham synthesis process. With the exception of Parylene-F, the precursors (dimer starting materials) for all these polymers are commercially available. All of these polymers follow a polymerization mechanism similar to that described in the previous few subsections, although certain deposition parameters such as the threshold condensation temperature (ceiling temperature) and optimum pyrolysis temperatures are different. Parylenes are particularly attractive candidates as interconnect materials for low dielectric constant applications and there are several reports on the synthesis and properties of parylene thin films in literature.[32-36]

Properties

Chemical vapor polymerized parylenes are in general highly crystalline and insoluble in most of the available solvents even at elevated temperatures. As attractive candidates for

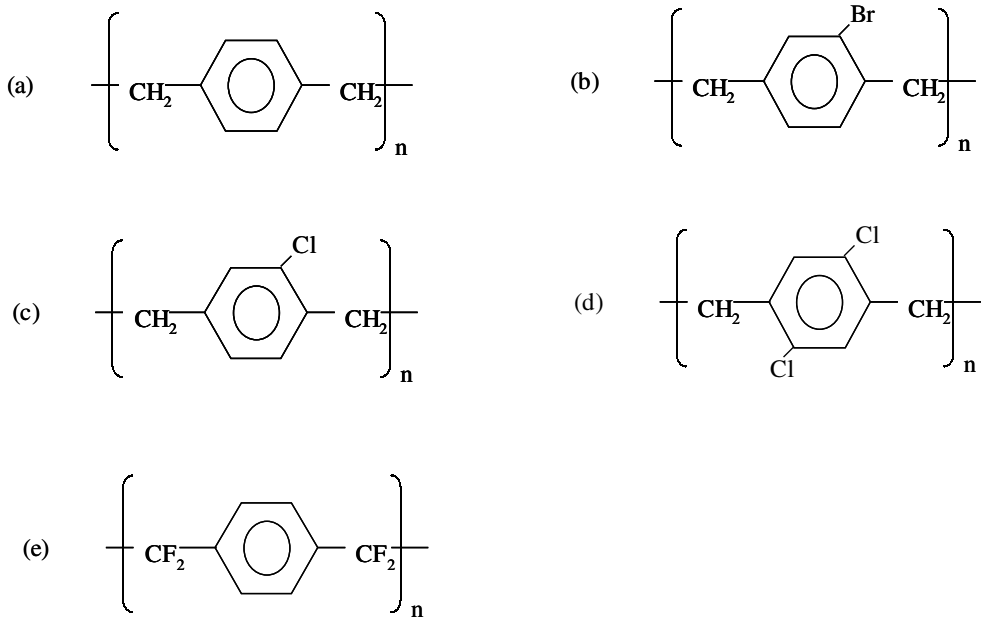

Fig. 8: Vapor deposited parylene analogues (a) polyparaxylylene (PPX-N), (b) polybromoparaxylylene, (c) polychloroparaxylylene (PPX-C), (d) polydichloroparaxylylene (PPX-D), and (e) polytetrafluoroparaxylylene (AF-4).

interconnect materials, they have been thoroughly investigated in literature in terms of their crystal structure, thermal, electrical and optical properties.

1. Crystal Structure

Crystallinity of parylenes is limited to submicron range domains dispersed randomly in an amorphous matrix. The crystal structure and morphology of parylenes are strongly dependent on the substrate temperature. Early reports indicated that at substrate temperatures above -50°C, polymerization occurs first followed by crystallization.[37] Below -50°C however, a change in mechanism occurs. The adsorbed monomer first crystallizes and polymerization follows.[37] In both the cases, the resultant films are highly crystalline (~ 60 %). Paraxylylene-N exists in two crystalline forms, a and b, the difference being that, the crystal structure of a is monoclinic while that of b is hexagonal. Under the typical deposition conditions of Gorham process, parylene crystallizes in a form, but it may undergo a transition to b upon heating or by stretching.[27] The details of parylene crystal structures and their unit cell parameters can be found elsewhere.[38-39]

2. Thermal Properties

Parylenes are in general, high melting point (>300°C) polymers. They exhibit different decomposition mechanisms when annealed in air (or oxygen) and inert atmospheres. In inert environment, melting is almost always accompanied by decomposition. In this case, it is not clear whether the process involves decomposition as a prelude to melting, or a merely concurrent phenomenon or a combination of both.[5] In any case, thermal degradation in inert atmospheres occurs at temperatures exceeding 400°C. When annealed in air or oxygen ambient, however, decomposition occurs at much lower temperatures (around 250°C). It has been proposed that, in oxygen ambient, peroxy radicals formed during annealing attack the CH_2 bonds in parylenes, resulting in chain scission leading to decomposition.[40] Studies of films annealed in air showed a drastic incorporation of oxygen on the surface of the film.[41]

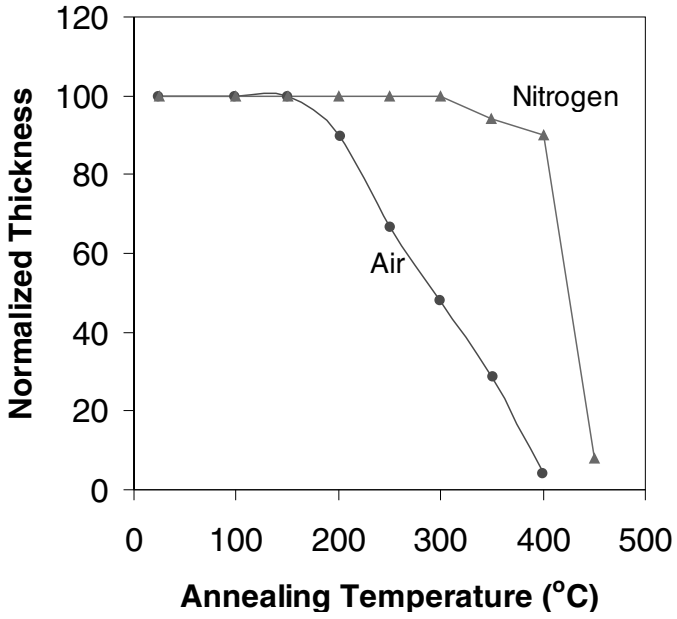

Fig. 9: Dynamic TGA of Parylene-N in N_2 and air environment.[41]

Thermal stability is an important criterion for microelectronic applications and hence has been the focus of several studies. Figure 9 shows the dynamic thermogravimetric analysis (TGA) of Parylene-N in both inert and oxygen environments. It is clear that, Parylene-N is stable up to about 480°C in inert ambient, beyond which it gradually decomposes.

3. Electrical Properties

Parylenes exhibit outstanding electrical properties as insulating films. Characterization of electrical properties is usually done by filling a parallel plate capacitor with the polymer sandwiched in between and measuring the electrical capacity. Parylenes in general show very low dielectric constants ranging from 2.4 to 3.2 (refer to Table 1), and the dielectric constant is invariant of annealing temperature. The low dielectric constant is due to the fact that in these polymers, electronic polarization is the only significant contribution to the dielectric constant. In addition, the highly symmetrical, nonpolar nature of the polymers results in an extremely low dielectric dissipation factor. It is also noteworthy that parylene thin films have a high dielectric breakdown strength (> 2 MV/cm). These properties along with the unique advantages CVP offers, account for the tremendous increase in interest in the fabrication of these polymer thin films, as will be explained in greater detail in section 5.1.

4. Optical Properties

In general optical properties of thin films are extremely important in applications such as optical waveguides, antireflection coatings and optical filters. Parylene thin films are transparent throughout the visible spectrum with refractive indices ranging from 1.609 to 1.678. Additionally, parylene thin films exhibit birefringence, i.e., the refractive index measured in the plane of the films differs from that measured in perpendicular direction to the film thickness. The cross-sectional birefringence could be attributed to the stresses setup during the deposition process.[5] The refractive indices were found to be independent of the thickness of the film.

Table 1 summarizes all the above mentioned properties of parylene thin films deposited using CVP.

Table 1. Summary of the Mechanical, Thermal, Electrical, and Optical Properties of Parylene Thin Films Deposited Using CVD[32,42,43,102]

Property	PPX-N	PPX-C	PPX-D	PPX-F (AF-4)
Mechanical				
Tensile Strength (psi)	6000 – 11000	10000	4000 - 13000	6200
Density (gm/cc)	1.1	1.29	1.42	1.51
Elongation to Break (%)	20 - 250	200	10	100
Water Absorption (%, 24 hrs)	< 0.1 %	< 0.1 %	< 0.1 %	-
Thermal				
Melting Point (°C)	420	290	380	500
Linear CTE (10^3/°C)	3 – 8	3 – 8	3 – 8	-
Glass Transition Temp. (°C)	60 – 70	80 – 100	80 – 100	110
Thermal Conductivity @ 25°C (cal/s.cm. K)	2.9×10^{-4}	2×10^{-4}	-	-
Oxidation Temperature (°C) (slow)	150	180	-	250
Electrical				
Dielectric Constant (1 MHz)	2.65	2.95	2.8	2.32
Dissipation Factor (1 MHz)	6×10^{-4}	1.3×10^{-2}	2.3×10^{-3}	7×10^{-4}
Breakdown Strength (MV/m)	2.3	1.9	> 2	> 2
Volume Resistivity (ohm-cm)	1.4×10^{17}	8.8×10^{16}	2×10^{16}	5×10^{16}
Surface Resistivity (ohm)	10^{13}	10^{14}	5×10^{16}	1.3×10^{14}
Optical				
(λ = 632.8 nm)				
Refractive Index (in plane)	1.665	1.647	1.645	1.55
Refractive Index (out of plane)	1.609	1.629	1.678	1.45

CVP of Polyimides

In comparison to parylenes, chemical vapor deposition (more commonly called vapor deposition polymerization, VDP) of polyimides is more recent. Chemical vapor deposition or VDP of polyimides was first reported independently by Iijima et al.[44] and Salem et al.[45]

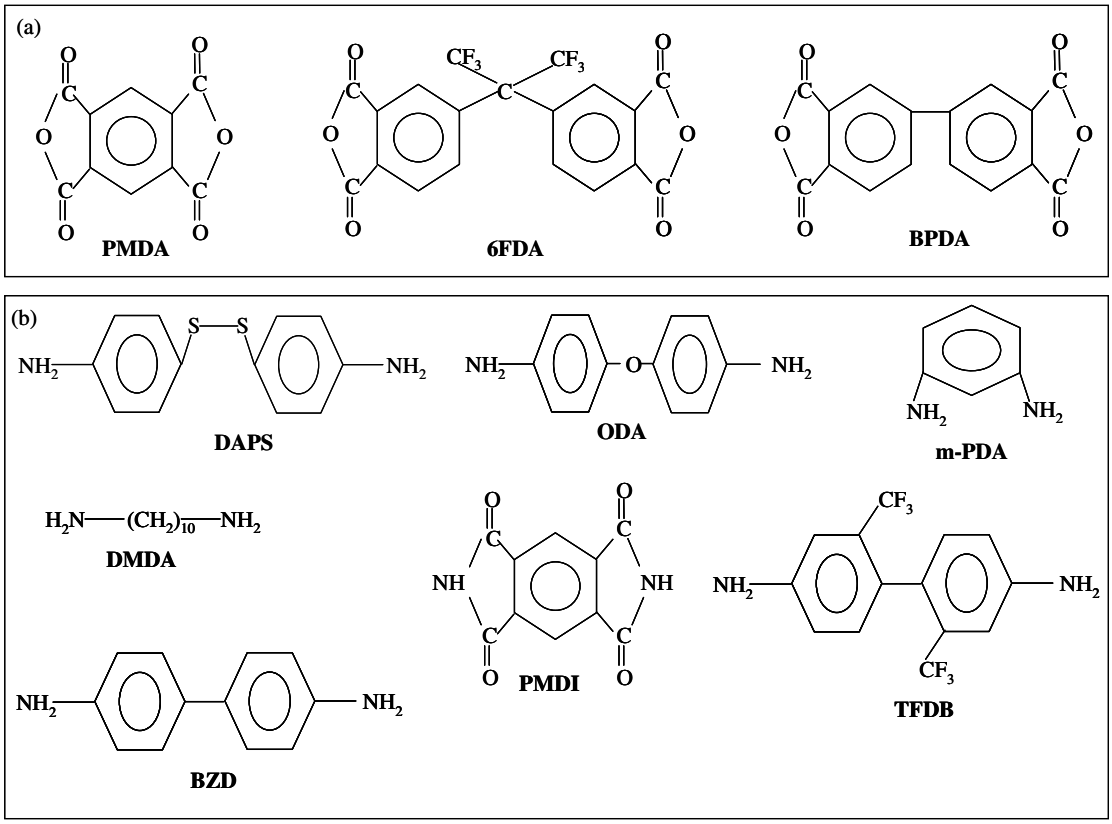

Fig. 10: Precursors for the VDP of polyimides (a) diamines and (b) dianhydrides.

Unlike parylenes, polyimides however, can also be prepared by a spin coating technique, and is investigated widely in literature.[46,47] Only recently, several polyimides have been synthesized by vapor deposition polymerization technique. The preparation techniques and the properties of the films are discussed in the following sections.

Polymerization Mechanism and Thin Film Formation

Chemical vapor polymerization of polyimides follows a different route from that of parylenes described above, in that, it is usually a two step process. First the monomers are adsorbed on the surface of the substrate resulting in the formation of a short-chained oligomer intermediate, and then the films are cured at a higher temperature (~ 300°C) to form the desired polyimide. Several aromatic diamine and the dianhydride precursors studied in this regard, are shown in Figure 10. VDP of polyimides involves two precursors viz., aromatic diamines and aromatic dianhydrides, and therefore the deposition system is different from that of parylenes. Figure 11 shows a setup commonly used for VDP of polyimides,[48] although other types of deposition systems were also reported.[49] In this setup, the source heaters are first calibrated to obtain the desired flux from each component. After codeposition onto a substrate maintained at temperatures below 50°C, a mixture of reacted and unreacted material is obtained,[50] which when subjected to a heat treatment process (curing) undergoes a cyclodehydration resulting in a uniform film of polymer. Several aromatic polyimides have been prepared in this manner, the polymerization scheme is given in Figure 12. The transition from

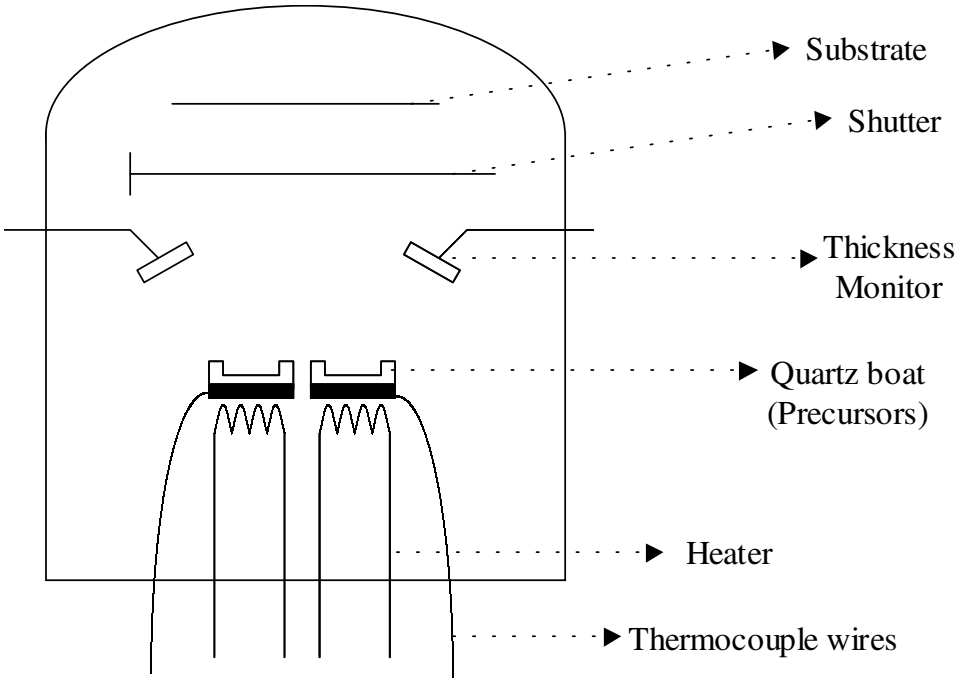

Fig. 11: Experimental setup for the VDP of polyimides.[48]

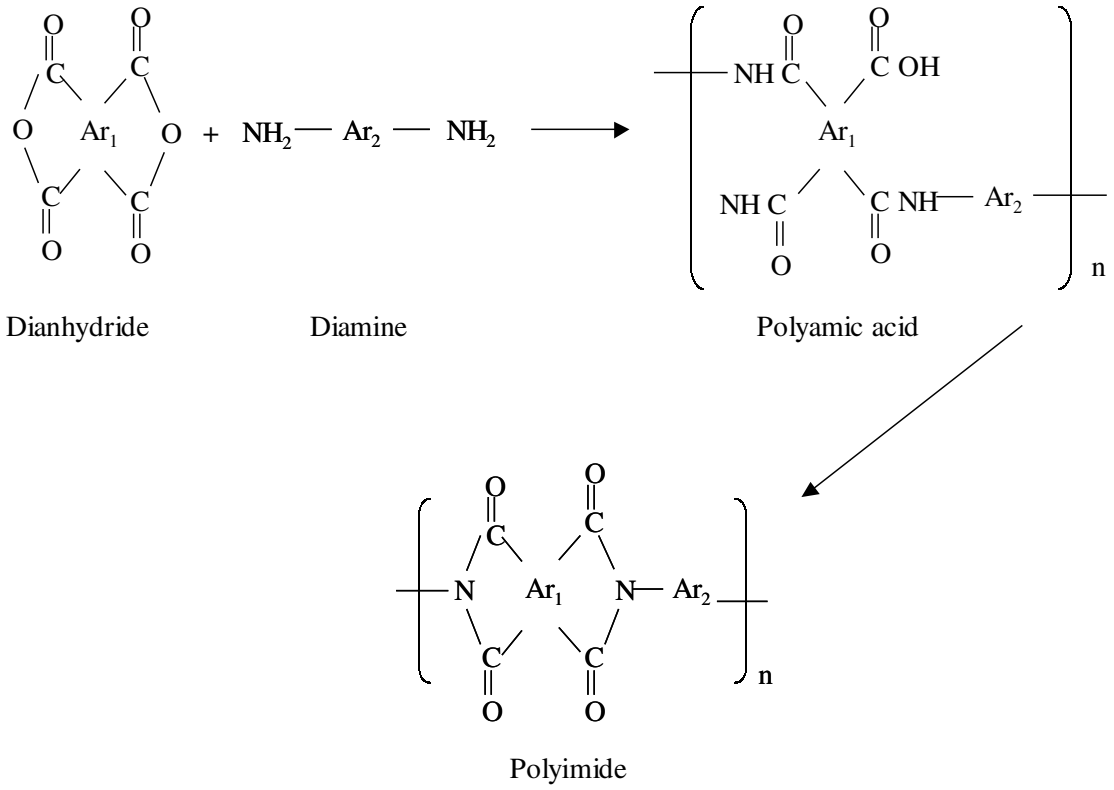

Fig. 12: Reaction pathway showing vapor deposition polymerization of aromatic polyimides.[48]

the intermediate to the polyimide was confirmed by infrared absorbance spectra of PMDA/ODA polyimide.[51]

VDP of polyimides is usually performed in vacuum (pressures $<10^{-3}$ Pa). Just as in any CVD process, the deposition parameters greatly influence the properties of the polyimide thin films. The effect of a few notable ones viz., substrate temperature and the relative fluxes of the precursor vapors is the focus of the next section.

Influence of Deposition Parameters

1. Substrate Temperature

Under typical deposition conditions of polyimides, the substrate is maintained at near room temperature (<50°C). As the substrate temperature is increased, the deposition rate is observed to decrease[45,52] with few exceptions.[53] It was suggested that the sticking coefficients of the organic precursors decrease with increasing substrate temperatures, resulting in lowered growth rate. In general, reducing the substrate temperature can increase the sticking coefficients of organic precursors, but this adversely affects the yield of chemically reacted intermediate species. At substrate temperatures below -20 oC, it was found that PMDA and ODA do not react and only form a molecular mixture.[54] It was also observed that, within this range, films grown at lower substrate temperatures have a shorter chain length.[51] In addition, films prepared at relatively higher substrate temperatures tend to exhibit higher molecular orientation perpendicular to the substrate.[53] In summary, lower substrate temperatures yield high deposition rate thin films (> 40 nm/min) but inherently contain unreacted species, which requires subsequent annealing.

2. Relative Amounts of Fluxes

As the VDP of polyimides involves two precursors, diamine and dianhydride, the relative amounts of fluxes of the precursor vapors need to be controlled carefully to obtain high quality polyimide thin films. The effects of both excess dianhydride as well as the diamine components have been studied and reported in literature,[45,51,52] It was observed that, excess dianhydride (PMDA) undergoes desorption when cured after deposition leading to poor thermal stability. Excess diamine (ODA) component on the other hand leads to undesirable chemical reactions. For instance, it was proposed that under conditions of excess ODA, following imidization, the free amino groups react with imide carbonyl groups resulting in the formation of imine links.[53] These imine links are unstable beyond 300°C, consequently, the films also exhibit poor thermal stability. The optimum relative fluxes need to be determined for each polymer separately taking into consideration the differences in the surface residence time of the species.

Properties of VDP Polyimide Thin Films

Interest in polyimide synthesis has been primarily driven by their excellent thermal stability, although processing problems have hindered their commercial viability until recently. In addition, polyimides have remarkable solvent resistance along with excellent electrical and mechanical properties. More recently, they are being thoroughly investigated based on their electrical properties for use in microelectronic industry. Several reviews on application of polyimides in the microelectronic industry are available in literature.[55,56] Since, polyimide thin films have been deposited by spin coating traditionally, comparative studies of vapor deposited films to spin coated films have been conducted and the properties obtained from both techniques were observed to be largely similar. A detailed description of all the polyimides synthesized primarily by spin coating is available in literature.[57] There were however, some differences such as higher purity in VDP films, which could be attributed to the absence of solution-related problems like solvent retention. Also, the average molecular weight of the polymers prepared from VDP and spin coating are different, (~13000 ± 1000 for VDP films and 20000-40000 for films made by spin coating.[51] In this section, some of the properties of polyimide thin films prepared by vapor deposition polymerization are discussed.

1. Crystal Structure

Kubono et al. studied the dependence of molecular orientation of vapor deposited

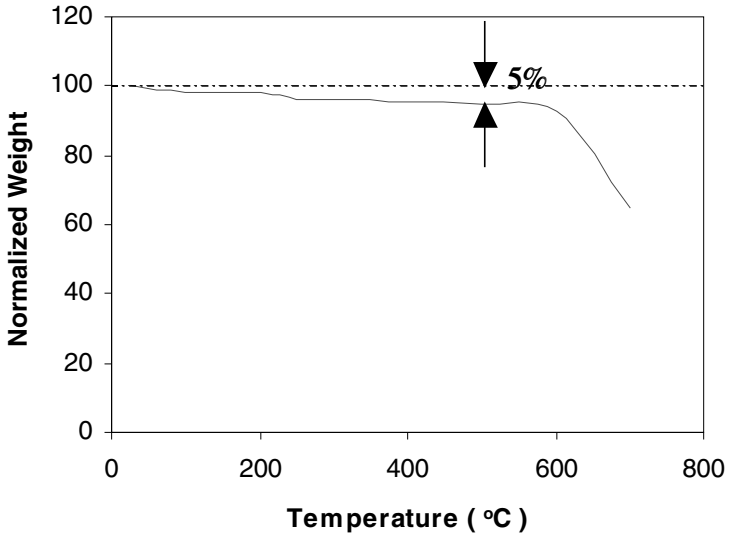

Fig. 13: Weight loss vs temperature for VDP, cured PMDA-ODA polyimide thin film.[45]

polyimide films on the substrate temperature.[53] Their studies revealed that, the films deposited at high substrate temperatures (125 and 175°C) exhibit a molecular orientation preferentially in the plane normal to the substrate, unlike solution based spin coated films, and undergo little change in orientation even upon annealing. Iida et al studied molecular orientation using wide-angle x-ray diffraction technique, and observed that the x-ray peak intensity increases with annealing, indicating an increase in crystallinity, but the crystalline order vanishes completely at 300°C.[58] Also, estimations of inter-planar distance using x-ray diffraction studies yielded a value of 2.7 nm for VDP films, while the corresponding value for spin cast films was 1.45,[57,59] although further studies need to be conducted to explain these differences.

2. Thermal Properties

The post deposition processing parameters (curing temperature, time) have a profound impact on the thermal properties of polyimide thin films. It has been observed that, films cured at around 300°C for 1 hour exhibit markedly superior thermal stability as compared to those that were not cured.[42,60] Cured PMDA-ODA polyimide thin films showed less than 5% weight loss even at 500°C (with the onset of thermal degradation occurring at 470°C in nitrogen ambient) whereas uncured films showed a loss of about 23%.[45] The lower thermal stability of uncured films could be due to the presence of 30-50% unreacted material in the film. Upon curing the amount of unreacted material is reduced considerably resulting in higher thermal stability of the cured films. In comparison to PMDA-ODA films, BPDA-OTD polyimides show a slightly higher thermal degradation temperature of 530°C.[60] This was attributed to the rigid, rod-like structure of these polymers. The thermal stability of PMDA-ODA polyimide film can be seen in Figure 13.[45]

3. Electrical Properties

Along with their excellent high temperature stability, polyimides also possess remarkable electrical properties. A detailed review of the electrical and optical properties of polyimides can be found in Ref. 62. Electrical properties of polyimides were primarily investigated in view of their low dielectric constants and insulating properties. Figure 14 shows the dependence of electrical conductivity of vapor deposited and

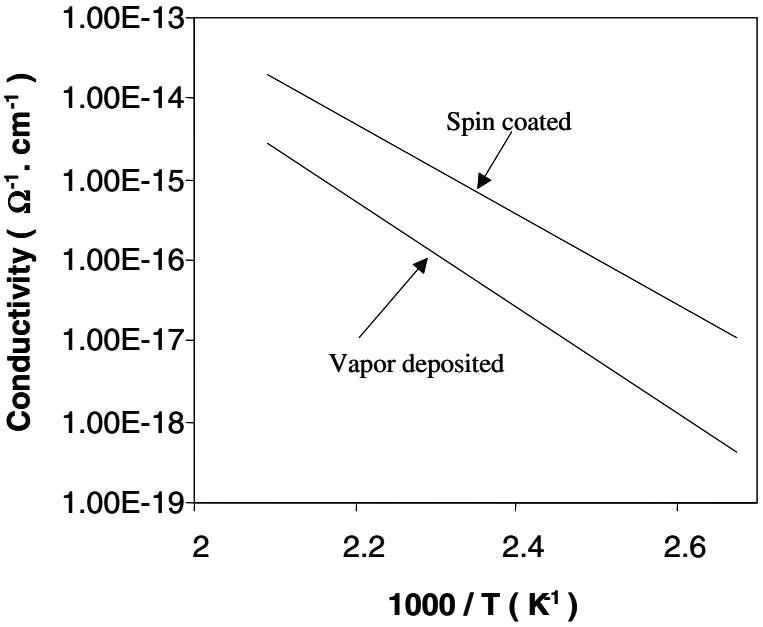

Fig. 14: Electrical conductivity as a function of temperature (a) vapor deposited and (b) spin coated.

spin coated films on annealing temperature.[48] It is clear that, vapor deposited films show significantly lower conductivity compared to spin coated films. This difference in conductivity can be attributed to the lower level of impurities such as dusts, retained solvent etc., in the VDP films compared to those prepared by conventional solution technique. The dielectric constant of the vapor deposited polyimide was found to be 2.9, which is considerably lower than that of spin coated films (ε_r = 3.2 - 3.5).[51] The dielectric dissipation factor is also lower for VDP films ($\tan\delta$ = 0.008 for VDP films and 0.010 for spin coated films). The dielectric breakdown strength was greater than 2 MV/cm.[60]

4. Optical Properties

In general, polyimides exhibit a high refractive index typically between 1.6 and 1.7 and hence can be of definite practical interest particularly as antireflection coatings. Also, similar to parylene thin films, polyimides exhibit anisotropic optical properties. The reported values of refractive index of polyimides were $n_{\parallel}$ = 1.653 and $n_{\perp}$ = 1.624 before curing and $n_{\parallel}$ = 1.695 and $n_{\perp}$ = 1.653 after curing. The birefringence ($n_{\perp}$ - $n_{\parallel}$) was found to be –0.042 after curing which was again lower in magnitude than the films prepared using spin coating (-0.078).[45] Assuming birefringence is a result of the anisotropy in chain orientation, it was suggested that vapor deposited thin films have more or less random molecular orientation, whereas the films prepared by spin coating are oriented primarily in the plane of the substrate. The anisotropy of spin coated and VDP grown polyimide thin films was also detected using internal reflection infrared spectroscopy and corroborated these suggestions.[61] This reduced anisotropy in VDP films could play an important role in the optical applications of polyimide thin films.

Table 2 shows all the above mentioned characteristics of VDP grown polyimide thin films.

Polynapthalenes

Polynapthalenes are essentially insoluble, infusible polymers, resistant to oxidation,

Table 2. Summary of the Properties of Polyimide Thin Films Deposited Using CVD[42,45,48,60]

Polyimide	T_{curing} (°C)	n	ε_r	Breakdown Strength (MV/cm)	$I_{Leakage}$ (@ 5V) (pA/cm^2)	$T_{decomposition}$
6FDA-BDAF	300	1.58	2.7	-	-	350
PMDA-BAPP	400	-	2.7	-	-	420
PMDA-meMDA	400	-	3.1	-	-	450
PMDA-ODA	400	1.78	3.0	4	7	470
PMDA-OTD	400	-	3.0	-	-	520
BPDA-OTD	400	-	2.9	2	10	530

radiation and exhibit excellent thermal stability. A complete discussion of napthalenes, their synthesis (solution based), and properties is presented in a review article by Speight et al.[63] However, there have been relatively few reports of studies on vapor deposited napthalenes. Lang et al. deposited polynapthalene and poly-fluorinated-napthalene using chemical vapor deposition, and reported the properties of these thin films.[28] Their synthesis technique and properties are discussed in the subsequent sections.

Polymerization Mechanism and Thin Film Formation

Chemical vapor deposition of polynapthalene differs from the parylene and polyimide systems in terms of the deposition process. As mentioned in earlier sections deposition of parylenes and polyimides occurs on cold surfaces, and the deposition rate decreases with increasing substrate temperature. In other words, deposition is done in a "hot wall" reactor. In contrast, CVD of polynapthalenes is performed in a "cold wall" reactor, meaning that the substrate is maintained at a high temperature (~350°C) while the surrounding wall temperature is kept at near room temperature. A schematic of the CVD reactor setup employed by Lang et al. can be found in Ref. 28. 1,2-Diethynylbenzene and 1,2-diethynyl-tetrafluorobenzene were used as the precursors, the synthesis of which can be found elsewhere.[64] The precursors were vaporized in vacuum, and the vapor was transported into the hot chamber where the substrates were placed. Polymer film formation requires the substrates to be maintained at 350°C. Unlike the parylenes where bond dissociation occurs, in this case, the high temperature surface of the substrate causes chemical bond rearrangement leading to the formation of free radicals. Condensation of these free radicals is immediately followed by polymerization. The proposed polymerization scheme is shown in Figure 15.

Properties

Polynapthalenes are in general, rigid rod-like low molecular weight aromatic polymers and are insoluble in most common solvents. Thin films of polynapthalene deposited by CVD are microcrystalline as deposited, and show a low dielectric constant (ε_r = 2.4), with high dielectric breakdown strength (3 MV/cm), along with excellent thermal stability (dissociation temperature ~570°C).[28] CVD studies have so far been done primarily in view of their low dielectric constants, for use as intermetallic dielectrics in ULSI interconnect applications.

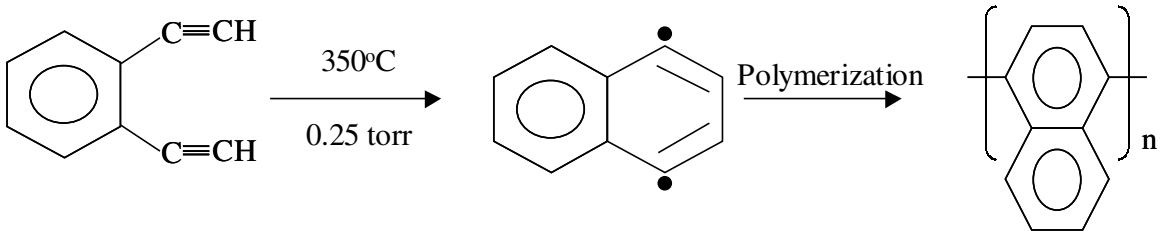

Fig. 15: Polymerization scheme of polynapthalenes.[28]

Poly(p-phenylene vinylene)

Conjugated polymers like poly(1,4-phenylene-vinylene), PPV, or more generally Poly(arylene-vinylenes), PAVs have evoked considerable interest as electrically conductive and nonlinear optical materials. More recently, electroluminescence properties of PPV have attracted substantial attention, since it was first reported in 1990.[65] Direct synthesis of PPV has been limited by its insolubility. Hence, the most commonly used routes are based on soluble polymer precursors[65] or soluble conjugated precursors.[66] The latter process is also commonly referred to as the sulfonium-based poly-electrolyte precursor route. PPV thin films from these solution-based routes, however, have problems related to contamination by solvents and oxidative defects in the polymer.[67,68] CVP is an alternate method for the deposition of high quality thin films of PPV. Reported first by Iwatsuki et al.,[69] it was investigated for electroluminescence applications by Staring et al.[70]

The advantage of CVP, apart from the elimination of solvent induced contamination and oxidative defects, is that it is compatible with traditional inorganic semiconductor processes in the microelectronic and optoelectronic industry. This would be extremely important in the integration of polymer and inorganic semiconductors into hybrid devices with a minimum of processing steps. Moreover, CVP allows the mixture of monomeric compounds in any ratio, thus facilitating the deposition of graded films.

Several researchers have used various precursor materials and processing parameters in order to produce fully conjugated PPV with desirable properties.[69-72] Furthermore, Schafer et al.[73] demonstrated that segmented PPVs, with varying segmentation ratio, can be produced by the CVP process.

Mechanism

Conjugated polymer preparation by CVP is a two step process. The first step involves chemical vapor depostion of an unconjugated precursor polymer. The second involves the conversion of the unconjugated polymer into a conjugated polymer. This is done by dehydrohalogenation, or dehydrogenation, of the unconjugated polymer to induce the formation of a carbon-carbon double bond.

Initial work in this area was done by Iwatsuki et al.,[74] who used the two-step process to synthesize a highly conjugated, poly-2,5-thienylene-vinylene (PTV) film. The mechanism of film formation was as follows:

1. A starting precursor, (2.2)(2,5) thiophenophane, was sublimed at 100°C. The evaporated precursor was then cracked at a pyrolysis temperature of 580°C and the deposited at a substrate temperature of 0°C to produce an insoluble poly-2,5-thienylene-ethylene (PTE) film. Figure 16 shows the CVP deposition of PTE film.
2. This PTE film was then dehydrogenized using 2,3-dichloro-5,6-dicyano-1,4-benzoquinone (DDQ) to produce a PTV film. Figure 17 shows the conversion scheme.

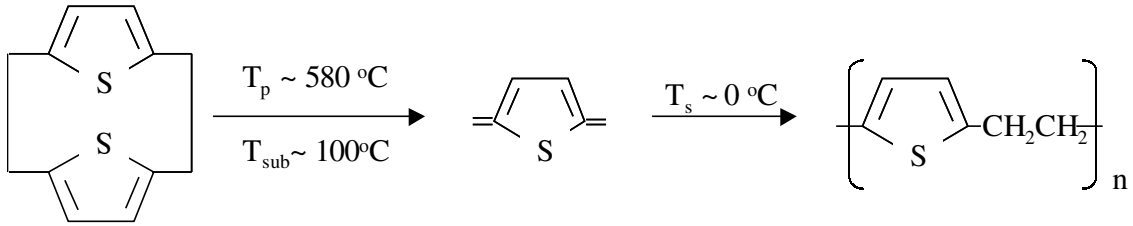

Fig. 16: Reaction scheme for PTE film by CVP of [2.2] (2,5) thiophenophane presursor.[74] T_p: pyrolysis temperature, T_{sub}: sublimation temperature of precursor, T_s: substrate temperature during CVD.

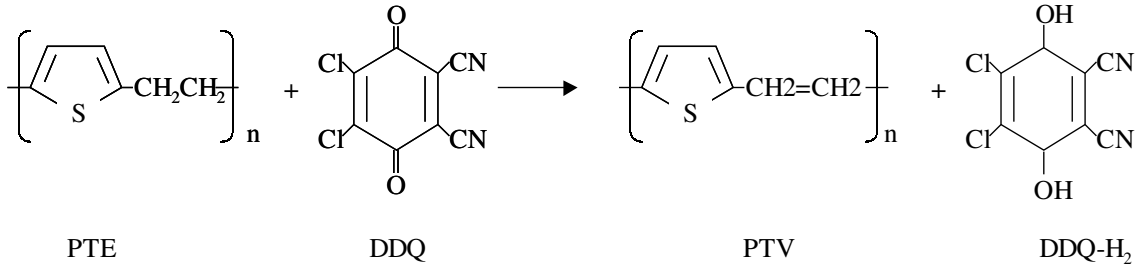

Fig. 17: Reaction scheme for PTV film by dehydrogenation of PTE using DDQ.[74]

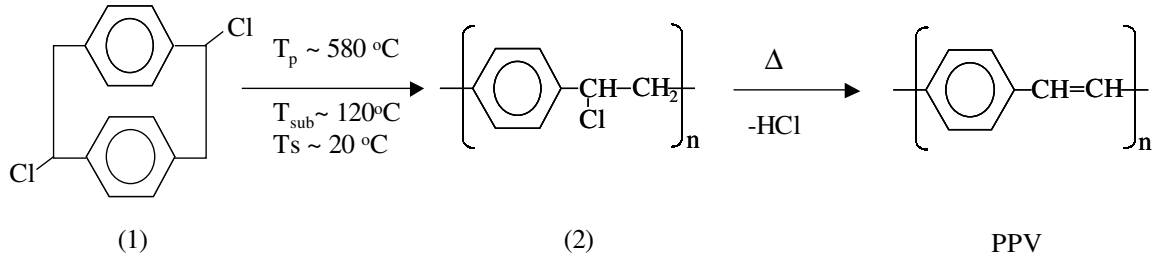

Fig. 18: Reaction scheme for PPV by thermal dehalohydrogenation of (2) film. (2) is formed by the CVP of (1), the dimer (1, 9-dichloro-2, 2-paracyclophane).[69] T_p: pyrolysis temperature, T_{sib}: sublimation temperature of precursor, T_s: substrate temperature during CVD.

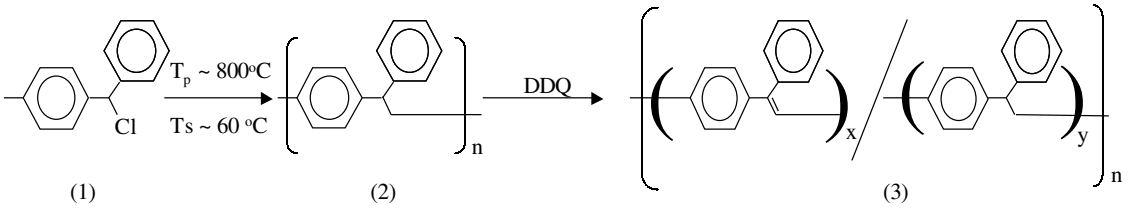

Fig. 19: Reaction scheme for segmented PPV (3), by dehydrogenation of soluble precursor polymer (2), using DDQ. (2) is deposited by CVP of (1).[73] T_p: pyrolysis temperature, T_s: substrate temperature during CVD.

Iwatsuki et al. followed up on this by using a similar process to produce PPV films.[69] Some modification, however, were introduced into the process. In the first step, poly-phenylene-ethylene (PPE) was deposited by the Gorham process.[11] When this was attempted to be converted to PPV by dehydrogenation, using DDQ, the PPE film was found to be extremely stable. Therefore, a leaving group (chlorine) was introduced which, was not only stable during the vapor deposition process but was also easily removable during the conversion of PPE to PPV. Figure 18 shows the two step process for the formation of PPV film.

Later researchers followed essentially the same process, substituting monomer precursors instead of the dimer, to produce PPV films.[70-72] The monomers were evaporated and the vapors carried into the pyrolysis chamber, where they were pyrolyzed at ~800°C. The reactant species were then transported to the substrate maintained at 60°C to form the precursor polymer film. This film was then thermally converted to PPV at 150-320°C.[70-72] Scafer et al.[73] have further shown that PPV can be produced via the dehydrogenation route introduced by Iwatsuki et al.[74] They showed that soluble a-phenyl substituted poly-p-xylylene can be prepared by CVP of 1-α-chlorobenzyl-4-methylbenzene. The parylene was then dehydrogenated by DDQ resulting in PPV. This process could be used to produce both segmented and unsegmented PPVs. The segmentation ratio was controlled by the molar ratio of the parylene to DDQ, in the dehydrogenation step. The reaction scheme is shown in Figure 19.

Composition and Structure

One of the major compositional hurdles of PPV produced by CVP is aliphatic hydrocarbon incorporation. This indicated incomplete conjugation which interrupts the conjugated π-bond structure of the polymer, thereby influencing the energy bad-gap and peak emission wavelength. Staring et al.[70] indicated that all their films had aliphatic hydrocarbon incorporation. Further studies[71,75] indicated that secondary reactions taking place during processing might be the cause of this aliphatic hydrocarbon incorporation.

1. Composition

Use of different monomer precursors indicated that symmetrically substituted monomers (α,α'-dihalogeno-p-xylenes) resulted in significantly larger amounts of aliphatic hydrocarbon incorporation as compared to unsymmetrically substituted monomers (α,α-dihalogeno-p-xylenes).[71] Figure 20 shows the reaction schemes for PPV deposition using symmetrically and unsymmetrically substituted monomers.

Vaeth and Jensen[75] indicated that, fragmentation of precursors during pyrolysis was the major source of aliphatic hydrocarbon incorporation. This fragmentation was also observed in parylenes, which prompted the introduction of (2,2) paracyclophanes[11] and α,α'-

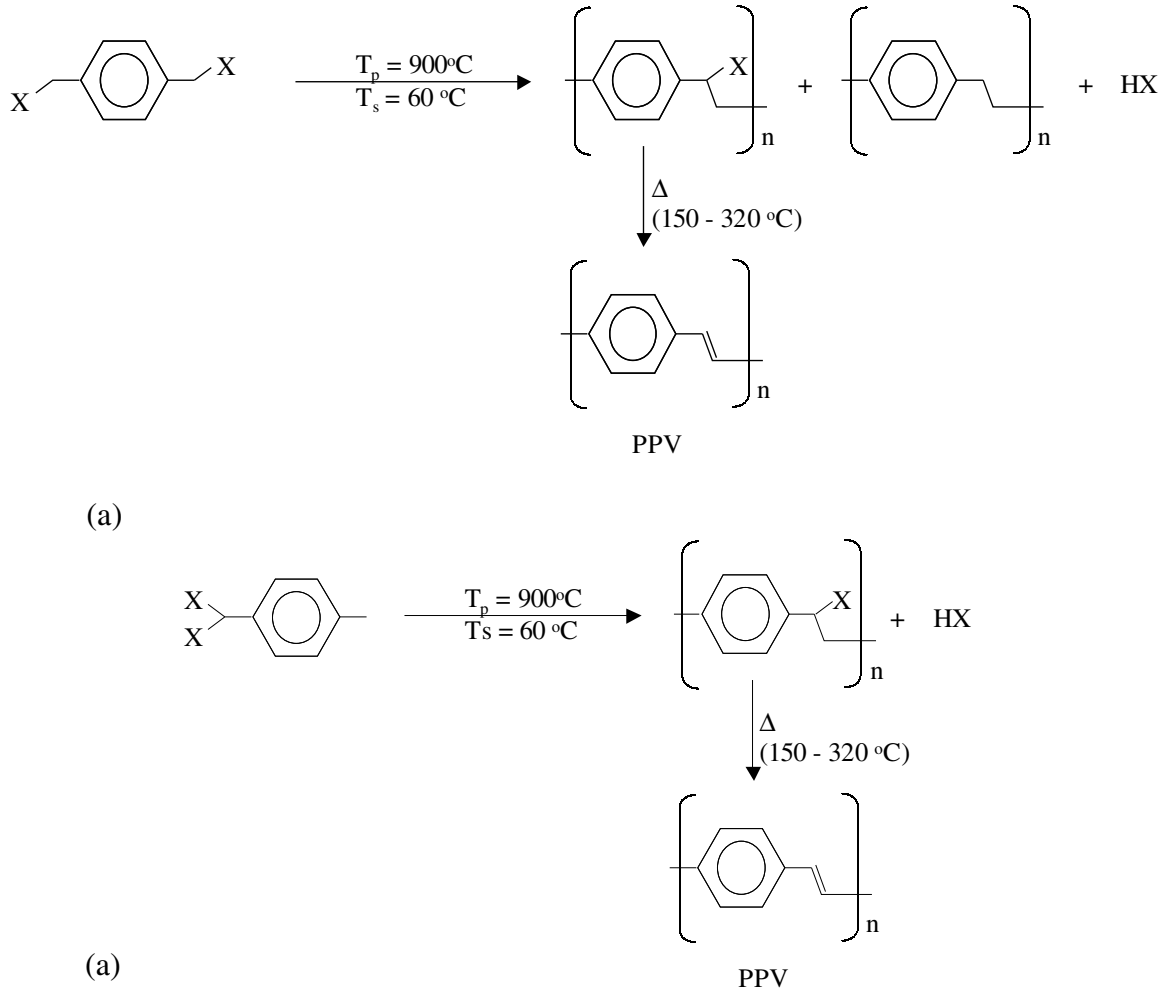

Fig. 20: Reaction scheme for PPV using CVD from (a) symmetrically and (b) unsymmetrically subsituted monomers. (a) shows a possible route for aliphatic hydrocarbon incorporation by formation of parylene during polymerization.[71]

dibromo-p-xylylenes, in conjunction with metal promoters[76,77] in order to reduce the pyrolysis temperatures. Thus, in the case of PPV, use of chlorine as the leaving group, instead of bromine, and lowering the pyrolysis temperature would lead to lesser fragmentation and consequently lesser aliphatic hydrocarbon incorporation.[75]

2. Structure

PPV samples prepared by solution based sulfonium precursor routes were found to be polycrystalline.[78] PPV thin films prepared by CVP, however, show a structure that is dependent on the annealing/conversion temperature.[71] At annealing temps < 200°C, the PPV samples were found to be amorphous, while annealing temperatures > 250°C yielded a polycrystalline structure with small and highly distorted crystals. The reason for this was suggested to be that PPV exhibits a glass transition at about 220°C.[71]

Properties

Interest in PPV has centered on its potential use as an active element in light emitting devices.

Hence the majority of studies of its properties have focussed on electroluminescence and photoluminescence.

1. Electroluminescence

Electroluminescence studies of CVP-PPV, by Staring et al., showed a maximum efficiency was 0.002% at 35V for devices with ~550 nm thickness.[70] They reported that thinner devices have lower threshold voltages for light emission, but often burn out before light emission can be observed. Vaeth and Jensen indicated that layered thin films (~ 60 nm) with high integrity can be fabricated by lowering the substrate temperature to about 25 from 60°C.[79] The reduction in the thickness of the films resulted in lower turn-on voltages, comparable to the ones obtained by solution-based route. Also, the use of chlorine as a leaving group, resulted in even lower turn on voltages. This was suggested to be due to residual chlorine from the thermal conversion, which dopes the polymer, thus changing the carrier injection properties of the film.[79]

Schafer et al.[71] suggested that the reason for such a low efficiency of CVP-PPV devices might be due to the fact that the indium-tin oxide (ITO) electrode, used in typical LED devices was destroyed by the hydrogen halogenides released during the CVP process. Replacement by neutral gold electrodes was shown to produce electroluminescence at a threshold field of the order of 106 V/cm, which is comparable to that of solution based PPV.[65] Further, the use of soluble parylene route to produce PPV, would avoid the generation of hydrogen halogenides during CVP, thereby eliminating the corrosive effect on ITO.[73]

2. Photoluminescence

Photoluminescence spectra of CVD-PPV films, show a blue-shift in the maximum PL wavelength relative to the maximum PL wavelength of solution-based PPV.[70-73, 75,79] This result was attributed to the higher degree of disorder in CVD-PPV films as compared to solution based PPV films. This has been attributed to aliphatic hydrocarbon incorporation, which reduces the effective conjugation length. Thus, PPV films from precursor with bromine as the leaving group (Br-PPV) have been found to have peak PL relatively blue-shifted as compared to Cl-PPV.[75]

Polyazomethines

Polyazomethines belong to a class of polymers that have highly ordered molecular orientation. These materials are important for their electronic, optical and nonlinear optical properties.[80,81] Specifically, polyazomethines have been studied for their electroluminescence and nonlinear optical properties. Conventional synthesis of polyazomethine involves the solution-based route, and suffers from the same limitations as mentioned earlier [section 1]. Also, second order non-linearity in solution deposited polymers is typically induced by a process called poling. This process involves applying a high electric field at a temperature close to the polymer's glass transition temperature (T_g) after the film is formed by spin coating.[82,83] The poling technique, however, suffers from inherent drawbacks such as the creation of a free volume that allows the relaxation of the polymer. The metastable structure due to poling can also be disordered by thermal disturbances. Various methods, ranging from cross-linking[83] to high T_g polymer,[84] have been proposed to overcome this problem. Moreover, the host matrix inhibits the mobility of the chromophores (molecular species, introduced for polarity), during poling.

Yoshimura et al. suggested that all the above mentioned problems associated with conventional poling of spin-coated polymers can be overcome by applying an electric field to the CVP process.[85] This process (called E-CVD) results in an as-deposited poled polymer, as the chromophores align themselves during the polymerization process itself. Since, aligned chromophores tend to de-align themselves due to thermal disturbances (brownian motion), a high T_g polymer is temporally more stable. CVP allows for the deposition of high T_g polymers at room temperature. Thus, the problems associated with thermal disturbance and the host matrix as well as the free volume would be greatly reduced. This is another of the process

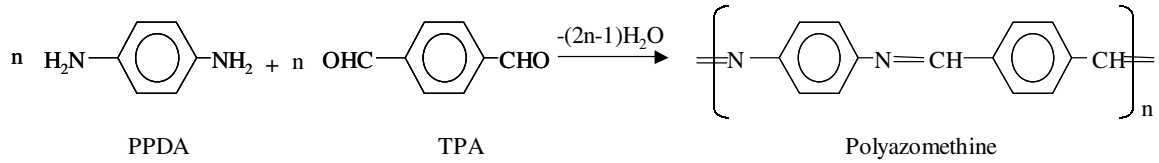

Fig. 21: Reaction scheme for CVD synthesis of azomethine conjugated polymer, poly.

advantages of CVD as compared to solution based techniques.

Synthesis

CVP of polyazomethine involves the introduction of two monomers separately and simultaneously into the deposition chamber to form a polymer on the substrate. The starting monomers are p-phenylenediamine (PPDA) and terephthalaldehyde (TPA). These monomers are sublimed in separate chambers and then introduced into a vacuum chamber. The sublimed monomer gases are held at pressures ranging from 10^{-3} to 10^{-1} torr. The deposition rate was found to be dependent on the gas pressures, which were controlled by changing the temperature of the monomer chambers from 120-150°C. Thus deposition rates ranging from 0.1 to 10 A°/s were obtained.[86,87] Weaver and Bradley deposited polyazomethines by simultaneous introduction of co-sublimed monomer gases into a deposition chamber held at 3×10^{-1} Pa.[88] Figure 21 shows the reaction scheme.

Tatsuura et al. employed the earlier mentioned E-CVD process to deposit polyazomethine conjugated polymer films with second order nonlinear optical properties.[87] The monomers used were 4-methoxy-o-phenylenediamine (MPDA) and o-phtalaldehyde (o-PA). Ortho-type monomers were used to ensure a total dipole moment for the polymer in the direction perpendicular to the chain. Figure 22 shows the structure of the monomers and the resultant polymer.

The energy gap of the polymer depends on the deposition rate.[87] Figure 23 gives the variation of the absorption peak height and energy gap as a function of the deposition rate. It can be seen that as the total deposition rate decreases the absorption peak height increases and the energy gap decreases. This was suggested to be due to the increase in conjugation length, which was attributed to the increased time allowed at lower deposition rates, for the monomers to combine to form the polymer.[87]

Properties

1. Electroluminescence

Electroluminescence (EL) studies done on CVP Polyazomethines indicated that it is primarily an electron transport polymer with a turn-on field ~ 105 V/cm.[88] This turn-on field is much better than that reported for solution processed PPV LEDs,[65] and is in the same range as the some of the best values reported for the CVP-PPV.[79] However, EL emission was only observed when a hole-transporting layer was introduced. They suggested that this might be due to the high ITO/polyazomethine energy barrier which injection of holes from the ITO electrode.[88]

2. Nonlinear Optical Properties

Second order: polyazomethine possesses both donor and acceptor groups at the molecular level, which when aligned gives a poled polymer. Tatsuura et al. fabricated an as-deposited poled polymer film by applying an in-situ electric field during CVD and reported on the second order nonlinear optical properties of the obtained film.[87] The polymer film refractive index was reported to be about 1.68 at 632.8 nm. Second order NLO susceptability, β, was found to be

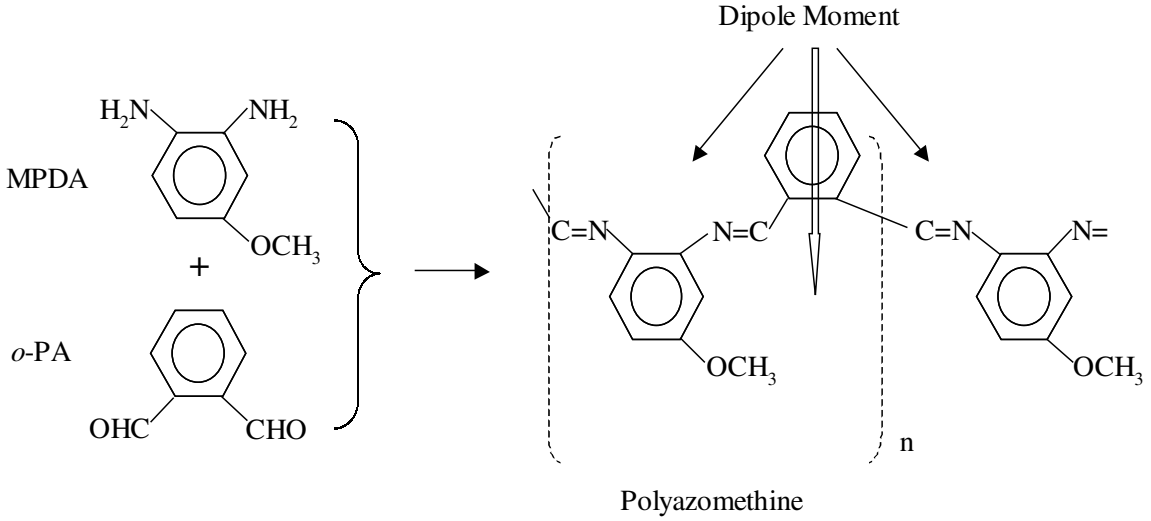

Fig. 22: Reaction scheme for CVD synthsis of polyazomethine with second-order nonlinear properties. The possible dipole moment is shown.[87]

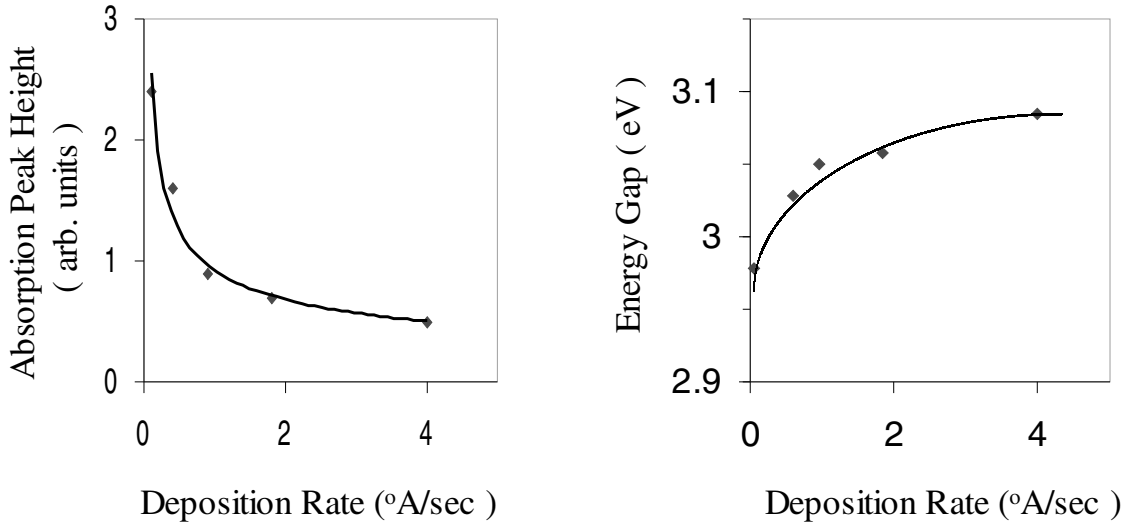

Fig. 23: Peak absorption and energy gap as functions of deposition rate of polyazomethine.[87]

3 – 5 times that of para-nitroaniline.[87] An electro-optic (EO) signal, though small, was observed after heat treatment of the polymer at 80°C for 5 hrs. The EO coefficient, however, was not reported.

Third order: The third order nonlinearity of polyazomethine is derived from its linearly conjugated structure. Furthermore, its long conjugated structure results in a high electro-optic (EO) coefficient.[89] McElvain et al.[90] studied the third-order NLO properties of polyazomethines. They reported the $\chi^{(3)}$ peak susceptibility values for poly-nitrilo-1,4-phenylenenitrilomethylidyne-1,4-phenylene-

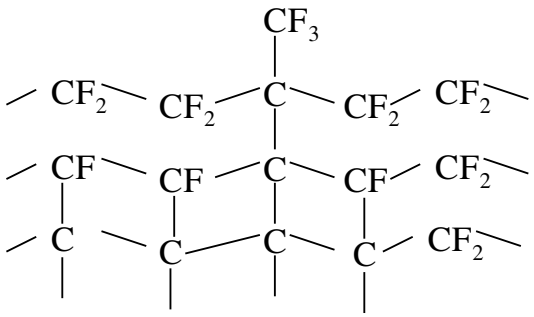

Fig. 24: Structure of a typical Teflon like fluoromonomer obtained by plasma enhanced CVD.[18]

methylidyne (PNPP) and poly-nitrilo-2,5-azinylnitrilomethylidyne-1,4-phenylene-methylidyne (PNAP), to be 2.8 × 10-11 e.s.u and 1.8 × 10-11 e.s.u respectively. Orientation of the films was using a SiO_2 underlayer was found to enhance the $\chi^{(3)}$ value of PNPP by about two times to 6.24×10^{-11} e.s.u.[90]

Novel Polymeric Materials using CVP

In addition to the above-mentioned conventional polymers, there are a few novel materials that are uniquely deposited by CVD. The following section discusses the deposition and properties of these materials.

CVP of Fluoropolymers

The unique capabilities of chemical vapor deposition are clearly demonstrated by the thin films belonging to this class of polymers. Yasuda et al first studied and reported the polymerization of organic compounds in glow discharge.[15,16,91] Polymerization of organic compounds in the presence of plasma is quite different from the conventional chemically or radiatively initiated polymerization. For instance, polymerization of styrene in conventional polymerization can be done using several means of initiation such as radiation, pyrolysis induced, etc., to create the free radical species. But the propagation is essentially the same step, addition reaction of the free radical on to the vinyl double bond of styrene. In this case, two factors namely, the concentration of the reactive species and the presence of the vinyl double bond are extremely essential for the polymerization to occur, and the absence of either implies no polymerization. Also, there is a balance between the number of free radicals generated and consumed. In plasma polymerization, the presence of plasma creates several reactive species and the balance between the production and consumption of reactive species is not necessary. This induces additional property of crosslinking in plasma derived polymer films, as in the case of styrene. Consequently, plasma polymerized styrene is not the same as polystyrene. Also, there are several reactive species in a plasma. This excess and variety of reactive species can be exploited to form an entirely new class of materials called plasma polymerized fluorinated monomers (PPFMs). These are not "polymers" in the conventional sense, as in, there is no one repeating unit. This can be understood more clearly by looking at Teflon-like (Dupont, Wilmington, DE), amorphous fluorinated polymer (Teflon AF), shown in Figure 24. Several such polymers have been studied by Yasuda et al and are shown in Table 3.[91] In the following discussion, we will examine the deposition and polymerization of plasma polymerized fluorinated monomers (PPFM) more closely.

Table 3. List of All the Plasma Polymerized Organic Monomers[91]

Ethylene	Acetylene	Acrylic acid
Tetrafluoroethylene	Styrene	Propionic acid
Benzene	Cyclohexane	Vinyl acetate
Hexafluorobenzene	Ethylene oxide	Methyl acrylate

Plasma Polymerized Fluorinated Monomers (PPFM): Thin Film Formation

Plasma polymerization is a very complicated process, and the overall growth rate is a function of several independent factors such as the type of discharge, reactor geometry, properties and temperature of the substrate, pressure, type and composition of the feed gas and so on. As a result, formulation of a generalized reaction mechanism is not easy. However, attempts were made to formulate the overall mechanisms of plasma polymerization, and can be applied to many cases.[15]

Plasma polymerized fluorinated monomers (PPFMs) are deposited by a freon fed glow discharge. Glow discharge (also called "cold plasma") is essentially a non-equilibrium system generated in the presence of an electric field. Typically, plasma consists of a significant density of neutral atoms, ions, molecules, electrons and free radicals, all at different temperatures, thereby creating a "non-thermodynamic condition".[92] Freon fed plasmas are commonly used to deposit PPFMs. Freon-fed plasmas are of particular interest because of their versatility in enabling (1) deposition. of plasma polymerized fluorinated monomers (PPFM) and (2) plasma etching of a variety of substrates. Both these processes are inherently competitive and present in any system. The rates of deposition and etching can be controlled by the plasma parameters such as the composition of the feed gas, plasma pressure, substrate temperature etc, and the desired process, deposition or etching, can be achieved.

Fluorocarbon plasmas produce two different kinds of reactive species in the glow, namely, CF_x and F atoms. The density of CF_x determines the rate of deposition while that of F atoms, the rate of etching.[93] Therefore, to achieve high deposition rates, CF_x to F ratio is to be maintained high. As is the case of any CVD process, deposition starts with the adsorption of the species on the surface, thereby creating an active surface site, and polymerization occurs by the reaction of the active species in the plasma with the surface active sites, resulting in film formation. The properties of the film are clearly a function of the several plasma-surface interactions along with process parameters such as the substrate temperature, composition of the feed gas and so on. The effects of some of these parameters on the growth rate of teflon AF is discussed below.

Influence of Deposition Parameters

A thorough understanding and careful control of plasma parameters can enable the process to be tailored to the desired application. It must be acknowledged however, that in spite of an impressive number of studies reported, an accurate prediction of the molecular structure of plasma polymers is not available. However, attempts have been made to examine the effects of various deposition parameters on the growth of plasma derived polymer thin films, and some of the results are summarized below.

1. Effect of Gas Feed Composition

As mentioned earlier, freon-fed plasmas generate the two species CF_x radicals and F atoms. CF_x radicals adsorb on the surface and contribute to the film grown. In contrast, F atoms react with the substrate and contribute to etching. It should be noted that both these processes are competitive and occur concurrently. Therefore, it is obvious that for the film deposition process to dominate the etching, the density of CF_x

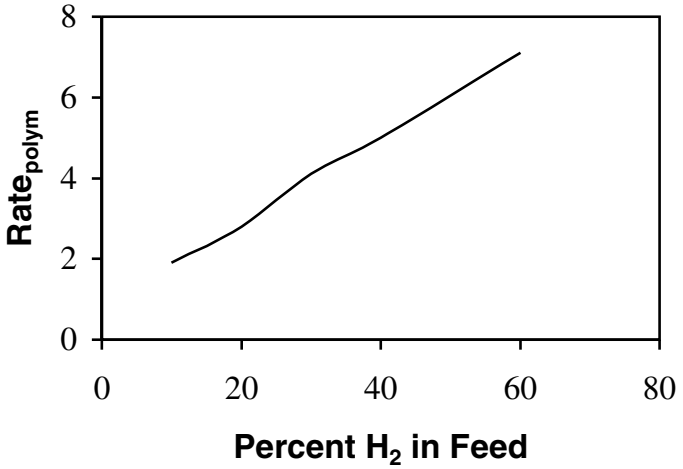

Fig. 25: Polymerization rate as a function of H in the feed gas as an additive to C_2F_6.

radicals in the plasma should be much greater than that of F atoms. Agostino et al studied the density of various reactive species in the plasma (CF, CF_2, CF_3, and F atoms) as a function of the composition of gas feed. It was expected that the order of increasing polymerizing capability would be $C_2F_4 > C_3F_8 > C_2F_6 > CF_4$.[94] To further reduce the etching effect in the plasma different gases such as hydrogen and hydrocarbons are often used as "F atom scavengers." Figure 17 shows the rate of polymerization as a function of the percentage of additive (H_2) in the feed gas.[94] It was observed that the rate of polymerization increases with the addition of H in the feed gas, as shown in the figure.[94]

2. Substrate Temperature

It has been widely reported in literature that the polymerization rate of PPFMs is adversely affected by the substrate temperature.[94,95] Agostino et al proposed a possible mechanism to explain this behavior.[95] They proposed that polymerization mechanism is composed of two steps namely, adsorption of the species on the surface and subsequent polymerization. As the substrate temperature is increased, the species adsorbed on the surface have a higher tendency to desorb before polymerization, leading to lower polymerization rates. The rate of polymerization as a function of substrate temperature is shown in Figure 25. From the figure, it is clear that, at very low substrate temperatures, the activation energy is close to zero, while at higher temperatures, the adsorption process is the rate limiting step and correspondingly the polymerization rate involves a substantial activation energy.

These plasma polymerized thin films have become increasing popular in the last few years, particularly, teflon like polymers, owing to their exceptional properties some of which are described below.

Properties

For a long time, teflon has been recognized to have the lowest dielectric constant with very good mechanical strength. However, a few problems such as cold creep which arises primarily from the crystallinity, and poor adhesion have hindered its applicability. On the other hand, plasma polymerization of fluoropolymers (PPFMs) have improved adhesion and lower crystallinity, thereby reducing creep, and is currently investigated for numerous low dielectric constant as well as optical applications. Some of these properties of PPFMs are described in brief in the following sections.

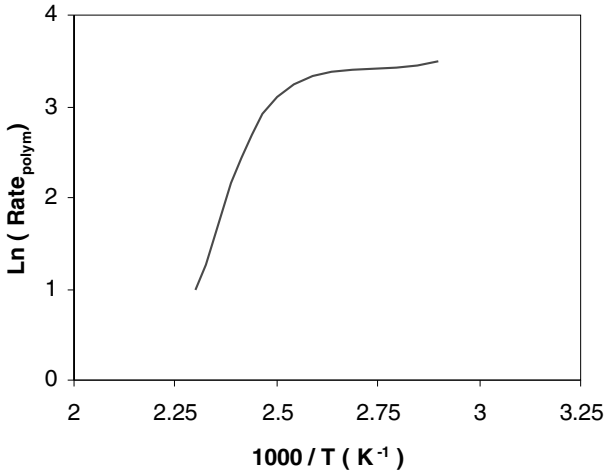

Fig. 26: Rate of polymerization vs. substrate temperature, for C_2F_6-50% H_2 feed mixture.[94]

1. Molecular Structure

Two distinct molecular structures of teflon-like fluoropolymers have been identified by Agostino et al.[95] Figure 26 shows the two structures reported. It can be seen that the first is clearly not a conventional "polymer", in the sense, there is no one repeating unit. It is a scrambled structure with variable C/F ratio and crosslinking. There are no long chains of CF_2 and therefore it is not teflon in the real sense. The C/F ratio could be varied resulting in a variation in properties of the material. The second case could be observed to be more ordered and oriented structure, comprising brush like segments. These are often referred to as after glow fluoropolymers or AG fluoropolymers. Several comparative studies on the two structures, varying the C/F ratios can be found in literature.[96,97]

2. Thermal and Electrical Properties

As mentioned before, Teflon AF has the lowest dielectric constant of most polymeric materials ($\varepsilon_r \sim 2.0$) and a dielectric loss ($\tan\delta$) close to 0.02.[98] Both dielectric constant and loss were found to be dependent on process parameters such as feed gas composition. Low dielectric constants (~2.1) were obtained for films with a high ratio of CF_x species to F atoms in the plasma.[99] The leakage currents obtained were of the order of 10^{-8} A/cm^2.[99] A thorough thermal stability study of PPFM films was done independently by Theil et al.[98] and Endo et al.[99] It was observed that although films obtained from CF_4 feed gas had the lower dielectric constant (2.1), those obtained from C_4F_8 exhibit higher thermal stability. This suggests a tradeoff between thermal stability and dielectric constant. Figure 27 depicts the results of thermal stability studies on PPFMs obtained using three different feed gases.[100]

Novel Copolymers by Thermal CVD

The dry nature of CVD process enables copolymerization more easily than solution based techniques. This approach has been utilized to tailor the thermal and electrical properties of parylene thin films for ULSI applications. One of the first reports of vacuum copolymerization of xylylene was done with maleic anhydride as the comonomer.[101] Subsequently, 9-vinylanthracene, 4-vinylbiphenyl and perfluoro-octyl methacrylate were successfully copolymerized with parylenes, and reported in

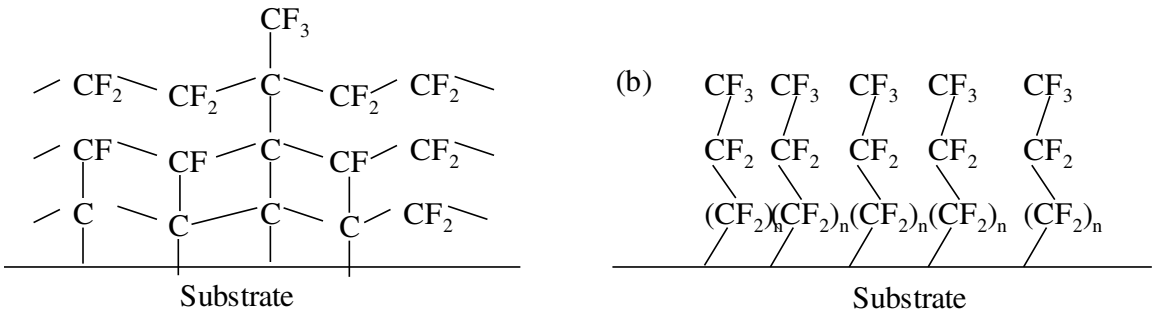

Fig. 27: Molecular structures of fluoropolymers obtained using PECVD of fluorinated monomers.[18]

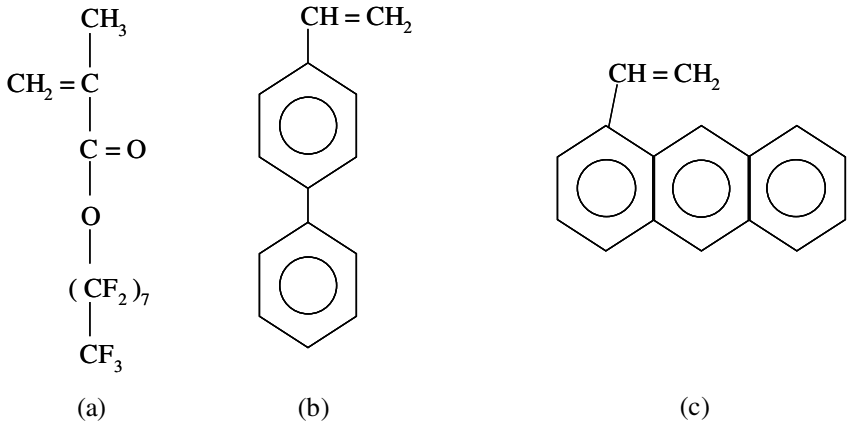

Fig. 28: Thermal CVD reactor to deposit SiO_2-PPXC nanocomposites and parylene based copolymers.

detail by Gaynor and Desu.[101-104] Figure 28 shows the reactor used to fabricate the copolymer thin films. Figure 29 shows the various monomers used for copolymerization with parylene.

It was observed that, these copolymers have superior properties as compared to homopolymers of parylene with respect to dielectric constant and thermal stability. Copolymerization of PPX-C with perfluoro-octylmethacrylate resulted in reduction of dielectric constant from 2.68 to 2.19 at optical frequencies.[101] Copolymerizing PPX-N with vinylbiphenyl yielded an increased thermal stability in oxygen to 450°C.[101,102] Although the idea of copolymerization is not at all novel, it is the solventless approach for the fabrication of these copolymers at near room temperature that is novel and is expected to open up interesting avenues for microelectronic applications.

Silicon Dioxide-Polymer Nanocomposites by Thermal CVD

Traditionally, nanocomposite materials have been developed using solution based (sol-gel)[105] or by sputtering.[106] It was not possible to deposit organic-inorganic nanocomposites by

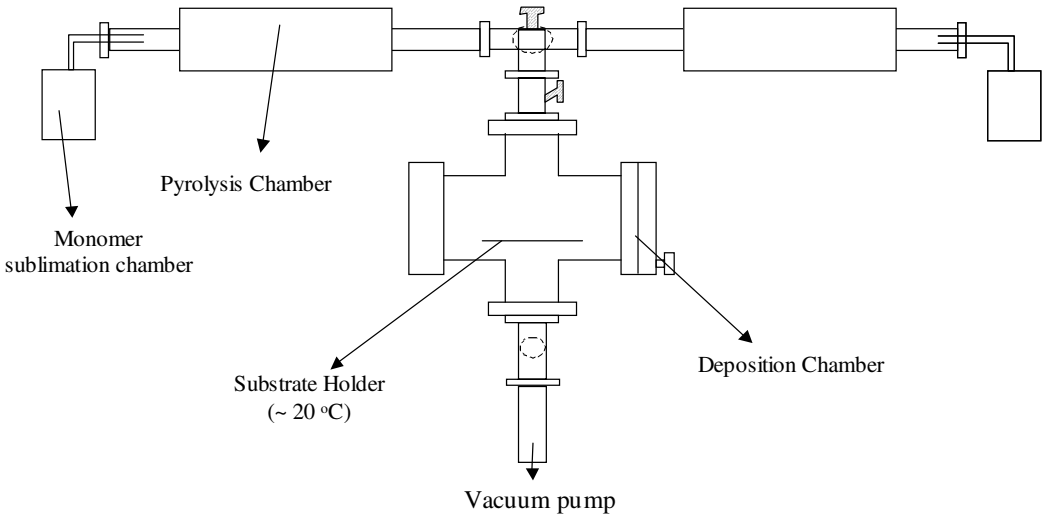

Fig. 29: Chemical structures of comonomers used for copolymerization with parylenes.[102]

CVD owing to the large difference between the deposition temperatures of the oxides (> 600°C) and the ceiling temperature of polymers (Tthr, max = 130°C). Recently, in our group, we have developed a novel thermal CVD based nanocomposite thin film synthesis technology.[107,108] It is expected that the synthesis of these nanocomposites could have a tremendous impact especially in microelectronic devices, and hence is discussed briefly in this review. Although several organic-inorganic nanocomposites could be synthesized by this technique, the following discussion focusses on the film formation and properties of Parylene-SiO_2 nanocomposites.

PPX-C/SiO_2 Nanocomposite Thin films: Synthesis

Conventionally, SiO_2 thin films are deposited at temperatures exceeding 600°C by thermal CVD. Therefore to enable co-deposition of SiO_2 and parylene thin films in the form of nanocomposites, it was necessary to first develop a near room temperature silica (SiO_2) synthesis technique. Desu first demonstrated the possibility of near room temperature deposition of silica thin films using di-acetoxy-ditertiary butoxy silane (DADBS).[109,110] Parylene-C and SiO_2 were then co-deposited in a reactor shown in Figure 28. Parylene was polymerized using Gorham process. The versatility of the co-deposition process can be seen from the wide range of compositions deposited in this technique. Compositional variation was achieved by achieved by careful control over the deposition parameters. Thin films with a wide range of properties could be obtained using this technique as will be shown below.

Properties

Transmission electron spectroscopy (TEM) studies of the co-deposited thin films revealed a continuos polymer phase with a largely inter-dispersed SiO_2 regions on a 5-50 nm scale, confirming the nanocomposite morphology. As mentioned in section 3.1.3, parylene thin films obtained are typically highly crystalline. In contrast, SiO_2 is an amorphous material. From X-ray diffraction analyses, it was observed that by increasing the relative amount of polymer in the nanocomposite, the crystallinity was

Table 4. Properties of PPX-C/SiO_2 Nanocomposite Thin Films Deposited Using Thermal CVD[107,108]

Property	PPX-C	SiO_2	88% PPX-C
Refractive Index (630 nm)	1.639	1.432	1.616
Dielectric Constant @1 MHz	2.88	4.26	3.07
Dissipation Factor	0.0013	0.001	0.021
Leakage Current (A/cm^2 @ 1 MV/cm)	$< 2 \times 10^{-11}$	$< 1 \times 10^{-11}$	2.8×10^{-11}
Dielectric Breakdown Strength (MV/m)	1.9	>5	>4
Weight loss at 415°C (N_2 ambient)	11%	4%	< 1%

correspondingly increased. Also, the dielectric constant (which along with thermal stability was the focus of the study) could be varied gradually from 3.9 (100% SiO_2 film) to 2.8 (100% PPXC) in the same manner.[107,108] Furthermore, it was observed that thermal stability of the nanocomposite films was considerably higher than that of pure polymers. Table 4 shows some of the properties of these polymer-silica nanocomposites.[107,108]

Applications of CVD Polymers

Although there are relatively only few polymers synthesized using CVD, these polymers have found place in numerous applications in microelectronics, optical devices, biomedical industry, corrosion resistant and protective coatings, and even in the automobile industry. Any attempt to review all of these applications would be over-ambitious. In this section, a few of them are briefly discussed, selected primarily based on the number of reports available in literature. For each application, first, the requirements imposed on the candidate materials are listed. Then the rationale of choice of these polymers and the CVD process, and finally, the performance of the polymers, along with their shortcomings, are discussed.

Microelectronic Applications

Low-k Dielectric Applications in ULSI

As can be deduced from the frequent mention of dielectric constants in sections about properties of CVD polymers in this review, a majority of CVD polymers are targeted towards low dielectric constant interconnect applications in ultralarge scale integrated circuits (ULSI). The urgent need to develop a suitable material and process for this application can be sensed by the sheer number of papers published in this area. For an in-depth understanding, the reader is referred to some excellent review articles in literature.[111-113]

The next generation of high performance microchips are expected to contain as many as 0.5 billion transistors on a single chip. This enormous density imposes stringent demands on interconnect wiring technology. In a typical microchip, several layers of copper or aluminum interconnect wiring are separated by a dielectric insulator. Currently, SiO_2 and its analogues with a dielectric constant (er) of about 3.9 are being used as the interlayer dielectrics. There are several problems associated with higher density of interconnect wiring resulting in increased metal resistance and dielectric capacitance. They include increased signal delays, cross talk, electromigration, loss of noise level immunity,

Table 5. Requirements for Low k Dielectrics, as Formulated by SEMATACH[114]

Electrical	Mechanical	Chemical	Thermal
Low Dielectric Constant	Thickness Uniformity	High Chemical Resistance	High Thermal Stability
Highly Isotropic Dielectric Constant	Adhesion	High Etch Selectivity	High Glass Transition Temperature
Low Leakage Current	Low Stress	Low Moisture Absorption	Low Thermal Shrinkage
High Breakdown Strength	High Tensile Modulus	Low Solubility in Water	High Thermal Conductivity
Low Dissipation Factor	High Hardness	Low Gas Permeability	
High Reliability	Low Shrinkage	High Purity	
	Low weight loss	No Metal Corrosion	
	High Crack Resistance	Long Storage Life	
		ESH Compatibility	

high power consumption among others. Currently used SiO_2 based dielectrics fall short of the requirements imposed by high density microchips. This has fueled a frantic search for an alternate dielectric material to replace SiO_2. The requirements for a material to replace SiO_2 are manifold, and are often referred to as Sematach criteria. These are listed in Table 5.[114]

The basic properties to be evaluated for a new interlayer dielectric are as follows:

1. Chemical and physical properties comprising residual stress, density, shrinkage, moisture absorption, impurities, etch rate etc.
2. Electrical properties comprising dielectric constant, dielectric loss, breakdown strength and leakage current, and
3. Thermal properties such as response to heat treatment cycles and thermogravimetric analysis (TGA), out gassing, etc.

Although several inorganic materials such as SiOF, SiBN, BN, are being investigated,[111] polymers are also rigorously investigated primarily owing to their low dielectric constants and excellent insulating properties. In this regard, paraxylylenes (parylenes), polyimides, polynapthalenes, and amorphous fluoropolymers are pursued. Table 6 shows the results of various studies conducted in this direction in the form of their advantages and shortcomings.

It is clear that, although there is not yet, a clear winner in the race for low dielectric constant materials, CVD polymers offer great potential as interlayer dielectric materials in future generation high density microchips.

Encapsulation and Packaging Applications

Once the microchip is made, mounting it on a board and providing protective device protection constitutes chip encapsulation and packaging. Chip on board (COB) assembly is a direct surface mount technology and is very popular in packaging applications owing to its low cost and size reduction.[116] CVD polymers are becoming increasingly popular for this application, primarily due to the conformal nature of the coatings obtained using CVD technique. There are several reviews in literature describing the details of the process and candidate materials, particularly for high density

Table 6. Polymers for Low k Dielectrics, Advantages, and Limitatons

Polymer	Advantages	Limitations
Parylenes	High purity, conformal CVD films, Thoroughly understood mechanism and properties, Compatible with manufacturing processes, Excellent electrical, Excellent chemical resistance and barrier properties	Low oxidation temperature* Shrinkage when annealed in N_2 Anisotropy in properties
Polyimides	Excellent electrical properties, Excellent barrier properties, eg., H_2O High thermal Stability	Two step deposition process CVD films not completely characterized
Polynapthalenes	Excellent electrical Properties Good thermal Properties Insoluble in all solvents	Cumbersome precursor synthesis Process not well established
PPFMs, particularly, Teflon AF and polytetrafluoro ethylene	Excellent electrical Properties (Lowest dielectric constant among most polymers < 2)	Poor thermal stability Adhesion problems High thermal expansion coefficients

devices.[115] The material property considerations of this application include high mechanical strength, low moisture permeation, good interfacial adhesion, excellent thermal stability, high dielectric strength, low dielectric constant, and high resistivity along with environmental issues such as radiation resistance. The polymeric materials under scrutiny for this application are polyimides, parylenes, and plasma derived polymers such as polymethyl methacrylate (PMMA).[116]

Lithographic Resists in Microfabrication

Due to the inherent dry nature of CVD technique, CVD polymers can be utilized as dry resist coatings. Dry resist lithography is advantageous over conventional wet resist techniques because, the whole process can be performed in a unified vacuum chamber. The following are the steps involved in a typical lithographic process.

1. First the resist is applied on the substrate conventionally using spin coating of the solution.
2. Next, the pattern is delineated in the resist.
3. Then, the patterned resist is developed by a dry process, followed by etching of the substrate through the resist mask window.
4. Finally, the stripping of residual resist is also done by a dry process. The advantages of utilizing plasma polymerization for resist coating are two fold
    1. The whole process can be made completely dry and
    2. Spin coating demands that the substrate be flat, while plasma derived coatings can be applied to nonplanar surfaces (even spherical substrates) efficiently. A detailed description of the

lithographic process can be found in Reference 84. Plasma polymerized Methyl methacrylate (PMMA) along with several copolymers of PMMA have been investigated for lithography.[116]

Optical Applications

Light Emitting Devices

The light emitting devices, LEDs and lasers, are the largest application of solid-state devices in the optoelectronic industry. They offer obvious advantages to other light sources in their simpler fabrication procedures, low cost and simpler drive circuitry and high reliability. Traditional light emitting diodes (LEDs), based on inorganic semiconductors such as GaAs, are not easily or economically usable in large-area devices. This has prompted a search for organic and polymer LEDs. The first LED containing luminescent polymer thin films was introduced by Burroughes et al.[65] in 1990. Since then, polymer LEDs have attracted wide attention due to various advantages they offer over inorganic LEDs, such as cheap fabrication technology, light-weight, large-area devices and mechanical flexibility. Also, growth of inorganic thin films requires a close lattice match with the underlying substrate unlike crystalline organic thin films, which can be grown with a substantial lattice mismatch. Furthermore, the peak emission color can be easily tuned by a simple modification of the polymer backbone. Molecular organic LEDs (OLEDs) offset some of the disadvantages inherent in inorganic materials, but suffer from their own shortcomings. Most OLEDs are not stable over long time periods owing to re-crystallization. They also suffer from low mechanical strength. Both of these disadvantages can be overcome by using polymer LEDs (PLEDs). For a more in-depth comparison, the reader.[117]

Some of requirements of the materials for LED applications are high luminescence (~200 cd/m_2), low addressing voltage (<10V), high energy yield, tunability (for different colors) and a reasonably long lifetime (of the order of 10^3 hours). Polymers that satisfy almost all these requirements are currently possible with spin-cast techniques. The best results have been from PPV and its derivatives.[118] A comprehensive review on the electroluminescence properties of polymers and applications can be found in literature.[118-120]

CVP-PPV has been reported to have an output of 20 cd/m^2 at a turn-on voltage of 4.5 V for 600A° thick film.[79] The output increases rapidly as the applied voltage is increased. Figure 30 shows the light output vs. voltage for the best CVP-PPV.[79] Also, CVP-polyazomethine films have been reported with low turn on fields of 6×105 V/cm,[88] making them good candidates for LED applications.

Semiconductor polymer lasers have been investigated only very recently. Though no study of lasing property studies have been reported on CVP conjugated polymers, studies on solution-based derivatives of PPV, show excellent prospects. Some of the advantages of conjugated polymers for laser applications are high photoluminescence efficiency, low self-absorption and that they can be electrically pumped in a diode configuration. Some good reviews on the applications of conjugated polymers for laser applications[121] and of organic materials in general, for laser applications[122] can be found in literature.

Non-Linear Optical Applications

Optoelectronic and photonic devices have made tremendous progress lately. The role of these devices has changed from passive, display devices and sensors, to active components in information systems. This trend is expected to continue towards the realization of fully integrated optoelectronic devices, if not photonic (all-optical) devices. Nonlinear optics is expected to play a major role in this technology. The major problems with the development of optical communication, hitherto, have been the incoherency of light sources and the lack of suitable guiding media.[123] With the advent of lasers, as a source of high intensity coherent light, nonlinear optics is expected to take off. Novel NLO polymers are expected to overcome the material property drawbacks of conventional inorganic NLO materials, like GaAs/AlGaAs

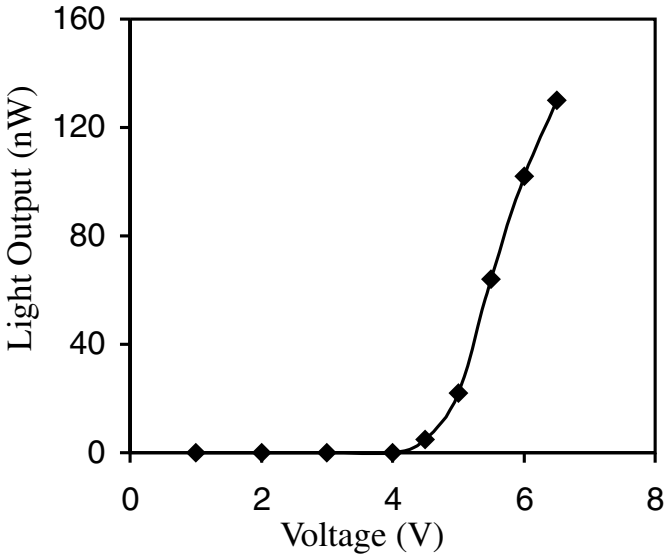

Fig. 30: Light output for single layer PPV device (obtained from chlorinated precursor), Thickness of PPV film = 700°A.[79]

and $LiNbO_3$, such as their fragility, high dielectric constant and processing and integration difficulties.[124] CVP is expected to play a significant role in the integration of polymers in existing silicon devices.

1. Second-order

Second order nonlinear optical properties are utilized in the construction of waveguides and electro-optic modulators, among others. This portends new possibilities for the development of low cost optoelectronic integrated devices for telecommunication and datacommunication. The advantage of polymers for these applications is derived from their low dielectric constants and high $\chi^{(2)}$ susceptibilities. This $\chi^{(2)}$ susceptibility allows for the switching of optical signals from one path to another, by the application of an electric field.

Second order optical nonlinearity can be induced in polymeric systems containing dipolar (donor-acceptor) chromophores.[125] The chromophore can be a molecular species attached to the host chain or it can be incorporated in the polymeric structure itself. In general, a good chromophore has an electron donating group connected to an electron accepting group by a large p-conjugated group. Noncentrosymmetric ordering of the chromophores is achieved by poling using an electric field. This is done by applying a high electric field at a temperature just below the glass-transition temperature (T_g) of the polymer. CVP allows for the in-situ application of the electric field during polymerization, thereby aligning the chromophores. This has some inherent advantages over the poling technique, as mentioned earlier [section 3.5].

Among polymers with second order non-linear optical properties, CVP has only been used for polyazomethines [section 3.5] and polyimides [section 3.2]. Polyazomethine deposited by E-CVD, was reported to have a β, 3 - 5 times that of paranitroaniline.[87] An EO response was also observed after heating the film at 80°C for 5 hrs, indicating that the alignment in polymer was thermally stable. Transparent polyimide films, with second order NLO properties, have been noted for their high T_g.[126] However, they have generally been prepared using solution based techniques. A good overview of a class of transparent polyimides, flourinated polyimides, with an emphasis on waveguide applications can be obtained.[127]

Yoshimura et al.,[85] applied an electric field to the CVP process of polyamic acid, a precursor of polyimide, to align the NLO molecules during polymerization. They reported that a slight dichromism was observed in the film for the light polarized parallel and perpendicular to the direction of the aligning field. Though not too large, this indicated that a poled polymer can be fabricated without subsequent poling by heating. They followed it up by fabricating an electro-optic waveguide from an epoxy-amine polymer film, using E-CVD.[128]

2. Third-Order

Third-order properties involve self-focusing or defocusing, four wave mixing, optical bistability and optical Kerr effect.[129] This frequency mixing phenomenon gives rise to the dependence of the refractive index of the material on the intensity of the incident light waves. This provides a basis for all optical processing of information, which can be used to develop photonic devices. One of the major drawbacks of all-optical switching and logic devices is that they require large amounts of input optical power. This limitation is sought to be overcome by the development of novel polymers with large $\chi^{(3)}$ susceptibility. Theoretical models predict large non-resonant third order nonlinearity associated with delocalized p-electron systems. Furthermore, the molecular structures do not have to be noncentrosymmetric, though they must possess anharmonicity.[129]

Conjugated polymers satisfy these requirements and have thus emerged as the most widely studied materials for their $\chi^{(3)}$ susceptability. Some of the examples of conjugated polymers, that have been studied for their third order NLO properties, are polydiacetylenes, poly-p-phenylenevinylenes and polythiophenes. However, CVD has only been used in the case of poly-p-phenylenevinylenes (PPV) [section 3.4], although $\chi^{(3)}$ values have not been reported. An excellent review of third order nonlinear optical properties of PPV in general, can be found in literature.[130] Recently, McElvain et al.[90] reported the $\chi^{(3)}$ values of CVD polyazomethines to be ~10-11 e.s.u, with a near doubling of the $\chi^{(3)}$ values for oriented polyazomethine films.

Coating Applications

Biomedical Applications

In addition to microelectronic and optical applications, polymers deposited using thermal and plasma assisted CVD are increasingly being used in several biomedical applications as well. For instance, drug particles microencapsulated with parylenes provide effective control release activity.[27] Plasma polymerized tetrafluoroethylene, parylenes and ethylene/nitrogen mixtures can be used as blood compatible materials.[131,132] An excellent review of plasma polymers used in biomedical applications can be found in reference 131.

Protective Coatings Applications

A low cost thin parylene coating on fuel system seals, O-rings, hoses and diaphragms in automobiles, improves the resistance to alternative fuels preventing corrosion and premature failure of car fuel systems.[43] The nature of CVD process enables formation of very thin coatings which otherwise cannot be deposited. This property has been exploited for better preservation of old books and documents and extended to fragile artifacts, since very thin parylene coating is sufficient to reduce their brittleness.[27] Parylenes are also used as electroinsulation coatings in miniature transformers and motor armature.[27] Parylene coatings have also been proposed for use to provide corrosion protection for a number of thin porous inorganic materials.[27] Furthermore, CVD polymers such as parylenes are hydrophobic and their coatings can be used to transport ultrapure water.[27]

Summary

In this paper, the fundamentals of chemical vapor deposition have been reviewed with emphasis on polymer thin films. CVD, being a vapor deposition technique offers several unique advantages over conventional thin film

deposition techniques such as solution based methods, sputtering etc. Moreover, plasma enhanced CVD polymers have specific properties such as higher degree of crosslinking, which otherwise cannot be achieved. There are, however, relatively few distinct families of polymers that can be deposited using CVD, namely, parylenes, polyimides, polyphenylene vinylenes, and polynapthalenes. More recently, there have been reports of novel materials, such as plasma polymerized fluorinated monomers (PPFM), and inorganic-organic nanocomposites. The deposition mechanisms along with details of polymerization have been discussed, with emphasis on the influence of deposition parameters on the film properties. These polymers are being used, and investigated for future potential applications in varied technologies, the notable ones being, low dielectric constant interconnect materials and optical devices along with protective, moisture repellant and corrosion resistant coatings applications. Clearly, the excellent properties of polymers combined with the unique advantages offered by CVD (such as the ability to deposit uniform, high purity ultra thin coatings) are yet to be fully exploited.

References

1. S. Sivaram, *Chemical Vapor Deposition*, International Thomson Publishing Inc. 1995.
2. Arthur Sherman, *Chemical Vapor Deposition for Microelectronics*, Noyes Publications, 1987.
3. H.O. Pierson, *Handbook of Chemical Vapor Deposition*: Principles, Technology and Applications, Noyes Publications, 1992.
4. H.S.W. Massey and E.H.S. Burhop, *Electronic and Ionic Impact Phenomena,* Oxford University Press, London, 1952.
5. R.S. Corley, H.C. Haas, M.W. Kane, and D.I. Livingston, *Journal of Polymer Science*, Vol.13, 1954, p.137.
6. B. McCarrol and E. Ehrlich, *Condensation and Evaporation of Solids*, Gordon and Breach, NY, 1964, p.521.
7. W.F. Gorham, *Encycl. Polym. Sci. Technol*., vol.15, 1971, p.98.
8. S. Kubo and B. Wunderlich, *Journal of Polymer Science and Polymer Physics*, Vol.10, 1972, p.1949.
9. J. Bloem and J. Giling, *VLSI Electronics Microstructure Science*, Academic Press, Florida, Vol.12, 1985, p.91.
10. R. Sarangpani and R. Singh, *Rev. Sci. Instrum*., Vol.68, (No.3), 1997, p.1564.
11. W.F. Gorham, *Journal of Polymer Science A-1*, Vol.4, 1966, p.3027.
12. R. Reif, *Handbook of Plasma Processing Technologoy*, Noyes Publications, New Jersey, 1990, p.268.
13. R.S. Rosler, W.C. Benzing, and J. Baldo, *Solid State Technol*., Vol.19, (No.6), 1976, p.45.
14. S.C. Brown, *Basic Data of Plasma Physics*, John Wiley & Sons, NY, 1959.
15. H. Yasuda and T. Hsu, *J. Polym. Sci: Polym. Chem*., Vol.15, 1977, p.81.
16. H. Yasuda and C.E. Lamaze, *J. Appl. Polym. Sci*., Vol.17, 1973, p.1519.
17. R. dAgostino, F. Cramarossa, and F. Fracassi, Plasma Deposition, Treatment and Etching of Polymers, Academic Press Inc., 1990, p.95.
18. R. dAgostino, Plasma Processing of Polymers, Kluwer Academic Publishers, 1997, p.3.
19. M. Szwarc, *Disc. Faraday Soc*., Vol.2, 1947, p.48.
20. B. Bartlett, L.J. Buckley, D.J. Godbey, M.J. Schroeder, C. Fontenot, and S. Eisinger, *J. Vac. Sci. Tech. B*, Vol.17, (No.1), 1999, p.90.
21. F. Cacialli and P. Bruschi, *J. Appl. Phys*., Vol.80, (No.1), 1996, p.70.
22. S. Tatsuura, W. Sotoyama, and T. Yoshimura, *Appl. Phys. Lett*. Vol.60, 1992, p.1158.
23. M. Szwarc, *J. Polym. Sci*., Vol.16, 1948, p.128.
24. M. Szwarc, *J. Polym. Sci*., Vol.6, 1951, p.319.
25. W.F. Beach, *Macromolecules*, Vol.11, (No.1), 1978, p.72.
26. J.F. Gaynor, S.B. Desu, and J.J. Senkevich, *Macromolecules*, Vol.28, 1995, p.7343.
27. L. Alexandrova and R. Veragraziano, Unpublished Private Communication.
28. C.I. Lang, G.R. Yang, J.A. Moore, and

T.M. Lu, *Proceedings of Mater. Res. Symp*., Vol.381, 1995, p.45.
29. W.F. Beach, C. Lee, D.R. Bassett, T.M. Austin, and R. Olson, *Encycl. Polym. Sci. Eng*., 2nd edn., John Wiley & Sons, Vol.17, 1989, p.990.
30. S. Ganguly, H. Agrawal, B. Wang, J.F. McDonald, T.M. Lu, G.R. Yang and W.N. Gill, *J. Vac. Sci. Techol*., Vol.A15, (No.6), 1997, p.3138.
31. F.E. Cariou, D.J. Valley, and W.E. Loeb, IEEE Trans. Parts; Mater. Packg., Vol.54, 1965.
32. D. Mathur, G.R. Yang, and T.M. Lu, *Journal of Materials Res*., Vol.14, (No.1), 1999, p.246.
33. P. Simon, S. Mang, A. Hasenhindl, W. Gronski, and A. Greiner, *Macromolecules*, Vol.31, 1998, p.8775.
34. A.S. Harrus, M.A. Plano, D. Kumar, and J. Kelly, *Proceedings of Materials Res. Symp*., Vol.443, 1997, p.21.
35. R. Vedula, V. Simkovic, and S.B. Desu, *Proceedings of Mat. Res. Symp*., 1998.
36. S.C. Selbrede and M.L. Zucker, *Proceedings Mat. Res. Symp*., Vol.476, 1997, p.219.
37. M. Szwarc, *Polym. Eng. Sci*., Vol.16, (No.7), 1976, p.473.
38. K.J. Miller, H.B. Hollinger, J. Grebowic, and B. Wunderlich, *Macromolecules*, Vol.23, 1990, p.3885.
39. N.S. Murthy and H.G. Kim, *Polymer*, Vol.25, 1984, p.1093.
40. B. Joesten, *Journal Applied Polym. Sci*., Vol.18, 1974, p.439.
41. P.K. Wu, G.R. Yang, J.F. McDonald, and T.M. Lu, *J. Electronic. Mat*., Vol.24, (No.1), 1995, p.53.
42. N. Majid, S. Dabral, and J.F. McDonald, *Journal of Electronic Materaials*, Vol.18, (No.2), 1989, p.301.
43. J. Pyle, *Machine Design*, 1993, p.77.
44. M. Iijima, Y. Takahashi, K. Inagawa, and A. Itoh, *Journal of Vac. Soc. Jpn*., Vol.28, 1985, p.437.
45. J.R. Salem, F.O. Sequeda, J. Duran, W.Y. Lee, and R.M. Yang, *Journal of Vac. Sci. Technol. A 4*, 1986, p.369.
46. B.C. Auman, *Proceedings of Materials Res. Soc. Symp*., Vol.381, 1995, p.19.
47. Y.K. Lee, S.P. Murarka, and B. Auman, *Proceedings of Materials Res. Soc. Symp*., Vol.443, 1997, p.71.
48. Y. Takahashi, M. Iijima, K. Inagawa, and A. Itoh, *J. Vac. Sci. Technol. A5*, Vol.4, 1987, p.2253.
49. C.W. Hutchings and M. Grunze, *Rev. Sci. Instrum*., Vol.66, 1995, p.3943.
50. M. Iijima and Y. Takahashi, *Macromolecules*, Vol.22, 1989, p.2944.
51. T. Strunskus and M. Grunze, *Polyimides*, Dekker, NewYork, 1996, p.187.
52. R.G. Pethe, C.M. Carlin, H.H. Patterson, and W.N. Unertl, *Journal of Mater. Res*., Vol.8, 1993, p.3218.
53. A. Kubuno, H. Higuchi, S. Umemoto, and N. Okui, *Thin Solid Films*, Vol.232, 1993, p.256.
54. C. Hahn, T. Strunskus, D. Frankel, and M. Grunze, *Journal of Electron Spectrosc. Relat. Phenom*., Vol.54/55, 1990, p.1123.
55. S.D. Senturia, *ACS Symp. Ser*., Vol.346, 1987, p.428.
56. R.J. Jensen, *ACS Symp. Ser*., Vol.346, 1987, p.466.
57. A. Golzhauser, S. Panov, M. Mast, A. Schertel, M. Grunze, and C. Woll, *Surface Sci*., Vol.334, 1995, p.235.
58. K. Iida, T. Nohara, K. Totani, S. Nakamura, and G. Sawa, *Japan Journal of Appl. Phys*., Vol.28, 1989, p.2552.
59. N. Takahashi, D.Y. Yoon and W. Parrish, *Macromolecules*, Vol.17, 1984, p.2583.
60. S. Ukishima, M. Iijima, M. Sato, Y. Takahashi, and E. Fukada, *Thin Solid Films*, Vol.308/309, 1997, p.475.
61. V. Liberman, V. Malba, and A.F. Bernhardt, *Proceedings of Mat. Res. Soc. Symp.,* Vol.443, 1997, p.15.
62. M.I. Bessenov, M.M. Koton, V.V. Kudryavtsev, and L.A. Laius, Polyimides, Thermally Stable Polymers, Consultants Brueau, NewYork and London, 1987, p.171.
63. J.G. Speight, P. Kovacic, and F.W. Koch, *Journal Macromol. Sci. Revs. Macromol. Chem*., Vol.C5, 1971, p.295.
64. S. Takahashi, Y. Kuroyama, K. Sonogashira, and N. Hagihara, *Synthesis*, 1980, p.627.

65. J.H. Burroughes, D.D.C. Bradley, A.R. Brown, R.N. Marks, K. Macay, R.H. Friend, P.L. Burns, and A.B. Holmes, *Nature*, Vol.347, 1990, p.539.
66. D. Braun and A.J. Heeger, *Appl. Phys. Lett*., Vol.58, 1991, p.1982.
67. B.R. Hsieh, H. Antoniadis, M.A. Abkowitz, and M. Stolka, *Polym. Prep*., Vol.33, 1992, p.414.
68. F. Papadimitrakopoulos, K. Konstandinidis, T.M. Miller, R. Opila, E.A. Chandross, and M.E. Galvin, *Chem. Mater*., Vol.6, 1994, p.1563.
69. S. Iwatsuki, M. Kubo, and T. Kumeuchi, *Chem. Lett*., 1991, p.1071.
70. E.G.J. Staring, D. Braun, G.L.J.A. Rikken, R.J.C.E. Demandt, Y.A.R.R. Kessener, M. Bouwmans, and D. Broer, *Synth. Met*., Vol.67, 1994, p.71.
71. O. Schafer, A. Greiner, J. Pommerehne, W. Guss, H. Vestweber, H.Y. Tak, H. Bassler, C. Schmidt, G. Lussem, B. Schartel, V. Stumpfln, J.H. Wendorff, S. Spiegel, C. Moller, and H.W. Spiess, *Synth. Met*., Vol.82, 1996, p.1.
72. K.M. Vaeth and K.F. Jensen, *Adv. Mater*., Vol.9, 1997, p.490.
73. O. Schafer, S. Mang, E. Arici, G. Lussem, C. Unterlechner, J.H. Wendorff, and A. Greiner, *Macromol. Chem. Phys*., Vol.199, 1998, p.807.
74. S. Iwatsuki, M. Kubo, and H. Yamashita, *Chem. Lett*., 1989, p.729.
75. K.M. Vaeth and K.F. Jensen, *Macromolecules*, Vol.31, 1998, p.6789.
76. A.V. Pebalk, I.Y. Kardash, and A.N. Pravendnikov, *Polym. Sci. U.S.S.R*., Vol.23, 1981, p.2101.
77. L. You, G.R. Yang, C.I. Lang, P. Wu, J.A. Moore, J.F. McDonald, and T.M. Lu, *Proceedings of Mater. Res. Symp.,* Vol.282, 1993, p.593.
78. V. Massardier, V.B. Cajipe, T.P. Nguyen, and V.H. Tran, *Synth. Met*., Vol.75, 1995, p.169.
79. K.M. Vaeth and K.F. Jensen, *Appl. Phys. Lett*., Vol.71, (No.15), 1997, p.2091.
80. D.S. Chemla and J. Zyss, Nonlinear Optical Properties of Organic Molecules and Crystals, Academic, New York, 1987.
81. P. Prasad and D. Williams, Introduction to Nonlinear Optical Effects in Molecules and Polymers, Wiley, New York, 1991.
82. K.D. Singer, M.G. Kuzyk, W.R. Holland, J.E. Sohn, S.J. Lalama, R.B. Comizzoli, H.E. Katz, and M.L. Schilling, *Appl. Phys. Lett*., Vol.53, 1988, p.1802.
83. D. Jungbauer, B. Reck, R. Twieg, D.Y. Yoon, C.G. Willson, J.D. Swalen, *Appl. Phys. Lett*., Vol.56, 1990, p.2610.
84. J.W. Wu, J.F. Valley, S. Ermer, E.S. Binkley, J.T. Kenney, G.F. Lipscomb, and R. Lytel, *Appl. Phys. Lett*., Vol.58, 1991, p.225.
85. T. Yoshimura, S. Tatsuura, and W. Sotoyama, *Thin Solid Films*, Vol.207, 1992, p.9.
86. T. Yoshimura, S. Tatsuura, W. Sotoyama, A. Matsuura, and T. Hayano, *Appl. Phys. Lett*., Vol.60, (No.3), 1992, p.268.
87. S. Tatsuura, W. Sotoyama, K. Motoyoshi, A. Matsuura, T. Hayano, and T. Yoshimura, *Applied Physics Letters*, Vol.62, (No.18), 1993, p.2182.
88. M.S. Weaver and D.D.C. Bradley, *Synth. Met*., Vol.83, 1996, p.61.
89. T. Yoshimura, *Physics Rev. B*, Vol.40, 1989, p.534.
90. J. McElvain, S. Tasuura, F. Wudl, and A.J. Heeger, *Synth. Met*., Vol.95, 1998, p.101.
91. H. Yasuda and T. Hsu, *J. Polym. Sci: Polym. Chem*. Vol.15, 1977, p.2411.
92. N. Morosoff, Plasma Deposition, Treatment and Etching of Polymers, Academic Press Inc., 1990, p.1.
93. R.D. Agostino, F. Cramarossa, and F. Illuzzi, *J. Appl. Phys*., Vol.61, 1987, p.2754.
94. R.D. Agostino, F. Cramarossa, F. Fracassi, and F. Illuzzi, Plasma Deposition, Treatment and Etching of Polymers, Academic Press Inc., 1990, p.95.
95. R.D. Agostino, *Proceedings of Mater. Res. Soc. Symp*., Vol.476, 1997, p.185.
96. D.G. Castner, K.B. Lewis, D.A. Fisher, B.D. Ratner, and J.L. Gland, *Langmuir*, Vol.9, 1993, p.537.
97. A. Kiaei, A.S. Hoffman, B.D. Ratner, and T.A. Horbett, *Journal of Appl. Polym. Sci. Polym. Symp*., Vol.42, 1988, p.269.

98. J.A. Theil, F. Mertz, M. Yairi, K. Seaward, G. Ray, and G. Kooi, *Proceedings of Mater. Res. Soc. Symp*., Vol. 476, 1997, p.31.
99. K. Endo and T. Tatsumi, *J. Appl. Phys*., Vol.78, (No.2), 1995, p.1370.
100. K. Endo, T. Tatsumi, Y. Matsubara, and T. Horiuchi, *Proceedings Mater. Res. Soc. Symp*., Vol.443, 1997, p.165.
101. J.F. Gaynor and S.B. Desu, *Journal of Mat. Res*., Vol.9, (No.12), 1994, p.3125.
102. J.F. Gaynor and S.B. Desu, *J. Mat. Res*., Vol.11, (No.1), 1996, p.236.
103. J.F. Gaynor, J.J. Senkevich, and S.B. Desu, *Journal of Mat. Res*., Vol.11, (No.7), 1996, p.1842.
104. K.J. Taylor, M. Eissa, J.F. Gaynor, S.P. Jeng, and H. Nguyen, *Proceedings of Mat. Res. Symp*., Vol. 476, 1997, p.197.
105. M. Benaissa, K.E. Gonsalves, and S.P. Rangarajan, *Appl. Phys. Lett*., Vol.71, (No.25), 1997, p.3685.
106. E. Holtz, U.S. Patent # 5.158,933.
107. J.J. Senkevich and S. B. Desu, *Chem. Mater*., Vol.11, (No.7), 1999, p.1814.
108. J.J. Senkevich and S.B. Desu, *J. Vac. Sci. Tech. B*, Vol.18, (No.1), 2000, p.321.
109. S.B. Desu, *J. Am. Cer. Soc*., Vol.72, (No.9), 1989, p.1615.
110. J.J. Senkevich and S.B. Desu, *Adv. Mater. CVD*, Vol.10, (No.4), 1998, p.92.
111. T. Homma, *Mater. Sci. Engin*., Vol.R23, (No.6), 1998, p.243.
112. S.P. Murarka, *Mater. Sci. Engin*., Vol.R19, 1997, pp.3-4.
113. H. Treichel, B. Withers, G. Ruhl, P. Ansmann, R. Wurl, Ch. Muller, M. Dietlmeier, and G. Maier, Handbook of Low and High Dielectric Constant Materials and their Applications, Vol.1, 1999, p.1.
114. C.H. Ting and T.E. Seidel, *Proceedings of Mater. Res. Soc. Symp*., Vol.381, 1995, p.3.
115. D.S. Soane and Z. Martynenko, Polymers in Microelectronics, Fundamentals and Applications, 1989, p.213.
116. R.D. Agostino, F. Cramarossa, F. Fracassi, and F. Illuzzi, Plasma Deposition, Treatment and Etching of Polymers, Academic Press Inc., 1990, p.425.
117. V. Bulovic and S.R. Forrest, *Electroluminiscence II*, Academic Press, San Diego, CA, 2000.
118. A.J. Heeger, *Solid State Comm*., Vol.107, (No.11), 1998, p.673.
119. F. Cacialli, *Photonic Polym. Sys*., Marcel Dekker Inc., New York, 1998, p.103.
120. G. Wang, C. Yuan, Z. Lu, and Y. Wei, *Photonic Polym. Sys*., Marcel Dekker Inc., NY, 1998, p.217.
121. F. Hide, B.J. Schwartz, M.A. Diaz-Garcia, A.J. Heeger, *Synth. Met*., Vol.91, 1997, p.35.
122. G. Kranzelbinder and G. Leising, *Rep. Prog. Phys*., Vol.63, 2000, p.729.
123. P. Battacharya, Semiconductor Optoelectronic Devices, Prentice-Hall Inc., New Jersey, 1994.
124. G.F. Lindsay, Second Order Nonlinear Optics, ACS Symp. Series, 601, Washington DC, 1995.
125. G.R. Meredith, J.G. Van Dusen, and D.J. Williams, *Macromolecules*, Vol.15, 1982, p.1385.
126. M.H. Davey, V.Y. Lee, L.M. Wu, C.R. Moylan, W. Volksen, A. Knoesen, R.D. Miller, and T.J. Marks, *Chem. Mater*., Vol.12, 2000, p.1679.
127. S. Ishibashi and H. Takahara, *SPIE Conf*., Vol.3799, 1999, p.254.
128. S. Tatsuura, W. Sotoyama, and T. Yoshimura, *Appl. Phys. Lett*., Vol.60, (No.14), 1992, p.1661.
129. P.N. Prasad and D.J. Williams, Introduction to Nonlinear Optical Effects in Molecules and Polymers, John Wiley & Sons, Inc., New York, 1991.
130. A. Samoc, M. Samoc, M Woodruff, and B. Luther-Davies, *Photonic Polym. Sys*., Marcel Dekker Inc., New York, 1998, p.373.
131. B.D. Ratner, A. Chilkoti, and G.P. Lopez, Plasma Deposition, Treatment and Etching of Polymers, Academic Press Inc., 1990, p.463.
132. D. Klee, H. Thelen, H. Bienert, D. Vorwerk, and H. Hocker, *J. Mater. Sci: Mater. Med*., Vol.10, 1999, p.443.

Chemical Vapor Deposition
Jong-Hee Park, T.S. Sudarshan, editors, p287-330
DOI:10.1361/chvd2001p287

Chapter 9

CVD of Metals: The Case of Nickel

Constantin Vahlas and Laurent Brissonneau
Centre Interuniversitaire de Recherche et d'Ingénierie des Matériaux
Ecole Nationale Supérieure de Chimie de Toulouse
118 Route de Narbonne, 31077 Toulouse cedex 4
France

Introduction

Processing of metallic thin films by chemical vapor deposition has been rapidly developed during the past few years, mainly due to numerous potential applications in the microelectronics industry. Research groups worldwide publish in this or allied fields. Contributions come from diverse scientific domains, such as coordination and theoretical chemistry, chemical engineering, and of course materials science. Such an interest from the scientific community reveals that CVD is an attractive route for the deposition of metallic films. However, there are numerous and complex problems to solve before optimizing it.

Most metals have actually been deposited in thin films by CVD. Even today, many precursors that are proposed in the literature for this process as well as corresponding processing conditions are tested trial and error. The lack of advanced fundamental studies often leads to an incomplete understanding or validation of the proposed solutions. Within this frame, the best known processes are those referring to the most popular metals in the microelectronics industry: aluminum, copper, and tungsten. For a review of the CVD of these metals, the reader is invited to consult references.[1,2]

This chapter focuses on the chemical vapor deposition of nickel. The raison d'être for the selection of this metal comes from the numerous applications in which nickel films are implied

today. Still in the microelectronics domain, it is used as interconnections in integrated circuits or as ohmic contact, especially in applications requiring improved corrosion resistance relatively to that of copper and aluminum. In this aim it can be even preferred to gold for economical reasons. Concerning integrated circuit repair, laser CVD (LCVD) of nickel from nickel tetracarbonyl $Ni(CO)_4$ is proposed as a reliable process for IC rewiring.[3] Ni has also been recently proposed for ohmic contacts to n-type doped SiC, a promising material for high power and high temperature device applications.[4,5] Indeed, as severe thermal or electrical cyclic stresses will be applied on these devices, the ohmic contact with SiC must be stable enough so that the properties of the component are kept constant during its life. Nickel is a material of choice for this application as the Ni_2Si phase formed after Ni deposition is in thermodynamic equilibrium with SiC. For this application, the deposition of approximately 200 nm nickel layer by electron beam evaporation techniques is actually preferred. The stability of nickel gallides and aluminides also make nickel an attractive material for ohmic contact with the III-V semiconductors.[6]

Nickel plating is also extensively used for decorative and corrosion resistance applications. In most cases, it is electrolytically deposited. However, some applications can require high purity films or good conformal coverage that can be better performed by the CVD process.

Nickel is also present in numerous alloys in the form of thin films, such as Au-Ge-Ni or NiP_2, that have been used in microelectronics for specific applications.[7] Nickel silicides have been used as contacts on silicon,[8] and have been investigated as diffusion barriers.[9]

The fabrication of microelectromechanical systems (MEMS), e.g. actuators and sensors, is also one of the promising applications for nickel films. Nickel is currently electroplated into pre-form molds. One typical process is the LIGA process*, where pure or alloyed nickel films are deposited on isolating plastic surfaces (mainly PMMA) structured by x-rays lithography.[10] In this field, the CVD process mainly concerns polysilicon, but it is obvious that the advantages of CVD (high purity, good conformal coverage) could be extended to nickel if convenient precursors are proposed. Still in concern with the LIGA process, metallic structures from a plastic predecessor (mould tool obtained from the LIGA process) can be processed by electroplating if a conducting layer is deposited on the insulating plastic structure. This layer can be obtained by the metal-organic CVD (MOCVD) technique, in view of the low deposition temperature imposed by the plastic substrate.[10]

Processing of nickel molds for mandrels, and coating of plastic molds[11] have also been proposed by MOCVD from $Ni(CO)_4$. The metallization of composites or plastic isolating structure by nickel is of interest in aeronautical applications as protection against strong electrical discharges such as caused by lightning.[12] In the nuclear industry, nickel layers are used for the protection of uranium blocks in nuclear reactors.[13] They have been also proposed for the encapsulation of contaminated graphite wastes from gas-cooled nuclear reactors, in order to reduce the emission of radionucleides.[14]

Nickel is also interesting because of its magnetic properties or those of its compounds: Pure or iron alloyed (e.g. Permalloy) nickel films have been grown by CVD for the fabrication of magnetoresistive sensors.[15] Films of Co_xNi_y of various magnetic properties,[16] and ferromagnetic nickel and nickel boride thin films,[17] have been obtained by LCVD. Ferrites containing nickel have also been obtained from various CVD processes.[18-19] Thin films processing of these materials is of great interest for integration in high frequency microwave devices. Nickel oxide thin films can be used in numerous applications due to their optical properties.[20,21]

Nickel is also interesting for its catalytic properties. In particular, the hydrogenation of alcenes and the reaction of water gas (reaction

* *LIGA (LIthograghic, Galvanoformung und Abformung). LIGA is alternative to silicon-based micro-fabrication process, consisting of three main steps: deep x-ray lithography, electroforming, and plastic molding.*

between C and H_2O to provide CO and H_2) are catalyzed by supported nickel. Within this frame, CVD is an interesting alternative to the impregnation and co-precipitation methods.[22] CVD prepared nickel membrane catalysts have been proved to be more useful then those prepared by the classical adsoption-oxidation method.[23] Palladium and nickel containing porous membranes have been fabricated by CVD for catalysis applications or for the detection and purification of hydrogen.[24] Also, bimetallic alloys such as Ni-Pt present interesting catalytic properties.[25]

Deposition of a nickel layer by fluidized bed CVD can improve sintering in powder metallurgy applications. The process can be used as a "premixing" step of the composite, for example on W particles.[26] A similar technique can also be used to improve the wettabilty of ceramics like SiC by the molten Al during the fabrication of metal matrix composites.[27]

Finally, it can be added that very thin nickel films are used as seed layers for the growth of fullerenes[28] and of silicon carbide SiC whiskers,[29] and that C/Ni multilayers are used as x-ray mirrors.[30,31]

In view of the above applications and of the fact that extensive literature is actually available on the CVD of aluminum, copper, and tungsten, processing of nickel films has been chosen in this chapter as an introduction to the actual challenges in the CVD of metals. This field is large, especially if it is considered to include deposition on substrates such as preforms, membranes or, particles. Because of space limitations no attempt has been made to provide a comprehensive overview. Although the choice of materials to be discussed was of necessity subjective, it is expected that the present approach will be useful for the investigation of different cases of metal CVD.

In many of the previously mentioned applications, the substrate or one of its elements on which deposition occurs, is temperature sensitive. This is typically the case for organic or polymeric materials. It may also be interesting to limit diffusion effects from and to the substrate. Consequently, low deposition temperatures are often necessary for the deposition of thin films. MOCVD can meet this condition. Nickel tetracarbonyl $Ni(CO)_4$ is the first compound that was used for the MOCVD of nickel.[32] Ni films from $Ni(CO)_4$ are indeed obtained at low temperature and are weakly contaminated by heteroatoms. Numerous processes integrating Ni thin films are actually using $Ni(CO)_4$. However, due to the high toxicity of this precursor and of its by-product carbon monoxide CO (their threshold limits for human exposure are 10^{-3} ppm and 10^{-2} ppm respectively,[33] non toxic substitution precursors are being investigated. A bibliographic synthesis concerning the different precursors that have been used for the CVD of nickel, the corresponding processing conditions and the properties of the obtained films will be presented in the first part of this chapter.

Among the different complexes that have been used as starting materials for the CVD of nickel, nickel-biscyclopentadienyl ($Ni(C_5H_5)_2$ nickelocene or $NiCp_2$) a priori satisfies most of the criteria that characterize an ideal precursor in MOCVD as have been listed.[34] Indeed, it is volatile,[9,35,36] rather inexpensive, and easy to purify. It is thermodynamically[9,37] and kinetically[38] stable in inert atmosphere up to 300°C. Its decomposition temperature is given at the melting point, 173°C. In hydrogen atmosphere it can easily yield nickel,[37] and the two cyclopentadienyl ligands can be hydrogenated into cyclopentadiene C_5H_6, cyclopentene C_5H_8, or cyclopentane C_5H_{10}. Among them, the last two are quite stable in commonly adopted operating conditions.

Different studies have been conducted in order to verify the ability of nickelocene to yield nickel films with satisfactory properties.[9,39-42] The main conclusion that has been drawn from these efforts is that, as is generally the case for many precursors using cyclopentadienyl ligands, nickelocene leads to carbon incorporation in the deposits. For this reason mainly, nickelocene has not been extensively used for deposition of nickel thin films by MOCVD. However, a literature review reveals that the question of carbon incorporation in nickel films processed from nickelocene has not

been extensively investigated. Only two reports deal with this point. In the most cited reference,[40] nickelocene has been used with no addition of hydrogen in the gas phase. These conditions necessarily lead to carbon incorporation, as the ligand C_5H_5 alone is not a stable radical. In the second report,[42] carbon incorporation has been studied as a function of deposition temperature. Nevertheless, no other parameters have been studied for their influence on the carbon content of the deposits. Based on these partial results and without an extended investigation of the conditions that may prevent the incorporation of carbon in the deposits, it has been concluded that the use of nickelocene leads to considerable contamination of nickel films. Because it has been admitted that this process is not compatible with the fabrication of pure nickel films, it has not been extensively investigated in terms of other important parameters such as growth rate or morphology. Moreover, the mechanisms that control the carbon incorporation and more generally the decomposition of the precursor and the formation of the deposit have not been clearly identified. For this reason, no concise proposal has been formulated to optimize the deposition conditions and to reduce the carbon content of the films. This situation confirms what has been previously mentioned on the drawbacks that are originated from the relative lack of fundamental studies of the CVD of metals. For this reason the second and main part of this chapter, is dedicated to a detailed investigation of the growth rate, the morphology and the carbon content of thin films of nickel processed from nickelocene, and of the composition of the gas phase during this process. Based on these results, a mechanism will be proposed that holds for the decomposition of nickelocene, for the subsequent growth of nickel films, and for the possible incorporation of carbon therein. This part is based on a series of articles recently published by the authors.[43-49] Detailed information on different parts of the following sections (e.g. experimental details) can be found therein.

The aim of the present approach is not to optimize the processing conditions for a given application *per se,* but rather to contribute to a better understanding of this process, thus providing the elements for the selection of optimum operating conditions as a function of the desired application. Furthermore, deposition from nickelocene is considered here as a model system. Indeed, as previously discussed, questions on the deposition mechanisms are still open, despite the apparent simplicity of this system. Their elucidation should help to understand and thus to optimize similar processes for the deposition of metallic thin films in general, and particularly when using metallocenes or precursors containing cyclopentadienyl ligands.

Precursors for the CVD of Ni

A list of precursors for the CVD of Ni until 1993 has been compiled by Zinn et al.[50] Numerous compounds have been proposed since then. In the following paragraphs, these precursors are first presented. Then, deposition conditions are detailed for those from which Ni films with satisfactory properties have been obtained.

Families of Precursors

In Table 1 are listed the different precursors together with their acronyms that have been used for the CVD of nickel. Mainly two types of ligands and their derivatives are currently used in organometallic chemistry to achieve high volatility, and have been used for the synthesis of these compounds: the cyclopentadienyl C_5H_5, and the b-diketone $CH_3COCH_2COCH_3$. In most of these compounds, nickel is found in the oxidation state (+ II).

In the first family, $NiCp_2$, a green solid, has been often used for the deposition of nickel films[9,38-42] (and the present report), and also for the deposition of NiO[20] or for the doping with nickel of other films.[62] Its methyl derivative, $Ni(MeCp)_2$ also seems promising.[51] $Ni(\eta_5\text{-}C_5Me_2)(\eta_3\text{-}C_3H_5)$ has been proposed by Zych et al.[17] It is highly volatile but less stable than $NiCP_2$ and seems to be sensitive to air.

Table 1. List of Different Precursors that have Been Proposed for the CVD of Ni

Name	Formula	Abbreviation	Reference
Cyclopentadienyl Family			
Nickel Biscylopentadienyl	$Ni(\eta_5\text{-}C_5H_5)_2$	$NiCp_2$ Nickelocene	9, 38-42, 44-46
Nickel Bis (1-1' Dimethyl Cyclopentadienyl	$Ni(\eta_5\text{-}CH_3C_5H_4)_2$	$Ni(MeCp)_2$	51
Nickel Allyl Pentamethylcyclopentadienyl	$Ni(\eta_5\text{-}C_5(CH_3)_5)(\eta_3\text{-}C_3H_5)$	Cp*Ni (Allyl)	17
β-Diketone Family			
Nickel Bis (2,4 Pentanedione) Acetylacetonate	$Ni(CH_3COCHCOCH_3)_2$	$Ni(acac)_2$	52
Nickel-Bishexafluoropentanedione or Nickel Bis (Hexafluoroacetylacetonato)	$Ni(CF_3COCHCOCF_3)_2$	$Ni(hfa)_2$	53
Nickel-Bis (Hexafluoropentanedionate) N, N, N', N'', N'' - Pentamethydiethyl-Enetriamine	$Ni(CF_3COCHCOCF_3)_2$ $(CH_3)_2NC_2H_4NCH_3C_2H_4N(CH_3)_2$	$Ni(hfa)_2$ PMDETA	21
Nickel-Bis (Hexafluoropentanedionate) N, N, N', N', Tetramethylethylenediamine	$Ni(CF_3COCHCOCF_3)_2$ $(CH_3)_2NC_2H_4N(CH_3)_2$	$Ni(hfa)_2$ TMEDA	21
Nickel Bis (Hexafluoroacetylacetonato) Bis (Pyridine)	$Ni(CF_3COCHCOCF_3)_2$ $(C_5H_5N)_2$	$Ni(hfa)_2$-2pyr	54
Nickel Bis (:2,2,6,6-Tetramethyl-3,5-Heptandionato)*	$Ni(C(CH_3)_3COCHCOC(CH_3)_3)$	$Ni(thd)_2$	54,55
Nickel Bis-(Hexafluoropentanedionate) Ethylenediamine*	$Ni(NH_2C_2H_4NH_2)$ $(CF_3COCH_2COCF_3)_2$	$Ni(en)(hfa)_2$	56
Other Compounds			
Nickel Dimethylglyoximato or Nickel Bis (2,3 Butanedionedioximato)	$Ni(NO(CCH_3)_2NOH)_2$	$Ni(dmg)_2$	55
Nickel Bis (3,4-Hexanedionedioximato)	$Ni(NO(CC_2H_5)_2NOH)_2$	$Ni(deg)_2$	7
Nickel Bis (N (3-Hydroxyimino-2-Methylbutyl-2)-Hydroxylamine	$Ni(NOC_2H_4CH_3CNOHCH_3)_2$	$Ni(HL^*)_2$	57
Nickel Bis (2-Imino-Pen-En-4-Trifluoroacetylacetonato)	$Ni(CH_3COCHCNHCF_3)_2$	$Ni(ktfaa)_2$	54
Nickel Bis(2-Imino-Pen-En-4-Onato)*	$Ni(CH_3COCHCNHCH_3)_2$	$Ni(kaa)_2$	54
Nickel Bis(2-Imino-Pent-2-En-Onato)	$Ni(CH_3CNHCHCOCH_3)_2$	$Ni(apo)_2$	13, 58
Nickel N, N' Bis Ethylenebis (2,4-Pentandion-Iminoato)*	$Ni(CH_3COCHCNCH_2\text{-}CH_3)_2$	Ni(enacac)	58
Nickel Tri-Ethanediamine Bis (2-Trifluoro Propane_One)	$Ni(NH_2C_2H_4NH_2)_3$ $(CF_3CO_2)_2$	$Ni(en)_3(CF_3CO_2)_2$	56

Contd...

Table 1. Continued

Nickel Bis-Trifluororacetate Bis (N, N' Dimethylethylenediamine)	$Ni(CH_3NHC_2H_4NHCH_3)_2$ $(CF_3COO)_2$	$Ni(dmen)_2(CF_3CO_2)_2$	59
Nickel Dichloride	$NiCl_2$		23, 27, 60, 61

Acronyms	
Cp	Cyclopentadienyl or η_5-C_5H_5
acac	acetylacetonate or 2,4 pentanedione or $CH_3COCH_2COCH_3$
hfa	hexafluoroacetylacetonate or; 1, 1, 5, 5, 5 hexafluoro 2, 4 pentanedione (oudionato) $CF_3COCH_2COCF_3$
dmg	diméthylglyoxime or 2, 3 butanedionedioximato
deg	3,4 hexanedionedioximato
en	ethanediamine ou ethylenediamine
enacac	ethylene bis (2,4-pentandion-iminoato)
dmen	dimethylethylenediamine
thd	2, 2, 6, 6-tetramethyl-3, 5-heptandionato
apo	2-amino-pent-2-en-onato or acetylactoiminato
HL*	(3-hydroxyimino-2-methylbutyl-2)-hydroxylamine
PMEDTA	pentamethylethylenetriamine, $(CH_3)_2NC_2H_4NCH_3C_2H_4N(CH_3)_2$
TMEDA	tetramethylethylenediamine, $(CH_3)_2NC_2H_4N(CH_3)_2$
ktfaa	2-imino-pen-en-4trifluoroacetylacetonato
kaa	2-imino-pen-en-onato

The base compound in the second family is $Ni(acac)_2$. It has been used for the deposition of thin films of nickel,[52] or Ni-Pd alloys for the processing of membranes on porous substrates.[24] Its fluorinated derivative, $Ni(hfa)_2 \bullet 2H_2O$ was the first alternative nickel precursor to $Ni(CO)_4$,[53] but it has not been further investigated. The reason for this is the difficult control of its volatility which varies due to the number of attached water ligands. The hfa ligand results in highly volatile compounds. For this reason it is present, together with other ligands, in numerous precursors: $Ni(hfa)_2$-2pyr[54] (this compound presents however the drawback of a reduced stability), or $Ni(hfa)_2$-PMDETA and $Ni(hfa)_2$-TMEDA which have been used for the deposition of NiO.[21] Other precursors that belong or are near to this group have not yielded metallic nickel films. These are $Ni(thd)_2$[54,55] and $Ni(en)(hfa)_2$.[56] $Ni(hfa)_2$DME, $Ni(hfa)_2$diglyme, and $Ni(hfa)_2$diglyme. H_2O decompose during evaporation.[21] Saito et al.[63] also proposed different volatile compounds containing the hfa ligand and its ethylenediamine substitutes.

More recently, other precursors have also been synthesized for the deposition of nickel films. They usually contain Ni-N bonds in order to avoid the incorporation of oxygen or carbon atoms in the films. It has thus been reported that high quality nickel films can be obtained from $Ni(deg)_2$[7] and from $Ni(dmg)_2$.[55] Decomposition and volatility of other similar compounds have also been investigated, but not their compatibility with CVD.[7] Ni(ktfaa)[54] and $Ni(HL^*)_2$[57] yield satisfactory growth rates. Good quality nickel films starting from $Ni(apo)_2$ have been obtained by Leonov et al.[13] $Ni(dmen)_2(CF_3CO_2)_2$ [59] and the ionic compound $Ni(en)_3(CF_3CO_2)_2$[56] lead to the (co-)deposition of the metastable nickel carbide Ni_3C. Finally, $Ni(dmen)_2(hfa)_2$,[64] $Ni(kaa)_2$,[54] and Ni(enacac)[55] have been proposed for the CVD of nickel films without satisfactory results, but their usefulness as nickel precursors has not been exhaustively investigated.

$NiCp_2$, $Ni(hfa)_2 \bullet 2H_2O$, $Ni(dmg)_2$, and $Ni(acac)_2$ are commercially available products having low cost and easily controllable purity. The other precursors reported in Table 1 can be synthesized following relatively simple, but careful operation procedures. Among these products, cyclopentadienyl derivatives can be easily purified by sublimation. However, being slightly sensitive to the air, they must be handled in inert atmosphere, and they present a reduced although not negligible toxicity.

Deposition Conditions

All but $Ni(CO)_4$ among the previously mentioned compounds are solid in standard conditions. $Ni(MeCp)_2$ and $Ni(hfa)_2$-PMDETA have low melting points, respectively 37°C and 34°C. Cyclopentadienyl compounds possess convenient volatility for CVD, permitting molar fractions in the input gas between 10^{-4} and 10^{-2} for sublimation temperatures lower that 150°C and even 100°C. This is less valid for the other compounds. Volatilization temperatures vary between 100°C for $Ni(hfa)_2$, $Ni(hfa)_2$-PMDETA and $Ni(hfa)_2$-TMEDA, and 220°C for $Ni(acac)_2$ and $Ni(dmg)_2$. Thermodynamic data on the vapor pressures of the most common compounds ($NiCP_2$, $Ni(dmg)_2$,...) are available[55] (and present report). These, as well as data on weight loss permitted relations such as Ln(P) = A-B/T between vapor pressure and temperature for many of these compounds. Most of them are generally decomposed at temperatures that are 20° higher than the ones required for their volatilization, thus allowing for their convenient transport to the deposition area.

Although many reports are available on deposition performed at atmospheric pressure, low pressure operation is convenient in order to obtain satisfactory molar fractions of the precursor (of the order of 10^{-3}) at relatively low (if possible less than 100°C) volatilization temperature, and also to achieve improved conformal coverage of the substrates. Only few investigations have been performed with varying deposition pressure.[41] It is worth noting that $Ni(HL^*)$ and $NiCp_2$ have been decomposed in molecular beam epitaxy (MBE) conditions, but with a high carbon contamination for the latter.[40]

In the absence of additional hydrogen in the input gas, deposition temperatures are generally elevated. For example, deposition occurs at 550°C for $NiCp_2$[40] and at 540°C for

$Ni(dmg)_2$.[55] For all these precursors, the use of hydrogen allows a decrease of 150°C to 250°C for the deposition temperature which becomes relatively low, but still higher than that for deposition from $Ni(CO)_4$. In view of the generally high reactivity of the precursors with hydrogen, the latter is injected in the input gas just before the deposition zone. The transport of the precursor takes place with an inert gas, whose flow rate is typically of the same order of magnitude as that of hydrogen. The most commonly adopted deposition conditions for different precursors are reviewed in Table 2.

Deposits Characteristics

Growth rates for films processed from $Ni(CO)_4$ (15-800 $\mu m.h^{-1}$) are by far the highest among the different nickel precursors. Results for growth rates are also reported in Table 2. Those followed by a star correspond to thermally activated processes. Results reported by Borisov et al.[57] (3-20 $\mu m.h^{-1}$) are remarkable, particularly in view of the adopted deposition technique (metal organic chemical beam epitaxy, MOCBE). Growth rates are generally lower than 0.2 $\mu m.h^{-1}$. $Ni(deg)_2$ (3 $\mu m.h^{-1}$) and $NiCp_2$ (>1 $\mu m.h^{-1}$) are the precursors allowing higher growth rates, but at elevated deposition temperatures for the former.

Most of the characteristics of the films reported in the literature have been obtained using x-ray diffraction (XRD). In the absence of analytical techniques such as x-ray photoelectron spectroscope (XPS), Auger electron spectroscope (AES), or electron probe microanalysts (EPMA), it is difficult to compare the performance of different precursors in this domain. Generally speaking, the use of hydrogen produces weakly contaminated films.[65] High purity films have been obtained from $Ni(MeCp)_2$,[6] from $Ni(deg)_2$[7] and from $Ni(dmg)_2$[58] although oxygen may be present in the latter.

Concluding Remarks

The choice of a precursor is conditioned by the application of the nickel film. If the operating environment requires the lowest possible temperature, $Ni(CO)_4$ remains the best choice, because deposition temperature for all other precursors exceeds 150°C. $NiCp_2$ (as it will be demonstrated in the following paragraphs) and $Ni(hfa)_2$ are good candidates for deposition around 200°C, because these commercially available complexes have satisfactory volatility and produce relatively pure deposits. However, films processed from $NiCp_2$ present a residual carbon contamination which, even at very low levels, may be prohibitive for some applications. If high purity is mandatory, $Ni(MeCp)_2$, $Ni(dmg)_2$, and $Ni(den)_2$ are the more interesting precursors. However, each one presents important drawbacks: low growth rates for $Ni(MeCp)_2$, reduced volatility for $Ni(dmg)_2$, and decomposition at relatively high temperatures for $Ni(den)_2$ with, nevertheless, high growth rates.

Processing of Ni Films from Nickelocene

Experimental

Most metal CVD in industry is carried out in single-wafer, cold wall systems. The results reported here concern deposition in 2.1 cm diameter horizontal reactor, where substrates were placed on an inductively heated graphite susceptor positioned immediately after a quartz ramp. The precursor containing carrier gas was mixed with excess hydrogen just before the deposition area. He was also occasionally used as a dilution gas. In all runs total flow rate Q and He flow rate through the sublimator $Q_{He,Ni}$ were kept constant at 80 sccm and 30 sccm respectively. Several depositions were performed around a main set of operating conditions with code name A3 that was defined by T = 175°C, P = 1 atm, hydrogen flow rate Q_{H_2} = 50 secm, and $X_{NiCp_2} = 1.8 \times 10^{-3}$, obtained by thermoregulating $NiCp_2$ at 102°C. The most important of these conditions and their evolution relative to conditions A3 are schematically presented in Figure 1.

Polished and depolished, inert (turbostratic carbon, glass and silica) and metallic ((200) oriented copper polycrystals, and Ni-25 at.%

Table 2. Deposition Conditions that Have Been Used for Different Nickel Precursors

Precursor	Degradation Temperature (°C)	Volatilization Temperature (°C)	Deposition Temperature (°C)	Pressure (Torr)	Hydrogen	Growth Rate ($\mu m.h^{-1}$)	Reference
$NiCp_2$	150-170	27	550	5.10^{-4}	No	0.05-0.1	40
		100-120	190-230	50-550	Yes	0.2-0.8	41
		<130	180-350	760	Yes	0.8-2	39
		120	200-350	760	Yes		42
Ni $(MeCp)_2$	38	35	280	760	Yes	0.05	6
$Ni(acac)_2$	238	200-220	250-350	760	Yes	0.1-0.15*	52
		350-400	350-400	1	Yes		24
$Ni(hfa)_2, 2H_2O$		135	200-350	760	Yes		53
$Ni(dmg)_2$	250	240	300-450	15	Yes	0.15*	55
$Ni(deg)_2$	241	200	350-450	23	Yes/No	1.5-3*	7
$Ni(apo)_2$		130	300	760	Yes		13
$Ni(hfa)_2$		80-120	300-800	1.5-760	Yes	0.15	21
PMDETA							
$Ni(en)(hfa)_2$	180	140-160	200-400	0.03-0.15	No		56
Ni(Ktfaa)	460	200	200-400	760	Yes		54
$Ni(hfa)_2$, 2pyr	420	200	200-400	760	Yes		54
$Ni(HL^*)_2$		25	225-300	10^{-4}	No	3-20*	57

* Thermally activated processes

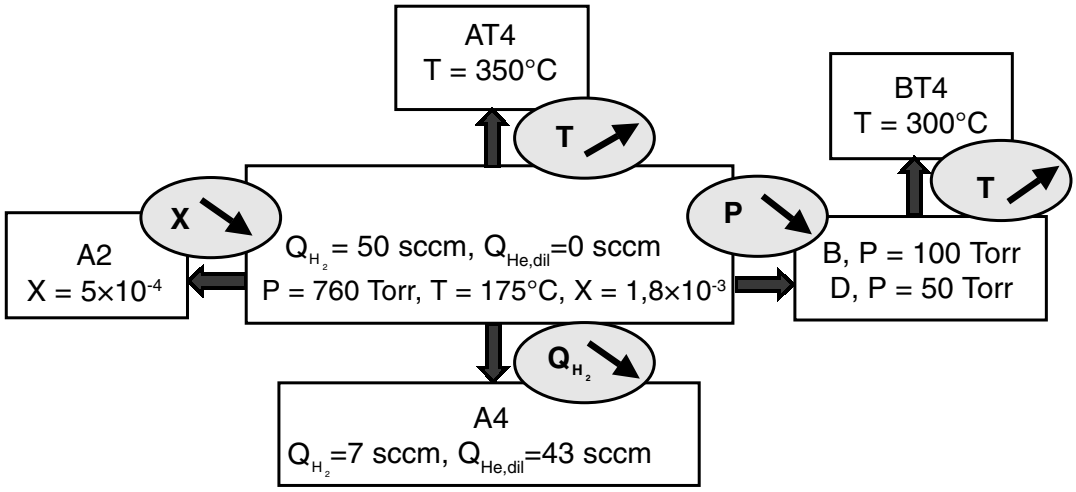

Fig. 1: Schematic representation showing the main set (A3) and other deposition conditions, and their evolution relative to the main set.

Cr, Ni_3Cr alloys) were used as substrates. The investigation of the composition of the gas phase in the vicinity of the growing surface during deposition was performed by on-line mass spectrometry with an electron impact ionization quadripole mass spectrometer (QMS). Sampling of the gas phase was achieved via a 2 mm diameter stainless steel tube. The tube was positioned parallel to the flux with its entry 1 mm above the substrates. It was connected to the QMS through a molecular leak valve.

Growth Rate

The obtained growth rates in different conditions are schematically presented in Figure 2 similarly to Figure 1. Intensity of gray scale is qualitatively proportional to the growth rate. In all experiments, an incubation period was observed before deposition occurred. The duration of the incubation period depended on processing conditions and especially on the nature of the substrate. It was shortest on the copper substrates (about 15 minutes) and longest on inert and polished substrates. In conditions A4 (atmospheric pressure, low hydrogen flow rate Q_{H_2}), it could be as long as 2 hours. The reported periods correspond to the interval between the opening of the mass flow meters and the observation of the change in color of the substrate through the reactor walls. Consequently, they overestimate the incubation period, defined by the time between the arrival of the input gas and the formation of the first nuclei on the surface. Deposition was observed neither for temperatures higher than 350°C nor for pressures lower than 20 Torr. Films were deposited at a pressure lower than 100 Torr only in the presence of copper substrates.

Higher growth rates were obtained on Ni_3Cr substrates. Although incubation period was shorter on copper or on unpolished substrates, because these substrates were generally placed downstream, the observed growth rates were comparable with those on polished substrates placed upstream. This was true when the duration of the experiment was long enough after the formation of the film on the polished substrates.

Growth rate did not depend on temperature between 150 and 225°C, in agreement with reported results.[39,41] Below 150°C, growth rate was low, and films grew only at the end of the susceptor. Above 200°C, deposits preferentially occurred at the beginning of the susceptor. Above 250°C growth rate was lower than

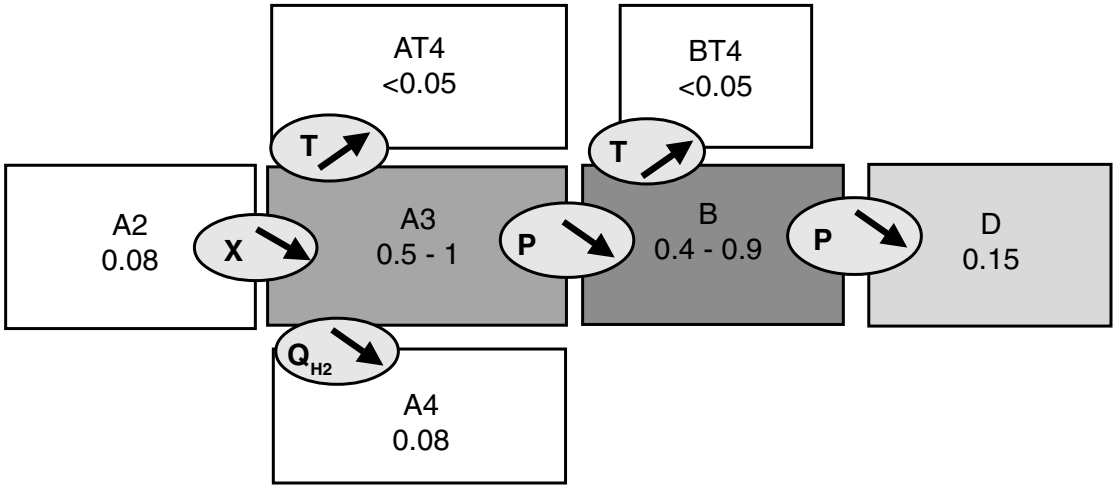

Fig. 2: Schematic representation of the growth rate of the nickel films (μm*h^{-1}) in different processing conditions. Intensity of gray scale is qualitatively proportional to the growth rate.

0.05 μm.h^{-1}. In these conditions deposits preferentially occurred on the colder part of the reactor, e.g. the walls above the susceptor or the quartz ramp. Based on these remarks, it appears that the optimum deposition temperature in the present configuration and in the investigated operating conditions is between 160°C and 180°C. In this temperature range deposition rate was more or less uniform on the susceptor.

The detrimental effect on the growth rate of the increase of the temperature above 250°C can not be attributed to the depletion of the precursor due to gas phase reactions. Indeed, this type of reaction occurs only above 400°C in the adopted experimental conditions, when particles of "soot" are deposited on the substrate. In-situ FTIR studies of the gas phase,[66] showed that gas phase reactions begin at 250°C for a value of X_{NiCp_2} five times higher than the one adopted in the present study, and that these reactions are slow below 350°C. Also, this effect can hardly be attributed to detrimental aerodynamic phenomena, because the Rayleigh number of the reactor in the investigated operating conditions at atmospheric pressure is lower than 50. This value is too low compared to 1708 which is the critical value for the formation of longitudinal roll, i.e. when buoyancy forces become predominant.[67] The detrimental effect of the increase of the temperature on the growth rate is attributed instead to the enhancement of the desorption rate of the precursor from the surface of the substrate. Indeed, when the activation energy for desorption of the precursor is higher than the activation energy for its decomposition, the increase of temperature can result in slower reaction rates, because apparent activation energy for the deposition process becomes negative.[2] In the next paragraph it is shown that this indeed holds for the case of nickelocene.

It is generally admitted that the overall reaction for the deposition of nickel from nickelocene is:[9, 42]

$$Ni(C_5H_5)_2 + n\,H_2 \rightarrow Ni(s) + 2\,C_5H_{5+n}(g) \qquad (1)$$

where n = 0, 1 3 5. n = 0 corresponds to the radical C_5H_5, n = 1 to C_5H_6, n = 3 to C_5H_8, and n = 5 to C_5H_{10}. Assuming that the decomposition of the precursor is achieved by the hydrogenation of a ligand, the activation energy for the decomposition of nickelocene can be estimated by the activation energy for the hydrogenation of a C_5H_5 radical. For the hydrogenation of C_5H_6 to C_5H_8 on the surface of nickel boride NiB, Wang et al.[68] found an activation energy of 7 kJ.mol^{-1}, while for the

hydrogenation of C_5H_6 to C_5H_7 in gas phase combustion, Zhong and Bozzelli[69] calculated an activation energy of 11 kJ.mol^{-1}. In analogy to the deposition of palladium from CpPd(η^3-C_3H_5)[22] and of platinum from $CpPtMe_3$,[70] nickel deposition from $NiCp_2$ is likely to be autocatalytic.[39] Indeed, nickel is expected to dissociate molecular H_2 to atomic hydrogen, making easier the hydrogenation of the ligand. For this reason, the previously proposed values of the activation energy for the hydrogenation of C_5H_6 can be considered as an upper limit for the case of $NiCp_2$. On the other hand, the energy of adsorption of nickelocene on Ag (100) has been estimated by Welipitiya et al.[71] to be of the order of 50 kJ.mol^{-1}. This is certainly a lower limit of the activation energy for the desorption from the surface of the substrates in the present study because more bonds can be formed on a rough surface than on a smooth (100) surface. It is thus concluded that the desorption energy for nickelocene is much higher than its decomposition energy, and that the increase of the temperature should lead more to a faster desorption of the nickelocene rather than to the formation of a nickel film.

Van den Brekel[41] reported a linear relation between X_{NiCp_2} and growth rate, indicating that under the conditions for which X_{NiCp_2} is increased (conditions A2 to A3), the surface is not saturated with nickelocene, and that the limiting step in this process is of first order with respect to the precursor. This step can correspond either to the transport of $NiCp_2$ through the diffusion layer or to a particular surface reaction.

Experiments in conditions A4 show that nickel deposition can be obtained from $NiCp_2$ with a reduced quantity of hydrogen in the gas phase. It has been reported[39] that nickel deposition from nickelocene without additional hydrogen requires high temperature (at least 350°C at atmospheric pressure) and leads to high carbon contamination. Stauf et al.[40] obtained nickel films by evaporating nickelocene at low pressure only above 550°C. These films were also heavily contaminated with carbon. On the other hand, Dormans[9] failed in depositing nickel with H_2 as carrier gas, because of premature decomposition of $NiCp_2$ in the sublimator. In the present experiments, although Q_{H_2} is systematically higher than that of nickelocene (the molar ratio $H_2/NiCp_2$ is 310 and 40 in conditions A3 and A4 respectively), the growth rate is still highly dependent on Q_{H_2}. It thus appears that the surface reaction between $NiCp_2$ and H_2 becomes the limiting reaction for the investigated gas phase concentrations of H_2. If the decomposition reaction takes place with atomic hydrogen on the surface, it must be assumed that there is a competition for the occupation of the adsorption sites between He and H_2, because both kinds of molecules in the gas phase are in excess relative to the available adsorption sites. Considering that growth rate is approximately divided by 5 when H_2 pressure is divided by 7.5, the partial order with respect to H_2 for the growth rate of nickel is about 0.8. Concerning deposition of cobalt from cobaltocene $CoCp_2$, it has been reported[72] that dependence on H_2 partial pressure is stronger, because replacement of half of H_2 by He leads to the inhibition of the deposition. This dependence has been attributed to the decrease of the rates of the reactions with n = 3 or n = 5 in relation (2). The partial order of these reactions with respect to H_2 would be about 3 and 5 respectively.[72] A high partial order with respect to H_2 for the decomposition of $CoCp_2$ comparatively to that of $NiCp_2$ is certainly possible because cobalt is not as good a catalyst as nickel for the dissociative adsorption of hydrogen. However, concerning the decomposition of $NiCp_2$, and in agreement with the mechanism proposed by Kaplin et al.,[42] it is more likely that the dissociation of the metal - ligand bond occurs just after the first hydrogenation of the ligand yielding C_5H_6, and that C_5H_8 and C_5H_{10} are products of sequential hydrogenation of the C_5 cycles.

Comparison of conditions A3, B and D, reveals that despite the change of total pressure, Q_{H_2} remains unchanged. Hence, although the partial pressure of H_2 decreases when pressure is decreased, the number of hydrogen molecules above the surface per unit time should be the same, because H_2 is a light molecule with a high diffusion rate. Lowering the pressure leads to enhancement of the diffusion of heavy rather

than light species in the boundary layer.[67,73] Consequently, the decrease in pressure should lead to an increase in concentration of nickelocene molecules on the surface. This higher number of $NiCp_2$ molecules should lead to a higher deposition rate, unless they compete with H_2 for the occupation of the adsorption sites following a Langmuir-Hinshelwood mechanism. In such a case, decreasing pressure decreases and even prevents the dissociative adsorption of H_2 molecules on the surface. As a result, hydrogen is only available in molecular form, but its reaction with adsorbed nickelocene should not be favored at such a low temperature. At 100 Torr (conditions B) the depletion of adsorbed hydrogen atoms is balanced by the higher density of adsorbed nickelocene molecules. However, as pressure becomes lower than 100 Torr, the surface should be almost covered by $NiCP_2$, and very few H_2 molecules can be dissociatively adsorbed. The area covered by a nickelocene molecule is at least that covered by a cyclopentadienyl ligand, which has been estimated by Avery[74] to be about 0.4 nm^2, considering Van der Waals interactions. In the present conditions, approximately 15 nickelocene molecules react on the surface per second and per nm^2. Thus, as only a maximum of three nickelocene molecules can be adsorbed per nm^2, surface sites will be saturated if a nickelocene molecule remains adsorbed on the surface for at least 0.2 s. The duration of the adsorption for a molecule is generally given as a function of its adsorption energy E_{ads},[75] equation (2).

$$t = 10^{-12} \times \exp\left(\frac{E_{ads}}{R \times T}\right) \qquad (2)$$

At 175°C, $t > 0.2$ s for $E_{ads} > 100$ $kJ.mol^{-1}$. For the value of 50 $kJ.mol^{-1}$ given by Welipitiya et al.,[71] the adsorption time is only 7×10^{-7} s. The extreme sensitivity on E_{ads} does not allow a precise estimation of the adsorption time in the present case. However, the value of 50 $kJ.mol^{-1}$ proposed for E_{ads} is certainly under-estimated, because it concerns an atomically smooth surface. On a surface under growth conditions that are far from the Frank-van der Merwe mode[76] as it will be shown in the next section, kinks and steps are more abundant, and the nickelocene molecule can form two or more bonds with the surface leading to an approximately two or more times higher adsorption energy. The increase of the number of surface-nickelocene bonds yields adsorption duration that is consistent with the presented assumptions.

Morphology

Figure 3 presents an SEM micrograph of a film deposited on carbon in conditions A2. The film was scratched from the substrate with a pliers. Thickness and morphology of the interface and of the surface are shown, the latter being observed from different angles. The high plasticity of the film is also illustrated. The observed nodular morphology corresponds to a Völmer-Weber growth mode.[76] This mode is due to low chemical affinity between substrate and deposit and generally induces low nucleation rates. A typical example is the deposition of a metal on an insulator. It has recently been shown that, in such a case, where the deposition reaction is faster on the deposit rather than on the substrate, formation of islands rather than of a continuous layer is favored in CVD compared to PVD processes, due to the autocatalytic nature of the former.[77]

Nodule size depends on the deposition conditions, on the chemical nature and the morphology of the substrates and on the thickness of the films. General trends of the influence of the deposition parameters on the nodule size can be obtained from the SEM micrographs of Figure 4, illustrating surfaces of films processed in different conditions. The number by the code at the upper left part of each micrograph is the grain size (nm). The number at the lower left side is the thickness of the film (μm). Thickness is comparable (0.6 ± 0.4 μm), except for that of the left micrograph of conditions A3 (2.7 μm). In this way, the differences in nodule size when changing deposition conditions can be mainly attributed to parameters other than thickness. All films in this figure have been deposited on polished,

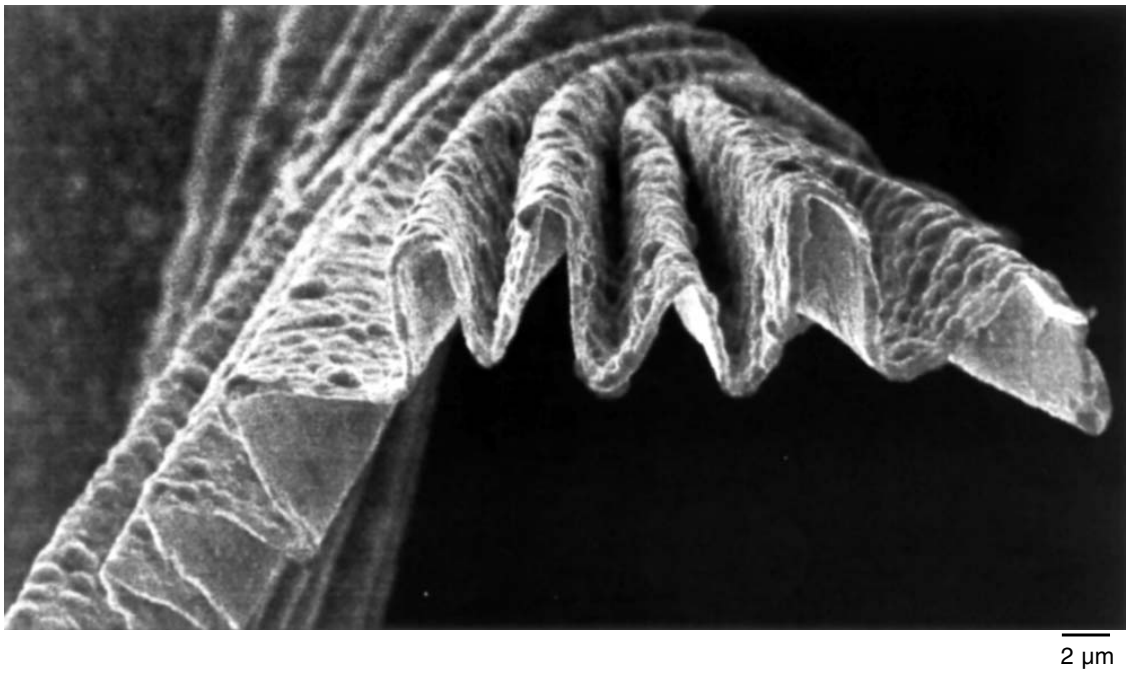

Fig. 3: SEM micrograph of a nickel film deposited on a polished inert (carbon) substrate, in conditions A2. The film has been scratched from the substrate with a pliers.

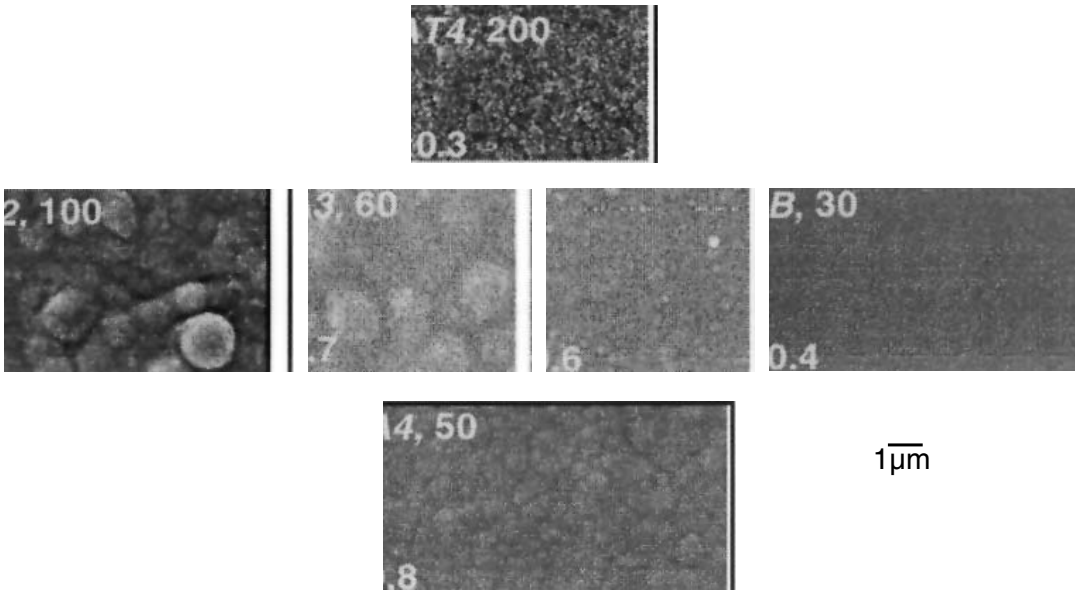

Fig. 4: Surface morphology of films processed in different conditions. Thickness (μm) is given in the lower left side, and grain size (nm) is given by the code at the upper left side of each micrograph.

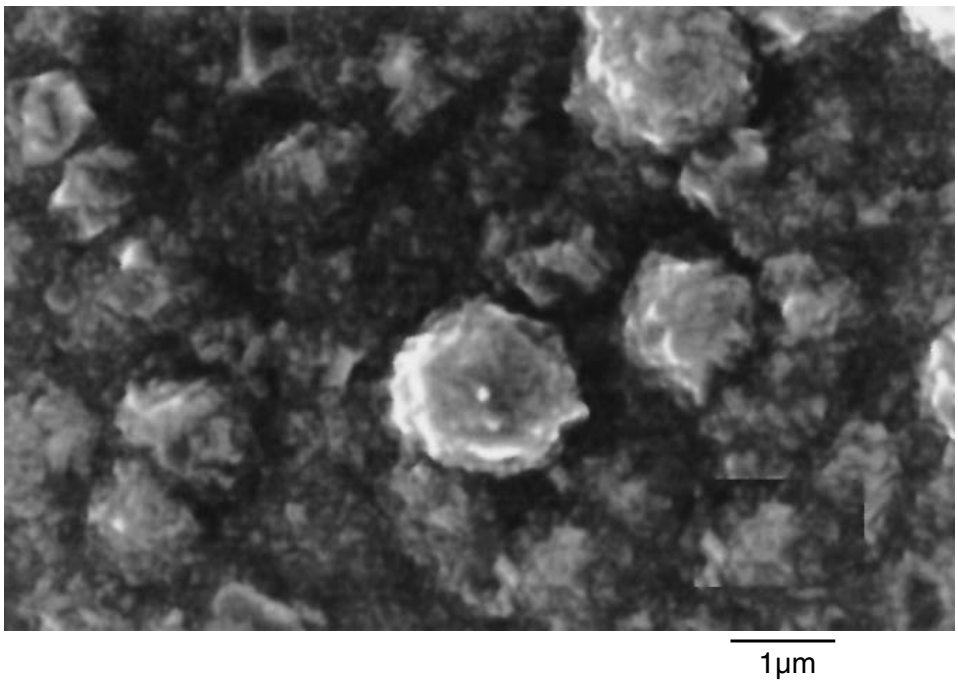

Fig. 5: Surface morphology of a film deposited in conditions A2. It is shown that nodules are composed of smaller grains.

chemically inert substrates. Nodules of films deposited on rough or on chemically active substrates such as Ni_3Cr or copper, are generally smaller than those of films deposited on inert substrates during the same experiment.

For comparison among different morphologies of Figure 4, the right micrograph of conditions A3 will be taken as reference. Nodule size increases with increasing thickness of the films (conditions A3). For thinner films, nodule size is roughly equal to film thickness, while for the thicker films, nodule size is lower than the thickness of the film. Decreasing X_{NiCp_2} leads to increasing nodule size (A2). The same, but in lesser extend happens when Q_{H_2} is decreased (A4). Decreasing pressure and increasing temperature lead to the decrease of nodule size (B and AT4 respectively).

As shown in the SEM micrograph of Figure 5, nodules are composed of small grains, in agreement with the results of Andreev et al.[39] The mean size of the crystallites that compose these grains has been estimated from the full width at mean height (FWMH) of the (111) and (200) peaks of the XRD diagrams obtained in theta-theta and in grazing incidence configuration, by using the Laüe-Scherrer relation. The evolution of grain size follows that of nodules. In Figure 6 are presented two bright field transmission electron microscope (TEM) micrographs of a cross section of a sample processed in conditions A2. It is shown that grains are smaller in the vicinity of the substrate than near the surface of a film. This trend has been confirmed by FWMH measurements because for two films processed in the same conditions, the thicker one exhibits a larger mean size of the nickel crystallites.

The size of the crystallites decreases with decreasing pressure or with increasing X_{NiCp_2}. It increases with increasing temperature. No preferential orientation was found on inert substrates. Annealing at 300°C for 30 min in vacuum, of films deposited on copper substrates, yields a (200) preferential orientation.

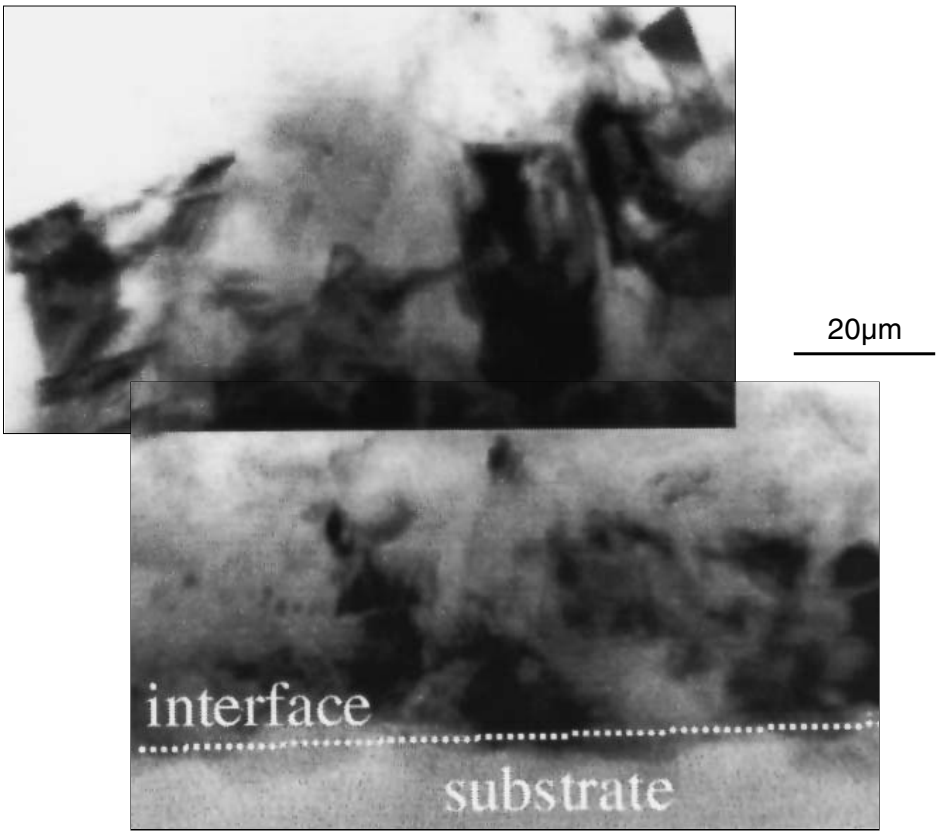

Fig. 6: Bright field TEM cross section micrographs of a film processed in conditions A2. Grains are shown near the substrate (lower part) and the surface (upper part).

Results indicate that deposition is facilitated on active (copper, Ni_3Cr) compared to inert substrates. This is attributed to an easier decomposition of the precursor on copper or Ni_3Cr rather than on glass or carbon surfaces. Hydrogen can be dissociatively adsorbed on Ni_3Cr substrates enhancing the decomposition of $NiCp_2$. On copper substrates, the dissociative adsorption of hydrogen is not easy. In that case, the enhanced nucleation is certainly due to the good wetting of the nickel on the copper surface. The equilibrium wetting angle for a nickel particle on a copper surface has been estimated to be 45°[**]. This is a relatively low value indicating that only a small number of nickel atoms is necessary for the nickel nucleus to be stable on the copper surface.

The observed differences in morphology of the films can be explained by differences of supersaturation of the precursor above the

[**] The wetting angle θ is calculated from the Young Dupré relation: $\sigma_{Cu} = \sigma_{Ni/Cu} + \sigma_{Ni}*\cos\theta$. Mean surface energies σ_{Cu} and σ_{Ni} are 1.78 $J*m^{-2}$ and 2.28 $J* m^{-2}$ for copper at 925°C and for nickel at 1060°C respectively.[78] The interfacial energy $\sigma_{Ni/Cu}$ is the sum of a crystallographic term resulting from the parametric misfit, and of a chemical term due to the difference of the bonding energy between copper atoms and nickel atoms relatively to the bonding energy between copper and nickel atoms. In the present case, the crystallographic term is low (~0.01 $J*m^{-2}$) due to the low parametric misfit (3%) between copper and nickel. The chemical term is the product of the fraction of bonds of each atom through the interface (here 0.25) with the molar exchange energy in the nickel-copper solution (estimated to be ~25 $kJ*mol^{-1}$), divided by the molar interfacial surface ($3.6 * 10^{-4}$ $m^2 * mol^{-1}$). $\sigma_{Ni/Cu}$ roughly equals 0.18 $J*mol^{-1}$. Based on these results, θ equals 45°.

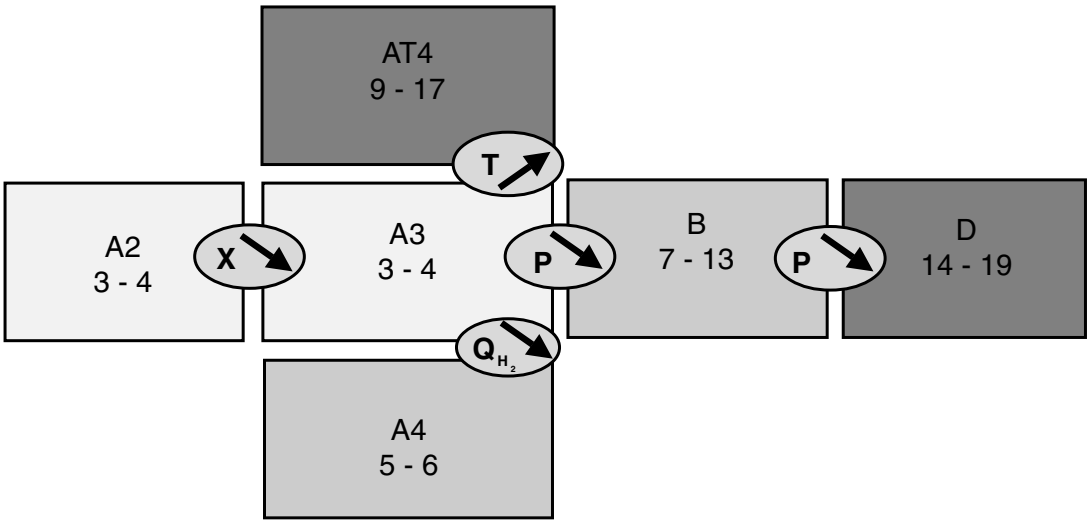

Fig. 7: Carbon content of the nickel films (at.%) in different processing conditions. Intensity of gray scale is qualitatively proportional to the carbon content.

surface in the investigated operating conditions. When X_{NiCp_2} is low (conditions A2), supersaturation is low and the number of nuclei formed on the surface decreases. Consequently, the nodule size increases. When pressure is decreased, the concentration of nickelocene, i.e. its supersaturation above the surface, increases because diffusion through the boundary layer is enhanced.[***] This should enhance the nucleation rate. Due to the decrease of available adsorption sites, surface diffusion rate also decreases. Indeed, Monte-Carlo simulations of nucleation and growth processes in CVD showed that lower surface diffusion induces a higher nucleation rate and a lower nodule size.[77]

The increase in nodule size with increasing temperature is due to the enhancement of surface diffusion and to the higher number of vacant sites due to increased desorption. The higher nodule size with decreasing concentration of H_2 can not be explained in terms of differences in supersaturation or in activation energy. This behavior can be attributed to the fact that hydrogen is probably adsorbed preferentially on nickel rather than on the substrates leading to a decrease of its concentration on the latter. Finally, the increase of grain size with increasing temperature is attributed to the excess energy that is available for rearrangement of nickel atoms while at the same time the number of crystal defects is reduced. Finally, the increase of grain size with decreasing attributed to the decrease of the reaction rate in these conditions, allowing more time for the nickel atoms to be reorganized in more stable positions.

Carbon Content

The carbon content of the films as determined by EPMA is schematically presented in Figure 7 for different deposition conditions, similarly to Figures 1 and 2. Intensity of gray scale is qualitatively proportional to the carbon content. When the partial pressure of hydrogen decreases (conditions A4) and when total

[***] This possibility has already been made in the previous paragraph to explain the variation of the growth rate with the pressure.

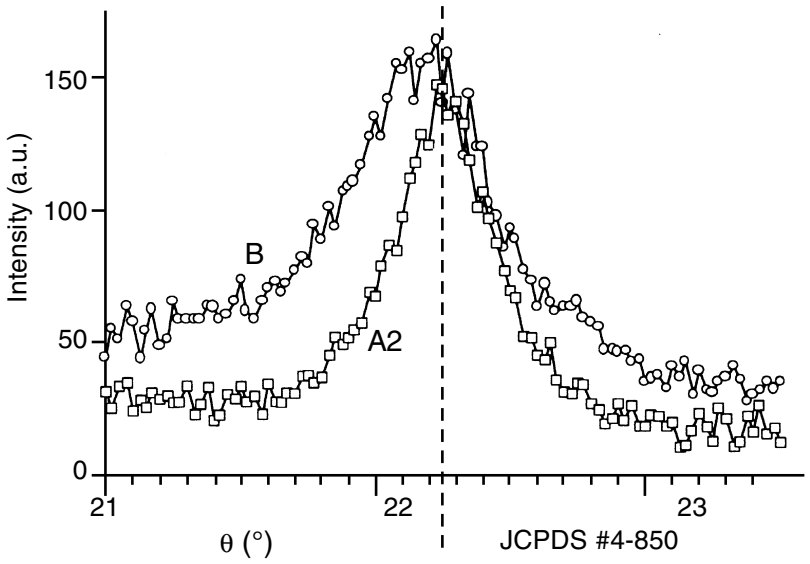

Fig. 8: X-ray diffraction spectra focused on the (111) Ni peak of films processed in conditions A2 (□) and B (O). The reference position for fcc Ni is shown for comparison.

pressure decreases (conditions B or D), carbon incorporation respectively slightly or strongly increases. In conditions B or D, carbon concentration varies from one experiment to another. For the same sample, the results are reproducible within ± 0.5 at.% from one EPMA measurement session to another. It is worth noting that the carbon content of 99.99% pure Ni foils was found to be 3-4 at.% in the same conditions of analysis. This value corresponds to the lower detection limit of the spectrometer. It is due both to the residual contamination of the apparatus and to the interference between the third order Ni L_{α}. and L_{β}, and the C K_{α} fluorescence peaks. Secondary ions mass spectrometry (SIMS) analysis of the films with negative primary ions distinguished the carbon concentration of only one heavily contaminated sample (conditions B, 10 at.% C) from samples with 3-4 at.% C (conditions A3) or even 5-6 at.% C (conditions A4). It was thus not possible to conclude by this technique that films processed in conditions A3 are carbon free. It will be shown in the next paragraphs that these films are indeed slightly contaminated with carbon. Finally, SIMS showed that the concentration profile of carbon remains unchanged along the thickness of the deposits.

Kaplin et al.[42] carried out experiments under conditions similar to A3 but with a higher molar fraction and with nitrogen N_2 as carrier gas. The carbon content in their films is higher than in those deposited in conditions A3 and is closer to that of films deposited in conditions B. The authors reported that the carbon content in nickel films increases with increasing temperature reaching a maximum of 17 at.% at 300°C before decreasing again at 350°C.

The C_{1s} XPS peak is slightly shifted towards the carbide position. However, it was not possible to obtain unambiguous evidence on the coexistence of two different chemical forms for the incorporated carbon. By comparison, for iron films with a carbon content lower than that reported in the present study, lzaki and Omi[79] obtained additional, well defined XRD peaks (compared to carbon peaks due to apparatus contamination at about 285 eV) for interstitial carbon at 283 eV. Also, XRD fcc Ni peaks of

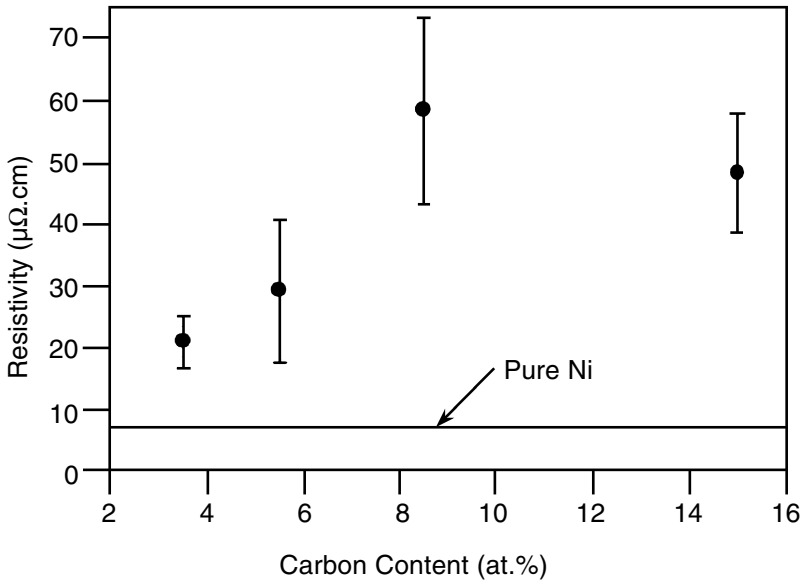

Fig. 9: Resistivity of Ni films as a function of their carbon content.

carbon contaminated films are shifted, although not systematically, towards lower theta values. This is clearly illustrated in Figure 8, where the (111) Ni peaks of two samples processed in conditions A2 and B are shown. Indeed, the peak position of the carbon-free film (A2) is the same as the reference for fcc Ni,[80] while that of the film containing 8-9 at.% carbon (B) corresponds to an enlargement of the unit cell from 0.3521 to 0.3528 nm. Similar enlargement of the unit cell has been observed by Aouni et al.[81] for Ni films containing 10 at.% carbon relative to those containing 1 at.% carbon. Finally, from Figure 8 it can also be noticed that the FWMH of the films is higher in conditions B than in conditions A2 revealing a decrease of grain size in the former. This behavior has been previously discussed.

Figure 9 shows the evolution of the electrical resistivity of the as processed films as a function of their carbon content. Resistivity of bulk Ni (6.84 μΩ∗cm) is also reported for comparison. Error bars show deviations both among different samples with the same carbon content, and among different positions within the same sample. Two unambiguous conclusions can be drawn from Figure 9. First, resistivity of the films is systematically higher than that of bulk Ni. This can be at least attributed to the numerous grain boundaries in the films. Second, the lowest values correspond to films with low carbon content, such as the ones deposited in conditions A3 and A4. Resistivity of films deposited in conditions B and D is higher. It is concluded that, in addition to thickness and morphology, the presence of the previously mentioned forms of carbon is also deleterious to the electrical properties of the films.

Figure 10 illustrates the variation of magnetization (M) as a function of applied field at 5 K for films processed in conditions A3 and B (film containing 7 at.% C). The (111) XRD Ni peak of these samples is not shifted relative to the reference position, in contrast to the 8-9 at.% C containing film whose XRD pattern is shown in Figure 8. In addition, the variation of M of a pure Ni foil and of a film processed in conditions B, containing 7 at.% C and annealed at 700°C for 3 hours under vacuum (approximately 10^{-4} Torr) is shown in this figure

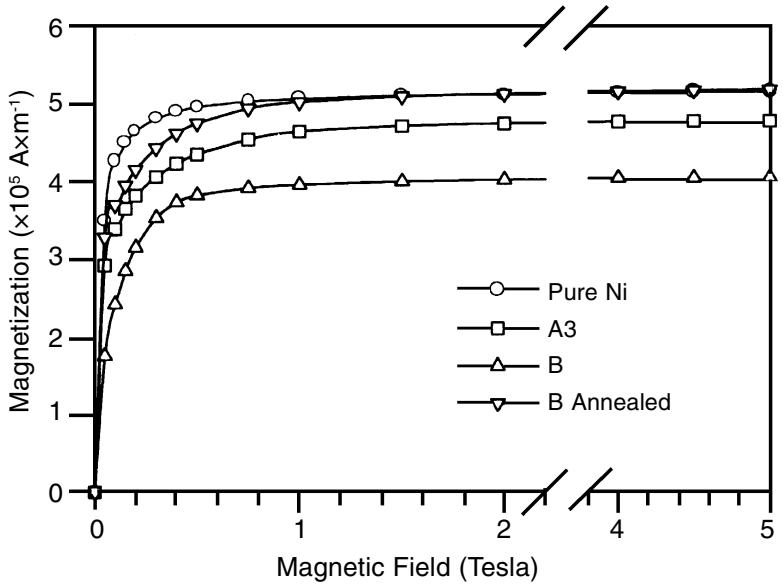

Fig. 10: Variation of the magnetization M, as a function of the magnetic field at 5 K for different samples: a pure Ni foil (O), a film deposited in conditions A3 (□), a film deposited in conditions B containing 7 at.% C(Δ), and the same film annealed for 3 h at 700°C in vacuum (∇).

for the same conditions. It appears that all samples exhibit a typical ferromagnetic behavior, characterized by increased magnetization with increasing magnetic field before reaching a plateau corresponding to the saturation magnetization value (M_s). M_s decreases with increasing temperature. This is illustrated in Figure 11, where M_s of each sample is plotted against $T^{3/2}$. A linear relation between the two parameters appears from this plot, characteristic of Bloch's law.[82] In Table 3, M_s at 5 K and at 300 K of the above investigated samples are shown, and are compared with some reported values for Ni layers. Table 3. Saturation magnetization M_s, at 5 and 300 K of samples A3, B, pure Ni, and B annealed. Some values of M, for various Ni layers from literature are also reported for comparison.

The results drawn in Figure 11 and tabulated in Table 3 indicate that M_s decreases with increasing carbon content of the as processed films. This is in agreement with literature information following which impurities such as boron, carbon or oxygen decrease the magnetization of nanocrystalline Ni powders,[85] and thin films.[17,83] It has also been reported that M_s, decreases when carbon has diffused in Ni, in particular if the non ferromagnetic nickel carbide Ni_3C is formed.[31] It is worth noting that magnetization of the films processed in conditions A3 is lower than that of the pure Ni sample, and that their M_s at 300 K is close to that of other carbon containing LCVD Ni films, deposited from nickelocene.[83] In agreement with a previous conclusion it thus appears that, although carbon contamination of films processed in conditions A3 is not detectable by EPMA, these deposits are carbon contaminated. This contamination level is high enough to affect their magnetic properties.

Sella et al.[31] observed that annealing Ni(C) films at 200°C under vacuum led to an increase in M_s, indicating that carbon atoms are segregating out of the crystal lattice. Such a diffusion mechanism of carbon at grain boundaries could explain that M_s of a sample processed in conditions B and annealed is close to that of bulk crystalline Ni.

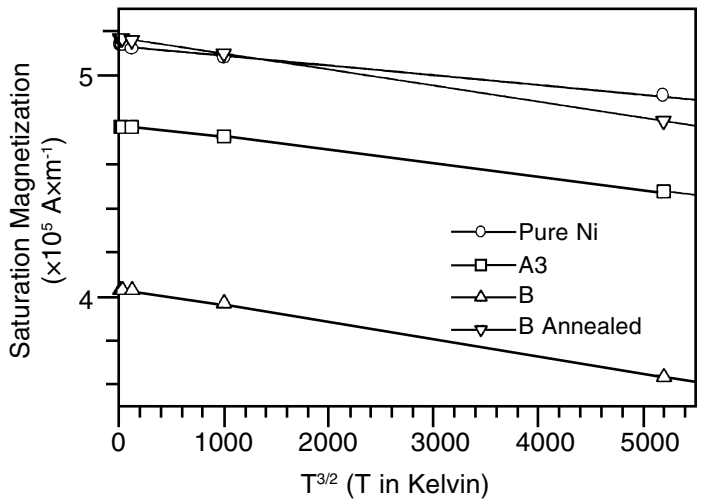

Fig. 11: Variation of the saturation magnetization M_s, as a function of $T^{3/2}$ for the samples of Figure 10.

Table 3. Saturation Magnetization M_s at 5 and 300 K of Samples A3, B, Pure Ni, and B Annealed. Some Values of M_s for Various Ni Layers from Literature are also Reported for Comparison

	Pure Ni Foil	**A3**	**B (7 at.% C)**	**B (7 at.% C) Annealed**
M_s ($.10^{-5}$ A.m^{-1}) at 5 K	5.14	4.77	4.03	5.17
M_s ($.10^{-5}$ A.m^{-1}) at 300 K	4.90	4.47	3.63	4.79
Reference	31	83	84	17
Material	PVD Ni/C	LCVD Ni (C)	Amorphous	Ni(B)
	Multilayer		Ni Layer	Thin Films
M_s($.10^{-5}$ A.m^{-1}) at 300 K	1.3 - 5.1	4.4	3.0	2.3

For amorphous Ni films, Tamura and Endo observed a reduced M_s value at 300 K compared to that of the crystalline state.[84] In the present case, the grain size of the deposits is systematically higher than 20 nm, i.e. at least one order of magnitude higher than the limit value which affects magnetizationd.

In Figure 12 the variation of the magnetic susceptibility as a function of temperature for a film processed in conditions B (7 at.%C) is presented. The Curie temperature T_c for this sample was measured from the heating and the cooling parts of this diagram. It slightly decreases after the annealing (approximately

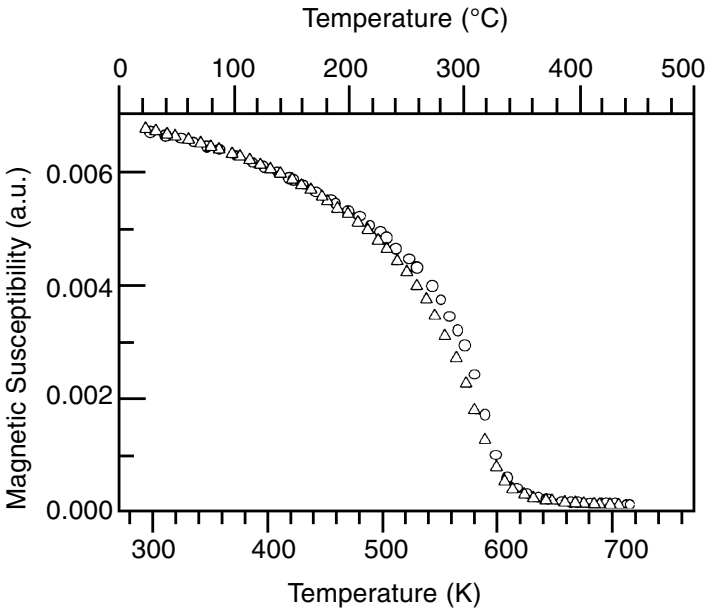

Fig. 12: Evolution of the magnetic susceptibility as a function of temperature during a heating (O), and a cooling (Δ) ramp, of a film processed in conditions B (7 at.% C). The corresponding T_C was determined as 335 ± 2°C.

3 hrs. above 400°C), but the magnetic susceptibility remains unchanged at low temperatures. T_c of the reference sample and of the films processed in conditions A3 remain unchanged after heating and cooling. Both T_c and magnetic susceptibility at low temperature of the films processed in conditions B (12 at.%C) significantly increase after annealing. Table 4 shows the T_c of the reference sample and the three films. It appears that T_c decreases with increasing carbon content of the films.

Decomposition of Nickelocene and Carbon Contamination: Reaction Schemes

Reaction (2) takes into account neither the carbon incorporation in the films nor the production of methane (CH_4), identified as one among the major by-products during this process. Thus, it is necessary to introduce a more complete scheme for the representation of these phenomena. A model will be proposed in order to understand, at least qualitatively, the influence of the main parameters on the reaction rates. It is based on the following assumptions.

a. Steady-state is reached in the reactor.
b. Residence time of the gases does not influence the rate of the reactions. Because most of them take place on the surface, reaction time is controlled by the time of adsorption on the substrate.
c. The hydrogenated derivatives of the C_5H_5 ligand are stable. They can be either desorbed from the substrates or further hydrogenated. Indeed, the dehydrogenation of C_5H_6[86] and of C_5H_8[74] proceed with C_5H_5 as an intermediate species, and both take place in the absence of hydrogen. Thus, although dehydrogenation reactions are possible, they should be slow and in any case, their decomposition is described by that of C_5H_5.
d. The carbon incorporated in the films is produced either from the condensation of

Table 4. Curie Temperature T_C for Four Ni Samples: A Pure Ni Foil, One Film Processed in Conditions A3, and Two Films Processed in Conditions B Containing 7 and 12 at.% C

	Pure Ni	A3	B (7 at.% C)	B (12 at.% C)
T_C (Heating Ramp)	360°C	350°C	336°C	333°C
T_C (Cooling Ramp)	360°C	350°C	334°C	343°C

cyclic parts or from the decomposition of the ligand, following a reaction scheme similar to those observed for the dehydrogenation of C_5H_6 or C_5H_8 but with C_5H_5 as starting species. Partial and total decompositions lead respectively to the incorporation of aliphatic (free) and carbidic (interstitial) carbon.

Following the proposed model, two types of reactions are in competition (Table 5). Those concerning the hydrogenation of the ligands (followed by desorption) (Reactions 3a to 8 in Table 5). Those concerning their decomposition, eventually leading to the incorporation of carbon (Reactions 9a to 12 in Table 5). In Table 5, the two branches of this reaction scheme are summarized. Although H_2 is written in its gaseous state, it is likely that it reacts in most cases under atomic form on the surface.[75] All other species are considered to be absorbed on the surface, unless otherwise specified.

Reaction (2) corresponds to the successive reactions (3) to (8). Because H_2 is dissociatively adsorbed on Ni, numerous highly reactive hydrogen atoms are available on the surface and consequently, hydrogenation reactions (3), (5) and (7) are catalysed on nickel. Reactions (9b and 10) describe the decomposition of the ligand C_5H_5. Incorporation of aliphatic carbon is represented by reaction (10a); that of interstitial or graphitic carbon is represented by reaction (10b). Incorporation of condensed species is represented by reactions (9c) and (9d). The methanation of carbon on nickel, reaction (12), has been extensively studied[75,87] and references therein), generally from decomposition of CO, because it plays a key role in many industrial processes. The hydrogenation of carbon atoms on nickel carbide surface has been studied by using surface characterization techniques.[88, 89] Finetti et al.[89] showed that 0.2 monolayer of carbon adsorbed on nickel can be only partially removed between 50°C and 75°C under a H_2 partial pressure P_{H_2} of 75 Torr, a residual quantity of carbon remaining on the surface after hydrogenation. By contrast, for experiments at 180°C, carbon is completely removed from the surface by methanation. Using a simple kinetic model to fit their experimental data, the authors propose that one among the four simple elementary steps $CH_x + H \rightarrow CH_{x+1}$ (x = 0, 1, 2 or 3) is a hundred times slower than the others. Following He et al.[88] this rate-limiting step corresponds to x = 2. These authors also showed that hydrogenation is induced by H* radicals and not directly by H_2. The total activation energy calculated for carbon hydrogenation to CH_4 is about 87 $kJ.mol^{-1}$.[89] Small size of crystallites, yielding surface with high density of reactive sites (as is the case of a growing surface by the CVD process), induce higher reactivity.[87] Following Zinn et al.,[65] metals like Ni, Pd or Pt, which catalyse this methanation reaction, can be deposited pure, without carbon incorporation.

According to the above presented reaction scheme, the level of carbon incorporation in the films will depend on the rate of reactions (9), v_9, which describe the decomposition of the cyclopentadienyl ligands, relative to the rate of reactions (3), V_3, which describe their hydrogenation. In order for the model to be complete, rates v_{11} and v_{12} must also be

considered, since part of the produced carbon is removed via the corresponding reactions (11) and (12). Two methods are presented for the comparison of these reaction rates.

The first method consists in a direct comparison of the rates between reactions (3) and reactions (9). Reactions (3) lead to the deposition of one nickel atom for one $NiCp_2$ molecule and to the production of two ligands that yield C_5H_8 and C_5H_{10}. Reactions (9) are the starting point for the incorporation of carbon in the films and for the production of CH_4 (assuming reaction rate v_{11} is negligible, $v_9 = v_{10} + v_{12}$). Assuming that most of the $NiCp_2$ molecules are decomposed via reactions (3) in typical CVD conditions, the production of CH_4 relative to each C_5H_5 ligand can be illustrated by the ratio

$$\frac{CH_4}{C_5H_8+C_5H_{10}}$$

This allows a direct comparison of the ratio $v_{12}/(v_6 + v_8)$ in different conditions. Because reaction rate v_5 is considered to be negligible, $v_3 \simeq v_6 + v_5$ based on assumption of steady state. Thus, this molar ratio should be $2^* v_{12}/v_3$, i.e. equal to the number of molecules of CH_4 formed for each half atom of deposited Ni. The rate of carbon incorporation per deposited nickel atom (i.e. the ratio v_{10}/v_3) is directly given by the carbon content of the films. As reaction (9) is related to C_5H_5, each ligand yields 5 carbon atoms, and ratio v_9/v_3 is provided by $(v_{10} + v_{12})/5$. Hence, the following relation can be obtained:

$$\frac{v_{10}}{v_4} = \frac{1}{5} \times \left(\text{at.\% C} + \frac{CH_4}{C_5H_8+C_5H_{10}} \right) \qquad (13)$$

This method provides a direct estimation of the ratio v_9/v_3. Its main drawback comes from the simultaneous consideration of two different kinds of measurements since EPMA and mass spectrometry have been used respectively for the determination of the first and the second terms in the right side of equation (13).

The second method consists in a comparison of the hydrogenation rates. As it can be expected, all reactions which should lead to pure Ni films are hydrogenation-type, in contrast to reactions which lead to carbon containing deposits. Hence, the two branches of Table 5 should have an inverse relationship with hydrogen. For example, it has been reported that the hydrogenation reaction of C_5H_6 to C_5H_8 On nickel boride NiB presents a partial order of 1 relatively to P_{H2}.[68] On the contrary, dehydrogenation reaction and C-C bond dissociation of C_2H_6 on the Ni surface presents an order of -2.5 relative to P_{H_2}.[90] Consequently, in processing conditions for which reactions (3) are favored, reactions (9) should not be, and *vice versa.* This shows that if the ratio of the rates v_3 for two sets of operating conditions can be established, it then becomes possible to compare the ratio of the rates of the two concurrent reactions (3) and (9).

It was not possible to evaluate v_3 by means of the present mass spectrometric measurements. C_5H_8 and C_5H_{10} are the two cyclic hydrocarbons whose molar ratio was quantitatively determined in all investigated conditions. Their ratio corresponds to the ratio of the reaction rates v_6/v_8, or to that of v_6/v_7 because steady-state is assumed. v_6/v_7 illustrates the ratio of the rate of desorption over that of hydrogenation for C_5H_8. At constant temperature, desorption rate depends on surface coverage. Thus, the comparison of this ratio for two experiments performed in different conditions yields a direct comparison between the hydrogenation rates of C_5H_8, provided temperature remains unchanged.

Because reactions (3), (5) and (7) are all hydrogenation reactions of cyclopentadienyl derivatives, it can also be assumed that their rates will vary the same way. Thus, the comparison of molar ratios,

$$\frac{C_5H_8}{C_5H_{10}}$$

for deposition at the same temperature, allows the comparison of the reaction rates of the "clean" decomposition of nickelocene (3). The higher this ratio, the less nickelocene decomposed following reaction (3).

This second method relies on the determination of the ratio

$$\frac{C_5H_8}{C_5H_{10}}$$

Table 5. Two Branches of the Proposed Reaction Scheme for the Deposition of Ni Films from Nickelocene

Decomposition of the Precursor with Hydrogenation of the Ligands	**Decomposition of the Precursor with Decomposition of the Ligands**
Dissociation of the Two Ni-Ligand Bonds:	**Decomposition of the First Ligand:**
$Ni(C_5H_5)_2 + ½\ H_2\ (g) \rightarrow NiC_5H_5 + C_5H_6$ (3a)	$Ni(C_5H_5)_2 \rightarrow C_xH_yNiC_5H_5 + C_{5-x}H_{5-y}$ (9a)
$Ni(C_5H_5) + ½\ H_2\ (g) \rightarrow Ni(s) + C_5H_6$ (3b)	Similar decomposition involving a ligand attached to a chemisorbed Ni:
C_5H_6 from reaction (3) can either be desorbed (4) or hydrogenated (5)	$C_5H_5 \rightarrow C_xH_y + C_{5-x}H_{5-y}$ (9b)
$C_5H_6 \rightarrow C_5H_6\ (g)$ (4)	Carbon incorporation is induced by the decomposition of species $C_{5-x}H_{5-y}$ and C_xH_y (10a), or by their direct incorporation in the deposit (10b):
$C_5H_6 + H_2\ (g) \rightarrow C_5H_8$ (5)	$C_{5-x}H_{5-y} \rightarrow C_uH_v(Ni) + C_wH_z\ (g)$ ($w \leq 5-x$ and $z < 5-y$) (10a)
C_5H_8 can be either desorbed (6) or hydrogenated (7, 8):	$C_{5-x}H_{5-y} \rightarrow C(s)$ ou $C(Ni)$ (10b)
$C_5H_8 \rightarrow C_5H_8\ (g)$ (6)	Condensation reactions can also lead to carbon incorporation by the formation of heavy olefins:
$C_5H_8 + H_2\ (g) \rightarrow C_5H_{10}$ (7)	$2\ C_5H_5 \Leftrightarrow C_{10}H_{10}$ (9c)
$C_5H_{10} \rightarrow C_5H_{10}\ (g)$ (8)	$n\ C_5H_6 \Leftrightarrow (C_xH_y)_m + k\ H_2$ (9d)
	with $m*x = 5*n$; $m*y + 2*k = 6*n$
Some of these species can react with hydrogen and give more stable molecules: $C_{5-x}H_{5-y} + n\ H_2 \rightarrow C_{5-x}H_{5-y+2n}\ (g)$ (11)	
Incorporated carbon can also react with hydrogen to yield CH_4. This reaction removes the incorporated carbon from the deposit:	
$C(Ni) + 2H_2 \rightarrow CH_4\ (g)$ (12)	

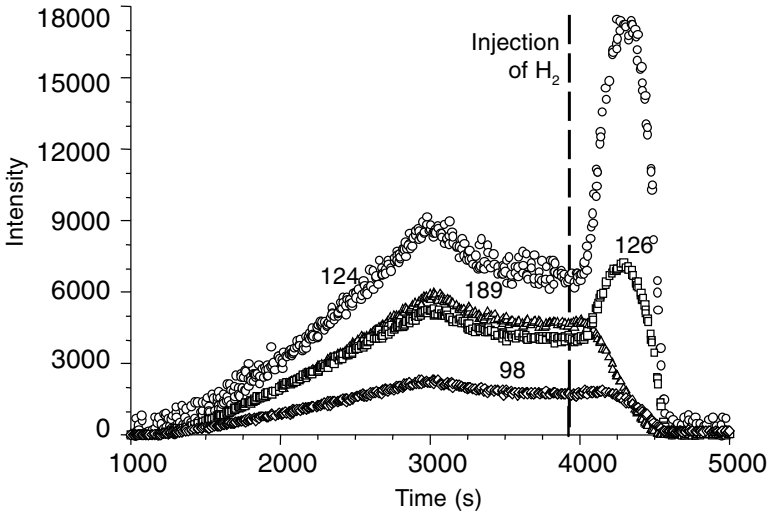

Fig. 13: Variation of masses m/q = 97, 123, 125, 188 as a function of time. Dotted line indicates the addition of H2 in the input gas. P = 100 Torr, T = 100 °C.

The approach appears less direct than the first one, but this parameter is based exclusively on mass spectrometric results and varies in a larger scale compared to the ratio v_9/v_3. Both ratios

$$\frac{C_5H_8}{C_5H_{10}} \text{ and } \frac{CH_4}{C_5H_8+C_5H_{10}}$$

allow the investigation of the relative rates between reactions (3) and (9), leading respectively to pure and to carbon contaminated Ni films. The mass spectrometric study of the gas phase described below is mainly focused on the investigation of these two ratios.

Investigation of the Gas Phase

Investigation of the gas phase was performed during deposition of Ni films. Three types of mass spectrometric experiments were realized.

a. In conditions B, at 100°C, where H_2 was replaced by He. In the course of the analysis, H_2 was also injected in the gas phase. He and H_2 flow rates were chosen in such a way that pressure in the mass spectrometer remained unchanged.
b. During deposition in conditions A3, A4, AT4, B and D.
c. In conditions A3 or B, during which, after the signal is stabilized, temperature was increased in increments of 25 or 50° up to 350°C.

From the last two types of experiments, the molar ratios

$$\frac{C_5H_8}{C_5H_{10}} \text{ and } \frac{CH_4}{C_5H_8+C_5H_{10}}$$

in the reactor, involving C_5H_8, C_5H_{10} and CH_4, were quantified following a calibration procedure reported in [46].

Gas Phase Analysis in the Absence of H_2

Figure 13 shows the variation with time of masses 97, 123, 125, and 188 at P = 100 Torr, T = 90°C, and a molar fraction of $NiCp_2$ 1.5×10^{-3}. The vertical dotted line indicates the replacement of He by H_2 in the input gas. Other

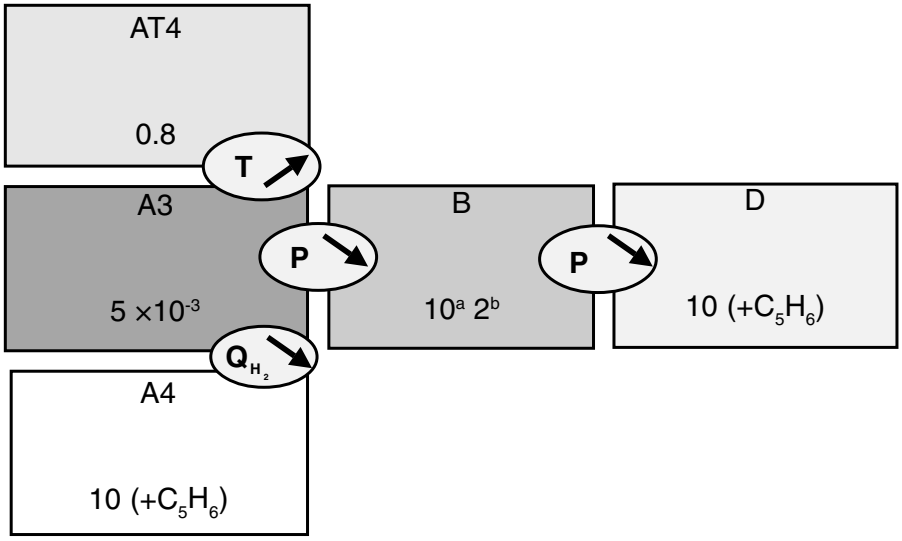

Fig. 14: C_5H_8/C_5H_{10} molar ratio during different processing conditions. Intensity of gray scale is inversely proportional to the C_5H_8/C_5H_{10} ratio, i.e. qualitatively proportional to the hydrogenation of the cyclopentadienyl ligands. In conditions B values ([a]) and ([b]) correspond respectively to the beginning of the experiment and to analysis in the presence of copper substrates.

masses, namely m/q = 58, 65, 66, and 124 were identified in these conditions but they have not been reported in the figure for clarity. Before the introduction of H_2, intensities increase with time and finally attain a stable value indicating a stationary regime. Masses 65 and 66 are attributed to C_5H_6. Mass 188 is attributed to $NiCp_2$ in contrast to masses 124 and 125 which do not belong to its mass spectrum. Intensities of masses 123 and 97 are stronger than in the spectrum of $NiCp_2$ (three to four times for the former). These results indicate that, in addition to $NiCp_2$, there should exist at least one other Ni containing species in the gas phase above the substrate.

The injection of H_2 results in:

a. A rapid and strong increase of the intensities of masses 123 and 125 in the same ratio as before the injection of H_2, followed by a rapid decrease,
b. A weak increase of mass 124 (as well as 58 and 97) followed, as for the previous masses, by a rapid decrease, and
c. A strong decrease of the intensity of mass 188 along with an increase in intensity of masses 123 and 125.

The decrease of the intensity of mass 188 and the simultaneous increase of masses 123 and 125 indicate that the latter can not be attributed exclusively to fragments of $NiCp_2$ in the gas phase. These masses are attributed to the ions $HNiCp^+$ and H_2NiCp^+, which, as it will be shown below, can be provided by the H_2NiCp, and possibly HNiCp molecules,

Evolution of the C_5H_8/C_5H_{10} Ratio

In Figure 14, the evolution of the C_5H_8/C_5H_{10} ratio during different processing conditions is schematically illustrated. Intensity of gray scale is inversely proportional to the C_5H_8/C_5H_{10} ratio, i.e. qualitatively proportional to the hydrogenation of the cyclopentadienyl ligands. In conditions B values ([a]) correspond to the beginning of the experiment and values ([b]) to utilization of copper substrates.

The C_5H_8/C_5H_{10} ratio generally decreases before reaching a stable value. In conditions A3, almost all ligands (~99.5%) are fully hydrogenated to yield C_5H_{10}, and no C_5H_6 can be detected. For higher temperature (350°C, conditions AT4), the ratio C_5H_8/C_5H_{10} increases by almost a factor of 100 and approximately equals one, indicating that half of the ligands are desorbed in the form of C_5H_8 instead of being hydrogenated to yield C_5H_{10}. The highest value of the C_5H_8/C_5H_{10} ratio (~10), was obtained at low H_2 flow rate (conditions A4). C_5H_6 was also detected in these experiments. Its quantity decreases with time, varying from 50% to 10% of the total cyclopentadienyl derivatives. The C_5H_8/C_5H_{10} ratio also increases with decreasing pressure from conditions A3 to B and D. In conditions D it attains a value comparable to that in conditions A4. Moreover, C_5H_6 is detected during the first steps in both conditions B and D. It represents 2% to 10% of the total amount of the cyclopentadienyl derivatives in conditions B, and 25% in conditions D. The decrease with time of the value of C_5H_8/C_5H_{10} in conditions B is faster when a copper substrate is placed upstream of the sampling tube. When the copper substrate is not present or is placed downstream, this transition period is much longer, and it lasts approximately until a nickel film is visible on the glass or silica SiO_2 substrates placed upstream.

Figure 15 shows the values of the ratios

$$\frac{C_5H_8}{C_5H_{10}} \text{(15a) and} \frac{C_5H_6}{C_5H_8+C_5H_{10}} \text{(15b)}$$

obtained from experiments where temperature was increased from 150°C to 350°C. These experiments have been performed at 100 Torr in conditions similar to deposition conditions B and at 760 Torr in conditions similar to deposition conditions A3 (or AT4). They are compared with results reported by Kaplin et al.[42] who operated close to conditions A3 and AT4, but with a higher molar fraction of nickelocene and with N_2 as carrier gas. Lines are guides to the eye. As already noticed at 175°C, the C_5H_8/C_5H_{10} ratio is about 100 times higher at 100 Torr than at 760 Torr. Both ratios increase very slowly with temperature. Ligands are more hydrogenated in the present experiments than in those of Kaplin et al. In particular, these authors observed much more C_5H_6, especially above 300°C.

The evolution of the composition of the gas phase was also investigated during cool down and with the saturator by-passed, after a deposition experiment had been completed. It was found that during a transition period when by-products were still observable, the decrease of the temperature induced a strong decrease of the signal attributed to C_5H_6 and C_5H_8, and a strong increase of the signal attributed to C_5H_{10}.

Evolution of the $CH_4/(C_5H_8 + C_5H_{10})$ Ratio

In Figure 16 the evolution of the $CH_4/C_5H_8 + C_5H_{10}$ ratio during different processing conditions is schematically illustrated. Intensity of gray scale is proportional to the value of this ratio. This value is very close to 0. 1 in all cases, except in conditions A3, in which case it is about 5×10^{-3}. The evolution of the $CH_4/C_5H_8 + C_5H_{10}$ ratio with temperature at 760 Torr and at 100 Torr is shown in Figure 17. At 760 Torr it is negligible at low temperature, but it sharply increases above 275°C. At 100 Torr, it remains stable in the order of a few percent from 175°C to 300°C, before strongly increasing. For both pressures, the values of the ratio $CH_4/C_5H_8 + C_5H_{10}$ are comparable above 300°C.

Some films deposited in conditions B were annealed at 300°C under the same (except for the presence of $NiCp_2$) atmosphere as during deposition. In these experiments, the signals attributed to the cyclopentadienyl derivatives were very weak, whereas the signal attributed to CH_4 was very strong. It is remarkable that the signal attributed to the nickelocene also becomes observable, whereas it was not observable during deposition experiments.

Other Masses

Masses m/q 27, 29, 37, 39, 40, 41, 43, that have not been attributed up to now to specific molecules, were observed in low quantities. They probably correspond to hydrocarbons with 2 or 3 atoms of carbon. They were detected mainly during experiments in conditions A4

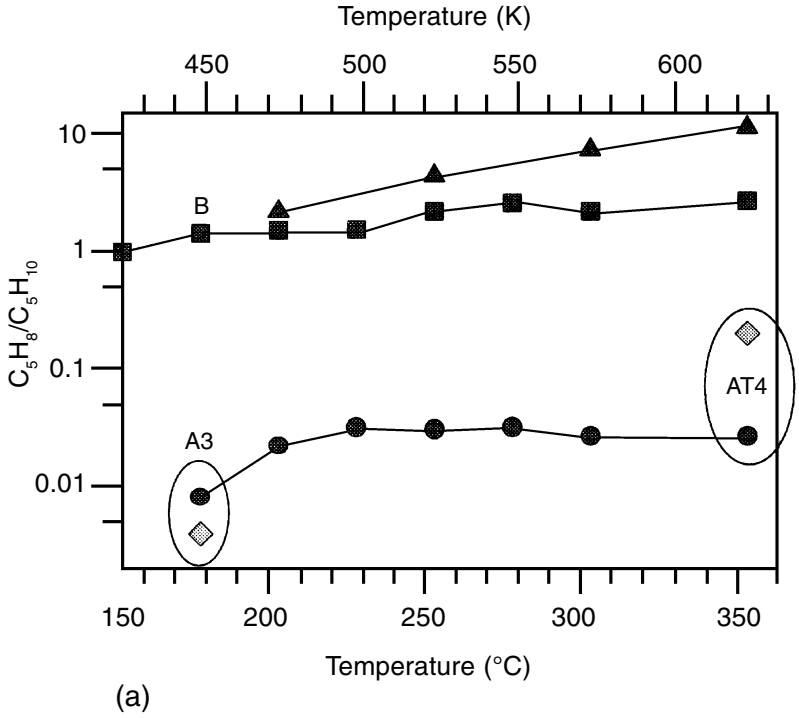

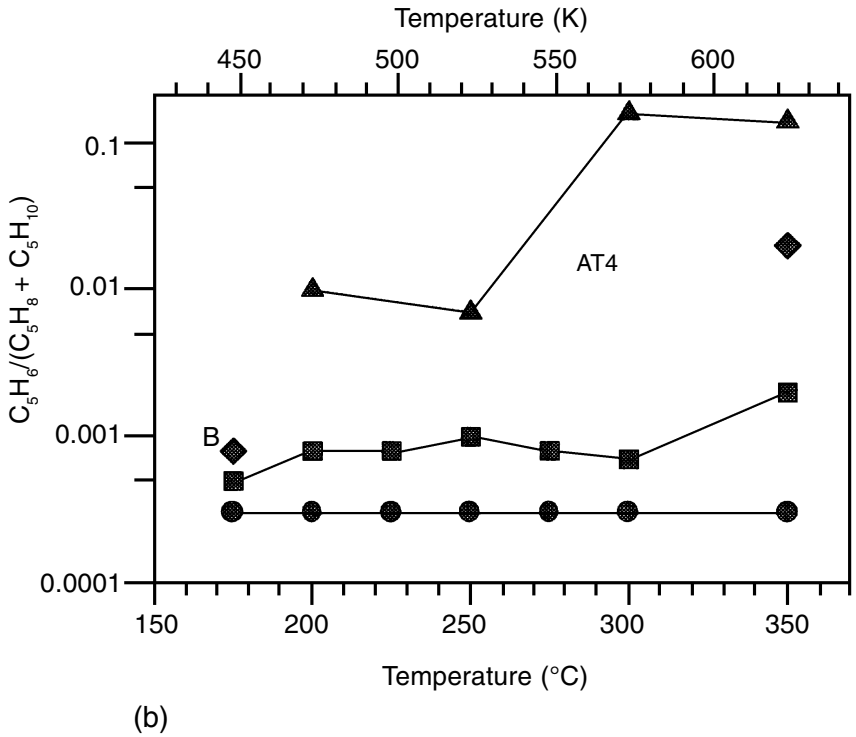

Fig. 15: Variation of the molar ratios (a) C_5H_8/C_5H_{10} and (b) $C_5H_6/(C_5H_8 + C_5H_{10})$ as a function of temperature for experiments performed at P = 760 Torr (•) and at 100 Torr (■). Corresponding results from Kaplin et al.[34] (▲) are also reported. Points (◆) correspond to experiments performed at constant temperature.

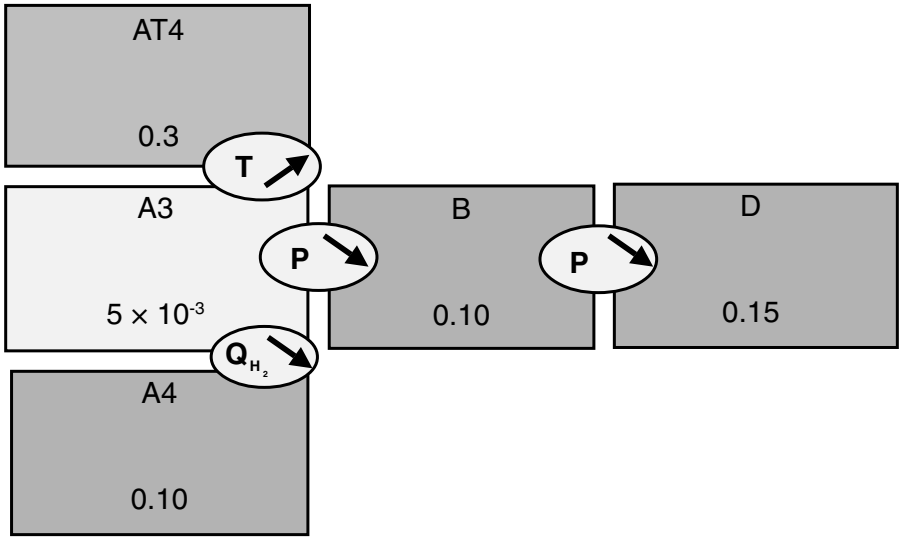

Fig. 16: $CH_4/(C_5H_8 + C_5H_{10})$ molar ratio during different processing conditions. Intensity of gray scale is qualitatively proportional to the value of the $CH_4/(C_5H_8 + C_5H_{10})$ ratio.

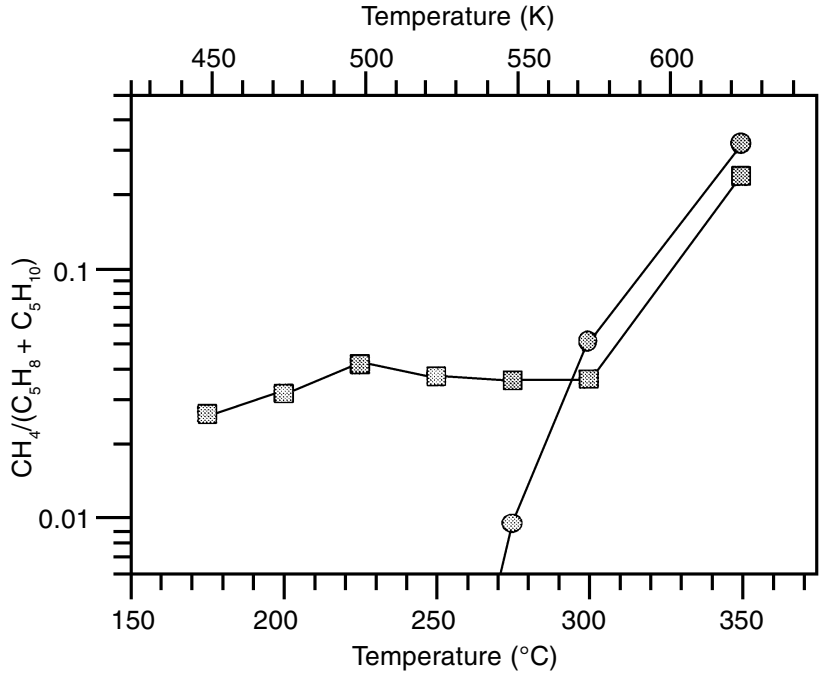

Fig. 17: Variation of the molar ratio $CH_4/(C_5H_8/C_5H_{10})$ as a function of temperature during experiments performed at 760 Torr (•) and at 100 Torr (■).

and to a lesser extent during experiments using conditions B and D. Masses heavier than those corresponding to C_5H_{10} were detected only in very weak quantities. These results differ from those reported in[42] where molecules corresponding to condensed species were detected, especially for deposition temperatures above 300°C.

Growth Mechanisms

Results

Variation with Time

Hydrogenation rate increases with time, before reaching a stationary value. In conditions B, this transition period is strongly reduced when a copper substrate is placed on the susceptor, upstream of the sampling tube. This transition period is attributed to the time that is necessary to cover the substrates with nickel. When nickel is present, hydrogenation is catalysed. Consequently, decomposition of nickelocene is enhanced, and deposition of Ni becomes autocatalytic.[39]

Variation with Temperature

Because desorption rates are different, it is not possible to directly compare the C_5H_8/C_5H_{10} ratio, i.e. the hydrogenation rates between two experiments at different temperatures. Consequently, in such conditions the C_5H_8/C_5H_{10} ratio does not allow the comparison between rates v_4 and v_{10}. However, the increase of this ratio with increasing temperature (Figure 15a) clearly shows that the desorption rate of the ligands becomes higher than their hydrogenation rate. Inversely, it becomes lower when temperature is decreased below 175°C as was shown from the gas phase analysis during cooling of the reactor at the end of the experiments. This is attributed to a higher activation energy for desorption than for hydrogenation. It is recalled that the adsorption energy of nickelocene on nickel growing films is certainly higher than that found by Welipitiya et al. for $NiCp_2$ on Ag (100), i.e. 50 kJ/mol^{-1},[71] that C_5H_6 is desorbed from the surface of Cu only above 350°C,[86] and that the energy for the hydrogenation of a ligand was estimated to be lower than 11 kJ.mol^{-1} (see section on the growth rate). This result confirms that the lower reaction rates observed at temperatures above 250°C are due to higher desorption rates of nickelocene in these conditions. The hydrogenation reaction and thus the reduction of $NiCp_2$ by H_2 is slow compared to desorption above 250°C.

When temperature is increased, the amount of CH_4 greatly increases (Figure 17), especially above 300°C. Following Kaplin et al.,[42] the amount of carbon in the deposits increases with increasing temperature up to 300°C and decreases at 350°C. It is concluded that when temperature is increased, reaction (12) increases faster than reaction (9) which increases faster than reaction (3). Thus, the activation energies for these three reactions should be related as: $E_A(3) < E_A(9) < E_A(12)$. Considering the values mentioned above, $11 < E_A(9) < 87$ kJ.mol^{-1}. Generally speaking, the activation energy for hydrogenolysis reactions on transition metals is between 64 and 100 kJ.mol^{-1}.[75] The increase in temperature leads to an increase in the amount of carbon incorporated in the films, until the methanation reaction can remove it, mainly at temperatures higher than 300°C. The strong increase of the production of CH_4 above 300°C at 100 Torr suggests a change for the mechanism of the ligand decomposition. Considering the similar amount of CH_4 produced at 760 Torr above 300°C, this mechanism, characterized by a higher activation energy, should be the same in these two conditions.

Variation with Hydrogen Flow

Hydrogenation strongly decreases when the hydrogen flow is decreased as illustrated by comparison of the values of the C_5H_8/C_5H_{10} ratio in conditions A3 and A4 (Figure 14). If the rate of reaction (7) is written in the classical form:

$$v_7 = K \cdot P^{\alpha}(H_2) \qquad (14)$$

then $\alpha \simeq 3.5$ according to the values of the above ratio obtained for experiments in conditions A3 and conditions A4. Coefficient K includes the activity of nickelocene on the surface. This activity is thus assumed to be the same in conditions A3 and A4; i.e. adsorption of nickelocene is only weakly influenced by the

hydrogen coverage of the surface. The value of α is significantly higher than that of 0.8, estimated for a similar relation applied to reaction (3). However, these calculations only reveal trends. They show that reactions (3) and (7) vary in the same way, even if the latter is more sensitive towards P_{H_2} than the former. Further measurements are necessary to obtain precise values for partial orders α.

The amount of incorporated carbon in the deposits processed in conditions A4, is 5-6 at.%, i.e. slightly higher than that of films deposited in conditions A3 (Figure 7). From Figure 16 it can also be noticed that in conditions A4, approximately 20 molecules of CH_4 are produced when 100 atoms of Ni are deposited. This is considerably higher than in conditions A3 (about 1 CH_4 per 100 deposited Ni atoms). These two results show that according to relation (13), the rate of ligand decomposition (9) increases relatively to reaction (3) when hydrogen flow rate is decreased. They also indicate that in conditions A4, despite a very low hydrogenation rate, methanation reaction (12) is very efficient permitting removal of 80% of the carbon produced by reactions (9) and (10). Because many other light molecules have been detected in conditions A4, reaction (11) helps to remove some parts of the decomposed ligands from the nickel surface. Because in conditions A_3 H_2 flow rate is higher than in conditions A4, the methanation rate for a given quantity of carbon should also be higher. In view of the high efficiency of the methanation reaction in conditions A4, the amount of carbon in films processed in conditions A3 should be less than the number of methane molecules formed per atom of deposited nickel, that is to say inferior to 1 at.%.

Variation with Pressure

Comparison of the values of the ratio C_5H_8/C_5H_{10} in conditions A3 and B, or B and D shows that the hydrogenation rate strongly decreases when pressure is decreased. This behavior is to be related with the decrease of the growth rate with decreasing pressure below 100 Torr. Because the growth rate of films is comparable in conditions A3 and B, and reaction (4) is slower in conditions B (as reaction (8) is slower), the number of nickelocene molecules on the surface should be higher in conditions B to balance the slower hydrogenation rate. This is attributed to a better diffusion of nickelocene in the boundary layer at low pressure. In such a case, the increased number of nickelocene molecules should saturate the adsorption sites for hydrogen, as has already been proposed. Consequently, less hydrogen should be dissociated on the surface and be available for nickelocene decomposition or ligands hydrogenation.

Following Figure 14, in conditions of low H_2 flow rate (A4) hydrogenation is slower than conditions B, and of the same order of magnitude as in conditions D. On the other hand, production of CH_4 is comparable in conditions B, D, and A4. Moreover, the amount of carbon is higher in conditions B (7-12 at.%) and D (14-19 at.%) than in conditions A4. Although the hydrogenation reaction is faster, the methanation reaction is less efficient in conditions B than in conditions A4, and the ligand decomposition is favored. This implies, according to relation (13), that the rate of reaction v_9 relative to reaction v_3 is faster at low pressure, independently of the decrease of the hydrogenation rate.

It is worth noting that the increase of the decomposition reaction of the ligands and the decrease of the efficiency of methanation are not only a consequence of the decrease of the hydrogenation reaction. Conditions that favor reaction (3) (or (12)) must discourage reaction (9) and *vice versa.* In a following paragraph, these phenomena will be correlated with the surface saturation of nickelocene.

Variation with the Molar Fraction or the Carrier Gas

The lower hydrogenation rates in the experiments reported by Kaplin et al.[42] compared with those in conditions A3 can be explained by the higher molar fraction of nickelocene or by the use of N_2 as carrier gas in their experiments. A higher concentration in the gas phase induces a higher concentration on the surface, which should lead to a saturation of

the sites for the adsorption of hydrogen. It is recalled that in the experiments reported by these authors, carbon content is also higher than that in films processed in conditions A3. By contrast, it is closer to that observed for conditions B, for which the surface has been said to be saturated with nickelocene.

Because hydrogenation is obviously a surface reaction between adsorbed H* and ligands, its 'rate must depend on the competition for adsorption sites between molecules of the carrier gas and H_2. N_2 is larger than He, and its adsorption energy is certainly higher. Thus, a similar flow rate of these two carrier gases will lead to a different surface coverage. It is possible that more adsorption sites for H_2 are occupied by the carrier gas when N_2 rather than He is used, leading to a slower hydrogenation rate.

Comparison with Equilibrium Calculations

Total and partial equilibrium calculations were performed using the GEMINI2 software,[91] in order to determine whether the variations in operating conditions can change along with the products of the reaction or their quantity by displacing the equilibrium.

Total equilibrium calculations considered:

a. fcc Ni, graphite and the nickel - carbon Ni(C) solid solution,
b. nickelocene, and
c. C_xH_y hydrocarbons with $\times \leq 6$, and also toluene, naphtalene, anthracene and phenantrene that have been detected during the pyrolysis of nickelocene.[38]

Data for all species were taken from the SGTE data bank,[92] except for nickelocene,[37] and for C_5H_5 and C_5H_6.[93] Results show that in a large domain of operating conditions, including those investigated in the present work, the Ni(C) solid solution is the only stable condensed phase. Carbon solubility in Ni is very low (below 0.1 at.%). CH_4 is the only stable gas under these conditions. In view of the misfit between calculated and experimental results (the latter showing that CH_4 is not the major gas and that carbon content in the film is higher) it is concluded that equilibrium was not attained in the experiments.

Partial equilibrium calculations considered fcc Ni as condensed species, and the cyclopentadienyl radical and its hydrogenated derivatives as gaseous species. Following this list, the only possibility for nickelocene is to be decomposed into solid Ni, while sufficient time is allowed for the ligands to reach equilibrium through hydrogenation reactions. However, ligands are not allowed to be decomposed. The results are illustrated in Figure 18 where the evolution of the calculated molar ratio C_5H_8/C_5H_{10} as a function of temperature is reported at 100 Torr and 760 Torr. No C_5H_6 was found below 500°C. In this figure, experimental results obtained in similar conditions are also reported. From the comparison between experimental and theoretical results, it appears that equilibrium for the hydrogenation reaction (7) is far from being reached, except at 350°C and atmospheric pressure. Consequently, the experimentally shown evolution of C_5H_8/C_5H_{10} with varying operating conditions can not be attributed to the displacement of the equilibrium with the pressure or temperature.

Finally, the same gaseous species were considered, with fcc Ni being replaced by the Ni(C) solid solution. Within this scheme, ligands were allowed to be hydrogenated or to be completely decomposed leading to the incorporation of carbon in Ni. The absence of CH_4 does not allow this carbon to be removed by a methanation reaction. The results show a slight increase of carbon solubility in Ni relative to the results of total equilibrium calculations: Carbon content in Ni is now 4×10^{-4} at.% at 175°C and 0.01 at.% at 350°C at atmospheric pressure, and slightly higher at 100 Torr. Although trends from calculations and from experiments are similar, the misfit between them is still high. The evolution of carbon incorporation in the deposits in different operating conditions can not be attributed to equilibrium displacement.

The decrease of the intensity of mass 188 and the simultaneous increase of those of masses 123 and 125 after the injection of hydrogen (Figure 13) indicate that the last two masses can not be attributed exclusively to fragments of $NiCp_2$ in the gas phase. We

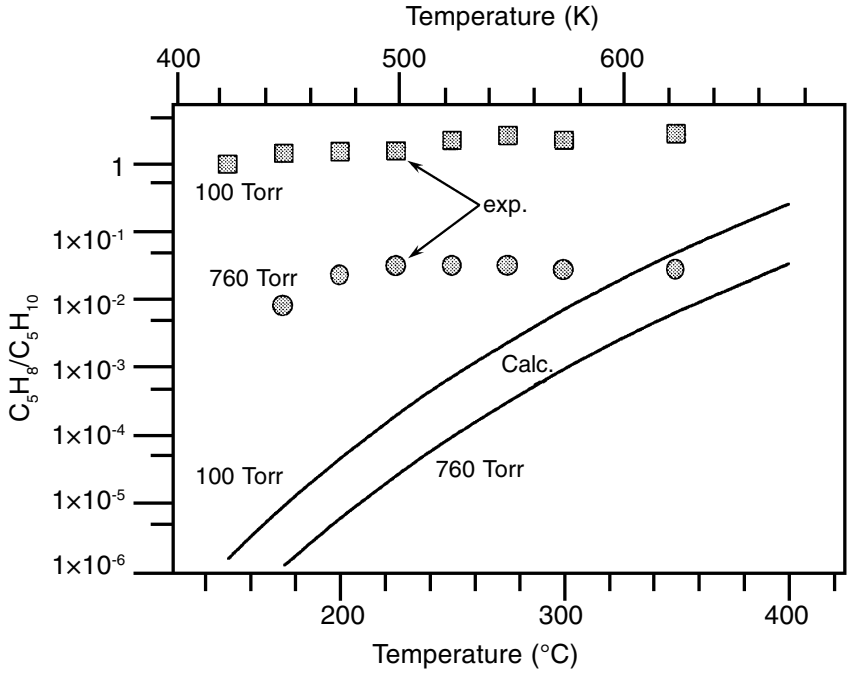

Fig. 18: Comparison of the C_5H_8/C_5H_{10} ratio as a function of temperature at 760 Torr and at 100 Torr, calculated in partial equilibrium conditions and corresponding experimental values.

attribute these masses to the ions $HNiCp^+$ and H_2NiCp^+, which can be provided by the H_2NiCp, and possibly HNiCp molecules. In agreement with the work of Pradeep et al.,[94] hydrogen atoms in these molecules are considered to be linked to nickel. In such a case, these species ran be formed from the reaction of hydrogen with the nickel cyclopentadienyl radical NiCp, which in turn is formed as an intermediate product during the dissociation of $NiCP_2$ (reaction 3a).

In order to investigate the stability of NiCp and of its hydrogenated forms, quantum chemistry calculations have been performed using the density functional theory.[47] The characteristics of the Ni-Cp bond have been optimized for the above compounds together with those of the Ni-H bond in H_2NiCp, and HNiCp. In Figure 19 an energy diagram of the dissociation energies (BDE) of the first and the second bonds of the two cyclopentadienyl ligands linked to Ni in $NiCP_2$ is presented. It can be noticed that the first BDE is considerably higher than the second by, 90 kJ/mol.

The BDEs of Ni-H bonds in HNiCp, and H_2NiCp are approximately 300 kJ/mol, their difference being less than 20 kJ/mol. Although the Ni-Cp BDE is weaker in H_2NiCp relatively to NiCp (230 instead of 310 kJ/mol), these values suggest that both the Ni-H and the Ni-Cp bonds are quite strong. Consequently, if hydrogen is available in the vicinity of NiCp, the formation of HNiCp and H_2NiCp, can not be excluded.

Based on the above calculations, both the free energy function (FEF) and the standard enthalpy of formation $\Delta H°_f(298)$ of NiCp were obtained, the first from its structure and normal mode of vibration by applying the harmonic-oscillator, rigid-rotator approximation, and the second from a Born-Haber thermodynamic cycle.[95] The thermodynamic description of NiCp, together with that of the other participating compounds, permitted a second series of partial equilibrium calculations of the

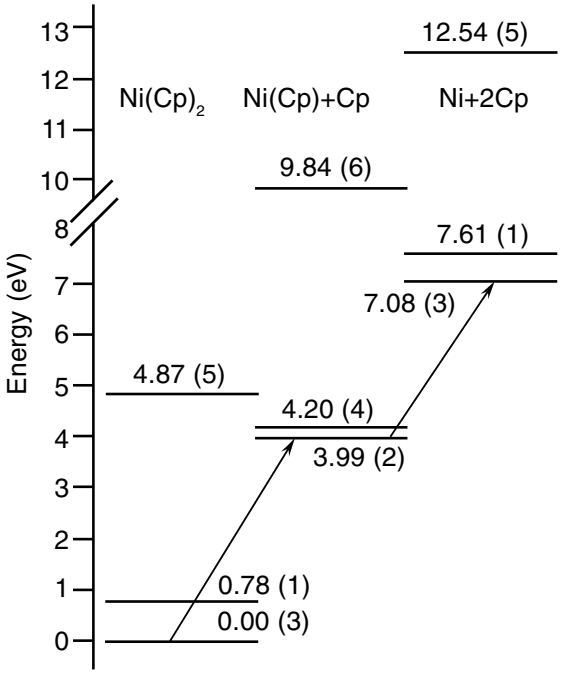

Fig. 19: Diagram of excitation energy (eV), predicted first bond dissociation energy (3.99 eV, lower arrow), and the sum of the first and the second bond dissociation (7.08 eV both arrows) of $NiCp_2$. Spin multiplicity is given in parenthesis. In all calculations the ground state of the cyclopentadienyl radical is considered.

metastable gaseous phase. It was then possible to obtain trends on the behavior of the gas phase in two different configurations, according to reaction (15) alone and to reactions (15) and (16) considered together:

$$Ni(C_5H_5)_2\,(g) \rightarrow Ni(C_5H_5)\,(g) + C_5H_5\,(g) \qquad (15)$$

$$Ni(C_5H_5)\,(g) \rightarrow Ni(s) + C_5H_5\,(g) \qquad (16)$$

The results are illustrated by the two diagrams of Figure 20, where the evolution of the molar fractions of $NiCp_2$, NiCp, and Ni(s) is reported as a function of temperature for two extreme values of pressure, 4×10^{-5} Torr, and 760 Torr. Calculations have also been performed at 13.3 kPa (100 Torr) and yield intermediate results between those illustrated in the diagrams of Figure 20. The main conclusions from these calculations are:

i. $NiCp_2$ is stable at atmospheric pressure.
ii. It yields NiCp or Ni(s) above 773K (500°C).
iii. At low pressures it is decomposed more easily and yields NiCp which can in turn yield Ni(s) above 623K (350°C). In these conditions NiCp becomes more stable above 723K (450°C), leading to a decrease in the quantity of Ni(s).

The lower stability of NiCp compared to that of $NiCp_2$ and Ni(s) has been experimentally confirmed for this [96] and related compounds.[97] This can also be expected from the lower BDE of the Ni-Cp bond in NiCp, relative to that of same bond in $NiCp_2$. It is thus shown that, in the absence of hydrogen, $NiCp_2$ can not decompose below 200°C via the dissociation of a Ni-Cp bond. This is consistent with the experimental results of Stauf et al.[40] who reported that in equivalent conditions deposition of nickel films is not possible below 550°C.

The decomposition of $NiCp_2$ in the presence of a comparable quantity of hydrogen following reaction (17) has then been investigated.

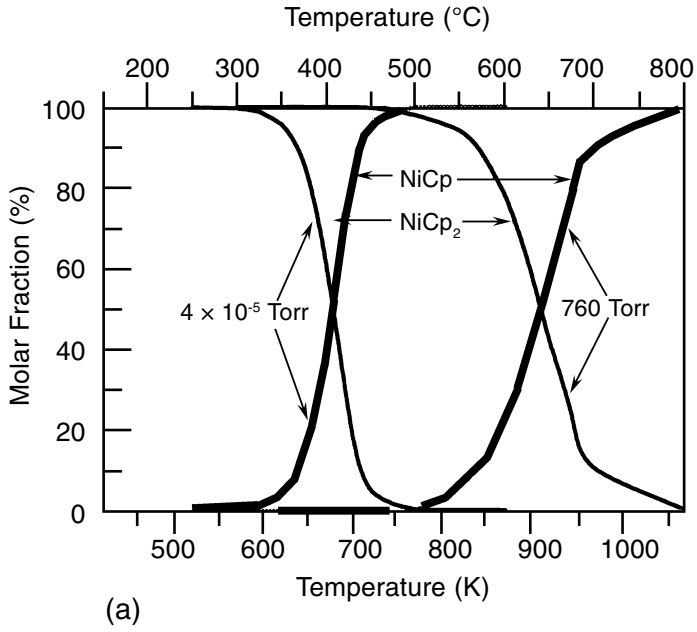

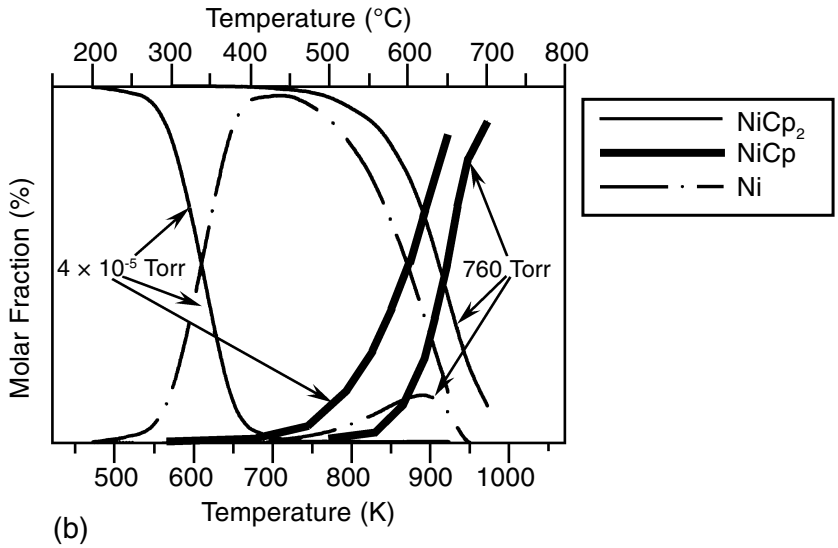

Fig. 20: Yield diagrams of stabilized species as a function of temperature for two pressures, 4×10^{-5} Torr and 760 Torr. Diagrams were obtained by partial equilibrium calculations within two chemical systems, one defined by equation (16) (diagram 20a) and the other by both equations (16) and (17) (diagram 20b).

$$Ni(C_5H_5)_2(g) + \tfrac{1}{2}H_2(g) \rightarrow C_5H_6(g) + Ni(C_5H_5)(g) \quad (17)$$

The results show that, if partial hydrogenation of the ligands through a limited quantity of hydrogen is allowed, NiCp starts forming above 200°C at very low pressure, and that this limit increases with increasing pressure. Hence, at atmospheric pressure, NiCp is stabilized above 300°C, to be compared with 550°C when there is no hydrogen available

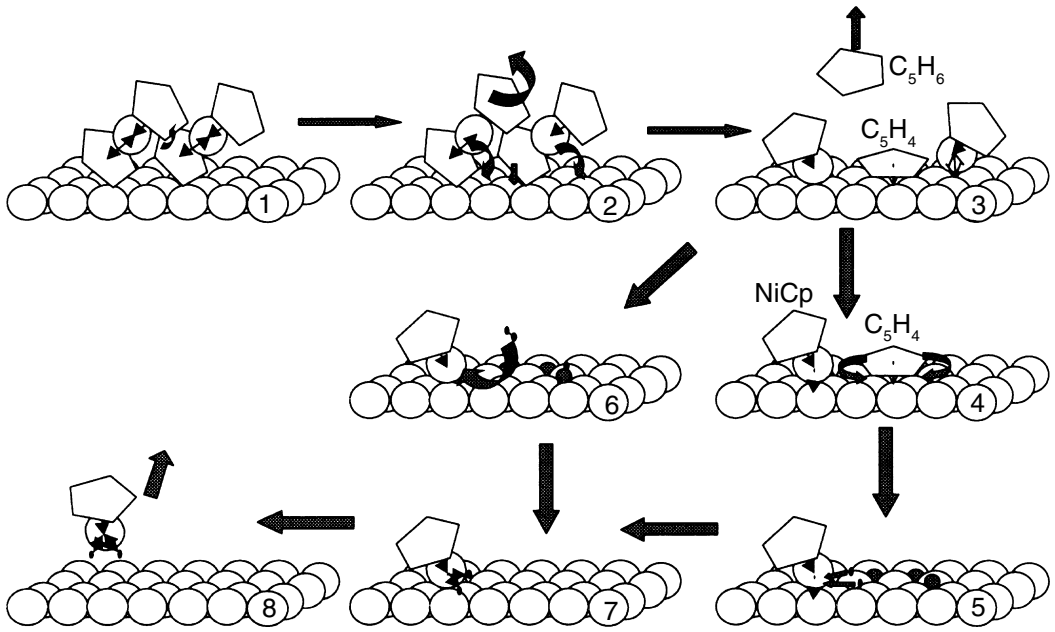

Fig. 21: Schematic representation of the reaction between adsorbed molecules of $NiCp_2$. (See text for detailed description of each step.)

(previous calculations). Finally, if nickel is allowed to form in these conditions, it is found that, in the presence of a minimum amount of hydrogen, $NiCp_2$ is decomposed at room temperature and yields Ni(s) and C_5H_6. NiCp is stabilized above 650°C.

Mechanism for Carbon Incorporation

From the previous sections, the following points can be made. Nickelocene and the cyclopentadienyl ligands are hydrogenated with atomic hydrogen produced from the dissociative adsorption of H_2 on the surface. Carrier gas, H_2 and precursor compete for the adsorption sites. Nickelocene can almost completely cover the surface and thus prevent the adsorption of H_2. Even with low hydrogenation rate, the methanation reaction can be very efficient for the cleaning of the surface. Hence, a decrease in hydrogenation results in limited carbon incorporation (conditions A4).

When the surface is almost saturated with nickelocene, decomposition of ligands is enhanced (reactions (9) and (10)), methanation becomes less efficient, and more carbon is incorporated in the nickel. This behavior can not be solely explained by the competition between hydrogenation and dehydrogenation reactions. Indeed, hydrogenation of ligands is slower in conditions A4 than in conditions B or D. Inversely, dehydrogenation of ligands leading to carbon incorporation and methanation reactions are faster in conditions B and D than in conditions A4. Reactions (10) certainly correspond to a high activation energy mechanism that is predominant above 300°C. We propose another mechanism for lower temperatures, which is based on the saturation of the surface with nickelocene. This mechanism is schematically presented in Figure 21 which approximates the relative dimensions among the involved atoms. The cyclopentadienyl

ligand is represented by a pentagon. The mode of adsorption of nickelocene molecules is as proposed by Welipitiya et al. for high coverage,[71] although a different mode has very recently been proposed.[98]

Following this mechanism, the reaction of the decomposition of the ligands is due to the reaction between two neighbor molecules of nickelocene. Hydrogen is transferred from a ligand of the first to a ligand of the second molecule of nickelocene (step 1). The first molecule is decomposed yielding NiCp and C_5H_4, whereas the other gives C_5H_6 and NiCp (steps 2 and 3). C_5H_4 would be expected to serve as precursor for the incorporation of carbon in the growing films following a dehydrogenation process proposed by Sun et al.[86] (step 4). The available hydrogen could react with the adsorbed NiCp to yield H_2NiCp or HNiCp (steps 5 and 7). It has been shown from *ab initio* calculations that these species can be stable relative to NiCp. Once HNiCp or H_2NiCp have been formed on the surface, they are expected to be desorbed more easily than NiCp, due to a decrease of the energy of the bond between nickel and the surface (step 8). If excess hydrogen is now directly injected in the gas phase (as was done during the analysis of the gas phase in section 5b) hydrogenation of NiCp could be performed directly from molecular H_2 (steps 6 and 7). Consequently, production of H_2NiCp should be enhanced relative to the previous case, and also relative to the production of HNiCp.

In summary, the reaction between two nickelocene molecules would necessarily lead to the decomposition of one ligand, with a weak probability for carbon from this reaction to be hydrogenated into CH_4. This or similar hydrogen exchange-based reaction mechanisms between two metalorganic molecules have already been proposed by Druzhkov et al.[99] for nickelocene decomposition, and by Russel[97] for the decomposition of $FeCp_2$ and $CpMo(CO)_3$.

According to this decomposition mode, carbon should be in the deposit in an aliphatic or carbidic form, due to the more or less complete decomposition of C_5H_4. The condensed cyclic form is less probable by this mechanism unless C_5H_4 can react with other C_5H_4 cycles, or with a nearby NiC_5H_5 radical, before it is decomposed. The mechanism presented in Figure 21 requires lower activation energy than the direct decomposition of the C_5H_5 ligands, which takes place at 350°C,[74,86] and is responsible for an increase in CH_4 above 300°C.

Summary and Conclusions

In view of the properties of the deposited films and of the corresponding processes, the most promising precursors for nickel CVD are $Ni(CO)_4$ (which, despite its high toxicity presents important advantages relative to the other precursors), $NiCp_2$, $Ni(MeCp)_2$, $Ni(hfa)_2$, $Ni(dmg)_2$, and $Ni(den)_2$. The choice of the most appropriate among them will depend on the intended application.

Thin films of nickel can be grown from nickelocene in the presence of hydrogen at rates up to 1 $\mu m.h^{-1}$ depending on the deposition conditions and the nature and the substrate surface morphology. The most appropriate temperature interval for this is between 160°C and 180°C. Smooth films are obtained during processing below 100 Torr, but these conditions are detrimental to the growth rate. Above 225°C desorption of nickelocene is favored over its decomposition. It appears that, although not optimized, the growth rate of Ni films from $NiCp_2$ is intrinsically limited due to the saturation of surface sites and to the competition between $NiCp_2$ and hydrogen for adsorption and, consequently, can not be significantly increased by modifying the operating conditions.

Carbon is incorporated in the films in interstitial, in aliphatic and/or organic forms. Carbon content is attributed to the high surface coverage of nickelocene, whether this high concentration is due to high molar fraction of the precursor or to low operating pressure. An increase in temperature above 250°C and, to a lesser extent, a decrease in hydrogen flow rate lead to an increase of carbon incorporation in the films. Interstitial carbon deforms the Ni lattice and is responsible for degradation of magnetic properties of the deposited films.

The gas phase study during deposition associated with the determination of the composition of the films revealed that the deposition reaction can be described by a Langmuir-Hinshelwood mechanism, i.e. that nickelocene prevents H_2 adsorption by occupying most of the adsorption sites. This high surface coverage is obtained by an increase of the nickelocene molar fraction or by a decrease of the total pressure. Thus, the hydrogenation reaction and deposition rate strongly decrease for high nickelocene surface coverage. The high surface coverage also induces reactions between nickelocene molecules. Many of these reactions are directly responsible for carbon incorporation, because they produce active species that decompose easily, and they prevent removal of the carbon by methanation. Dehydrogenation of the ligand under thermal conditions is responsible only for a weak part of the contamination. Carbon is present both in the intestinal and aliphatic or organic forms. These conclusions can be extended to other MOCVD processes with precursors containing cyclopentadienyl ligands. They could explain the generally high carbon contamination in deposits obtained from such precursors. Because the surface concentration of the precursor should be relatively low, films having good electrical or magnetic characteristics should be processed with low deposition rates. On the other hand, it seems that nickelocene can be a very convenient precursor for Ni films for applications that do not require optimum electrical properties.

Chemical vapor deposition in general, and CVD of metals in particular is a complex process. Comprehension of the underlying mechanisms requires a multi-disciplinary approach, and different scientific and technological skills. For example, the coupling of gas phase analysis with the microstructure of the material was demonstrated in this chapter. It was confirmed that mass spectrometry is a powerful analytical instrument. However, in order to propose a surface reaction scheme, it was necessary to make different assumptions. This kind of study is complementary to high vacuum investigation of surface reactions. Indeed, operating conditions in the latter are far from practical deposition conditions, and for this reason, extrapolation of conclusions to the real process may not be reliable. On the other hand, these fundamental investigations are valuable in determining the different steps of the proposed reaction schemes.

Acknowledgments

Major parts of this chapter are based on the Ph.D. thesis of L.B., performed through a grant from the French Ministry of Education and Research. We are indebted to A. Castillo for technical assistance, to A. Reynes and M. Parioleau for help with the mass spectrometry work, to R. Sahnoun and C. Mijoule for the *ab initio* calculations, to D. de Caro, R. Madar and D. Boursier for the magnetic measurements, to P. de Parseval, and C. Armand, for EPMA and SM4S analysis, to J.K. Kang and S.W. Rhee for FFIR measurements, to F. Maury for fruitful discussions, and to an anonymous referee for valuable remarks.

References

1. T.T. Kodas and M. Hampden Smith, *The Chemistry of Metal CVD*, Weinheim, Germany, VCH, 1994.
2. J.R. Creighton and J.E. Parmeter, Metal CVD for Microelectronic Applications, An Examination of Surface Chemistry and Kinetics, *Critical Review in Solid State Materials Science,* Vol.18, 1993, pp.175-238.
3. S. Leppävuori, J. Remes, and H. Moilanen, Laser Chemical Vapor Deposition of Cu and Ni in Integrated Circuit Repair*, SPIE*, Vol.2874, 1996, pp.272-282.
4. M.W. Cole, C. Hubbard, C.G. Fountzoulas, D. Demaree, A. Natarajan, R.A. Miller, D. Zhu, and K. Xie, The Reliability of Ni Contacts to n-SiC Subjected to Pulsed Thermal Fatigue, *Electrochemical and Solid-State Letters,* Vol.2, 1999, pp.97-99.
5. J. Crofton, P.G. Mcmullin, J.R. Williams, and M.J. Bozack, High-Temperature Ohmic

Contact to n-Type 6H-SiC Using Nickel, *Journal of Applied Physics,* Vol.77, 1995, pp.1317-1319.

6. H.D. Kaesz, R.S. Williams, R.F. Hicks, J.I. Zink, Y.J. Chen, H.J. Muller, Z. Xue, D. Xu, D.K. Shuh, and Y.K. Kim, Deposition of Transition Metal and Mixed Metal Thin Films from Organometallic Precursors, *New Journal of Chemistry,* Vol.14, 1990, pp.527-534.
7. J.D. Martin, P.H. Hogan, K.A. Abboud, and K.H. Dahmen, Variations on Nickel Complexes of the Vic-Doximes, An Understanding of Factors Affecting Volatility Toward Improved Precursors for Metal-Organic Chemical Vapor Deposition of Nickel, *Chemistry of Materials,* Vol.10, 1998, pp.2525-2532.
8. E. Hökelek and G.Y. Robinson, Aluminum/ Nickel Silicide Contacts on Silicon, *Thin Solid Films,* Vol.53, 1978, pp.135-140.
9. G.J.M. Dormans, OMCVD of Transition Metals and their Silicides Using Metallocenes and (di) Silane or Silicon Tetra-Bromide, *Journal of Crystal Growth*, Vol.108, 1991, pp.806-816.
10. A. Thies, G. Schanz, E. Walch, and J. Konys, Chemical Deposition of Metals for the Formation of Microstructures, An Alternative Method to Galvanoforming, *Electrochimica Acta*, Vol.42, 1997, pp.3033-3040.
11. S. Balog, Chemical Vapor Deposition of Nickel Molds, Proceedings of the 66th Annual Technological Conference, American Electroplating Society, Vol.66, (No.5), 1979, pp.1-9.
12. F. Fau Canillac, Métallisation De Matériaux Composites Organiques par Dépôt Chimique en Phase Vapeur à partir de Sources Organométalliques, Ph.D. Thesis #626, Institut National Polytechnique de Toulouse, France, 1992.
13. M.R. Leonov, V.A. Ilyushenkov, and N.I. Kiselev, Preparation of Two-Layer Coatings Containing Uranium or Thorium Dioxide and Metallic Nickel, *Radiochemistry,* Vol.39, 1997, pp.239-242.
14. F. Caturla, F. Molina, M. Molina-Sabio, and F. Rodriguez-Reinoso, Electroless Plating of Graphite with Copper and Nickel, *Journal of Electrochemical Society,* Vol.142, 1995, pp.4084-4090.
15. P.A. Lane, P.J. Wright, P.E. Oliver, C.L. Reeves, A.D. Pitt, and J.M. Keen, Growth of Iron, Nickel, and Permalloy Thin Films by MOCVD for use in Magnetoresistive Sensors, *Chemical Vapor Deposition,* Vol.3, 1997, pp.97-101.
16. Y.G. Jim and D. Byun, *Journal of Applied Physics,* Vol.70, 1991, pp.6062-6064.
17. D. Zych, A. Patwa, S.S. Kher, J.T. Spencer, J. Kushneir, A.J. Goodby, N.M. Boag, and P.A. Dowben, Novel Methods for the Fabrication of Ferromagnetic Nickel and Nickel Boride Thin Films, *Journal of Applied Physics,* Vol.76, 1994, pp.3684-3687.
18. P. A. Lane, Liquid Injection Metal Organic Chemical Vapor Deposition of Nickel Zinc Ferrite Thin Films, *Journal of Crystal, Growth,* Vol.192, 1998, pp.423-429.
19. G.F. Dionne, *IEEE Trans on Magnetics,* Vol.31, 1995, pp.3853-3855.
20. W.C. Yeh and M. Matsumura, Chemical Vapor Deposition of Nickel Oxide Films from bis-pi-Cyclopentadienyl-nickel, *Japan Journal of Applied Physics Part I.* Regular Papers Short Notes & Review Papers, Vol.36, 1997, pp.6884-6887.
21. C.I.M.A. Spee, H.L. Linden, A. Mackor, K. Timmer, and H.A. Meinema, Development of Novel Nickel (B-Diketonate) 2 Ligand Complexes as Precursors for MOCVD of Nickel and Nickel Oxide, *Proceedings Materials Research Society*, Vol.415, 1996, pp.93-98.
22. J.C. Hierso, C. Satto, F. Feurer, and P. Kalck, Organometallic Chemical Vapor Deposition of Palladium Under Very Mild Conditions of Temperature in the Presence of Low Reactive Gas Partial Pressure, *Chemical Materials,* Vol.8, 1996, pp.2481-2485.
23. T. Nishikawa, T. Ono, N. Kakutani, M. Yano, and Y. Ogo, Preparation of Ni Membrane Catalyst Supported on Ceramic Filter by CVD Method, Member of Faculty of Engineering, Osaka City University,

Vol.32, 1991, pp.37-46.

24. G.Y. Meng, L. Huang, M. Pan, C.S. Chen, and D.K. Peng, Preparation and Characterization of Pd and Pd-Ni Alloy Membranes on Porous Substrates by MOCVD with Mixed Metal Beta-diketone Precursors, *Material Research Bulletin,* Vol.32, 1997, pp.385-395.
25. J.F. Faudon, F. Senocq, G. Bergeret, B. Moraveck, and G. Clugnet, Preparation and Characterization of Ni-Pt Catalysts by X-Ray Diffraction Analytical Microscopy and EXAFS, *Journal of Catalysis,* Vol.144, 1993, pp.460-471.
26. B.E. Williams, J.J.J. Stiglich, and R.B. Kaplan, CVD Coated Tungsten Powder Composites, Part I, Powder Processing Characterization, Presented at Tungsten and Tungsten Alloys - Recent Advances, A. Choson and E. Chen, eds., 1991, pp.95-101.
27. C.C. Chen and S.W. Chen, Nickel and Copper Deposition on $A1_2O_3$ and SiC Particulates by Using the Chemical Vapor Deposition Fluidized Bed Reactor Technique, *Journal of Materials Science,* Vol.32, 1997, pp.4429-4435.
28. C. Crowley, R. Taylor, H.W. Kroto, D.R.M. Walton, P.C. Cheng, and L.T. Scott, Pyrolytic Production of Fullerenes, *Synthetic Materials,* Vol.77, 1996, pp.17-22.
29. I.C. Leu, M.H. Hon, and Y.M. Lu, Chemical Vapor Deposition of Silicon Carbide Whiskers Activated by Elemental Nickel, *Journal of Electrical Society,* Vol.146, 1999, pp.184-188.
30. R. Krawietz, B. Wehner, D. Meyer, K. Richter, H. Mai, R. Dietsch, S. Hopfe, R. Scholz, and W. Pompe, Investigation of the Thermal Stability of Ni/C Multilayers by X-Ray Methods, *Fresenius' Journal of Analytical Chemistry,* Vol.353, 1995, pp.246-250.
31. C. Sella, K. Youn, R. Barchewitz, M. Arbaoui, and R. Krishnan, Structure and Properties of WIC and Ni/C Multilayer Films, *Thin Solid Films,* Vol.164, 1988, pp.405-409.
32. L. Mond, C. Langer, and F. Quincke, Action of Carbon Monoxide on Nickel, *Journal of Chemical Society,* Vol.14, 1885, pp.749-752.
33. R.C. Weast, *Handbook of Chemistry and Physics*, 66th ed., Boca Raton, FL, C.R.C. Press, 1985.
34. F. Maury, Recent Trends in the Selection of Metal-Organic Precursors for MOCVD, *Journal of de Physique IV,* Vol.C5, 1995, pp.449-463.
35. L.A. Torres-Comez, G. Barreiro-Rodriguez, and F. Mendez-Ruiz, Vapor Pressures and Enthalpies of Sublimation of Ferrocene, Cobaltocene and Nickelocene, *Thermochemistry Acta,* Vol.124, 1988, pp.179-183.
36. A.G. Turnbull, Thermochemistry of Biscyclopentadienyl Metal Compounds. II. Entropy of Sublimation, *Australian Journal of Chemical,* Vol.20, 1967, pp.2757-2760.
37. A.G. Turnbull, Thermochemistry of Biscyclopentadienyl Metal Compounds I. Preparation and Themal Stability, *Australian Journal of Chemical,* Vol.20, 1967, pp.2059-2067.
38. L.M. Dyagileva, O.N. Druzhkov, and Y.A. Andrianov, Gas-Phase Pyrolysis of Nickelocene, *Journal of General Chemistry of USSR,* Vol.1, 1977, pp.82-85.
39. O.N. Andreev, O.P. Bespal'ko, V.P. Marii, L.N. Vyshinskaia, and G.A. Ruzuvaev, Nickel Deposition from Thermal Decomposition of Nickelocene, *Metalloorganitcheskaya Khimiya,* Vol.1, 1988, pp.1184-1186.
40. G.T. Stauf, D.C. Driscoll, P.A. Dowben, S. Barfuss, and M. Grade, Iron and Nickel Thin Film Deposition via Metallocene Decomposition, *Thin Solid Films,* Vol.153, 1987, pp.421-430.
41. C.H.J. Van den Brekel, R.M.M. Fonville, P.J.M. Van der Straten, and G. Verspui, CVD of Ni, TiN, TiC on Complex Shapes, Presented at Proceedings of the 8th International Conference on Chemical Vapor Deposition, *Proceedings of the Electrochemical Society*, Vol.81, (No.7), 1981, pp.142-156.

42. Y.A. Kaplin, G.V. Belysheva, S.F. Zhil'tsov, G.A. Domrachev, and L.S. Chernyshova, Decomposition of Nickelocene in Presence of Hydrogen, *Journal of General Chemical USSR,* Vol.50, 1980, pp.100-103.
43. L. Brissonneau and C. Vahlas, Precursors and Operating Conditions for the Metal-Organic Chemical Vapor Deposition of Nickel Films, *Annales de Chemie - Science des Matériaux,* Vol.25, pp.81-90.
44. L. Brissonneau and C. Vafflas, MOCVD Processed Ni Films from Nickelocene. Part I, Growth Rate and Morphology, *Chemical Vapor Deposition,* Vol.5, 1999, pp.135-142.
45. L. Brissonneau, D. deCaro, D. Boursier, R. Madar, and C. Vahlas, MOCVD Processed Ni Films from Nickelocene. Part II, Carbon Content of the Films, *Chemical Vapor Deposition,* Vol.5, 1999, pp.143-149.
46. L. Brissonneau, A. Reynes, and C. Vahlas, MOCVD Processed Ni films from Nickelocene. Part III, Investigation of the Gas Phase, *Chemical Vapor Deposition,* Vol.5, (No.6), 1999, pp.281-290.
47. L. Brissonneau, R. Sahnoun, C. Mijoule, and C. Vahlas, Investigation of nickelocene decomposition during chemical vapor deposition of nickel, *Journal of the Electrochemical Society*. in Press.
48. L. Brissonneau, C. Vahlas, and A. Reynes, Processing of Pure Ni MOCVD Films, Presented at Advanced Interconects and Contact Materials and Processes for Future Integrated Circuits Symposium, *Proceedings of Material Research Society Symposium*, Vol.514, 1998, pp.491-496.
49. L. Brissonneau, A. Reynes, and C. Vahlas, Morphology and Carbon Content of Nickel Films Deposited from Nickelocene, Presented at International Symposium on Chemical Vapor Deposition, CVD-XIV and EUROCVD 11, *Proceedings of the Electrochemical Society*, Vol.97, (No.25), 1997, pp.1580-1587.
50. A.A. Zinn, L. Brandt, H.D. Kaesz, and R.F. Hicks, Nickel, Palladium and Platinum, *The Chemistry of Metal CVD,* T.T. Kodas and M.J. Hampdens-Smith, eds., Weinheim, VCH, 1994, pp.329-355.
51. H.D. Kaesz, R.S. Williams, R.F. Hicks, Y.A. Chen, Z. Xue, D. Xu, D.K. Shuh, and H. Thridandam, Low Temperature Organometallic Chemical Vapor Deposition of Transition Metals, *Proceeding of Material Research Society Symposium*, Vol.131, 1989, pp.395-400.
52. T. Maruyama and T. Tago, Nickel Thin Films Prepared by Chemical Vapor Deposition from Nickel Acetylacetonate, *Journal of Materials Science,* Vol.28, 1993, pp.5345-5348.
53. R.L. Van Hemert, L.B. Spendlove, and R.E. Sievers, Vapor Deposition of Metals by Hydrogen Reduction of Metal Chelates, *Journal of Electrochemical Society,* Vol.112, 1965, pp.1123-1126.
54. P.P. Semyannikov, V.M. Grankin, and I.K. Igumenov, Investigation of Thermolysis Mechanism of Gas Phase of Ni(II) Chelates by Mass Spectrometry, International Symposium on Chemical Vapor Deposition, CVD-XIV and EUROCVD 11, The Electrochemical Society Proceeding, Vol.97, (No.25), 1997, pp.89-96.
55. M. Becht, J. Gallus, M. Hunziker, F. Atamny, and K.H. Dahmen, Nickel Thin Films Grown by MOCVD Using Ni(dmg)2 as Precursor, *Journal of Physique IV,* Vol.C5, 1995, pp.465-472.
56. M. Urrutigoity, C. Cecutti, F. Senocq, J.P. Gorrichon, and A. Gleizes, Preliminary Study of $(Ni(en)_3)$ $(CF_3CO_2)_2$ and Ni(en) (hfpd)2 as Precursors for Metalorganic Chemical Vapour Deposition, Structural Properties and Thermal Behaviors, Inorganica *Chimical Acta,* Vol.248, 1996, pp.15-21.
57. V.O. Borisov, V.V. Bakovets, L.F. Bakhturova, and I.P. Dolgovesova, Kinetics of Nickel Deposition from Ni(HL*)2 Vapor, *Inorganic Materials-Engl Tr,* Vol.31, 1995, pp.1026-1027.
58. M. Becht, F. Atamny, A. Baiker, and K.H. Dahmen, Morphology Analysis of Nickel Thin Films Grown by MOCVD, *Surface Science,* Vol.371, 1997, pp.399-408.

59. L. Brissonneau, A. Kacheva, F. Senocq, J.K. Kang, S.W. Rhee, A. Gleizes, and C. Vahlas, MOCVD of Ni and Ni_3C Thin Films from Ni(dmen)2 (CF3OO)2, *Journal de Physique* IV, Vol.9, 1999, pp.597-604.
60. S. Motojima, K. Haguri, Y. Takahashi, and K. Sugiyama, Chemical Vapor Deposition of Nickel Phosphide Ni_2P, *Journal of Less-Common Metals,* Vol.64, 1979, pp.101-106.
61. S. Kher and J.T. Spencer, The Chemical Vapor Deposition of Pure Nickel and Nickel Boride Films from Borane Cluster Compounds, *Proceedings of Material Research Society Symposium*, Vol.250, 1992, pp.311-316.
62. S.D. Hwang, N. Remmes, P.A. Dowben, and D.N. McIlroy, Nickel Doping of Boron-Carbon Alloy Films and Corresponding Fermi Level Shifts, *Journal of Vacuum Science Technology,* Vol.A15, 1997, pp.854-859.
63. Y. Saito, T. Takeuchi, Y. Fukuda, and K. Sone, On Some Mixed Chelates of Nickel (II) which are Highly Volatile, Fusible and Soluble in Nonpolar Solvent, *Bulletin of the Chemical Society of Japan,* Vol.54, 1981, pp.196-199.
64. F. Senocq, M. Urrutigoity, Y. Caubel, J.P. Gorrichon, and A. Gleizes, Preliminary Studies of $(Ni(dmen)_2$ $(CF_3CO_2)2$, Ni (deen)2 $(CF_3CO_2)2$ and Ni(en) $(CF_3C(O)$ $CHC(O)CF_3)_2$ as Precursors for Metalorganic Chemical Vapor Deposition, Structures, Thermal behaviors and Vapor Pressures, *Inorganic Chemical Acta,* Vol.288, 1999, pp.233-238.
65. A. Zinn, B. Niemer, and H.D. Kaesz, Reaction Pathways in Organometallic Chemical Vapor Deposition (OMCVD), *Advanced Materials,* Vol.4,1992, pp.375-378.
66. J.K. Kang and S.W. Rhee, *Unpublished Results.*
67. W.L. Holstein, Design and Modelling of Chemical Vapor Deposition Reactors, *Progress in Crystal Growth and Characterization,* Vol.24, 1992, pp.111-211.
68. W.J. Wang, M.H. Qiao, J. Yang, S.H. Xie, and J.F. Deng, Selective Hydrogenation of Cyclopentadiene to Cyclopentene over an Amorphous NiB/SiO_2 Catalyst, *Applied Catalysis A*, Vol.163, 1997, pp.101-109.
69. X. Zhong and J.W. Bozzelli, Thermochemical and Kinetic Analysis on the Addition Reactions of H, O, OH, and HO_2 with 1,3 Cyclopentadiene, *International Journal of Chemical Kinetics,* Vol.29, 1997, pp.893-913.
70. Z. Xue, H. Thridandam, H.D. Kaesz, and R.F. Hicks, Organometallic Chemical Vapor Deposition of Platinum. Reaction Kinetics and Vapor Pressures of Precursors, *Chemical Materials,* Vol.4, 1992, pp.162-166.
71. D. Welipitiya, C.N. Borea, C. Waldfried, C. Hutchings, L. Sage, C.M. Woodbridge, and P.A. Dowben, The Adsorption of Nickelocene. Part I, Molecular Bonding on Ag(100), *Surface Science,* Vol.393, 1997, pp.34-46.
72. G.J.M. Dormans, G.J.B.M. Meekes, and E.G.J. Staring, OMCVD of Cobalt and Cobalt Silicide, *Journal of Crystal Growth,* Vol.114, 1991, pp.364-372.
73. M.L. Hitchman and K.F. Jensen, Chemical Vapor Deposition, Principles and Applications, Academic Press, London, 1993.
74. N.R. Avery, Bonding and Reactivity of Cyclopentene on Pt (III)*, Surface Science,* Vol.146, 1984, pp.363-381.
75. G.A. Somorjai, *Chimie des Surfaces et Catalyse, Ediscience International*, Paris, 1995.
76. J.A. Venables and G.D.T. Spiller, Nucleation and Growth of Thin Films, *Surface Mobilities on Solid Materials Fundamental Concepts and Applications,* NATO ASI series, 1983, pp.341-404.
77. D.P. Adams, T.M. Mayer, E. Chason, B.K. Kellerman, and B.S. Swartzentruber, Island Structure Evolution During Chemical Vapor Deposition, *Surface Science,* Vol.371, 1997, pp.445-454.
78. R.T. DeHoff, *Thermodynamics in Materials,* McGraw-Hill, New York, 1993.
79. M. Izaki and T. Omi, Structural Characterization of Martensitic Iron Carbon Alloy Films Electrodeposited from an Iron (II) Sulfate Solution, *Metallurgical*

Material Transactions, Vol.27A, 1996, pp.483-485.

80. JCPDS Card #4-850, *Powder Diffraction Files, PDF-2 Database, International Center* for *Diffraction Data, Newton Square, PA.*
81. A. Aouni, A. Pianelli, and E. Bauer Grosse, Etude Structurale et Stabilité Thermique de dépôts $Ni_{1-X}C_X$ é1aborés par pulvérisation Cathodique, *Revue de Métallurgie,* Vol.9, 1992, p.597.
82. Saturation Magnetization follows Bloch's Relation, $M_s(T) = M_s(0)*[1-B*T^{3/2}]$ where $M_s(0)$ is the Saturation Magnetization at 0K and B is the Bloch Constant, See F. Bloch, Z. *Physics,* Vol.61, 1931, p.206.
83. Y.G. Kim, D. Byun, C. Hutchings, P.A. Dowben, H. Hejase, and K. Shröder, Fabricating Magnetic Co-Ni-C Thin Film Alloys by Organometallic Chemical Vapor Deposition, *Journal of Applied Physics,* Vol.70, 1991, pp.6062-6064.
84. K. Tamura and H. Endo, Ferromagnetic Properties of Amorphous Nickel, *Physics Letters,* Vol.29A, 1969, pp.52-53.
85. H.E. Schaefer, H. Kisker, H. Kronmüller, and R. Würschum, Magnetic Properties of Nanocrystalline Nickel, *Nanostructural Materials,* Vol.1, 1992, pp.523-529.
86. D.H. Sun, B.E. Bent, and J.G. Chen, Chemistry of Cyclopentadiene on a Cu(100) Surface, Detection of Cyclopentadienyl (C_5H_5) Species as Reaction Intermediates, *Journal of Vacuum, Science Technology,* Vol.A15, 1997, pp.1581-1585.
87. F. Van Looij and J.W. Geus, The Reactivity of Carbon-Containing Species on Nickel, Effects of Crystallite Size and Related Phenomena, *Catalysis Letters,* Vol.45, 1997, pp.209-213.
88. H. He, Y. Okawa, and K. Tanaka, Hydrogenation of Carbidic Carbon on the Ni(100) Surface, *Surface Science,* Vol.376, 1997, pp.310-318.
89. P. Finetti, R.G. Agostino, A. Derossi, A. Santoni, and R. Rosei, Hydrogenation of Carbidic Carbon on Ni(III), *Surface Science,* Vol.262, 1992, pp.1-7.
90. J.H. Sinfelt, Catalytic Hydrogenolisis on Metals, *Catalysis Letters,* Vol.9, 1991, pp.159-172.
91. Gibbs Energy Minimizer (GEMINI2), THERMODATA, Grenoble, France, 1994.
92. Scientific Group Thermodata Europe (SGTE), available on line from THERMODATA, BP 66 F-38402 Saint Martin d'HèRes, France and Royal Institute of Technology, S-10044, Stockholm, Sweden.
93. M. Karni, I. Oref, and A. Burcat, Ab Initio Calculations and Ideal Gas Thermodynamic Functions of Cyclopentadiene and Cyclopentadiene Derivatives, *Journal of Physics Chemical Reference Data,* Vol.20, 1991, pp.665-683.
94. T. Pradeep, J.S. Patrick, B. Feng, S.A. Miller, T. Ast, and R.O. Cooks, Concerted Hydrogen Rearrangement in Nickelocene Cation and The formation of NiH_2^+, *Journal of Physics Chemical,* Vol.99, 1995, pp.2941-2945.
95. L. Brissonneau, Dépôt Chimique en Phase Vapeur De Couches Minces De Nickel à Partir De Précurseurs Métal-Organiques Ph.D. Thesis #1500, Institut National Polytechnique De Toulouse, France, 1998.
96. E. Hedaya, The Techniques of Flash Vacuum Pyrolysis. The Cyclopentadienyl Radical and its Dimer, *Accounts for Chemical Research,* Vol.2, 1969, pp.367-373.
97. D.K. Russel, Gas-Phase Pyrolysis Mechanisms in Organometallic CVD, *Chemical Vapor Deposition,* Vol.2, 1996, pp.223-233.
98. D.L. Pugmire, C.M. Woodbridge, and M.A. Langell, Orientation of Nickelocene on Ag (100), *Surface Science Letters,* Vol.411, 1998, pp.L844-L848.
99. O.N. Druzhkov, Y.A. Andrianov, and L.M. Diagyleva, Mass Spectra of Dicyclopentadienyinickel and Bis (Isopropyleyclopentadienyl) Nickel, *Zhurnal Obshchei Khimii,* Vol.47, 1977, pp.1836-1841.

Chemical Vapor Deposition
Jong-Hee Park, T.S. Sudarshan, editors, p331-377
DOI:10.1361/chvd2001p331

Chapter 10

CVD Diamond, Diamond-Like Carbon, and Carbonitride Coatings

Priyadarshini Karve
Department of Applied Physics, Sinhagad College of Engineering
Sinhagad Technical Education Society
Wadgaon Budruk, Pune 411 041, India

J. Prabhjyot Pal
Physical and Materials Chemistry Division
National Chemical Laboratory, Pune 411 008, India

S.B. Ogale
Department of Physics and Department of Materials Science
University of Maryland, College Park, MD 20742

Preamble

The advantage of thin films and coatings in imparting desired properties to the surface of a relatively unimportant substrate material is well established. This aspect of the thin film and coating technology has a tremendous scope in tribology. The possibility of coating a tool surface with a hard wear resistant coating to enhance tool life is a highly attractive proposition.

Diamond, which is the hardest known material, is a natural choice for tribological application. In fact, this has been one of the major motivating factors to develop the synthesis of this unique allotrope of carbon in the thin film form. Today, diamond thin films and coatings are considered to be technologically important to a wide variety of applications due to their remarkable combination of extreme properties.

Many new phases of carbon have been discovered as an offshoot of attempts of artificial synthesis of diamond. Among these, a class of amorphous carbon and hydrocarbon phases exhibits properties close to those of diamond. These diamond-like phases are therefore considered to be promising technological materials.

Among the various compounds of carbon, the carbides of different elements have a special significance from the tribological point of view. Many of these materials, for instance WC, SiC, and TiC, are mechanically hard and have found use in the tribological industry. The carbonitride (or what can also be called the carbide of nitrogen) is an important constituent of this class of materials. In the last decade or so, the theoretical prediction of crystalline carbonitride phases that could be harder than diamond has generated much interest in the synthesis of this material.

CVD Diamond

Introduction

Diamonds were first discovered in India as early as about 800 BC. The early diamond mines were the alluvial gravel in the banks or beds of active or dried up rivers in which diamond and other heavy and hard crystals had been concentrated by the action of the flooding water. The most famous Indian mine was at Kollur near Hyderabad where several historical diamonds (the chief among them being the *Koh-i-Nur*) were found. Although most of the Indian diamond mines dried up by the 18th century, the mines at Panna in Madhya Pradesh are still operational and some new fields in the vicinity are soon to be opened for commercial exploitation.

Fortuitously, just as India's supply of diamond was running out, deposits were discovered in Brazil and just as Brazil's were nearly exhausted, huge supplies were found in Africa. Today the African continent is the major supplier of natural diamond to the world. Most gem diamonds come from the coastal deposits in South West Africa whereas Zaire and Angola mines yield industrial quality diamonds. Sizable deposits have also been discovered in Siberia in the erstwhile U.S.S.R in the 1950's, and in northwest Australia in the 1970's. In the 1990's, large diamond deposits have been discovered in northern U.S.A and are estimated to last for about 12 years.

In the early days diamonds were chiefly considered as precious stones to be used for decorative purposes as well as for financial transactions. There are historical evidences to indicate that diamond grit was being used for polishing gem diamonds and for cutting and engraving on glass in the 16th century. But today diamond has proved itself to be a giant among materials not only as a decorative gemstone or as an abrasive tool but also from the scientific and industrial point of view, by virtue of an astonishing combination of a variety of extreme properties.

Diamond is the purest and crystallographically the most perfect substance that occurs in nature though composed of one of the commonest elements on earth, i.e., carbon. It is the hardest natural material and yet can be broken with the blow of a hammer. It can withstand attack by the strongest chemicals and harshest radiation and yet thermodynamically it is metastable. It is the best thermal conductor as well as a good electrical insulator.

Unfortunately, in spite of its immense usefulness, widespread use of diamond in industry has been prevented by its rarity. Even with modern mining techniques, on an average, 250 tons of host rock must be mined and processed in order to produce 1 carat of diamond.[1] As a result, since ancient times, attempts have been made to synthesize this material.

Towards the end of the 18th century a British chemist, Smithson Tennant, showed that diamonds are composed of nothing but carbon a discovery that gave a more scientific direction to synthesis efforts. By the beginning of the 19th century, it was known that carbonaceous materials, heat and pressure are required for diamond formation. Finally, success in artificial synthesis was achieved in the middle of the 20th century by two routes: the High Pressure High Temperature (HPHT) route leading to the formation of diamond grit and the Low Pressure

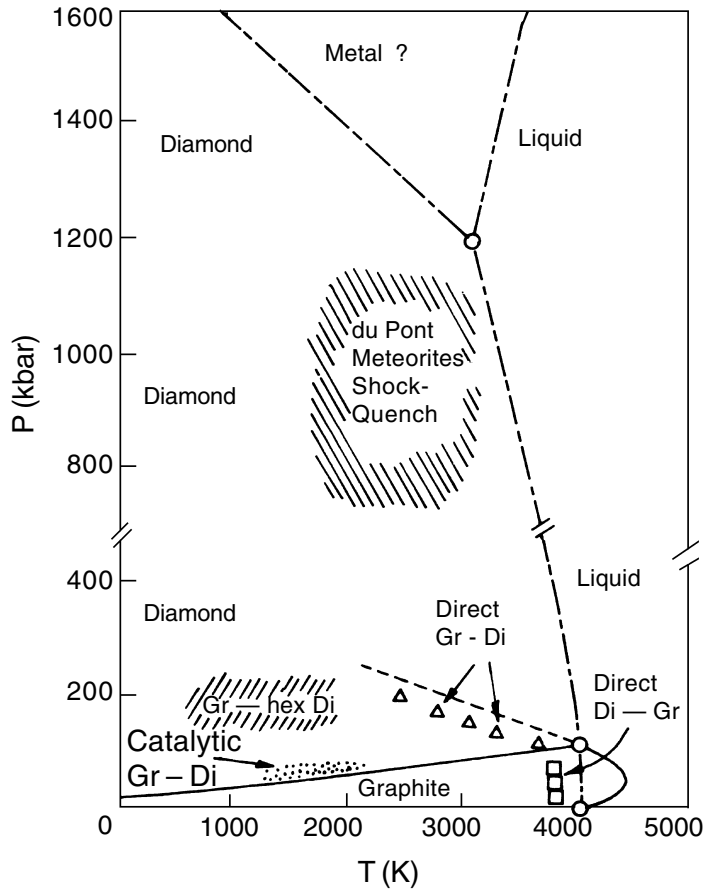

Fig. 1: Phase diagram of carbon.[3]

Low Temperature (LPLT) route leading to the deposition of polycrystalline films of diamond on nondiamond substrates. The HPHT route has also been used for making gem quality diamond stones of different colors.[2] This route involves subjecting graphite to high pressure and high temperature (i.e., conditions at which diamond is thermodynamically the more stable form of carbon than graphite) in the presence of a metal such as iron, nickel, cobalt, manganese, and chromium or tantalum to act as a solvent as well as a catalyst. The LPLT methods, on the other hand, involve low pressure deposition of diamond from the vapor phase. The thermodynamic conditions favoring diamond formation, corresponding to both these routes are presented in the phase diagram of carbon[3] depicted in Figure 1.

The realization of the LPLT route has opened up a wide vista of exciting probable applications for diamond. This is because it offers the novel possibility of obtaining diamond as thin films, coatings or even as free standing thin sheets, ribbons, and tubes.

Low Pressure Low Temperature Synthesis of Diamond

The growth of diamond on diamond seed crystals from low pressure low temperature decomposition of acetylene in the presence of mercury vapor was reported by von Bolton as early as 1911, but the claim went unnoticed for nearly half a century. Systematic studies of the vapor synthesis of diamond began in 1950's.[4,5]

Pioneering work in this field was done by Eversole in the U.S.A who patented a low pressure vapor synthesis process in 1958 and also by a Russian research group headed by Derjaguin. The processes developed in the early days involved thermal decomposition of hydrocarbons or hydrogen + hydrocarbon gas mixtures, the substrate was diamond and the process involved many cycles of growth followed by etching to remove the excessive graphitic deposits. Eversole's process involved etching by hydrogen at a temperature above 1000°C and pressure above 50 atm. The Russian group used oxidation in air at atmospheric pressures to remove the graphite.

In spite of the success achieved, interest in the field remained limited due to very low growth rates (a few Å/sec) and co-deposition of a large quantity of graphite. In the U.S.A., Eversole's work was continued by Angus, laying the groundwork for a better understanding of the processes involved in the vapor growth of diamond.[6,7] Meanwhile, Derjaguin demonstrated the use of gas activation techniques leading to a dramatic increase in diamond growth rate and reduction in graphite co-deposition.

In 1976, Derjaguin, Spitzyn and Bouilov showed that diamond nucleation is possible on nondiamond substrates such as copper. This proved to be a major breakthrough attracting the attention of the entire materials science community towards this field. In the early 1980's a team of scientists led by Matsumoto in Japan demonstrated the nucleation and continuous low pressure growth of good quality diamond on various nondiamond substrates using different gas activation techniques. This set off an intensive research activity in Japan, Western Europe and the U.S.A.[8] Since then a number of experimental procedures for producing well-crystallized diamond have been demonstrated. Since the last decade or so, scientists all over the world have actively taken up research in this field.

Synthesis Techniques

Most of the synthesis techniques used for diamond deposition fall in the category of chemical vapor deposition, using a dilute mixture of a carbon containing gas in hydrogen as the starting material. There are a few techniques based on the principle of physical vapor deposition, generally using graphite as the carbon source, but so far these methods have enjoyed limited success.

All the major CVD techniques for producing diamond films involve pyrolysis of a carbonaceous gas and simultaneously activation of the gas phase to produce a selective etchant such as atomic hydrogen to remove nondiamond carbon phases from the growing film. The various techniques differ mainly in the means used for gas activation. Some basic activation techniques that have been used by various researchers involve:[9]

1. Activation by high temperature: hot filament/hot surfaces, laser heating, arc discharge and arc plasma jets, chemically induced hot gas flames, etc.
2. Activation by electric or electromagnetic gas discharge: microwave and radio frequency discharge, DC and AC glow discharge, plasma jets induced by RF, microwave, DC, systems involving alteration of activated gas volumes and surface areas by magnetic confinement or other methods, etc.
3. Combinations of 1 and 2 : HF + microwave, HF + DC discharge, HF + bias, e.g., electron assisted CVD, etc.

Some commonly used CVD systems are schematically shown in Figure 2.

Each deposition method has its own advantages and drawbacks, and therefore the choice of the method depends on the end use of the deposit. For instance, Hot Filament CVD (HFCVD) is considered to be a good choice for coating diamond on cutting tools for tribological applications. For optical and electronic applications, where phase purity is critically important, Microwave Plasma CVD (MPCVD) is considered to be more suitable. Bulk polycrystalline diamond pieces for thermal management applications are more easily fabricated using high rate deposition methods such as DC or RF plasma torch or combustion flame. The various diamond deposition processes are summarized and compared in Table 1.[10]

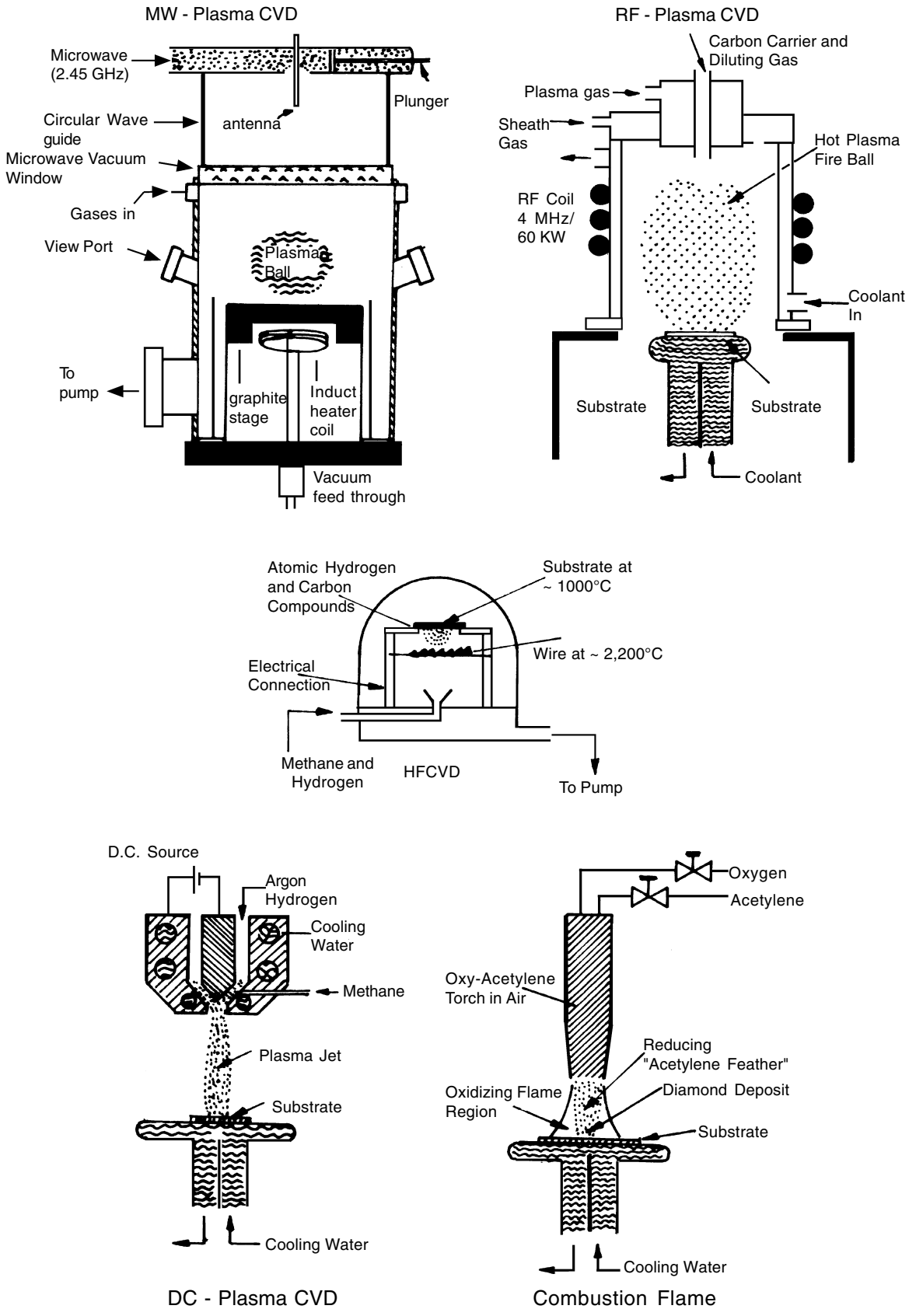

Fig. 2: Schematic representation of diamond CVD systems.

Table 1. CVD Diamond Processes[10]

Method	Dep. Rate (mm/hr)	Dep. Area (cm^2)	Quality (Raman)	Advantages	Drawbacks
Flame	30-100	< 1	+++	Simple	Area, Stability
Heated Filament	0.3-2	100	+++	Simple, Large Area	Contamination, Stability
Low Pressure DC Discharge	< 0.1	70	+	Simple, Large Area	Quality, Rate
Medium Pressure DC Discharge	20-250	< 2	+++	Rate, Quality	Area
DC Plasma Jet	930	< 2	+++	Highest Rate, Quality	Area, Stability, Homogeneity
Low Pressure RF	< 0.1	?	-/+	Scale Up	Quality, Rate, Contamination
Thermal (1 atm) RF	180	3	+++	Rate, Quality	Area, Stability, Homogeneity
Microwave (0.9-2.45 GHz)	1 (Low Pressure) 30 (High Pressure)	40	+++	Quality, Stability, Reasonable Rate, Area	Rate, Area
Microwave (ECR 2.45GHz)	0.1	< 40	-/+	Area (?), Low Pressure	Quality, Rate, Contamination

Another approach to diamond synthesis involves energetic ion or laser beams to produce local areas where, for short duration, carbon atoms are subjected to pressure and temperature conditions that reach into the diamond stable region of the carbon phase diagram. After rapid quenching to ambient temperature and pressure, diamond thus formed remains metastable with respect to graphite. Attempts to deposit diamond by such techniques have been only moderately successful.

Polycrystalline diamond formation has been reported using high energy (a few tens of keV) carbon ion implantation in diamond[11-13] or suitable nondiamond substrates,[14-16] by ion beam deposition using carbon ions,[17] by low energy (< 1 keV) implantation with carbon or methane ions,[18-20] by ion beam sputtering of graphite,[21] by DC magnetron sputtering of a vitreous carbon target in Ar + H_2 plasma,[22] etc.

Laser-induced phase transformation from graphite to diamond was first achieved by the Russian group of Derjaguin et al., by irradiating ultrafine graphite powder with a CO_2 laser beam, and was later confirmed by Roy et al.[23] Various other researchers have reported diamond synthesis by similar techniques (e.g., 24-27). Diamond formation by laser ablation of graphite too has been claimed (e.g., 28, 29).

Recently a new technique has been reported under the name of the QQC process.[30] It utilizes a combination of lasers and does not require vacuum, H_2 ambient or substrate pretreatments. The main source of carbon is CO_2 and the films have been deposited on different metal and ceramic substrates.

Characterization of Diamond Coatings

The vast variety of allotropic forms available for carbon along with the crystal size variation within crystalline phases necessitates a precise definition of diamond, but also makes

it extremely difficult to formulate. A working definition was suggested by Messier et al.[31] According to this definition, diamond deposition is confirmed by:

1. A crystalline morphology visually discernible by electron or optical microscopy,
2. A single phase polycrystalline structure identified by x-ray or electron diffraction, and
3. A laser Raman spectrum typical of natural diamond, i.e., the presence of the Raman active line at 1332 cm^{-1}.

Various characterization techniques are used to evaluate the quality of diamond coatings on the basis of the criteria put down in this definition. Broadly the major categories of CVD diamond analysis include chemical characterization, i.e., identification of the different carbon phases in terms of composition and bonding, and physical characterization, i.e., investigation of structural and morphological properties such as defects and interfaces. The most commonly used techniques are laser Raman spectroscopy, scanning electron microscopy and x-ray diffraction.[32] Examples include XRD analysis and Raman spectrum of a polycrystalline diamond film grown by HFCVD technique and oriented diamond film grown by MPCVD technique.[33] Scanning electron microscopy is used to characterize the morphology of a polycrystalline and (100) oriented film.[34]

Chemical Vapor Deposition of Diamond

The processes involved in the low pressure synthesis of diamond are not yet clearly understood, but various models have been proposed on the basis of thermodynamic and / or chemical kinetic considerations and a number of *in situ* as well as *ex situ* diagnostic studies. Figure 3 is a schematic representation of the diamond deposition process as it is understood today.[35]

The following 11 criteria are generally accepted guidelines for the CVD of diamond films.

Criterion 1

The reaction gases used must contain relatively low concentrations of volatile carbon compounds (typically about 1-2% by volume) with a high excess of hydrogen.

In vapor deposition of diamond, growth occurs at the gas-solid interface in a carbon-hydrogen system and not in an elemental carbon system. Under these conditions diamond growth is favored because a diamond surface saturated with hydrogen is more stable than a carbon surface free of hydrogen, i.e., a graphitic deposit.[8] Once a diamond layer is buried under another growing diamond layer, it is metastable with respect to graphite.

Hydrogen influences the CVD of diamond in many ways.[36]

In the gas phase, atomic hydrogen is necessary to initiate the gas phase chemical kinetics for production of the reactive hydrocarbonaceous radicals required for carbon deposition by the following reactions.

$$CH_n + H \leftrightarrow CH_{n-1} + H_2$$
$$CH_n + CH_{n'} \leftrightarrow C_2H_m + xH$$

Atomic hydrogen is also critical to surface reactions leading to diamond deposition. It stabilizes the diamond nuclei by passivating the dangling bonds to form the more stable hydrogen saturated diamond surfaces. It also produces vacant sites for attachment of the hydrocarbonaceous radicals onto the diamond surface, enabling the film to grow. Furthermore, atomic and molecular hydrogen present in the CVD environment act as solvents for graphite. The rate at which graphite is etched by hydrogen is several orders of magnitude faster than that for diamond. Atomic hydrogen can also repair sp^2 bonded defect structures in the growing film.

Figure 4 shows the SEMs of diamond deposition on Si(100) substrates under identical HFCVD condition, except for the ambient deposition pressure. The cauliflowerlike growth in (a) corresponds to the deposition pressure of 80 Torr, whereas the better faceted growth in (b) corresponds to a pressure of 20 Torr. This clearly indicates the importance of the concentration of atomic hydrogen reaching the substrate surface in deciding the diamond film quality. The chance that the hydrogen atoms produced near the

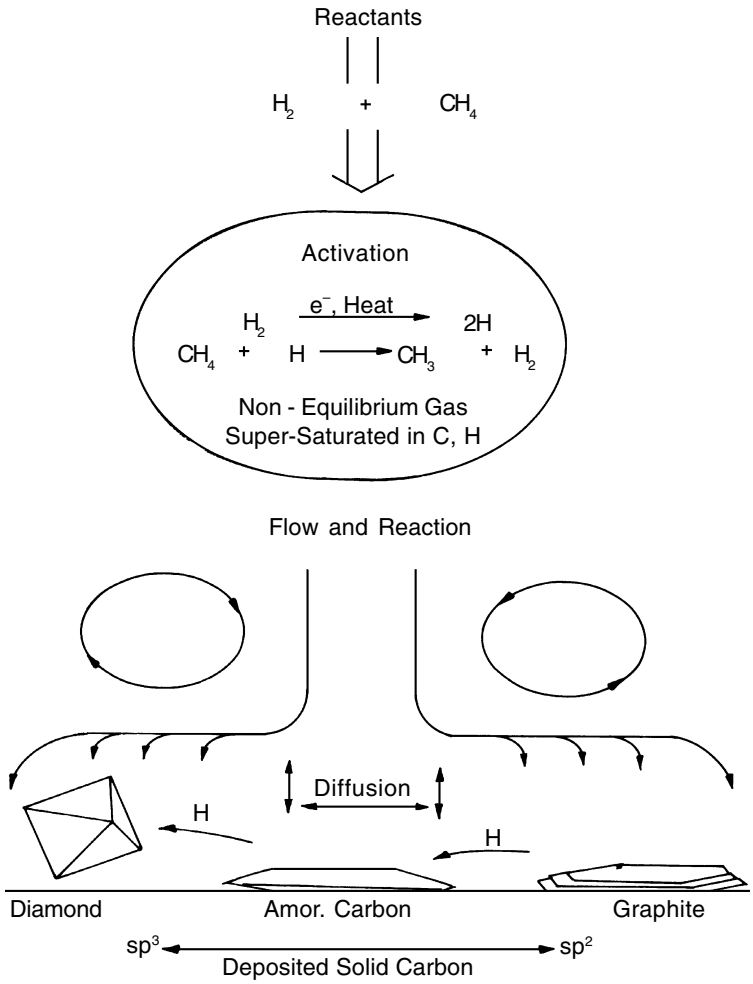

Fig. 3: Schematic representation of diamond deposition process.[35]

filament will recombine before reaching the substrate is higher for the case of the higher ambient pressure of 80 Torr.

Various studies (e.g., 37-46) have shown that the role of atomic hydrogen can also be served by atomic oxygen, OH radicals, atomic halogens, etc., which can be termed H atom surrogates. As a result, addition of small quantities of the source materials of these radicals to the source gas mixtures has been observed to be beneficial for diamond CVD.

Criterion 2

Appreciable CVD diamond growth rates cannot be achieved without some form of gas activation.

In the early experiments of thermal CVD using methane + hydrogen gas mixtures, a temperature of about 1000°C and a pressure less than 0.1 atm meant that the formation of graphite was predominant.[8,47] An activation energy is required to produce carbon and/or hydrogen radicals so that the gas phase and surface reactions leading to predominantly diamond deposition can proceed at a significant rate.[48]

Criterion 3

The chemical nature of the carbon source does not seem to be critical to the nucleation density, growth rate or quality of the deposit.

A number of studies (e.g., 49,50) have shown that the relative concentrations of the

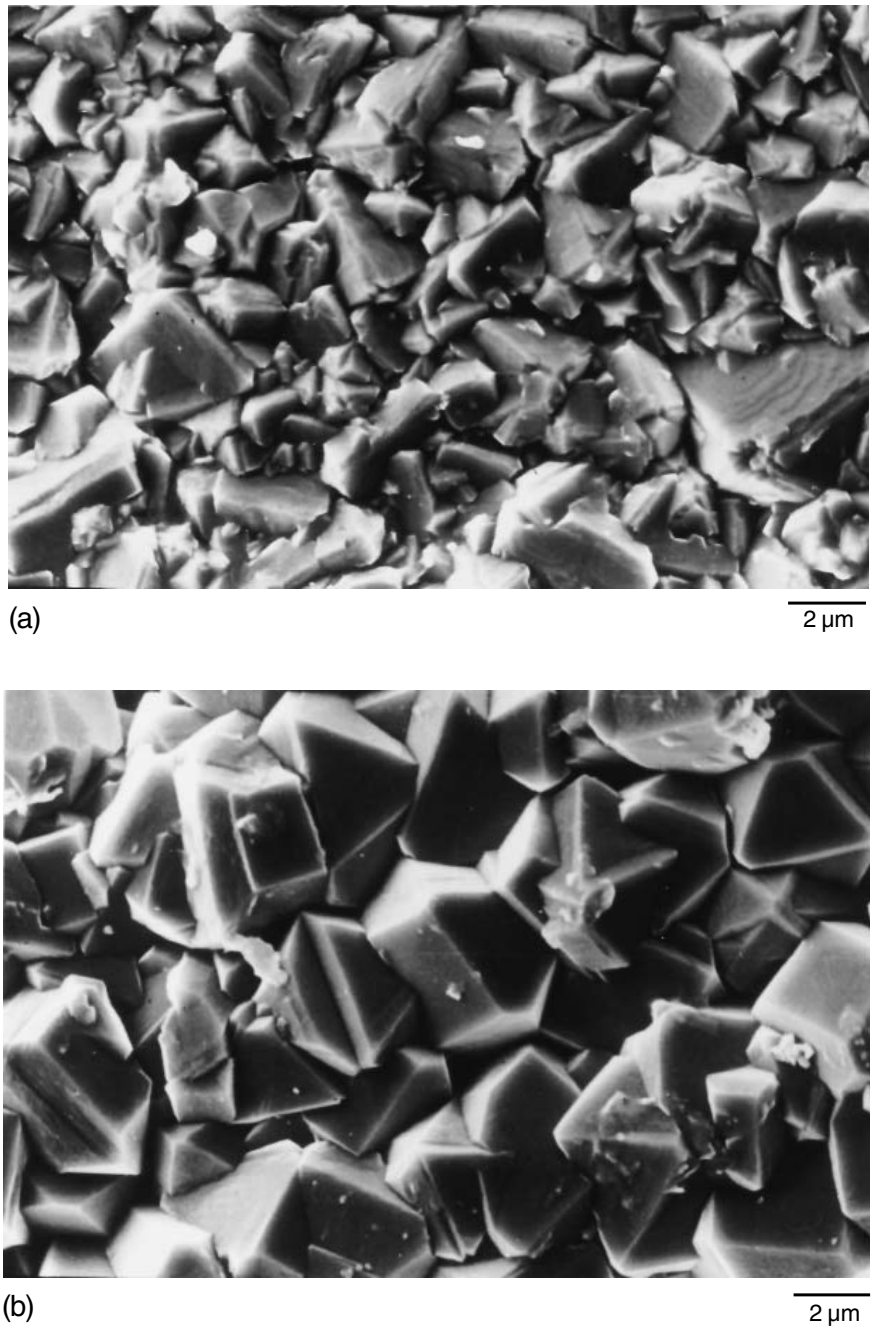

Fig. 4: SEMs of diamond films deposited on Si(100) substrates, under identical HFCVD conditions, except for ambient deposition pressure, (a) 80 Torr and (b) 20 Torr.

different stable hydrocarbon species and their dependence on temperature are both insensitive to the choice of precursor gas. Bachmann et al.[51] have suggested that irrespective of the starting molecular gas composition, diamond deposition is possible as long as the C-H-O composition falls within a narrow domain of an atomic C-H-O phase diagram that provides the common basis for all low pressure diamond CVD methods. The phase diagram is shown in Figure 5.

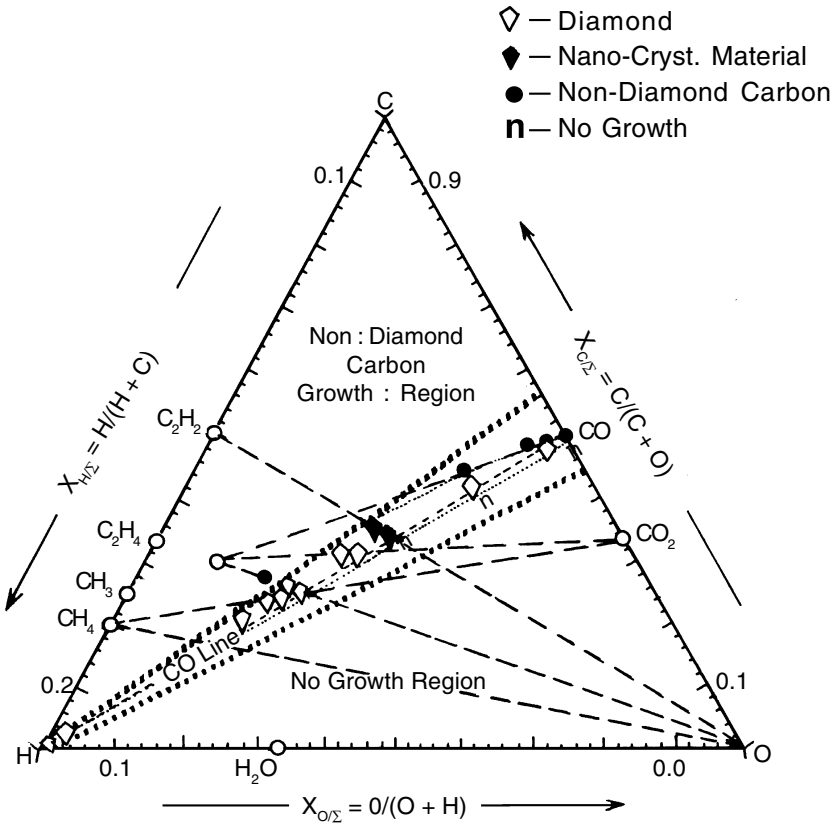

Fig. 5: C-H-O phase diagram.[51]

On similar lines, diamond deposition regions have been calculated in C-H-O-F and C-S-F phase diagrams, for gas mixtures containing chlorinated or fluorinated hydrocarbons, halogens and other agents of proper composition.[52]

The various carbon sources that have been used so far include methane (which is the most commonly used source), acetylene, alcohols, amines, ethers, carbon monoxide, etc.,[53] as well as, vapors of different hydrocarbon liquids, e.g., propylene oxide (C_3H_6O), 1,3-dioxolane ($C_3H_6O_2$) and dimethylcarbonate ($C_3H_6O_3$).[54]

Criterion 4

Diamond growth comes mainly from single carbon radicals such as methyl and/or acetylene.

Various *ex situ* as well as *in situ* diagnostic studies of activated gas mixtures in different deposition systems[55-57] as well as chemical kinetics calculations[37,58,59] have attributed diamond growth to single carbon radicals such as methyl and/or acetylene. The results of actual experiments[50-62] as well as the theoretical models[63,64] of CVD diamond growth have indicated that CH_3 is the dominant growth species, and for essentially identical temperature and pressure, the rate of diamond formation and its quality are significantly lower for C_2H_2 growth species.

Criterion 5

Nucleation from the vapor phase is not a determining factor in the relative kinetics of formation of either graphite or diamond on a substrate. Which of these two competing structures wins out depends on the kinetics of growth.

If the rate of impingement of atoms onto the growing phase is about the same for both

structures and the attachment step is not the rate controlling step, then the most stable polymorph should win. It has been suggested[65] that even though graphite has the lower bulk free energy, as a thin film it is possible that on suitable substrates the diamond structure will yield lower free energy for the substrate-film combination. The reason for this could be that the contribution of the interface energies to the difference in total free energy between the two substrate-film systems is a significant deciding factor.

There are two schools of thought regarding the question why well crystallized diamond is formed in CVD.[66] According to one school, graphite is etched by hydrogen at a rate higher than diamond. Thus diamond is kinetically stable with respect to graphite. In this case, the deposition mechanism and species involved are the important factors. However, this mechanism does not explain the dependence of deposit quality on the substrate properties. According to the second school, diamond surfaces are stabilized by termination with hydrogen. Any of the three principal low-index surfaces of diamond, if hydrogenated, have lower heats of formation than any of the low-index planes of hydrogenated graphite or lonsdaleite. Thus the bulk instability of diamond is irrelevant. If the nature of the deposited carbon is controlled by the structure of its surface during growth, the issues of interest involve (a) which surfaces lead to lowest free energy and (b) how equilibrium between the substrate and the deposit are influenced by the deposition parameters.

None of the two approaches can explain all the experimental data satisfactorily and it is generally believed that a combination of both mechanisms is prevalent during diamond CVD.

Criterion 6

Many substrate materials have been used for diamond deposition. They can be loosely classified into three groups:

- Diamond crystals,
- Carbide forming materials and their carbides (Si, Mo, W, SiC, WC, etc.,
- Materials that do not interact with carbon (Cu, Au).[67]

Diamond nucleation on nondiamond substrates seems to be prevented only if the carbon is too rapidly removed by diffusion into or by chemical reaction with a particular substrate. A stable surface with respect to carbon atoms is the key factor for nucleation. A study of diamond nucleation on metal substrates[68] revealed that dense and uniform nucleation occurs on substrates like copper and platinum that have no interaction with carbon and therefore represent a stable surface. Substrates like iron have a distinct solubility for carbon and carbon diffuses into the substrate until it is completely saturated. As the time to reach saturation is dependent on the substrate thickness, this can significantly delay the onset of diamond nucleation. As far as the carbide forming substrates such as silicon, tungsten, etc., are concerned, the carbon atoms arriving onto the substrate react with the substrate surface to form a surface carbide layer which thereafter acts as the stable barrier to further diffusion of carbon into the substrate. Due to the high stability of the carbide and low solubility of carbon in these substrates, the incubation period in this case is relatively small.[69] Figure 6 shows the SEMs of diamond deposition on copper (non-reacting) and chromium (carbide-forming) substrates. The copper-diamond interface is sharp suggesting that the deposited carbon has contributed almost exclusively to diamond growth, whereas the chromium-diamond interface distinctly indicates deposition of an intermediate layer before onset of diamond growth.

The carbon atoms arriving at the substrate surface must exceed a certain concentration at the solid-gas interface to reach and exceed the critical nucleus size. Therefore the diamond nucleation density as well as the growth rate are dependent on the relative rates of bulk and surface diffusion of carbon atoms.[69,70] These are different for different substrates. Thus, the nucleation process needs a temperature dependent incubation time which is related to the time required to form critical size diamond clusters on the substrate surface. The nucleation rate, which is initially negligible, reaches a maximum after a certain time period and tends to zero for longer deposition times.[71]

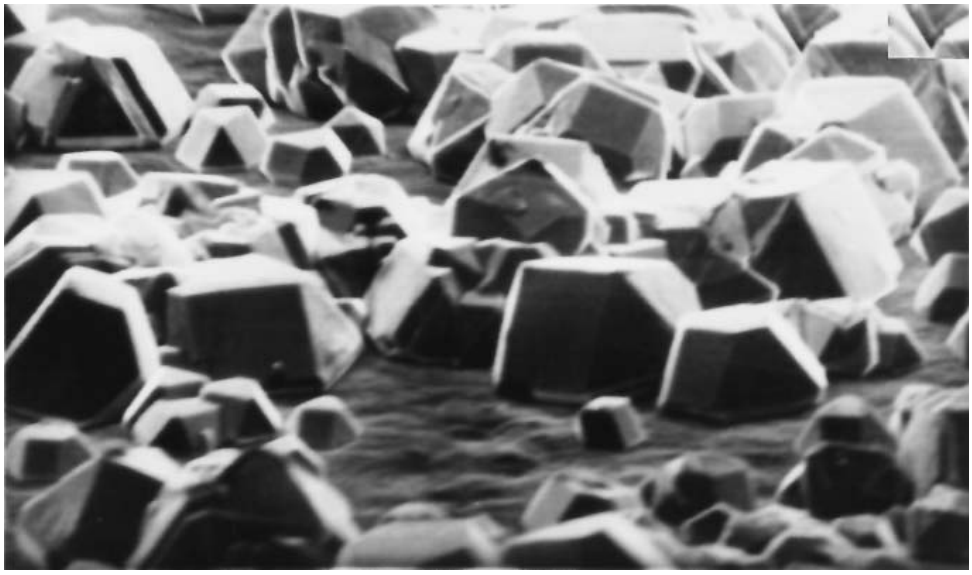

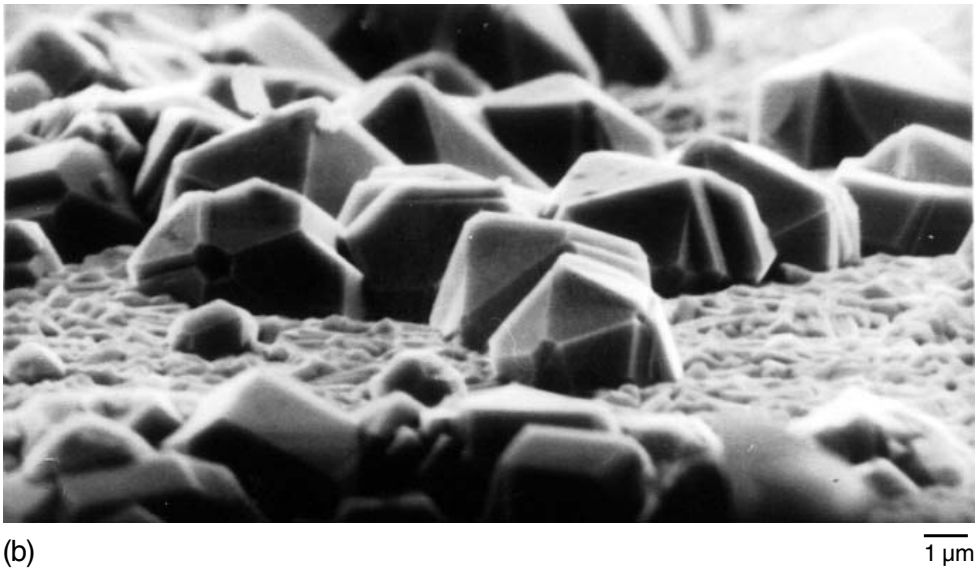

Fig. 6: SEMs of CVD diamond films on (a) copper and (b) chromium.

Criterion 7

For high quality diamond film formation the substrate temperature has to be between 800°C and 1100°C.[53]

The upper temperature limit for the vapor growth of diamond is determined by the kinetics of the diamond-to-graphite solid state transformation and how these kinetics are influenced by structural imperfections. The thermodynamics of the deposition process place a lower limit on the deposition temperature depending on the gas concentration-pressure

combination being used in a particular setup.[8] The crystalline or amorphous growth from the vapor phase is balanced by the rate of arrival of the precursors from the gas phase and the rate of their diffusion across the substrate surface. While the gas phase parameters decide the rate of arrival, the substrate temperature influences the rate of surface diffusion and therefore the growth microstructure.[72] The crystal morphology of the film has been shown to depend on the substrate temperature within the optimal range.[73]

However, a number of researchers have reported deposition of good quality diamond films at much lower substrate temperatures using oxygen containing gas mixtures (e.g., 74-77). Stiegler et al.[78] have shown that the low temperature limit of diamond growth is mainly influenced by the carbon content in the gas mixture, allowing a reduction of the growth temperature by reducing the carbon source gas concentration. It has been shown[75,78] that etching by the additional oxygen compensates for the increased nondiamond carbon deposition at the reduced substrate temperature.

Criterion 8

Various substrate surface pretreatments have been reported to increase nucleation density.

Because of the long incubation period involved in the formation of a stable surface before onset of nucleation, the nucleation density observed on most substrates, for practically feasible deposition periods, is too little. Different substrate pretreatments have been attempted to improve the nucleation density.

The most common technique involves abrading the substrate surface with hard powders (preferably diamond), or ultrasonic treatment in a slurry of an abrasive powder (preferably diamond grit) in an organic liquid for a prolonged period. This type of pretreatment leads to embedding of the abrasive particulates into the surface as well as mechanical damage to the substrate, both of which are believed to enhance the nucleation density.[79-81] The maximum nucleation enhancement is observed when diamond grit is used, and this has been attributed to implantation of diamond particles into the substrate surface. Considerable enhancement in diamond nucleation has also been observed on substrates pretreated in a bed of diamond particles fluidized by nitrogen gas.[82] However mechanical abrasion of the substrate during the surface pretreatments is undesirable in many applications (e.g., semiconductor electronics), hence nucleation enhancing buffer layers have also been used.[83-88]

A bias nucleation process has been developed to overcome the problem of the low diamond nucleation density on untreated nondiamond substrates wherein a negative bias is applied to the substrate during deposition.[89-92]

Criterion 9

The nuclei are randomly distributed, the distribution depending on the balance between the flux of the arriving carbon atoms and the carbon diffusion rate.

The growth of nuclei first leads to formation of individual rapidly growing crystals. The nuclei form either single or bicrystals exhibiting reentry corners, growth spirals and growth steps for easy atomic attachment. Once the optimal nucleation density (in accordance with the surface diffusion rate) has reached the minimum distance between near neighboring crystals, no further individual nuclei are formed. However, existing crystals continue to grow in all directions until they touch and form a layer. Bulk diffusion controls the number of nuclei, and the period required to reach the necessary minimum concentration for nucleation, whereas surface diffusion determines the distance between a nucleus and its near neighbors. In early growth stages, small crystals are liable to be redissolved if the bulk diffusion rate is high. In short, the films are formed by a two step process, the growth of individual crystals followed by the growth of the layer.[9]

An *in situ* characterization study of HFCVD deposition[93] has suggested that three kinetic periods are involved in diamond deposition: firstly, an incubation period, secondly, a limited diamond growth period and finally an unlimited diamond growth period. It has been shown that[94] three mechanisms of particle formation are operational during diamond CVD.

a. In the early stages, a Guassian type distribution of particle size develops. With time the group shifts towards larger diameters without significant broadening or change of population. This group of particles does not seem to have any preference for specific growth sites.
b. Thereafter, a second group of particles appears at the low end of the size scale, nucleated preferentially along the scratches produced during surface pretreatment. The growth rate of these particles is slow leading to a bimodal size distribution.
c. In the later stage of substrate coverage, there is an avalanche of particle formation.

It has been proposed that both sources 1 and 2 particles originate from the diamond residue left from the surface pretreatment. Source 1 particles grow from large size seeds. The scratches may contain smaller seeds which grow at a lower rate to give source 2 particles. Source 3 particles form close to larger particles approaching each other. This may be due to minute diamond residues acting as nuclei for new growth, or to faster carbon diffusion from the diamond deposit increasing the local carbon concentration.

Criterion 10

The crystallographic morphology of the films exhibits dominance of cubic {100} and octahedral {111} surfaces and {111} twin planes. Cubo-octahedra exhibiting both {100} and {111} surfaces are common.

Crystal surfaces are either rough surfaces with zero step free energy or flat surfaces with positive step free energy. The rough crystal faces grow by random addition of growth units whereas the flat faces grow layerwise. Due to the finite step free energy in the case of the flat face, an activation barrier has to be overcome to form a new growth layer. Therefore flat faces are also the slowest growing faces. In the case of diamond, both {100} and {111} are the flat faces. Because the morphology of a crystal is determined by the slowest growing faces, these are the dominant surfaces observed in CVD diamond.[95]

The ratio of total surface energy to volume is the most important factor in determining the morphology at the nucleation stage. The lowest ratio is exhibited by an octahedron composed of {111} planes. Therefore the initially formed crystal is octahedral, which is the equilibrium shape. At the growth stage the important factor is the specific surface energy of each growing plane. Therefore the growth shape is dependent on the relative growth rate of constituent planes which in turn depends critically on the growth conditions.[96-98] Figure 7 shows the variation in crystal shapes with the ratio of growth rates for the <100> and <111> axes.[99]

The <111> penetration twins on both {100} and {111} faces of the CVD diamond crystals have been identified and they have been shown to play a major role in determining the film morphology.[99-100]

Criterion 11

Homoepitaxy of diamond is possible whereas heteroepitaxy is difficult but not impossible.

Several researchers have reported successful deposition of homoepitaxial diamond films on natural as well as HPHT diamond substrates (e.g., 101-104).

Heteroepitaxy of diamond on c-BN has been successful (e.g., 105,106) due to the identical crystal structures with a close lattice match (only 1.3% mismatch) between the two and the high surface energy (~ 4.8 J/m^2) of the c-BN (111) plane.[66,107] The heteroepitaxy of diamond on silicon could be the key to electronic device applications of diamond. However, diamond has a large lattice mismatch with silicon (52%) and a much higher surface energy than silicon (6 J/m^2 for diamond, 1.5 J/m^2 for silicon). In spite of this, there are several reports of oriented diamond film deposition on substrates like silicon, silicon carbide, etc., by various techniques (e.g., 108-112).

Exciting Application Possibilities for Diamond Coatings

The crystal structure of diamond combined with the strong interatomic chemical bonding accounts for most of its unique properties. Although the properties of CVD diamond are slightly inferior to those of natural single crystal diamond (due to the presence of nondiamond

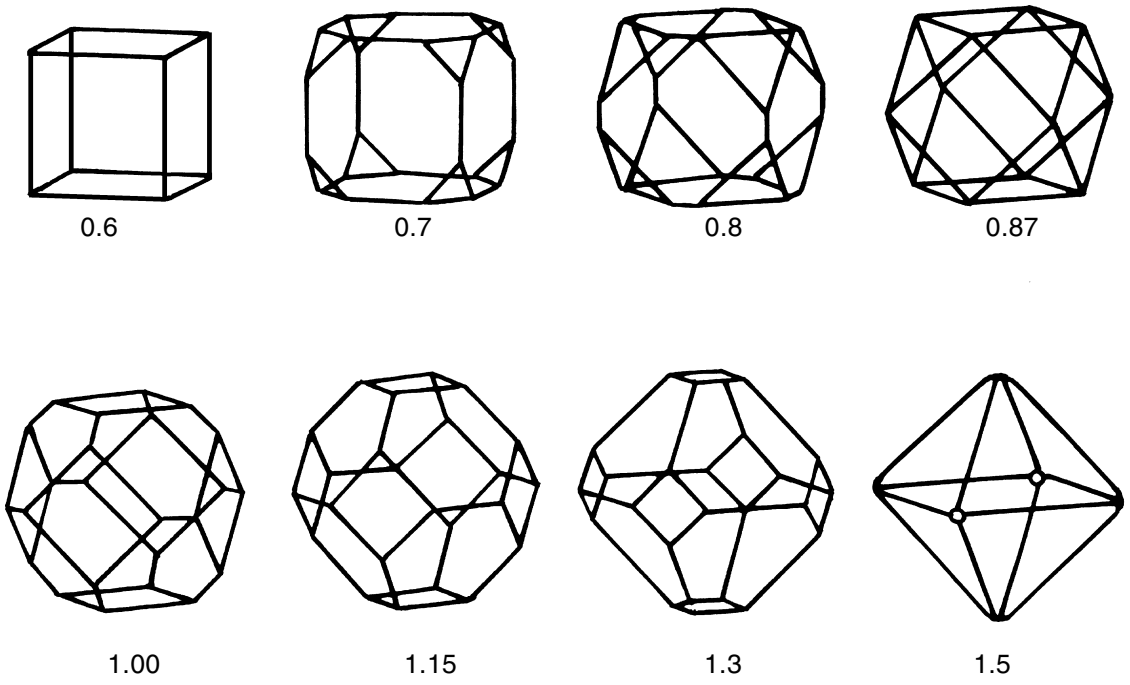

Fig. 7: Cubo-octahedral shapes for different values of <100> growth rate/<111> growth rate.[99]

carbon and the polycrystalline nature of the film), the advantages of the thin film formed onto a nondiamond substrate, more than compensate for the shortcomings.[113,114] CVD technology has the potential to coat diamond onto aircraft turbine blades, microprocessor chips, surgical instruments, LEDs and innumerable other substrates. Consequently a number of potential uses are envisaged from super computer heat sinks and heat seeking missile windows to gourmet knives. A comparison of the properties of diamond with other competing materials and the possible applications for CVD diamond are listed in Table 2.[115]

Due to its extreme hardness, diamond has long been used for cutting, drilling, mining and milling everything from the hardest rock to the softest aluminum. The advent of HPHT synthesis methods led to the concept of Polycrystalline Diamond (PCD) tools, and diamond coating synthesis methods have brought in the concept of applying diamond coating to the cutting edge of a hard nondiamond tool. The cutting performance of the PCD tools and the comparatively cheaper diamond coated carbide tools with good quality adherent diamond films are comparable.[116] For good adhesion between diamond film and a tungsten carbide tool surface, diamond "anchoring roots" are embedded between the carbide grains.[117] Another possible application for polycrystalline diamond coatings is decorative, scratch or wear resistant and corrosion resistant surfaces to be used for industrial, medical, optical, chemical and other applications.[118]

Diamond has potential application as human implant coatings because it fulfills the main requisites for use in human implants: biocompatibility and chemical stability. *In vitro* studies of stimulation of human monocytes by diamond particles have shown encouraging results.[119] Diamond coatings have been deposited on surgically implantable substrates such as ceramics used in dental implants,[120] stainless steel, titanium and molybdenum used for prosthetic devices,[121] etc.

There are an increasing number of applications that require a material with high

thermal conductivity as well as high strength and minimum weight. e.g., Aerospace applications include heat exchangers in hypersonic vehicles operating over a wide temperature range of 20-930°C, cooling fins in space power systems operating upto 780°C. In electronics, high performance multichip modules involve power density levels difficult to cope with using conventional packaging materials. CVD diamond may be the material for such applications with its unique combination of properties.[122] Already, use of diamond has successfully improved normal 2D packaging approaches, making possible the exciting prospect of simple, practical 3D packaging approaches.[123,124] Recently a composite CVD diamond-silicon heat spreader has been demonstrated[125] to have superior properties at a production cost comparable to that of the conventional materials like AlN and CuW. The highest thermal conductivity combined with the highest elastic constant make diamond useful in surface acoustic wave devices for high frequency operations and telecommunication. Diamond based SAW device has an edge over other materials since it can be operated at higher frequencies which means that more information can be transmitted.[126] Figure 8 shows SEMs of good quality diamond deposition on a micropatterned silicon substrate. The SEM in (c) is that of a free standing patterned diamond film produced by etching out the patterned silicon substrate. The SEM is recorded from the interface side and clearly demonstrates the faithful reproduction of the substrate patterns by the film. Such suitably patterned diamond slabs can be useful as heat sinks in microelectronics applications.

Due to its transparency[127] to a wide range of wavelengths from the infrared to the ultraviolet region, as well as to x-rays, combined with its radiation hardness and mechanical sturdiness, diamond is an ideal choice as a window material for lasers, x-ray sources, etc. A systematic evaluation of properties such as IR absorption, elastic properties, mechanical strength and thermal properties has been carried out to reveal that CVD diamond has significant advantage in IR applications in adverse environments as compared to other candidate materials.[128-130] Figure 9 shows the FTIR transmission spectrum of a free diamond film obtained by HFCVD technique.[131] Good quality diamond deposition has been possible on substrates like ZnS suggesting the possibility of using diamond as a protective coating for optical components.[132] Recently a novel x-ray mask using a diamond-SiC double membrane has been demonstrated.[133] With the realization of epitaxial/oriented, large area and excellent quality freestanding diamond membranes, the possibility of commercial use of diamond windows has come quite close to reality.

Boron doping leads to p type semiconducting diamond, and although n type doping has proved to be elusive, a number of prototype electronic devices have been demonstrated using CVD diamond, such as thermistors,[134] field effect transistors,[135] Schottkey diodes,[136] field emission arrays[137-138] etc. For example, Figure 10 shows the device structures and corresponding resistance versus temperature characteristics of diamond thin film thermistors.[139] Okano et al.[140] have been able to achieve p as well as n type doping using the HFCVD technique with B_2O_3 and P_2O_5 as the respective precursors. They have successfully fabricated p-n devices, also. Because hydrogen-terminated diamond surfaces have negative electron affinity, they are expected to emit electrons spontaneously. This has led to attempted development of 'cold cathodes' miniaturized vacuum diodes that might have application in microelectronics and flat panel displays. A high concentration of nitrogen can be achieved in diamond films using urea as the gaseous nitrogen source. Such films show very low threshold electron emission, which encourages the development of cold cathode technology.[141]

Diamond-Like Coatings

Introduction

The research effort directed towards artificial synthesis of diamond under low pressure low temperature conditions led to the

Table 2. The Extreme Properties of Diamond Compared to Competing Materials and the Possible Areas of Application[115]

Properties of Diamond		Comparison with Competitors	Possible Applications
Vickers' Hardness	12000-15000 kg/mm^2	Hardest Material Known	Tribological Tools, Wear Resistant Coatings
Friction Coefficient	0.1 (in air)	Very Low in Air; Higher if Kept Clean in Vacuum	
Young's Modulus	1.2×10^{12} N/m^2	Twice that of Alumina, Highest Mechanical Strength	Stiff Membranes for Lithography Masks, Lightweight Coatings and Diaphragms for Audio Devices
Sound Velocity	18.2 km/s	1.6 Times that of Alumina	
Chemical Inertness	Inert	Resistant to all Acids, Bases and Solvents at Room Temperature	Corrosion-Protective Coatings
Range of Transmittance	0.22-2.5 mm, > 6 mm	In the ir, Orders of Magnitude Higher than Other Material	Uv-Vis-IR Windows and Coatings, Microwave Windows, Optical Filters, Optical Waveguides
Refractive Index	2.41	1.6 Times that of Silica	
Band Gap	5.45 eV	1.1 for Si, 1.43 for Gaas, 3.0 for b-Sic	High Power Electronics, High Freq., High Temp. Semicond. Devices, Lasers, Detectors
Electron/Hole Mobility	1900/1600 cm.Amp/s	1500/600 for si, 8500/400 for Gaas	
Dielectric Constant	5.5	11 for Si, 12.5 for Gaas	
Thermal Conductivity	20 W/cm.K	4 Times that for Cu or Ag	Insulating Heat Sinks for Electronic Devices
Thermal Expansion Coefficient	0.8×10^{-6} /K	Value at Room Temperature Close to that for Sio_2	Thermally Stable Substrates e.g., X-ray Lithography Masks
Luminescence	430 mm	Blue Luminescence Scarce	Blue leds, displays

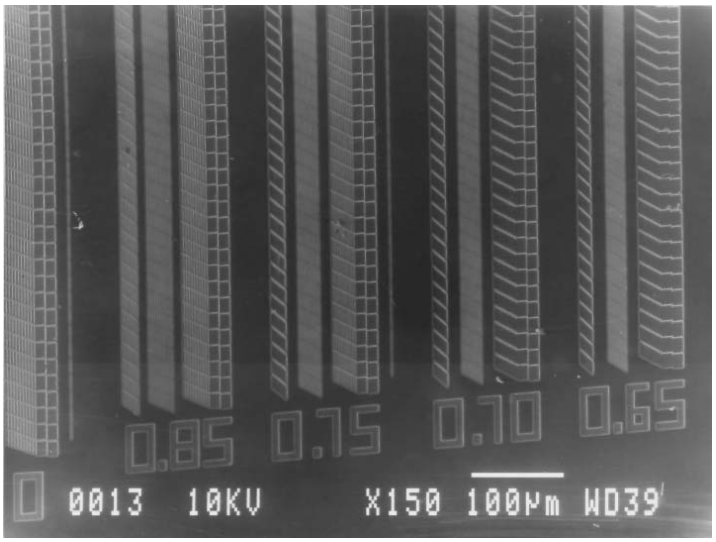

(a)

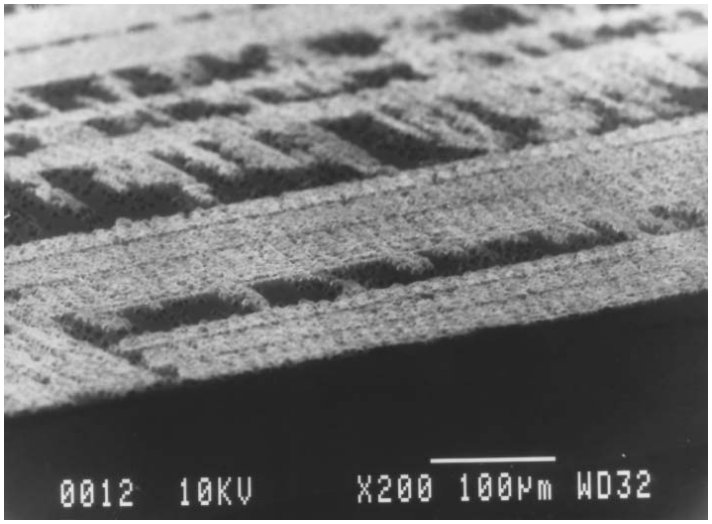

(b)

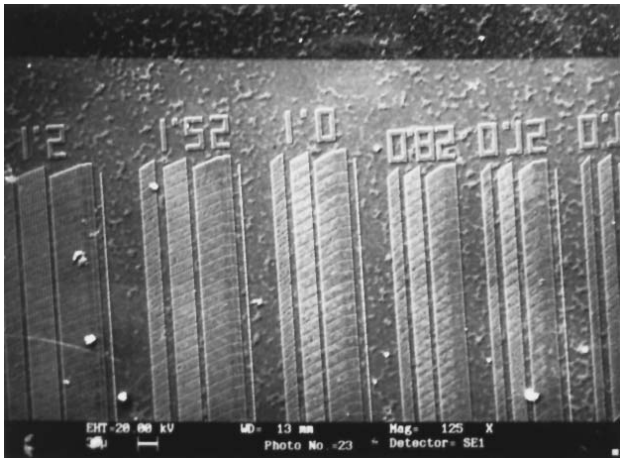

(c)

Fig. 8: SEMs of (a) micropatterned silicon, (b) diamond deposition along the patterns of (a), and (c) free-standing micropattrned diamond film, from the interface side.

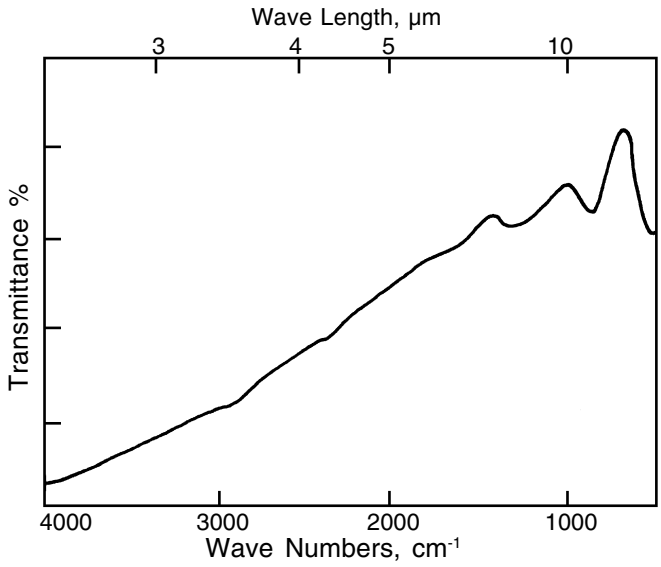

Fig. 9: FTIR transmission spectrum of a free standing diamond film obtained by HFCVD.[131]

discovery of a new class of materials, namely the "diamond-like" phases. Diamond-like hydrocarbon phases were first noticed by Schmellenmeier in 1953,[142] but their unusual properties and structure remained unnoticed for nearly three decades. These films possessed properties between those of graphite and diamond but closer to those of diamond. The term "diamond-like" carbon or DLC was first coined by Aisenberg and Chabot[143] when they produced these carbon films by ion beam deposition in 1971. Different models were suggested to explain the structure of diamond-like carbon materials in the 1980's.

In the present paper, the term DLC refers to amorphous, pure carbon coatings with diamond like properties while DLHC indicates the amorphous diamond-like hydrocarbon form. Both types contain a significant amount of sp^3 carbon sites. There is little or no hydrogen present in the former type while the latter type contains 17 to 60 atomic percent of hydrogen.[144]

The atomic number density of DLHC (more than 0.19 gram-atom per cubic centimeter) falls between that of admantane and diamond. It is greater than normal hydrocarbons with the same atomic composition and increases with increase in the average coordination number of carbon atoms from 3 to 4 as the amount of hydrogen is increased. DLC has atom number density approximately between 0.19 and 0.28 gram-atom per cubic centimeter with properties different from those of DLHC. Also, the properties are different from those of other tetrahedrally bonded amorphous materials (for example, a-Si and a-Ge), because of the very strong bonding between carbon atoms and the mixture of sp^3 and sp^2 bonds present in the network.[144]

Because diamond like materials contain a mixture of both sp^3 and sp^2 sites and hydrogen, they can therefore be considered to be an intermediate between diamond, graphite and polymeric hydrocarbon. The mixed bonding means that the properties of diamond like materials are generally inferior to those of diamond. However, these materials have certain advantages that make them competitive to diamond coatings in a number of applications. These advantages are listed below.

1. There are deposition techniques by which diamond like coatings can be deposited at

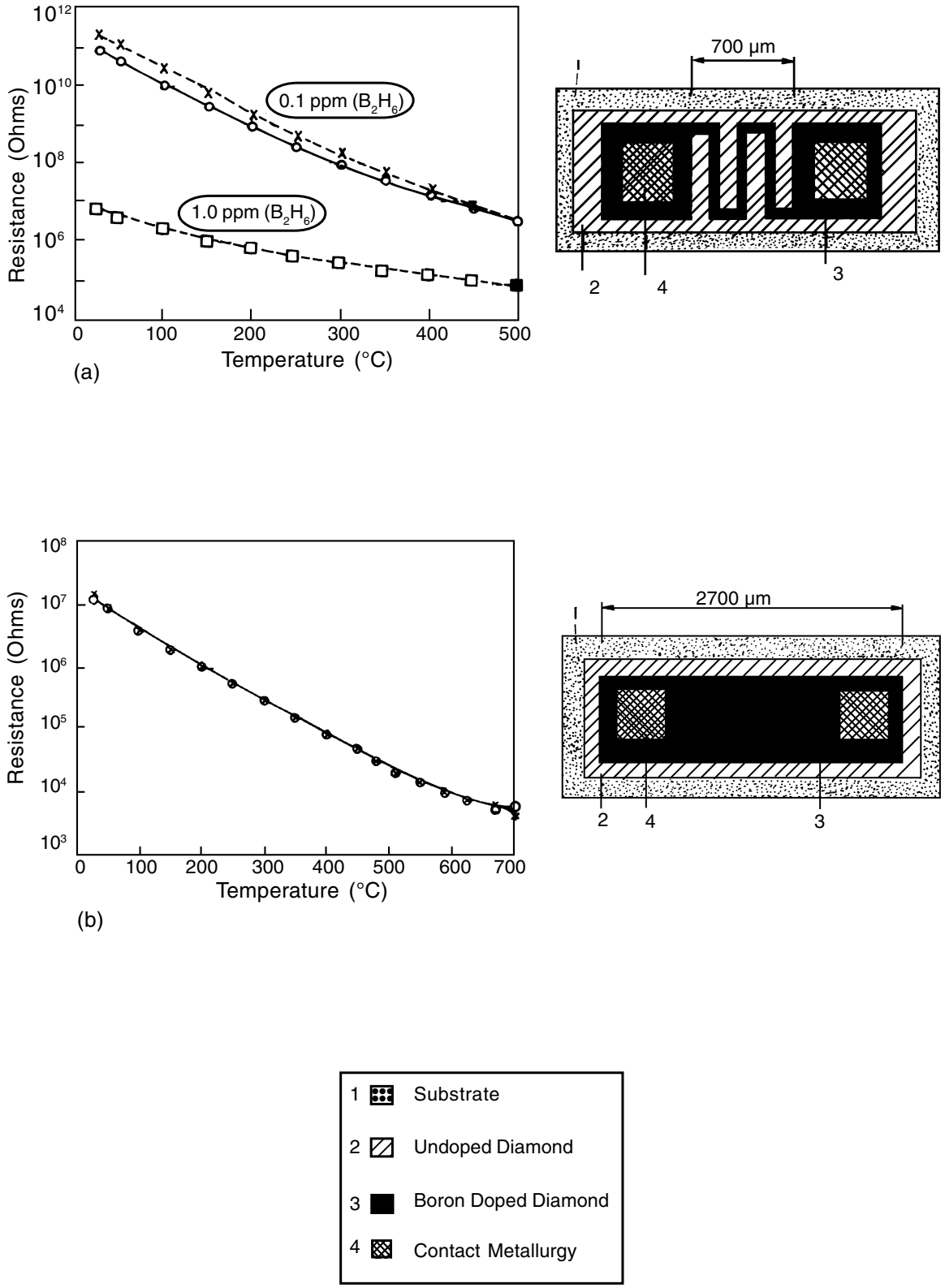

Fig. 10: Device structures with (a) serpentine and (b) rectangular geometry and corresponding resistance Vs. Temperature characteristics of a diamond thin film thermistor. The serpentine structure was doped with o.1 ppm or 1.0 ppm diborane whereas the rectangular structure was doped with 0.1 ppm diborane.[139]

low temperatures (< 100°C). This implies that it is possible to coat plastics, polymers and ferrous substrates without degrading their quality. This has, so far, not been possible by diamond deposition techniques.

2. There are deposition techniques by which diamond like films can be deposited over larger areas compared to those using diamond film synthesis methods.
3. Diamond like coatings are basically amorphous and therefore smooth whereas diamond coatings are polycrystalline and hence rough. As a result, the diamond like coating experiences lower sliding friction in wear resistance applications and tends to provide better protection than a diamond coating inspite of the comparatively lower hardness.
4. In addition to being transparent to IR (like diamond), the refractive index of DLC can be tailored to suit a particular application (unlike that of diamond). This gives diamond like coatings a significant edge over diamond in some special applications, e.g., as antireflection coatings on germanium optics.

Deposition Methods

A variety of deposition techniques, some involving physical vapor deposition (i.e. a solid carbon source and/or a hydrocarbon source gas) and others involving chemical vapor deposition (i.e. a hydrocarbon source gas), can be used for deposition of DLC and DLHC films.[145] Various factors such as deposition rate, film properties, film adherence, sample coverage, process control and scale up need to be considered for diamond like films to be used for practical applications. Such factors favor sputtering, plasma deposition and ion plating techniques. Generally, the fundamental/investigative studies of the film formation process and film structure have been carried out using the techniques like mass selected ion beam (MSIB) and plasma deposition. The different techniques can be classified depending upon the carbon source used for depositing diamond like materials, and these are shown schematically in Figures 11 and 12.

Out of all the CVD and PVD techniques, RF plasma deposition from a hydrocarbon source gas[146] is the most popular method. The schematic of the RF plasma configuration used for diamond like film deposition is shown in Figure 13. The RF power is capacitively coupled to the substrate electrode, and the counter electrode is either a second electrode or the grounded walls of the chamber. The deposition rate is highest for gases of low ionization potentials and large molecular weights. Films deposited with acetylene appear to have the best properties, having the highest hardness and a reasonably high deposition rate. In all the plasma assisted chemical vapor deposition methods RF plasma CVD,[147,148] electron cyclotron resonance plasma CVD,[149] pulsed arc-discharge,[150,151] etc. the small possible substrate size (few square centimeters) and high deposition temperature (300 - 600°C) limit the choice of substrates that can be coated by these methods.

The physical vapor deposition techniques such as direct Ion Beam Deposition,[152] MSIB Deposition,[18,153,154] Ion Beam Sputtering,[155] Magnetron Sputtering,[156] Laser Plasma Deposition[157] and Ion Assisted Deposition[158] have been extensively used for diamond like film deposition at room temperature. In all these techniques, the key to formation of a diamond like film is the bombardment of the film, during its growth, by the energetic species (20 - 500 eV) which apparently is necessary for the graphite to diamond like transition.[159]

In ion beam deposition, carbon ions are generated either from a solid source (ion sputtering of graphite) which gives ions of the form C_m^+ or from a gaseous source (ion-induced decomposition of hydrocarbon gas) resulting in ions of the form $C_mH_n^+$. Growth rates using a solid carbon source are very low as compared to those obtained using the gaseous source. In both the cases, the substrate also receives a large flux of neutral species. Figure 14 shows the schematic of direct ion beam deposition used by Aisenberg and Chabot[143] for the formation of diamond like films from a solid carbon source.

The technique of MSIB deposition allows deposition of single ion species by passing the ion beam through a magnetic mass analyzer for e/m selection. Figure 15 shows the general layout of the MSIB technique used for the deposition of

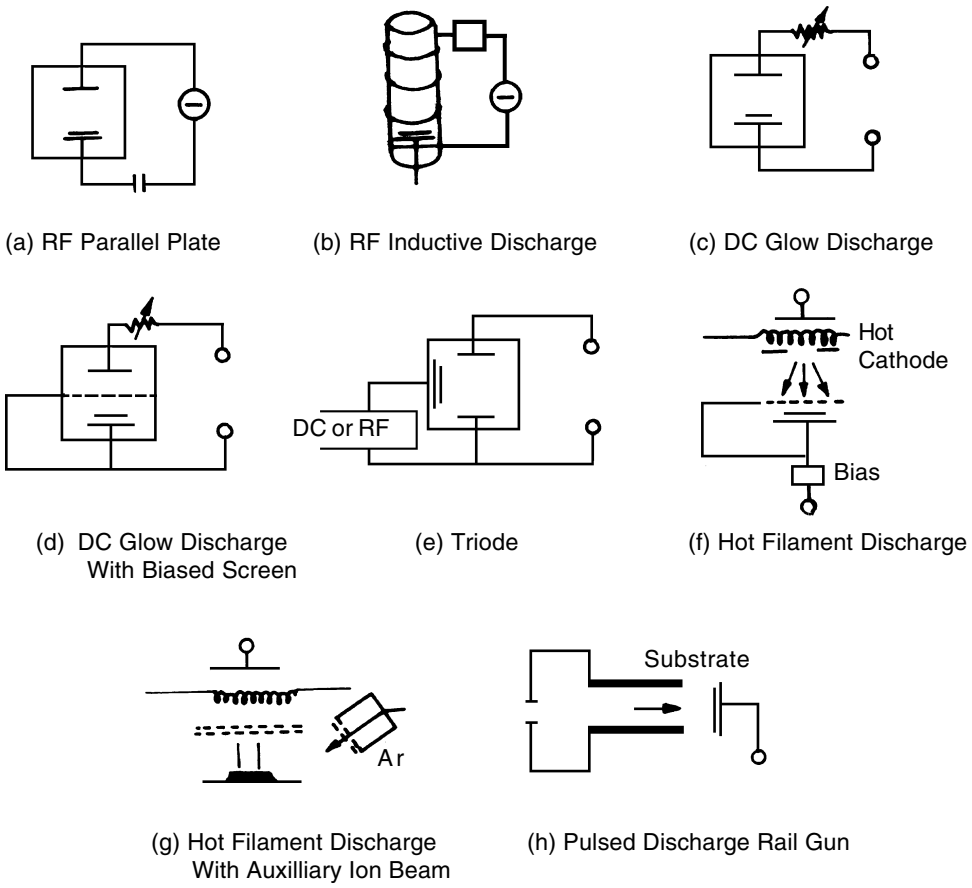

Fig. 11: Methods of growing diamondlike materials from hydrocarbon gases.[145]

DLC. This technique was first used by Aksenov et al.[160] It results in the formation of diamond like amorphous carbon with the highest percentage of sp^3 bonded carbon (90 ± 5%),[161] highest hardness,[162,163] highest density ($1.6 \pm 0.2 \times 10^{23}$ atoms cm^{-3})[163] and highest resistivity (3×10^9 Ω - cm)[153,164] reported to date, as compared with the diamond like carbon phases obtained from any of the other deposition processes. Also, MSIB DLC films retain their structure even at temperatures as high as 800°C, while the diamond like films deposited by other techniques graphitize between 350 - 400°C. Martin et al.[165] and Antilla et al.[166] reported that when hydrogen was added to the DLC film growth environment during the MSIB technique, the films became hydrogenated. These films were more transparent, and the hardness was less compared to DLC films. This was consistent with the predictions of Robertson[167] and observations by Jansen et al.[168] that hydrogen introduction during ion beam sputter deposition of DLC film leads to an increase in the electrical resistivity, the optical gap and the sp^3 to sp^2 ratio, but a decrease in the density. The deposition rate for this method can be maximized by using a carbon arc as an ion source.[169] However, the main practical problem with this technique is the high compressive stress in the films which limits the adhesion for films over 500 Å thick.[170]

Various sputtering methods are used for the deposition of diamond like films (refer to Figure 14). It is possible to coat a substrate with a diamond like film by ion beam sputtering using the same ion sources that are used for (non-mass-analyzed) direct ion beam deposition.[171] In ion beam sputtering, a beam of typically 1 kV argon ions is directed onto a graphite target. A

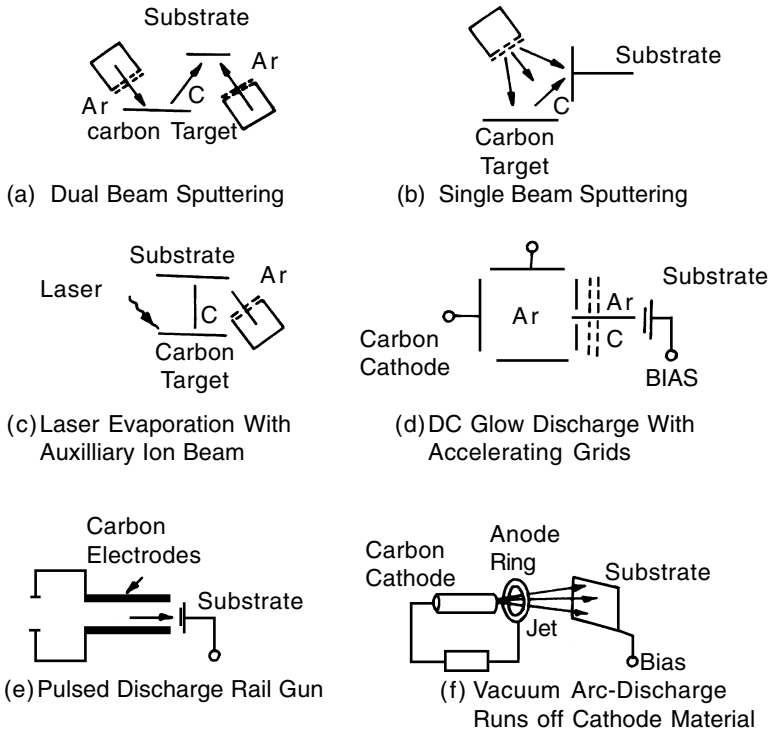

Fig. 12: Methods of growing diamondlike materials using solid carbon source.[145]

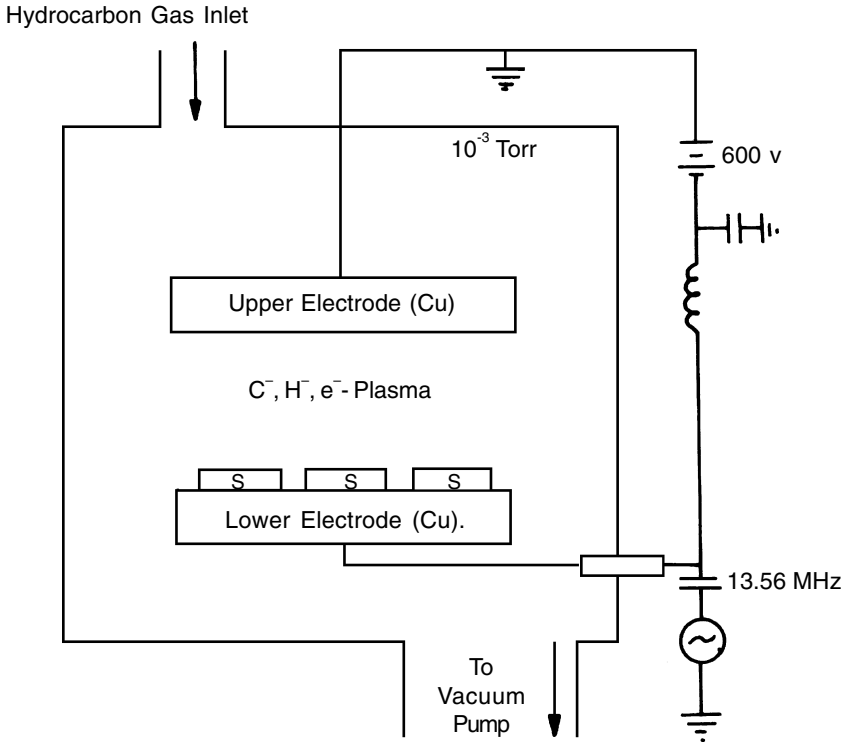

Fig. 13: RF Plasma deposition method.[145]

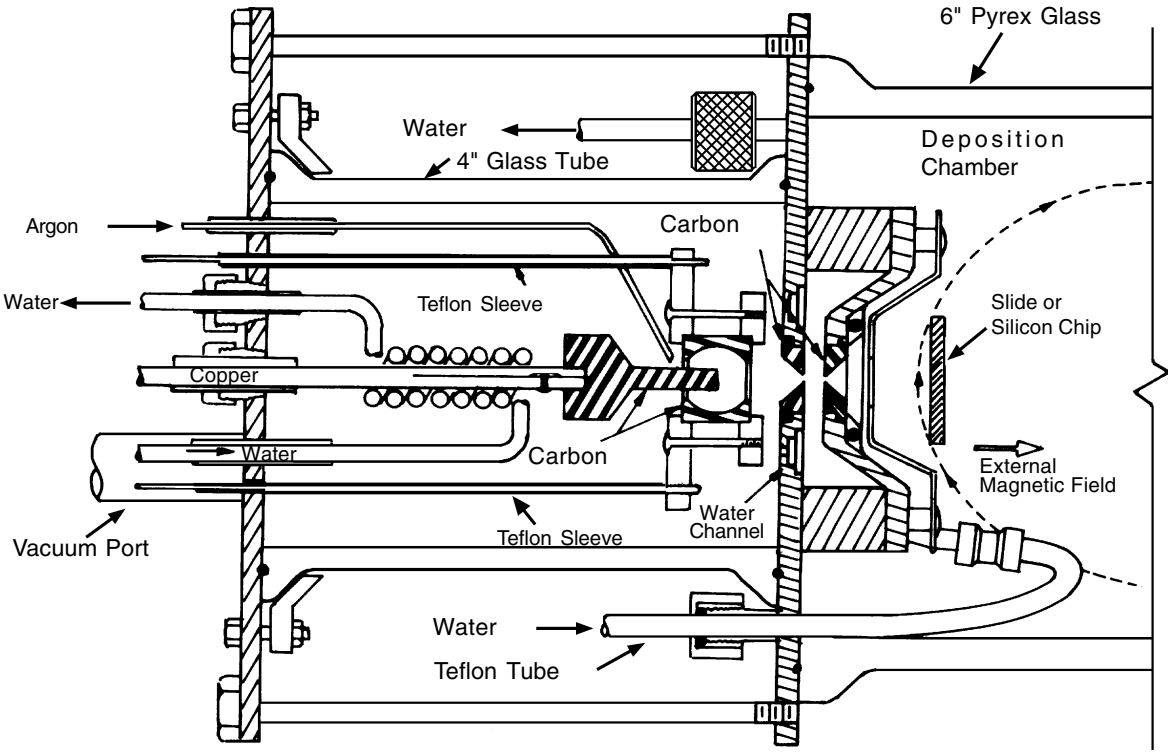

Fig. 14: Direct Ion beam depostion method.[143]

second argon ion beam can be directed at the substrate to provide bombardment to the growing film and the method is known as dual ion beam sputtering.[172] Ion beam sputter deposition suffers from low growth rates (< 0.06 mm/h, 0.006 mm/h).[173,174] Higher growth rates can be achieved by using hydrocarbon gas,[173] but this leads to deposition of DLHC films. Magnetron sputtering yields higher growth rates as compared to ion beam sputtering.[175] The advantages of sputtering are good process control and ease of scale-up to larger apparatus.

Laser ablation of a graphite target (refer to Figure 14) can produce carbon ion plasma.[176] The resulting films are diamond like if the laser power exceeds a certain threshold. The diamond like film is found to consist of a nano-scale mixture of diamond grains embedded in an amorphous carbon matrix. It has the advantage of high hardness yet moderate internal stress. Cuomo et al.[177] compared the ion beam sputtered diamond like film and laser ablated diamond like film and found that in the material deposited at the same temperature, the sp^3 fraction can be higher for laser ablation than for ion sputtering. This is partly attributed to the difference in the mean energy of the atoms or ions being deposited in these two processes. In ion beam sputtering the energy is of the order of 5 eV[178] while for laser ablation it is significantly higher, 10-20 eV. However, there is a disadvantage in the laser ablation technique which is the comparatively smaller coating area.

In ion assisted deposition, there are two methods: one is decomposition of hydrocarbon oil using energetic ions[158,179] and the other is evaporation of graphite with concurrent bombardment of the growing film with energetic ions.[180-181] With these methods, diamond like films with reasonably good properties can be deposited over large areas (1 m^2) at low temperatures (< 140°C).

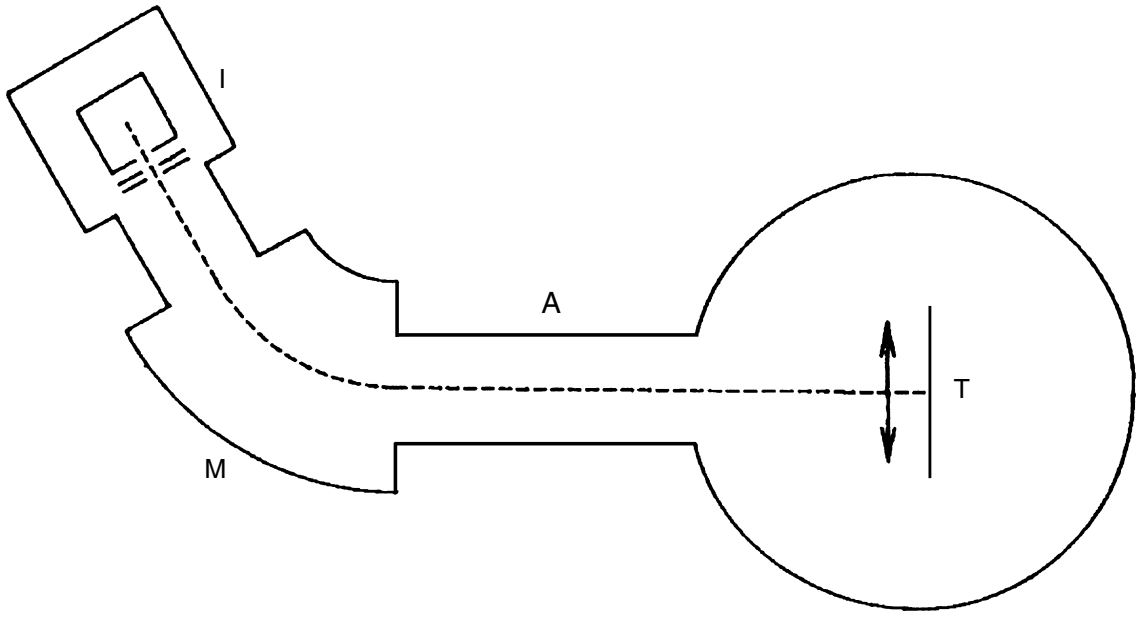

Fig. 15: General layout of MSIB technique (I-ion source, M-analysis magnet, A-acceleration or deceleration stage and T-target chamber).[162]

Critical Growth Parameters

The fundamental processes involved in the nucleation of diamond like films during the ion beam deposition processes, the critical role of the impinging ion energy and the differences in the basic mechanisms of depositing carbon ions versus the use of argon ions (in the case of ion assisted deposition) are still not well understood. In the following sections some of the established concepts are reviewed and discussed.

Type of Substrate

Because the ion-assisted processes enable deposition at temperatures less than 100°C, deposition of diamond like coatings has been attempted on a wide range of substrates, e.g., stainless steel,[182] Copper,[183] ceramics,[184] optical materials (plastics, polymers and polycarbonates),[185,186] glasses,[187] quartz,[188] sapphire,[189] infrared-transmitting optical materials[190] such as germanium, zinc sulfide and zinc selenide, and a variety of electronic grade materials. Although thin films can be produced on most of the substrates, the adhesion of the coating to the substrate and the tribological properties of the coating vary widely. Generally, sputtering of the substrate prior to deposition has been employed to improve adhesion. In addition, thin interlayers also have been employed for the same purpose. An intermediate silicon layer has been used to improve the adhesion of diamond like films on metals (such as Co, Cr and their alloys) that are used for magnetic recording media.[191] In the case of ZnS, a thin interlayer of Ge or Si has been used for the same purpose.[189] The adhesion of diamond like films on a stainless steel substrate has also been improved by plasma nitriding of the substrate prior to deposition,[192] preliminary hardening of the substrate with ion implantation and additional thermal treatment, or by etching of the coating surface with ions of reactive gas.[193]

Deposition Pressure

The pressure during deposition decides the diamond like film composition and therefore its properties. The film growth rate is also critically

dependent on the pressure (10^{-2}-10^{-9} Torr). Direct ion beam based techniques employ pressures in the submillitorr region. Techniques like ion plating and plasma deposition utilize pressures in the millitorr region and in these cases, it is possible to obtain films at high growth rates. However, the films deposited by these techniques have poorer optical and electronic properties than those produced by ion beam processes.

Ion Energy Considerations

The single most widely studied process parameter in deposition of diamond like films by ion beam based techniques is the energy of the incident energetic particles. Several researchers have shown that many of the important film properties can be directly controlled by manipulation of the particle energy.

In direct ion beam deposition processes, ion energy in the range of a few tens of eV to a few tens of keV is used for diamond like film deposition. Careful control of ion energy in high-vacuum systems employing mass filtering of carbon ions (as in MSIB) has been shown to produce crystalline diamond materials up to several micrometers in size.[194]

Growth Mechanisms

Ion beam based PVD processes have the advantage of the production of metastable species by the condensation of energetic particles. The energy contained in the condensing particle is employed in preferentially rearranging the bonding structure on the material surface. The fundamental chemistry and physics occurring on the surface is still not well understood. Some theories have been proposed, most of which have addressed specifically the MSIB technique.

It was suggested by Spencer et al. in 1976[195] that the diamond like films are formed due to preferential sputtering of sp^2 sites compared to sp^3 sites. Later in 1990, Lifshitz et al.[196] observed that this was unlikely due to the low sputtering yield of carbon and suggested the 'subplantation model'. This model proposes that film growth from hyperthermal species occurs via the 'subplantation' or shallow implantation mechanism which is characterized by three stages. In the first stage the hyperthermal species transfer their energy to the target atoms with incorporation or diffusion of these species as interstitials in the subsurface layer. In the second stage, the excess energy of the atoms excited in the first stage is expended within the target and the atoms reach thermal equilibrium with the surrounding atoms. This stage is followed by the third stage of long term relaxation which consists of processes such as diffusion of vacancies and interstitials, phase transformations and chemical reactions, ultimately determining the final structure of the material. The final structure of the film is dependent upon

a. The 'mold' effect of the substrate matrix which determines the possible site occupancies of the penetrating species and places constraints on initial evolution of the new phase,
b. Preferential displacement of atoms with low displacement energy, and
c. Diffusion rates of vacancies and interstitials created in the deposition process.

The subplantation growth of diamond like material takes place as follows. The penetration of carbon into subsurface layers of the substrate matrix leads initially to the formation of a carbide layer. With increase in the carbon fluence, there is further increase in the local carbon concentration in the subsurface layers, resulting in a 2D graphitic layer which finally becomes 3D bulk carbon while the substrate atoms are removed due to sputtering and/or ion-mixing. The structure of the film is graphitic or sp^3 diamond like depending on the incident ion energy. This is followed by the growth of a pure carbon layer on the substrate surface.

Lifshitz et al.[196] also studied the effect of carbon ion energy and substrate temperature on diamond like film deposition. They observed that there exists an optimal energy range within which it is possible to obtain good quality diamond like films and that the film quality deteriorates with increasing substrate temperature.

It was argued that at low carbon ion energies (but high enough to trap carbon in the subsurface layers), there is no target atom

displacement, and the carbon atoms are trapped as interstitials. This induces a high stress, and the ions lose their energy via thermal spikes which provide a highly excited environment. This, combined with the 'mold' effect of the substrate matrix, favors the formation of metastable phases at low ion energies. At medium ion energy the displacement energy of the diamond phase is very low as compared to that for the graphitic phase. Therefore, apart from the mold effect and the thermal spike phenomenon, preferential displacement of sp^2 bonded carbon as compared to that of the sp^3 phase contribute to the sp^3 rich diamond like film formation. At higher ion energies the damage is high for all constituents i.e., displacement energies for both diamond and graphitic constituents are high. This ion-induced damage overrides all the other effects resulting in an amorphous material of sp^n (n = 1,2,3) hybridization. However, the optimized ion energy range has been recently reported to be 30 eV - 10 keV for DLC deposition by hyperthermal carbon species (MSIB).[197]

As far as the effect of substrate temperature was concerned, it was suggested that at temperatures lower than 70°C, impingement of low energy carbon ions creates immobile carbon interstitials and therefore the sp^3 rich phase is formed. With increasing temperature the mobility increases and the atoms diffuse to the surface releasing the internal stress to form the thermodynamically stable sp^2 phase.

In this model, it has been assumed that the incident ions cause a preferential displacement of the graphitic carbon and increase the possibility of sp^3 diamond-like bond formation in the optimal ion energy range. This assumption is based on the values of the displacement threshold of graphite and diamond as 30 eV and 80 eV respectively. Robertson[159] observed that the values are actually much closer to each other, namely, in the range of 25-42 eV for graphite[198] and in the range of 37-45 eV for diamond.[199-200] He, therefore, proposed that sp^3 bonding is promoted by the ion flux causing a quenched-in density increase. A local high density results when an incident ion penetrates the subsurface layer of the substrate and sits in an interstitial position. At low ion energies the ion does not penetrate the substrate sufficiently and just sticks to the surface forming an sp^2 rich phase. At higher energies penetrating ions increase the localized density, but their kinetic energy is dissipated in a thermal spike resulting in relaxation of the excess density. The greater the energy, the greater is the probability of relaxation. Therefore, the optimum ion energy is determined by a balance between a sufficient penetrative yield and a small relaxation of the density increment. However, there are some discrepancies between this model and the experimental data. On the other hand, it has been shown recently that particle bombardment of carbon phases leads to more atomic displacements in graphitic structures than in sp^3 bonded structures.[201] This indicates that the displacement thresholds are significantly different for graphite and diamond phases, so that the preferential displacement of graphite assumed by Lifshitz et al. may be a valid argument.

Characterization of DLC

DLC films have been characterized by a variety of methods. To detect and quantify the carbon-carbon bonding in DLC, electron spin resonance,[202] electron diffraction,[203] Raman spectroscopy,[204-206] optical spectroscopy,[207] infrared spectroscopy,[208,209] photoelectron spectroscopy,[210,211] electron energy loss spectroscopy,[212,213] nuclear magnetic resonance,[214,215] etc. have been used. Optical and IR spectroscopies give the transmittance, band gap and refractive index. Raman spectroscopy yields structural information which can also be obtained from electron spin resonance and electron diffraction techniques. Nuclear magnetic resonance is used for precise determination of the sp^3 to sp^2 bonding proportion in the film. The hydrogen concentration is measured by elastic recoil detection analysis.[215] XPS and EELS give compositional information of these films. In all these techniques, measurements are sensitive to changes in the film structure and properties. However, in very few can the measurements be subsequently interpreted simply in terms of the actual concentration of sp^3 and sp^2 hybridized carbon atoms. All the characterization studies

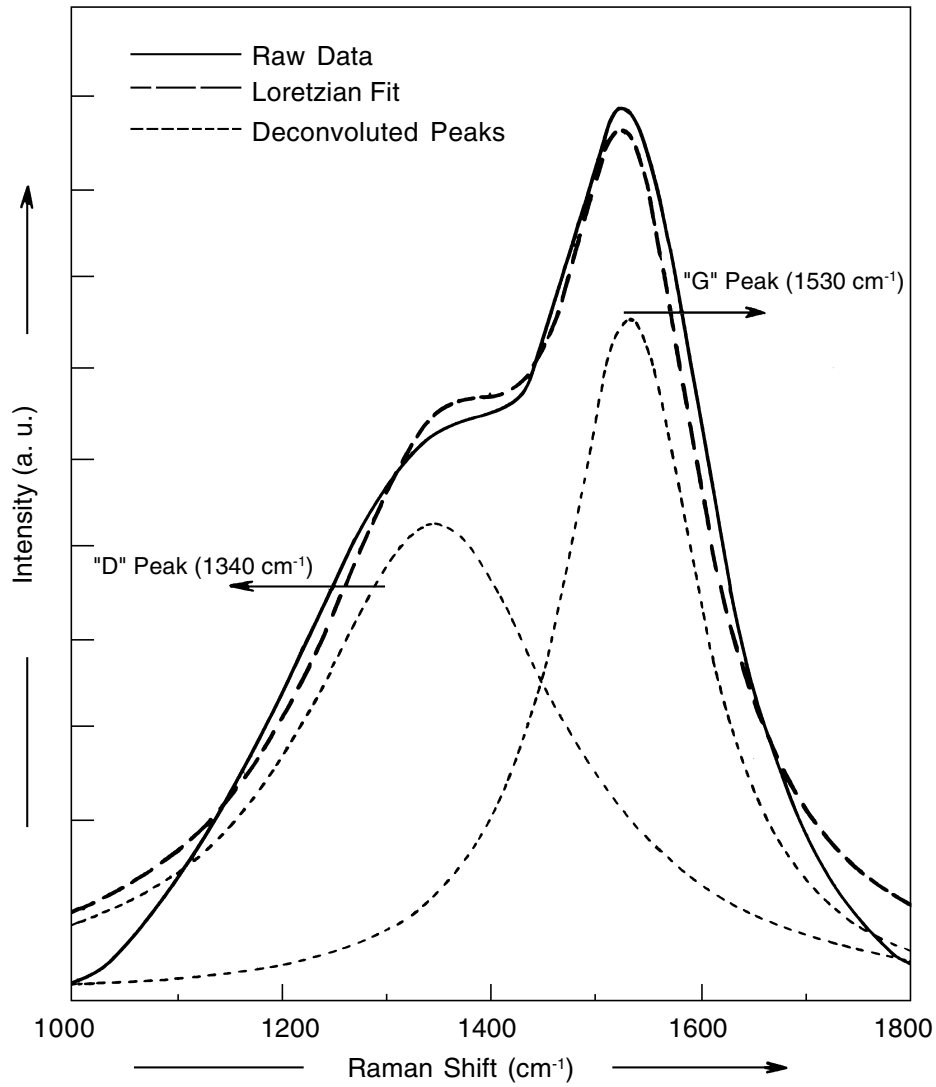

Fig. 16: Raman spectrum of DLC film deposited by IBAD technique.

indicate that the chemical structure and physical properties of the films are quite variable, depending on the deposition techniques and film growth conditions.

Extensive study has been carried out on the tribological properties of DLC. Different types of tribo-testers such as ball-on-disk[216] and pin-on-disk[217,218] have been used at low sliding speed or reciprocating conditions to find the friction coefficient as well as the wear rate of the coating.

Figure 16 shows the Raman spectrum of a DLC film deposited by the IBAD technique. The Raman spectra for diamond like materials provide information on the sp^2 bonding. The characteristic features of Raman spectra of diamond like materials consist of a graphite-like (G) peak and a disorder (D) peak in the regions 1500-1550 cm^{-1} and 1330-1380 cm^{-1} respectively. The relative intensities of the G and D peaks can be used to indicate qualitatively the concentration of graphite crystallites of

varying sizes in relation to the host disordered amorphous network. Typically, the Raman spectrum of an excellent quality amorphous DLC consists of a broad band centered around 1500-1550 cm^{-1} representing a highly disordered network of carbon-carbon bonds.[197,204]

Structure of Diamond-Like Films

Due to the nearly infinite bonding possibilities for the sp^2 and sp^3 sites, an enormous variety of 3D carbon networks can be imagined for DLC. Mertz et al.[219] have described several continuous networks solely of tetrahedrally and trigonally bonded carbon that have yet to be observed experimentally.

Experimentally the structure of DLC (produced by the MSIB technique) has been investigated by electron diffraction and by neutron scattering.[220] These films have high hardness, density and electrical resistivity, close to those of diamond. This material exhibits amorphous nature similar to the so-called amorphous diamond, a form which was thought unlikely to exist because of bonding constraints imposed on the carbon network. However, studies show that these films are structurally equivalent to those of a-Si and a-Ge indicating a high percentage of tetrahedral bonding. Wang et al.[221] simulated an amorphous carbon network for such DLC films with 80% sp^3 and 20% sp^2 bonded carbon.

Beeman et al.[205] proposed a random covalent network of sp^2 and sp^3 bonded atoms in which the bond angles and bond lengths are distorted from their equilibrium conditions.

Robertson et al.[222] and Tamor et al.[223] suggested a defect graphite model wherein diamond like material is considered as a mixture of conductive islands of sp^2 graphite embedded in an insulating sp^3 matrix. Tetrahedrally coordinated carbon atoms (sp^3) enable 3D cross-linking, making these films extraordinarily hard. At the same time, graphite clusters composed of three fold coordinated sp^2 hybrids are responsible for the electrical and optical properties. This model seems to accommodate all of the properties reported for diamond like material grown from largely neutral atoms and from ions arriving with low kinetic energies. However, it is not able to explain the structures formed from fully ionized plasmas and from ion beams.

In some models, hydrogen is included as a network terminator i.e., it passivates the dangling bonds within the films. It also has the effect of substituting for carbon-carbon bonds leading to reduction in 3D rigidity of the structure. This random structure consists mostly of carbon atoms that are bonded to one another with either sp^3 or sp^2 coordination. It is defined by Yoshikawa et al.[224] as a random covalent network of aromatic regions linked by polymeric networks. Angus and Hayman[225] reason that in DLHC films with low hydrogen concentration, medium range order due to formation of sp^2 bonded microcrystals relieves the compressive stress caused by a constrained random distribution of covalent sp^2 and sp^3 bonds. On the other hand, Collins et al.[226] proposed a distribution of sp^3 bonded microcrystals linked by sp^2 and sp^3 bonded atoms to explain the high density of the samples prepared by laser ablation. In all these arguments, the role of hydrogen on the structure has not been clearly explained.

Properties and Potential Applications of Diamond Like Films

Table 3 lists the properties of diamond like materials prepared by different techniques in comparison with diamond and graphite.[167]

The excellent properties of the diamond like materials combined with the low deposition temperature and high deposition rate, make these coatings very promising materials for the future. They have many potential applications as protective coatings for industrial products.[227] Of course the properties of diamond like films never match those of diamond. The films are intrinsically smooth and amorphous, and can be used in coating applications where a plane, mechanically hard and wear/corrosion resistant surface is desirable.

By changing the deposition conditions and hydrogen content it is possible to progress from a coating that is fully compatible with the soft

Table 3. Properties of Various Diamond Like Materials Prepared by Different Deposition Techniques[167]

	Density (g/cc)	Hardness (GPa)	Sp^3 %	H at. %	Band Gap (eV)
Diamond	3.5	100	100	0	5.5
Polycrystalline Diamond	3.5	100	100	0	5.5
Graphite	2.267	-	0	0	- 0.04
Glassy Carbon	1.3 - 1.55	2 - 3	0	-	0.01
Evap. Carbon	1.8 - 2.0	2 - 5	< 5	-	0.4 - 0.7
PECVD DLC/DLHC	1.9 - 2.2	15 -30	-	-	1.1 - 3.0
MSIB DLC	2.5 - 3.0	100	90 ± 5	< 9	1.5 - 2.0
Laser DLC/DLHC	-	40	60	-	0.5 - 3.0
Hard DLHC	1.6 - 2.2	10 - 40	30 - 60	20 - 40	0.8 - 1.5
Soft DLHC	0.9 - 1.6	< 5	50 - 80	40 - 65	1.5 - 4
Polythene	0.92	0.01	100	67	6

polymeric substrate to a hard diamond like exterior surface.

Values of microhardness range from 40-100 GPa for DLC coatings and from 5-40 GPa for DLHC coatings depending upon hydrogen percentage. These hardness values compare favorably with diamond and silicon carbide[225] respectively. It is observed that hardness and wear resistance of a DLHC film decrease as hydrogen content increases[168,228] i.e., as the proportion of sp^3 bonded C-H increases. It is speculated that the large decrease in hardness and wear resistance with an increase in the percentage of hydrogen is most likely caused by the development of regions of soft polymeric material. When these soft regions percolate through the entire structure, the hardness reduces greatly and the films are unable to support the large internal compressive stress.[229]

DLC films are much harder than DLHC films,[230] especially films prepared by MSIB techniques. Because hydrogen is not present, it can not be responsible for stabilization of the sp^3 sites. Stress relief in DLC films with high sp^3 to sp^2 ratio is achieved possibly by the development of medium-range or long-range order, such as clustering or formation of crystalline regions.[225]

Diamond like films exhibit fairly good wear resistance,[231,232] abrasive resistance,[233] and sliding coefficient of friction.[218,233] These properties help it find applications in the bearing industry and in those machine components where relative sliding is involved. Bearings coated with these films will be silent in operation due to less friction. This also means that the life of the bearing can be increased, thereby reducing the running cost of the machine.

Diamond like films are amorphous, smooth and lightweight. The ability to produce very thin (2-6 nm) and smooth films together with low atomic number makes these films an ideal material for use as protective coatings on x-ray mirrors.[234] Also, these films are scratch/chemical resistant and block ultraviolet radiation. These properties taken together can revolutionize the spectacle and goggle industry. These properties

also render diamond like films a promising watchglass coating. Improvement in scratch resistance by a factor of 6 has been obtained for plastic lenses coated with these films. Figure 17 shows the optical micrographs of an uncoated and a 30 nm thick DLC coated, float glass samples subjected to identical ball-on-disk wear tests. The uncoated sample shows a fairly prominent scratch whereas the DLC coated sample shows a very faint wear track. Figure 18 shows percent haze vs. number of test cycles for Taber tested uncoated polycarbonate and DLC-coated polycarbonate substrates. The ratio of haze of uncoated polycarbonate to haze of DLC coated polycarbonate is presented for two data points.[187] Figure 19 shows the number of scratch defects vs. number of grocery items scanned for uncoated float glass window, Diamonex DLC-1 and Diamonex DLC-2 coated float glass windows. The estimated average lifetimes for each window are also presented.[187]

The properties of these films like good surface hardness, excellent wear resistance, chemical inertness and environment durability can be put to good use in the automobiles industry.[235] This is also a good candidate material for the hermetic coating on optical fibres.[236] The development of diamond like coating specifically for automotive polymers seems to offer great promise and could increase the use of low cost polymer material. When plastic is substituted for heavier material, the vehicle weight is reduced and this translates directly into energy saving through reduced fuel consumption.

These films can be used as a protective overcoat to increase the life of many other potentially useful coatings in different applications, for example, the soft Indium-Tin Oxide film used in photovoltaic applications,[237] soft $YBaCu_2O_3$ superconducting thin films,[238] etc. provided the diamond like overcoat does not alter or influence the basic properties of the underlying soft coating.

The smooth and wear resistant DLC coatings have been shown to provide excellent protection to discs for use as magnetic recording media without affecting the inherent properties of the magnetic material. The DLC coating on the recording head can prevent wear of the magnetic layer and subsequent data loss.[239]

Diamond like films have excellent transmission in the infrared region,[240] thereby making them a promising candidate for protective coatings for IR windows. Figure 20 shows IR transmission of DLC-coated ZnSe. The DLC coating thickness was approximately 1 μm.[187]

DLHC films with precise control over refractive index and thickness also have been deposited on silicon solar cells as antireflection coatings resulting in an increase in cell efficiency by 40% and on germanium windows as transparent protective coatings.[225]

It is observed that diamond like films adhere strongly to quartz, glass and to substrates such as high molecular weight polyethylene (HMPE). These films are smooth with low coefficient of friction, non toxic[241] and biocompatible.[242] In one study,[243] *in vitro* studies were carried out using three cell culture lines. These were macrophages that ingest debris and foreign material as part of immune response; fibroblasts that produce the material of connective tissues in the body and osteoblasts that are bone forming cells. These tissues were grown on DLC coated and uncoated (control) discs. Lactate dehydrogenase (LDH), a material released during cell death was used as a measure of cell viability. Figure 21 indicates LDH release from

a. Macrophages,
b. Fibroblasts, and
c. Oestoblasts like cells.

These figures show no difference in LDH release between the DLC and control specimen indicating a good degree of bio-compatibility of DLC coating. In view of the combination of bio-compatibility and wear resistance exhibited by the DLC coatings, they can be used as protective and smooth coatings on contact lenses for opthalmological application[244] and on artificial heart valves to reduce friction.[245] Also, polymer substrates coated with these films can be used as joints in artificial limbs.[246]

The high film hardness and high chemical inertness makes DLC films more suitable as passivation layers for sensor devices as compared to other materials such as Si_3N_4 and SiO_2.[247]

DLC films can also be used as dielectric layers for thermal management systems. In this case, the DLC film is coated on copper inserts used as heat transfer devices in multichip

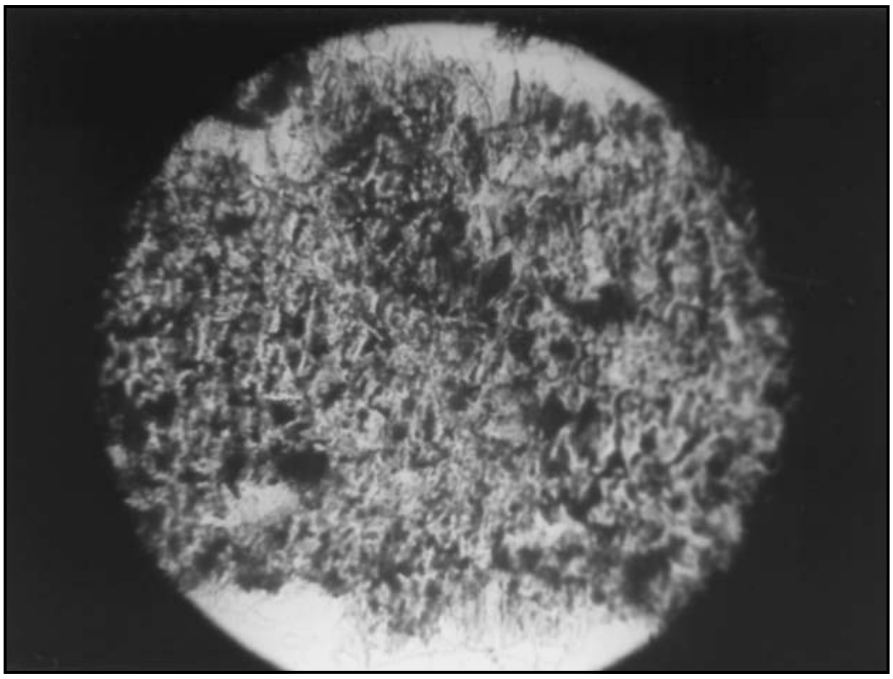

(a)

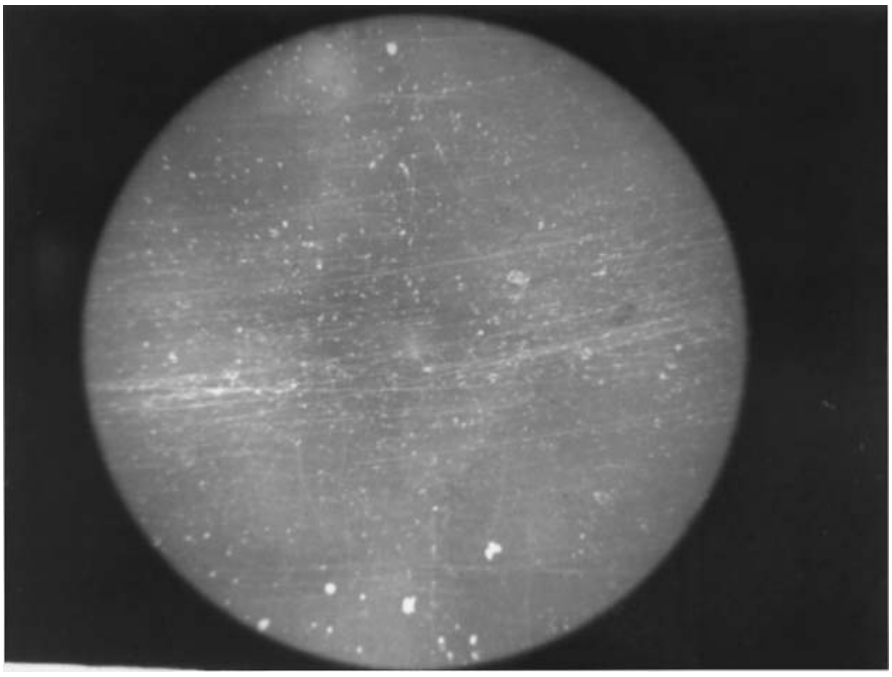

(b)

Fig. 17: Optical micrographs of Ball-on-Disk wear tested (a) uncoated float glass and (b) 30 nm DLC coated float glass.

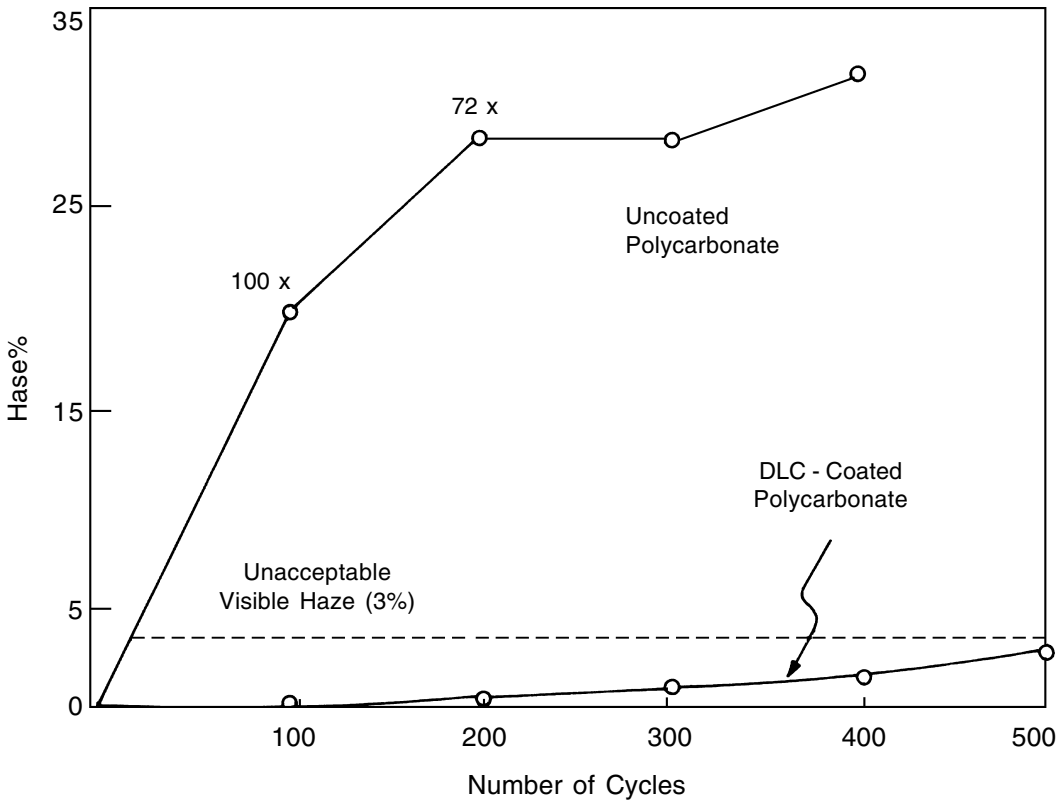

Fig. 18: Percent haze vs. number of test cycles for Taber tested uncoated polycarbonate and DLC-coated polycarbonate substrates.[187]

modules. The DLC layer provides electrical insulation as well as protection from abrasion to the soft copper metal.[187]

There are various applications of DLC in the electronics industry too. For example, DLC coating has been demonstrated to lead to an increase in the electron emission of molybdenum emitters.[248]

Carbonitride Coatings

Introduction

In 1989, Liu and Cohen performed theoretical calculations to investigate the structural and physical properties of β-C_3N_4, a metastable binary phase of carbon and nitrogen.[249] It was predicted that this material possesses low compressibility with bulk modulus and hardness exceeding that of diamond. This phase is structurally similar to β-Si_3N_4 with Si replaced by C, but unlike the ionically bonded β-Si_3N_4, it is a covalently bonded crystalline material.[250] These results suggested that β-C_3N_4 could be a good protective coating for technological applications.

Synthesis Techniques

Because of the theoretical predictions much interest has been generated in the deposition of C-N films in the hope of realizing new phases. Synthesis has been attempted by various techniques, such as reactive sputtering,[251] laser ablation of graphite in nitrogen ambient,[252] chemical vapor deposition,[253] ion beam assisted deposition,[254] dual ion beam sputtering,[255] high dose nitrogen ion implantation into carbon thin

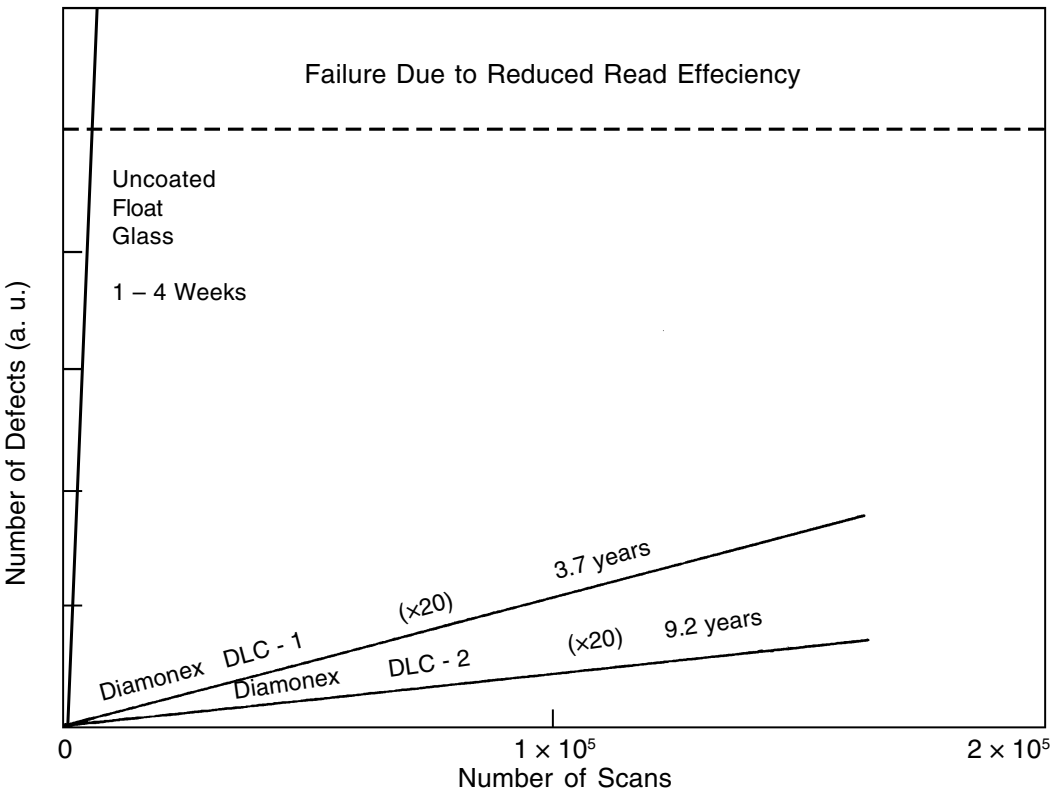

Fig. 19: Number of scratch defects vs. number of grocery items scanned for uncoated float glass window, Diamonex DLC-1 and Diamonex DLC-2 coated float glass windows and the corresponding estimated average lifetimes.[187]

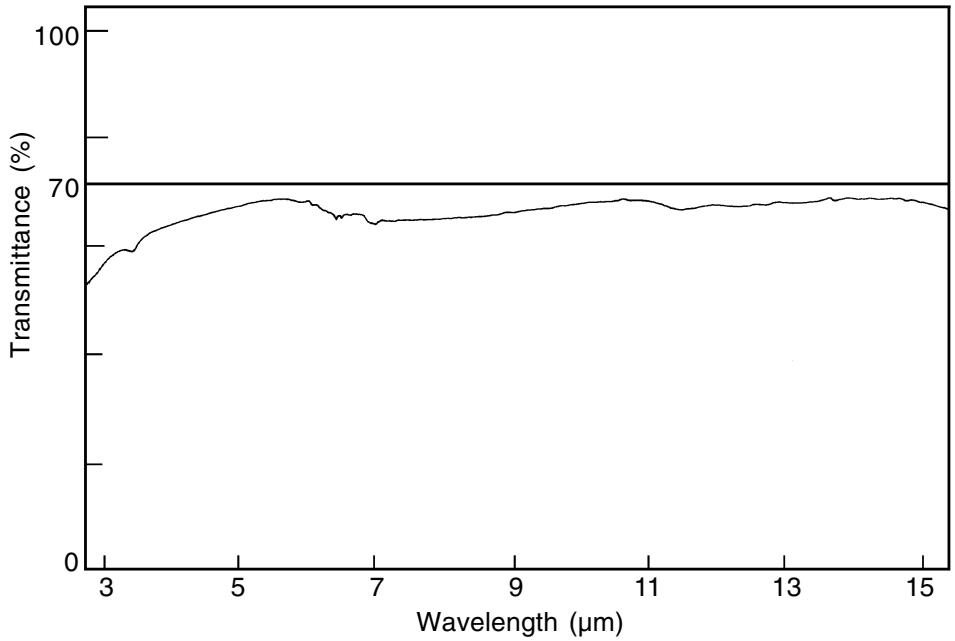

Fig. 20: IR transmission of DLC-coated ZnSe. The approximate transmission of uncoated ZnSe (70%) is also pesented for reference.[187]

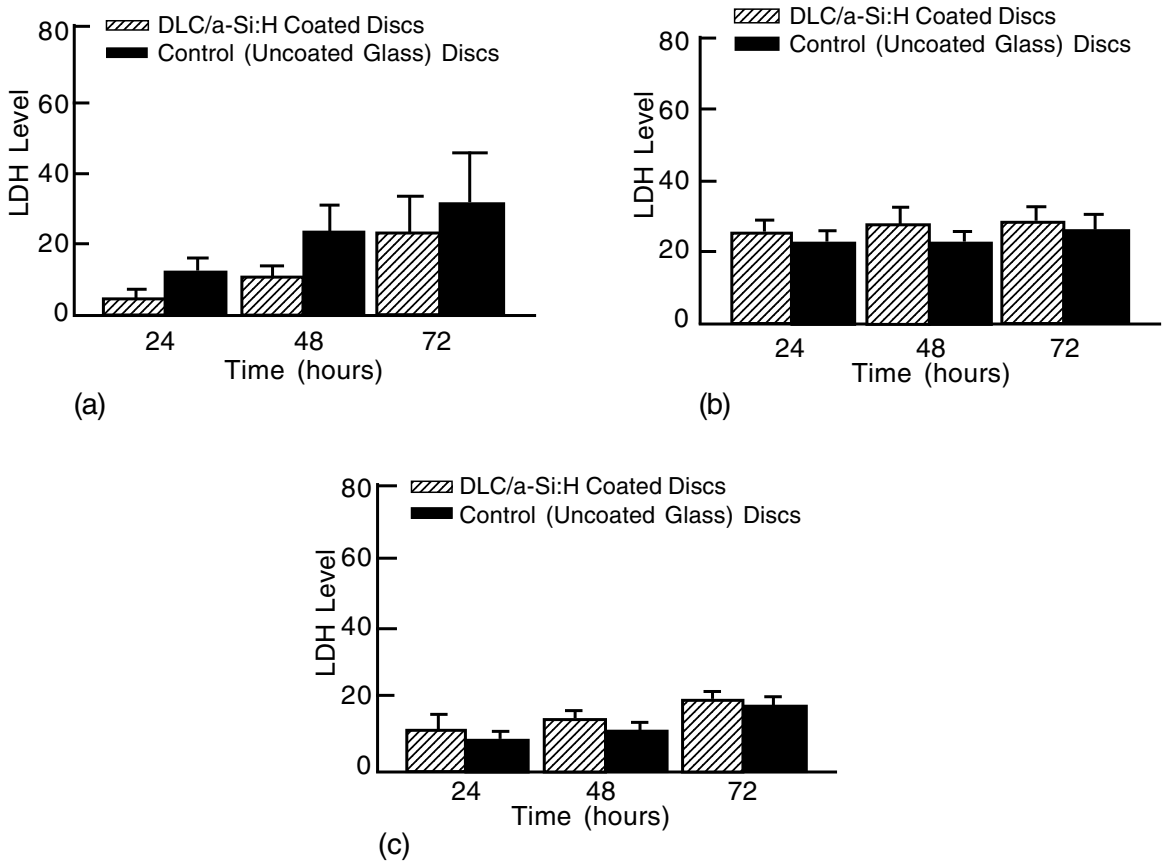

Fig. 21: LDH (Lactate dehydrogenase, an enzyme released at cell death is used as a measure of cell viability) release from human cells which indicates that there is no significant difference between the DLC and control samples.[243]

film,[256] ionized cluster beam deposition,[257] ionized magnetron sputtering,[258] nitrogen ion beam bombardment of C_{60} films,[259] etc. However, with all these techniques only amorphous carbonitride films, termed CN_x films, with N/C ratios between 0.3 and 0.5 (as compared to 1.33 required for the β-C_3N_4 stoichiometry) could be obtained. In some of these films small crystallites with dimensions ~ 0.5 μm embedded in an amorphous matrix have been found.[246,251,260]

Nitrogen ion implantation of the carbonitride films was also carried out to further increase the nitrogen percentage in the film to obtain the desired stoichiometry of β-C_3N_4. For carbonitride films deposited by cathodic arc,[261] no evidence of the β-C_3N_4 crystal structure was found and the films were primarily sp^2 bonded. On the other hand, for carbonitride films deposited by IBAD,[262] nitrogen ion implantation led to an increase in nitrogen percentage in the films and crystalline β-C_3N_4 with crystallite size of about 30 nm could be detected.

High pressure and high temperature methods have also been tried for synthesizing the predicted superhard crystalline phases of carbonitride. Wixom et al.[263] used shock compression of nitrogen containing material but could obtain only diamond. Carbonitride films prepared by pyrolysis of several organic compounds with high nitrogen content in a

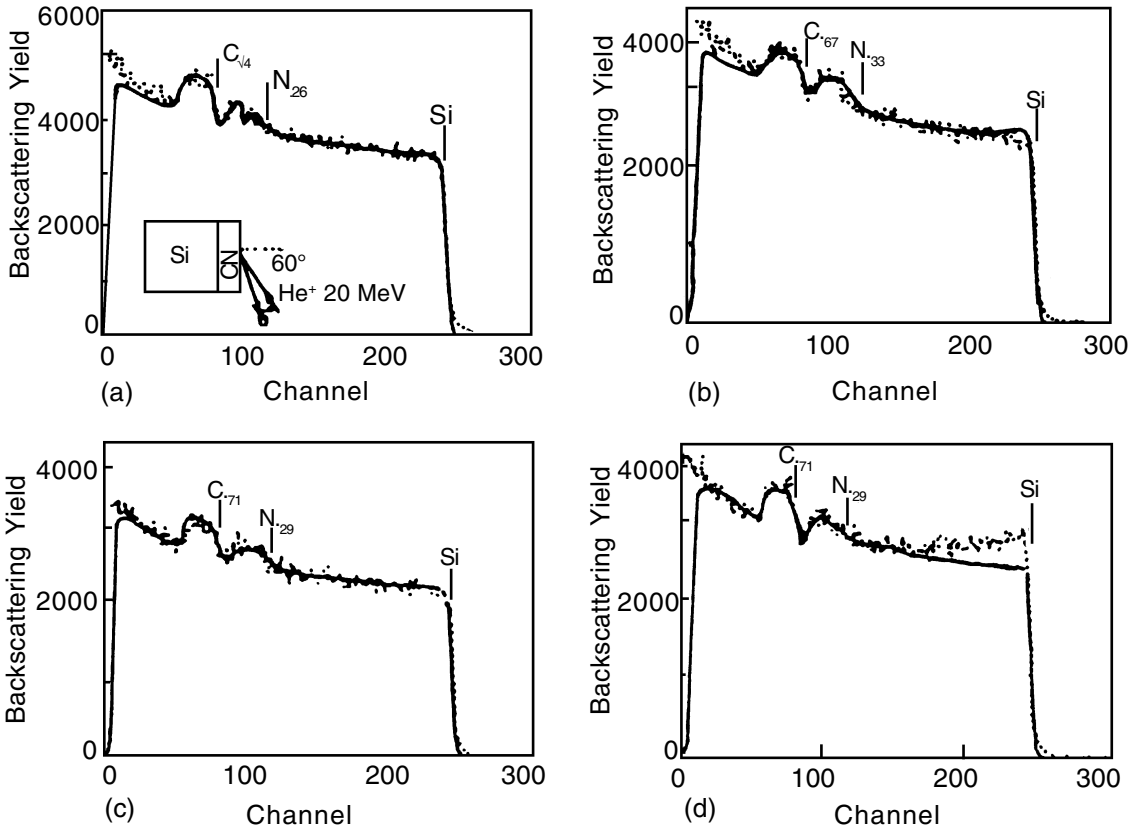

Fig. 22: RBS spectra of carbonitride films deposited, at different temperatures, using IBAD technique.

medium pressure closed vessel by Maya et al.[253] were amorphous without any evidence for the existence of sp^3 carbon and C-N bond formation.

However, in recent times, there have been several reports on synthesis of the crystalline form of carbonitride. Zhang et al.[264] synthesized crystalline carbonitride films with large crystalline grains up to ~10 μm (from SEM and XRD spectra) in size by RF plasma assisted hot filament chemical vapor deposition. Li. et al.[265] claimed to have synthesized polycrystalline C_3N_4 films (from XRD data) at ambient temperature by RF diode sputtering. From Auger electron spectroscopy, the N/C ratio was computed to be 1.33 as required for C_3N_4 stoichiometry.

However, in some reports, electron diffraction patterns of the carbonitride films that were indexed as β-C_3N_4 structure[251,264,265] were later observed to fit to other carbon phases. It was also shown that the published diffraction data can be re-indexed as α-C_3N_4,[266,267] the phase of carbonitride which was found to be more stable than β-C_3N_4. In a recent report by Chen et al.,[268] α and β phases of pure crystalline C_3N_4 in films deposited on nickel by bias assisted hot filament chemical vapor deposition have been confirmed by XRD and TEM measurements. However, none of the above-mentioned reports refer to the hardness and other tribological and related properties of these phases.

Figure 22 shows RBS spectra of amorphous (Raman spectra similar to amorphous diamond like films) carbonitride films deposited at different temperatures using IBAD.[269] Using this technique, maximum nitrogen incorporation was 33% as compared to 57% required for β-C_3N_4 stoichiometry. The XPS spectra (C 1s and N 1s) of the film with 33% nitrogen are shown in Figure 23. From these spectra the percentage of single bonded carbon and nitrogen is obtained

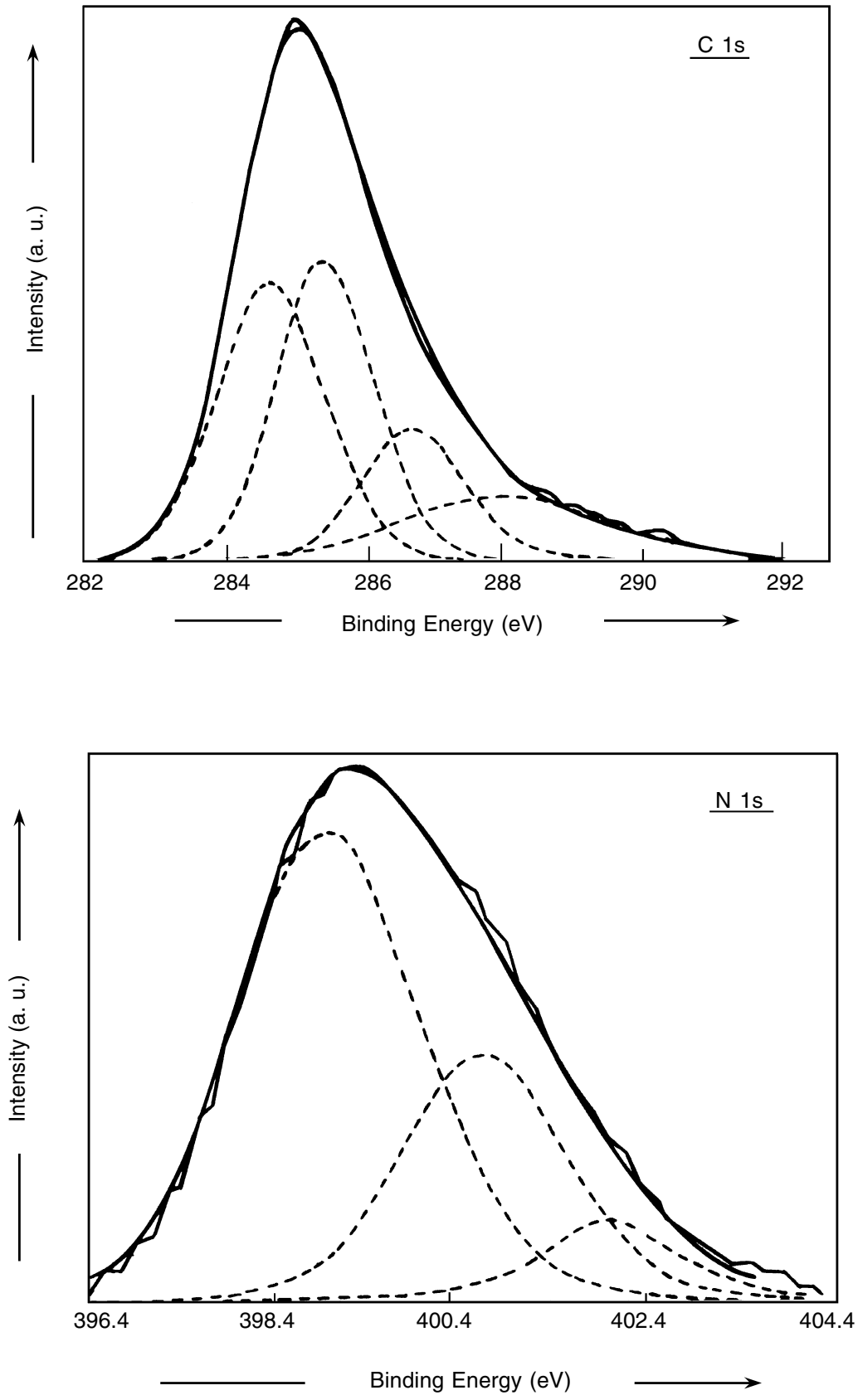

Fig. 23: C 1s and N 1s spectra of a carbonitride film with 33% nitrogen.

to be of the order of 40% indicating the presence of sp^2 and sp bonded carbon and nitrogen in the film.

Carbonitride Phases and Potential Applications

To date, amorphous carbonitride thin films (CN_x) containing up to ~50 % nitrogen have been reported, but these are not pure phases and contain C ≡ N impurity which increases with increasing nitrogen percentage. Nevertheless, these films have been found to be extremely resistant to plastic deformation with very high elastic recoveries. Also, these amorphous CN_x films have hardness significantly greater than the amorphous hard carbon films (~5 -15 GPa) generally used as protective overcoats for computer hard disc surfaces. It was shown that the CN_x coatings achieve wear rates 3-4 times lower than those of amorphous hard carbon films tested under similar conditions, suggesting that CN_x can potentially be a replacement overcoat material for next-generation computer disc surfaces.[270-271]

Another amorphous phase of carbonitride, C_2N phase with sp^2 bonding, was shown to be a stable phase[272] which exhibits high electrical resistivity and thermal conductivity similar to that of diamond-like films. The diamond-like properties and non-diamond-like bonding make C_2N an attractive candidate for applications such as thermal management in high-performance microelectronics.

Various other forms of carbonitride with high hardness have been suggested, such as fullerene-like carbonitride[273] and crystalline carbonitride composite.[274]

Teter and Hamley predicted several additional prototype structures by considering chemical systems with β-C_3N_4 type of bonding topology and by locating dense structures in the system.[267] These are graphite-C_3N_4 and α-C_3N_4 which are energetically favored relative to β-C_3N_4 and a cubic form of C_3N_4 that may have a zero-pressure bulk modulus exceeding that of diamond and which may be metastable at zero pressure.

As mentioned earlier, the structure of β-C_3N_4 was predicted to be similar to that of β-Si_3N_4 with carbon replacing the silicon in a complex network of CN_4 tetrahedra linked at the corners. This structure would be carbon four coordinated with nitrogen, and nitrogen three coordinated with carbon.[252] The stable form of carbonitride, α-C_3N_4, is predicted to possess a non-planar structure with the nitrogen incorporated as spheroidal cavities into a tetrahedral lattice. The structure of α-C_3N_4 has been described as an ABAB... stacking sequence of layers of β-C_3N_4 and its mirror image.[271]

A recent report[275] claims to have discovered the β-C_3N_4 phase as predicted by Liu and Cohen, with hardness equal to that of diamond. It reports nanoindentation tests on these coatings indicating a high elastic recovery and hardness. The same authors in their review[276] of carbon nitride films prepared by different techniques conclude that there is not enough evidence that β-C_3N_4 can be produced as large crystals. On the other hand, in another recent paper,[277] x-ray powder diffraction patterns and structure factors of hypothetical crystalline C_3N_4 have been recalculated. The authors have observed discrepancy between the calculated diffraction intensities and the experimental ones for the synthesized compounds. The computational method used here was also applied to Si_3N_4 and the corresponding calculated XRD patterns matched the experimental ones taken from the joint committee on powder diffraction standards cards, indicating the reliability of the computational pragramme. This implies that, in so far as phase identification is concerned, none of the claims regarding successful synthesis of crystalline C_3N_4, α-C_3N_4 and defect zincblende C_3N_4 are convincing.

Thus, current research appears to be a long way from the carbonitride being synthesized in its predicted crystalline forms. However, if crystalline C_3N_4 is synthesized, it would have several potential applications similar to diamond and diamond-like carbon, due to its high hardness, elasticity and thermal conductivity. Because of the promising application possibilities, the search continues for crystalline C_3N_4.

Acknowledgments

The authors will like to thank S.M. Kanetkar (now at DGP Hinoday, Pune), Rajiv Joshi (IBM, Yorktown heights), R. P. Sharma (Maryland) and Atul Kulkarni (Multiarc, Pune) for their contributions to certain phases of the work carried out at the Department of Physics, University of Pune.

References

1. C.M. Welbourn, *The Fourth International Conference on the New Diamond Science and Technology Abstracts*, 1994, pp.75-86.
2. M. O'Donoghue, *Gemstones*, Chapman and Hall, U.K., 1988, pp.176-182.
3. F.P. Bundy, *Journal of Geophysics Research*, Vol.85, 1980, pp.6930-6935.
4. R.C. DeVries, *Annual Review Materials Science*, Vol.17, 1987, pp.161-187.
5. B.V. Derjaguin and D.B. Fedoseev, *Science Amercian*, Vol.233, 1975, pp.102-104.
6. J.C. Angus, H.A. Will, and W.S. Stanko, *Journal of Applied Physics*, Vol.39, 1968, pp.2915-2922.
7. S.P. Chauhan, J.C. Angus, and N.C. Gardner, *Journal of Applied Physics*, Vol.47, 1976, pp.4746-4754.
8. K.E. Spear, *Journal of Amercian Ceramic Society*, Vol.72, 1989, pp.171-191.
9. B. Lux and R. Haubner, *RM and HM*, 1989, pp.158-163.
10. P.K. Bachmann and H. Lydtin, *Diamond and Diamond-Like Films and Coatings*, R.E. Clausing, L.L. Horton, J.C. Angus, and P.Koidl, eds., Plenum, New York, 1991, pp.829-836.
11. T.E. Derry and J.P.F. Sellschop, *Nuclear Instruments Methods*, Vol.91, 1981, pp.23-27.
12. R.S. Nelson, J.A. Hudson, D.J. Mazey, and R. Piller, *Proceedings of Royal Society of London*, Vol.A386, 1983, pp.211-224.
13. S.T. Lee, W.M. Lau, L.J. Huang, Z. Ren, and F. Qin, *Diamond and Related Materials*, Vol.4, 1995, pp.1353-1358.
14. S.T. Lee, S. Chen, G. Braunstein, X. Feng, I. Bello, and W.M. Lau, *Applied Physics Letters*, Vol.59, 1991, pp.785-787.
15. J.F. Prins, *Thin Solid Films*, Vol.212, 1992, pp.11-19.
16. J.F. Prins, *Diamond and Related Materials,* Vol.2, 1993, pp.646-655.
17. E.G. Spencer, P.H. Schmidt, D.C. Joy, and F.J. Sansalone, *Applied Physics Letters,* Vol.29, 1976, pp.118-120.
18. T. Miyazawa, S. Misawa, S. Yoshida, and S. Gonda, *Journal of Applied Physics,* Vol.55, 1984, pp.188-193.
19. A. Antilla, J. Koskinen, M. Bister, and J. Hirvonen, *Thin Solid Films*, Vol.136, 1986, pp.129-134.
20. J.L. Robertson, S.C. Moss, Y. Lifshitz, S.R. Kasi, J.W. Rabalais, G.D. Lempert, and E. Rapoport, *Science*, Vol.243, 1989, pp.1047-1050.
21. M. Kitabatake and K. Wasa, *Journal of Applied Physics*, Vol.58, 1985, pp.1693-1695.
22. M. Basu, A.B.M. Maity, S.N. Kundu, S. Chaudhari, and A.K. Pal, *Proceedings of National Conference on Thin Film Characterization and Applications*, Sa.K. Narayandass and D. Mangalraj, eds., Allied Publishers Limited, 1996, pp.301-315.
23. D.V. Fedoseev, B.V. Derjaguin, and R. Roy, *Proceedings of Second International Conference New Diamond Science and Technology*, R. Messier, J.T.Glass, J.E. Butler, and R. Roy, eds., MRS, 1991, pp.439-442.
24. S.B. Ogale, A.P. Malshe, S.M. Kanetkar, and S.T. Kshirsagar, *Solid State Communication*, Vol.84, 1992, pp.371-376.
25. N. Kikuchi, Y. Ohsawa, and I. Suzuki, *Diamond and Related Materials*, Vol.2, 1993, pp.190-196.
26. R. Roy, *Fourth International Conference on the New Diamond Science and Technology Abstracts*, 1994, pp.51-52.
27. S.D. Roy, Ph.D. Thesis, 1998, p.60.
28. E.B.D. Bourdon, P. Kovarik, and R.H. Prince, *Diamond and Related Materials*,Vol.2, 1993, pp.425-431.

29. M.C. Polo, J. Cifre, G. Sanchez, R. Aguiar, M. Varela, and J. Esteve, *Diamond and Related Materials*, Vol.4 1995, pp.780-783.
30. P. Mistry, M.C. Turchan, S. Liu, G.O. Granse, T. Baurmann, and M.G. Shara, *Inn. Materials Res.*, Vol.1, 1996, pp.193-196.
31. R. Messier, A.R. Badzian, T. Badzian, K.E. Spear, P. Bachmann, and R. Roy, *Thin Solid Films*, Vol.153, 1987, pp.1-9.
32. W. Zhu, H.S. Kong, and J.T. Glass, *Diamond Films and Coatings Development, Properties and Applications*, R.F. Davis, ed., Noyes Publications, 1991, pp.244-248.
33. P.J. Ellis, D.S. Buhaento, and B.R. Stoner, *Diamond and Related Materials*, Vol.4, 1995, pp.406-409.
34. P. Kania and P. Oelhefen, *Diamond and Related Materials*, Vol.4, 1995, pp.425-428.
35. P.E. Pehrsson, F.G. Celii, and J.E. Butler, *Diamond Films and Coatings Development, Properties and Applications*, R.F. Davis, ed., Noyes Publications, 1991, pp.68-71.
36. J.E. Butler, R.L. Woodin, *Phil. Transactions of Royal Society London*, U.K., Vol.A342, 1993, pp.209-214.
37. T. Kawato and K. Kondo, *Japanese Journal of Applied Physics*, Vol.26, 1987, pp.1429-1432.
38. Y. Saito, K. Sato, H. Tanaka, K. Fujita, and S. Matsuda, *Journal of Materials Science,* Vol.23, 1988, pp.842-846.
39. S.J. Harris and A.M. Weiner, *Applied Physics Letters*, Vol.55, 1989, pp.2179-2181.
40. M. Frenklach, R. Kematick, D. Huang, W. Howard, K.E. SPear, A.W. Phelps, and R. Koba, *Journal of Applied Physics*, Vol.66 1989, pp.395-399.
41. Y. Liou, A. Inspektor, R. Weimer, D. Knight, and R. Messier, *Journal of Materials Res.*, Vol.5, 1990, pp.2305-2309.
42. R.A. Rudder, G.C. Hudson, J.B. Posthill, R.E. Thomas, and R.J. Markunas, *Applied Physics Letters,* Vol.59, 1991, pp.791-793.
43. P.K. Bachmann and D.U. Wiechert, *Diamond and Related Materials*, Vol.1, 1992, pp.422-427.
44. T. Kotaki, Y. Amada, K. Harada, H. Uyama, and O. Matsumoto, *Diamond and Related Materials,* Vol.2, 1993, pp.342-346.
45. H. Lux, *Diamond and Related Materials,* Vol.3, 1994, pp.277-281.
46. R. Beckmann, B. Sobisch, and W. Kulisch, *Diamond and Related Materials*, Vol.4, 1995, pp.256-260.
47. S. Sato, *New Diamond*, English, ed., Vol.2, 1990, pp.15-19.
48. W.A. Yarbrough and R. Messier, *Science*, Vol.247, 1990, pp.688-696.
49. C.H. Wu, M.A. Tamor, T.J. Potter, and E.W. Kaiser, *Journal of Applied Physics*, Vol.68, 1990, pp.4825-4829.
50. C.A. Rego, P.W. May, C.R. Henderson, M.N.R. Ashfold, K.N. Rosser, and N.M. Everitt, *Diamond and Related Materials*, Vol.4, 1995, pp.770-776.
51. P.K. Bachmann, D. Leers, and H. Lydtin, *Diamond and Related Materials*, Vol.1, 1991, pp.1-12.
52. E.G. Rakov, A.V. Modin, and A.V. Grunsky, *Journal of Chemical Vapor Deposition*, Vol.6, 1997, pp.30-38.
53. P.K. Bachmann and R. Messier, C and EN Vol.67, 1989, pp.24-29.
54. C.F. Chen, S.H. Chen, T.M. Hong, and S.H. Wu, *Diamond and Related Materials*, Vol.2, 1993, pp.732-736.
55. Y. Mitsuda, Y. Kojima, T. Yoshida, and K. Akashi, *Journal of Materials Science*, Vol.22, 1987, pp.1557-1562.
56. F.G. Celli, P.E. Pehrsson, H.T. Wang, and J.E. Butler, *Applied Physics Letters,* Vol.52, 1988, pp.2043-2045.
57. W.A. Yarbrough, K. Tankala, and T. DebRoy, *Proceedings of Second International Conference, New Diamond Science and Technology*, R. Messier, J.T. Glass, J.E. Butler, and R. Roy, eds., MRS, 1991, pp.341-346.
58. M. Frenklach and H. Wang, *Physical Review B*, Vol.43, 1991, pp.1520-1545.
59. Z. Chen, G.P. Wirtz, and S.D. Brown, *Journal of Amercian Ceramic Society*, Vol.75, 1992, pp.2107-2115.
60. L.R. Martin and M.W. Hill, *Applied Physics Letters*, Vol.55, 1989, pp.2248-2249.
61. C.J. Chu, M.P. D'Evelyn, R.H. Hange, and

J.L. Margrave, *Journal of Materials Res.* Vol.5, 1990, pp.2313-2315.
62. N. Ota and N. Fujimori, *The Fourth International Conference on the New Diamond Science and Technology Abstracts*, 1994, pp.57-61.
63. S.J. Harris and L.R. Martin, *Journal of Materials Res.*, Vol.5, 1990, pp.2313-2316.
64. K. Larsson, S. Lunell, and J.O. Carlsson, *Diamond and Related Materials*, Vol.2, 1993, pp.949-951.
65. E.S. Machlin, *Journal of Materials Res.,* Vol.3, 1988, pp.958-963.
66. W.B. Yarbrough, *Journal of Vacuum Science Technology*, Vol.A9, 1991, pp.1145-1149.
67. W.A. Yarbrough, A. Inspektor, and R. Messier, *Amorphous Carbon*, S. Alterovitz and J. Pouch, ed., TranTech Publications, Switzerland, 1989.
68. M. Kawarada, K. Kurihara, and K. Sasaki, *Diamond and Related Materials, Vol.*2, 1993, pp.1083-1089.
69. R. Haubner and B. Lux, *Diamond Films Technology*, Vol.3, 1994, pp.209-213.
70. P.O. Joffreau, R. Haubner, and B. Lux, R and HM, 1988, pp.186-189.
71. P. Ascarelli and S. Fontana, *Diamond and Related Materials*, Vol.2, 1993, pp.990-996.
72. J. Stiegler, T. Lang, M. Nygard Fergusson, Y. Von Kaenel, and E. Blank, *Diamond and Related Materials,* Vol.5, 1996, pp.226-229.
73. S. Matsumoto, *Journal of Materials Science Letters*, Vol.4, 1985, pp.600-603.
74. T.P. Ong and R.P.H. Chang, *Applied Physics Letters*, Vol.55, 1989, pp.2063-2065.
75. Y. Liou, R. Weimer, D. Knight, and R. Messier, *Applied Physics Letters*, Vol.56, 1990, pp.437-439.
76. Y. Murakawa, H. Yamashita, and H. Miyadera, *Journal of Vacuum Science Technology*, Vol.A9, 1991, pp.76-79.
77. S. Jin and E. Svillano, *The Fourth International Conference on the New Diamond Science and Technology Abstracts*, 1994, pp.62-66.
78. J. Stiegler, T. Lang, M. Nygard-Fergusson, Y. Von Kaenel, and E. Blank, *Diamond and Related Materials*, Vol.5, 1996, pp.226-229.
79. Y. Chakk, R. Kalish, and A. Hoffman, *Diamond and Related Materials*, Vol.5, 1996, pp.1074-1079.
80. S.S. Eskildsen *Proceedings of Second International Conference on the Applications of Diamond and Related Materials*, M. Yoshikawa, M. Murakawa, Y. Tzeng, and W.A. Yarbrough, eds., MYU, Tokyo, 1993, pp.297-305.
81. P. Karve, S.R. Sainkar, and S.T. Kshirsagar, *Materials Letters*, Vol.34, 1998, pp.387-391.
82. T. Takarada, T. Okazaki, K. Kato, and Y. Nakaike, *The Fourth International Conference on the New Diamond Science and Technology Abstracts*, 1994, p.61.
83. T. Hartnett, R. Miller, D. Montanari, C. Willingham, and R. Tustison, *Journal of Vacuum Science Technology*, Vol.A8, 1990, pp.2129-2132.
84. R. Haubner and B. Lux, *Diamond Films Technology*, Vol.3, 1994, pp.209-213.
85. I. Endler, A. Leonhardt, H.J. Scheibe, and R. Born, *Diamond and Related Materials*, Vol.5, 1996, pp.299-302.
86. I.Y. Konyashin and M.B. Guseva, *Diamond and Related Materials*, Vol.5, 1996, pp.575-579.
87. S.M. Kanetkar, A.A. Kulkarni, A. Vaidya, R.D. Vispute, S.B. Ogale, S.T. Kshirsagar, and S.C. Purandare, *Applied Physics Letters*, Vol.63, 1993, pp.740-742.
88. P. Karve, J.P. Pal, S.C. Patil, A.A. Kulkarni, S.M. Kanetkar, N. Parikh, B. Patnaik, and S.T. Kshirsagar, *Diamond and Related Materials*, Vol.5, 1996, pp.1527-1530.
89. S. Yugo, A. Izumi, T. Kanai, T. Kimura, T. Muto, and S. Yugo, *Applied Physics Letters*, Vol.58, 1991, pp.1036-1038.
90. S. Yugo, T. Kimura, and T. Kanai, *Diamond and Related Materials*, Vol.2, 1992, pp.328-331.
91. B.R. Stoner, G.H. Ma, S.D. Wolter, and J.T. Glass, *Physical Review*, Vol.B45, 1992, pp.11067-11084.
92. J. Robertson, *Diamond and Related Materials*, Vol.4, 1995, pp.549-556.
93. S. Moulin and A.M. Bonnot, *Diamond and Related Materials*, Vol.4, 1995, pp.750-754.

94. J. Stiegler, Y. Von Kaenel, M. Cans, and E. Blank, *Journal of Materials Research*, Vol.11, 1996, pp.716-719.
95. W.J.P. Van Enckevort, G. Janssen, W. Vollenberg, J.J. Schermer, and L.J. Giling, *M. eal. Diamond and Related Materials*, Vol.2, 1993, pp.997-1003.
96. J.S. Kim, M.H. Kim, S.S. Park, and J.Y. Lee, *Journal of Applied Physics*, Vol.67, 1990, pp.3354-3357.
97. Ch. Wild, N. Herres, and P. Koidl, *Journal of Applied Physics*, Vol.68, 1990, pp.973-978.
98. Ch. Wild, P. Koidl, W. Muller-Sebert, H. Walcher, R. Kohl, N. Herres, R. Locher, R. Samlenski, and R. Brenn, *Diamond and Related Materials*, Vol.2, 1993, pp.158-168.
99. R.E. Clausing, L. Heatherley, E.D. Specht, and K.L. More, *Proceedings of Second International Conference New Diamond Science and Technology*, R. Messier, J.T. Glass, J.E. Butler, and R. Roy, eds., MRS, 1991, pp.575-581.
100. M.A. Tamor and M.P. Everson, *Journal of Materials Research,* Vol.9, 1994, pp.1839-1842.
101. A.R. Badzian, T. Badzian, and L. Pilione, *RM and HM*, 1990, pp.92-99.
102. H. Shiomi, K. Tanabe, Y. Nishibayashi, and N. Fujimori, *Japanese Journal of Applied Physics*, Vol.29, 1990, pp.34-37.
103. C.J. Chu, M.P. D'Evelyn, R. Hauge, and J.L. Margrave, *Journal of Applied Physics*, Vol.70, 1991, pp.1695-1705.
104. Y. Avigal, C. Uzan-Saguy, and R. Kalish, *Diamond and Related Materials*, Vol.2, 1993, pp.462-467.
105. R. Haubner, *RM and HM*, Vol.9, 1990, pp.70-75.
106. A. Argoitia, J.C. Angus, J.S. Ma, L. Wang, P. Pirouz, and W.R.L. Lambrecht, *Journal of Materials Research*, Vol.9, 1994, pp.1849-1853.
107. S. Koizumi, T. Murakami, T. Inuzuka, and K. Suzuki, *Applied Physics Letters*, Vol.57, 1990, pp.563-565.
108. B.R. Stoner and J.T. Glass, *Applied Physics Letters*, Vol.60, 1992, pp.698-700.
109. R. Kohl, Ch. Wild, N. Herres, P. Koidl, B.R. Stoner, and J.T. Glass, *Applied Physics Letters*, Vol.63, 1993, pp1792-1794.
110. X. Jiang and C.P. Klages, *Diamond and Related Materials*, Vol.2, 1993, pp.1112-1113.
111. D.K. Milne, P.G. Roberts, P. John, M.G. Jubber, M. Liehr, and J.I.B. Wilson, *Diamond and Related Materials*, Vol.4, 1995, pp.394-400.
112. Q. Chen, Y. Chen, J. Yang, and Z. Lin, *Thin Solid Films*, Vol.274, 1996, pp.160-166.
113. A.H. Deutchman and R.J. Partyka, *Advanced Materials and Processes*, Vol.6, 1989, pp.29-33.
114. P.K. Bachmann, *Physics World*, 1991, pp.32-36.
115. P.K. Bachmann, D. Leers, and D.U. Wiechert, *Journal of De Physique IV, Colloque C2, Supply, Au J. de Physique II*, Vol.1, 1991, pp.C2-907-915.
116. N. Narutaki, H. Usuki, Y. Yamane, and T. Ito, *Surface Modification Technologies*, T.S. Sudarshan and J.F. Braza, eds., The Institute of Materials, Vol.5, 1992, pp.259-271.
117. C. Tsai, J.C. Nelson, W.W. Gerberich, J. Heberlein, and E.P. Fender, *Diamond and Related Materials*, Vol.2, 1993, pp.617-620.
118. H. Mohrbacher, B. Blanpain, J.P. Celis, and J.R. Roos, *Diamond and Related Materials*, Vol.2, 1993, pp.879-884.
119. L. Nordsletten, A.K.M. Hogasen, Y.T. Konttinen, S. Santavirta, P. Aspenberg, and A.O. Aasen, *Biomaterials*, Vol.17, 1996, pp.1521-1524.
120. J. Cifre, M.C. Polo, G. Sanchez, A. Lousa, and J. Esteve, *Diamond and Related Materials*, Vol.4, 1995, pp.798-801.
121. N.A. Morrison, I.C. Drummond, C. Garth, P. John, D.K. Milne, G.P. Smith, M.G. Jubber, and J.I.B. Wilson, *Diamond and Related Materials*, Vol.5, 1996, pp.1118-1124.
122. D.S. Hoover, S.Y. Lynn, and D. Garg, *Solid State Technology*, 1991, pp.89-93.
123. R.C. Eden, *Diamond and Related Materials*, Vol.2, 1993, pp.1051-1058.
124. A. Partha, *Journal of Microelectron*,

Vol.27, 1996, pp.9-13.

125. M. Nagai, Y. Yamamoto, K. Tanabe, Y. Kumazawa, and N. Fujimori, *Proceedings of SPIE 3235*, 1997, pp.302-309.
126. J.T. Glass, B.A. Fox, D.L. Dreifus, and B.R. Stoner, *MRS Bulletin*, Vol.23, 1998, pp.49-57.
127. M. Kohzaki, K. Higuchi, S. Noda, and K. Uchida, *Diamond and Related Materials*, Vol.2, 1993, pp.612-616.
128. W.A. Yarbrough, N.D. Rosen, L.J. Pilione, and W.D. Drawl, *Proceedings of SPIE 1112*, 1989, pp.176-181.
129. C.A. Klein, *Diamond and Related Materials*, Vol.2, 1993, pp.1024-1032.
130. E.J. Coad, C.S.J. Pickles, G.H. Jilbert, and J.E. Field, *Diamond and Related Materials*, Vol.5, 1996, pp.640-647.
131. H.W. Ko, S.E. Hsu, S.J.Yang, M.S. Tsai, and Y.H. Lee, *Diamond and Related Materials,* Vol.2, 1993, pp.694-698.
132. M.C. Costello, D.A. Tossell, D.M. Reece, C.J. Brierley, and J.A. Savage, *Diamond and Related Materials*, Vol.3, 1994, pp.1137-1143.
133. H. Noguchi, Y. Kubota, and T. Takarada, *Journal of Electrochemical Society*, Vol.144, 1997, pp.3304-3307.
134. P.R. Chalker, C. Johnson, J.A.A. Crossley, J. Ambrose, C.F. Ayres, R.E. Harper, I.M. Buckley-Golder, and K. Kobashi, *Diamond and Related Materials*, Vol.2, 1993, pp.1100-1106.
135. B.A. Fox, M.L. Hartsell, D.M. Malta, H.W. Wynands, C.T. Kao, L.S. Plano, G.J. Tessmer, R.B. Hernard, J.S. Holmes, A.J. Tessmer, and D.L. Dreifus, *Diamond and Related Materials*, Vol.4, 1995, pp.622-627.
136. H. Kiyota, E. Matsushima, K. Sato, H. Okushi, T. Ando, M. Kamo, Y. Sato, and M. Iida, *The Fourth International Conference on the New Diamond Science and Technology Abstracts*, 1994, p.86.
137. E.I. Givargizov, L.L. Aksenova, A.V. Kuznetsov, P.S. Plekhanov, E.V. Rakova, A.N. Stepanova, V.V. Zhirnov, and P.C. Nordine, *Diamond and Related Materials*, Vol.5, 1996, pp.938-945.
138. N.A. Fox, W.N. Wang, T.J. Davis, J.W. Steeds, and P.W. May, *Applied Physics Letters*, Vol.71, 1997, pp.2337-2339.
139. J.P.Bade, S.R. Sahaida, B.R. Stoner, J.A. Von Windheim, J.T.Glass, K. Miyata, K. Nishimura, and K.Kobashi, *Diamond and Related Materials*, Vol.2, 1993, pp.816-819.
140. K. Okano, T. Iwasaki, H. Kiyota, H. Maekawa, T. Kurosu, and M. Iida, *Surface Modification Technologies*, T.S. Sudarshan and J.F. Braza, eds., The Institute of Materials, Vol.5, 1992, pp.235-244.
141. K. Okano, S. Koizumi, S. Silva, P. Ravi, and G.A.J. Amartunga, *Nature*, Vol.381, 1996, pp.140-144.
142. H. Schmellenmeier, *Z. Physics Chemical*, Vol.205, 1955, pp.349-352.
143. S. Aisenberg and R.W. Chabot, *Journal of Applied Physics*, Vol.42, 1971, pp.2953-2958.
144. J. Robertson, *Surface Coatings Technology*, Vol.50, 1992, pp.185-203.
145. Status and Applications of Diamond and Diamond like Materials: An Emerging Technology, National Materials Advisory Board, 1990.
146. P. Koidl, C. Wild, B. Dischler, J. Wagner, and M. Ramsteiner, *Materials Science Forum*, Vol.52, 1990, pp.41-69.
147. J.W. Zou, K. Reichelt, K. Schmidt, and B. Dischler, *Journal of Applied Physics*, Vol.65, 1989, pp.3914-3918.
148. C. Srividya and S.V. Babu, *Chemical Materials*, Vol.8, 1996, pp.2528-2533.
149. K. Kamata, T. Inoue, K. Maruyama, and I. Tanabe, *Japanese Journal of Applied Physics*, Vol.29, 1990, pp.L1203-1205.
150. A.V. Stainshevsky, and L.Yu. Khriachtchev, *Diamond and Related Materials*, Vol.5, 1997, pp.1355-1361.
151. M. Hakovirta, *Diamond and Related Materials*, Vol.5, 1996, pp.186-189.
152. P.H. Gaskell, A. Saeed, P. Chieux, and D.R. McKenzie, *Physical Review Letters*, Vol.67, 1991, pp.1286-1289.
153. S. Kasi, H. Kang, and J.W. Rabalais,

Physical Review Letter, Vol.59, 1987, pp.75-78.
154. Y. Lifshitz, G.D. Lempert, E. Grossman, I. Avigal, C. Uzan-Saguy, R. Kalish, J. Kullik, D. Marton, and J.W. Rabalais, *Diamond and Related Materials*, Vol.4, 1995, pp.318-323.
155. C. Weissmantel, C. Schurrer, F. Frohlic, P. Grau, and H. Zscheile, *Thin Solid Films*, Vol.146, 1979, pp.93-107.
156. N. Savvides, *Journal of Applied Physics*, Vol.59, 1986, pp.4133-4145.
157. C.B. Collins, *Applied Physics Letters*, Vol.54, 1989, pp.216-218.
158. A.M. Jones, C.J. Bedell, G. Dearnaley, C. Johnston, and J.M. Owens, *Diamond and Related Materials*, Vol.1, 1992, pp.416-421.
159. J. Robertson, *Diamond and Related Materials*, Vol.2, 1993, pp.984-989.
160. I.I. Askenov, V.A. Belous, V.G. Padalka, and V.M. Khoroshikh, *Fountzoulas Plazmy*, Vol.4, 1978, pp.758-764.
161. S.D. Berger, D.R. Mckenzie, and P.J. Martin, *Philos. Mag. Letters*, Vol.57, 1988, pp.285-290.
162. I.I. Askenov, S.I. Vakula, V.G. Padalka, V.E. Strel'nitskii, and V.M. Khoroshikh, *Soviet Physics Technology Physics*, Vol.25, 1980, pp.1164-1169.
163. J. Koskinen, *Journal of Applied Physics*, Vol.63, 1988, pp.2094-2097.
164. A.I. Maslov, G.K. Dmitriev, and Y.D. Chistyakov, *Instruments Expert Technical*, Vol.28, 1985, pp.662-665.
165. P.J. Martin, R.P. Netterfield, and T.J. Kinder, *Thin Solid Films*, Vol.193/194, 1990, pp.77-83.
166. A. Antilla, J. Koskinen, R. Lappalainen, J.P. Hivonen, D. Stone, and C. Paszkiet, *Applied Physics Letters*, Vol.50, 1987, pp.132-134.
167. J. Robertson, *Philos. Trans. Royal Society*, Vol.A342, 1993, pp.277-286.
168. F. Jansen, M. Machonkin, S. Kaplan, and S. Hark, *Journal of Vacuum Science Technology*, Vol.A3, 1985, pp.605-611.
169. M. Kuhn, P. Meja, and F. Richter, *Diamond and Related Materials*, Vol.2, 1993, pp.1350-1358.
170. D.R. McKenzie, D. Mueller, B.A. Pailthorpe, Z.H. Wang, E. Kravtchinskaia, D. Sega, P.B. Lukins, P.D. Swift, P.J. Martin, G. Amartunga, P.H. Gaskell, and A. Saeed, *Diamond and Related Materials*, Vol.1, 1991, pp.51-60.
171. J.C. Angus, J.E. Stultz, P.J. Shiller, J.R. MacDonald, M.M. Mirtich, and S. Domitz, *Thin Solid Films*, Vol.118, 1984, pp.320-329.
172. B.A. Banks and S. Rutledge, *Journal of Vacuum Science Technology*, Vol.21, 1982, pp.807-815.
173. C. Weissmantel, K. Bewilogua, K. Breuer, D. Dietrich, U. Ebersbach, H.J. Erler, B. Rau, and G. Reiss, *Thin Solid Films*, Vol.96, 1982, pp.31-44.
174. S. Fujimori, T. Kasai, and T. Inamura, *Thin Solid Films*, Vol.92, 1982, pp.71-80.
175. N. Savvides, *Materials Res. Forum*, Vol.52, 1990, pp.407-413.
176. F. Davanloo, T.J. Lee, D.R. Sander, H. Park, and C.B. Collins, *Journal of Applied Physics*, Vol.71, 1992, pp.1446-1453.
177. J.J. Cuomo, J.P. Doyle, J. Bruley, and J.C. Liu, *Applied Physics Letters*, Vol.58, 1991, pp.466-468.
178. M.W. Thompson, *Defects and Radiation Damage in Metals*, Cambridge University Press, 1969.
179. G. Costas Fountzoulas, *Proceedings of Materials Research Society Symposium*, Vol.396, 1996, pp.569-574.
180. F. Rossi, B. Andre, A.V. Veen, P.E. Mijnarends, H. Schut, M.P. Delplancke, W. Gissler, J. Haupt, G. Lucazeau, and L. Abello, *Journal of Applied Physics*, Vol.75, 1994, pp.3121-3129.
181. S.J. Bull, *Diamond and Related Materials*, Vol.4, 1995, pp.827-836.
182. Y. Liu, A. Erdemir, and E.J. Meletis, *Surface Coatings Technology*, Vol.82, 1996, pp.48-56.
183. E. Marotta, N. Bakhru, A.Grill, V. Patel, and B. Meyerson, *Thin Solid Films*, Vol.206, 1991, pp.188-194.
184. E. Ali, C. Bindel, R.F. George, and P. Wilbur, *Tribology Transactions*, Vol.39, 1996, pp.735-742.
185. A.R. McCabe, A.M. Jones, and S.J. Bull, *Diamond and Related Materials*, Vol.3,

1994, pp.210-209.
186. J. Lankford, C.R. Blanchard, C.M. Agrawal, D.M. Micallef, G. Dearnaley, and A.R.M.C. Cabe, *Nuclear Methods*, Vol.B80-81, 1993, pp.1441-1445.
187. F.M. Kimock and B.J. Knapp, *Surface Coatings Technology*, Vol.56, 1993, pp.273-279.
188. J. Koskinen, R. Lappalainen, A. Antilla, and J.P. Hirvonen, *Diamond and Related Materials*, Vol.3, 1994, pp.52-55.
189. M.J. Mirtich, D. Nir, D.M. Swec, and B.A. Banks, *Journal of Vacuum Science Technology*, Vol.A4, 1986, pp.2860-2864.
190. A.H. Lettington, *Philos. Transactions Royal Society*, Vol.A342, 1993, pp.287-296.
191. A. Grill, B. Meyerson, and V. Patel, *Journal of Materials Research*, Vol.3, 1988, pp.214-218.
192. E. Cellier and J.F. Nowak, *Diamond and Related Materials*, Vol.3, 1994, pp.1112-1120.
193. Sh. Trakhtenberg, S.A. Plotnikov, O.M. Bakunin, S.G. Yakovleva, A.A. Nechaev, S.D. Gorpinchenko, A.B. Vladimirov, L.G. Korshunov, N.V. Gavrilov, and V.N. Mizgulin, *Diamond and Related Materials*, Vol.4/7, 1995, pp.1020-1024.
194. E.F. Chaikovskii, V.M. Puzikov, and A.V. Semenou, *Sov. Physics Crystal.*, Vol.26, 1981.
195. E.G. Spencer, P.H. Schmidt, D.C. Joy, and F.J. Sanasalone, *Applied Physics Letters*, Vol.29, 1976, pp.118-120.
196. Y. Lifshitz, S.R. Kasi, J.W. Rabalais, and W. Eckstein, *Physical Review*, Vol.B41, 1990, pp.10468-10480.
197. S.Prawer, K.W. Nugent, Y. Lifshitz, G.D. Lempert, E. Grossman, J. Kulik, I. Avigal, and R. Kalish, *Diamond and Related Materials*, Vol.5, 1996, pp.433-438.
198. B.T. Kelly, *Physics of Graphite,* Elsevier, U.K., 1981, pp.87.
199. H.J. Steffen, D. Marton, and J.W. Rabalais, *Physical Review Letter*, Vol.68, 1992, pp.1726-1729.
200. J. Koike, D.M. Parkin, and T.E. Mitchell, *Applied Physics Letters*, Vol.60, 1992, pp.1450-1452.
201. M. Zaiser and F. Banhart, *Physical Review Letter*, Vol.79, 1997, pp.3680-3683.
202. D. Mueller and D.R. Mckenzie, *Thin Solid Films*, Vol.108, 1983, pp.257-264.
203. S. Craig and G.L. Harding, *Thin Solid Films*, Vol.97, 1982, pp.345-361.
204. R.O. Dillon, J.A. Woolam, and V. Katkanant, *Physical Review*, Vol.B29, 1984, pp.3482-3489.
205. D. Beeman, J. Silverman, R. Lymds, and M.R. Anderson, *Physical Review*, Vol.B30, 1984, pp.870-875.
206. N. Savvides, *Journal of Applied Physics*, Vol.59, 1986, pp.4133-4145.
207. B. Dischler, A. Bubenzer, and P. Koidl, *Solid State Communication*, Vol.48, 1983, pp.105-112.
208. F.R. McFeely, S.P. Kowlaczyk, L. Ley, R.G. Cavell, R.A. Pollak, and D.A. Shirley, *Physical Review*, Vol.B9, 1974, pp.5268-5278.
209. D.Wesner, S. Krummacher, R.Carr, T.K. Shum, M. Strongin, W. Eberhardt, S.L. Weng, G. Williams, M. Howella, F. Kampas, S. Heald, and F.W. Smith, *Physical Review*, Vol.B28, 1983, pp.2152-2158.
210. J. Fink, Th. Muller-Heinzerling, J. Pfluger, B. Scheerer, B. Dischler, P. Koidl, A. Bubenzer, and R.E. Sah, *Physical Review*, Vol.B30, 1984, pp.4713-4718.
211. C. Gao, Y.Y. Wang, A.L. Ritter, and J.R. Dennison, *Physical Review Letter*, Vol.62, 1989, pp.945-948.
212. S. Kaplan, F. Jansen, and M. Machonkin, *Applied Physics Letters*, Vol.47, 1985, pp.750-753.
213. R.H. Jarman, G.J. Ray, R. W. Standley, and G.W. Zajac, *Applied Physics Letters*, Vol.49, 1986, pp.1065-1067.
214. K.Tanaka, M. Okada, T. Kohno, M. Yanokura, and M. Aratani, *Nuclear Instruments Methods*, Vol.B58, 1991, pp.34-39.
215. B. Schultrich, H.J. Scheibe, G. Grandremy, D. Drescher, and D. Schneider, *Diamond and Related Materials*, Vol.5, 1996, pp.914-918.
216. H.Dimigen, H. Hubsch, R. Memming, *Applied Physics Letters*, Vol.50, 1987, pp.1056-1058.

217. F.M. Kustas, M.S. Misra, D.F. Shephard, and J.F. Froechtenigt, *SPIE Diamond Opticals*, Vol.3, 1990, pp.1325-1328.
218. I.I. Askenov, and V. Strel'nitskij, *Proceedings of First European Conference on Diamond and Diamond Like Carbon Coatings*, Crans-Montana, 1990.
219. K.M. Mertz, R. Hoffman, and A.T. Balaban, *Journal of American Ceramic Society*, Vol.109, 1987, pp.6742-6749.
220. D.R. McKenzie, D. Muller, and B.A. Pailthorpe, *Physical Review Letter*, Vol.67, 1991, pp.773-776.
221. C.Z. Wang and K.M. Ho, *Physical Review Letter*, Vol.71, 1993, pp.1184-1187.
222. J. Robertson, E.P. O'Reilly, *Physical Review*, Vol.B35, 1987, pp.2946-2957.
223. M.A. Tamor and C.H. Wu, *Journal of Applied Physics*, Vol.67, 1990, pp.1007-1012.
224. M.Yoshikawa, G. Katagiri, H. Ishida, A. Ishitani, and T. Akamatsu, *Journal of Applied Physics*, Vol.64, 1988, pp.6464-6468.
225. J.C. Angus and C.C. Hayman, *Science*, Vol.241, 1988, pp.913-921.
226. C.B. Collins, F. Davanloo, D.R. Jander, T.J. Lee, H. Park, and J.H. You, *Journal of Applied Physics*, Vol.69, 1991, pp.7862-7870.
227. A.H. Lettington, *Philos. Transactions Royal Society A., Physics Science Engineering*, Vol.342, 1993, pp.287-296.
228. K. Miyoshi, J.J. Pouch, and S.A. Alterovitz, *Materials Science For.*, Vol.53-54, 1989, pp.645-651.
229. J.C. Angus and F. Jansen, *Journal of Vacuum Science Technology*, Vol.A6, 1988, pp.1778-1781.
230. K. Miyoshi, *Surface Coatings Technology*, Vol.44, 1990, pp.799-806.
231. K. Miyoshi, R.L.C. Wu, and A. Garscadden, *Surface Coatings Technology*, Vol.54-55, 1992, pp.428-433.
232. I. Garnev and V. Orlinov, *Diamond and Related Materials*, Vol.4, 1995, pp.1041-1049.
233. H. Xioming, L. Hengde, and L. Wenzi, *Proceedings of International Surface Science Engineering*, 1995, pp.15-23.
234. D.E. Savage, J. Kleiner, N. Schimke, Y.H. Phang, T. Jankowski, J. Jacobs, R. Katiotis, and M.G. Lagally, *Journal of Applied Physics*, Vol.69, 1991, pp.1411-1424.
235. D.P. Dowling, K. Donnelly, T.P. O'Brien, A. O'Leary, T.C. Kelly, and W. Neuberger, *Diamond and Related Materials*, Vol.5, 1996, pp.492-495.
236. N. Kumar, B. Singh, S. DiVita, N. Vallestero, A. Samiul, and R.H. Williams, *Proceedings of International Wire Cable Symposium,* 1995, pp.325-333.
237. *Abrasion Wear Resistant Polymeric Substrate Product***,** U.S. Patent issued to F.M. Kimock, B.J. Knapp, and S.J. Finke, Patent No. 5,190,807, 1993.
238. L. Ganapathi, S. Giles, and Rama Rao, *Applied Physics Letters*, Vol.63, 1993, pp.993-995.
239. H.C. Tsai and D.B. Bogy, *Journal of Vacuum Science Technical*, Vol.A6, 1987, pp.3287-3295.
240. K. Enke, *Applied Optics*, Vol.24, 1985, pp.508-513.
241. T.L. Parker, K.L. Parker, I.R. McColl, D.M. Grant, and J.V. Wood, *Diamond and Related Materials*, Vol.3, 1994, pp.1120-1125.
242. S. Mitura, P. Niedzielski, D. Jachowicz, M. Langer, J. Marciniak, A. Stanishevsky, E. Tochitsky, P. Louda, P. Couvrat, M. Denis, and P. Lourdin, *Diamond and Related Materials*, Vol.5, 1996, pp.1185-1188.
243. R. Butter, M. Allen, L. Chandra, A.H. Lettington, and N. Rushton, *Diamond and Related Materials*, Vol.4, 1995, pp.857-861.
244. V.V. Sleptsov, V.M. Elinson, N.V. Simakina, A.N. Laymin, I.V. Ysygankov, A.A. Kivaev, and A.D. Musina, *Diamond and Related Materials*, Vol.5, 1996, pp.483-485.
245. E. Watchel, P. Villars, A. Armini, and M. Spector, *Surface Modification Technologies*, T.S. Sudarshan and J.F. Braza, eds., The Institsute of Materials, Vol.5, 1992, pp.125-138.
246. J. Lankford and C.R. Blanchard, *Nuclear*

Instruments Methods, Vol.B80-81, 1993, pp.1441-1445.

247. H. Voigt, F. Schilthelm, T. Lange, and T. Kullick, and R. Ferreti, *Sens. Actuators,* Vol.B44, 1997, pp.441-444.
248. C.M. Lin, F.Y. Chuang, J.T. Lai C.H. Wang, T.Y. Hsiu, M. Yokoyama, I.N. Lin, J.H. Tsai, C.M. Huang, and W.C. Wang, *Tenth International Vacuum Microelectron, Conference Technical Dig*., 1997, pp.131-140.
249. A.Y. Liu and M.L. Cohen, *Science*, Vol.245, 1989, pp.8419-8421.
250. A.Y. Liu and M.L. Cohen, *Physical Review Letter*, Vol.B41, 1990, pp.10727-10734.
251. K.M. Yu, M.L. Cohen, E.E. Haller, W.L. Hansen, A.Y. Liu, and I.C. Wu, *Physical Review*, Vol.B49, 1994, pp.5034-5037.
252. C.Niu, Y.Z. Lu, and C.M. Lieber, *Science*, Vol.261, 1993, pp.334-336.
253. L. Maya, D.R. Cole, and E.W. Hagaman, *Journal of Amercian Ceramic Society*, Vol.74, 1991, pp.1686-1688.
254. K. Ogata, J.F.D. Chubaci, and F. Fujimoto, *Journal of Applied Physics*, Vol.76, 1994, pp.3791-3796.
255. P. Prieto, C. Quiros, E. Elizalde, A. Fernandzes, J.M. Martin, and J.M. Sanz, *Nuclear Instruments Methods*, Vol.B122, 1997, pp.534-537.
256. H. Xin, C. Lin, S. Zhu, S. Zou, X. Shi, H. Zhu, and P.L.F. Hemment, *Nuclear Instruments Methods*, Vol.B103, 1995, pp.309-312.
257. J.Y. Feng, C.P. Long, F.W. Zhang, Z. Yi, and Y.D. Fan, *Wuli Xuebao*, Vol.45, 1996, pp.1068-1072.
258. D. Li, Y.W. Chung, S. Lopez, M.S. Wong, and W.D. Sproul, *Proceedings of International Conference Surface Science and Engineering,* 1995, pp.101-106.
259. Z.M. Ren, Y.C. Du, Z.F. Ying, F.M. Li, J. Lin, Y.Z. Ren, and X.F. Zong, *Applied Physics A: Materials Science Process*, Vol.A64, 1997, pp.327-330.
260. J.P. Riviere, D. Texier, J. Delafond, M. Jaouen, and E.L. Mathe, *Materials Letters*, Vol.22, 1995, pp.115-118.
261. Z.M. Ren, Y.C. Du, Y. Qiu, J.D. Wu, Z.F. Ying, X.X. Xiong, and F.M. Li, *Physical Review*, Vol.B54, 1995, pp.5274-5277.
262. A.R. Merchant, D.G. McCulloch, D.R. McKenzie, Y. Yin, L. Hall, and E.G. Gerstner, *Journal of Applied Physics*, Vol.79, 1996, pp.6914-6919.
263. M.R. Wixom, *Journal of Amercian Ceramic Society*, Vol.73, 1990, pp.1973-1978.
264. Y. Zhang, Z. Zhou, and H. Li, *Applied Physics Letters*, Vol.68, 1996, pp.634-636.
265. Y.A. Li, Z.B. Zhang, S.S. Xie, and G.Z. Yang, *Chemical Physics Letters*, Vol.247, 1995, pp.253-256.
266. Y. Guo and W.A. Goddard III, *Chemical Physics Letters*, Vol.237, 1995, pp.72-76.
267. D.M. Teter and R.J. Hemley, *Science*, Vol.271, 1996, pp.53-55.
268. Y. Chen, G. Liping, and E.G. Wang, *Philos. Mag. Letters*, Vol.75, 1997, pp.155-160.
269. J. Prahjyot Pal, S.C. Patil, S.M. Kanetkar, S.B. Ogale, L. Ganapathi,and P. Rama Rao, *Bulletin Materials Science*, Vol.17, 1994, pp.829-839.
270. S.V. Hainsworth, H. Sjoestroem, T.F. Page, and J.E. Sundgren, *Proceedings of Materials Research Society Symposium*, Vol.436, 1997, pp.275-280.
271. E.C. Crutiongico, D. Li, Y.W. Chung, and C.S. Bhatia, *Journal of Tribology*, Vol.118, 1996, pp.543-548.
272. Z.J. Zhang, P. Yang, and C.M. Leiber, *Proceedings of Materials Research Society Symposium*, Vol.388, 1994, pp.271-282.
273. S.J. Sjostrom, M. Stafstrom, and J.E. Sundgren, *Physical Review Letter*, Vol.75, 1995, pp.1336-1339.
274. D. Li, X. Chu, S.C. Cheng, X.W. Lin, V.P. Dravid, and Y.W. Chung, *Applied Physics Letters*, Vol.67, 1995, pp.203-205.
275. J.M. Gil, J.F.M. Gil, M. Sarikaya, M. Qian, M.J. Yacaman, and A. Rubio, *Journal of Applied Physics*, Vol.81, 1997, pp.2555-2558.
276. M.J. Yacaman, M.J. Gil, F.J. Gil, M. Sariyaka, and M.X. Qian, *Materials Chemistry and Physics*, Vol.47, 1997, p.109.
277. B. Wang, *Physical Review*, Vol.B58, 1998, pp.11890-11893.

Chemical Vapor Deposition
Jong-Hee Park, T.S. Sudarshan, editors, p379-399
DOI:10.1361/chvd2001p379

Chapter 11

CVD Diamond Films in Tribological Applications*

Ali Erdemir
Energy Technology Division
Argonne National Laboratory
Argonne, IL 60439

Abstract

Diamond, the hardest material known, offers several outstanding properties, such as high mechanical strength, chemical inertness, and very attractive friction and wear properties. Accordingly, these and other relevant properties make diamond very attractive for a wide range of tribological applications including machining, bearings, microelectromechanical systems, surgical tools, mechanical seals, etc. This chapter provides an overview of the tribological properties of chemical vapor deposited (CVD) diamond films used in machining and in various friction and wear applications. Specifically, it presents the current state of the art of making high-quality diamond films (such as nanocrystalline diamond) that provide ultralow friction and wear coefficients, and it addresses the prospects for future applications. Particular emphasis is placed on tribological issues associated with metal cutting and contact sliding. Smooth diamond films obtained by polishing and controlling grain size will also be discussed, and their potentials for future tribological applications will be assessed. It will be shown that during cutting and sliding, diamond films can undergo gradual abrasive wear and phase transformation and that transformation products trapped at sliding interfaces may dominate sliding wear performance. Based on structural and fundamental tribological knowledge, the chapter will emphasize the importance of surface physical and chemical effects on friction and

* Work supported by U.S. Department of Energy, under Contract W-31-109-Eng-38.

wear and will describe new deposition procedures that can lead to the formation of smooth, nanocrystalline diamond films that afford ultralow friction and wear to sliding tribological interfaces.

Introduction

In recent years, overwhelming interest has been shown in the production and use of high quality diamond coatings on metallic and ceramic substrates for various mechanical, electronic, optical, and tribological applications. Properties that make diamond coatings very attractive for such applications include extreme mechanical hardness and strength, excellent chemical inertness, broad optical transparency, high refractive index, wide band gap, low or negative electron affinity, transparency in light sources from deep UV through the visible to the far infrared, excellent thermal conductivity, extremely low thermal expansion, and a naturally low friction coefficient (comparable to that of Teflon ™).[1-11] The combination of these exceptional qualities in one material is very rare and makes it ideal for numerous industrial applications. In fact, if it were inexpensive and abundant, diamond would undoubtedly be the material of choice for many engineering applications.

Some of the present industrial uses of diamond coatings include cutting tools, optical windows, heat spreaders, acoustic wave filters, flat-panel displays, photomultiplier and microwave power tubes, night vision devices, and sensors.[9,10] Because its thermal conductivity and electrical insulation qualities are high, diamond is used for heat sinks in x- ray windows, circuit packaging, and high-power electronic devices. Moreover, the high chemical stability and inertness of diamond make it ideal for use in corrosive environments and in prosthetic devices that require biocompatibility.[12]

Natural gem-quality diamonds are expensive and difficult to machine and fabricate into useful shapes for general industrial purposes. Except for a few cases (i.e., diamond-studded rotary drill bits, dressers, diamond-tipped glass cutters, fine superabrasive powders in grinding wheels), natural diamond is not used for industrial purposes.[13,14] However, synthetic polycrystalline diamonds (PCD) have been available in industry for a long time (more than 30 years). They are mostly produced by a high-pressure/high-temperature (HPHT) method in which diamond is crystallized from metal solvated carbon at pressures from 50 to 100 Kbar and at temperatures of 1600 to 2000°C.[15] Worldwide production of PCDs is estimated to be ≈75 metric tons/year. These diamonds are micrometer-size powders or particulates that are used mostly as superabrasives in grinding and polishing media. It is possible to sinter these diamond powders with metallic or ceramic binders (such as Co, Ni, and TiC, etc.) at high pressures and temperatures and then use them as tool bits or sharp blades in metal-cutting operations.

Prospects for inexpensive and large-scale production of diamond increased tremendously in the mid 1970s when researchers discovered that diamond can be grown as thin coatings at low deposition pressures (10^2-10^3 Pa) from hydrocarbon/hydrogen mixtures by chemical vapor deposition (CVD). Since then, there has been an explosion in diamond and related- material research with the expectation that CVD will allow faster, cheaper, and easier production of diamond. CVD diamond technology was proved to be more versatile in coating intricate shapes and could be less expensive than HPHT.[16-18]

Currently, diamond coatings can be produced by several methods. The methods most widely used are plasma-enhanced CVD, hot-filament CVD, microwave CVD, DC-arc jet, etc.[10,19,20] These methods are very robust, well-developed, and widely-adopted by researchers and industry, and they have greatly expanded the application possibilities for diamond coatings in cutting tools and other industrial fields. At present, more and more cutting-tool manufacturers and commercial coaters are offering diamond-coated tools at reasonable costs. Initially, only tool inserts were coated with diamond, but nowadays complex tools such as drills, endmills, and taps are also coated with diamond.[18,19,21,22] Figure 1 shows a collection of cutting tools coated with CVD diamond.

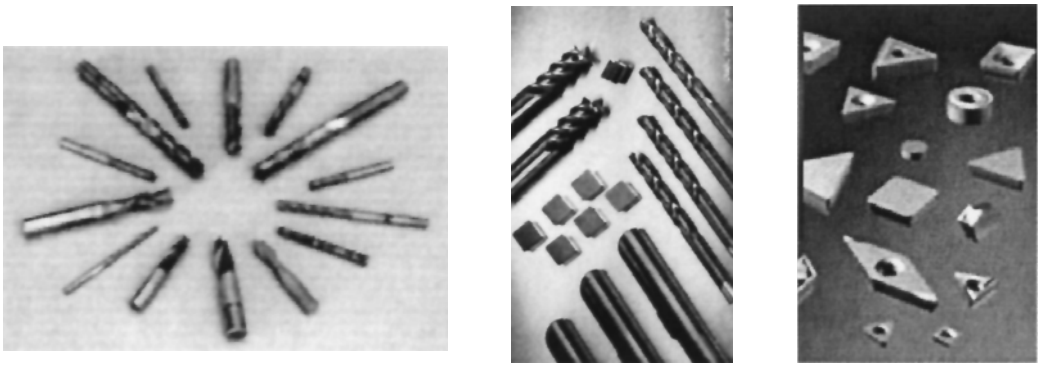

Fig. 1: Some examples of diamond coated tools (Courtesy of sp^3 and Crystallume Co.).

Early studies on diamond film growth date to when HP-HT synthesis of diamond was being explored. Tube oven experiments by Eversole and Angus[16,23] in the 1960s and low- pressure synthesis of diamond from hydrocarbon gas mixtures by Derayagin and Fedoseev[24] in the 1970s can be regarded as the earliest attempts to produce synthetic diamond coatings. In fact, Eversole of Union Carbide was able to produce a diamond phase by a thermal pyrolysis method in 1962. Progress was very slow until John Angus of Case Western University found a way in which graphite is etched simultaneously as the diamond is deposited in the presence of atomic hydrogen in the system. His work motivated Derayagin and Fedoseev[24] to focus on the use of hydrogen/hydrocarbon mixtures for low-pressure diamond growth. Since these studies, great strides have been made in the production of high- quality diamond coatings. Nowadays, high-quality diamond coatings can be produced by several methods at fairly high growth rates (e.g., plasma-jet method) over very large deposition areas.[25-29] These methods reduced cost and increased the prospect for large-scale applications of diamond films. The high-quality diamond coatings produced today exhibit most of the desired mechanical properties of natural diamonds.[4,30]

Low-pressure synthesis of diamond coatings involves the use of hydrogen and methane gas mixtures. Typical deposition pressures in these syntheses are 10^2-10^3 Pa, and the gas mixture consists of mostly hydrogen and very little methane. In the case of microwave CVD, 0.5 to 5% methane is mixed with hydrogen gas and introduced into the deposition reactor. Plasma conditions in the CVD methods are tailored to dissociate hydrogen/hydrocarbon mixtures into ionic or highly energetic species that are essential for the initial nucleation as well as subsequent growth of these coatings. For a long time, atomic hydrogen had been considered critically important for the initial nucleation and subsequent growth of diamond, but recent studies have indicated that thin diamond coatings can be produced in the near absence of hydrogen in a microwave plasma.[26] Typical substrate temperatures for diamond deposition are 700-1000°C. Deposition of diamond at temperatures below 700°C has also been demonstrated, but growth rates are reduced drastically, and the amount of nondiamond precursors in these coatings is substantially greater.[25]

High-quality diamond coatings are structurally microcrystalline and largely made up of tetrahedrally bonded carbon atoms. Thick coatings are composed of large columnar grains that are highly faceted and generally rough. These coatings tend to grow continuously rougher as the film becomes thicker. The generally rough surface finish of these coatings precludes their immediate use for sliding tribological applications. When used in such applications, sharp asperities cause high friction and very high wear losses on mating surfaces.[31-33] The

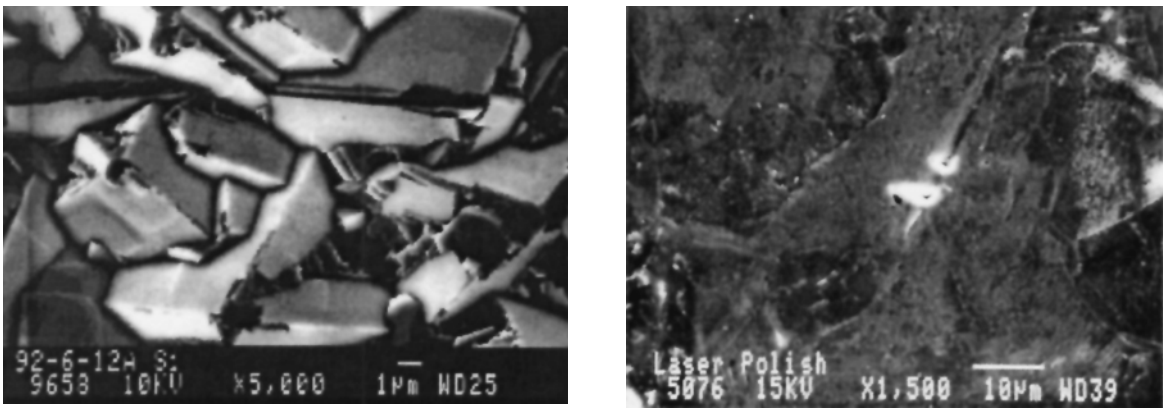

(a) (b)

Fig. 2: Surface morphology of a typical CVD diamond film (a) before and (b) after laser polishing.

rough microcrystalline coatings can be polished by laser beams, fine diamond powders, or by rubbing against hot iron or nickel plate.[34,35] Figure 2 shows the surface morphology of a rough film before and after laser polishing. The polished coatings can provide friction coefficients comparable to that of natural diamond.[36-38] However, the polishing processes are tedious, very time-consuming, and in the case of complex geometries, impractical.

Despite the high interest in using diamond coatings for diverse tribological applications, their widespread utilization in the industrial world has not yet met expectations.[39-44] Until now, only carbide and certain ceramic tools have been coated successfully with diamond and made available commercially. Although prototypes of other tribological parts (such as mechanical seals[45] have also been prepared with diamond coatings, their large-scale utilization has not yet been realized. Major limitations to much larger applications of diamond coatings are high-temperature requirements, small deposition areas, slow growth rates, rough surface finish, and most important, high cost.

The primary goal of this chapter is to provide an overview of the recent developments in the production and uses of diamond coatings for tribological applications. A brief description of the friction and wear mechanisms of diamond in general and diamond coatings in particular will be presented first. This will be followed by a discussion of the tribological performance and applications of these coatings in cutting tools and other fields. Special emphasis will be placed on the effects of film microstructure, adhesion, and surface morphology on tribological Performance.

Synthesis of Diamond Coatings

Deposition Methods

Diamond coatings are produced primarily by several CVD methods, including laser-assisted, microwave, and hot-filament CVD, plasma-jet, combustion flame, etc.[19-22] Typical deposition pressures in these methods are 10^2-10^3 Pa, and the gas mixture consists of mostly hydrogen and very little methane. In the case of microwave CVD, 0.5 - 5% methane is mixed with hydrogen gas and introduced into the deposition reactor. Small amounts of oxygen and nitrogen can also be blended. Typically, a 2.45 GHz microwave power source is used to initiate and maintain a gas discharge plasma in which substrates are immersed. At the very high deposition temperatures of CVD (typically 700 to 1000°C), electrons intensely interact with the hydrogen rich gas mixture, and the ionic species created during this interaction lead to the formation of diamond nuclei on the surfaces of suitable substrates.

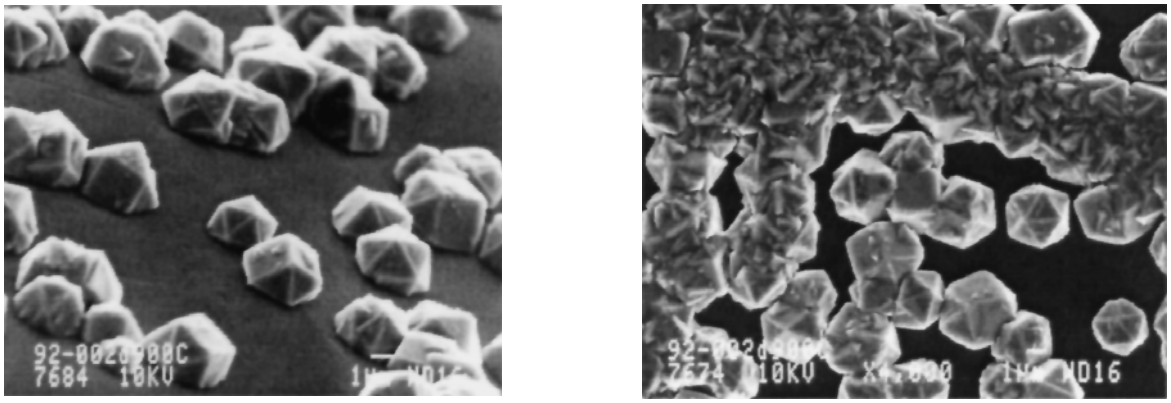

(a) (b)

Fig. 3: (a) Initial and (b) intermediate growth morphologies of microwave CVD diamond films.

Hydrogen is extremely important for the synthesis of high-quality diamond coatings. It plays - a critical role in the stabilization of the sp^3 bond character of the growing diamond surface and controls the size of the nuclei, dissolution of carbon and generation of condensable carbon radicals in the gas phase, abstraction of hydrogen from hydrocarbons attached to the surfaces, and production of vacant surface sites where sp^3-bonded carbon precursors can be attached. It etches most of the double or sp^2 -bonded carbon from the surface, and thus hinders the formation of graphitic and/or amorphous carbons.[29] Briefly, the thermodynamics and kinetics of diamond film growth are very complex and involve a nonthermal gas-phase equilibrium and complex surface reactions. Depending on growth conditions, amorphous carbon, graphite, and diamond, or a combination of all three may be produced.

In the case of hot-filament CVD, refractory metal filaments (e.g., W, Ta, Re, etc.) are electrically heated to very high temperatures (between 2000 and 2700°C) to produce the necessary amount of atomic hydrogen that is necessary for the reasons mentioned above for the synthesis of diamond. Except for combustion flame CVD, hot-filament CVD is considered the simplest of all of the methods and also the most inexpensive. Plasma-jet and laser-assisted CVD methods rely on a plasma torch or laser to attain the very high temperatures that are needed to produce the atomic hydrogen that is essential for diamond nucleation and growth. Several excellent articles that describe the principles of each deposition method have appeared in recent scientific journals and reference books.[20,26,44]

Microcrystalline Coatings

Most coatings produced by the methods mentioned above consist of coarse grains, are generally rough, and tend to grow continuously rougher as the film becomes thicker (see Figure 2a). During the initial stage of film growth, nucleation starts at preferred sites; eventually, independent nuclei form. As these nuclei grow, they close the gaps between them and merge to form a continuous film. (Figure 3 shows initial and intermediate stages of the diamond film growth on a Si wafer). Thereafter, the growth process and growth rates are dominated by nearby neighbors and growth orientation. Grains with more favorable growth orientation will grow the fastest and overshadow grains with less favorable growth orientation. Grains with less favorable growth orientation will be buried between the large grains.

As mentioned above, most CVD and plasma-jet methods require large amounts of atomic hydrogen, which leads to the etching of the small diamond grains, preventing continuous renucleation and allowing only diamond grains that have attained a certain critical ratio of bulk

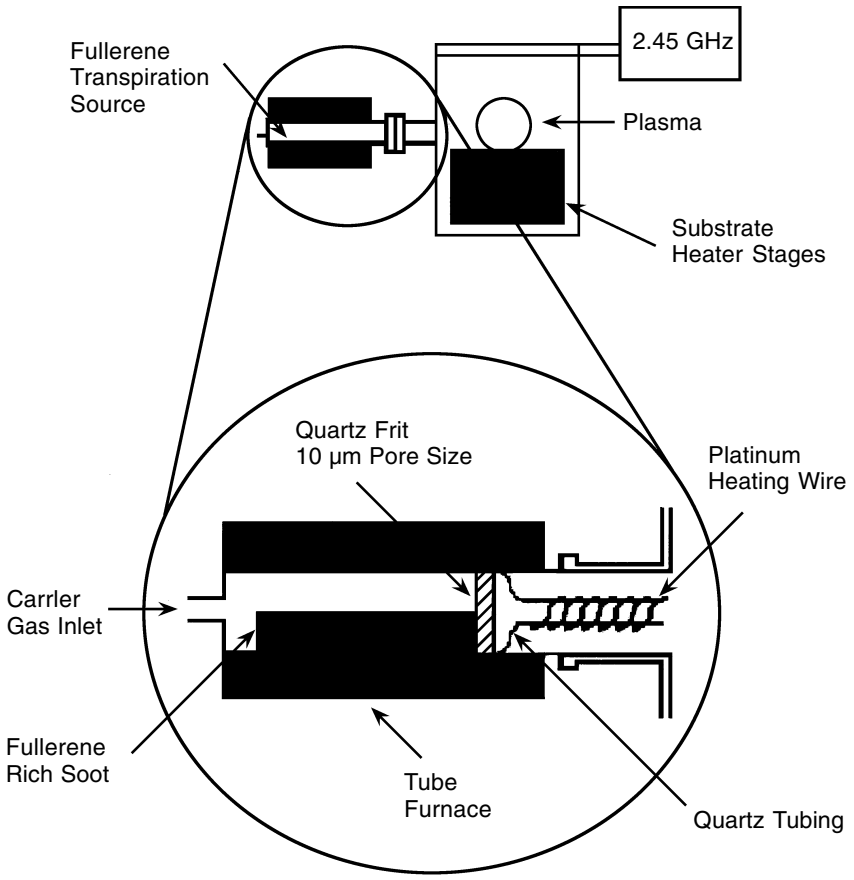

Fig. 4: Schematic layout of a modified microwave CVD reactor for nanocrystalline diamond deposition.

to surface atoms to survive. Consequently, these coatings consist primarily of large grains that continue to grow at the expense of smaller grains, with a typical RMS surface roughness value of ≈ 10% of the film thickness. The generally rough nature of these coatings has limited their widespread application in many engineering fields, including tribology. Effective polishing techniques are now available but they increase the cost of coated work pieces.

Nanocrystalline Coatings

Recently, new methods have been developed for depositing nanocrystalline diamond (NCD) coatings with a very smooth surface finish. In these methods, a higher than normal C/H ratio is used in a microwave plasma or a DC-bias is applied to the substrates to increase nucleation density.[45-47] Although the growth rates are somewhat reduced, the surface finish of the resultant diamond coatings is much smoother (i.e., ≈25 nm, RMS). Deposition of NCD coatings has also been achieved by microwave plasmas that consist primarily of Ar, with either C_{60}, or CH_4 as the carbon precursor, in the near absence of atomic hydrogen and the structural, mechanical, and tribological properties of these films were reported.[26,47-50] The reactor is essentially a modified version of microwave CVD, the details of which are depicted in Figure 4. To introduce C_{60} into the reactor, a quartz transpirator, shown in Figure 4, was attached. Fullerene-rich soots, containing ≈10%

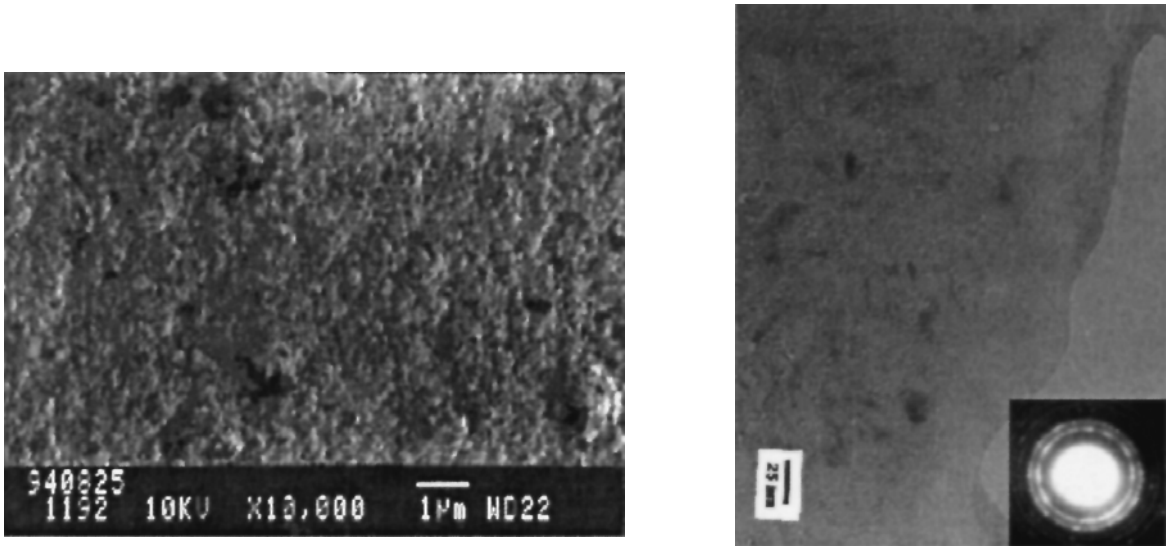

(a) (b)

Fig. 5: Plan view (a) SEM and (b) TEM micrographs of nanocrystalline diamond film.

C_{60}, are placed in the transpirator. The soot was heated to 200°C under vacuum for 2 hours to remove residual gases and hydrocarbons. During operation, the tube furnace and transport tube were heated to between 550 and 600°C to sublime C_{60} into the gas phase. Argon gas was passed through the transpirator to carry the C_{60} vapor into the plasma. To ensure that C_{60} was transported into the chamber, a silicon wafer was placed in front of the transport tube while maintaining a 14 sccm argon flow. With the reactor pressure at 100 torr and the transpirator at 600°C, a 1.7-mg brown film was deposited on the wafer in one hour. The film displayed only strong C_{60} infrared absorption features. The measured Raman spectrum was also attributed to C_{60}. Based on these measurements, the transpirator is considered an effective source of C_{60} for diamond growth. The NCD coatings can also be grown under similar low hydrogen content conditions with CH_4 instead of C_{60} as the carbon source.

The NCD coatings can be grown on various substrates including single-crystal silicon wafers, sintered SiC, W, WC, Si_3N_4, etc. Initially, a bias of - 150 V is applied to enhance diamond nucleation density. Film growth is monitored in-situ by laser reflectance interferometry to determine growth rate and to stop growth at the desired film thickness. The substrate temperature may vary between 700 and 950°C, and the total gas flow rate is ≈100 sccm. A typical gas composition for NCD diamond film can be 97% Ar, 2% H_2 and 1% C_{60} or CH_4 at a total pressure of 1.33×10^4 Pa and a microwave power of 800 W. Figure 5 shows plan-view SEM and TEM photomicrographs of an NCD film produced at Argonne National Laboratory.

The growth mechanism of NCD coatings differs significantly from that of a conventional diamond film produced by other CVD methods described in a series of recent papers. Specifically, extraction of a carbon dimer (C_2) from C_{60} and CH_4 molecules with subsequent insertion into the diamond surface has recently been proposed for the growth of these coatings.[47,51-53] C_2 dimers, the major diamond growth species, are inserted directly into the diamond surface. The resultant coatings are phase-pure NCD, with an average grain size of ≈15 nm, as can be seen in plane-view and cross-sectional TEM photomicrographs in Figures 5a and b. The

carbon dimer growth mechanism is unique in that it is capable of producing a continuous diamond coating that can be as little as 30-60 nm thick.

Polishing of Rough Diamond Coatings

The high-quality microcrystalline diamond coatings are rough and often nonuniform in thickness or slightly bowed because of internal stresses and difference in deposition rate from the edges to the center of the samples. The generally rough surface finish of these coatings precludes their immediate use for most machining and wear applications. When used in sliding-wear applications, such rough coatings cause high friction and very high wear losses on mating surfaces.[32,33,54] The rough diamond coatings can be polished by laser beams, mechanical lapping with fine diamond powders, ion-beam or plasma etching, and thermomechanical polishing with hot iron or nickel plates.[34,35,55,56] Mechanical lapping and polishing with hot iron plates, the most widely used methods, allow polishing of large areas. Depending on the polishing method, one can achieve mirror-finish surfaces with an RMS surface roughness of 10 nm or less. Figure 2b shows the surface morphology of a diamond film before and after laser polishing. The polished coatings can provide friction coefficients comparable to that of natural diamond.[36-38,55] However, the polishing processes are tedious, time-consuming, and, in the case of complex geometries, impractical. Depending on the desired film thickness or the degree of original roughness, it may be necessary to remove large amounts of material before a smooth surface is obtained.

Tribology of Diamond Coatings

Despite high interest in using diamond coatings for diverse tribological applications, their widespread utilization for these purposes has not yet met expectations. Until now, only carbide and certain ceramic tools have been coated successfully with diamond and made available for commercial use. Although prototypes of other tribological parts (such as mechanical seals) have also been prepared with diamond coatings, their large-scale utilization has not yet been realized. Among the reasons for this are rough surface finish, poor adhesion, oxidation when used at elevated temperatures, high fabrication cost, limitations on substrate materials, and most important, insufficient reliability/repeatability in actual applications. They cannot be used to machine iron or iron-base materials, which constitute the largest segment of industrial machining. Diamond can only be deposited on select substrates such as W, Mo, WC, Si, SiC, and Si_3N_4. Also, they cannot be produced on the surfaces of iron-base alloys (such as tool steels), which are used the most in tribology.

As elaborated above, conventional diamond coatings are generally rough and composed of large grains. Depending on deposition conditions, these grains can have <111> or <100> type crystallographic growth orientations. Figure 6 shows plan-view SEM photomicrographs of two films with <111> and <100> growth orientation. These films were grown in a H_2/CH_4 plasma. Figure 7 shows the friction coefficients of the two coatings shown in Figure 6 as a function of time. After an initial run-in period, the friction coefficients of both coatings decrease. The friction coefficient of film with a <100> growth orientation stabilizes at ≈ 0.1, whereas that of the film with a <111 > growth orientation remains high and unsteady but continues to decrease steadily during successive sliding passes.[50]

The high friction coefficients of rough diamond coatings with <111> orientation can be attributed to the abrasive cutting and ploughing effects of sharp surface asperities on the softer counterface pins. If a favorable <100> growth orientation is present, such coatings can also afford low friction coefficients to sliding surfaces, despite relatively higher measured surface roughness. Previous studies also demonstrated a close correlation between higher surface roughness and greater friction.[32,33,50,54,57-60] When polished or NCD diamond coatings are used in sliding-contact experiments, very low friction coefficients are also attained (Figure 8).[36,37,48-50,57]

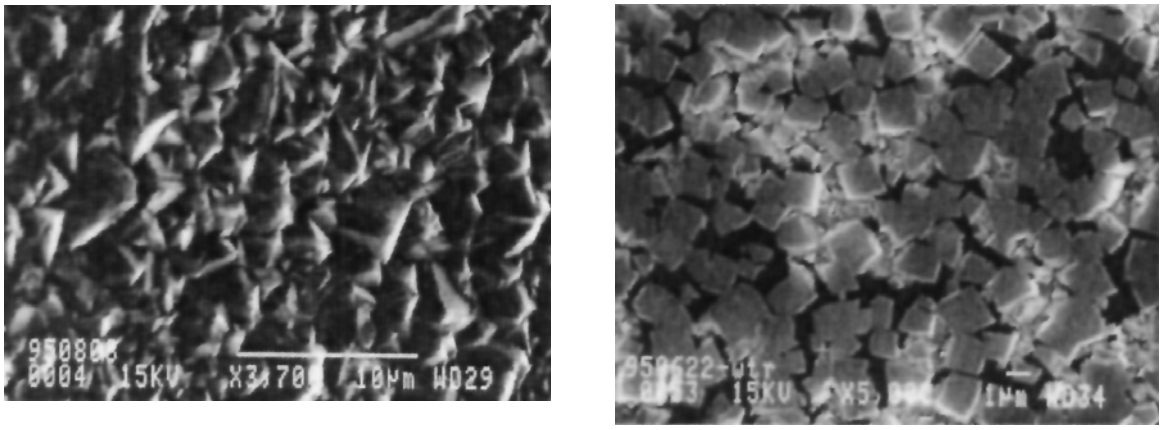

(a) (b)

Fig. 6: Plane-view SEM photomicrographs of diamond films with (a) <111> and (b) <100> growth orientations.

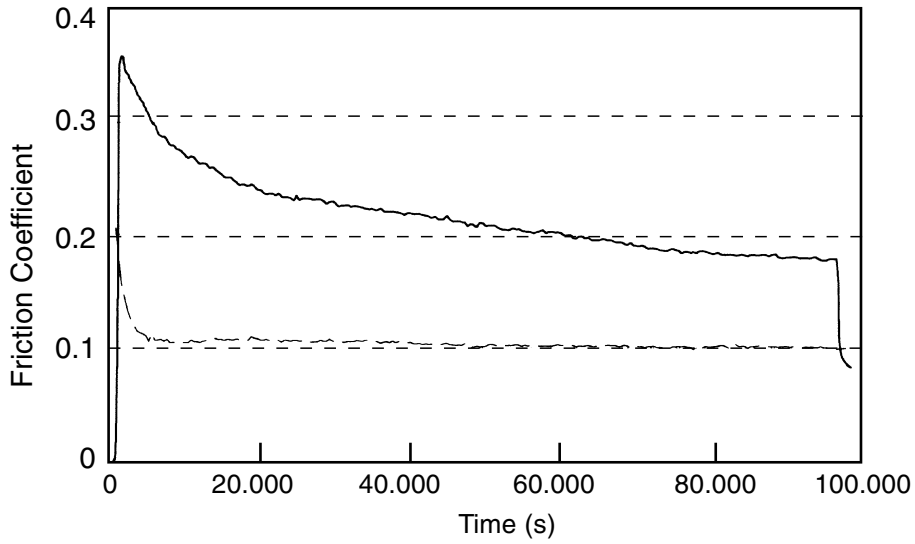

Fig. 7: Effect of crystallographic growth orientation on friction performance of CVD diamond films.

In general, previous studies confirmed the notion that regardless of grain size, diamond coatings with a smooth surface finish provide very low friction coefficients to mating surfaces. Figure 9 illustrates the close relationship between surface roughness and friction coefficients of diamond films.

Mechanistically, the low-friction nature of cleaved diamond and/or smooth diamond coatings has long been attributed to the highly passive nature of their sliding surfaces.[61-64] Specifically, it has been postulated that gaseous adsorbates such as hydrogen, oxygen, or water vapor can effectively passivate the dangling surface bonds of diamond (as illustrated in Figure 10, which was taken from Ref 65). When the dangling bonds become highly passive, the adhesion component of friction is diminished.

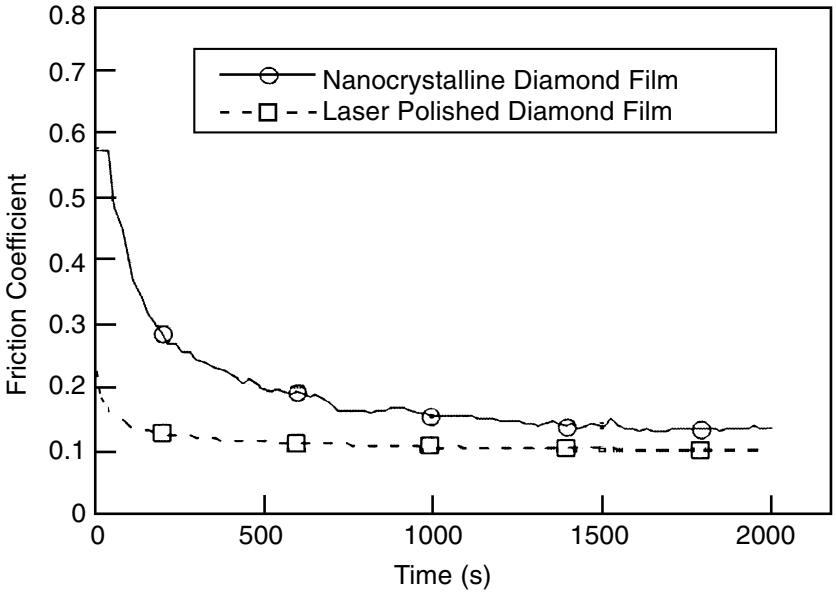

Fig. 8: Friction coefficients of nanocrystalline and laser-polished diamond film.

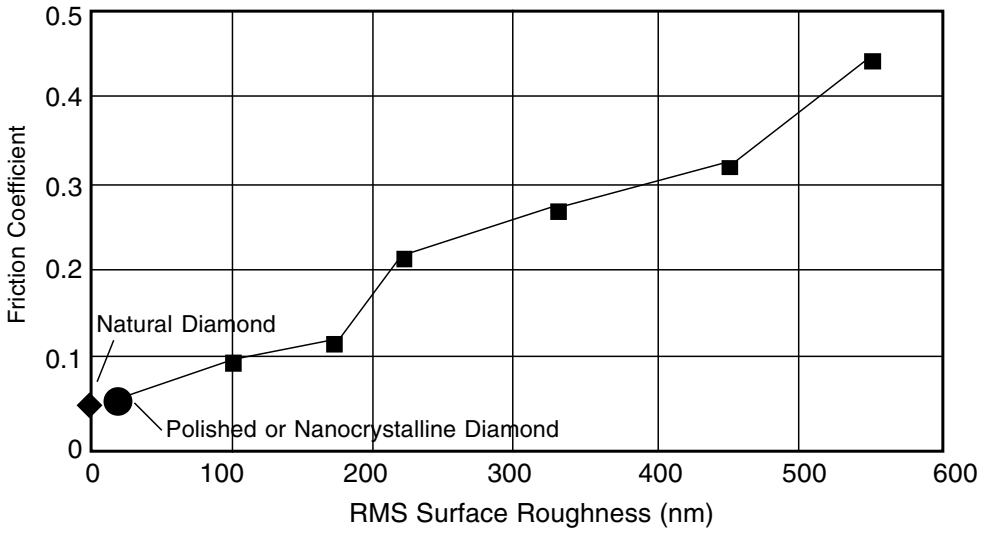

Fig. 9: Correlation between friction coefficient and surface roughness of diamond films.

Recent fundamental studies have showed that, when adsorbed gases are removed from the sliding surfaces of diamond, the friction coefficient increases rapidly, because the dangling surface bonds are reactivated and are available to form strong bonds across the sliding contact interface.[66] Conversely, if the surface of diamond is exposed to air, the friction coefficient

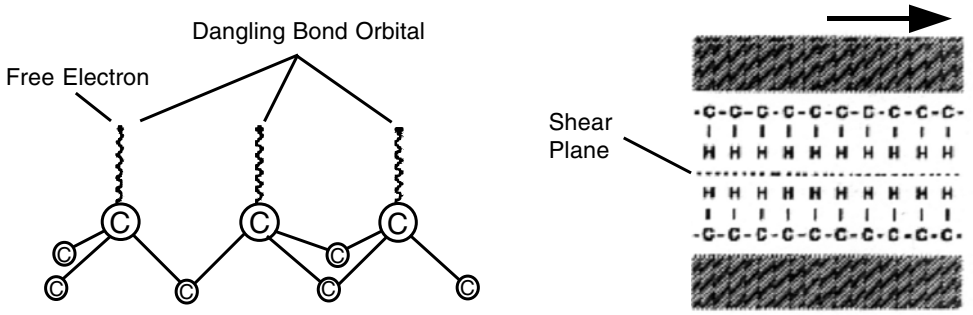

Fig. 10: Schematic representation of surface dangling bonds of diamond and passivation by hydrogen.[65]

drops precipitously, mainly because of the repassivation of dangling surface bonds.

Apart from physical roughness and chemical passivation effects, phase transformation or structural changes can also play a major role in the friction and wear performance of diamond coatings.[67] The extent of such changes may be dominated by environmental species or by ambient temperature.[68,69]

Phase transformation most often is the result of extreme contact pressures and high frictional heating at the local asperity levels. Real contact occurs first between these asperities and their tips can either fracture or undergo phase transformation because of the extreme pressures and high frictional heating.[69-71] Thermodynamically, graphite is the most stable form of carbon whereas diamond is metastable. It is known that when excited thermally or by ion bombardment, diamond can transform to a graphitic form.[72,73] The graphitic debris particles can gradually accumulate at the sliding contact interface and then begin to dominate the long-term sliding friction and wear performance of these coatings. Previous research by Erdemir et al. [69] and Jahanmir et al.[71], revealed that most of the debris particles derived from sliding diamond surfaces exhibited a graphitic microstructure. Specifically, Raman spectroscopy, electron diffraction, and electron-energy loss spectroscopy (EELS), and TEM have concurrently confirmed the presence of highly disordered graphitic debris particles at sliding interfaces.[69]

Tribological Applications

Over the years, great strides have been made in the deposition, characterization, and industrial applications of diamond coatings.[74-78] Our fundamental understanding of the structure, properties and performance of these coatings has increased tremendously in recent years and this understanding has been used to design/ customize coatings that can meet the more stringent needs of particular applications. Although some applications are still in the exploratory stage and require further development, others have been fully developed and are offered on a commercial scale. In particular, cutting tools (i.e., inserts, end mills, microdrills, push pins, tab tools) have been commercially available from several industrial manufacturers.[18,21,23,78-84] These coated tools provide much improved performance during metal- cutting operations by allowing high-speed machining at increased feed rates. Some of the advantages that diamond provides in these applications are extreme hardness and wear resistance; good fatigue strength; high chemical inertness; excellent resistance to abrasion, erosion, and corrosion; high thermal conductivity, low friction; and excellent environmental compatibility. Currently, market share of diamond-coated tools in these applications is rather small. It can increase substantially if the cost of producing diamond on tool inserts is further reduced. Other potential applications for diamond coatings are

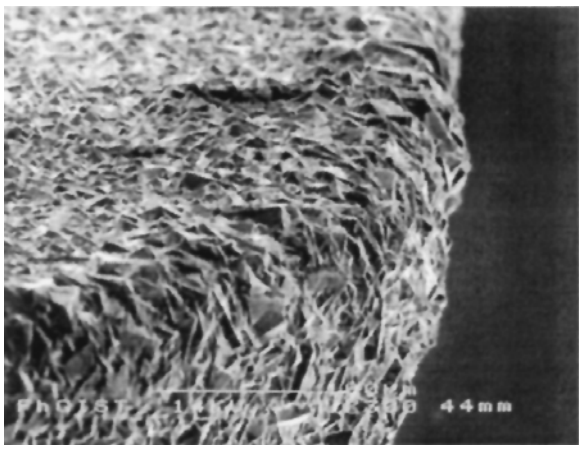

Fig. 11: Morphology of cutting edge of diamond-coated tool insert.

mechanical seals, sliding bearings, microclectromechanical systems (MEMS), wire-drawing dies, and various wear parts used against erosion and abrasion (e.g., jet nozzles).

Machining

For machining purposes, diamond has been used in three distinct forms. One form is based on the use of synthetic diamond powders produced by HPHT methods. Specifically, diamond powders are first sintered into the shape of a tool tip and then brazed on the cutting edges of a tool insert. A second form is based on the deposition of a relatively thick (i.e., 0.5-1mm thick) diamond film on an Si wafer from which small bits are laser-cut into a desired shape. Subsequently, the Si substrate is etched out and cut diamond bits are recovered. As a last step, the free-standing diamond bits are bonded or brazed onto the cutting edges of tool inserts or end mills. This technology competes well with the traditional products prepared by high- pressure sintering of synthetic diamond powders produced by the HPHT method. The third form is directly deposited on cutting tools by various methods (e.g., plasma-jet, hot-filament CVD, etc.). Figure 11 shows the morphology of the cutting edge of a diamond-coated tool insert.

CVD diamond coated tools perform as well as or better than the PCD diamonds in cutting and turning operations. However, edge chipping or deterioration due to easy cleavage of highly oriented needlelike diamond grains in CVD diamond may occur and limit the performance of the coated tools. Another fundamental difference between brazed and coated diamond tool bits is that a coated tool can be tailor-made to meet the specific machining needs of an application, whereas the brazed bits come in a strict form and cover only the areas of the sharp tips of inserts. In the case of coated tool bits, the shape of a base carbide insert can be prepared in such a way that it will allow better chip handling and breaking capability than very small brazeable diamond bits. The whole functional surface is coated with diamond and it can be prepared in any style or geometry to provide better efficiency and to overcome limitations on cut depth which is always a problem with brazed tool bits.

Diamond-coated tools are primarily used in the machining of nonferrous metals, alloys, and composite materials that are inherently very difficult to cut or machine. The range of materials that are suitable for machining by diamond-coated tools include aluminum and its alloys (in particular high-silicon aluminum alloys); magnesium and its alloys; copper, lead, and manganese alloys; graphite; carbon; plastics;

fiberglass composites; carbon-carbon composites; metal-matrix composites; epoxy resins; green ceramic; fiber-reinforced plastics; concrete; and tools for various mining and rock drilling operations; etc.[84-89] Another key application for diamond coatings is woodworking tools. However, diamond-coated tools cannot be used for machining of ferrous alloys and the alloys of groups IV^a, V^a, VI^a, VII^a, and VIII^a of the Periodic Table. Diamond can chemically react and/or dissolve and rapidly wears out in these materials at the high-temperatures that are generated during machining.

Diamond has been the material of choice for machining of high silicon containing aluminum alloys for automotive applications. In particular, hyper-eutectic aluminum-silicon alloys are increasingly being used in this industrial sector, mainly because they are lightweight (thus reducing overall weight of the car and hence improving fuel economy) and relatively strong and resistant to wear.[90-96] The major applications for aluminum silicon alloys include pistons, engine blocks and heads, wheels and chassis, and some transmission parts. The increased use of lightweight materials in the automotive sector is likely to continue; hence, the need for diamond-coated tools will increase.

The most important factor governing the success of a diamond-coated tool insert in cutting operations is strong bonding between the diamond coating and the substrate insert. If bonding is not intimate and strong, coatings are easily removed from the edges, and thus they lose their cutting performance and effectiveness. In fact, premature delamination of the diamond film in early trials represented the most common mode of tool failure. Residual stresses are inherent in all CVD-diamond coatings, and these stresses may significantly affect the film/substrate adhesion.[97-98] Diamond coatings are often deposited at high temperatures and a large mismatch in thermomechanical properties between the diamond coating and the underlying substrate results in large compressive stresses. The presence of a high stress in the coating can lead to various undesirable failure modes that can cause the film to delaminate, crack, or blister and thus destroy the entire structure. Other factors, such as film thickness, film roughness, substrate preparation and grain size, also affect film/substrate adhesion, and they must be considered with the residual stresses whenever the quality of a diamond coating is evaluated. Two other problems may occur when diamond is used in machining operations. One problem is oxidation. The other problem is that, despite its extreme hardness, diamond is brittle and can fracture, especially when forced in the direction of relatively weak cleavage planes.

Diamond coatings are mostly applied to WC-Co-based cemented carbide tool inserts, because these tools exhibit excellent toughness, hardness and high-temperature durability. Cobolt is mainly used as a binder and it also controls the toughness of the materials. In addition to strict process control during deposition, the selection and pretreatment of the substrate materials are extremely important for achieving strong adhesion between a diamond coating and the substrate material. In particular, the selection of the correct kind of WC-Co material is a must for achieving strong bonding and hence long wear life. In principle, lower Co content (< 5%) in cemented carbide is highly desirable, because Co has a detrimental effect on the adhesion of diamond coatings to carbide inserts. Due to its high mobility and vapor pressure at high temperatures, Co tends to interfere with the nucleation and growth processes. Specifically, it plays a catalytic role in the formation of nondiamond phases during the early stages of film growth. It also slows down the nucleation process and reduces nucleation density early on. Interfaces with a high proportion of nondiamond phases and low nucleation density suffer from poor adhesion. Too much Co can also increase the difference in thermal expansion coefficient between diamond and substrate; hence, during cooling, very high compressive stresses build up at the interface region. When these stresses are combined with the stresses associated with cutting action, premature adhesive failure occurs at or near the cutting edges. Briefly, it is important to use carbide substrates with very low Co content or to etch the Co out completely from the near surface, otherwise the coatings will not stick to the tools.

Because of the detrimental effect of Co, composition of the near surface of cemented carbides is controlled very closely by using various methods. Drills that are to be coated are prepared by methods that have been established in various studies as the most effective for cleaning them and removing surface Co.[99-102] If the surface Co is not removed, the coating process produces complex Co carbides rather than diamond on the surface of the tool. Because Co is the binder that holds the tool's WC grains together, the depth of the Co removal must be controlled with great care. If too much Co is removed from the surface, the tool will become weakened and its integrity near the surface will be hurt.

Several methods are used by industry for the removal of surface Co from tool inserts. Most of the methods involve selective etching of Co by chemical means. Some of the chemicals that have been proved to be effective in etching Co are HNO_2, HCl, and CH_3COOH. In one case, tool inserts are dipped in a solution of HNO_3 and water (mixed 1:1 by volume) and ultrasonically agitated for 15 minutes. They were then rinsed and ultrasonically cleaned in ultrapure water for 5 minutes. In another case, researchers heat-treated WC-CO substrates at very high temperatures for an extended period of time in a protective environment. Heat treatment causes grain growth in WC and hence roughens the surface, and it evaporates Co and thus reduces the amount of Co at or near the surface. Increased surface roughness provides better mechanical interlocking between diamond and WC grains, whereas the absence of Co insures higher nucleation density and better adhesive bonding. Formation of stable Co borides and silicides that can endure the high deposition temperatures of diamond has also been used in the past to prevent Co-associated problems.[103,104]

Various bond layers (i.e., W, Si, SiC, and Si_3N_4) have also been tried on tool inserts to achieve strong bonding. The effectiveness of bond layers is very dependent on the exact composition and thickness of the bond layer material. Researchers have tried to replace Co with Cu in an electrochemical cell and reported stronger bonding between diamond and Cu-treated tool surfaces.[85] A few other procedures have been developed by industry to achieve strong adhesion, but inasmuch as they are considered highly proprietary, very little is known about these procedures. Published case studies indicate that, depending on the material that is to be cut and cutting conditions, CVD diamond-coated tools can improve tool life from 25% to more than a factor of 40. Greater improvements in tool life are reported when the tools are used to cut aluminum-silicon alloys, green ceramics, and fiber-reinforced composites. Figure 12 shows the performance of uncoated and CVD diamond-coated carbide inserts while machining an A1Si alloy for a truck wheel application.

When the performance and price of CVD tools compare favorably with those of PCD tools, CVD tools may displace PCD tools in some applications. Woodworking tools represent another major market segment for diamond coatings. Tungsten carbide blades already comprise a large part of the woodworking tool market. CVD-diamond-coated tools have yet to be used in woodworking and, thus, they offer an excellent business opportunity.

Mechanical Seals

In addition to cutting tools, seals represent the next best application possibility for CVD diamonds. The mechanical seals market is very large. Over three million higher-end pumps rely on the tribological performance of SiC seals, which are ideal substrates for diamond film growth. In fact, because of its extreme hardness and low coefficient of friction, diamond is an ideal candidate for seal surfaces of rotating shafts. Improper use or leakage in mechanical pump systems can be very costly and cause environmental disasters. Total energy losses due to high friction and wear are estimated to be on the order of 10^{10} kwh/year, which translates into roughly $1 billion/year. Also, it is estimated that 10-15% of total hazardous emissions are due to leakage or catastrophic failure of mechanical seals. If properly applied, diamond coatings can extend the useful life of these components and

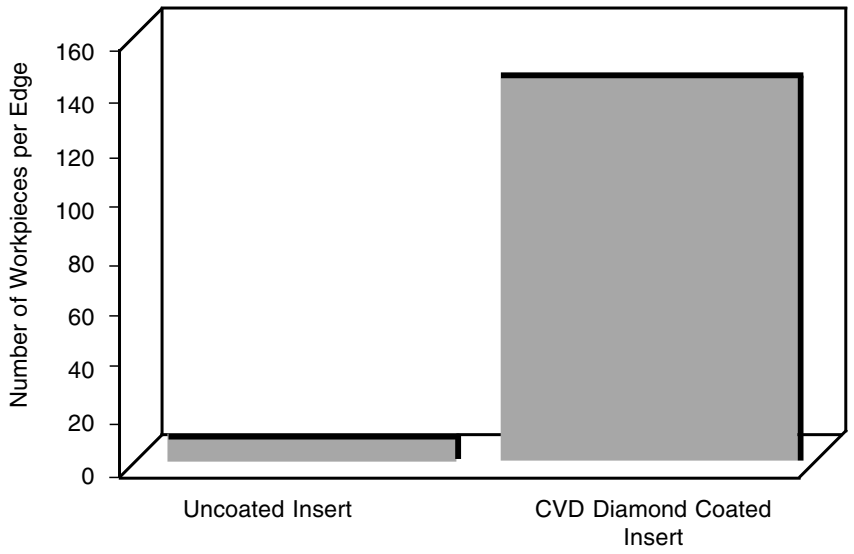

Fig. 12: Cutting performance of uncoated and CVD-diamond-coated insert while machining cast aluminum alloy that contained 7% Si (Cutting conditions: speed, 150-2500 m/min, depth of cut, 0.5-3 mm; feed rate, 0.25-0.8 mm/rev).[89]

also reduce energy losses because of the very low friction they afford to the sliding surfaces of seals. Early studies by Hollman et al. demonstrated that smooth diamond films can lead to substantial reductions in frictional torque and wear rates of shaft seals.[45,106]

Rough diamond coatings cannot be used in seal applications. One of the scaling faces (inserts) is mostly made out a soft carbon-graphite composite which wears out rather quickly when rubbed against a rough and superhard. Hard SiC inserts may also be used, but are much more expensive and when rubbed against rough diamond, suffer major wear losses. Polished or smooth, nanocrystalline diamond coatings will be more desirable for seal applications. Coated seals would be especially attractive in applications that require chemical inertness (especially in environments that involve concentrated acids or bases), pump grit slurries that cause rapid erosion in conventional seals, and in applications where a liquid lubricant is not permissible. Figure 15 shows a SiC seal coated with a nanocrystalline diamond film.

Figure 13 illustrates the effectiveness of a nanocrystalline diamond-coated carbide insert in preventing edge wear and loss of sharpness after machining a high-Si-containing AI alloy. CVD-diamond-coated tools were proved to be as good as or better than PCD tool inserts during turning of A1Si alloys and graphite. Figure 14 shows the tool life of CVD diamond in comparison to PCD- and TiN-coated carbide inserts during rough turning of graphite.[105] Diamond-coated tools have been available commercially for some time in many industrialized countries. Market share of coated tools is expected to increase steadily because prices are declining while performance and reliability are improving. Improved quality and reliability will certainly make diamond-coated tools last longer, cost less, and increase productivity.

Several companies are engaged in the production of CVD-diamond-coated tool inserts. DeBeers, Mitsubishi, Nachi-Fujikoshi, Norton, Kennametal, Sandvik, and Sumitomo are the major firms. Kennametal and Sandvik provide diamond-coated tools on a commercial basis. Based on the input of several tool insert manufacturers, the estimated world market for diamond-coated inserts is $10 to 20 million per year. As discussed above, CVD- diamond-coated inserts are primarily targeted for machining

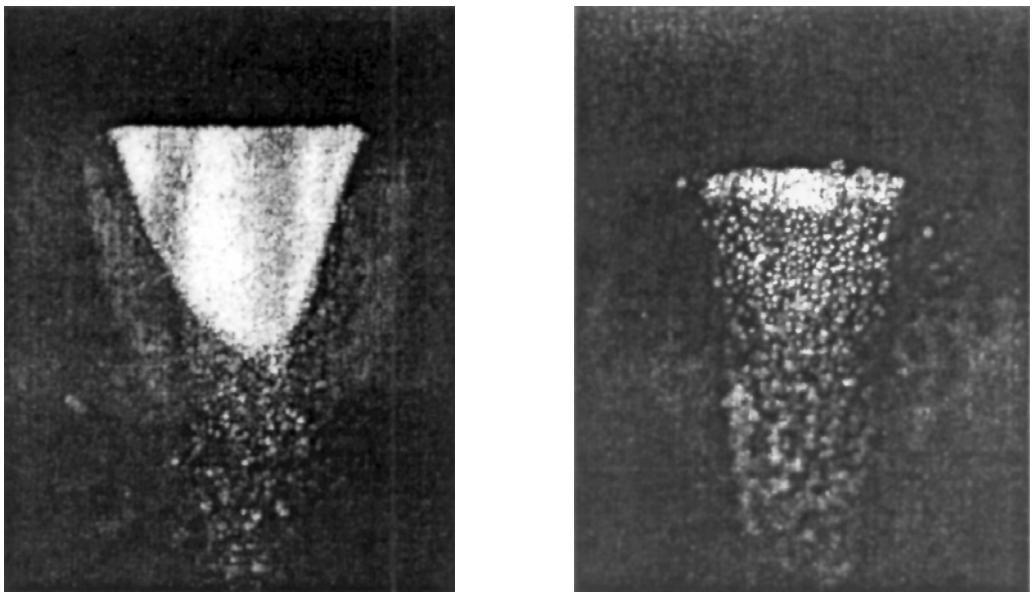

(a) (b)

Fig. 13: Extent of wear damage on (a) uncoated and (b) nanocrystalline diamond coated tool inserts after machining of hypereutectic aluminum-silicon alloy.

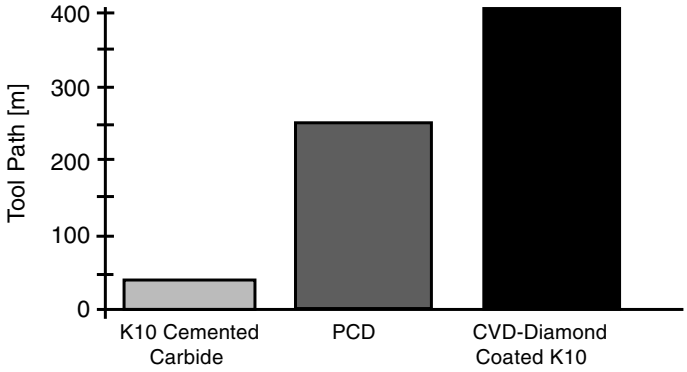

Fig. 14: Cutting performance of uncoated, PCD and CVD-diamond-coated tool inserts while milling graphite.[105]

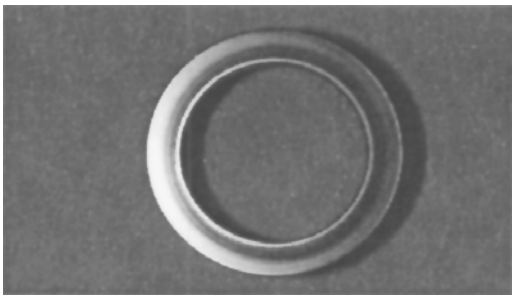

Fig. 15: Nanocrystalline-diamond-coated SiC face seal.

applications that involve high silicon aluminum alloys. The projected growth of the aluminum uses in automobiles indicates that the growth of the diamond-coated tool insert market will be significant.

Other Tribological Applications

Microelectromechanical systems (MEMS) represent a new class of moving mechanical assemblies that can be used for a wide range of applications, including sensors, actuators, high-precision positioning devices, etc. MEMS devices such as gear assemblies and micromotors have been largely fabricated by Si micromachining technology. However, Si exhibits very poor mechanical and tribological properties. When these microdevices used in a very high speed application, they suffer from unacceptably high friction and wear losses. Consequently, they are unsuitable for applications that use high speeds and realistic loads. Researchers have developed alternative fabrication methods that can allow production of MEMS devices from SiO^2, Si^3N4, or SiC-type materials. However, the tribological performance of these materials is also very poor; hence, they may not function well in a dynamic MEMS application.

Because of their excellent properties, researchers have recently been contemplating the use of diamond coatings for MEMS applications.[107-111] However, some difficulties have been encountered in fabricating diamond coatings and/or components with a morphology suitable for NMMS. The nanocrystalline diamond films discussed earlier appear to be better suited because their grain size is very small (i.e., 10-30 nm). With these films, it will be possible to attain film coverage at very small thicknesses (as thin as 50 nm) and thus preserve the fine structural features of the MEMS device. Conventional CVD films with 0.5-10-μm grains may not completely cover the surface of Si-based MEMS devices.

Other potential applications for CVD-diamond coatings include, woodworking tools, tab tools, push pins, high-precision microdrills, surgical blades, wire-drawing dies, and various wear parts that are used against erosion and abrasion (such as jet nozzles).

Summary and Future Directions

Over the years, great strides have been made in the deposition and characterization of diamond coatings. However, despite high interest in the use of diamond coatings for a wide range of applications only certain tool inserts have been successfully coated with diamond and made available for commercial uses. Although prototypes of other tribological parts (such as mechanical seals) have also been prepared with diamond coatings, their large-scale utilization has not yet been realized. Some of the reasons for the slow progress in the commercialization of diamond coatings are rough surface finish, problems with adhesion, high fabrication cost, and most important, insufficient reliability/repeatability in actual applications. This overview demonstrates that these coatings have much to offer for future tribological applications. It is anticipated that the uses of diamond coatings by industry will increase substantially if and when the reliability and quality control issues are adequately addressed and the unit cost is further reduced.

The results of previous studies suggest that the friction and wear performance of these films are controlled by physical roughness and chemical interaction with the surrounding environment. Tribo-oxidation, graphitization, gaseous adsorption/desorption can occur at the sliding contact interfaces of these films and control their friction and wear properties. As with other types of thin solid coatings, strong bonding between diamond films and substrate materials is an important prerequisite for long service life in most tribological applications. Existing data suggest that with proper process control and structural engineering, nanocrystalline diamond coatings with very smooth surface finishes can be obtained. These films can afford very low friction coefficients to sliding surfaces and are particularly suitable for mechanical shaft seals and MEMS applications.

Diamond coatings afford excellent life improvements to cutting tool inserts that are used to cut aluminum-silicon alloys and graphite. The cutting performance of coated-inserts is also impressive when cutting other alloys and composite materials. With recent advances in CVD technology, these inserts are expected to last even longer and cost less than before, and thus increase their market share in the metal-cutting industry. Briefly, the future of diamond coatings in tribological applications looks promising, because industrial needs for materials with unusual properties are constantly increasing.

Acknowledgments

This work is supported by the U. S. Department of Energy, under Contract W-31-109-Eng-38. The author thanks his research collaborators and students who participated in the reparation, testing, and characterization of the nanocrystalline diamond films discussed in this chapter.

References

1. C.A. Brookes and E.J. Brookes, *Diamond and Related Materials*, Vol.1, 1991, pp.13-17.
2. K. Miyoshi, *Diamond Films Technology*, Vol.8, 1995, pp.153-172.
3. S. Jin and H. Mavoori, *Journal of Electron. Materials*, Vol.27, 1998, pp.1148-1153.
4. J.E. Field, *The Properties of Natural and Synthetic Diamond*, Academic Press, London, 1992.
5. L.K. Bigelow and J. De Physique, Vol.3, 1993, pp.897-902.
6. A.K. Dua, *Materials Science Forum*, Vol.246, 1997, pp.91-104.
7. Status and Applications of Diamond and Diamond-like Materials, An Emerging Technology, National Materials Advisory Board, Washington, DC, 1990.
8. P.W. May, Endeavour, Vol.19, 1995, pp.101-106.
9. W.J.P. Van Enckevort, *Journal of Hard Materials*, Vol.1, 1990, p.247.
10. P.K. Bachmann, D. Leers, and D.U. Wiechert, Berichte der Bunsengesellschaft fuer Physikalische Chemie, Vol.95, 1991, pp.1390-1400.
11. H.J. Boving, W. Hanni, M. Maillat, J.P. Dan, and P. Niedermann, MRS Proceedings, Vol.383, 1995, pp.297-306.
12. G. Heinrich, T. Groegler, S.M. Rosiwal, and R.F. Singer, *Surface Coating Technology*, Vol.94-95, 1997, pp.514-520.
13. D. Hayes, *Industrial Diamond Review*, Vol.58, No.578, 1998, pp.80-81.
14. D. Hayes, *Industrial Diamond Review*, Vol.54, 1994, p.28.
15. H.P. Bovenkerk, J.B. Bundy, H.T. Hall, H.M. Strong, and R.H. Wentorf, *Nature*, Vol.184, 1959, p.1094.
16. J.C. Angus, Synthetic Diamond, Emerging CVD Science and Technology, K.E. Spear and J.P. Dismues, eds., John Wiley & Sons, Inc., New York, 1994, pp.21-39.
17. Y. Muranaka, H. Yamashita, and H. Miyadera, *Diamond and Related Materials*, Vol.3, 1994, pp.313-318.
18. R.Haubner and B.Lux, *International Journal of Refract. Metallurgical Hard Materials*, Vol.14, 1996, pp.111-118.
19. R. Haubner and B.Lux, *Diamond and Related Materials*, Vol.2, 1993, pp.l277-1294.
20. T.R. Anthony, *Proceedings of Workshop on Diamond and Diamond like Carbon Films*, F.A. Nichols and D.K. Moores, eds., Argonne National Laboratory, Argonne, IL, ANL-Conf-9202262, 1992, pp.117-164.
21. J. Karner, M. Pedrazzini, I. Reineck, M.E. Sjostrand, and E. Bergmann, *Materials Science and Engineering*, Vol.A209, 1996, pp.405-413.
22. J.E. Butler and H. Windischmann, MRS Bulletin, Vol.23, 1998, pp.22-27.
23. W.G. Eversole, U.S. Patents 3,030,187, and 3,030,188, 1962.
24. B.V. Deryagin and D.B. Fedoseev, *Sci. Am.,* Vol.233, 1975, pp.102-109.
25. A. Hatta and A. Hiraki, Low Pressure Synthetic Diamond, B. Dischler and C. Wild, eds., Springer-Veriag Berlin, Chapter

6, 1998, pp.103-117.
26. D.M. Gruen, S. Liu, A.R. Krauss, J. Luo, and X. Pan, *Applied Physics Letters*, Vol.64, No.12, 1994, pp.1502-1504.
27. N.J. Komplin and R.H. Hauge, Low Pressure Synthetic Diamond, B. Dischler and C. Wild, eds., Springer-Verlag Berlin, Chapter 7, 1998, pp.119-136.
28. R.T. Rozbicki and V.K. Sarin, *Thin Solid Films*, Vol.332, 1998, pp.87-92.
29. W. Banholzer, *Surface Coatings Technology*, Vol.53, 1992, pp.1-12.
30. K. Miyoshi, *Diamond Film Technology*, Vol.8, 1998, pp.153-172.
31. D.G. Bhat, D.G. Johnson, A.P. Malshe, H. Naseem, W.D. Brown, L.W. Schaper, and C.H. Shen, *Diamond and Related Materials*, Vol.4, 1995, p.921.
32. I.P. Hayward, *Surface Coatings Technology*, Vol.49, 1991, pp.554-559.
33. A.K. Gangopadhyay and M.A. Tamor, *Wear*, Vol.169, 1993, pp.221-229.
34. S.K. Choi, D.Y. Jung, S.Y. Kweon, and S.K. Jung, *Thin Solid Films*, Vol.279, 1996, pp.110.
35. R. Ramesham and M.F. Rose, *Thin Solid Films*, Vol.320, 1998, pp.223-227.
36. A. Erdemir, M. Halter, G.R. Fenske, A. Krauss, D.M. Gruen, S.M. Pimenov, and V.I. Konov, *Surface Coating Technology*, Vol.94-96, 1997, pp.537-541.
37. B. Buhshan, V.V. Subramanian, A. Malshe, B.K. Gupta, and J. Ruan, *Journal of Applied Physics*, Vol.74, 1993, pp.4178-4185.
38. B.K. Gupta, A. Malshe, B. Bhushan, and V.V. Subramanian, *Journal of Tribological*, Vol.116, 1994, pp.445-453.
39. M. Lahres and G. Joergensen, *Surface Coatings Technology*, Vol.96, 1997, pp.198-204.
40. S. Chikata, MRS Bulletin, Vol.23, No.9, 1998, p.61.
41. M. Seal, *Applications of Diamond Films and Related Materials*, third International Conference, A. Feldman et al., NIST Special Publication, Vol.885, 1995, pp.3-12.
42. K. Anda, S. Takehana, S. Yoshida, R. Watanabe, S. Takono, H. Ando, and F. Shimakura, *Surface Coatings Technology*, Vol.73, 1995, pp.115-120.
43. K.V. Ravi, *Synthetic Diamond*, Emerging CVD Science and Technology, K.E. Spear and J.P. Dismukes, eds., Electrochemical Society Monograph, John Wiley and Sons, New York, 1994, pp.419-504.
44. M.A. Cappelli and T.G. Owano, *Low Pressure Synthetic Diamond*, B.Dischier and C.Wild, eds., Springer-Verlag Berlin, Chapter 4, 1998, pp 59-80.
45. P. Holiman, O. Wanstrand, and S. Hogmark, *Diamond and Related Materials*, Vol.7, 1998, pp.1471-1477.
46. D.M. Bhusari, J.R. Yang, T.Y. Wang, S.T. Lin, K.H. Chen, and L.C. Chen, *Solid State Comm.,* Vol.107, 1998, pp.301-305.
47. D.M. Gruen, MRS Bulletin, Vol.23, No.9, 1998, pp.32-35.
48. C. Zuiker, A.R. Krauss, D.M. Gruen, X. Pan, J.C. Li, R. Csenesits, A. Erdemir, C. Bindal, and G. Fenske, *Thin Solid Films*, Vol.270, 1995, pp.154-159.
49. A. Erdemir, G.R. Fenske, and C. Bindal, C. Zuiker, A. Krauss, and D. Gruen, *Diamond and Related Materials*, Vol.5, 1996, pp.923-931.
50. A. Erdemir, C. Bindal, G.R. Fenske, C. Zuiker, R. Csencsits, A.R. Krauss, and D.M. Gruen, *Diamond Films Technology*, Vol.5, 1996, pp.31-47.
51. D.A. Horner, L.A. Curtiss, and D.M. Gruen, *Chemical Physics Letters*, Vol.233, 1995, pp.243-248.
52. D.M. Gruen, P.C. Redfern, D.A. Horner, P. Zapol, and L.A. Curtiss, *Journal of Physics Chemical*, Vol.B103, 1999, pp.5459-5467.
53. D.M. Gruen, C.D. Zuiker, A.R. Krauss, and X. Pan, *Journal of Vacuum Science Technology*, Vol.A13, No.3, 1995, pp.1628-1632.
54. I.P. Hayward, I.L. Singer, and L.E. Seitzman, *Wear*, Vol.157, 1992, pp.215-227.
55. S.M. Pimenov, A.A. Smolin, E.D. Obraztsova, V.I. Konov, U. Bogli, A. Blatter, E.N. Loubnin, M. Maillat, A. Leijala, and J. Burger, *Applied Surface Science*, Vol.92, 1996, pp.106-114.
56. A.M. Zaitsev, G. Kosaca, B. Richarz,

V. Raiko, R. Job, T. Fries, and W.R. Fahrner, *Diamond and Related Materials*, Vol.7, 1998, pp.1108-1117.
57. A. Erdemir, G.R. Fenske, A.R. Krauss, D.M. Gruen, T. McCauley, and R.T. Csencsits, *Surface Coatings Technology*, Vol.121, 1999, pp.565-572.
58. M. Kohzaki, K. Higuchi, S. Noda, and K. Uchida, *Journal of Materials Research*, Vol.7, 1992, pp.1769-1777.
59. S.J. Bull, P.R. Chalker, C. Johnston, and V. Moore, *Surface Coating Technology*, Vol.68-69, 1994, pp.603-610.
60. K. Miyoshi, R.L.C. Wu, A. Garscadden, P.N. Barnes, and H.E. Jackson, *Journal of Applied Physics*, Vol.74, 1993, pp.4446-4450.
61. F.P. Bowden and J.E. Young, *Proceedings of Royal Society*, London, Vol.208, 1951, pp.444-455.
62. F.P. Bowden and A. E. Hanwell, *Proceedings of Royal Society*, London, Vol.A295, 1966, pp.233-243.
63. S.V. Pepper, *Journal of Vacuum Science and Technology*, Vol.20, 1982, pp.643-646.
64. S. Chandrasekar and B. Bhushan, *Wear*, Vol.153, 1992, pp.79-89.
65. K. Holmberg, *Tribological*, Vol.12, 1998, pp.33-62.
66. M. Dugger, D.E. Peebles, and L.E. Pope, *Surface Science Investigations in Tribology*, Experimental Approaches, Y.W. Chung, A.M. Homolo, and G.B. Street, eds., ACS Symposium Series 485, American Chemical Society, Washington D.C., 1992, pp.72-102.
67. M.N. Gardos and B.L. Soriano, *Journal of Materials Research*, Vol.5, 1990, p.2599.
68. M.N. Gardos and K.V. Ravi, *Diamond Films Technology*, Vol.4, 1994, pp.139-165.
69. A. Erdemir, M. Halter, G.R. Fenske, R. Csencsits, A.R. Krauss, and D.M. Gruen, *Triboligical Transactions*, Vol.40, 1997, pp.667-675.
70. A. Erdemir and G.R. Fenske, *Triboligical Transactions*, Vol.39, 1996, pp.787-794.
71. S. Jahanmir, D.E. Deckman, L.K. Ives, A. Feldman, and E. Farabaugh, *Wear*, Vol.133, 1989, pp.73-81.
72. E.H. Lee, D.M. Hembree, G.R. Rao, and L.K. Mansur, *Physics Review*, Vol.48, 1993, pp.15540-15551.
73. E.H. Lee, M.B. Lewis, P.J. Blau, and L.K. Mansur, *Journal of Materials Research*, Vol.6, 1991, pp.610-617.
74. M. Seal, *Applications of Diamond Films and Related Materials*, Third International Conference, A. Feldman et al., eds., NIST Special Publication, Vol.885, 1995, pp.3-12.
75. S.J. Bull and A. Mathews, *Diamond and Related Materials*, Vol.1, 1992, p.1049.
76. K.V. Ravi, in Synthetic Diamond, Emerging CVD Science and Technology, K.E. Spear, and J.P. Dismukes, eds., *Electrochemical Society Monograph*, John Wiley and Sons, New York, NY, 1994, pp.419-504.
77. B. Lux and R. Haubner, *Diamond as a Wear-resistant Coating, Diamond Films and Coatings,* R.F. Davis, ed., NOYES Publications Park Ridge, New Jersey, 1993, pp.184-243.
78. M. Murakawa, *Materials Science Forum,* Vol.246, 1997, pp.1-28.
79. M. Murakawa and S. Takeuchi, *Surface Coatings Technology*, Vol.49, 1991, pp.359-365.
80. K. Kanda, S. Takehana, S. Yoshida, R. Watanabe, S. Takano, H. Ando, and F. Shimakura, *Surface Coating Technology*, Vol.73, 1995, pp.115-120.
81. J.F. Braza and T.S. Sudarshan, *Materials Science and Technology*, Vol.8, 1992, pp.574-581.
82. R.K. Zalavutdinov, A.E. Gorodetsky, A.P. Zakharov, Y.V. Lakhotkin, V.G. Ralchenko, N.V. Samokhvalov, V.N. Anikin, and A.I. Pjyanov, *Dimnond and Related Materials*, Vol.7, 1998, pp.1014-1016.
83. B. Lux and R. Haubner, *Ceramic International*, Vol.22, 1996, pp.347-351.
84. E. Kubel, *Manufacturing Engineering*, Vol.120, 1998, pp.44-46.
85. B. Lux and R. Haubner, *Low Pressure Synthetic Diamond*, B. Dischler and C. Wild, eds., Springer-Verlag Berlin Heidelberg, 1998, pp.223-242.

86. R. Komanduri and S. Nandyal, *International Journal of Mechanical Tools Manufacturing*, Vol.33, 1993, pp.285-296.
87. A. Inspektor, E.J. Oles, and C.E. Bauer, *International Journal of Ref. Metallurgical Hard Materials*, Vol.15, 1997, pp.49-56.
88. K. Saijo, M. Yagi, K. Shibuki, and S. Takatsu, *Proceedings of Materials Manufacturing*, Vol.8, 1993, pp.59-73.
89. J. Karner, M. Pedrazzini, I. Reineck, M.E. Sjostrand, and E. Bergmann, *Materials Science and Engineering*, Vol.A 209, 1996, pp.405-413.
90. S. Durante, G. Rutelli, and F. Rabezzana, *Surface Coatings Technology*, Vol.94-95, 1997, pp.632-640.
91. F. Deuerler, M. Pies, H. Van den Berg, R. Tabersky, and V. Buck, *Physica Status Solidi (A) Applied Research*, Vol.154, 1996, pp.403-422.
92. R. Keipke, H. Buchkremer-Hermanns, H. Weiss, and H. Ren, *Proceedings of Materials Manufacturing*, Vol.13, 1998, pp.603-610.
93. H.G. Prengel, W.R. Pfouts, and A.T. Santhanam, *Surface Coatings Technology*, Vol.102, 1998, pp.183-190.
94. C.H. Shen, *Key Engineering and Materials*, Vol.138-140, 1998, pp.25-55.
95. V.J. Trava-Airoldi, E.J. Corat, and V. Baranauskas, *Key Engineering and Materials*, Vol.138-140, 1998, pp.195-244.
96. C.H. Shen, *Surface Coatings Technology*, Vol.86-87, 1996, pp.672-677.
97. J.M. Olson and M.J. Dawes, *Journal of Materials Research*, Vol.11, 1996, pp.1765-1775.
98. J. Gunnars and A. Alahelisten, *Surface Coatings Technology*, Vol.80, 1996, pp.303-312.
99. S. Chatterjee, A.G. Edwards, A. Nichols, and C.S. Feigerle, *Journal of Materials Science*, Vol.32, 1997, pp.2827-2833.
100. K.L. Menningen, M.A. Childs, H. Toyoda, L.W. Anderson, and J.E. Lawler, *Journal of Materials Research*, Vol.9, 1994, pp.915-920.
101. E. Cappelli, S. Orlando, F. Pinzari, and P. Ascarelli, *Proceedings of MRS Symposium*, Vol.526, 1998, pp.361-365.
102. H.K. Toenshoff, A. Mohlfeld. C. Gey, and J. Winkler, *Surface Coatings Technology*, Vol.108-109, 1998, pp.543-550.
103. E.R. Kupp, W.R. Drawl, and K.E. Spear, *Surface Coatings Technology*, Vol.68-69, 1994, pp.378-383.
104. S. Kubelka, R.Haubner, B.Lux, R.Steiner, G.Stingeder, and M.Grasserbauer, *Diamond and Related Materials*, Vol.3, 1994, pp.1360-1369.
105. T. Leyendecker, O. Lemmer, S. Esser, and M. Frank, Proceedings of Third International Conference, *Applied Diamond Films and Related Materials*, A. Feldman, Y. Tzeng, W.A. Yarhrough, M. Yoshikawa, and M. Murakawa, eds., NIST SP-885, Washington DC, 1995, pp.183-190.
106. P. Hollman, H. Bjorkman, A. Alahelisten, and S. Hogmark, *Surface Coatings Technology*, Vol.105, 1998, pp.169-174.
107. H. Bjorkman, P. Rangsten, P. Holiman, and K. Hjort, *Proceedings of Summer Topical Meeting of the IEEE/LEOS*, Monterey, CA, IEEE Piscataway, NJ, 1998, pp.77-78.
108. M. Aslam and D. Schulz, *Proceedomgs of 8th International Conference, Solid State Sensors and Actuators, and Eurosensors IX. Part 2,* (of 2), 1995, Stockholm, Sweden, IEEE Piscataway NJ, Vol.9, No.2, pp.221-224.
109. M.Y. Mao, T.P. Wang, J.F. Xie, and W.Y. Wang, *Proceedings of IEEE Micro Electro Mechanical Systems Conference*, Amsterdam, 1995, pp.392-393.
110. R. Ramesham, *Thin Solid Films*, Vol.340, 1999, pp.1-6.
111. M.N. Gardos, *Proceedings of Electrochemical Society*, Vol.97, 1998, pp.465-481.

Chemical Vapor Deposition
Jong-Hee Park, T.S. Sudarshan, editors, p401-419
DOI:10.1361/cvd2001p401

Chapter 12

CVD Films for Electrical Insulation

J.H. Park
Materials Scientist
Energy Technology Division
Argonne National Laboratory
Argonne, IL 60439

W.D. Cho
Professor
Department of Metallurgical Engineering
University of Utah
Salt Lake City, UT 84112

Abstract

The requirements, development and fabrication of electrical insulator and corrosion protection coatings for high-temperature alloys using thermal CVD coatings have been demonstrated. This chapter focuses on the requirements and applications of electrical insulator coatings have been focused on magnetic cores in power transformers and on design of liquid-metal-cooled magnetic fusion reactors (MFRs)

In general electrical insulation coatings reduce or prevent unwanted flow of electrical current there exist several important technological applications of electrical insulator coatings when conductors are placed

within a magnetic field. Induced currents result when the conductors are moving. Magneto-hydrodynamic (MHD) forces and their influence on thermal hydraulics are major concerns for liquid-metal cooling systems.[1-2] Magnetic power transformers contain many thin sheets of insulated magnetic core plates.[3-5] The electrical steels used for laminated magnetic cores of power-frequency electrical equipment such as transformers, motors, and generators typically have some type of insulator coating to minimize interlaminar core loss due to circulating eddy currents. Pioneering work has been done by Loundermilk and Murphy on electrical steels,[4,5] Liu,[6] and Park and his collaborators[7-10] on the design of a liquid-metal cooling system for a first-wall/blanket in a magnetic fusion reactor (MFR) to describe the technology of insulating coatings. However for the latter application, corrosion resistance of structural materials and magnetohydrodynamic (MHD) forces and their influence on thermal hydraulics are major concerns.[1,2,7]

Requirements

Magnetic Cores

The purpose of magnetic cores in transformers, motors, generators, and other electromagnetic devices is to multiply and direct magnetic flux. To accomplish this task efficiently, the amount of energy wasted in heating the core must be minimized.[3] The loss of energy as heat is called core loss and is typically expressed in watts per unit weight of core material. The purpose of insulating coatings on electrical steel laminations is to minimize a component of total core loss called interlaminar loss. When a primary winding in a transformer is energized with alternating current, an alternating magnetic flux is induced in the core. This alternating flux induces a voltage in the secondary winding, thereby accomplishing the desired transformation of voltage, which is either an increase or decrease relative to the input voltage depending on the ratio of the number of turns in the primary and secondary windings. However, the varying magnetic flux also induces an alternating voltage in the core material, which gives rise to circulating electrical currents called "eddy" currents. In a solid core, these eddy currents are free to circulate throughout the entire cross section of the core, as shown in Figure 1(a) Resistive heating of the core by the induced eddy currents is a major component of total core loss and is called "eddy current loss" One way to minimize eddy current loss is to restrict the path of the eddy currents by using a laminated core structure composed of thin sheets electrically insulated from one another. Figure l(b) shows a laminated transformer core in which the eddy current paths are confined to each individual lamination.

This restriction of eddy current paths results in a large decrease in eddy current power loss (i^2R loss). The ratio of the eddy current loss in a laminated core with n laminations to a solid core with the same cross sectional area is $1/n^2$ Commercial transformer cores are fabricated from thin sheets of metallic core material to take advantage of this effect. The eddy current loss P_e within laminations of a magnetic core is given by the "classical" eddy current power loss equation

$$P_e = 3.39 \times 10^{-13} (B \bullet f \bullet t)^2 \ / \rho\delta \ \text{W/kg}, \qquad (1)$$

where B = magnetic flux density (gauss), f = frequency (Hz), t = lamination thickness (cm), ρ = electrical resistivity, and δ = density of the core material (g/cm^3). It is apparent that eddy current loss can be minimized by using thin laminations with high electrical resistivity Electrical steels are flat-rolled iron-silicon alloys designed specifically for use in laminated or wound magnetic core structures. When the laminations are perfectly insulated from one another, eddy currents induced in the core by the alternating magnetic flux cannot flow from one lamination to another. In most cases, it is not practical or necessary to have perfect insulation between laminations. Typically, the surface insulation on electrical steels is considered adequate if the interlaminar core loss is at most about 1% of the total core loss. The interlaminar eddy current loss is P_i (see Eq. 2) in a transformer core with uniform surface resistivity. Electrical systems containing large

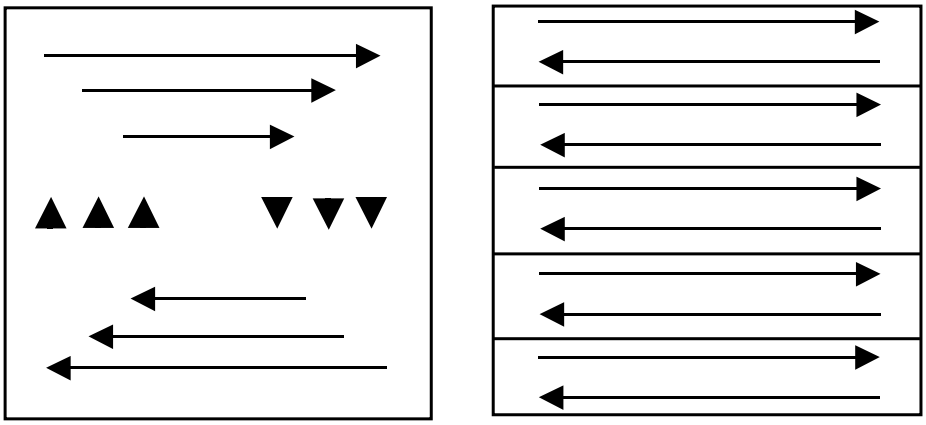

(a) Eddy Current in Solid Core (b) Eddy Current in Laminated Core

Fig. 1: (a) In a solid core eddy currents are free to circulate throughout the entire cross-section of the core and (b) While in a laminated transformer core, the eddy current paths are confined to each individual lamination.

cores that operate at high flux densities (such as large power transformers or generators) require much higher interlaminar resistance than do electrical systems with smaller cores. P_i is determined by

$$P_i = 2.54 \times 10^{-13} (B^2 \bullet f^2 \bullet t \bullet w^2)/r\delta \text{ W/kg} \quad (2)$$

Where B = induction magnetic flux (gauss), and r = surface resistivity (Ω-cm^2 per lamination). Therefore, interlaminar loss decreases with increasing surface resistivity. Figure 2 shows the surface resistivity required for t = 0.023 cm transformer core steel to maintain predicted interlaminar eddy current power loss, P_i, at B = 15 kG, and f = 60 Hz.

Magnetohydrodynamic (MHD) Forces in Liquid Metal Flows

If a liquid metal flows perpendicular to the magnetic field direction (Figure 3), a potential difference across the flow duct is induced in the metal coolant; this causes a high electrical current flow when the potential difference is short-circuited by the electrically conducting walls. The relationship between magnetic field (B), electrical current (I), and mechanical force (F), when the I is flowing perpendicular to B, results in F, which leads to MHD pressure drop (Δp). It has been shown that even in thin conducting walls, this would lead to a significant pressure drop. Calculated values of Δp of 8.6 MPa result if there is a conducting liner of 0.1 mm thickness.[11,12] A lower limit for the Δp would be achieved with perfectly insulated walls.[13] The product of coating resistivity (ρ_c) and coating layer thickness (t_c) should have a minimum value of $\rho_c \bullet t_c^3 \geq 100$ Ω.cm^2 is a target for the insulator coating in the liquid-metal for magnetic fusion reactors (MFRs). For example, if the coating material has a ρ_c value of 10^6 $\Omega \bullet$cm^2, it requires (t_c) of 10^{-4} cm, ie., 1 μm thickness of insulator coating. Therefore, conceptually, the higher the ρ_c value, a thinner coating is required. Reed et a1.[13] conducted tests to evaluate the MHD performance of electrical insulator coating that uses an Na-K eutectic as a liquid metal coolant; the Al_2O_3 insulator coatings on type 304 stainless steel. The present effort is focused on liquid lithium as a coolant. Vanadium and vanadium-base alloys (V-Ti or V-Ti-Cr) are leading candidate materials for structural applications.[l4] Some studies have concentrated on in-situ formation of AlN in liquid-lithium environments.[6-10] Subsequent work addressed

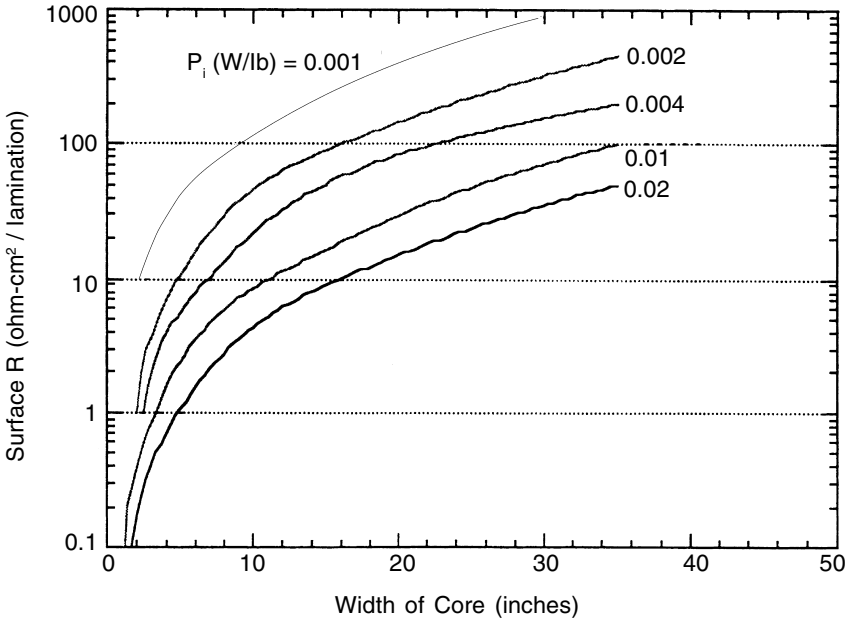

Fig. 2: Surface resistivity required for t = 0.023 cm transformer core steel to maintain predicted interlaminar eddy current power loss, P_i at B = 15 kG, and f = 60 Hz. (adapted from Ref. 4)

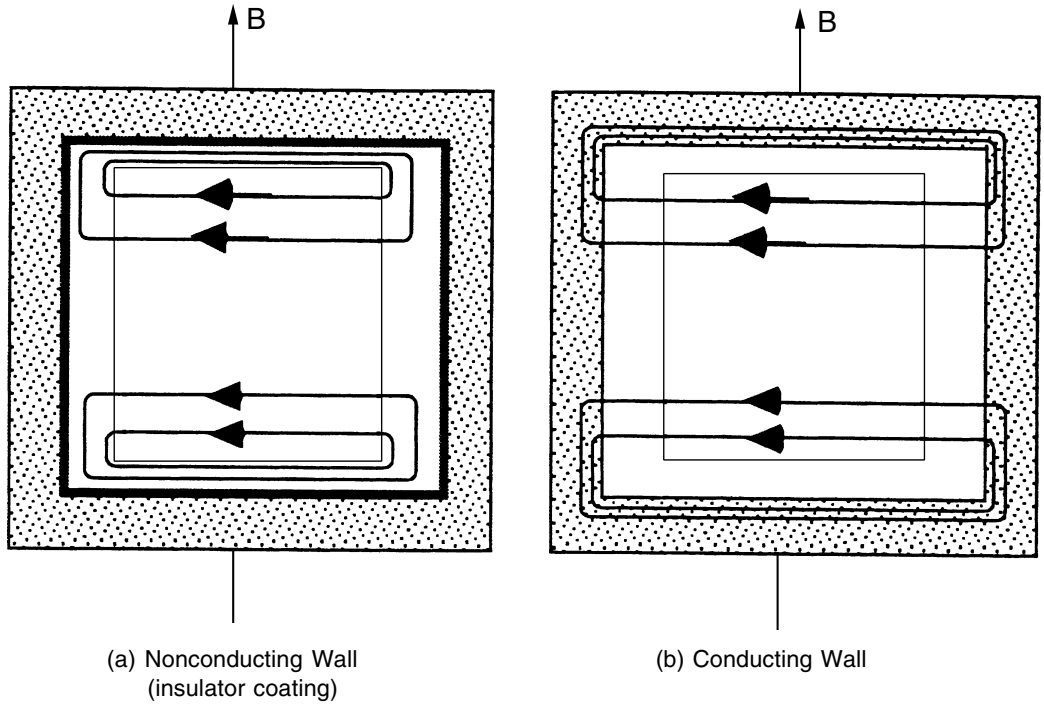

Fig. 3: Linduced current flows for two different walls and (a) for the non-conducting wall and (b) conducting wall under magnetic flux B.

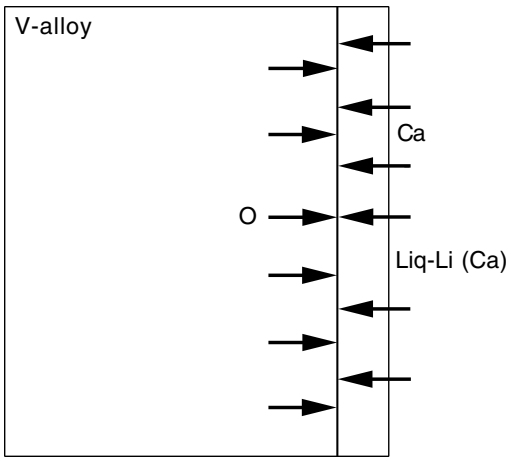

Fig. 4: Schematic diagram of CaO film growth in liquid-Li (Ca-bearing) environment.

in-situ formation of CaO in a liquid-lithium environment because the electrical resistivity of CaO is 10,000 times greater than that of AlN, and because there are many available insulator candidates, i.e, CaO, Y_2O_3, BeO, MgO, $MgA1_2O_4$, $Y_3A1_2O_{12}$ etc.[15-17] CaO has high thermodynamic stability in liquid lithium.[6-9,15] The coatings can be deposited on various shapes, such as the insides of tubes or irregular contours and angles, to prevent adverse currents generated by MHD forces from passing through the walls.[1,2] The coatings could also improve general corrosion resistance and act as a diffusion barrier for hydrogen isotopes, i.e., deuterium and tritium.[2,18,19]

Compatibility Screening Tests on Electrically Insulating Ceramics

As a first step, we need a compatibility screening test for the development of insulator coatings Results of compatibility tests on electrically insulating ceramic candidates in liquid Li are shown in Table 1.[7] In general, compatibility of ceramic insulators with liquid Li follows the criterion for thermodynamic stability. Although some ceramic materials are considered to be thermodynamically stable materials, e.g., sintered AlN and SiC (applied by chemical vapor deposition), they were not compatible with liquid Li in screening tests. We conclude that this behavior is caused by grain boundaries in AlN and SiC that are enriched in O, Si, C, or impurities that react with liquid Li. An example is sintered AlN. Electron energy dispersive-spectroscopy (EDS) analysis indicated that O contamination was predominant in AlN. Oxygen may form $A1_2O_3$ in the grain-boundary area, which is not stable in liquid Li. $A1_2O_3$, if present at grain boundaries, reacts with Li and thereby weakens the mechanical strength of AlN. As a result, O-enriched AlN appears to be brittle after exposure in liquid Li. When the O is gettered by the Y/Y_2O_3 phase present in AlN, sintered AlN remains intact after exposure to liquid Li. This presumably indicates that both AlN and Y_2O_3 are compatible with Li, as indicated in Table 1. Based on results of the liquid-Li compatibility tests, we proceeded with work to screen in-situ forming phases, which are then converted to ceramic insulators in liquid-Li environments. Figure 4 is a schematic diagram of CaO film growth in the liquid-Li (containing Ca) environment. Figure 5 shows SEM views of CaO film growth on the V-5 Cr-5Ti in the liquid-Li-5 at.% Ca thin film at 420°C and thick film grown at 800°C. The diffusion behavior of a growing CaO film could be predicted by the following trends:

Table 1. Liquid-Li Compatibility of Insulator Materials

Material	Composition (Form)	Compatibility/ Test Method[a]	Observation
SiC	SiC (CVD)	1/1	Reacted
	SiC (Si-enriched)	1/1	Reacted heavily
	SiC (Hot-pressed)	3/1	Intact
Si_3N_4	Si_3N_4 (Hot-pressed)	0/1	Specimen not Recovered
	Si-N-O (IBAD-coating)	0/1	Coating layer totally dissolved
Quartz	SiO_2 (Quartz tube)	0/1 and 2	Specimen not recovered
Rutile	Y_2O_3 (Single crystal)	0/1	Specimen not recovered
Yttria	Y_2O_3 (Sintered)	3/1	Intact
	Y_2O_3 (Hot-pressed)	3/1	Intact
YSZ	ZrO_2-10% Y_2O_3		
	(Sintered)	1/1	Reacted heavily
	(Single crystal)	1/1	Reacted heaviy
Chromia	Cr_2O_3 (Hot-pressed)	0/1	Specimen not recovered
A1N	A1N	3/2	Intact[7]
	A1N[b] (1-3% Y incorporated)	3/1	Intact
	A1N (Sintered-oxygen enriched)	2/1	Reacted
	A1 (V) N or A1N	3/2	A1N, Al (V) N, or Al-O-C-N formed in situ on V-5 Cr-5 Ti in Li
	A1-O-C-N		

- O transport in V-alloy is fast.
- Ca transport is faster than O in CaO film.[20]
- Concentration of Ca^{+2} is much higher than Li^{+1} because Li^{+1} is thermodynamically unstable when Ca metal is present.
- Ca^{+2} ion is much smaller than Li atom.
- Some possibility of isolated Li incorporation probably as atomic form in grain boundaries, triple points, or defected zone in CaO film.
- Possibility of Li^{+1} presence near the V-alloy/CaO film interface area due to oxygen potential is highest at interface

However, in practical applications, there are many concerns, and CaO should be considered as an in-situ healing option when the film is degraded during operation. Therefore, practical insulator coatings applied by high-temperature CVD are the primary option.

Table 1. Continued.

Material	Composition (Form)	Compatibility/ Test Method[a]	Observation
BN	BN (Hexagonal) BN (IBAD-coating)	0/1 0/1	Specimen not recovered Coating totally dissolved
Si	Si (Single crystal)	0/1	Specimen not recovered
Al_2O_3	Al_2O_3 (Ad 998-sintered)	0/1	Specimen not recovered
TiN[c]	[d]TiN (Pure & deped with Si, Mg, Al and O)	3/2	TiN formed on Ti in Li at >650°C
CaO	CaO CaO or Ca(V)O	3/2 3/2	700°C CaO formed on V-15 Cr-5Ti[e] 416°C CaO or Ca(V)O formed in-situ on V-5 Cr-Ti in Li
MgO	MgO	3/2	Intact[7] Intact[7] 416°C MgO or Mg(V)O formed in-situ on V-5Cr-5Ti in Li
BeO	BeO BeO BeO or Be(V)O	3/2 3/2 3/1 and 2	Intact[7] Intact[7] 416°C BeO or Be(V) O formed in-situ on V-5Cr-5Ti in Li
Y-A1 garnet	$Y_3Al_2O_{12}$	3/2	Intact[7]

[a]Compatibility with liquid-Li: 0 and 3 indicate not compatible and compatible, respectively, Test method; 1 indicates a test in flowing Li at 450°C for 315 to 617 hrs. 2 denotes capsule tests at 400°C for 100 hrs.

[b]ICP-Spectrochemical analysis of AlN indicated impurity levels (in wt.%); As<0.05, Ba 0.005, Ba 0.005, Be < 0.001, Ca 0.54, Co <0.02, Cr <0.002, Cu 0.006, Fe 0.015, Y 3.77, Y_2O_3 4.79, Mg 0.004, Mn <0.001, Ni 0.002, Pb <0.02, Sb <0.05, Sn <0.02, Sr <0.001, Ti 0.022, V <0.002, Zn <0.002, Zr <0.002, and Te <0.05. Before and after the test, only the Li was analyzed again, Li contents were <0.01 and 6.85, respectively.

[c]TiN is an electrical conductor.

[d]Type 304/316 stainless steel container for Li + N.

[e]Li + Ca used for this study.

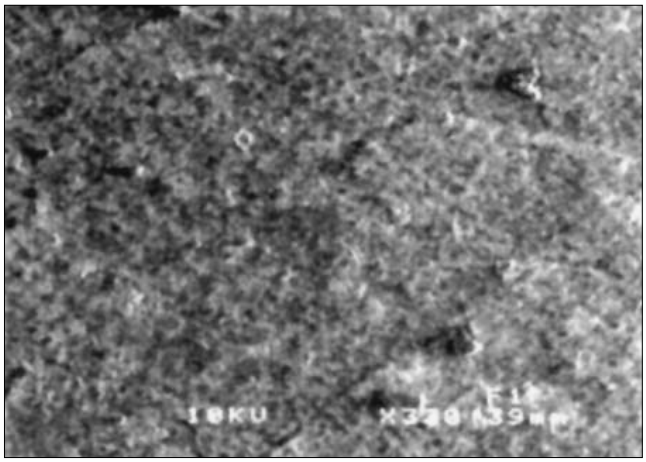

(a)

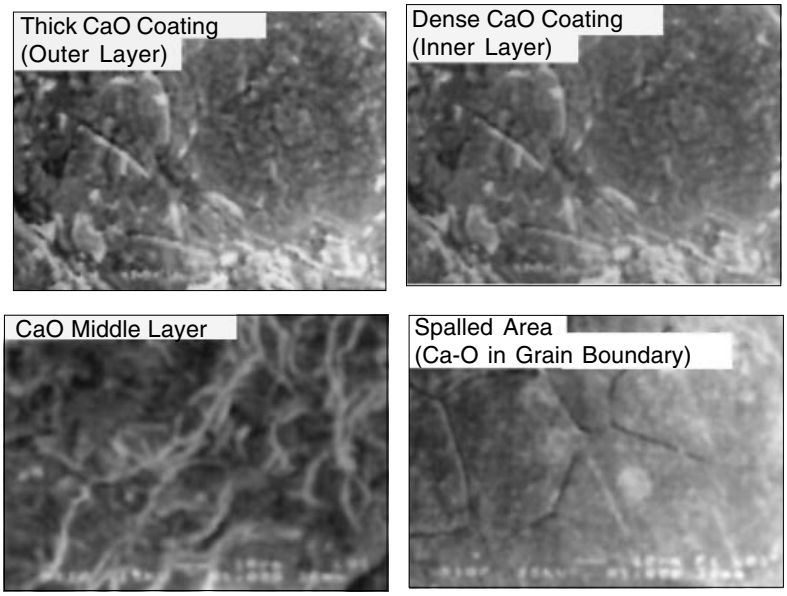

(b)

Fig. 5: (a) SEM Views of CaO film growth on V-5Cr-5Ti in liquid-Li-5at. %Ca thin film at 420°C and (b) Thick film at 800°C for various depths.

CaO Corrosion Behavior in Liquid Li

Based on the screening test shown in Table 1, CaO forms in-situ in liquid Li Therefore, CaO has been used as an insulator coating. However, we would like to consider possible corrosion in the liquid-Li environment, such as:

$$\underset{\text{(in V-4Cr-4Ti)}}{\underline{O}} + \underset{\text{(in liquid Li)}}{Ca} \rightarrow \underset{\text{(surface of V-4Cr-Ti)}}{CaO} \quad (3)$$

$$2\,Li_{(liq.)} + CaO \rightarrow Li_2O + Ca \quad (4)$$

Reaction 4 has a free energy change, ΔG, of +13 kcal/mole at 400°C, indicating that CaO should not be severely corroded by Li. This calculation, however, using the free energy of formation for solid Li_2O and CaO, does not represent the chemical reactions as they occur in flowing Li. Consequently, two additional potential corrosion mechanisms are considered here. Liquid Li is known to dissolve both Ca and O. The solubility of O in Li is ≈800 wppm

(≈ 350 appm) at 400°C, and the solubility of Ca in Li is 0.6 atomic fraction at 405°C. Consequently, the potential corrosion reaction should be written as

$$CaO_{(s)} \xrightarrow[Li_{(Liq.)}]{} Ca_{(Li)} + O_{(Li)} \qquad (5)$$

where $Ca_{(Li)}$ and $O_{(Li)}$, represent the species dissolved in liquid Li. The free-energy change for this reaction at 400°C can be calculated on the basis of the excess partial molar free energies of Ca and O in liquid Li, which have been measured, i.e., ΔG_f(400°C) kcal/g-atom. $Ca_{(Li)}$ = 9.4, $O_{(Li)}$ = 5.6 (estimated) and $CaO_{(s)}$ = 135. Therefore, the total ΔG for Reaction 3 is +120 kcal/mole. Even if the excess partial molar free energies of $Ca_{(Li)}$ and $O_{(Li)}$ are overestimated, the formation free energy of CaO is so high that the physical phenomena for the molar quantities for both assumed values are quite conservative Based upon the relationship

$\Delta G = -2303\ RT\ (\log k)$ or $\log k$

$= -\Delta G / (2.303 \bullet RT)$

$K \approx 1 \times 10^{-39} = [Ca_{(Li)}] \bullet [O_{(Li)}]$

$/[(CaO)_{(Li)}] \approx [Ca_{(Li)}] \approx [Ca_{(Li)}\} \bullet [O_{(Li)}]$

Hence, if the concentration of $[O_{(Li)}]$ is kept at 1 ppb in order to ensure replenishment of the CaO layer, then the normal concentration of $[Ca_{(Li)}] \approx 70$ ppm; even a value in the ppb range will be adequate. Therefore, in-situ formed CaO could be chemically stable.

Formation Mechanism of CaO Reactive Coatings

As we see in Table 1, CaO can be fabricated as a corrosion product between residual oxygen in metals, such as V-Cr-Ti alloys and dissolved Ca in Li. It is probable that CaO is intact in liquid Li. As we see in the screening test results in Table 1. O is mostly an interstitial impurity (especially, in BCC metals like V-alloys). When it is exposed to liquid-Li-bearing Ca, the corrosion product CaO could form on the metallic surface. Based on the screening process, we recognize that the O reacts with Ca in Li. When the V-substrate contains a slightly higher O concentration in the near-surface, CaO is produced If the surface oxidized as oxide films, calcium vanadate films could be fabricated as well. Formation of CaO at the V/CaO interface is expected for good adhesion properties because we can assume that the bonding nature follows the reaction scheme. In this case, if the difference in Gibbs free energy of reaction becomes negative, the lowest ΔG°(T) will have the best chance to form reactive CVD coatings. However, the original state of the substrate can vary among metallic or intermetallic substrates, as well as among oxides, nitrides. O-N, or carbides etc. If the insulator layer grows at the interface of the metal/film, for example, we consider that the Ca^{+2} cations move inward via the CaO coating layer and that this layer could achieve greater adhesion, as shown above. However, in general when the film grows by outward diffusion through the coating layer, the metal ions move from the substrate to the scale/environment interfaces, leaving vacancies in the substrate. Cations will be generated at the metal/coating interface, and metal atoms may be generated near a grain boundary or dislocation. In general, the vacancies coagulate near the interfaces and therefore total bonding strength decreases. When the cations have gone, the interfaces are almost in a floating state in a dynamic situation. Based on the reaction/diffusion profile at high temperature, oxide insulator coatings should form by surface oxygen charging initially, followed by oxygen-reactive vapor, (eg., Ca/CaO) that forms an adhesive CaO insulator coating on the metallic substrate. The principle of this process is similar to oxidation of metals in oxygen environments, that is, cation and anion sources are exchanged with each other.[17]

Our recent study (Ref. 31) on the internal oxidation of Ag-l.2 at% Mg and Ag-0.25 at% Mg-0.25 at% Ni showed that the clustering of oxygen active elements, R, with oxygen atoms O, varied with the ratio r = (O/R). The lower amount of R in the alloy has higher r-values Temperature dependent r-values indicated that lower temperatures showed higher r-values. Therefore, we can apply these phenomena in the oxygen-charging step or the CVD process.

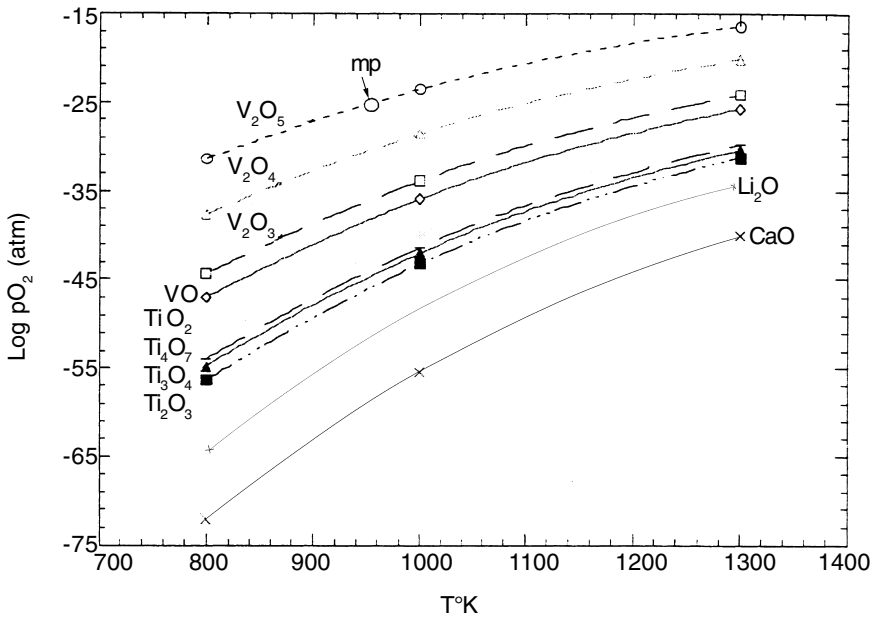

Fig. 6: Thermodynamic stability of several possible oxide phases that can form on V-Cr-Ti alloys; with Li, and Ca in oxygen-containing environments.

Oxygen Charging of Surfaces of V-Cr-Ti Alloys

The near-surface region of the specimens was charged with oxygen by heating the specimens for 2-3 hrs. argon (99.999% pure, with 5-10 ppm oxygen), or in a 1% CO-CO_2 gas mixture or air to form vanadium oxide at 625-650°C.[21-23] Figure 6 shows the thermodynamic stability of solid-state oxide phases as a function of equilibrium partial pressure of oxygen and temperature, that can form when V-Cr-Ti alloys with liquid Li, and Ca are exposed to oxygen-containing environments. It is well known that O can be incorporated into the interstitial sublattice in body-centered cubic (bcc) V and its alloys. Thus, if O or N is present in the alloy (as a reactant), these elements may have a higher affinity for solutes such as Ca, Y or Mg dissolved in Li than do the alloy elements. In the bcc lattice of V-5 Cr-5 Ti, O can occupy interstitial sites within the lattice up to several atomic percent. Oxygen charging of V-5Cr-5Ti was conducted for up to 48 hrs. at temperatures between 500 and 1030°C in flowing high-purity Ar and N_2 (99.999%) that contained O as an impurity. Diffusion coefficients of O and N in V indicate that O diffuses faster than N by 10 to 1800.[24,25] This property is very important for in-situ formation of CaO. Oxygen charging in a nitrogen atmosphere lowers the diffusion rate (≈5%) because of N participation. Based on metallographic information and weight gain, we can control the depth of the O-charged layer by exposure temperature and time in flowing Ar or N_2 atmospheres. Oxygen concentration in the near-surface layer was calculated from the weight gain, surface area, and thickness of the hardened region. It ranged from 250 ppm (as received) to ≈2-3%, depending on position within the layer and exposure conditions. Normal oxygen charging was performed in air at 400°C to avoid melting of V_2O_5 (690°C) during oxidation.[21] A blue amorphous layer (≈ 1 μm thick) formed at the surface. Samples charged with O in high-purity Ar or N_2

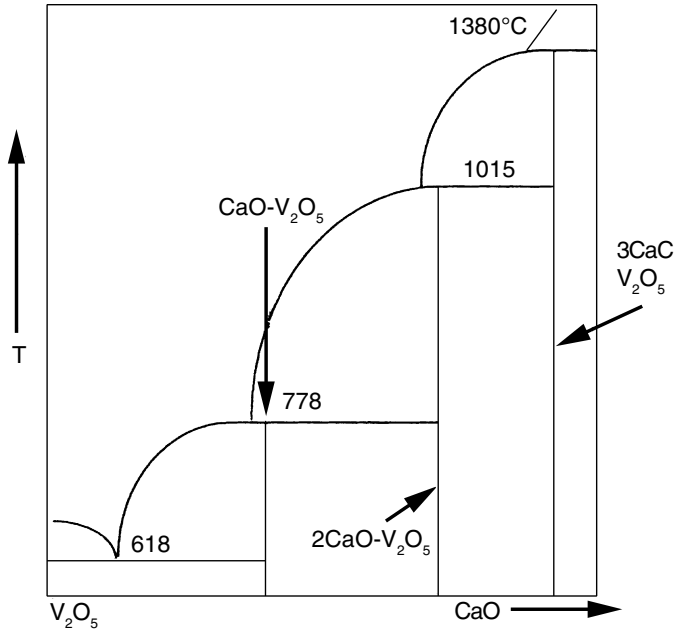

Fig. 7: $CaO\text{-}V_2O_5$ phase diagram. (adapted from Ref. 26.)

atmospheres showed the same x-ray spectra before and after O charging (except for lattice parameter changes). When we measured ohmic resistance (two-point contact) on the surfaces of heat-treated specimens at room temperature, the specimens charged with O in high-purity Ar or N_2 showed the same ohmic values before and after O charging.[*1] The blue oxide that formed in air at 400°C had a resistance of ≈5 Ω, not very high compared to values for most metal oxides. This oxide is not stable in liquid Li.

Chemical Vapor Deposition of CaO and Calcium Vanadate Films

Figure 7 is a phase diagram for the V-Ca-O system.[26] Figure 8 shows a schematic diagram of the CVD apparatus. For cleaning a Type 304 SS chamber was heated to 850°C within ≈1 hr. while purging with 99.999% argon and was then cooled.

Vanadium-alloy samples and a calcium source vessel were then placed near the bottom and top of the chamber, respectively. The calcium source at the top of the furnace remained at room temperature when the furnace was heated. The vanadium alloy specimens in these experiments were either charged with oxygen for 2-3 hrs. in argon that contained 5-10 ppm oxygen or oxidized in air to form vanadium oxide. Several specimens were retained to quantify oxygen uptake during the oxygen-charging step. Subsequently, the stainless steel chamber was evacuated with a vacuum pump, and the calcium reservoir was lowered into the hot zone of the furnace to evaporate calcium, which was deposited on and reacted with the oxygen-charged and oxidized vanadium alloy surfaces at 800-850°C for 1.5 - 4 hrs. The formation of several vanadates ($Ca\text{-}V_xO_y$) can be predicted from the CaO-vanadium oxide phase diagram.[26] These phase relationships are the basis for the formation of vanadate coatings on vanadium and its alloys. Calcium reacts with the precharged oxygen surface and diffuses through the CaO or $Ca\text{-}V_xO_y$ layer. Reactions for the formation of the coatings are

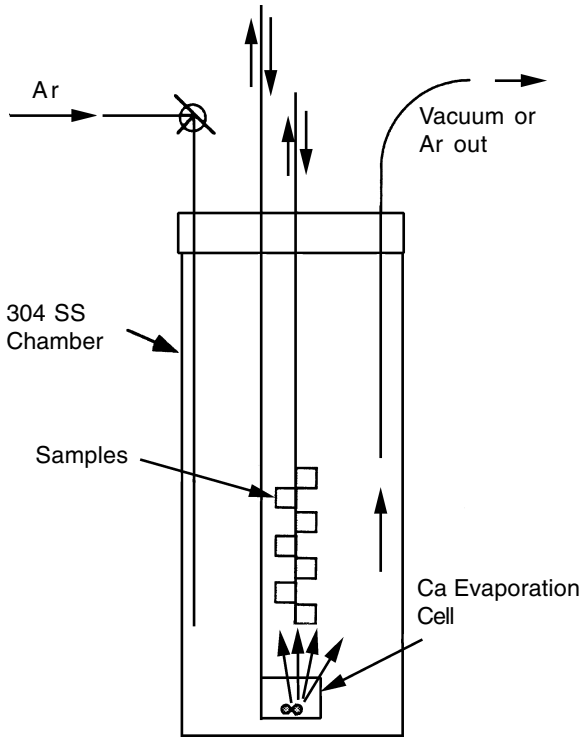

Fig. 8: Schematic diagram of CVD apparatus.

$$Ca_{(vapor)} + \underline{O}_{(alloy)} = CaO \quad (6)$$

and

$$Ca_{(vapor)} + V_xO_{y(alloy\ surface)} = CaV_xO_y \quad (7)$$

where $\underline{O}$ represents oxygen activity at the interface between the CaO and the oxygen-charged vanadium alloy. These reactions occur spontaneously, and the probable rate-determining step is ionic diffusion (Ca^{+2}) through the CaO layer. Figure 9 shows the results of x-ray diffraction analysis and of visual examination by SEM. We tried to obtain a good cross-sectional view of the microstructure, but this was difficult due to the reactive CaO with water during the polishing procedure. EDS analysis of the surface of a CaO coating formed on v-4% Cr-4% Ti at 850°C indicated >97 at.% calcium, and a 15-80 at calcium content in the calcium vanadate coatings. SEM of CVD coatings on V-4% Cr-4% Ti at 850°C revealed uniform surfaces with grain sizes of 0.7-3 μm for CaO and 3-8 μm for the calcium vanadate coatings. The x-ray diffraction spectrum of the CaO coating on V-4% Cr-4% Ti clearly showed the two sets of peaks for CaO and V-4% Cr-4% Ti and indicated no other phases. The x-ray beam can penetrate ≈40 μm into CaO, and when film thickness is ≈3 μm the spectrum of the V-4% Cr-4% Ti substrate is also present. Sublimation of calcium in a relatively low vacuum of 10^{-4} to10^{-5} torr, when oxygen was present as an impurity, enabled the formation of CaO clusters by oxidation of calcium vapor inside the chamber. After coating the V-4% Cr-4% Ti specimens at 800 or 850°C for electrical resistance measurements, we cooled the system to room temperature while purging with 99.999% argon. In one experiment the calcium reservoir was raised to the top of the furnace (cool region) and the specimens remained at temperature for 3-5 hrs. to determine if any additional oxidation occurred. No appreciable

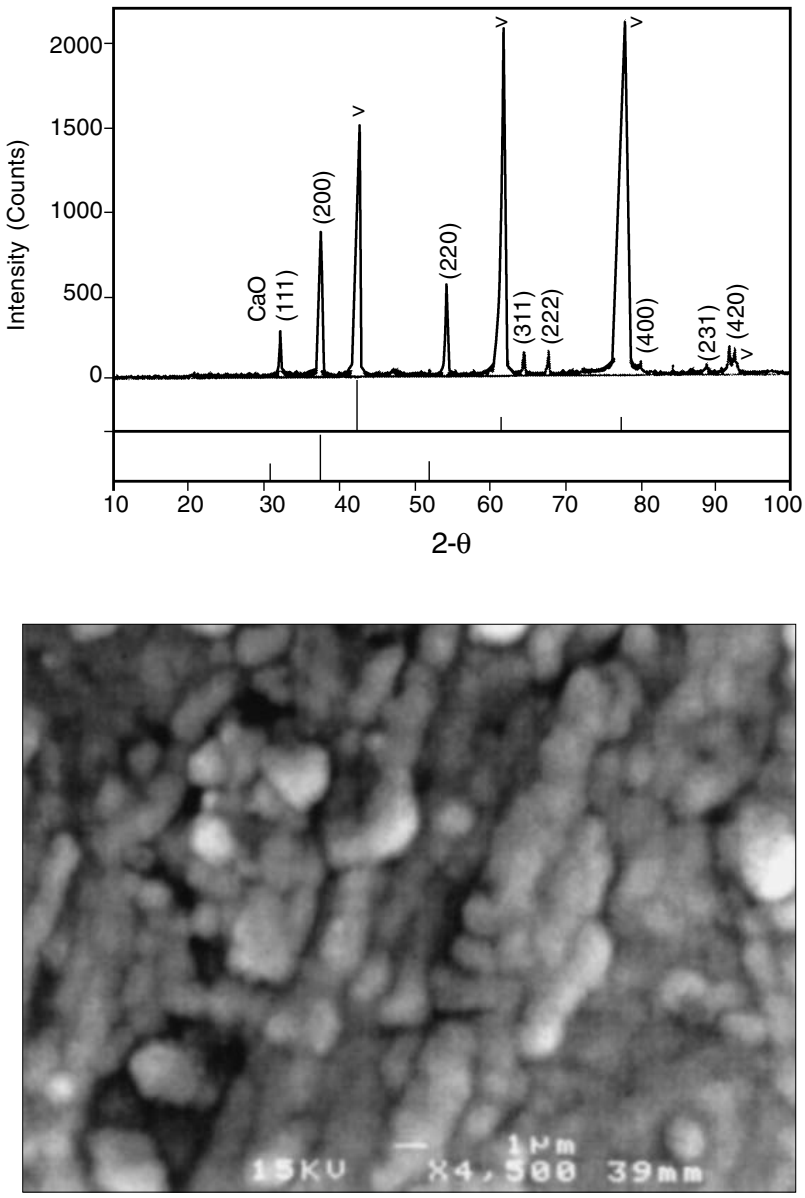

Fig. 9: Results for the X-ray diffraction analysis and visual examination done by SEM.

weight gain or loss was detected after CaO had been deposited. The weight gain for CaO coatings on V-4% Cr-4% Ti specimens at 230 min. (≈4 hrs) was determined over the range of 309-883°C and is given by

$$\log (\text{Wt. gain, g/cm}^2) = -0.983-2444/T\ (K) \quad (8)$$

which corresponds to coating thicknesses of ≈0.02 to 2.4 μm at 309-883°C for a CaO density of 3.346 g/cm^3.

To determine the electrical resistance of the coatings and facilitate SEM/EDS analysis, the samples were coated with gold by sputter-deposition of an array of ≈l-mm-diameter discs on the surface of the coatings (Figure 10). When placed in contact with gold foil, the disc provided a good electrical connection over a large area of the specimen. Ohmic resistance was measured at 25-500°C in air (Figure 11) Only the specimen charged with oxygen in

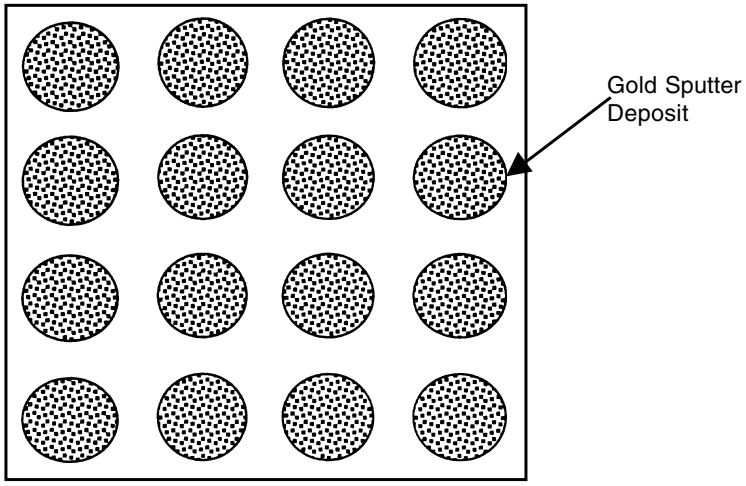

Fig. 10: Schematic diagram of gold sputter coating on a CaO coating for electrical resistivity measurements.

99.999% argon and coated with calcium by CVD exhibited insulator behavior. The specimens that were oxidized in air and in a 1% CO-CO_2 gas mixture and coated by CVD showed semiconductor behavior.[27-28] CaO coatings on V-4% Cr-4% Ti exhibited high ohmic insulator characteristics even when a small amount of vanadium existed in the CaO. However, the coating becomes conductive when the vanadium concentration reached >15 wt.%. Despite the highly resistive nature of CaO, when vanadium is incorporated in the material, a calcium vanadate phase that exhibits semiconductor behavior forms in local regions. To explore this hypothesis, CaO and Ca-V-O coatings were produced on vanadium-base alloys by chemical vapor deposition (CVD) and metallic-vapor processes to investigate their electrical behavior. In some cases, CaO-coated samples exposed in liquid lithium displayed semiconductor behavior, and we sought the reason for this phenomenon. To examine the electrical behavior of CaO-V_xO_y specimens, several calcium vanadates were synthesized by a self-reactive method. Calcium and vanadium pentoxide (V_2O_5) were mixed in various proportions (5-90 wt.% calcium) and allowed to react in vacuo by self-ignition in sealed capsules. An exothermic reaction occurred in ≈2 s. The synthesized samples were examined by scanning electron microscopy/electron-energy dispersive-spectroscopy (SEM/EDS), and electrical resistance was determined. All samples fabricated by these methods were conductive and the results were similar to those of lga and Nishihara,[27] except for single phase CaO, which showed high resistance.[28] The results summarized in Table 2 indicate that calcium vanadates do not provide sufficient electrical resistance for insulator coatings in MFR applications, Therefore, phase-pure CaO coatings are required for the MFR applications.

Environmental Aspects of CaO Coating

It is desirable to demonstrate the principles of both thermodynamic and kinetic behavior for the surface incorporation of the most common environmental reactive chemical species, i.e., CO_2 and H_2O, with the CaO.[29-30]

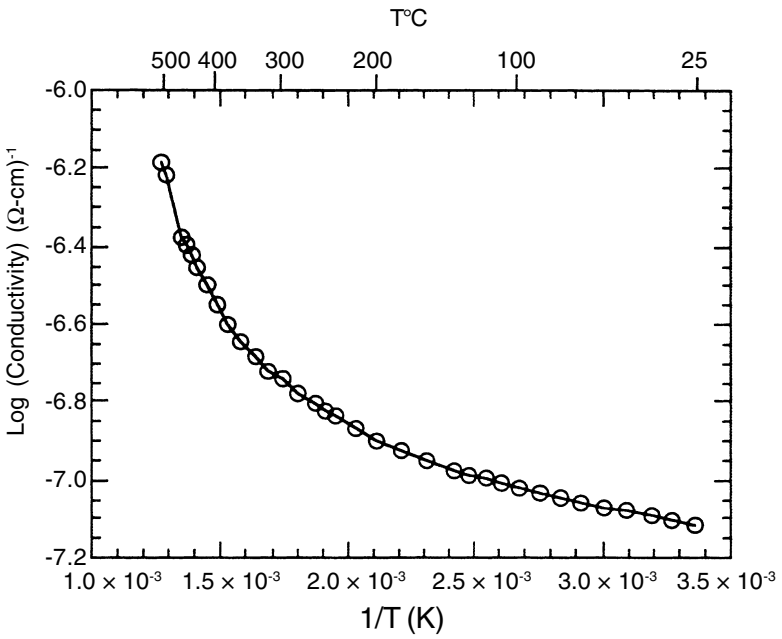

Fig. 11: Log conductivity vs. 1/T for CaO coating in air.

Table 2. Observation of Films Fabricated in this Study

Exam	CaO	Calcium Vanadates
Visual	Good, no spallation	Good, no spallation
EDS	>97 at.% Ca	15-80 at.% Ca
Grain size (μm)	Very fine, 0.7-3 μm	Coarse, 3-8 μm
X-ray diffraction[*2]	CaO	Calcium vanadates
Electrical property	Insulator	Semiconductors

[*2] X-ray beam penetrates ≈40 μm into CaO. Thus for film thickness of ≈3 μm, spectrum of V-4% Cr-4% Ti substrate is also present.

Thermodynamic Aspects

The Reactions of CaO in CO_2 and H_2O Environments are :

$$CaO + CO_2 = CaCO_3 \quad (9)$$

$$CaO + H_2O = Ca(OH)_2 \quad (10)$$

Under equilibrium conditions, the equilibrium partial pressures of CO_2 and water vapor are defined by the reactions

$$pCO_2 = \exp(\Delta G^\circ_{CaCO_3}/RT) \quad (11)$$

and

$$pH_2O = \exp(\Delta G^\circ_{Ca(OH)_2}/RT) \quad (12)$$

where $\Delta G^\circ_{CaCO_3}$ and $\Delta G^\circ_{Ca(OH)_2}$ are the standard Gibbs free energies of formation of the $CaCO_3$ and $Ca(OH)_2$, respectively, in Eqs. 9 and 10. From Eqs. 11 and 12, it appears that one should be able to deduce the conditions for caborization or hydration; however, a further reaction must be considered, namely

$$CaCO_3 + H_2O = Ca(OH)_2 + CO_2 \quad (13)$$

with equilibrium condition

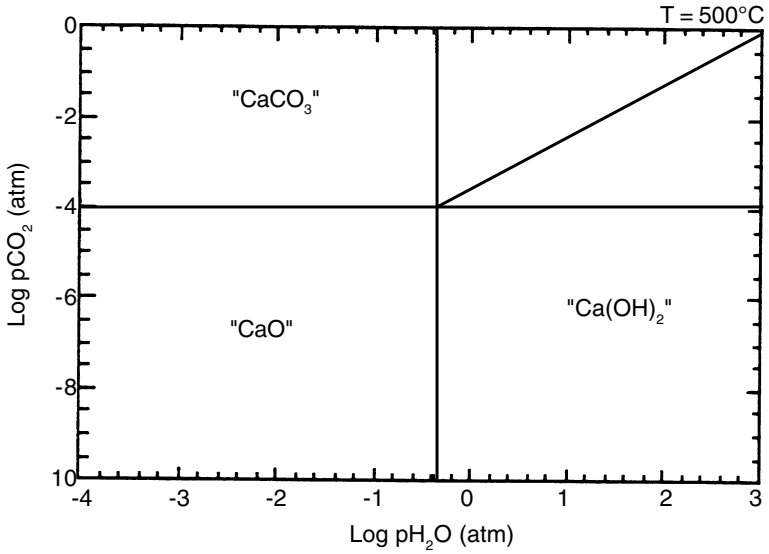

Fig. 12: Thermochemical diagram for H_2O-CO_2-CaO system at 500°C.

$$(pCO_2/pH_2O)_{eq} = \exp$$

$$[(\Delta G^\circ_{CaCO_3} - \Delta G^\circ_{Ca(OH)_2}/RT] \quad (14)$$

when the unity activity for the solid phases. Examination of Eqs. 11,12, and 14 permits the identification of various situations that the type of surface correction products can be formed, as follows:

- If both gas-phase pCO_2 and pH_2O are lower than those of the equilibrium partial pressures then CaO is stable; (notation: the equilibrium partial pressures of CO_2 and H_2O as $pCO_{2,eq}$ and pH_2O_{eq})
- If gas-phase pCO_2 < and gas-phase pH_2O > pH_2O_{eq}, then only $Ca(OH)_2$ is stable;
- If gas-phase $pCO_2 > pCO_{2,eq}$ and gas-phase $pH_2O < pH_2O_{eq}$, then only $CaCO_3$ is stable;
- If gas-phase $pCO_2 > pCO_{2,eq,}$ and gas-phase $pH_2O > pH_2O_{eq,}$ then both $Ca(OH)_2$ and $CaCO_3$ should be stable and will form surface products.

However, reference to Eq. 6 indicates that only one phase will form, depending on which of the following two conditions prevail:

(a) $(pCO_2/pH_2O)_{gas} > (pCO_2/pH_2O)_{eq}$

This condition will cause Reaction 13 to proceed to the left, and $CaCO_3$ will be stable where the $BaCeO_3$ is in contact with the gas phase

(b) $(pCO_2/pH_2O)gas < (pCO_2/pH_2O)_{eq,}$

This condition will cause Reaction 13 to proceed to the right, and $Ca(OH)_2$ will be stable where the CaO is in contact with, the gas phase. We can represent the possible reaction product as a function of gas chemistry in order to construct a thermochemical diagram that depicts the stability range of various condensed phases as functions of the thermodynamic activities of the two components of reactive gas such as CO_2 and H_2O in air, etc. Based on the above analysis, we can build the thermochemical diagram for CaO and $CaCO_3$ and $Ca(OH)_2$ at 500°C by using literature values as a function of pCO_2 and pH_2O (see Figure 12).

Kinetic Aspects

in Figure 12, one sees that proposed reactions 9, 10, and 13 will be applied to evaluate thermodynamic stability; however, this will be reconsidered when the kinetics are

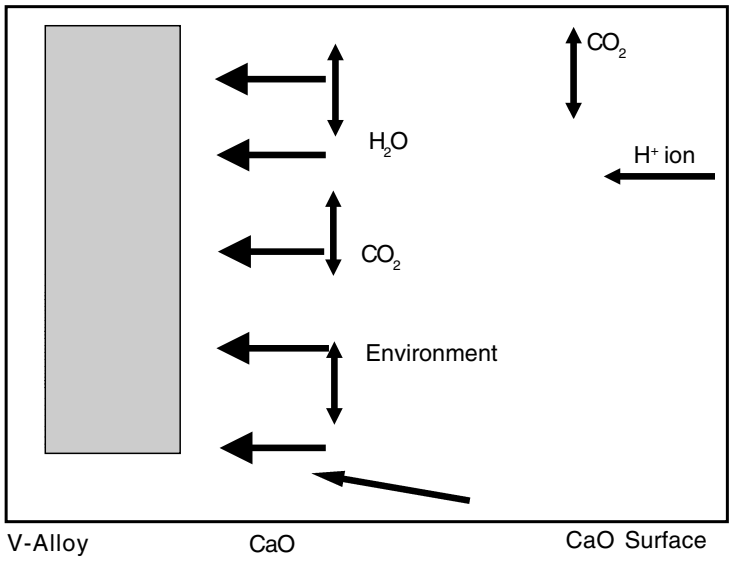

Fig. 13: CaO surface exposed to environment containing H_2O and CO_2.

hindered by the sluggish solid-state diffusion process, such as oxidation of metals (e.g., presence of very thin aluminum oxide scale on the aluminum). Figure 13 shows the CaO surface exposed to H_2O and CO_2 environments. Eventually. CO_2 reacts only at the surface to form a monolayer of CO_2, via chemical reaction and or chemical (d/de)sorption. The result of CO_2 incorporation at the CaO surface could be explained as $CaCO_3$ surface blocking by CO_2 at the surface for the continuous reaction. Ca ions should be extruded to the surface. However, Ca ion diffusivity in the CaO is expected to be extremely low, and therefore CO_2 mostly interacts only at the surface. However, protons from water will be diffused into the bulk CaO, depending on chemical potential gradient. (Ad/de)sorption phenomena has been analyzed recently for the proton conducting ceramic materials.[32]

Summary of Electrically Insulating Films

The requirements and development of electrical insulator coatings using thermal CVD coatings have been demonstrated. For electrical insulator coatings. their requirements and application have been focused on the magnetic core in power transformers, and on the design of liquid-metal-cooled MFRs

CaO and calcium vanadate films were prepared on vanadium alloys and Types 304 and 316 SS by chemical vapor deposition (CVD) and high-temperature metallic vapor deposition at 800-850°C. The films were examined by optical and scanning electron microscopy and by electron-energy-dispersive and x-ray diffraction analysis. We found that when the ratio of calcium to vanadium in the oxide coating was >0.9, the film was a good insulator, whereas when the ratio R < 0.8, the coating layer exhibited semiconductor or metallic-conduction behavior However, in some cases, when a CaO-coated sample was immersed in liquid lithium, semiconductor behavior was observed even though the calcium/vanadium ratio > 0.98 over a wide surface area. We attribute the semiconductor behavior to local regions that contained a conductive calcium vanadate phase in the CaO coating. The formation of either vanadate or titanate phases in thin (1-5 μm) coatings may not provide sufficient

electrical resistance for MFR applications and could present potential problems for liquid-metal compatibility. We have applied the oxygen charging and reactive CVD technique to other oxides e.g., MgO, (BeO), $MgAl_2O_4$, etc., to determine their suitability for insulator coatings in MFRs applications.

Acknowledgments

This work has been supported by the U.S. Department of Energy. Fusion and Fossil Energy and Basic Materials Program, under Contract W-31-109-Eng-38 Drs. K. Natesan, R. Mattas, C. Reed, and D.L. Smith (Argonne National Laboratory)and Wiffen (US Department of Energy) helped with discussions and collaboration throughout this work. L. Nowicki, D. Rink, B. Tani (ANL), and F. Deleglise (a visiting scientist from France) helped in the experimentals.

References

1. C.C. Baker, et al., *Tokamak Power System Studies FY 1985*, Argonne National Laboratory Report ANL/F, 1985, pp.85-2.
2. T. Kammash, *Fusion Reactor Physics*, Chapter 15, Ann Arbor Science Pub. Inc., Ann Arbor, MI, 1975, pp.405-439.
3. 15th Annual Magnetic Conference, Department of Electrical and Computer Eng., IIT, Chicago, 1996.
4. D.S. Loudermilk and R.A. Murphy, Overview of Technology of insulating Coatings for Grain-Oriented and Nonoriented Electrical Steels.[3]
5. M. Lessny, Coating Technology Update. [3]
6. Y.Y. Liu and D.L. Smith, *Ceramic Electrical Insulators for Liquid Metal Blankets*, *Journal of Nuclear Materials,* **38**, 1986, pp.131-133.
7. J.H. Park, T. Domenico, G. Dragel, and R.W. Clark, *Development of Electrical Insulator Coatings for Fusion Power Applications*, Fusion Engineering and Design, **27** ,1995, pp.682-695.
8. J.H. Park and W.D. Cho, *Fabrication of Intermetallic Coatings for Electrical Insulation and Corrosion Resistance on High Temperature Alloys*, Surface Modification Technologies IX, eds., T.S. Sudarshan, W. Reitz, and J.J. Stiglich, The Minerals, Metals and Materials Society, Warrendale PA, 1996, pp.151-166.
9. J.H. Park and T.F. Kassner, *CaO Insulator and Be Intermetallic Coatings on V-Base Alloys for Liquid Lithium Fusion Blanket Applications*, Presented for 16th IEEE/ NPSS Symposium on Fusion Engineering (SOFE '95), Champaign, Illinois, **5**, 1995.
10. J.H. Park and G. Dragel, *Development of Aluminide Coatings on Vanadium-Base Alloys in Liquid Lithium*, Fusion Reactor Materials Semiannual Progress Report for the Period Ending, DOE/ER-0313/13, 1993, pp.405-410.
11. K. Natesan, Development of Aluminide Insulator Coatings for Fusion Reactor Application, Argonne National Laboratory Report ANL/FPP/TM-278, ITER/US/95/ 1V-BL-03, 1995.
12. S. Malang and L. Buchler, MHD Pressure Drop in Ducts with Imperfectly Insulating Coatings. Argonne National Laboratory Report ANL/FPP/TM-269, 1994.
13. C.B. Reed, K. Natesan, T.Q. Hua, I.R. Kirillov, I.V. Vitkovski, and A. Anisimov, Experimental and Theoretical MHD Performance of a Round Pipe with a NaKcompatible $A1_2O_3$ Coating, *Proceedings of 3rd international Symposium on Fusion Nuclear Technology,* Los Angeles, 1994.
14. R.F. Mattas, B.A. Loomis, and D.L. Smith, Vanadium Alloys for Fusion Reactor Applications, JOM, **44**(8), 1992, 26 1992.
15. J.H. Park, Intermetallic and Electrical Insulator Coatings on High-Temperature Alloys in Liquid-Lithium Environments, in Elevated Temperature Coatings: Science and Technology I, eds. N.B. Dahotre. J.M. Hampikian, and J.J. Stiglich, The Minerals, Metals, and Materials. Section, 1995, pp.227-240.
16. J.H. Park, Intermetallic and Electrical Insulator Coatings on High-Temperature Alloys in Liquid Lithium: Materials and

Manufacturing Process **10**(5), 1995, pp.971-986.
17. J.H. Park, U.S. Patent#5769966.
18. R.E. Buxbaum, R. Subramanian, J.H. Park, and D L. Smith, Hydrogen Transport and Embrittlement for Palladium Coated Vanadium-Chromium-Titanium Alloys, *Journal of Nuclear Material,* Part A, **233-237**, 1996, pp.510-512.
19. J.H. Park, G.M. Dragel, R.A. Erck, D.L. Smith, and R.E. Buxbaum, Solubility of Hydrogen in V-4Cr-4Ti and Lithium, Fusion Reactor Materials Progress Report for the Period Ending 1995 (DOE/ER-0313/19), 1996, pp.59-62.
20. V. Kumar and Y.P. Gupta, *Cation Self-Diffusion in Single Crystal CaO*, *Journal of Physics Chemical Solid,* **30**, 1969, pp.677-685.
21. J.H. Park, D.S. Kuppermanl and E.T. Park, Mechanical Properties of and Phase Transformation in, V-Cr-Ti-O Solid Solutions; Proceedings of TMS Ann. Mtg., Anaheim, CA, 1996; in Elevated Temperature Coatings: Science and Technology II, eds. N.B. Dahotre and J.M. Hampikian, pp.323-332.
22. J.H. Park, D.S. Kupperman, E.T. Park, and G. Dragel, Physical Properties of O-and N-Containing V-Cr-Ti Alloys, Fusion Reactor Materials Progress Report for Period Ending Dec. 31, 1995 (DOE/ER-O313/19), 1996, pp.12-16.
23. J.H. Park and J. Gazda, Vanadium-Oxygen and Vanadium Nitrogen Solid Solutions, *Presented at 188th Electrochemical Sec. Mtg.,* Chicago, 1995.
24. $CaO\text{-}V_2O_5$ Phase Diagram, in Phase Diagrams for Ceramist, 1973.
25. J.H. Park, Electrically Insulating Films Deposited on V-4% Cr-4% Ti by Reactive CVD, presented at Chemical Vapor Deposition Session. *12th Surface Modification Technologies Conference,* held in Conjunction with Symp. of Matls Solutions at ASM International Conference, Chicago, 1998.
26. A.N. Morozov, Metallurg., **13**(12), 1938, p.24.
27. F. Iga and Y. Nishihara, *Metal-Insulator Transition with Oxygen Content in* $CaVO_{3-y}$, *Journal of Phyics Society,* Japan, **61**(6), 1992, pp.1867-1870.
28. J.H Park and W.D. Cho, Evaluating Electrically Insulating Films Deposited on V-4% Cr-4% Ti by Reactive CVD. Fusion Reactor Materials Semiannual Progress Report for the Period Ending 1996 (DOE/ER-0313/21), 1997, pp.52-56.
29. Gaskel, Introduction to Metallurgical Thermodynamics. 2nd Ed. McGraw-Hill, New York, 1981.
30. CRC Handbook of Chemistry and Physics, 71st Ed., 1991.
31. J.H. Park, B.C. Prorok, K.C. Goretta, U. Balachandran, and M.J. McNallan HighTemperature Internal Oxidation of Ag/12 at% Mg and Ag/0.25 at.% Mg-0.25 at.% Ni, Presentation for the Per Kofstad Memorial Symposium on High-Temperature Corrosion and Materials Chemistry at the at the Electrochemical Society Meeting, Honolulu, 1999.
32. J.H. Park, Surface and Interface Modification Science and Technology, 1999 World Korean Science and Engineers Symposium, Seoul, Korea, 1999.

Chemical Vapor Deposition
Jong-Hee Park, T.S. Sudarshan, editors, p421-433
DOI:10.1361/chvd2001p421

Chapter 13

CVD Films for Corrosion Protection Coatings

J. H. Park
Materials Scientist
Energy Technology Division
Argonne National Laboratory
Argonne, IL 60439

W. D. Cho
Professor Department of
Metallurgical Engineering
University of Utah
Salt Lake City, UT 84112

Abstract

The development of CVD films for high-temperature corrosion protection of ferrous alloy has focused on methods with and without addition of oxygen-active elements. CVD processes, which employ vapor-transport and heat treatment of a stabilized alloy substrate to deposit protection coatings, have performed extremely well. A very useful system of insulator/corrosion protection coatings, which can be used individually or together in energy-related industries, is described.

Corrosion resistance of structural iron-base alloys in high-temperature environments is typically achieved by formation of a continuous

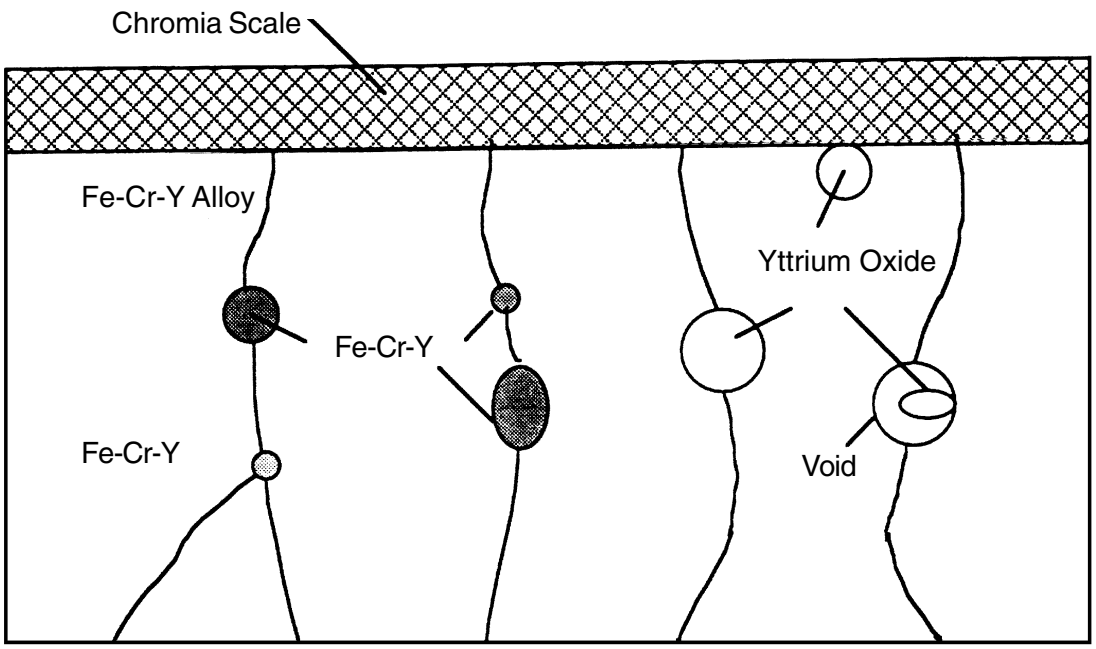

Fig. 1: Grain-growth inhibition by Fe-Cr-Y and Y_2O_3 segregated in alloy grain boundaries.

protective oxide scale such as chromium oxide or aluminum oxide, which acts as a diffusion barrier between the environment and the alloys.[1] Such coatings may cover the alloy surface only superficially and are subject to erosion or spallation under severe high-temperature conditions. Two fundamental goals that must be addressed in the development of more oxidation-resistant alloys are to (a) decrease the transport rate of metal ions and/or oxygen through the scale, and (b) improve scale adhesion to the alloy substrate.[2-5]

The use of "reactive elements" (e.g., yttrium, lanthanum, cerium) in alloys dates from the 1930s and influences the properties of both the scale and the alloy substrate during high temperature oxidation.[2] Alloys without oxygen-active elements exhibit outward caution migration during oxidation. However, when the reactive elements are present in the alloy, inward anion transport predominates during scale growth.[4] The reactive elements tend to inhibit grain growth, i.e., they stabilize the alloy substrate during high-temperature oxidation. Reactive elements in Fe-Cr alloys inhibit grain growth in the alloy and suppress Fe diffusion through the scale.[5,6] Oxidation rates decrease in the order Fe-25 Cr >> Fe-25 Cr-1 Ce > Fe-25 Cr-03Y. Transmission electron microscopy (TEM) and scanning electron microscopy (SEM) (done by King et al.[8]) confirmed the grain boundary segregation of the stable intermetallic phase of $Y_2(Fe,Cr)_{17}$[8-10] or Y_2O_3 for Fe-25Cr-(0.1-3)Y alloys and of Ce-Fe-Cr or CeO_2 for Fe-25Cr-(0.3-1)Ce as illustrated in the schematic drawing in Figure 1.

The objective of surface modification by CVD is to develop additional corrosion protection for high-temperature alloys (e.g., Fe-25Cr-0.3Y) beyond that achieved by reactive-element additions which will be effective for a long period. Because CVD is a high temperature process, the following topics must be discussed before we can develop successful high-temperature corrosion-protection coatings.[7]

Diffusion Approach

It has been generally reported that the addition of <1% of so-called reactive elements

to an alloy decreases the rate of scale growth and enhances scale adhesion. Grain-boundary transport could be the main contribution in high-temperature chromia forming oxidation. Therefore, measurements were made of bulk, dislocation, and grain-boundary diffusion of cations and anions in pure and Y-doped Cr_2O_3. There are mainly two volumes of collected references[3,11] which cover of the recent investigations on reactive elements[11-14] along with two volumes of overall views on the transport properties of the oxide materials[3,11] and high-temperature corrosion with a detailed description of the basic mechanisms.[10]

Chromia is thought to grow via outward diffusion of cations from the metal to the oxide/gas interface. When the scale formation proceeds by diffusion along short-circuit paths such as grain boundaries in the oxide layer, Eq. 1 describes the usual diffusion controlled oxidation kinetics:

$$x^2 = k_p t \quad (1)$$

where x is the oxide thickness, t is time, and k_p is the so-called parabolic rate constant. The expression for k_p must be modified to reflect the fact that grain-boundary diffusion is the dominant mechanism of mass transport in the scale.

This assumption could be applicable if, and only if, no open voids or micro cracks are present in the scale and there is perfect adhesion between the oxide scale and the alloy. However, real oxidation may not occur according to the assumption considered. Several research groups have demonstrated that bulk diffusion of cations as measured in chromia single crystals and polycrystals, is too slow to explain observed rates of oxidation in alloys that form a chromium oxide layer.[15-22] However, the calculated oxidation rate based on grain-boundary diffusivity is still 10 times too low to account for the measured oxidation rates (e.g., Cr, Cr-Y, Fe-25Cr, and Fe-25Cr-[Ce, or Y], etc., Ce, Y = 0.1-3 wt.%). This presumably tells us that other important mechanisms should be considered, e.g., a dynamic situation may increase the mass transport rate during chromia-forming oxidation. This question remains unresolved, but the cause could be surface diffusion near the wide-open grain boundaries generated. Vapor phase transport may occur near the interfaces of the alloy, with the scale based on a dynamic situation during high-temperature scale growth, and may be improperly compared to the chromia ceramic grain-boundary diffusion data with naturally forming grain-boundaries.

Our observation on grain-boundary data obtained with as-grown chromia scale in the chromium metal was identical with ceramic chromia, except that the as-grown scale showed small microcracks due to the sample-handling procedure. In alloys bearing reactive elements, inward diffusion of anions is the predominant process. In the case of Fe-Cr-Y alloys, no Fe diffused outward. However; when no Y was present in the alloys, Fe outward diffusion contributed to faster diffusion paths of FeO or Fe_3O_4 produced via fast channels in Cr_2O_3 scales.[23] This anion inward diffusion during oxidation of commercially developed alloys is a more advanced concept for the surface modification of high-temperature alloys. The direction of diffusion (either anion inward or cation outward), which defines the oxidation process, is very important for the development of any surface modification process, including high-temperature CVD.

Background Considerations for Alloy Substrates

The following basic alloy microstructures and impurities on the reacting surfaces art considered, i.e. (a) bulk (point defect-zero degree defect including impurities), (b) grain-boundaries (2-D defect), (c) dislocations (1-D defect), and (d) open microvoids during fabrication of the alloy

Bulk Conditions

Here, bulk means that only intrinsic defects are present for the pure substance or, in the case of impure substances, only point defects are formed due to impurity doping in a homogeneous solution.

Therefore, the related defect concentration depends on the impurity level and or temperature. When we consider the thermodynamics for the formation of point defects, vacancies are important, i.e., $N_v = N_v(T)$. Simultaneously, we could consider the mobility of defects as $B_v = B_v(T)$. In these expressions, N_v is defect concentration, B_v is the mobility of a point defect, and T is temperature. Interstitials are important defect species that are predominant in impurity doping. When the reacting species arrive on the surface at high temperatures, they will be bound on the surface or diffused into the substrate, depending mainly upon the temperature and concentration of the reacting species and time. In general, at higher temperatures, this process will accelerate as normally experienced in a thermally activated process. However, when the initial nucleation process is finished, an incubation period is expected until the free surfaces are covered by the reaction product. After this period, a different phenomenological process is expected due to diffusion through the reaction product.

In the high-temperature process, several possible diffusion schemes are considered for continuous scale formations namely:

(a). Alloy elements diffusing out through the formed scale.
(b). Reacting species diffusing in.
(c). Both (a) and (b) take place.

However, the processes are mainly controlled by the microstructures on the alloy substrate including such features as dislocations, grain boundaries, and open voids in the alloy substrates.

Grain Boundaries (2-D defects)

(a). Grain-growth and inhibition of Grain-Growth:
r = r (T, impurities)
where r = grain diameter.
(b). Impurities: Impurity segregation tendency in the alloy grain boundary, surface, and alloy/scale interface.
(i). Beneficial (strengthening agent) impurities
(ii). Weakening impurities
(c). Effective grain-growth inhibition: benefit from scale spallation.

Here, grain boundary transport behavior is not a concern in the alloy. Grain-boundary diffusion is high but the grain-boundary contribution is limited based on grain size. Larger grains contribute less, but smaller grains contribute more. We must consider the metal/scale interface as containing wide grain boundaries that move perpendicular to the substrate and provide a fast transport channel and thus does not depend on impurity segregation on the metal/alloy interface. However, this interface is very important, because dislocations in the alloy always connect directly with the scale. Therefore, proper treatment of this interface boundary is necessary to describe the relationship between alloy dislocations and the metal/scale interface. The primary question is "How can we coat the alloy dislocations," or, "How can we introduce beneficial impurities in the alloy dislocations?"

Dislocations (1-D defect)

Dislocations may be mobile or fixed and their densities depend on temperature and impurity concentration. They are typically directly related to mechanical behavior of an alloy. They also influence scale-growing mechanisms. When the alloy dislocations are moving around during scale growth, we can expect the formation of irregular interfaces, including open interface structures. The initial stage of scale growth starts from a nucleation-like process on the alloy surface. In general, the numbers of nuclear oxide particles along the metallic grain boundary and in grains are quite different during initial oxidation. In the grain boundary, $\approx = 1$ μm oxide particles are arrayed along the boundary, while other metal oxide particles in the grains are well separated from each other. This tells us that the transport through dislocations in the alloy is most crucial for continuous growth of scales on the alloy substrate. We could say that the grain boundary contains concentrated dislocations, and these dislocations could be the extra half plane that is strongly dependent on temperature. Therefore, when we consider passivation layer formation, i.e., an inert coating, blocking of the dislocation

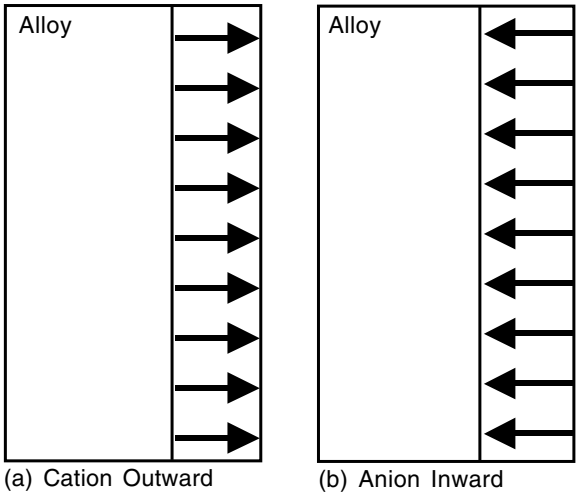

Fig. 2: Schematic view of two different diffusion processes during oxidation of alloys.

channels is the main concern. When we count the metal oxide particles on the alloy surface in the initial stage of oxidation, we could calculate the active dislocation numbers on each grain; these numbers depend principally on the orientation of individual grains Some metallic grains have more oxide particles and some have fewer oxide particles, and this is related to the number of active dislocations in the grain.

When we consider continuous scale growth, we can expect that the mobile species from the metal (cations diffusing out) will be supplied by alloy grain-boundaries, bulk defects, and dislocations. These diffusivities are quite different from each other: D(bulk) << D(dislocation) < D(grain boundary) < D(surface). Therefore, we expect the formation of voids around the alloy grain boundaries and dislocations as the scale continues to grow. The chief concerns, here, is "How can we prepare an inert state (kinetically and thermodynamically) for the point defects, for the grain boundaries, and especially for the dislocations in the alloy substrate?"

Scale Adhesion

Figure 2 shows schematic representations of two different diffusion processes by which we can predict the trend for scale adherence. When reactive elements are present in an alloy, scale adhesion is generally good. The main considerations are (a) stability of alloy substrates during high-temperature oxidation and anion inward diffusion and (b) oxide formation at the scale/alloy interface as shown in Figure 2. Some reactive elements (e.g., Y) provide both conditions satisfactorily, according to oxidation tests of Fe-Cr alloys with and without Y. The alloy containing Y showed good scale adhesion, but that without Y showed total spallation or poor bonding at metal/scale interfaces. The mast favorable behavior for Y was substrate stabilization during oxidation.[6] Figure 3 shows alloy grain-growth trends during oxidation of Fe-Cr alloys with and without reactive element additions. The trend is similar during annealing of the alloy (Figure 4).

According to the grain-growth behavior of the various Fe-Cr alloys without oxidation, Y alloying (0.1-3 wt.%) provided the most stable alloy substrate, as shown in Figure 3. and 4. In Ce-bearing alloys (0.3-1 wt.%). most Ce migrated to the specimen surface, and alloy grains became enlarged during annealing. However, preheated samples of Fe-25 Cr did not show spallation. This could indicate that the stabilized grain samples showed a higher

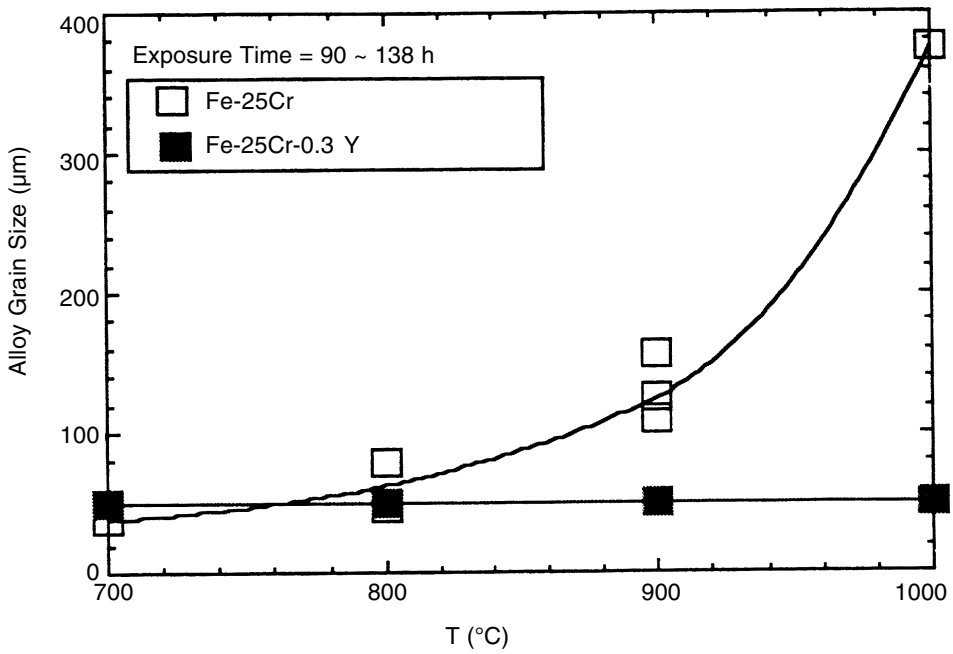

Fig. 3: Grain-size variation in Fe-25 Cr and Fe-25 Cr-0.3 Y alloys during oxidation at 700 to 1000°C.

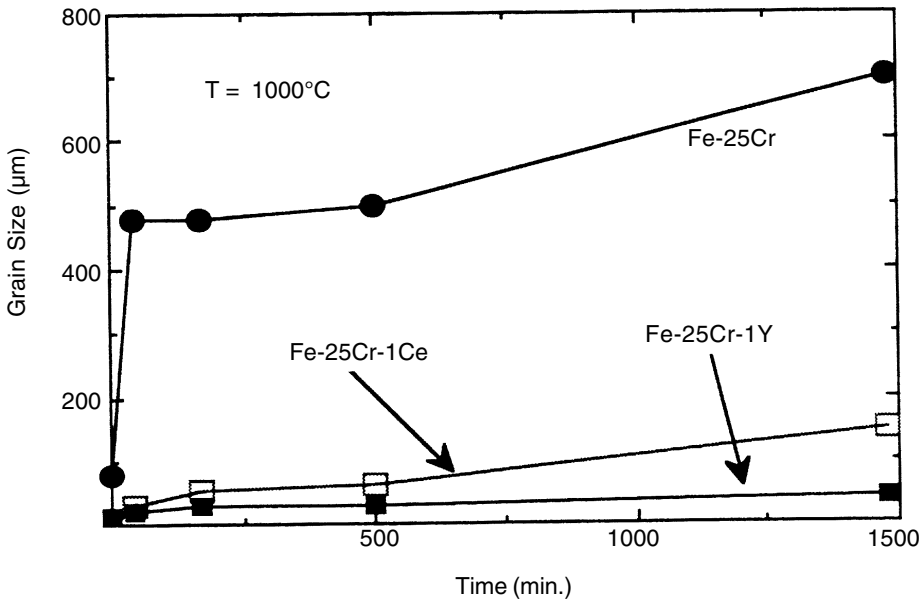

Fig. 4: Grain-size variation in Fe-25Cr, Fe-25Cr-1Ce, and Fe-25Cr-1Y alloys as a function of annealing time.

degree of adhesion. On the other hand, longer oxidation times showed outward Fe diffusion, which caused the oxidation process to be more rapid than that of pure chromia forming oxidation.[6]

Surface Modification by High Temperature CVD

Nucleation Sites/Adsorbed Layers

The nature of the nucleation sites has always been of great interest. Many investigators have proposed that nucleation is favored at sites of higher energy, i.e., at defects such as dislocations, grain boundaries, impurities, etc. Others have concluded that homogeneous nucleation takes place in the adsorbed layer. It appears that the particular mechanism that predominates is dependent on the metal and the pretreatment of its surface, the temperature, and the oxygen pressure (e.g., the degree of super saturation in the adsorbed layer). Oudar[23-24] has proposed that at weak supersaturation and relatively high temperatures, defects in the adsorbed layer may anneal out, and only defects in the metal surface remain in appreciable numbers. Thus, for high degrees of supersaturation, the number of nuclei can greatly exceed the number of dislocations. Under these conditions, homogeneous nucleation is likely to predominate. Such a mechanism would also qualitatively explain the strong influence of oxygen pressure on the density of oxide nuclei at relatively high temperatures. When the oxide nuclei have grown laterally to form a continuous oxide film on the surface, the reaction mechanism changes completely.

Initial Oxidation

When we investigated the initial oxidation of metals in a reduced oxygen environment (e.g.. vacuum with oxygen pressures 10^{-4} to 10^{-3} torr), oxygen reacted to form small oxide islands (typically measuring a few micrometers in size)[25] These small oxides are well arrayed along the metal grain boundaries and are randomly distributed in the bulk, as shown in Figure 5. Grain boundaries could be a two-dimensional point defect array due to mismatching neighboring grains. In a two-dimensional view, this shows as a line defect on the surface. Most impurities are easily segregated in the grain boundaries. Therefore, when the oxidation starts, these point defects are more reactive than the perfect atomic lattice. As a result, more oxide particles are formed in the metallic grain-boundaries than in the bulk however, in the bulk, some the residue dislocation tips will be reacted. Those observations can be extended toward the practice of surface modification of high temperature metallic alloys by CVD. Oxygen can be replaced by other vapors that could be reactive with the metal to form useful coatings for the surface modification. This is explained in the next subsection.

CVD for Corrosion Protection Coatings

A surface modification can be defined on the basis of the above fundamental information, i.e., it slows the scale-forming process and improves adhesion at the interface between alloy substrate and scale. To improve the protective scale, we must slow the diffusion of either cations or anions through the film to the modified alloy surface. Most probably, thermodynamically stable oxides, such as $A1_2O_3$, Cr_2O_3, and SiO_2 can be selected for a new surface modification. These oxides also have low diffusivity of either cations (metal ions) or anions (i.e., oxygen or sulfur ions) and will provide an excellent diffusion barrier. However, when the elements are added to the base metal alloys to control spontaneous film-growing of such protective oxides, critical levels must be achieved that then greatly alter the mechanical properties. Rapp and collaborators[26-31] have tried extensive studies with high-temperature pack cementation to developed corrosion protection coatings. Such coatings on high-temperature alloys could be produced by CVD with a vapor source, followed by annealing to diffuse the

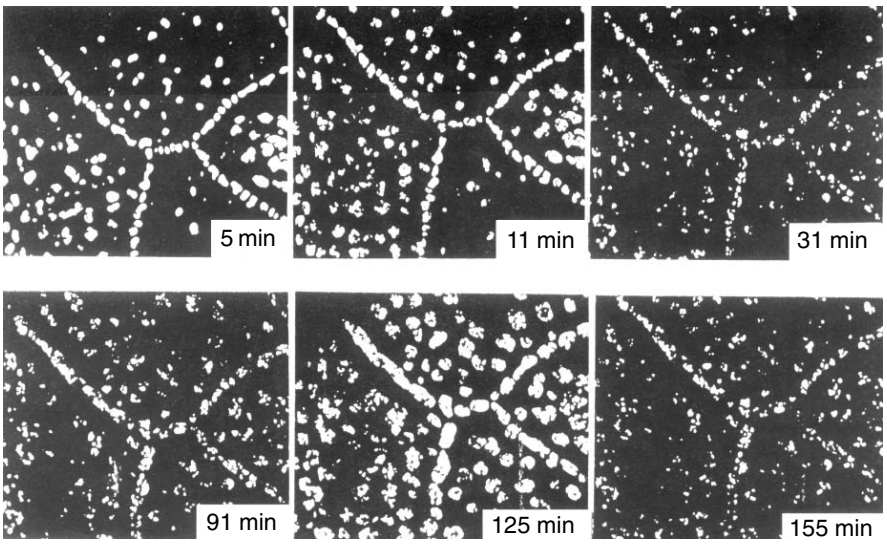

Fig. 5: In-situ TEM view for initial oxidation of Fe-25 Cr-20 Ni (T = 650°C, $pO_2 = 10^{-3}$ torr) with time. Small oxides are arrayed along metal grain boundaries and randomly distributed within the grains.

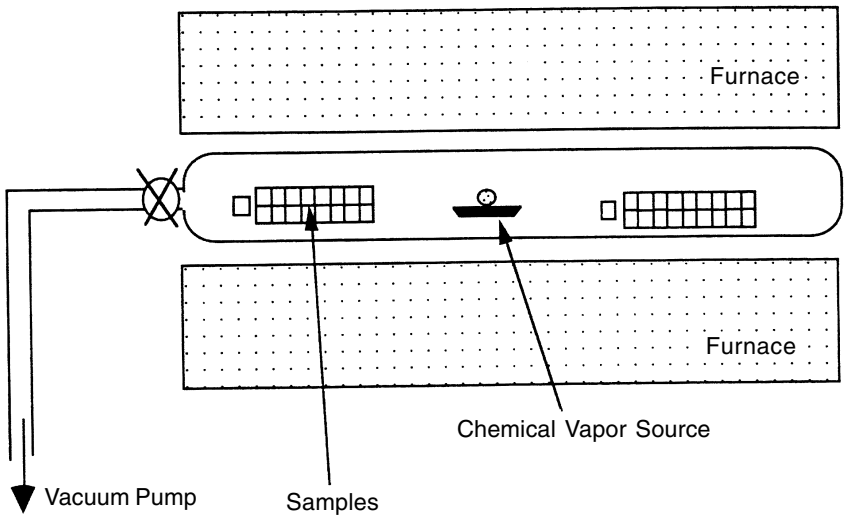

Fig. 6: Schematic view of CVD apparatus used in coating development.

vapor into the bulk alloy and then exposure to reactant vapor to form a stable phase by chemical reaction at the surface.[32] Figure 6 is a schematic view of the CVD apparatus used in coating development for this study. A powder mixture of NaF-Si-SiO_2 is a source of silicon vapor when it is heated. Figure 7 shows sample weight gain vs. position as measured from the vapor source after CVD coating for Fe-25 Cr-0.3Y and Fe-25 Cr-0.3Ce, respectively with

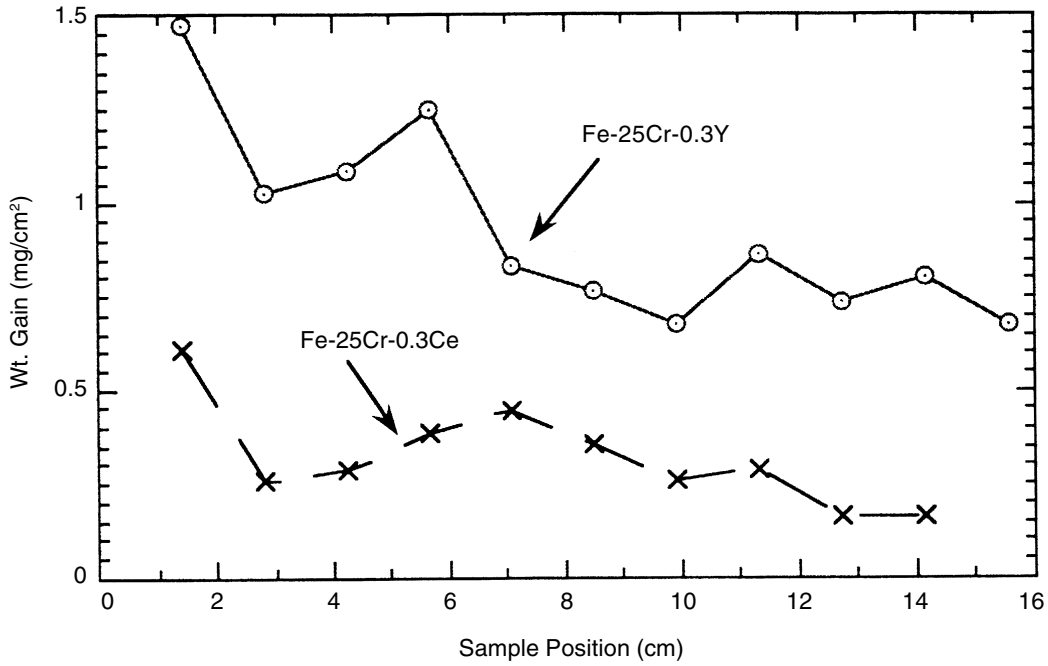

Fig. 7: Sample weight gain vs. position as measured from vapor source after CVD coating for Fe-25 Cr-0.3Y and Fe-25 Cr-0.3Ce.

investigations by SEM/EDS of the surfaces and SEM and TEM views with silicon map in the near grain boundary, it was seen that the silicon had diffused and reacted near the surface of the Fe-25Cr-0.3Y alloy. Silicon diffused into and around surface defects, figures, and microcracks that are normally the chemically active sites where corrosion begins on the alloy surface.

Oxidation/Sulfidation of Surface Modified Samples

To compare the corrosion behavior of coated and uncoated samples, several oxidation/sulfidation tests were performed at 700 to 1000°C in a thermogravimetric microbalance. Test results for oxidation of various samples in flowing air and sulfidation in 498-ppm H_2S/H_2 gas mixture for one month are shown in Figure 8.

Based on the above results from fundamental observations. A surface coating has been developed to provide additional corrosion protection beyond that achieved by reactive element additions to these alloys. An effective surface modification process was produced by CVD and subsequent chemical reaction in a controlled environment. The role of such protective surface modification is to protect the various microscopic surface sites (e.g., defects, fissures, microcracks) in the alloy surface that are chemically active locations for initial attack when the alloy is exposed to corrosive gases or oxygen at high temperatures. After sulfidation in 498-ppm H_2S/H_2 at 700°C for 55 days, and oxidation in air at 1000°C, the rate of weight change of the surface-modified alloy was much lower than that of uncoated alloys and of pure Cr. Surface modification by a CVD process improves the protection of alloys that are exposed to corrosive gases and/or oxygen at high temperatures. Without the benefit of an effective and long-lasting protective coating, the alloys are attacked initially at microscopic surface defects, fissures, and microcracks that are chemically active sites, Silicon addition to the surface of the alloy and subsequent heat treatment in a nitrogen-containing atmosphere

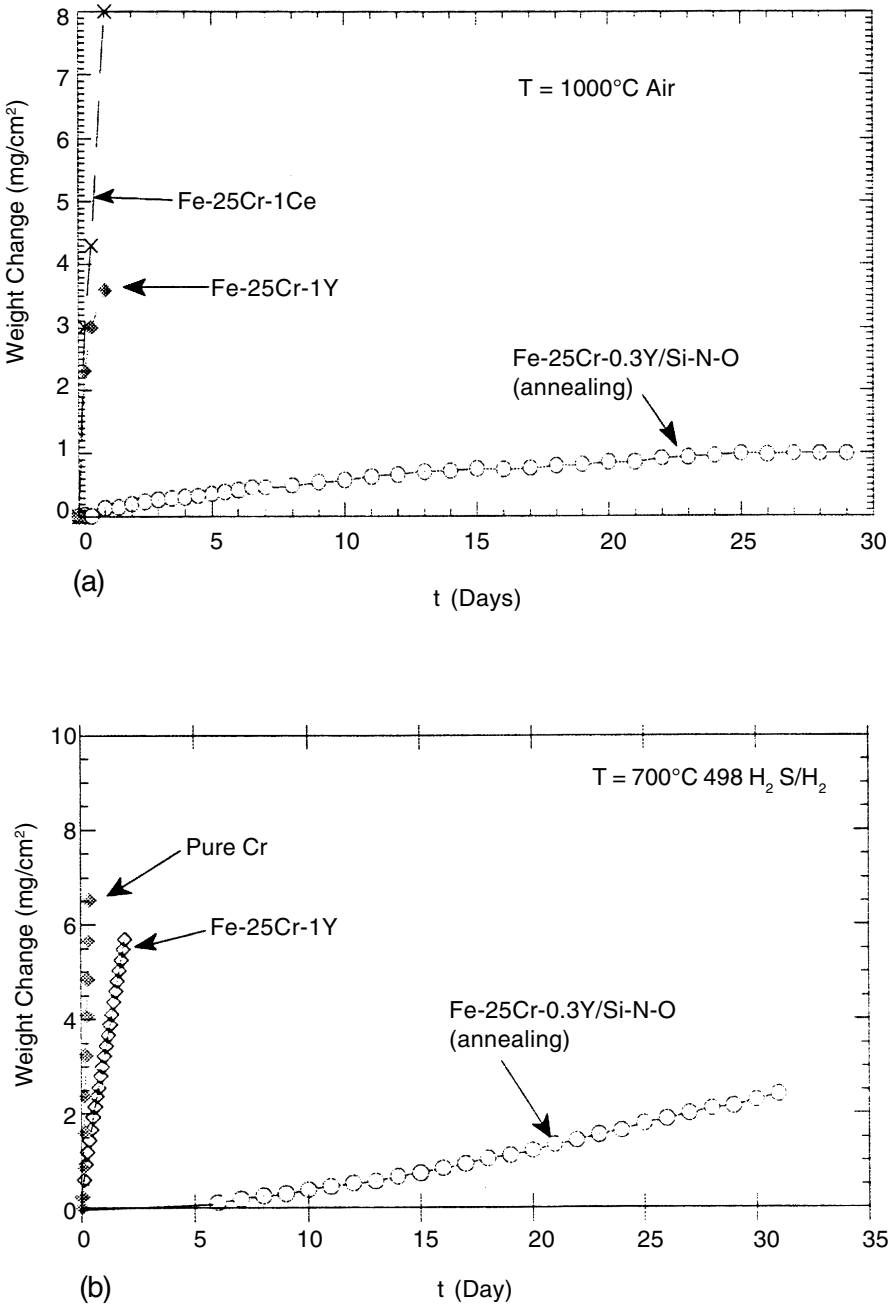

Fig. 8: Thermogravimetric results for (a) oxidation and (b) sulfidation, of various samples.

converts the silicon to an amorphous material that also contains oxygen and nitrogen. Without this heat treatment, the silicon itself is subject to attack by corrosive gases. It appears that the silicon blocks the various microscopic surface sites from attack by the corrosive environment. The choice of protective material can be made on the basis of the alloy to be protected and the specific environmental conditions. Figure 9 shows the SEM view for the cross section and

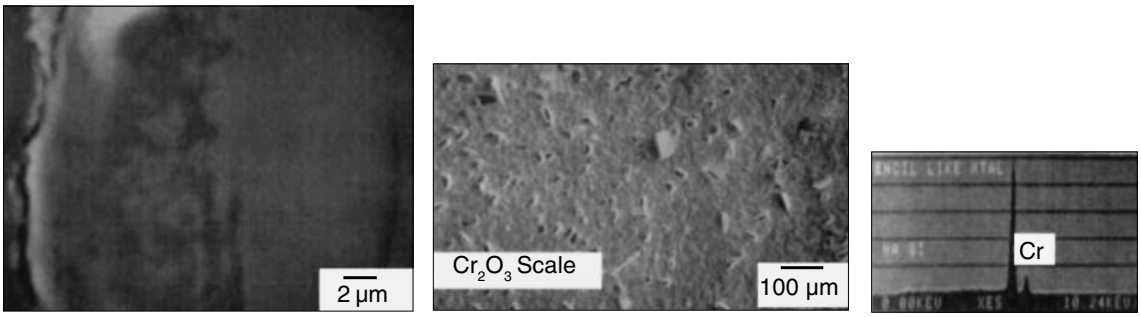

Fig. 9: SEM view of cross section and oxide surface as oxidized in air at 1000°C for 55 days, described in Figure 10(a) in chapter 12.

oxide surface as oxidized in air at 1000°C for 55 days and illustrated in Figure 8(a). Planar shaped chromia crystals are perpendicular to the surface. These crystals might grow by a surface diffusion process via wide-open grain boundaries or triple points on the grown protective layer. In the corundum structure, (ab)-plane diffusion is faster than the vertical c-direction. Therefore, these planar crystals are oriented in the direction of the (a,b)-plane. Similarly, Sem and x-ray element mapping for Cr, Fe, S, and Si sulfidation in 498-ppm H_2S/H_2 at 700°C for 55 days. We saw the oxide scale in the air oxidation. According to the results of X-ray studies, the weight gain in Figure 8(b) is due mostly to the Cr-S that forms via outward Cr diffusion during sulfidation.

This CVD process can be beneficial because it is technologically simple and relatively inexpensive. The silicon coating is extremely thin (1-2 µm) and penetrates the smallest defects, cracks, etc., on the alloy to be protected. Bonding of the protective coating to the surface occurs chemically in the same way that the corrosive gases would react, starting with the surface defects that are the active sites. Treatment with nitrogen-containing atmosphere then renders the silicon coating essentially inert to attack from corrosive environments. By comparison, low-temperature coatings may cover the surface only superficially and are thus subject to erosion or spallation under severe high-temperature conditions. The present method is beneficial for the fabrication of heat-resistant alloys.

Summary of Corrosion Protection Coatings

A durable protective coating for high-temperature alloys can be achieved by CVD. Normally, we must consider alloy stabilization in addition to chemical reaction in a controlled environment. The results define the nature of coatings for high-temperature corrosion protection, namely, a thin (1-2 µm) diffused silicon layer that covers the surface and penetrates even the smallest defects, cracks, etc., on the alloy to be protected. This surface modification treatment by CVD can be adapted to other alloys and is technologically simple and relatively inexpensive.

Acknowledgments

This work has been supported by the U.S. Department of Energy, Fusion and Fossil Energy, and Basic Materials Program, under Contract W-31-109-Eng-38. Drs. K. Natesan, R. Mattas, C. Reed, and D. L. Smith (Argonne National Laboratory), and W. Wiffen (US Department of Energy), helped with discussions and collaboration throughout this work. L. Nowicki, D. Pink. B. Tani (ANL), and F. Deleglise (a visiting scientist from France) helped in the experimental.

References

1. P. Kofstad, High Temperature Corrosion, *Elsevier Applied Science,* England, Essex, 1988; Nonstoichiometry, Diffusion and Electrical Conductivity in Binary Metal Oxides, Wiley Interscience, New York, 1972.
2. L. B. Pfeil, Improvements in Heat Resistant Alloys, British Patent No. 459, 1937, p.848.
3. W. E. King, ed., The Reactive Element Effect on High Temperature Oxidation After Fifty Years, *Materials Science Forum,* MRS, 1991.
4. C. Cotell, K. Przybylski, and G. J. Yurek, *Proceedings of Symposium on Fundamental Aspects of High Temperature Corrosion-II,* D. A. Shores and G. J. Yurek, eds., Boston, The Electrochemical Society, Inc., Pennington, NJ, 1986, p.103.
5. J. H. Park, Role of Yttrium in Enhanced Adhesion of Chromia Scale to Chromium, Materials Letter, **8**(10), 1989, pp.405-408.
6. J.H. Park and K. Natesan, Argonne National Laboratory Report, ANL/FE-92/1, 1992.
7. J.H. Park, U.S. Patent#5421913.
8. W. E. King, N. L. Peterson, and J. F. Reddy, *Journal of Physique,* **46**, 1985, pp.C4-423.
9. F. A. Shunk, Constitution of Binary Alloys, Second Supplement, McGraw-Hill, New York, 1969.
10. M. Hansen, Constitution of Binary Alloys, McGraw-Hill, New York, 1958.
11. M. A. Dayananda, S. J. Rothman, and W E. King, eds, Oxidation of Metals and Associated Mass Transport, *Proceedings of Symposium Metallurgical Society, AIME and MSD-ASM Atomic Transport Activity,* TMS-AIME Fall Meeting, Orlando, FL, 1986.
12. K. Przybyiski, A. J. Garratt-Reed, and G. J. Yurek, *Journal of American Ceramics Society,* **69**, 1986, p.C-264.
13. K. Przybylski, A. J. Garratt-Reed, and G. J. Yurek, Grain-boundary Segregation of Yttrium in Chromia Scale, *Journal of Electrochemical Section,* **135**, 1988, p.509.
14. K. Przybylski and G. J. Yurek, The Influence of Implanted Yttrium on the Mechanisms of Chromia Scales, *Material Science Forum,* **43**, 1989, p.1.
15. J. H. Park, W. E. King, and S. J. Rothman, Cation Grain-boundary Diffusion in Cr_2O_3 and Cr_2O_3 doped with Y_2O_3, *Journal of American Ceramics Society,* **70**, 1987, p.880.
16. W. E. King, J. H. Park, J. L. Routbort, and K. C. Goretta, Effect of Y_2O_3 Additions on the Plasticity of Sintered Cr_2O_3, Oxide Metals, **29**, 1988, pp.217-223.
17. W. E. King and J. H. Park, Effect of Gamma on Cation and Anion Grain Boundary Diffusion in Chromia, Collogue De Physique C1, **51**, 1990, pp.C1-551 to C1-556.
18. J. H. Park and K. Natesan, Electronic Transport in Thermally Grown Cr_2O_3, Metal Oxide, **33**(1/2), 1990, pp.31-54.
19. A. Dominguez - Ródriguez, A. R. DeAreilano - Lopez, K. C. Goretta, W. E. King ,J. H. Park, and J. L. Routbort, Creep of Cr_2O_3 and Yttrium Doped Cr_2O_3, *Material Science Technology,* **5**, 1989, pp.499-501.
20. J. H. Park and K. Natesan, Transport Properties and Oxidation in Chromium and Fe-Cr Alloys Exposed to Oxygen at High Temperatures, Presented at *1st International Conference on Materials,* Lake Geneva, WI, 1991.
21. A. Dominguez-Rodriguez, K. C. Goretta, W. E. King, J. H. Park, and J. L. Routbort, Creep of Chromia and Yttria-doped Chromia, *Material Science Technology,* **5**, 1989, pp. 499-501.
22. W. E. King and J. H. Park, Anion Grain Boundary Diffusion in Cr_2O_3 and $Cr_2O_3$0.09 Weight Percent Y_2O_3. *Proceedings of Materials Research Section,* **122**, 1989, pp.193-198.
23. J. Ouadar, Physics and Chemistry of Surface, Blackie, Glasgow/London, 1975.
24. J. Ouadar, in High Temperature Corrosion, R. A. Rapp., Ed., NACE, Houston, 1983, p.8.
25. K. Natesan and J. H. Park, Role of Alloying Additions in the Early Stage of Oxidation

of Fe-Base Alloys, presented at *Symposium on Corrosion and Panticle Erosion at High Temperatures,* IMS-AIME Annual Mtg., Las Vegas, 1989; Abstract in 118th TMS Annual Mtg & Joint TMS/SME Exhibit Technical Program, 1989, p.5.

26. S. C. Kung and R. A. Rapp, *Journal of Electrochemical Society,* **135**, 1988, p.731.
27. S. C. Kung and R. A. Rapp, Oxide Metal, **32**, 1989, p.1571.
28. S. C. Kung and R. A. Rapp, Oxide Metal, **34**, 1989, p.217.
29. F. D. Fredrick and R. A. Rapp, Oxide Metal, **40**, 1993, p.213.
30. R. Bianco and R. A. Rapp, *Journal of Electrochemical Society,* l40, 1993, p.1181.
31. R. Bianco, R. A. Rapp, and J. L. Smialek, *Journal of Electrochemical Society,* **l40**, 1993, p.1191.
32. J. H. Park and W. D. Cho, Surface Modification of High Temperature Alloys: A Protective and Adhesive Scale-Forming Process, Presented at *4th international Symposium on Processing and Fabrication of Advanced Materials IV,* Cleveland, Processing and Fabrication of Advanced Materials IV, eds. T. S. Srivatsan and J. J. Moore, 1995, pp.287-304.

Chemical Vapor Deposition
Jong-Hee Park, T.S. Sudarshan, editors, p435-463
DOI:10.1361/chvd2001p435

Chapter 14

Heat Treatment of CVD-Coated Tool Steels

O.H. Kessler
Stiftung Institut für Werkstofftechnik
Badgasteiner Str. 3
28359 Bremen
Germany

Abstract

This chapter deals with the post heat treatment of CVD (e.g. TiN) coated forming tools. Forming tools often need the advantages of CVD coatings compared to PVD coatings, such as normally better adherence, all-round coating and simpler equipment. CVD coated forming tools are very important for many fields of metalworking, e.g. forming of sheet metal, and are used on a large scale. For good performance of CVD coated forming tools, as for almost every coated component or tool, not only good coating properties, but also good substrate properties are necessary. This means for most CVD coated steel tools, that they must be subsequently quench hardened and tempered to restore high substrate strength which has been lost due to high coating temperature and the slow cooling rate. Different heat treatment paths with different complexities are discussed. Best substrate/coating properties and smallest distortion can be achieved by the most complex heat treatment path in the order quench hardening, tempering, CVD, quench hardening, tempering. At the various treatment steps several parameters, specific for CVD coated tools, must be taken into account (protective atmospheres, equalizing steps, etc.). The chemical composition, microstructure and hardness of CVD TiN coatings are usually not significantly influenced by subsequent quench hardening of the tools. Coating residual stresses can strongly be influenced depending on substrate volume

changes. Coating adhesion is usually enhanced due to the load support of the hardened tool steel. When the tool steel, coating and heat treatment are well coordinated with proper design, significantly longer lifetimes of CVD coated tools compared to uncoated tools can be obtained. In this case, the tools are profitable, although manufacturing costs are higher. Further improvements are possible by future developments, e.g. combined processes.

Introduction

Tools for metalworking nowadays are often coated with hard materials to reduce tool wear and enhance tool lifetime. Common coating processes are chemical vapor deposition (CVD) and physical vapor deposition (PVD), common hard materials are group IVb-VIb (Ti, V, Cr,) carbides, nitrides, etc. Beside many other differences, CVD coatings (especially high temperature HT CVD) are deposited at temperatures of about 1000°C while PVD coatings are carried out at lower temperatures of about 200-500°C. Coated tools for metalworking can be divided into three main groups: CVD coated cemented carbide cutting tools, PVD coated steel cutting tools and CVD coated steel forming tools:

- Cemented carbide cutting tools, e.g. inserts for turning, can easily be CVD coated without a post heat treatment, because their properties are only slightly influenced by the high CVD temperature.
- Slender steel cutting tools, e.g. drills, would be strongly influenced by the high CVD temperature and would need a post heat treatment to receive useful properties. Because this post heat treatment causes distortion of slender steel cutting tools, they are normally PVD coated at lower temperatures without a post heat treatment.
- Massive steel forming tools or punching tools are also strongly influenced by the high CVD temperature and need a post heat treatment to receive useful properties. But the distortion of these massive tools during post heat treatment can be controlled to a certain extent.

This chapter deals with the post heat treatment of CVD coated steel forming tools. Forming tools often need the advantages of CVD coatings compared to PVD coatings, such as normally better adherence, thorough coating coverage and simpler equipment. CVD coated forming tools are very important for many fields of metalworking, e.g. forming of sheet metal, and are used on a large scale.[1-5] Figures 1 and 2 show two examples of CVD coated and post heat treated steel forming tools: a drawing ring (M2, CVD TiC coated) and a segmented forming tool for an automobile door (D2, CVD TiN coated).

Fundamentals of Heat Treating CVD Coated Tool Steels

For good performance of coated tools, the properties of both coating and substrate should be optimized.[6-16] The coating (thickness some µm) contributes the friction, wear and corrosion reducing properties. The substrate contributes the mechanical load support for the thin coating and should therefore have a minimum hardness of ~58 HRC.

To understand the need for heat treating CVD coated steel tools, the temperature/time regime of the CVD process should be compared with the temperature/time dependence of the transformation behavior of different tool steels. Tool steels suitable for CVD coating should have these properties: high hardenability, secondary hardening behavior and austenitizing temperature near CVD temperature. Table 1 describes several such tool steels. Almost every type of tool steel has some qualities suitable for CVD coating, but most common for forming tools are high alloy cold work steels and high speed steels. Typical cooling curves in a hot wall CVD reactor are shown in Figure 3. After the CVD stage, the heating hood is removed from the reactor and replaced by a cooling hood, which cools the reactor with an air flow from outside. The cooling curves depend on the CVD batch size. Figure 3 shows slow cooling for a small batch

Fig. 1: Example of CVD coated steel tool, drawing ring. (Courtesy of VST Verschleiss Schutz Technik Keller GmbH & Co. KG, Schopfheim, Germany).

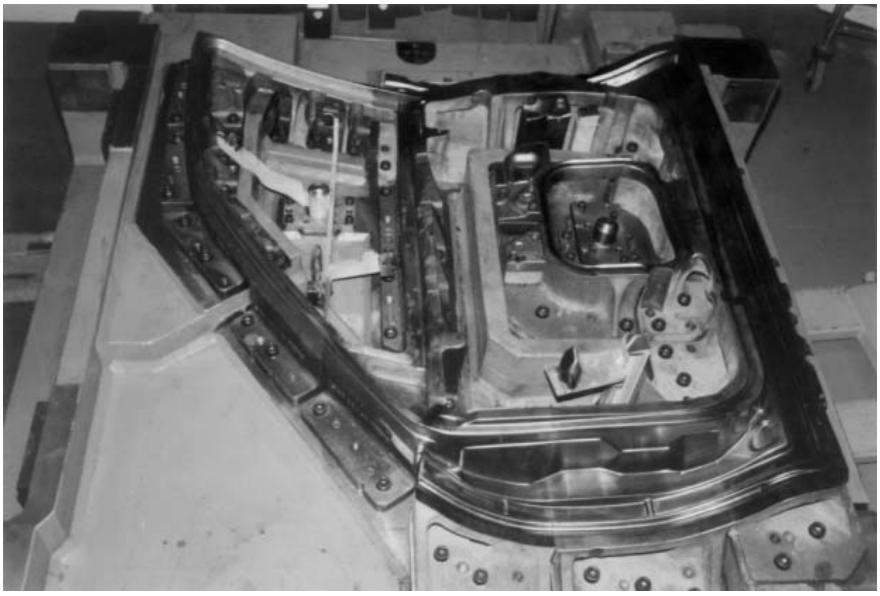

Fig. 2: Example of CVD coated steel tool, segmented forming tool for an automobile door. (Courtesy of VST Verschleiss Schutz Technik Keller GmbH & Co. KG, Schopfheim, Germany).

and an even slower cooling for a large batch. In all cases, cooling from the coating temperature lasts several hours, and these temperature/time regimes should be compared with the transformation behavior of the tool steel substrates. The transformation behavior can be taken from the (continuous cooling transformation CCT diagrams) such as Figures 4

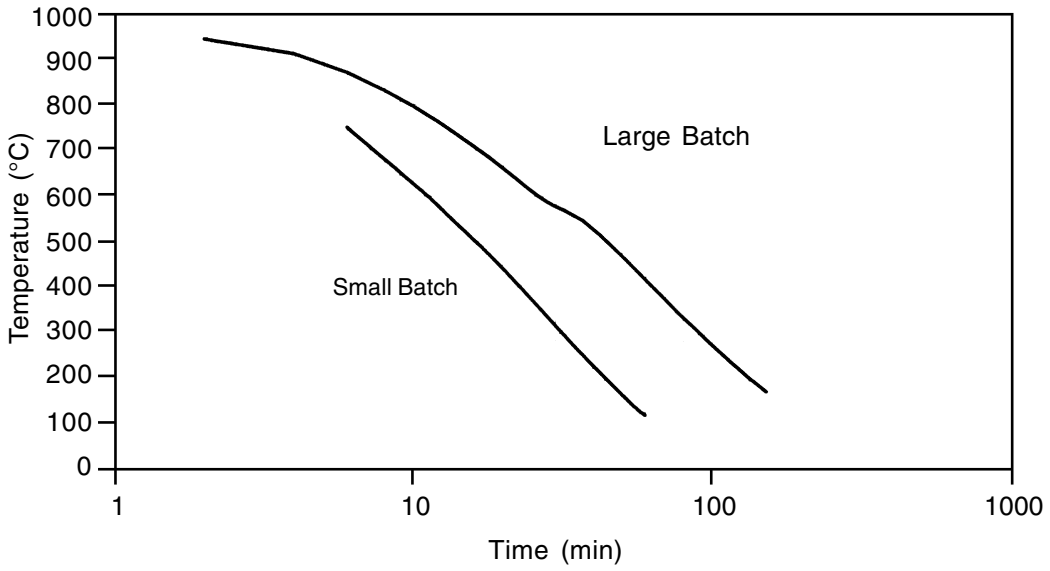

Fig. 3: Cooling curves after CVD coating.

Table 1. Tool Steels Suitable for CVD Coating[9-10]

Tool Steel Type	AISI	UNS	DIN	DIN No.
Molybdenum High Speed Steel Powder Metallurgical Molybdenum High Speed Steel	M2 "ASP23 PM" ~ M3 PM	T11302	HS 6-5-2 ~HS 6-5-3 PM	1.3343
Tungsten High Speed Steel	T5	T12005	HS 18-1-2-10	1.3265
High Alloy Cold Work Steel	D2 D3	T30402 T30402	X155 CrVMo 12-1 X210 Cr12	1.2379 1.2080
Medium Alloy Air Hardening Cold Work Steel	A2	T30102	X100 CrMoV5-1	1.2363
Oil Hardening Cold Work Steel	O2	T31502	90 MnCrV8	1.2842
Low Alloy Tool Steel	L3	T61203	100 Cr6	1.2067
Unalloyed Water Hardening Tool Steel	W110	T72301	C110 W2	1.1650
Hot Work Tool Steel	H13	T20813	X40 CrMoV5-1	1.2344

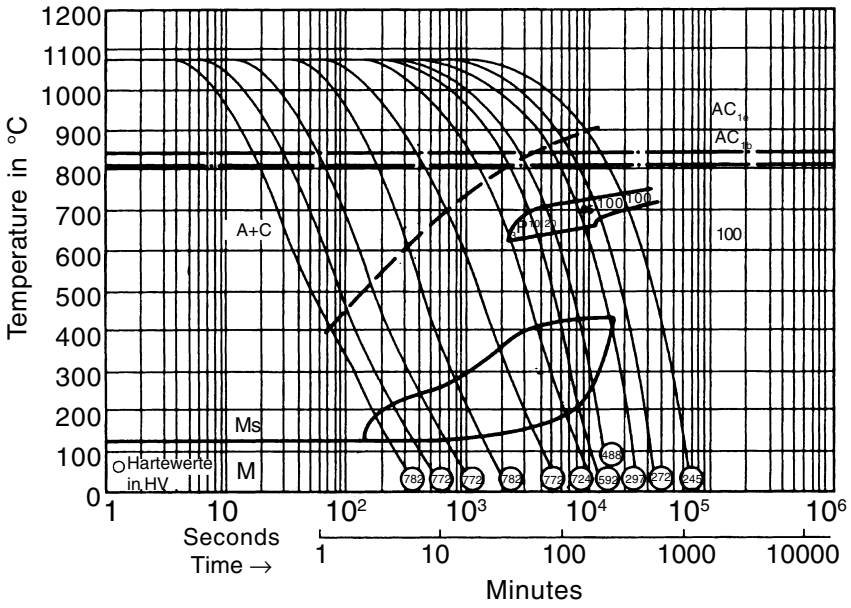

Fig. 4: CCT diagram of D2 tool steel. Source: Thyssen Edelstahlwerke AG, Werkzeugstähle, Druckschrift 1122/5, Ausgabe, June 1986.

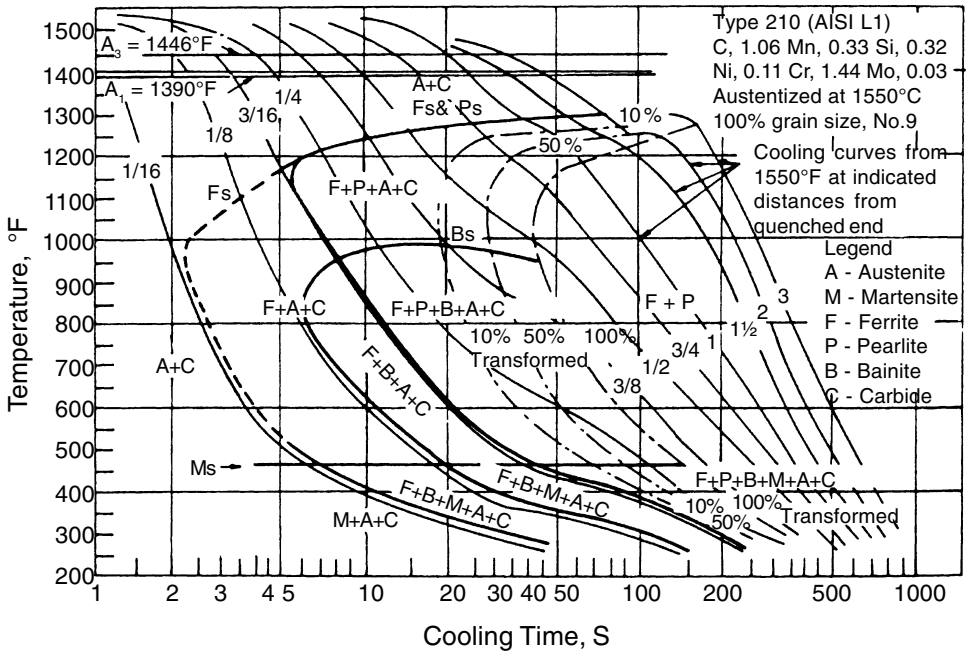

Fig. 5: CCT diagram of L1 tool steel.[17]

and 5 for a high alloy tool steel (D2) and a low alloy tool steel (L1), respectively.

Although the CCT diagrams have been determined for austenitizing conditions different from CVD coating, they can be used to get a rough estimation of the resulting tool steel microstructure and hardness after CVD coating and slow cooling. CVD coating and slow cooling of a small D2 batch may exceed the critical cooling velocity for martensite

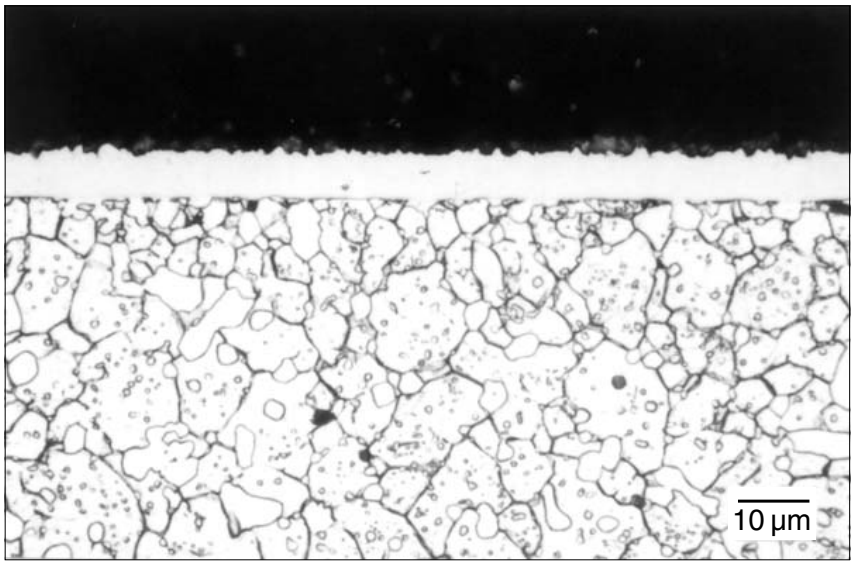

Fig. 6: Microstructure of D2/TiN, small batch, 10% alcoholic HNO_3 etch.

transformation in this high alloy tool steel. This is proven by the microstructure of a CVD TiN coated D2 in Figure 6, which consists of martensite, retained austenite (~10 vol.% by x-ray diffraction) and carbides with a hardness of 770 HV1. This is not an ideal microstructure of a quench hardened D2 (see below). With larger batches even this high alloy tool steel will fall below the critical cooling velocity for martensite transformation and contain pearlite/bainite phases. This is confirmed by the microstructure of a CVD TiN coated D2 in Figure 7, which consists of martensite, pearlite/bainite and carbides with a hardness of only 480 HV1. A low alloy tool steel like L3 will in every case fall below the critical cooling velocity for martensite transformation during cooling from CVD temperature. This results in a soft pearlite microstructure, as shown in Figure 8 for a CVD TiN coated L3 with a hardness of only 360 HV1.

These soft steel substrates do not sufficiently support the hard coatings under load, therefore they are not useful for a CVD coated forming tool and need to be post heat treated.[6-16] Different heat treatment paths of CVD coated steel tools are possible. The most complex heat treatment path (Figure 9d) consists of rough machining, stress relieving, finishing, quench hardening plus tempering and further finishing before CVD. The final finishing should result in a roughness R_{max} (DIN 4760) of a few µm or less. After CVD a further quench hardening plus tempering follows. Altogether Figure 9 shows four different heat treatment paths.

A. CVD/Tempering:
   Coating of soft substrates, cooling after coating sufficient for martensite formation.
B. CVD/Hardening/Tempering:
   Coating of soft substrates, cooling after coating not sufficient for martensite formation.
C. Hardening/Tempering/CVD/Tempering:
   Coating of hard substrates, cooling after coating sufficient for martensite formation.
D. Hardening/Tempering/CVD/Hardening/Tempering:
   Coating of hard substrates, cooling after coating not sufficient for martensite formation.

Basically, during the heat treatment of CVD coated tools the common rules for heat treating

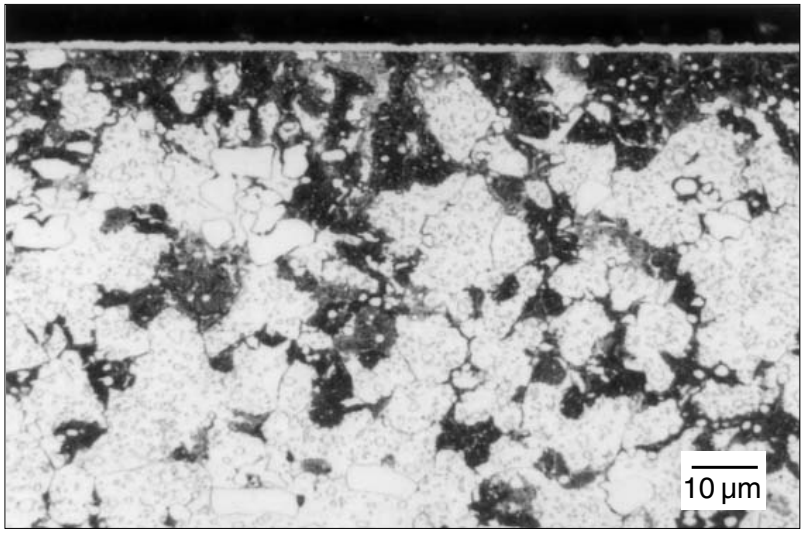

Fig. 7: Microstructure of D2/TiN, large batch, 10% alcoholic HNO_3 etch.

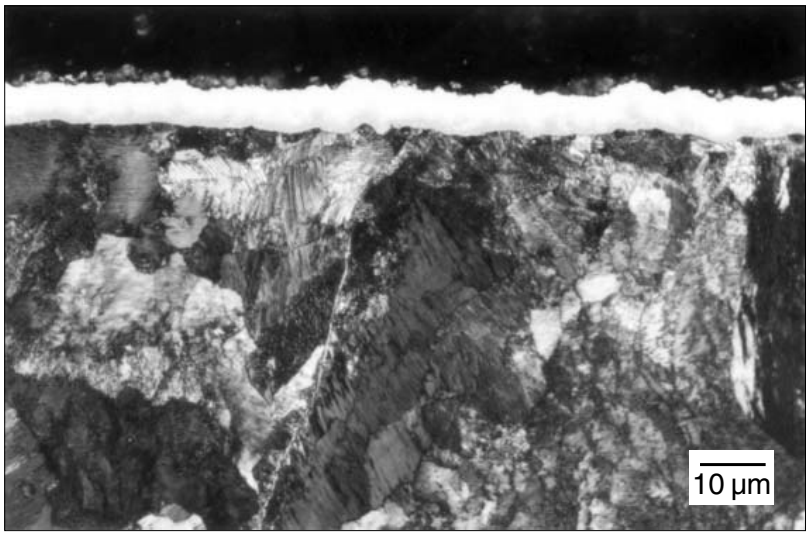

Fig. 8: Microstructure of L3/TiN, 3% alcoholic HNO_3 etch.

tool steels[18,19] must be followed. All of the above heat treatment paths require that quench hardening and tempering before and after CVD coating should be done in vacuum or protective atmosphere to protect either the surfaces to be coated or the CVD coatings from damages like oxidation. Further, preheating steps during heating and an equalizing step during quenching should be provided, to ensure uniform temperature which promotes uniform stress distribution in the tools. Oil quenching, gas quenching or even gas

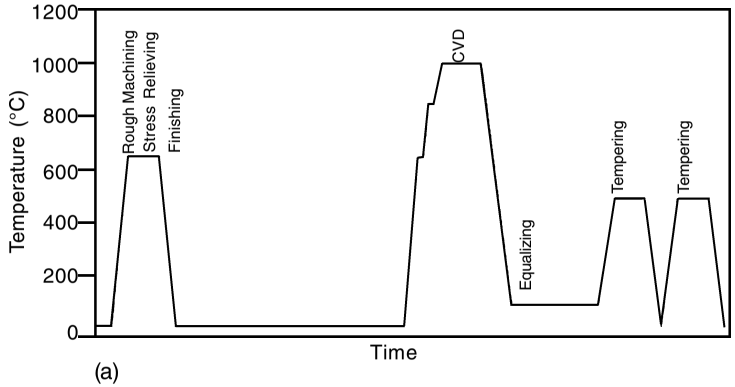

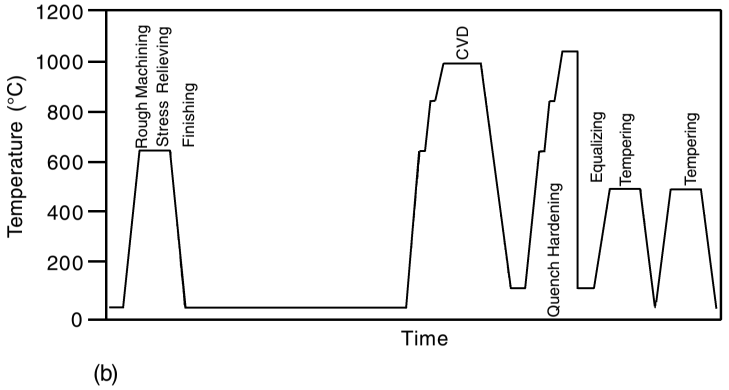

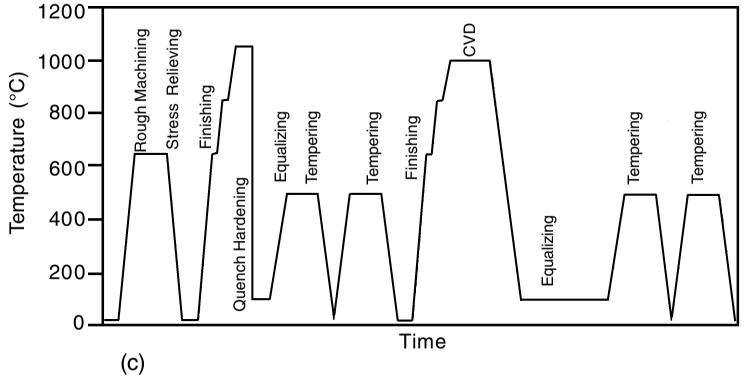

Fig. 9: Heat treatment paths. (Please see Fig. 9d in next page).

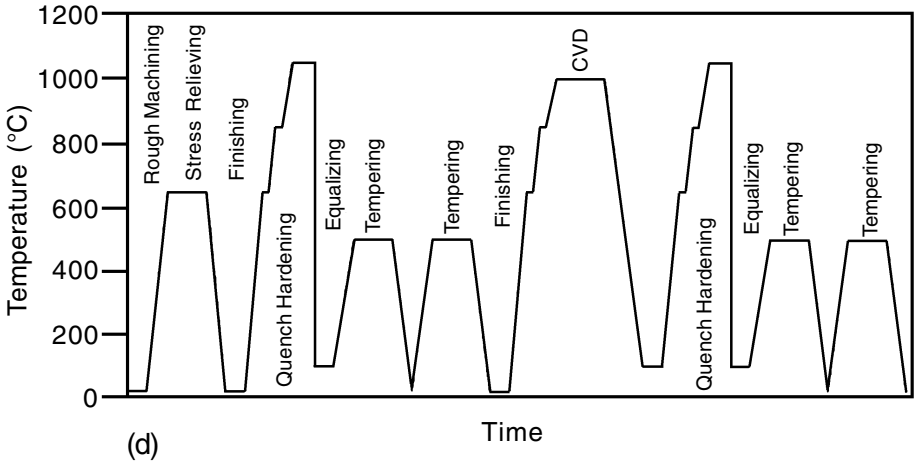

Fig. 9: Continued.

quenching with martempering can be used, depending on the tool steel, the tool dimensions and the available heat treatment equipment. The number and temperatures of tempering steps depend on the tool steel. High alloy tool steels such as D2 are tempered at secondary hardening temperatures, where besides the partial decomposition of martensite and retained austenite, fine alloy carbide precipitation occurs. These fine alloy carbide precipitates cause a hardness increase (Figure 10).[20] Besides unwanted new martensite is formed during cooling from the first tempering step.[21] Thus, multiple tempering, at least two times, should be performed, to temper this new martensite. Distortion during CVD and heat treatment should be minimized by adequate charging support of the tools.

Some characteristics of the different heat treatment paths are given in Table 2. The degree of complexity rises from heat treatment path A to D. But the simpler heat treatment paths have some problems concerning microstructures and properties of the tool steels and may not be sufficient for high quality forming tools. For low alloy tool steels, like L3, the hardness will be too low after heat treatment path A. For high alloy tool steels, like D2, the hardness may be high after heat treatment path A, but pre-eutectic carbide precipitation on grain boundaries may occur during cooling from CVD temperature (see CCT diagram, Figure 4) and significantly reduce the toughness. Further, CVD temperatures are usually lower than common austenitizing temperatures of high alloy steels. This results in less dissolved carbon and carbide forming elements (W, Mo, V,) in the austenite and prevents secondary hardening by fine alloy carbide precipitation during tempering (Figure 10). These problems can be solved by heat treatment path B with an additional quench hardening step after CVD.

Besides obtaining a useful tool steel microstructure, controllable distortion is another requirement of CVD coated forming tools, because the small coating thickness hinders post machining. Distortion due to heat treatment is influenced by many factors.[22, 23] One factor is the different specific volume of various phases in steel (Figure 11).[24] The heat treatment paths A and B have the following in common. Finishing and CVD coating are done in the soft annealed state of the tool steel (ferrite + carbides), whereas the final state of the tool steel is quench hardened and tempered (martensite + retained austenite + carbides). This difference in phases causes a difference in specific volume and thereby distortion of the tool. Heat treatment paths C and D try to avoid this

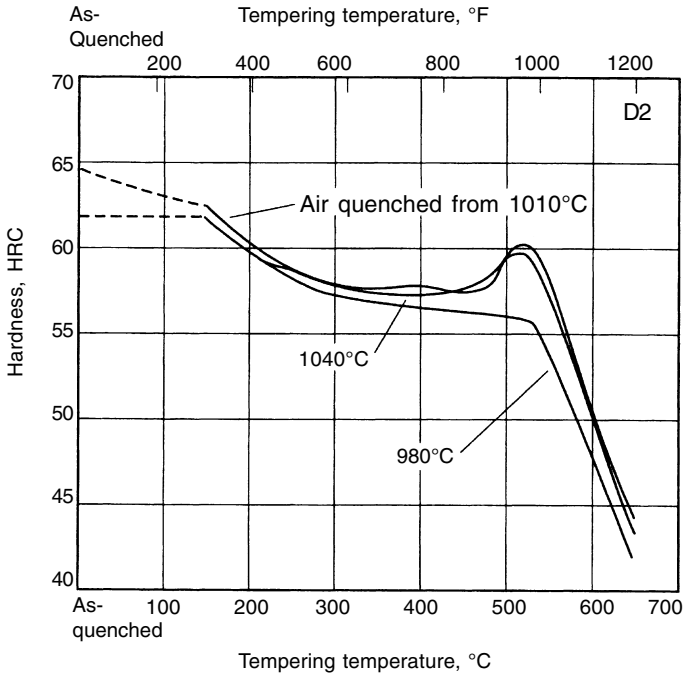

Fig. 10: Relationship between tempering temperature and hardness for D2 tool steel.

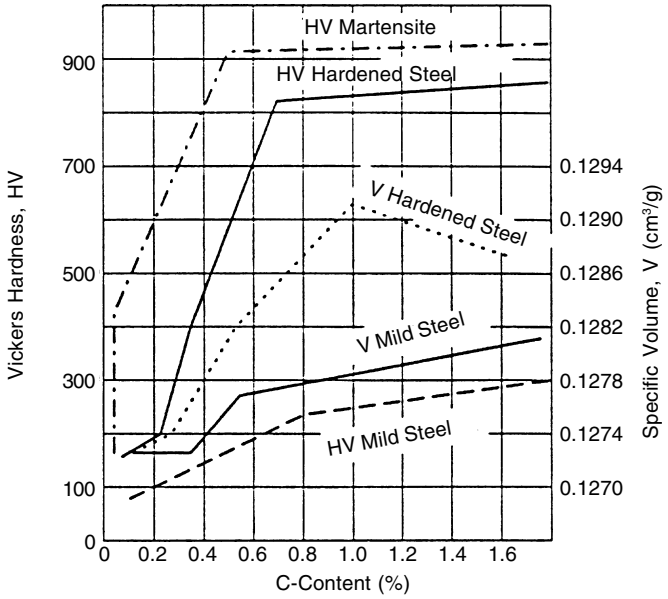

Fig. 11: Hardness and specific volume of steels in various states vs. cabon content.[24]

distortion by adjusting the desired final tool steel phases already before finishing and CVD, i.e. by an additional quench hardening and tempering before finishing and CVD. This results in the most complex, but also most successful heat treatment path D.

Case Studies

This chapter first describes some characteristic properties of CVD coatings and tool steel substrates, such as chemical composition, microstructure, hardness, residual

Table 2. Characteristics of Different Heat Treatment Paths + Good Properties, Possible Poor Properties

Heat Treatment Path	Complexity	Hardness	Carbide Precipitations on Grain Boundaries	Secondary Hardening	Distortion, Specific Volume
A	Low	(-)	-	-	-
B	Medium	+	+	+	-
C	Medium	(-)	-	-	(+)
D	High	+	+	+	+

stresses, adhesion and distortion. In this section the interaction of these properties in some practical case studies of CVD coated steel forming tools will be presented.

For the characteristic properties two representative examples are chosen: the CVD TiN coated and post heat treated high alloy tool steel D2 and the low alloy tool steel L3, both heat treated following path D. The complete heat treatment parameters are:

D2:

- Hardening + Tempering:
  1050°C, 20 min/oil/3× (500°C 1.5 h)
- Finishing
- CVD TiN:
  1000°C, 2.5 h/Furnace Cooling
- Hardening + Tempering:
  Vacuum 1050°C, 20 min/oil/3×
  (Vacuum 500°C, 1.5 h)
  Respectively:
  Vacuum 1050°C, 20 min/N_2 6 bar/3×
  (Vacuum 500°C, 1.5 h).

L3:

- Hardening + Tempering:
  830°C, 20 min/oil/180°C, 2 h
- Finishing
- CVD TiN:
  1000°C, 2.5 h/Furnace Cooling
- Hardening + Tempering:
  Vacuum 830°C, 20 min/oil/air 180°C, 2 h.

Even austenitizing temperatures above the CVD temperatures cause almost no changes in the chemical compositions of the D2 substrate and TiN coating as measured by GDOS (glow discharge optical spectroscopy), if the post CVD quench hardening is done in vacuum. Comparing Figures 12a (as coated) and 12b (coated + hardened) reveal no significant differences. The TiN coating (thickness ~5 µm) remains unchanged (nearly stoichiometric) and in the interface no significant interdiffusion due to austenitizing seems to occur. At lower austenitizing temperatures of L3/TiN in vacuum even fewer changes in chemical composition are expected.[25-30]

Significant, desirable changes are found in the microstructures of the CVD coated and subsequently heat treated tool steels. Compared to the non-optimal martensitic microstructure or the pearlite/bainite microstructure of D2/TiN in Figures 6 and 7, a useful microstructure for high alloy tool steels can be achieved by subsequent quench hardening and tempering. Figure 13a shows the quench hardened state. The D2 substrate consists of martensite, retained austenite (20-30 vol.% by x-ray diffraction) and carbides with a hardness of 800 HV1. After subsequently tempering three times at secondary hardening temperatures fine, alloy carbide precipitates are observed and the hardness increases (Figure 13b, 750 HV1). The TiN coating (thickness ~5 µm) remains unchanged, homogeneous and without microscopic defects. This is confirmed in SEM investigations (scanning electron microscope) of quench hardened and tempered D2/TiN, where a typical CVD coating microstructure consisting of columnar crystals with prismatic apices, but no pores, cracks or delaminations are found (Figure 14). Even higher hardness and

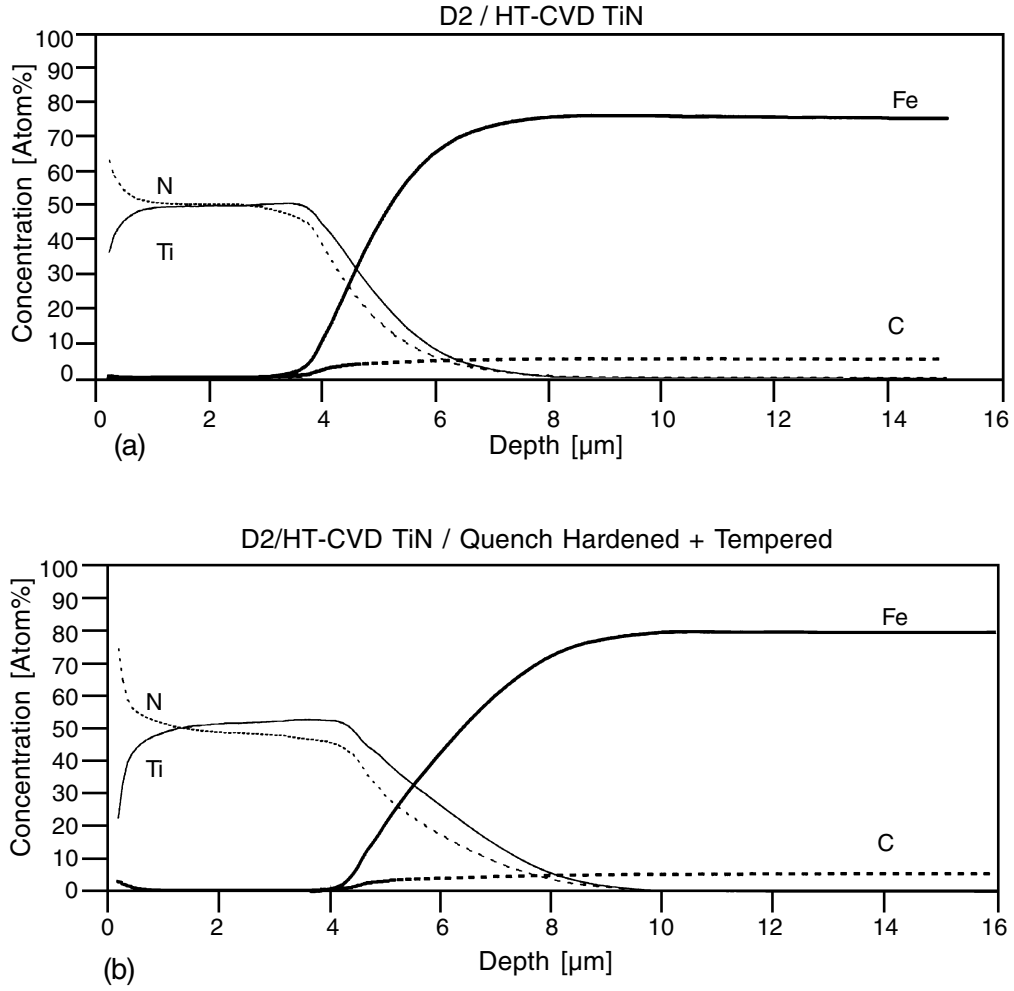

Fig. 12: (a) Chemical composition of D2/CVD TiN, measured by GDOS and (b) Chemical composition of D2/CVD TiN/quench hardened + tempered, measured by GDOS.

microstructure changes can be found in the CVD coated and subsequently heat treated low alloy tool steel L3/TiN. The soft pearlitic microstructure of the L3 substrate in Figure 8 turns into a predominantly martensitic microstructure with some retained austenite and carbides **a**fter quench hardening (Figure 15, 850 HV1). The TiN coating (thickness ~5 µm) remains unchanged, homogeneous and without microscopic defects. A further low temperature tempering step results in a small hardness decrease to 810 HV1 with almost no visible microstructure changes.[25-30]

A fundamental property of wear resistant CVD coatings for forming tools is their hardness. Thus coating hardness should not be reduced by subsequent quench hardening of the tools. Table 3 shows the microhardness measured on polished surfaces of CVD TiN and for comparison of PVD (reactive sputtered) TiN coatings in the as deposited and quench hardened state. Whereas the hardness of the PVD coating is significantly reduced by quench hardening, the hardness of the CVD coating remains almost constant. These results can be explained by changes in the coating

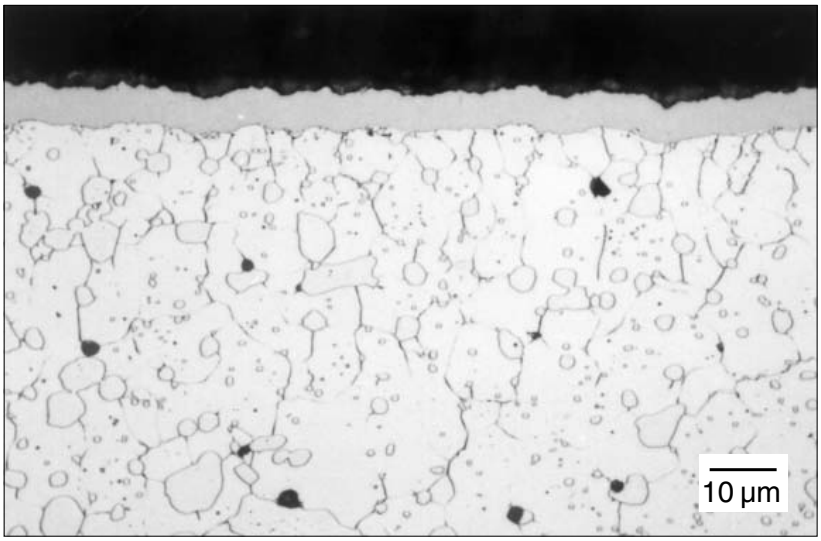

(a)

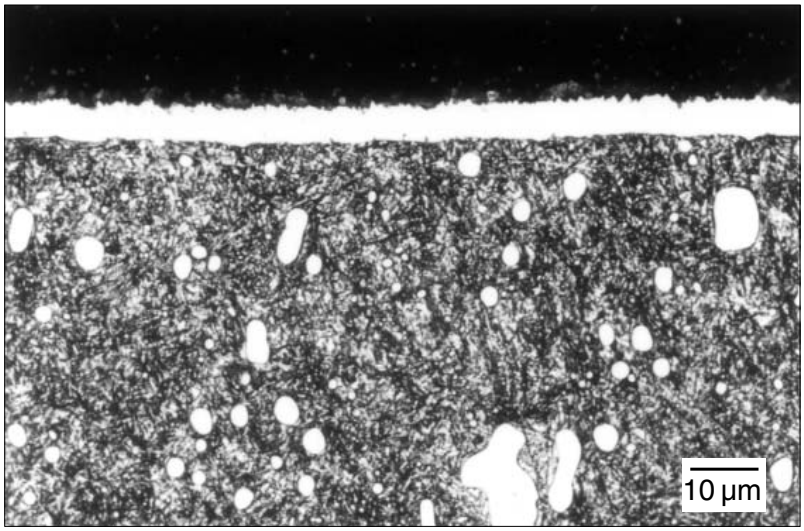

(b)

Fig. 13: (a) Microstructure of D2/CVD TiN/quench hardened, LVII 19-2/10, 1000 : 1 and (b) Microstructure of D2/CVD TiZ/quech hardened + tempered, LV 296.4/21.

microstructures, detected by evaluating half-widths (FWHM) of TiN interference lines in x-ray diffraction (Table 3). Large half-widths can be interpreted as a high density of lattice defects in the coating crystals, usually in conjunction with high hardness. The higher hardness and larger half-width of PVD TiN coatings compared to CVD TiN coatings in the as deposited state is attributed to their different growth mechanisms. This higher density of lattice defects in the PVD TiN coatings is relieved during quench hardening, namely during austenitizing, which is near the recrystallization temperature of TiN ($0.4\ T_S \approx 1000°C$). In CVD TiN coatings the

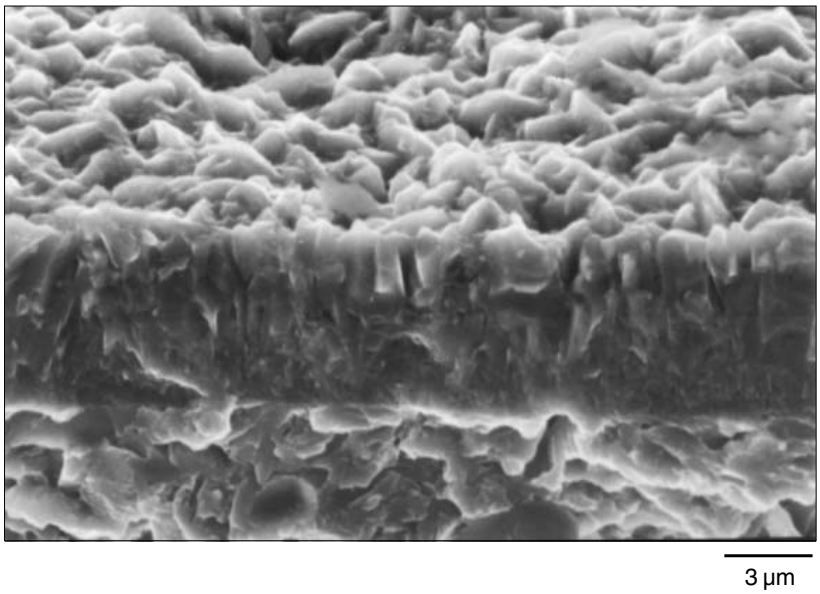

Fig. 14: SEM micrograph of D2/CVD TiN/quench hardened + tempered, CS VIII 22-3/14.

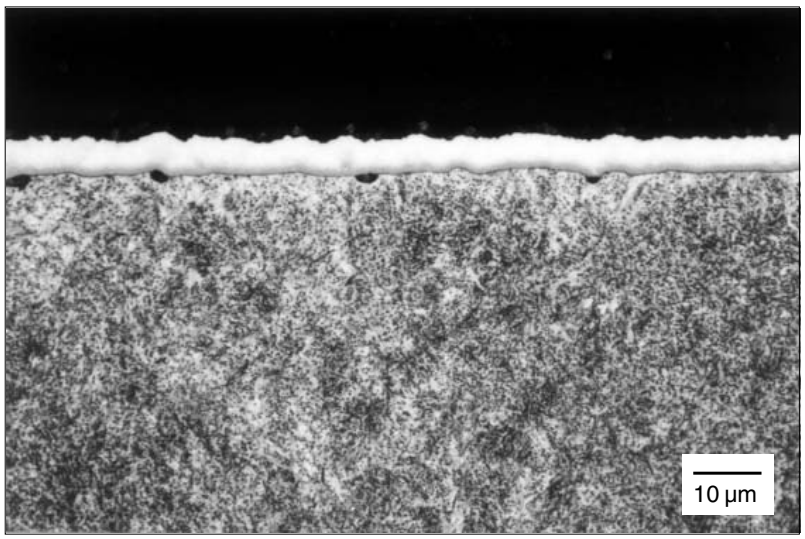

Fig. 15: Microstructure of L3/CVD TiN/quench hardened, LVII 32-6/33, 1000 : 1.

density of lattice defects is lower and thus not further reduced by quench hardening, as can be seen from their half-width and hardness values.

Beside microstructure and hardness, the residual stresses in coatings and substrates are of great importance for the practical behavior of CVD-coated tools. Residual stress depth profiles, measured by x-ray diffraction ($\sin^2\psi$ method) with stepwise sputtering of the surface, are shown in Figure 16. Because of the higher

Table 3. Coating Hardness

	Coating Hardness HV0.025 (each 9 Measurements, Coating Thickness ~ 5 µm)	Half-Width (FWHM) of TiN {220} Lines in X-ray Diffraction with Cr-Kα Radiation
4140: HT-CVD TiN	1800 ± 100	0.7°
4140: HT-CVD TiN / Quench Hardened	2000 ± 100	0.7°
4140: PVD TiN	3700 ± 200	2.7°
4140: PVD TiN /Quench Hardened	2800 ± 300	2.0°

thermal expansion coefficient of the steel substrate compared to the TiN-coating, as deposited CVD TiN coatings on steel substrates usually have high residual stresses of -2000 to -3000 N/mm^2. These high compressive residual stresses are beneficial for the practical behavior of CVD coated tools.

Residual stresses in CVD coatings develop during cooling from coating temperature due to different thermal contraction of coating and substrate as well as volume changes by phase transformations. Figure 17 shows the contraction of a CVD TiN-coating and a steel (L3) substrate during cooling from coating temperature (1000°C), assuming that coating and substrate are not bonded. The coating shrinks steadily according its thermal expansion coefficient. The substrate first shrinks according the thermal expansion coefficient of austenite. Then austenite transforms to ferrite and cementite and thereby the substrate volume increases. Finally the substrate shrinks according the thermal expansion coefficient of ferrite and cementite. Because coating and substrate are bonded, the coating is compressed by the stronger substrate contraction. Assuming the total substrate transformation at $A_1 = 723°C$, the resulting residual coating strain can be calculated by

$$\varepsilon_{coat,\,res} = \alpha_{coat}\,(20°C - T_c) - [\alpha_{aust}\,(723°C - T_c) + \varepsilon_{trans} + \alpha_{ferr}\,(20°C - 723°C)]$$

with

$\varepsilon_{coat,\,res}$ = Residual coating strain,
T_c = Coating temperature,
α_{coat} = Thermal expansion coefficient of the coating,
α_{aust} = Thermal expansion coefficient of austenite,
α_{ferr} = Thermal expansion coefficient of ferrite and cementite,
ε_{trans} = Strain by transformation austenite → ferrite + cementite.

From the residual coating strain, the residual coating stress can be calculated assuming a two-dimensional stress state in the thin coating.

$$\sigma_{coat,\,res} = \varepsilon_{coat,\,res}\,E_{coat} / (1 - \nu_{coat})$$

with

$\sigma_{coat,\,res}$ = Coating residual stress
E_{coat} = Young´s modulus of the coating
ν_{coat} = Poisson's ratio of the coating

In Table 4 the calculated coating residual stresses are compared with values measured by X-ray diffraction. The agreement is quite good, so the described model can be used to predict residual stresses in CVD coatings.

Post quench hardening and tempering of D2/TiN does not influence the coating residual stresses significantly (Figure 16a). This is due to the almost equal specific substrate volumes

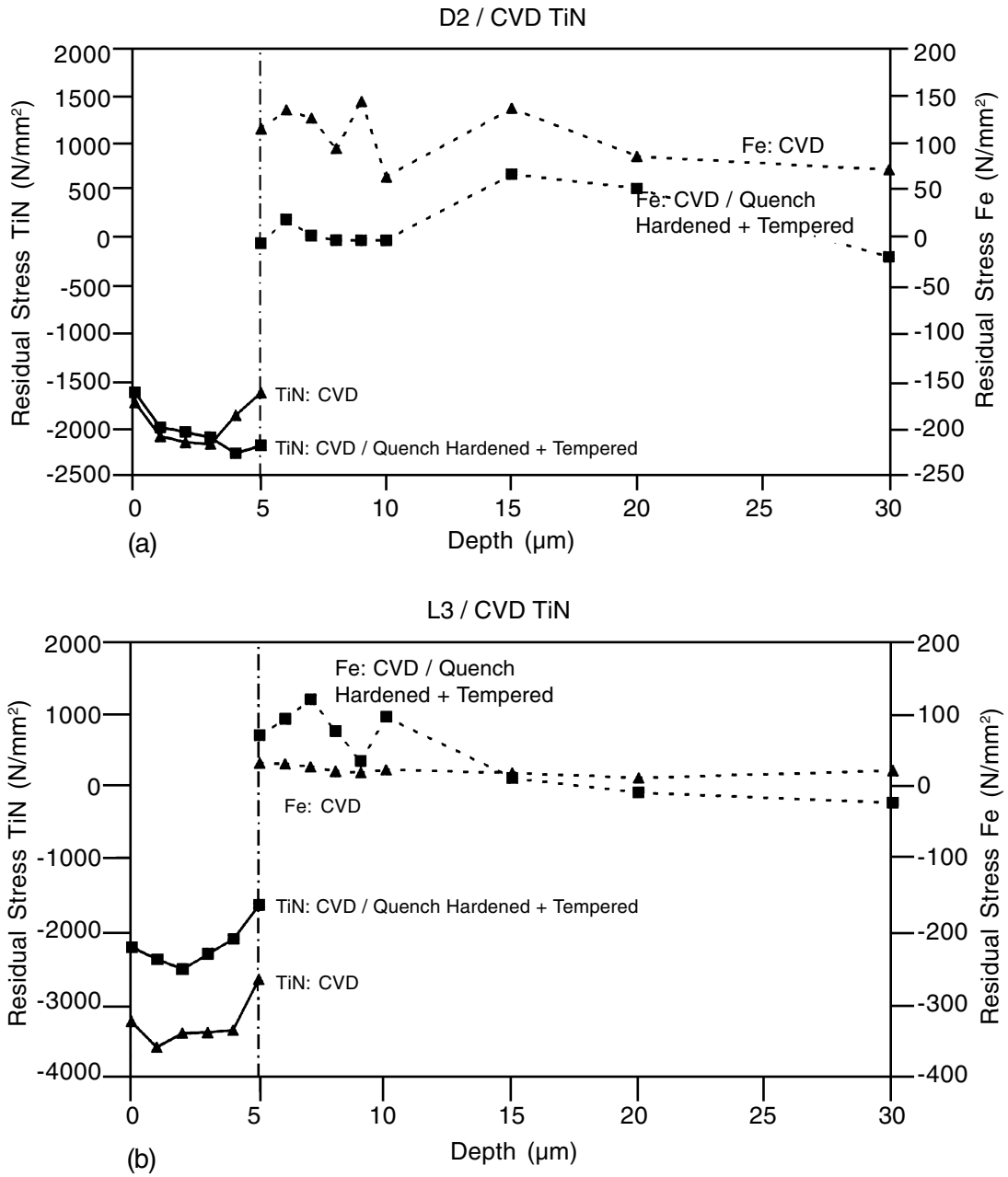

Fig. 16: (a) Residual stresses of D2/CVD TiN and D2/CVD TiN/quench hardened + tempered and (b) Residual stresses of L3/CVD TiN and L3/CVD TiN/quench hardened + tempered, measured by x-ray diffraction ($\sin^2\psi$-method).

of D2 in the CVD-coated and post heat treated state. The D2 substrate residual stresses are moved from slight tension to almost zero. In the low alloy tool steel L3/TiN, the coating residual stresses are strongly influenced by the post quench hardening. They decrease approximately by 1000 N/mm^2 (Figure 16b). This is due to the significant increase in the specific substrate volume of L3 from the as-deposited (pearlitic) to the quench hardened

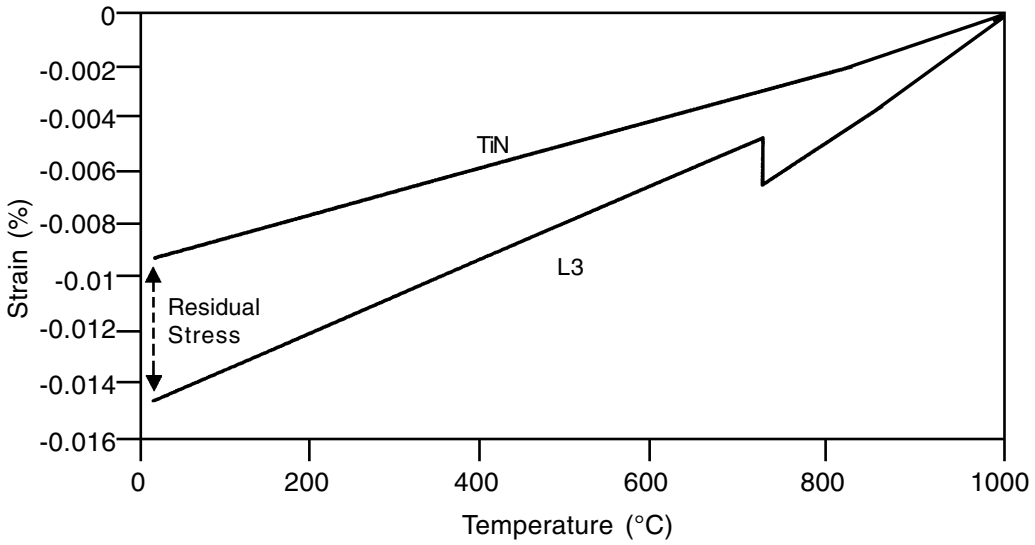

Fig. 17: Coating and substrate contraction during cooling from CVD temperature.

Table 4. Residual Stresses in As-Deposited CVD TiN Coating[29]

Substrate/Coating		4140/CVD TiN	L3/CVD TiN
Tc	°C	1000	1000
α_{coat}	10^{-6} 1/K	9.4	9.4
α_{aust}	10^{-6} 1/K	22.3	21.9
α_{ferr}	10^{-6} 1/K	14.5	14.3
ε_{trans}	10^{-3}	2.8	1.8
$\varepsilon_{coat,\ res}$	10^{-3}	-4.4	-5.1
E_{coat}	N/mm^2	430000	430000
ν_{coat}	-	0.2	0.2
$\sigma_{coat,\ res}$ calculated	N/mm^2	-2300	-2800
$\sigma_{coat,\ res}$ measured	N/mm^2	-1800	-3400

(martensitic) state. The coating is firmly bonded on the substrate and follows the volume change by reducing its compressive residual stresses. The L3 substrate residual stresses are moved to slight tension.[25-30]

Generally, residual stress changes in CVD coatings after quench hardening are caused by substrate volume changes (Figure 11). From these substrate volume changes, a substrate strain can be calculated assuming isotropy

Table 5. Residual Stresses in CVD TiN Coatings After Quench Hardening[29]

Substrate/Coating		L3/CVD TiN	D2/CVD TiN
Microstructure after CVD		Ferrite + Cementite	Martensite + 10% Retained Austenite + Carbide
$V_{sub, CVD}$	cm^3/g	0.1275	0.1281
Hardening		Quench Hardening	Quench Hardening + Tempering 500°C
Microstructure after Hardening		Martensite + 20% Retained Austenite	Tempered Microstructure + Carbide
$v_{sub, hard}$	cm^3/g	0.1284	0.1281
$\Delta\varepsilon_{coat, res}$	10^{-3}	2.3	0
$\Delta\sigma_{coat, res}$ Calculated	N/mm^2	1200	0
$\Delta\sigma_{coat, res}$ Measured	N/mm^2	1000	-280

Table 6. Critical Loads for Cohesive Failure in Scratch Tests

	Substrate Hardness HV1 (Each 9 Measurements)	Critical loads for cohesive failure in scratch tests [N] (each 9 scratch tests)
D2: HT-CVD TiN	770 ± 13	50 ± 5
D2: HT-CVD TiN/Quench Hardened + tempered	746 ± 6	50 ± 6
L3: HT-CVD TiN	359 ± 12	27 ± 4
L3: HT-CVD TiN/Quench Hardened + Tempered	814 ± 8	52 ± 3

material behavior. This substrate strain is transferred to the coating and causes a change in coating residual strain and thereby in coating residual stress.

$$\Delta\varepsilon_{coat, res} = \Delta\varepsilon_{sub} = (v_{sub, hard} - v_{sub, CVD}) / 3\, v_{sub, CVD}$$

$$\Delta\sigma_{coat, res} = \Delta\varepsilon_{coat, res}\, E_{coat} / (1 - \nu_{coat})$$

with

$\Delta\varepsilon_{coat, res}$ = Change in coating residual strain

$v_{sub, hard}$ = Specific substrate volume after quench hardening + tempering

$v_{sub, CVD}$ = Specific substrate volume after CVD

$\Delta\sigma_{coat, res}$ = Change in coating residual stress.

In Table 5 the calculated changes in coating residual stresses after quench hardening are compared with values measured by x-ray diffraction. The agreement is quite good, so the described model can be used to predict residual stresses in CVD coatings after quench hardening.

Another important property for the practical behavior of CVD-coated tools is coating

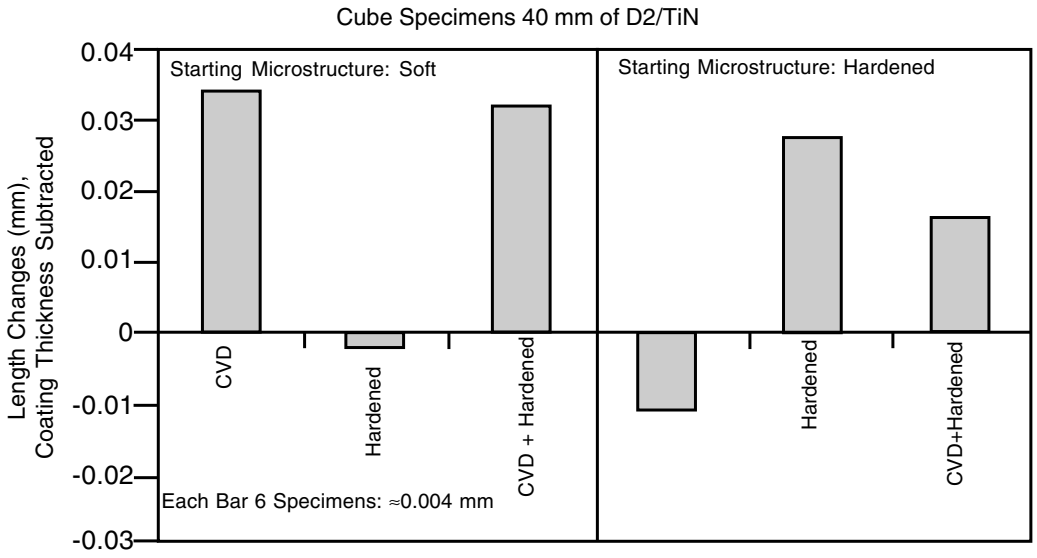

Fig. 18: Length changes of D2/CVD TiN/quench hardened + tempered, heat treatment paths B and D.

adhesion. Coating adhesion is difficult to measure; attempts have been made using the scratch test. Wherein cohesive failure (cracks in the coating) and adhesive failure (coating delaminations) can be distinguished. Because the results of scratch tests depend also on the substrate deformation, they can be interpreted in terms of substrate load support for the coating. This is shown in Table 6, where critical loads for cohesive failure in scratch tests and substrate hardness are tabulated for D2/TiN and L3/TiN as-deposited and post quench hardened. In the high alloy tool steel D2, substrate hardness and critical loads are high in both cases, whereas in the low alloy tool steel L3 the substrate hardness increase causes increased critical loads in scratch tests.[25-30]

The above mentioned differences between the heat treatment paths B and D concerning distortion are demonstrated in Figure 18. Soft annealed and quench hardened + tempered D2 microstructures are used as starting state for CVD TiN coating and subsequent heat treatment. The soft microstructure (Figure 18 left) leads to significant length changes of No.01%, especially after CVD, due to the difference in specific volumes between starting and final microstructure. The hardened microstructure (Figure 18 right) leads to smaller length changes, because the specific volumes of starting and final microstructure are similar. This result is still not optimized; by varying the tempering temperature the tool dimensions can be targeted on the desired values (Figure 19).[10]

The difference in specific volume is only one of many reasons for distortion during heat treatment.[22,23] Another important influencing factor is the quenching medium during hardening. Fluids or gases can be employed as quenching media. Advantage of fluids is the usually higher cooling power, which is necessary for low alloy steels and large tool dimensions. High alloy tool steels can profit from the main advantage of gases, the possibly lower distortion, due to controllable cooling power and absence of a re-wetting stage during cooling. This is proven in Figure 20, where CVD + hardening with oil quenching of D2/TiN cause significantly greater shape changes than CVD + hardening with gas quenching (6 bar nitrogen).[31,32]

Forming tools such as drawing rings, deep drawing dies or bending tools for sheet metal forming are typical examples of CVD-coated steel

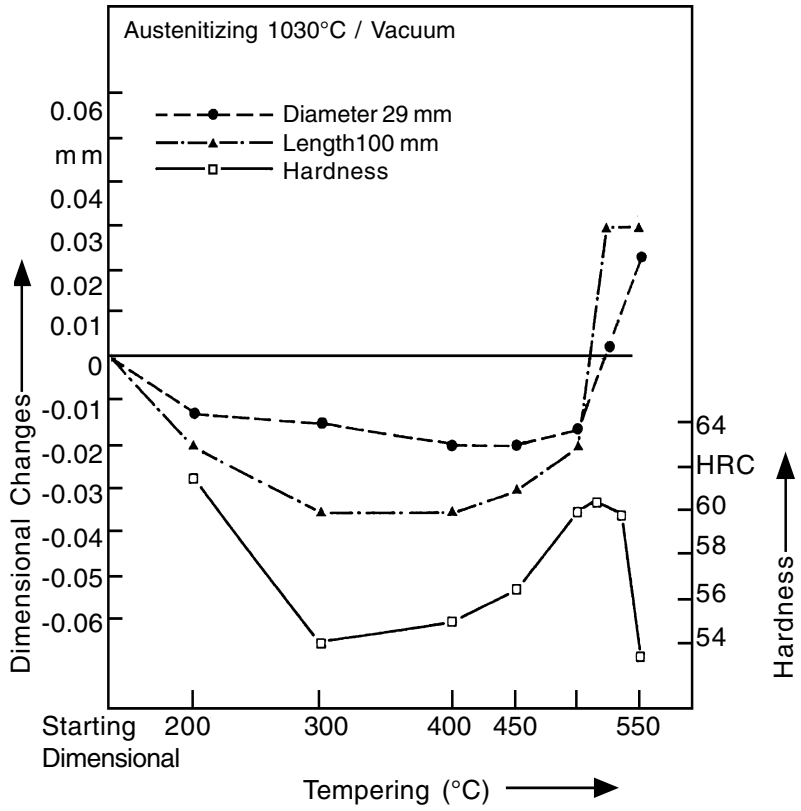

Fig. 19: Tool dimensions depending on tempering temperature.[10]

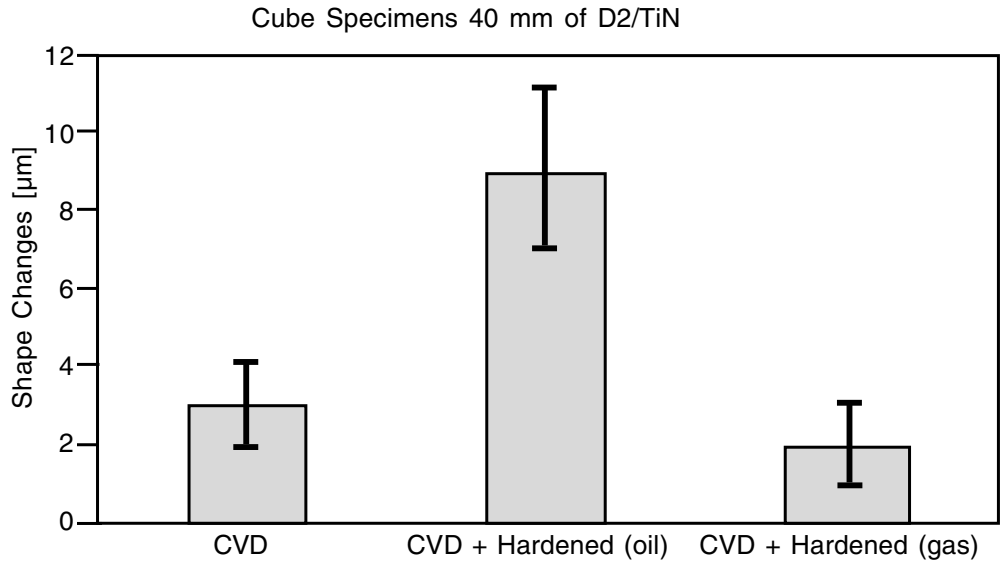

Fig. 20: Shape changes of D2/CVD TiN/quench hardened, oil and gas quenching.

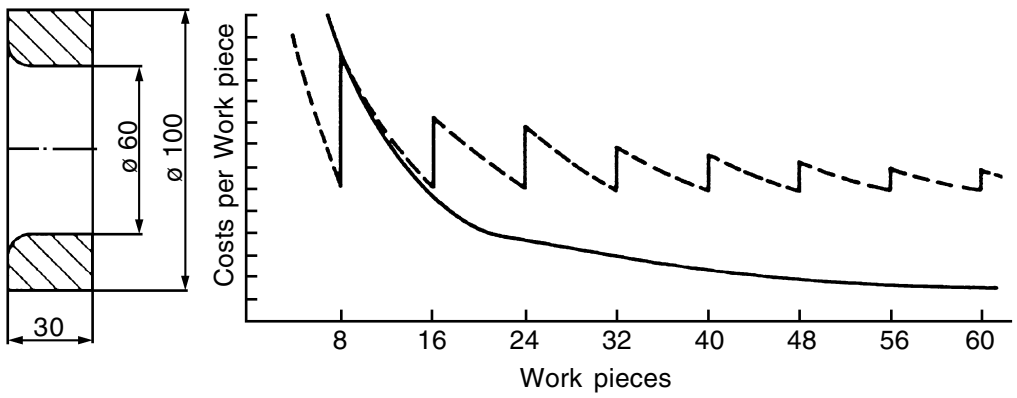

Fig. 21: Tool costs for uncoated (dashed line) and CVD coated (solid line) ~D2 drawing rings (schematically).[10]

Table 7. Case Studies, Practical Examples[9,10]

Tool	Workpiece, Operation	Tool Steel	Tool Treatment Without CVD	Tool Life Without CVD	Tool Treatment With CVD	Tool Life with CVD
Drawing Ring	Steel Sheet 2.25 mm, Drawing	≈D2	Hardening + Tempering + Electroplating (Cr)	100 000 Pieces	CVD TiC + Hardening + Tempering	1 000 000 Pieces ≈ 10× without CVD
Drawing Ring	Steel Sheet 0.8 mm, Drawing	≈ D2	Hardening + Tempering + Gas Nitriding	800 Pieces	CVD TiC + Hardening + Tempering	100 000 Pieces ≈ 100× without CVD
Deep Drawing Die	Steel Sheet 1 mm, Deep Drawing	≈D2	Hardening + Tempering (60 HRC)	200 000 Pieces With Reworking	CVD TiC + Hardening + Tempering	2 000 000 Pieces ≈ 10× Without CVD
Bending Tool	Steel Sheet 4 mm, Bending	D2	Hardening + Tempering (58 HRC)	1 000 Pieces With Reworking	CVD TiN + Hardening + Tempering	50 000 Pieces ≈50× Without CVD

tools. In Table 7 some of these CVD-coated and subsequently hardened high alloy steel tools are compared before and after CVD coating. "Before" conditions include nitriding and electroplating. In all cases a significant increase (10× to 100×) in tool life without reworking can be achieved by CVD-coating and post hardening. The increase in tool life overbalances the additional costs for coating and heat treatment in most cases. This is demonstrated in Figure 21, where tool costs of

uncoated and CVD-coated drawing rings are schematically plotted against the number of workpieces. Even for a relatively small number of workpieces, the CVD-coated tool becomes profitable. Further, machine downtime for tool change is minimized and workpiece quality is enhanced.[10]

This highlights the significant potential of CVD-coating and post hardening for forming tools. Two limitations should be mentioned.

1. These examples can not be generalized for every tool. Each tool with its own wear system consisting of wear partners, lubricants, environmental conditions, etc. should be analyzed and a specific tool steel, coating and heat treatment must be chosen.
2. Design, tool steel selection, machining, coating and heat treatment of a successfully coated tool should not happen independently in different divisions of a company or even different companies, but in cooperation, because many interactions exist between design, tool steel, machining, coating and heat treatment of tools.

Future Directions

Future developments of CVD-coated forming tools attempt to improve the quality and lifetime of tools as well as reduce manufacturing costs. Actual research examples of these future directions are:

- Interdiffusion between coating and substrate,
- Anisotropic distortion, and
- Combined processes.

Interdiffusion processes between coating and substrate during deposition and heat treatment occur due to the high CVD and austenitizing temperatures. They can strongly influence the chemical composition in the interface and affect tool quality, e.g. coating adhesion or load support of the substrate. Carbon diffusion from tool steel substrates into the coatings is a special problem. Carbon content in the coating depends on CVD atmosphere, temperature and pressure as well as on the carbon activity of the substrate and can be controlled to a certain extent.[33,34] Simultaneously, coating elements such as titanium can diffuse from the coating into the substrate. The consequences of this change in chemical composition of the substrate interface are not well known. Figure 22 (taper section 15°) shows a noticeable consequence in the microstructure of a low pressure (LP) CVD TiN-coated and post quench hardened unalloyed tool steel similar to W110, a soft pearlite interlayer. In a depth corresponding to the pearlite layer, titanium concentrations of up to 0.4 wt.% are measured by EPMA (electron probe micro analysis), whereas the base substrate contains almost no titanium (Figure 23). Titanium has diffused from the coating into the substrate. Such titanium concentrations are of great importance for the transformation behavior of steels. Titanium increases the critical cooling velocity for martensite transformation[35] resulting in pearlite instead of martensite in the substrate interface. This pearlite layer has a low hardness of ~500 HV 0.025 instead of ~900 HV 0.025 in the core and degrades load support for the coating. These interdiffusion processes must be understood and controlled to optimize coating /substrate-properties.

Distortion of CVD-coated tools during deposition and heat treatment strongly influences manufacturing costs, due to re-working of tools or assembling segmented tools. Here anisotropic dimensional changes of high alloy steels are of special interest, because they are very difficult to control. The anisotropic dimensional changes during quenching of a high alloy tool steel similar to D3 are demonstrated in Figure 24. Depending on forging reduction, longitudinal and transverse to the forging direction different dimensional changes are observed. At common high forging reductions, longitudinal dimensional changes are greater than transverse dimensional changes. This is explained by the tool steel microstructure with stretched carbides arranged in longitudinal lines.[36] Because the reason for this distortion behavior lies in the history of the tool before CVD and heat treatment, further attempts must be made to understand distortion not only as a result of heat treatment, but as a result of the

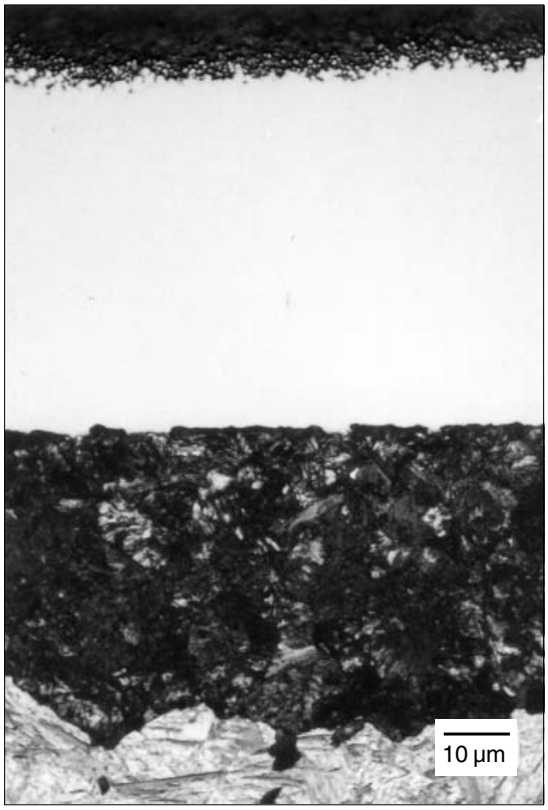

Fig. 22: Microstructure of ~W110/LP-CVD TiN/quench hardened, taper section 15°, 3% alcoholic HNO_3 etch.

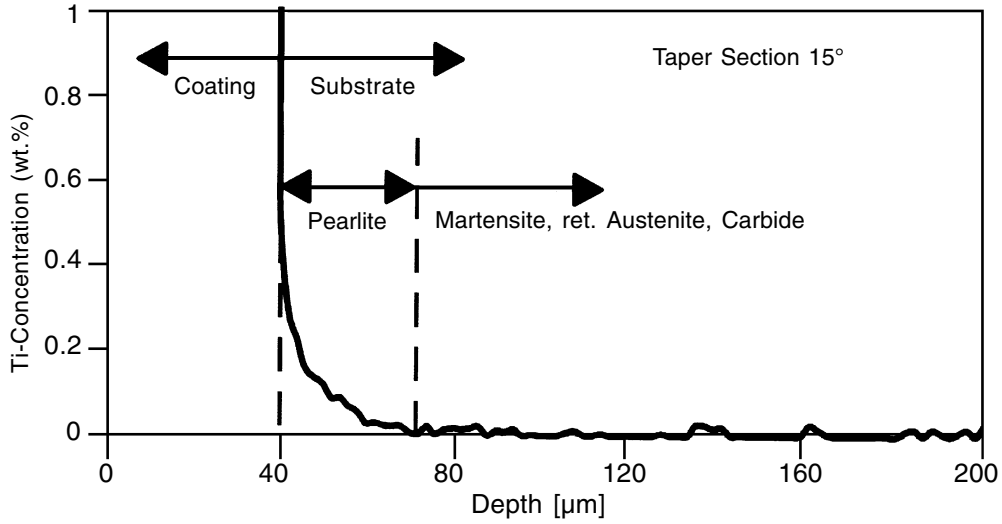

Fig. 23: Titanium content of ~W110/LP-CVD TiN/quench hardened (EPMA analyzis).

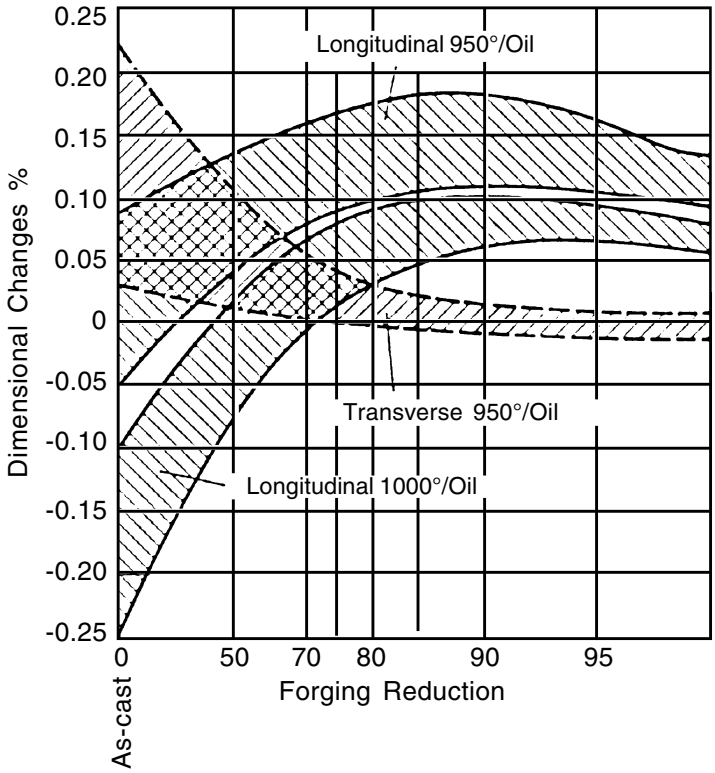

Fig. 24: Anisotropic dimensional changes during quench hardening of ~D3.[36]

whole manufacturing history of the tool, including design, steel selection, casting, forging, machining, coating and heat treatment.[22,23]

Although CVD coating and subsequent hardening is already a combined process, further improvement in tool quality may be achieved by combinations of CVD with other surface engineering technologies, e.g. CVD + induction hardening or carburizing + CVD.[37, 38] CVD + induction hardening offers the possibilities of selective hardening, reducing distortion and inducing compressive residual stresses in the substrate surface. Figure 25 shows an example of a CVD TiN-coated and induction hardened low alloy tool steel L3. The substrate surface hardness was ~880 HV1, the hardened substrate depth (80% surface hardness) extended to ~1 mm underneath an almost unchanged TiN-coating (thickness ~6 µm) with no microscopic defects.[39,40] From a large number of CVD + induction hardening processes, a window of successful process parameters was drawn into a continuous TTT-diagram of L3 for austenitizing. Figure 26 shows, that this window is relatively small and limited to high temperatures by coating damage, to low temperatures by insufficient hardening, to high times by full hardening and to low times by low load support for the coating. Similar diagrams can be drawn for other steels subjected to CVD + induction hardening.

Carburizing + CVD offers the possibilities of strengthening the substrate surface and inducing compressive residual stresses in the substrate surface. Further, it can be done sequentially in one chamber just by changing the atmosphere from low pressure carburizing to CVD. Figure 27 shows an example of a

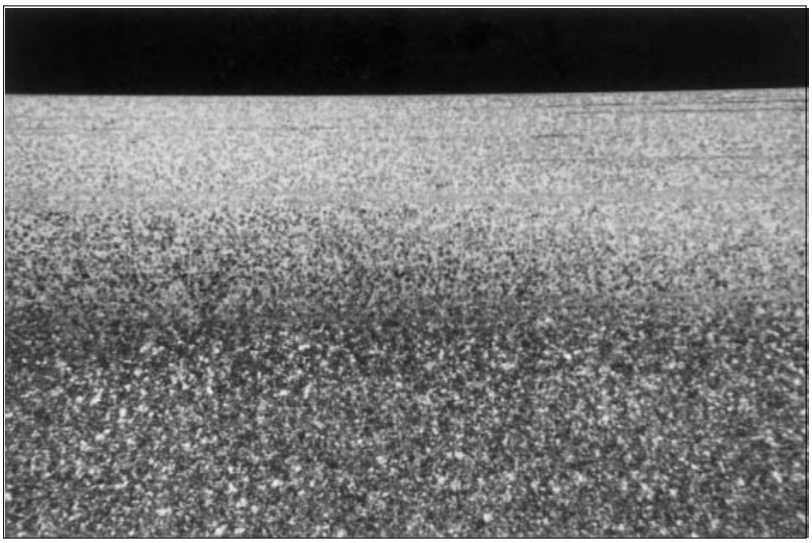

(a)

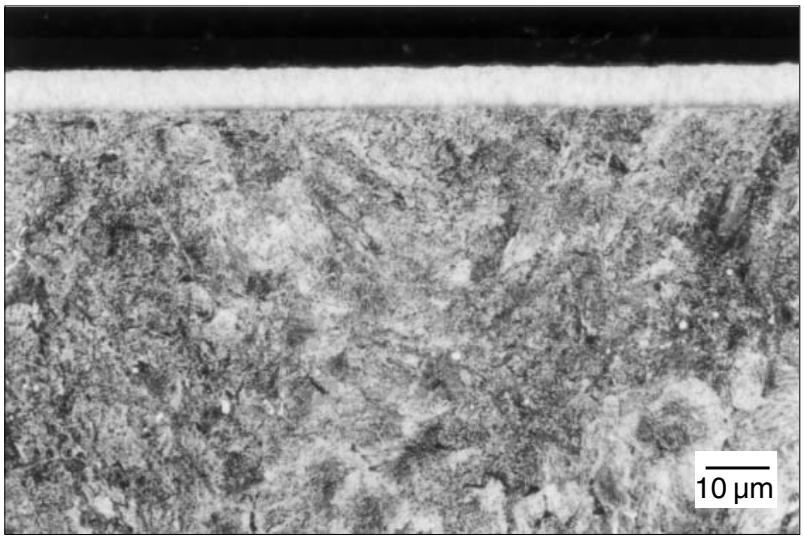

(b)

Fig. 25: Microstructure of L3/CVD TiN/induction hardened (a) substrate, 3% alcoholic HNO_3 etch and (b) surface, 3% alcoholic HNO_3 etch.

carburized, CVD TiN-coated and subsequently quench hardened (gas quenching 6 bar nitrogen) hot working tool steel H13. The substrate surface was carburized up to 0.6 wt.% carbon and a depth of ~1 mm. The substrate surface hardness was ~780 HV1, the core was ~600 HV1; the TiN-coating (thickness ~3 µm) remained almost unchanged with no microscopic defects.[41] These initial results, which of course must be optimized, highlight the significant potential of combined processes for CVD-coated forming tools.

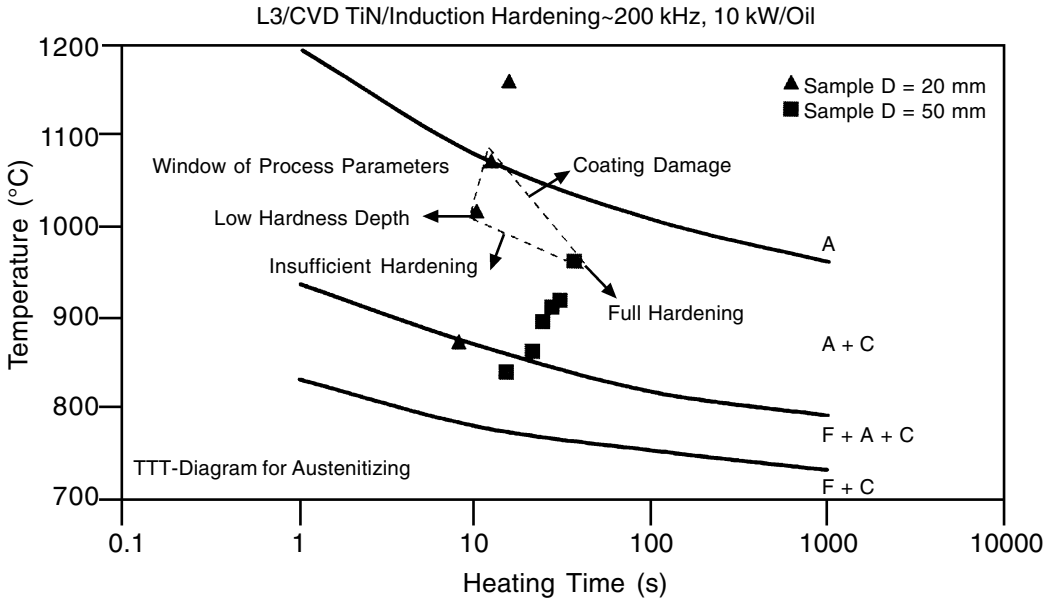

Fig. 26: TTT diagram for austenitizing of L3/CVD TiN/induction hardened.

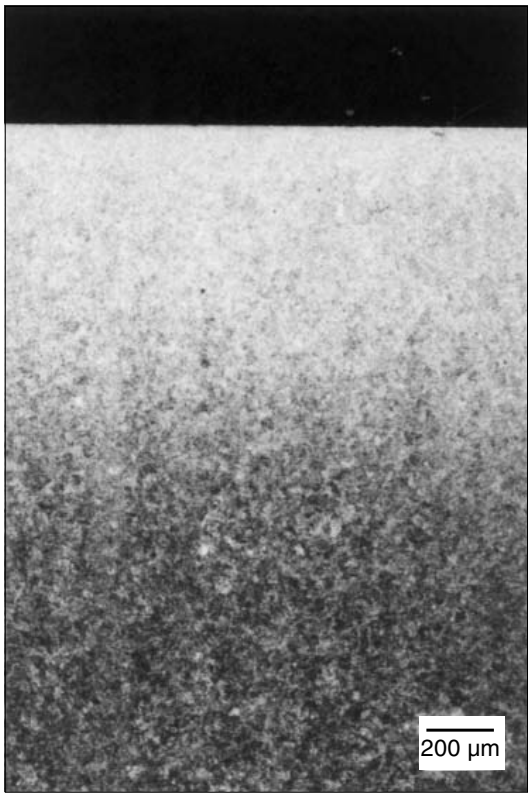

(a)

Fig. 27: Microstructure of H13/carburized/CVD TiN/quench hardened (a) survey, Fe-Cr-etch and (b) surface, Fe-Cr-etch. [Please see (b) in next page].

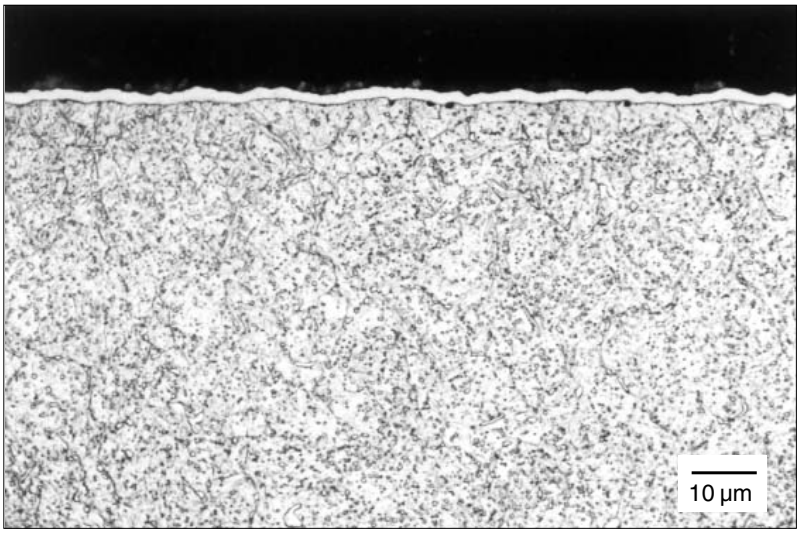

(b)

Fig. 27: Continued.

Summary

For good performance of CVD (e.g. TiN)-coated forming tools, as for almost every coated component or tool, not only good coating properties, but good substrate properties are necessary. This means for most CVD-coated steel tools, that they must be subsequently quench hardened and tempered to restore high substrate strength which has been lost during exposure to high coating temperature and slow cooling. Different heat treatment paths with different complexities are discussed. Best substrate/coating-properties and smallest distortion can be achieved by a complex heat treatment path in the order quench hardening, tempering, CVD, quench hardening, tempering. During the various treatment steps several parameters, specific for CVD-coated tools, must be taken into account (protective atmospheres, equalizing steps, etc.). The chemical composition, microstructure and hardness of CVD TiN-coatings are usually not significantly influenced by subsequent quench hardening of the tools. Coating residual stresses can strongly be influenced depending on substrate volume changes. Coating adhesion is usually enhanced due to the load support of the hardened tool steel. When design, tool steel, coating and heat treatment are well coordinated, significant longer lifetimes can be obtained on CVD-coated tools compared to uncoated tools. In this case, the tools are profitable, although manufacturing costs are higher. Further improvements are possible in the future by working on combined processes.

References

1. R.F. Bunshah and C.V. Deshpandey, Hard Coatings, *Vacuum*, **39**(10), 1989, pp.955-965.
2. Ch. Wick, Coatings Improve Tool Life Increase Productivity, *Manufacturing Engineering*, 1986.
3. K. Keller and F. Koch, *Beschichtete Umformwerkzeuge für die Blechverarbeitung*, Bänder Bleche Rohre, **7**, 1991, p.37.
4. R. Hegi, Vergleichende Betrachtung von PVD/CVD Techniken und Schichten, *Fachbroschüre Oberflächentechnik*, **3**, 1985, p.35.
5. G. Ebersbach and E. Mey, Anwendung von Hartstoffschichten zur Leistungssteigerung von Werkzeugen, *Stahlberatung*, **16**(3), 1989, p.18.
6. H.E. Hintermann, Tribological and

Protective Coatings by CVD, *Thin Solid Films*, **84**, 1981, p.215.
7. A. Oldewurtel, *Surface Treatment Methods*, Mold-Making Handb. for the Plastic Engineering, Carl Hanser, Munich, Germany, Distributed by Macmillan Publ. Co., New York, NY., 1983, pp.351-372.
8. A. Oldewurtel, Neuentwicklungen bei der Oberflächenbehandlung von Kaltumformwerkzeugen, Draht, **31**(2), 1980, p.78.
9. A. Oldewurtel and K.R. Eversberg, Mehrleistung mit CVD-Beschichteten Umformwerkzeugen, wt-Z.ind.Fertig., **75**, 1985, p.299.
10. A. Oldewurtel and K.R. Eversberg , CVD-Beschichtung von Werkzeugen, *Härterei-Technische Mitteilungen*, **44**(1), 1989, p.25.
11. K. Keller, Beschichtungen von Werkzeugen im Fahrzeugbau - Voraussetzungen, Herstellung und Erfahrung, Umformtechnisches Kolloquium, VDI-Gesellschaft Umform-technik, Düsseldorf, 1988.
12. A. Inzenhofer, Verbesserung des Verschleiß und Korrosionsverhaltens Metallischer Oberflächen durch Behandlung nach dem CVD-Verfahren Teil I, *Fachberichte Hüttenpraxis Metallweiterverarbeitung*, **22** (4), 1984, p.318.
13. A. Inzenhofer, Verschleißschutz durch CVD-Behandlung Standzeiterhöhung, *Industrie-Anzeiger*, **11**, 1988, p.28.
14. W. Schintlmeister, O. Pacher, W. Wallgram, and J. Kanz, Anwendung und Herstellung Von CVD-Hartstoffschichten für die Spanende und Spanlose Formgebung, *Metallurgical*, **34**(10), 1980, p.905.
15. E. Broszeit and H.M. Gabriel, Beschichten nach dem CVD-Verfahren, *Z. Werkstofftech*, **11**, 1980, p.31.
16. W. Ruppert, E. Horvath, and A.J. Perry, Werkstoffprobleme Von Stählen bei der Chemischen Abscheidung aus der Gasphase, *Härterei-Technische-Mitteilungen*, Vol.36(No.6), 1981, p.306.
17. G. Roberts, R. Cony, *Tool Steels*, ASM, 1985, p.342.
18. G. Krauss, *Steels – Heat Treatment and Processing Principles*, ASM, Metals Park, Ohio, 1990.
19. G.A. Roberts and R.A. Cary, *Tool Steels*, ASM, Metals Park, Ohio, 1985.
20. Heat Treating, *ASM Hand Book*, **4**, 1994, p.743.
21. A. Kulmburg, E. Kaiser, and F. Korntheuer, Vorgänge beim Anlassen von Warm-und Kaltarbeitsstahl, *Härterei-Technische Mitteilungen*, **44**(2), 1989, p.83.
22. K. Heeß, G. Besserdich, R.B. Damaschek, M. Ehlers, H.J. Grasemann, M. Hoferer, O. Keßler, T. Lübben, A. Majorek, S. Miskiewicz, G. Schmitt, B. Thoden, J. Volkmuth, D. Wiedmann, and H.W. Zoch, Maß und Formänderungen infolge Wärmebehandlung, Expert Verlag, Renningen, 1997.
23. J. Volkmuth, Eigenspannungen und Verzug, *Härterei-Technische Mitteilungen*, **51**(3), 1996, pp.145-154.
24. M. Tisza, *Physical Metallurgy for Engineers*, ASM International and Freund Publishing House, Israel, in Press, p.273.
25. O. Keßler, F. Hoffmann, and P. Mayr, Thermal Treatment of CVD and PVD Coated Steels, *Proceedings of Conference Surface Engineering*, Bremen, Germany, 1993, DGM.
26. O. Keßler, F. Hoffmann, and P. Mayr, Nachwärmebehandlung CVD und PVD hartstoffbeschichteter Stähle Teil I, *Härterei-Technische Mitteilungen*, **49**(1), 1994, pp.48-57.
27. O. Keßler, F. Hoffmann, and P. Mayr, Nachwärmebehandlung CVD und PVD hartstoffbeschichteter Stähle Teil II, *Härterei-Technische Mitteilungen*, **49**(3), 1994, pp.191-197.
28. O. Keßler, F. Hoffmann, and P. Mayr, Residual Stresses in CVD Coated and Thermal Treated Steels, *Surface Modification Technologies VIII*, T.S. Sudarshan and M. Jeandin, eds., The Institute of Materials, Nice, France, **8**, 1995, pp.940-943.
29. O. Keßler, Nachwärmebehandlung CVD und PVD hartstoffbeschichteter Stähle, Dissertation University Bremen, Papierflieger, Clausthal-Zellerfeld, Germany, 1995.
30. O. Keßler, F. Hoffmann, and P. Mayr,

Mechanical Properties and Structure of CVD Coated and Post Heat Treated Steels, *Surface and Coatings Technology*, **89**, 1997, pp.299-304.

31. O. Keßler, F. Hoffmann, and P. Mayr, Maß und Formänderungen bei der Gasabschreckung des unbeschichteten und CVD-beschichteten Werkzeugstahls X155CrVMo 12-1, *Härterei-Technische Mitteilungen*, **50**(6), 1995, pp.337-343.
32. O. Keßler, F. Hoffmann, and P. Mayr, Distortion of CVD Coated and Gas Quenched Tool Steels, Second International Conference on Quenching and the Control of Distortion, (Proceedings of Conference), Cleveland, Ohio, 1996, pp.171-178.
33. O. Keßler, F. Hoffmann, and P. Mayr, Interdiffusion During CVD Coating of Steels: Influences on structure and Properties, 11th Congress of the International Fed. for Heat Treatment and Surface Engineering/4th ASM Heat Treatment and Surface Engineering Conference in Europe, Florenz, (Proceedings of Conference), D. Fiarro and E.J. Mittemeijer, eds., Associazione Italiana di Metallurgia, **2**, 1998.
34. O. Keßler, F. Hoffmann, and P. Mayr, Microstructure and Property Changes Caused by Diffusion During CVD Coating of Steels, International Conference on Metallurgical Coatings and Thin Films, (Proceedings of Conference), San Diego, 1999, (to be published).
35. E. Houdremont, Handbuch der Sonderstahlkunde, Springer, Berlin, 1956.
36. J. Frehser, Anisotrope Maßänderungen bei der Wärmebehandlung ledeburitischer Chrom-Werkzeugstähle, Arch. Eisenhüttenwes., **24**(11/12), 1953, p.483.
37. O. Keßler, F. Hoffmann, and P. Mayr, Systematik der Kombinationsverfahren, *Härterei-Technische Mitteilungen*, **52**(.3), 1997, pp.150-155.
38. O. Keßler, F. Hoffmann, and P. Mayr, Combinations of Coating and Heat Treating Processes: Establishing a System for Combined Processes and Examples, International Conference on Metallurgical Coatings and Thin Films, (Proceedings of Conference), San Diego, B.D. Sartwell, J.H. Givens, C. Mitterer, and S.L. Rhode, eds., Elsevier, Amsterdam, 1998, pp.211-216.
39. K. Pantleon, O. Keßler, F. Hoffmann, and P. Mayr, Randschicht und durchgreifendes Härten Von 42CrMo4 nach CVD Beschichtung, *Härterei-Technische Mitteilungen*, **54**(3), 1999.
40. K. Pantleon, O. Keßler, F. Hoffmann, and P. Mayr, Induction Surface Hardening of Hard Coated Steels, *International Conference on Metallurgical Coatings and Thin Films, (Proceedings of Conference),* San Diego, 1999, to be published.
41. H. Surm, O. Keßler, F. Hoffmann, and P. Mayr, Carburized, CVD Coated and Gas Quenched Steels: Carbon Profile, Microstructure and Hardness, EUROMAT, (Proceedings of Conference), Munich, Germany, 1999, to be published.

Subject Index

Publication title	Product code
Chemical Vapor Deposition	#06682G

To order products from ASM International:

Online Visit www.asminternational.org/bookstore

Telephone 1-800-336-5152 (US) or 1-440-338-5151 (Outside US)

Fax 1-440-338-4634

Mail Customer Service, ASM International
9639 Kinsman Rd, Materials Park, Ohio 44073-0002, USA

Email CustomerService@asminternational.org

In Europe American Technical Publishers Ltd.
27-29 Knowl Piece, Wilbury Way, Hitchin Hertfordshire SG4 0SX, United Kingdom
Telephone: 01462 437933 (account holders), 01462 431525 (credit card)
www.ameritech.co.uk

In Japan Neutrino Inc.
Takahashi Bldg., 44-3 Fuda 1-chome, Chofu-Shi, Tokyo 182 Japan
Telephone: 81 (0) 424 84 5550